UAB
Universitat Autònoma de Barcelona

High-Tc Magnetic Spirals and Fe-based Frustrated Multiferroics

ARNAU ROMAGUERA CAMPS

High-Tc Magnetic Spirals and Fe-based Frustrated Multiferroics

by

ARNAU ROMAGUERA CAMPS

Thesis submitted for the degree of Doctor of Philosophy
PhD programme in Materials Science

Supervisors:
Prof. José Luis García-Muñoz
Dr. Javier Herrero Martín

Crystallography of Magnetic and Electronic Oxides and Surfaces
Institut de Ciència de Materials de Barcelona
Universitat Autònoma de Barcelona

January, 2023

Prof. José Luis García-Muñoz and Dr. Javier Herrero Martín

CERTIFY

that the work reported in the present by Arnau Romaguera Camps, entitled "High-Tc Magnetic Spirals and Fe-based Frustrated Multiferroics", has been done at the group of "*Crystallography of magnetic and electronic oxides and surfaces* (CMEOS)" in the Institut de Ciència de Materials de Barcelona (ICMAB-CSIC). This work constitutes the Doctoral Thesis Memory submitted by the interested person to the Facultat de Ciències de la Universitat Autònoma de Barcelona to apply for the degree of Material Science.

Bellaterra, January 30th, 2023

Signature:

Prof. José Luis García-Muñoz
Research professor at the Institut de Ciència de Materials de Barcelona (ICMAB-CSIC)

Signature:

Dr. Javier Herrero Martín
Beamline Scientist at the ALBA-CELLS Synchrotron Light Source in Barcelona

Com puc dir-ne fredor si m'ha encès tan sovint,
si tants cops m'ha inundat de desig i de vida,
si m'ha fos al seu foc –la raó feta instint–
i m'ha obert tot un món amb tan sols un bolígraf?

— *Física*. David Jou

Als meus pares

Abstract

This thesis work investigates frustrated magnetic oxides as potential materials to develop high-temperature multiferroicity. Multiferroic materials with magnetoelectric coupling are promising candidates for low-energy switching in data storage devices and might lead to ultra-low-power electronics. However, magnetoelectric multiferroics are rare because the mechanisms generating electric and magnetic polarization are often mutually exclusive. This research focuses on two specific ferrite systems: $YBaCuFeO_5$ and ε-Fe_2O_3, whose attractive magnetic and ferroic properties have the potential to be exploited beyond room temperature (RT).

In spiral-driven multiferroics the spin and ferroelectric orders are coupled "by construction". Most of the spiral magnetoelectric multiferroics investigated in recent years are geometrically or exchange frustrated magnets with low magnetic transition temperatures (T_S<50 K). The exceptional stability of the spiral magnetic order (at T_S) in the layered structure of $YBaCuFeO_5$ involves a non-conventional mechanism ("*spiral order by disorder*"). This original mechanism has been experimentally investigated and confronted to the theory by studying a large number of samples prepared or fabricated in the form of polycrystalline powders and single crystals. The influence of Fe/Cu cation disorder on the magnetic phase diagram was quantitatively studied using neutron and synchrotron techniques. Disorder allows tuning the spiral transition temperature by more than 200 K, up to well beyond RT. The interplay between disorder, stability and the detailed features of the incommensurate spiral order has been deciphered. Three different regimes are distinguished in the $YBaCuFeO_5$ phase diagram versus disorder, which set limits to T_S and the cycloidal component of the helicoidal order.

The lattice effects due to chemical pressure were also explored. As an alternative strategy to upgrade the properties of $YBaCuFeO_5$, several families of $YBa(Cu,M)FeO_5$ layered perovskites have been investigated. The impact of lattice, magnetic and spin-orbit coupling effects on the phase diagrams were determined and described for distinct divalent M-cations partially substituting Cu^{2+} ions. The study shows how the orientation and the stability of the spiral in $YBaCuFeO_5$, as well as the cycloidal component of the helix can be manipulated (even in opposite directions) by divalent B substitutions.

The limitations of neutron powder diffraction forced to study the real magnetic nature of the "so-called" spiral magnetic phase of $YBaCuFeO_5$ by means

of (i) unpolarized single-crystal neutron diffraction, (ii) spherical neutron polarimetry and (iii) synchrotron resonant magnetic X-ray scattering. Collinear modulated and non-collinear spiral models, including the analysis of magnetic and chiral domains, have been confronted to the experiments on crystals using these quantum-beam techniques. As well as the magnetoelectric response in single crystals.

The singular magneto-structural coupling, rich phase diagram and magnetic properties of the geometrically frustrated ε-Fe_2O_3 ferrite have been investigated by neutron and synchrotron techniques. This ferrite stands out for its huge coercive field (up to 2 T at RT), RT multiferroicity, mm-wave ferromagnetic resonance, non-linear magneto-optical effects, magneto-electric coupling, etc. Its complex magnetism and successive magnetic phases were thoroughly investigated and described. The nature of the incommensurate magnetic order, attributed by some authors to a spiral ground state, was investigated in zero and applied magnetic fields, and reinterpreted in the light of the models confronted to neutron data. Findings illustrate the interplay between the huge magnetic anisotropy, frustration, spin-lattice coupling and the stabilization of the super-hard ferrimagnetic phase in the 150-500 K interval.

Agraïments/Acknowledgements

Sembla que fos ahir quan, el primer dia de classe a l'institut, la professora de física va començar prometent-nos 'un viatge al·lucinant'. I tant, si ho ha sigut! Mai m'hauria imaginat que aquell viatge que començava acabaria sent tan gran, i encara menys que m'acabaria portant fins aquí. En aquest camí, que he de dir que ha estat llarg i difícil, han passat moltes coses que m'han ajudat a créixer com a persona i com a científic, especialment en aquests últims i intensos anys de dedicació a la tesi doctoral, que he pogut compartir amb moltes persones noves, però també amb els que ja hi eren. Així doncs, m'agradaria mostrar el meu agraïment a totes elles per, d'una manera o altra, haver-me ajudat a arribar fins aquí.

En primer lloc, expressar el meu sincer agraïment als meus supervisors, José Luis i Javier, per la seva constant dedicació i la confiança dipositada en mi des del primer dia, per l'orientació i el suport continuat. Pels incomptables viatges amb llargues hores i nits d'experiments compartides a Alba, Diamond i a l'ILL on he après tant. I sobretot, per la paciència i la passió amb què m'heu sabut transmetre els coneixements i les respostes a tantes i tantes preguntes, despertant-me la curiositat i motivació per descobrir les respostes de totes aquelles que encara no en tenen.

Igualment, agraeixo a Martí Gich la seva valuosa col·laboració i les aportacions en l'estudi de la fase Epsilon presentat en aquesta tesi. I a Vassil Skumryev la seva generositat pel temps dedicat a les mesures de magnetometria en monocristalls, i per ensenyar-me els detalls i les subtileses d'aquestes tècniques.

A tots els investigadors de la comunitat de tècniques neutròniques que d'alguna manera han contribuït en la discussió científica o amb els aspectes tècnics dels experiments realitzats. En especial m'agradaria mostrar la meva gratitud als responsables dels diferents instruments a l'Institut Laue-Langevin: a l'Oscar Fabelo per la seva inestimable ajuda, predisposició i les explicacions tan didàctiques sobre les tècniques i anàlisi de dades, a J. Alberto Rodríguez Velamazán, Gabriel Cuello, Navid Qureshi, Stanislav Savvin i Clemens Ritter.

Agraeixo també el suport als responsables de línia al sincrotró Alba: a Francois Fauth i Catalin Popescu per l'assistència en els experiments de difracció a MSPD, i a Javier herrero per les mesures d'absorció dutes a terme a BOREAS.

També a Alessandro Bombardi i Gareth Nisbet pels seus esforços i suport en la realització del complex estudi amb X-Ray Magnetic Resonant Scattering, realitzat a la línia i16 del sincrotró Diamond.

Així mateix s'agraeixen les eines computacionals que ofereixen el programari Fullprof, Isotropy i Mag2pol i el Bilbao Crystallographic Server.
A tots els tècnics dels serveis generals de l'ICMAB: a Bernat Bozzo per la seva ajuda amb les mesures magnètiques, a Anna Crespi per les explicacions en difracció de raigs X i la seva implicació en les mesures i en l'orientació de monocristalls, a Anna Esther Carrillo per les sessions de SEM, i a Roberta Ceravola per les mesures de termogravimetria. I no puc oblidar-me de la constant presència del personal del taller i de manteniment, Oriol Sabater i Jose Algar, que sempre han donat resposta qualsevol imprevist al laboratori, i del personal de neteja. Gràcies per la vostra assistència.
També agraeixo als companys i col·laboradors de l'ICMAB, especialment a Xiaodong Zhang, Zheng Ma, Nico Dix, Darla Mare, Adrian Crespo i Ruyong Li, els coneixements i experiències compartides dins i fora de l'ICMAB. Demano disculpes a tota la gent que em deixo, però la tesi ja és prou llarga! En resum, m'emporto un molt bon record de tothom amb qui he compartit espai al despatx, a la cafeteria i als laboratoris de l'ICMAB.
I per últim, però no per això menys important, gràcies als meus pares, germans i amics, i evidentment a tu, Lorena. Us he tingut al costat en tot moment i us heu preocupat per mi en els moments de màxim estrès. Gràcies per ser-hi i per animar-me sempre, sense vosaltres no ho hauria aconseguit.

Funding

This thesis, done as a part of the PhD Program in Materials Science of the Universitat Autònoma de Barcelona, has been possible thanks to a FPI (Formación de Personal Investigador) scolarship for the formation of doctors and the realization of doctoral theses, assigned by the Spanish Ministerio de Ciencia, Innovación y Universidades (MINCIU) [PRE2018-084769].
I acknowledge financial support from the Spanish Ministerio de Ciencia, Innovación y Universidades (MINCIU), through Projects No. MAT2015-68760-C2-1, RTI2018-098537-B-C21 and PID2021-124734OB-C22, cofunded by ERDF from EU, and "Severo Ochoa" Programme for Centres of Excellence in R&D [SEV-2015-0496 and CEX2019-000917-S].
I also acknowledge the Institut Laue-Langevin (ILL), the D1B-CRG (MINCIU), the Cells-Alba Synchrotron and Diamond Light Source national synchrotrons for provision of beam time. The Helmholtz-Zentrum Dresden-Rossendorf (European Magnetic Field Laboratory, HZDR Dresden) is acknowledged for experimental and technical support.

Contents

List of Abbreviations

AFM	Antiferromagnetic
APD	Avalanche PhotoDiode
CRG	Collaborating Research Group
CM	Commensurate
CSIC	Consejo Superior de Investigaciones Científicas
DM	Dzyaloshinskii-Moriya
FC	Field Cooling
FE	Ferroelectricity
FM	Ferromagnetic
FWHM	Full Width at Half Maximum
FY	Fluorescence Yield
FZ	Floating Zone
GKA	Goodenough-Kanamori-Anderson
HRPD	High Resolution Powder Diffraction
HS	High-Spin
ICMAB	Institut de Ciència de Materials de Barcelona
ILL	Institut Laue-Langevin
ICM	Incommensurate
JT	Jahn-Teller
LS	Low-Spin
ME	Magnetoelectric
MAD	Multi Analyzer Ddetector
MMM	Magnetoelectric Multiferroic Material
MPMS	Magnetic Property Measurement System

MS	Magnetostructural
MSG	Magnetic Space Group
MSPD	Materials Science and Powder Diffraction
MF	Multiferroic
ND	Neutron Diffraction
NN	Nearest-neighbor
NPD	Neutron Powder Diffraction
OFZ	Optical Floating Zone
PFY	Partial Fluorescence Yield
PSD	Position Sensitive Detector
PM	Paramagnetic
PPMS	Physical Properties Measuring System
RBCFO	RBaCuFeO$_5$
RMXS	Resonant Magnetic X-Ray Scattering
RE	Rare Earth
RT	Room Temperature
SG	Space Group
SCND	Single Crystal Neutron Diffraction
SNP	Spherical Neutron Polarimetry
SQUID	Superconducting Quantum Interference Device
SXRPD	Synchrotron X-Ray Powder Diffraction
TEM	Transmission electron microscopy
TEY	Total Electron Yield
TFY	Total Fluorescence Yield
TM	Transition Metal
TSFZ	Traveling solvent floating zone
VSM	Vibrating Sample Magnetometry
XAS	X-ray Absorption Spectroscopy
XMCD	X-Ray Magnetic Circular Dichroism
XRD	X-Ray Diffraction
XRPD	X-Ray Powder Diffraction
YBCFO	YBaCuFeO$_5$
ZFC	Zero-Field Cooling

Part I

Introduction

Chapter 1

Introduction and motivation

Transition metal (TM) oxides are one of the most interesting classes of materials in the field of correlated systems and functional magnetic compounds, presenting an extremely rich variety of properties caused by the strongly correlated nature of electrons that occupy the outer *d*-orbitals and the complex interplay and competition between orbital, charge and spin degrees of freedom (Figure 1.1). Putting all this in the background of an enormous number of lattice configuration possibilities, we can find systems displaying different types of physical phenomena: magnetic, charge and orbital ordering, cooperative Jahn-Teller effect, or high-temperature superconductivity. The interplay between lattice and the above mentioned phenomena many times lead to exotic transport and magnetic behavior: metal-insulator transitions (MIT), unconventional magnetic transitions, multiferroicity, giant magnetoresistance (MR) and more. This chapter will provide a brief overview of the most relevant concepts necessary to understand the magnetic, ferroelectric, or multiferroic properties and the interplay between them exhibited by the materials investigated in this work.

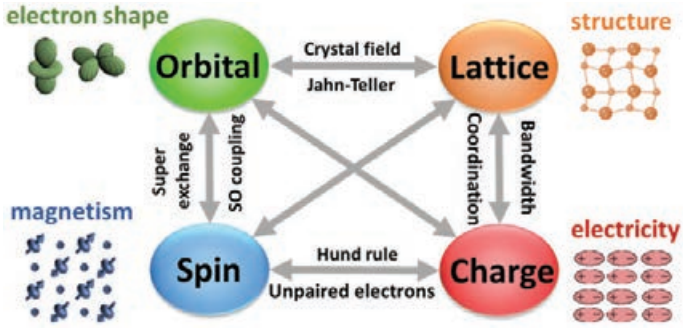

FIGURE 1.1: Scheme of the multi-degrees of freedom in highly correlated systems.

1.1 Multiferroic and Magnetoelectric Materials

1.1.1 A short history of magnetoelectric materials

Magnetism and electricity are two fundamental physical phenomena whose study dates back hundreds of years, starting from the magnetic properties of natural ferric stones (lodestones) and electric charge induced on amber when rubbed with a piece of fur, both described by Greek philosophers. Since then, the complexity of a countless number of devices based on Magnetism and Electricity has increased as a consequence of years of study. In particular, the discovery of magnetoelectrics (and more recently multiferroics), where the possibility to manipulate primary ferroic properties of a material (namely, ferroelectricity and ferromagnetism) by means of electric and magnetic fields, and the coupling between such properties, has generated until today a great interest due to its importance for the solid state physics as well as because of the possible technological applications that could be developed based on it.

Two independent events marked the discovery of the magnetoelectric (ME) effect. First, in 1888 W.C. Röntgen (before he discovered X-rays) demonstrated that a dielectric material moving in an electric field becomes magnetized, which was followed by the observation of the reverse effect, the electrical polarization of a moving dielectric in a magnetic field [1]. Second, in 1894, based on lattice symmetry considerations, Pierre Curie foresaw theoretically the possibility of inducing electric polarization in some crystals by applying a magnetic field, and vice versa, without having to move the sample [2]. The original conjecture of Pierre Curie was later considered by P. Debye in 1926 [3], who defined the term "magnetoelectric effect". However, this effect remained in the speculation until 1960, when the first experimental proof of magnetoelectricity was discovered by Astrov in Cr_2O_3 was discovered [4], inspired by Dzyaloshinskii's generic prediction one year earlier [5].

In the whole twentieth century, studies on the ME physics and corresponding materials were slow. Reasons of this background were due to the lack of available ME materials, and the poor ME performance observed. In addition, the ME theories in early years were generally phenomenological, lacking the ingredients of the modern electronic theory based on quantum mechanics. An extensive research on the correlated electronic materials did not appear until the late 1980s [6], and the colossal magnetoresistive manganites in the 1990s [7], which paved a good foundation for the advanced ME research. In 1994, H.

Schmid coined a new terminology in a proceeding publication: multiferroics, which denotes the coexistence of multiple ferroic orders in a single-phase material [8].
The long stagnation was finally folded up due to the two unexpected breakthroughs which were both discovered in 2003: the $BiFeO_3$ thin films [9] and the orthorhombic $TbMnO_3$ [10]. Although the strong magnetization of the reported $BiFeO_3$ thin films was later found to be non-intrinsic [11], it was the first time that a single-phase ME material providing good multiferroic behavior with potential room temperature applications was obtained. The orthorhombic $TbMnO_3$ displays only a weak polarization appearing only at low temperature (< 28 K) [10]. Despite its poor performance regarding the ferroelectric polarization and magnetism, it became a milestone due to the intrinsically strong ME coupling if offers. A few years later, another two interesting multiferroic materials were discovered: the orthorhombic $TbMn_2O_5$ [12] and the hexagonal $HoMnO_3$ [13], even these materials were reported either having a small polarization or presenting a low Néel (*i.e.*, antiferromagnetic ordering) temperature. Since then, the interest on this exciting subject has enormously grown, with a huge number of novel materials and ME phenomena emerging. Many publications on the fundamental research and different multiferroic materials have promoted the progress of this discipline [11, 14–22].

1.1.2 Magnetoelectric effect and multiferroicity

Magnetoelectricity

In the most general definition, the *magnetoelectric* (ME) effect denotes any coupling between the magnetic and the electric properties in matter (induction of magnetization by an electric field or of polarization by a magnetic field). A systematic progression of contributions to the ME effect is obtained from a power series expansion in the electric and magnetic fields $\mathbf{E}$ and $\mathbf{H}$ of the free energy of a material, *i.e.*,

$$\begin{aligned} F(\mathbf{E},\mathbf{H}) = F_0 - P_i^S E_i - M_i^S H_i - \frac{1}{2}\epsilon_0\epsilon_{ij}E_iE_j - \frac{1}{2}\mu_0\mu_{ij}H_iH_j \\ -\alpha_{ij}E_iE_j - \frac{1}{2}\beta_{ijk}E_iH_jH_k - \frac{1}{2}\gamma_{ijk}H_iE_jE_k - \cdots \end{aligned} \tag{1.1}$$

Differentiation of Eq. (1.1) leads to the polarization

$$P_i(\mathbf{E},\mathbf{H}) = -\frac{\partial F}{\partial E_i} = P_i^S + \epsilon_0\epsilon_{ij}E_j + \alpha_{ij}H_j + \frac{1}{2}\beta_{ijk}H_jH_k + \gamma_{ijk}H_iE_j + \cdots \tag{1.2}$$

and to the magnetization

$$M_i(\mathbf{E},\mathbf{H}) = -\frac{\partial F}{\partial H_i} = M_i^S + \mu_0\mu_{ij}H_j + \alpha_{ij}E_i + \frac{1}{2}\beta_{ijk}E_iH_j + \gamma_{ijk}E_jE_k - \cdots \tag{1.3}$$

where $\mathbf{P}^S$ and $\mathbf{M}^S$ denote the spontaneous polarization and magnetization, and $\hat{\epsilon}$ and $\hat{\mu}$ are the electric and magnetic susceptibilities. The i subindices refer to the three spatial dimensions. The tensor $\hat{\alpha}$ describes the *linear ME effect*, which corresponds to an electric polarization induced linearly by a magnetic field, and vice versa. Tensors $\hat{\beta}$ and $\hat{\gamma}$ describe higher-order ME effects [23].

Magnetoelectric multiferroics

Although the concept of *multiferroicity* was born to refer to materials that can exhibit more than one primary ferroic property[1] simultaneously in the same phase, nowadays its definition has been broadened including materials displaying nonprimary 'long range orders' (such as antiferromagnetism or ferrimagnetism) rather than the primary ferroic properties. Fig. 1.2 illustrates the classification of the materials regarding their magnetic and electric properties. As shown in this diagram, one must distinguish between magnetoelectricity and multiferroicity. A magnetoelectric material is a material in which one can induce both electric or magnetic polarization by means of external magnetic

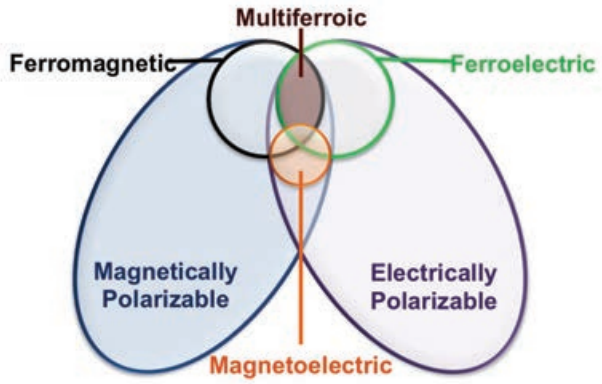

FIGURE 1.2: Classification of materials according to the magnetic and electric polarizability. Multiferroic and magnetoelectric conditions should be satisfied in MMMs. Figure adapted from Ref. [24].

[1]Ferromagnetism, ferroelectricity and ferroelasticity are primary ferroic properties. Magnetization, electric polarization or deformation appear spontaneously in these materials when a magnetic, electric or stress field is applied, respectively.

and electric fields, respectively, but not necessarily in the same phase. Instead, a multiferroic material is able to exhibit ferromagnetism and ferroelectricity in the same phase, but magnetic and electric properties are not necessarily coupled as in magnetoelectric materials. If a *magnetoelectric* material is *simultaneously ferromagnetic and ferroelectric* in the same phase, it is called a *Magnetoelectric Multiferroic Material* (MMM).

1.1.3 Characteristics and applications of MMMs

The difficulty in finding new potential MMMs lies on the fact that the intrinsic characteristics of ferroic properties are often mutually exclusive. This reduces enormously the number of potential MMM candidates. The main limiting factors are described below:

- **Symmetry conditions:** The possible terms appearing in the previously described (1.2) and (1.3) expansions above for the two different ferroic properties ($\mathbf{P}$ and $\mathbf{M}$) are constrained by different symmetries of the material: electric polarization ($\mathbf{P}$) is inverted under spatial inversion, and magnetization is inverted under a time-reversal. So, if the crystal structure of a compound contains a symmetry operation which reverses, for instance, z by -z, electric polarization will never show up along the z axis (it would be compensated). In other words, the Neumann's Principle has to be fulfilled: *the symmetry elements of the physical properties of the material have to include the symmetry operations of the point group of the crystal*. Thus, in order to have a multiferroic material, its symmetry must allow more than one primary ferroic property.

- **Physical conditions:** Each ferroic property require specific physical conditions that usually exclude one or the other property. For instance, ferroelectrics are necessarily insulators, while most ferromagnetic mterials are metals. Besides that, in $3d$ transition metal oxides, magnetic order arises from incomplete d orbitals, whereas ferroelectricity usually requires empty d shells.

Why are MMMs interesting?

What makes this rare kind of materials interesting is that, unlike classical magnetoelectrics, MMMs do not need any external field to become magnetically and electrically ordered in the same phase. However, since they are magnetoelectric, both order parameters can be controlled by external fields, either magnetic or electric. The possibility of controlling magnetism by electric fields and vice

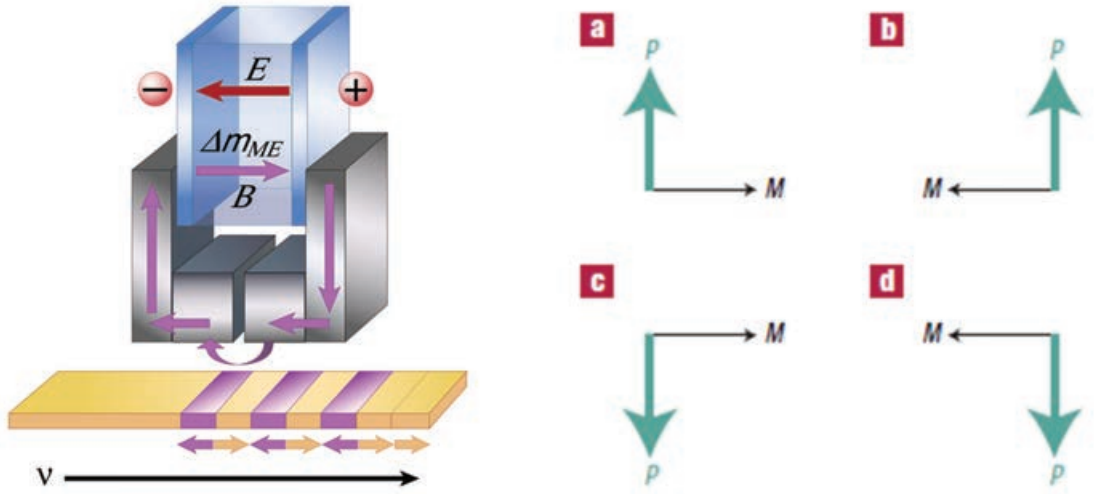

FIGURE 1.3: Left: Scheme of a magnetoelectric write head for magnetic hard disk. An electric field generates a bulk magnetic moment in a slab of magnetoelectric material, giving rise to a magnetic flux density. The gap in the flux closing yoke emits a stray field, which writes a magnetic "bit" into the moving track of the hard disk [26]. Right: Electric polarization P and magnetization M can assume four non-collinear states in a multiferroic crystal [25].

versa opens the door to possible technological applications that could be developed based on it. Electronic devices where the magnetization is controlled by an electric field are an example. Thanks to this coupling, it is possible to write magnetic bits in this class of materials by means of more energy efficient electric fields. Since electric current is no longer needed, energy losses produced by the heat coming from the Joule effect are avoided, and overheating of the system as well. For instance, nowadays, reading and writing systems and computers are based on Magnetic Random Access Memory (MRAM) devices, but MagnetoElectric Random Access Memory (MERAM) devices are being developed with the hope that one day they could replace them (Fig. 1.3). Multiferroic magnetoelectric materials also raise great interest in the aim of developing memory elements with more than the two states used by Boolean algebra. A four-state logic [Fig. 1.3(a-d)] would permit an exponential increase in computing capacity [25]. Coupled multiferroics with spiral or conical magnetic orders, where electric fields can interact with the spin chirality of the magnetic phase, arise as possible candidates. Unfortunately, the low temperatures at which such properties show up (tipically below 100 K) critically restrict the potential uses of these materials for spintronics and low-power ME devices.

1.1.4 Combining magnetism and ferroelectricity: types of magnetoelectric multiferroics

In 2009, D. Khomskii [27] proposed a classification of multiferroic materials in two two categories (type I and type II) according to the microscopic origin of ferroelectricity and its interplay with magnetic order.

Type I

This type of multiferroics were the first MMMs to be discovered, and they are the most numerous. As their ferroelectricity and magnetism have different sources, such properties display low coupling and appear rather independently. Usually ferroelectricity arises at higher temperatures than magnetic order does, making them bad candidates for technological applications. In their favour, they are multiferroics at relatively high tempeatures ($BiFeO_3$ multiferroic at RT), and display rather large electric polarization values (10-100 $\mu C/cm^2$). Whereas the microscopic origin of magnetism is essentially the same in these materials (exchange interactions between the localized moments lead to magnetic order), the situation with ferroelectrics is quite different. The following classification can be made according to the different ferroelectricity-driving microscopic mechanisms:

- **Perovskite-like structures**: One of the best-known ferroelectrics are the ABO_3 perovskites, like $BaTiO_3$ or $Pb(ZrTi)O_3$, which are interesting materials where different mechanisms can be used to induce ferroelectricity. One possible way is 'mixing' d^0 and d^n ions in the B position, which can result in ferroelectricity and magnetic order from different origins. Unfortunately, the coupling of magnetic and ferroelectric subsystems in mixed perovskites is rather weak.

- **Charge ordering**: Another mechanism can be charge ordering, often observed in transition metal oxides, especially those containing TM ions with different valence. If, after charge ordering, both sites and bonds turn out to be inequivalent, this can lead to ferroelectricity. Another similar possibility is when the bonds are inequivalent because of the structure of the material, the site-centered charge order appearing on top of that. Perovskite manganites, magnetite and frustrated $LuFe_2O_4$ are examples of this mechanism.

- **Ferroelectricity due to lone pairs**: Stereochemical activity of A-site lone pair atoms (which have outer free electrons), gives rise to ferroelectricity and magnetism arises from B-site cations. Apparently this is what happens in many

Bi^{3+}- and Pb^{2+}-containing ferroelectrics and multiferroics, such as $BiFeO_3$ and probably $PbVO_3$. These cations can also helps to improve the ferroelectric properties, like in $Pb(Zr_xTi_{1-x})O_3$.

- **Geometrically driven**: The geometry of the system itself may also cause ferroelectricity, as it is the case of $YMnO_3$, where the rotation of the rigid MnO_5 polyhedra to provide closer packing results in shifts of oxygen ions towards Y, resulting in electrical polarization.

Type II

This group is composed by materials in which ferroelectricity exists only in a magnetically ordered state, and is induced by a particular type of magnetism. Although the electric polarization is usually lower than in Type I multiferroics, they show a very strong coupling between the magnetism and the ferroelectricity. Discovered in the last decade, materials in this group are a novel class of multiferroics causing a renewed interest in this field. However, one of the main drawbacks on Type II MMMs is that in almost all such materials the magnetic orders associated to the magnetoelectric phase arise at relatively low temperatures and in narrow stability ranges. At least three subclasses can be distinguished depending on the origin of the electric polarization:

- **Non-collinear multiferroics**: Most type II materials materials belong to this group. In this class of multiferroics, the ferroelectricity appears associated to the cycloidal component of a spiral-like non-collinear magnetic structure. In this case, the ferroelectricity is ruled by the following expression [21, 28–31]:

$$\mathbf{P} \sim \mathbf{r}_{ij} \times (\mathbf{S}_i \times \mathbf{S}_j) \tag{1.4}$$

where $\mathbf{r}_{ij}$ is the translation vector between two neighboring spins, $\mathbf{S}_i$ and $\mathbf{S}_j$. This expression tells us that the polarization is always perpendicular to the spin-chirality vector ($\mathbf{Q} = \mathbf{S}_i \times \mathbf{S}_j$). In simple cases it can be translated to $\mathbf{P} \sim \mathbf{k} \times (\mathbf{S}_i \times \mathbf{S}_j)$, where $\mathbf{k}$ is the propagation vector of the magnetic structure. In such cases, only magnetic structures with a cycloidal component ($\mathbf{k} \perp \mathbf{S}_i \times \mathbf{S}_j$) would produce an electric polarization. Fig. 1.4(a-d) shows different examples of non-collinear spiral and conical magnetic structures. Although the mechanisms that drive the spin-induced electric polarization are still not firmly established, the microscopic mechanism of this polarization is connected with the spin-orbit interaction. Two main theories could explain it: the inverse

Dzyaloshinskii-Moriya (DM) interaction model [30] or the spin-current model (Katsura–Nagaosa–Balatsky model) [21, 31]. Nevertheless, magnetic frustration plays a fundamental role since it is what enforces the complex magnetic structures. Because of its relevance for this thesis, these concepts will be further explained in the following sections.

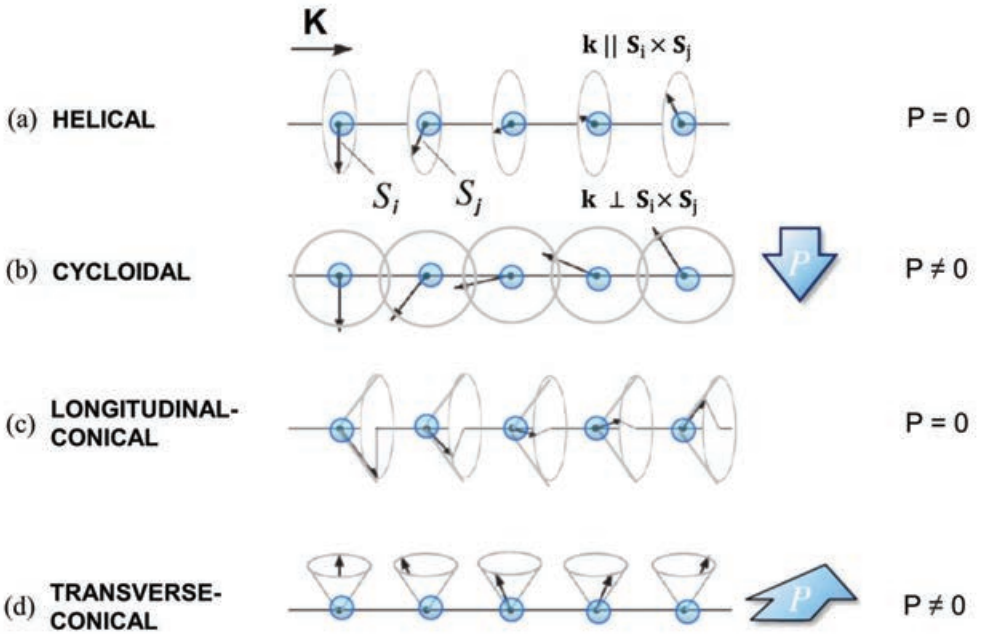

FIGURE 1.4: Schematic illustration of different types of spiral magnetic structures on a one-dimensional array of magnetic moments: (a) helical (or screw) type structure, (b) cycloidal structure, (c) longitudinal-conical and (d) transverse-conical magnetic orders. According to the spin current model or inverse DM model [21, 30] only spiral structures with a cycloidal component may give raise to polarization. Figure adapted from Ref. [32].

- **Exchange striction multiferroics**: The second group of magnetically driven ferroelectrics are those in which ferroelectricity appears in collinear magnetic structures (*i.e.*, with all magnetic moments aligned along a particular axis) without the necessary involvement of the spin-orbit interaction. In ferroelectric systems with collinear magnetic order, such as Ca_3CoMnO_6 [33], the exchange striction is usually the cause of the electric polarization because the magnetic coupling varies with the atomic positions. In the mentioned example, the polar phase emerges coupled to the magnetic transition into a magnetic structure of the type ↑↑↓↓. The different exchange striction between ferro and antiferro bonds (↑↑ and ↑↓) is different, giving raise to a ferroelectric distortion. In RMnO$_3$ manganites (where R is a small rare earth) the Mn magnetic order in the basal plane is of the type ↑↑↓↓. In this scenario the exchange striction causes

transverse displacements of oxygen atoms that cause the polarization to show up [34].

- **Other spin electronic mechanisms**: Another mechanism that can generate ferroelectricity is the 'electronic' ferroelectricity, observed in some frustrated magnets by L.N. Bulaevskii *et al.* in Ref. [35]. The polarization of a regular triangle with $\mathbf{S}_1$, $\mathbf{S}_2$ and $\mathbf{S}_3$ spins located its vertices is nonzero if the spin correlation function $\mathbf{S}_1(\mathbf{S}_2 + \mathbf{S}_3) - 2\mathbf{S}_2\mathbf{S}_3$ is nonzero.

1.2 Fundamental physics concepts on the magnetism of TM oxides

One important property that can be found in transition metal oxides is the magnetic order. This section provides a brief introduction on some relevant concepts necessary to understand the complex phenomenology behind the different materials that will be investigated along this manuscript.

1.2.1 Magnetic Order

Origin of the magnetic order

Magnetism is a direct consequence of the quantum nature of materials, based on the spins and Pauli's exclusion principle are on its basis. The magnetic ordered state is the eigenvector of the following Hamiltonian:

$$\mathcal{H} = \mathcal{H}_C + \mathcal{H}_{S-O} + \mathcal{H}_{CF} \tag{1.5}$$

where $\mathcal{H}_C$ takes into account the Coulomb repulsion between non-coupled electrons, $\mathcal{H}_{SO}$ refers to the spin-orbit interaction (proportional to $\hat{L} \cdot \hat{S}$) and $\mathcal{H}_{CF}$ is the crystal-field contribution derived from the Coulomb interaction between the electronic charge distribution $\rho_0(\mathbf{r})$ of an ion and the crystal field (surrounding charges) when it is embedded in a crystalline solid.

The total Hamiltonian can be simplified, within the Heisenberg model, as a function of the spins as

$$\mathcal{H} = -\sum_{ij} J_{ij}\mathbf{S}_i \cdot \mathbf{S}_j \tag{1.6}$$

where J_{ij} is the exchange constant between the two spins $\mathbf{S}_i$ and $\mathbf{S}_j$ (explicitly located at the atom positions). Its sign and value measures the strength of the

exchange interactions: $J_{ij} > 0$ tends to align the two spins parallel (ferromagnetic interaction) and $J_{ij} < 0$ tends to align them antiparallel (antiferromagnetic interaction). Below a certain temperature, those magnetic interactions can eventually "freeze" the spins so that the materials become magnetically ordered.
One necessary condition for magnetic order is that in the crystal lattice there should be atoms with unpaired electrons (as $3d$, $4f$ elements). However, if the temperature is high enough, the order is destroyed by thermal fluctuations giving raise to a disordered *paramagnetic* state. In this paramagnetic state, the response of the randomly fluctuating magnetic moments to an external field, *i.e.*, its magnetic susceptibility χ, usually follows the Curie-Weiss law:

$$\chi = \frac{C}{T - \Theta_p} \tag{1.7}$$

where C is the Curie constant and Θ_p is the paramgnetic temperature above which the material becomes paramagnetic. The latter is directly related to the exchange interactions.

Types of magnetic order

Below we provide an oversimplified picture of the main types of magnetic structures and characteristics that might arise in a magnetically ordered crystalline solid. A schematic representation of these types of magnetic order (ferromagnetism, ferrimagnetism and antiferromagnetism) and its magnetization/susceptibility as a function of the temperature is shown in Fig. 1.5:

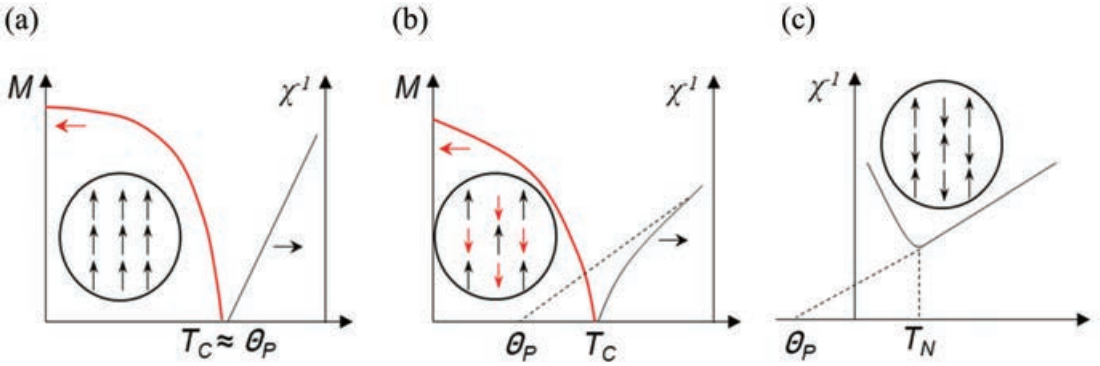

FIGURE 1.5: Schematic plots of the typical behaviour as a function of the temperature of magnetization, M, and the inverse of magnetic susceptibility, chi^{-1}, in the different types of magnetic order: (a) ferromagnetism, (b) ferrimagnetism and (c) antiferromagnetism.

(a) **Ferromagnetism**: The exchange interaction between neighbor spins is positive ($J_{ij} > 0$). Hence, magnetic moments are ordered displaying a parallel arrangement below the paramagnetic temperature, Θ_p. As a consequence, in the ordered state there is spontaneous magnetization, even in absence of any external magnetic field. Following the Curie-Weiss law the inverse magnetic susceptibiity tends to infinity ideally at the Curie temperature, $\Theta_p \approx \mathrm{T_C}$ according to Eq. (1.7), where the spontaneous polarization emerges.

(b) **Ferrimagnetism**: the exchange interaction is negative ($J_{ij} > 0$), leading to antiparallel alignment of the moments below $\mathrm{T_C}$. However, neighboring atoms do not have equal spin, and hence they do not compensate. In ferrimagnetism, the antiparallel non-nonequivalent moments can be described as two different ferromagnetic sublattices that interpenetrate each other in an antiparallel way, the different magnetic moments not cancelling each other, resulting in non-zero net magnetization. In these materials the inverse susceptibility tends to infinity at the curie temperature as well, but the paramagnetic temperature Θ_p does not coincide with $\mathrm{T_C}$.

(c) **Antiferromagnetism**: If the sublattices in a ferrimagnet have equal moments, the material is an antiferromagnet. Thus, the total magnetization cancels out and no spontaneous magnetization arises in the material when it becomes ordered below the Néel temperature, $\mathrm{T_N}$. The magnetic susceptibility displays a maximum at $\mathrm{T_N} \neq \Theta_p$.

Besides the three basic types of magnetic orders above introduced, which can be considered as simple structures, there are many others such as canted ones, amplitude modulated structures (sinusoid, fan-type structures, ...), circular helixes (or screw-type), elliptical spirals, cycloidal structures, conical, and so on. Some examples are shown in Fig. 1.4. Along this dissertation it will be important to distinguish between helical and cycloidal types of spiral magnetic structures. The difference between them lies in the relation between the rotation plane of the spins and the direction of the propagation of the vector **k**. Whereas in helical structures **k** is perpendicular to the rotation plane, in a cycloidal structure they are parallel. Because these exotic modulated structures usually do not show any spontaneous net magnetization, and due to the typically antiferromagnetic behaviour of their susceptibility temperature dependence, most of those exotic structures are often considered as antiferromagnets.

Description of magnetic structures: the magnetic propagation vector

As described in this section, referring to the type of magnetic order is often not sufficient to provide its complete and detailed description. In general, the magnetic structure can be defined as a periodic function where the orientation of the magnetic atom j in the unit cell l can be expanded in a Fourier series as the following sum:

$$\mathbf{m}_{lj} = \sum_{\mathbf{k}} \mathbf{S}_{\mathbf{k}j} e^{-2\pi i \mathbf{k}\cdot\mathbf{R}_l} \tag{1.8}$$

where $\mathbf{S}_{\mathbf{k}j}$ stands for the Fourier components of the distribution associated to the propagation vector $\mathbf{k}$.

As in conventional crystallography, magnetic structures are characterized by two features: the periodicity of the structure and the motif. When dealing with magnetic structures one must notice that even if they are periodic, these structure do not necessarily need to have the same periodicity as their associated crystal structures. In the three main cases, ferromagnetic, antiferromagnetic or ferrimagnetic, the periodicity of the magnetic structure is equal or an integer multiple of the crystal structure. However, this is not always the case, and for this reason a better approach to describe the periodicity of magnetic structures is the propagation vector formalism, $\mathbf{k}$. This vector, defined in the reciprocal space, is a mathematical object which describes the relation between the orientation of the equivalent atoms in different nuclear cells. For instance, let's consider the case of a nuclear cell with a single magnetic atom within it. From (1.8) it follows that for $\mathbf{k} = (0, 0, 0)$ the magnetic moments of atoms in contiguous nuclear cells are parallel. This is the case of a ferromagnetic structure where all of the moments are parallel, and the magnetic cell coincides with the nuclear one. Let us assume now that the situation is such that along a the moments are antiparallel. In this case, the magnetic unint cell would be doubled along the a axis with respect to the nuclear, *i.e.* $a_{mag} = 2a_{nuc}$, with a corresponding $\mathbf{k} = (\frac{1}{2}, 0, 0)$ propagation vector. In other words, $\mathbf{k} = (k_a, k_b, k_c)$ represent the wave vector that defines the phase difference between the moments of a magnetic modulation. When (k_a, k_b, k_c) are rational numbers, then the structure is called *commensurate*, and if not, it is called *incommensurate*.

1.2.2 The Dzyaloshinskii-Moriya interaction

After the discovery of the giant ME response in $TbMnO_3$ by Kimura *et al.* [10], the spin-driven ferroelectricity has become a central issue of the research field

of correlated electron systems. Common to all the spin-driven ferroelectricity is the breaking of space inversion by magnetic order. From the microscopic of view, several types of origins were theoretically proposed and intensive experimental studies have confirmed that these mechanisms really induce the electric polarization. In 1958, I.E. Dzyaloshinskii proposed a thermodynamic theory to explain the weak ferromagnetism observed in Cr_2O_3 [28]. This was the first time to postulate an asymmetrical exchange interaction which was subsequently elaborated as a consequence of the spin-orbit coupling by T. Moriya using quantum theory in 1960 [29]. It was later coined as the Dzyaloshinskii-Moriya (DM) interaction, as it is known today. The microscopic origin of this interaction is the relativistic correction to the exchanges in the presence of the spin-orbit (SO) coupling. The DM interaction plays a crucial role not only in the physics of multiferroics (mainly the so-called type-II multiferroics), but also in many subfields of magnetism.

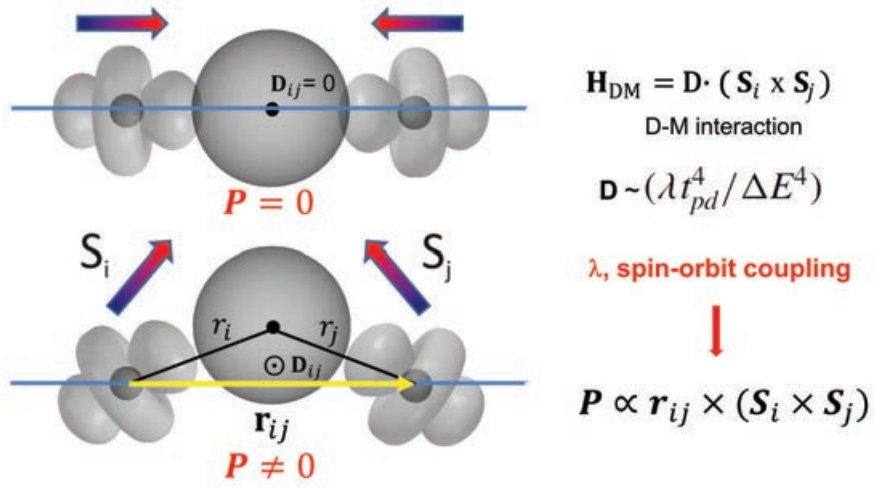

FIGURE 1.6: Electric polarization as induced by the displacement of the oxygen atoms due to the DM interaction. The direction of the DM vector $\mathbf{D}_{ij}$ is perpendicular to the plane.

The DM interaction is an antisymmetric, anisotropic exchange coupling between two spins on lattice bonds ij with no inversion center. For spins $\mathbf{S}_i$ and $\mathbf{S}_j$, a new term in the Hamiltonian is then given by

$$\mathcal{H}_{\mathrm{DM}} = \mathbf{D}_{ij} \cdot (\mathbf{S}_i \times \mathbf{S}_j) \tag{1.9}$$

where the Dzyaloshinskii-Moriya vector, $\mathbf{D}_{ij}$, is is finite when the crystal field does not have inversion symmetry with respect to the center between $\mathbf{S}_i$ and $\mathbf{S}_j$ (see Fig. 1.6). The effect of the DM interaction is often to provide a small

canting of the moments in an antiferromagnetic structure, resulting in a non-collinear order that produces weak ferromagnetism. Generally, in DM weak ferromagnets the non-collinear order is not at the origin, but a consequence of the of the structural distortion. An example are R_2CuO_4 rare earth cuprates [36, 37]. The induced weak ferromagnetism (WFM) has important implications for multiferroic properties and its applications.

Role of the DM interaction in spin-driven ferroelectricity

The relationship between the DM interaction and the onset of ferroelectricity in systems which show non-collinear spin order such as $TbMnO_3$ was proposed by I. Sergienko *et al.* [30]. Various types of spin order can have a potential to break the inversion symmetry and produce a spontaneous polarization. This has been valid for both collinear and non-collinear forms of magnetic order, when they are arranged in some specific lattice geometry. Some types of non-collinear cases are illustrated in Fig. 1.4. When the spins on the adjacent atomic sites are mutually canted, as Fig. 1.6, the horizontal mirror-plane symmetry is lost, resulting in the possible generation of a polarization along the vertical direction [20, 21, 30, 38]. Recently, it has also been shown theoretically [21] that the overlap of the electron wave function between the two atomic sites with canted spins generates a genuine electric polarization via the spin-orbit interaction.

When the spins form a transverse-spiral (cycloidal) modulation along a specific crystallographic direction [as the one shown in Fig. 1.4(b)], every nearest-neighbor spin pair produces a unidirectional local polarization as schematized in Fig. 1.6. A macroscopic polarization then can be generated, whose direction can be expressed as follows:

$$\mathbf{P} = A_0 \sum_{i,j} \mathbf{r}_{ij} \times (\mathbf{S}_i \times \mathbf{S}_j) \tag{1.10}$$

where A_0 is a constant and $\mathbf{r}_{ij}$ is the displacement vector connecting neighbouring $\mathbf{S}_i$ and $\mathbf{S}_j$ spins. The sign of $\mathbf{P}$ depends on a the chirality (clock-wise or counter-clock-wise) of the spins propagating along the spiral axis. In this class of spiral-spin multiferroics governed by the DM mechanism, the spontaneous polarization can be easily controlled by an external magnetic field along a specific direction [10, 39].

1.2.3 Magnetic frustration

Another important concept in the field of strongly correlated materials, from which many of the exotic magnetic and magnetoelectric phenomena arise in many TM metal oxides, is the '*magnetic frustration*'. In frustrated materials, the magnetic interactions can not be satisfied simultaneously. In other words, the competing interactions in the Hamiltonian contribute in such a way that the energy can not be minimized in a single ground state and becomes degenerated. The geometry of the crystal and the different competing interactions between different $\mathbf{S}_i$ and $\mathbf{S}_j$ couples can lead to complex magnetic structures.

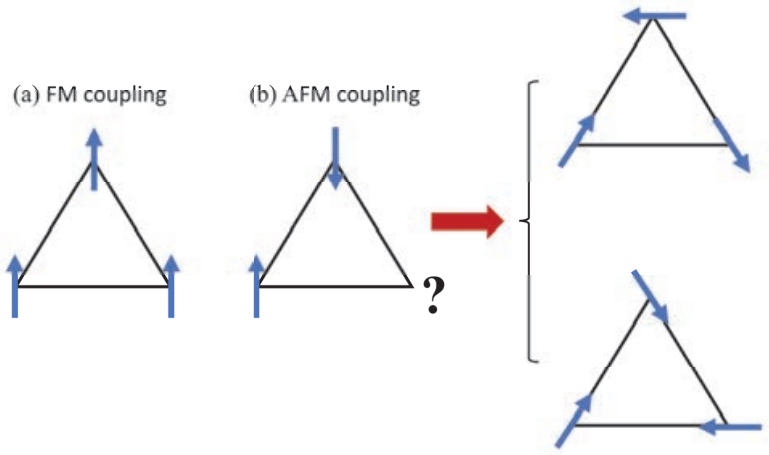

FIGURE 1.7: Scheme of the possible configurations for spins in a triangle. Whereas a FM coupling is compatible with the triangular lattice (a), in the case of AFM coupling magnetic frustration emerges from the geometry of the spin lattice, giving raise to different states. Figure adapted from Ref. [40].

To illustrate the latter case, Fig. 1.7 sows a scheme of the possible configurations for spins in a triangular lattice, where the origin of magnetic frustration is in the topology. If the interactions between nearest neighbors are ferromagnetic, they can all be satisfied simultaneously [Fig. 1.7(a)] and the ground state is unique. However, if the interactions between the nearest neighbors is antiferromagnetic, as in Fig. 1.7(b), the system does not have a unique spin configuration that minimizes the energy. In consequence, the ground state becomes degenerated and several spin structures may arise in the system.

1.3 YBCFO, a new high-Tc multiferroic with chiral spin order

The search of magnetoelectric multiferroic (MF) materials, where magnetic order combines with ferroelectricity (FE) and both are coupled to each other is an issue of keen interest in condensed matter physics and in spin-related emerging communication technologies. In many of these materials, the spontaneous appearance of electric polarization P is linked to the onset of incommensurate (ICM) magnetic order, where the spin-orbit coupling induces ferroelectric polarization in a noncollinear phase through the Dzyaloshinskii-Moriya (DM) interaction [15, 41, 42]. However, the magnetic frustration mechanisms giving raise to such noncollinear phases is produce low magnetic ordering temperatures (typically <100 K), critically restricting their potential uses for spintronics and low-power magnetoelectric devices. To very recently, the celebrated spiral magnetic orders in CuO and $YBaCuFeO_5$ were the only known examples of switchable, magnetism-driven ferroelectricity at zero field and temperatures above 200 K [19, 43–47]. In the former, the low monoclinic symmetry promotes frustrated magnetic interactions leading to a spiral magnetic multiferroic phase, stable only in the reduced range of 213 to 230 K [42]. Instead, the layered double perovskite $YBaCuFeO_5$ (YBCFO) with a structure AA'BB'O_5 is an exception to this phenomenon, since it displays magnetism-driven ferroelectricity at unexpectedly high temperatures ($T<T_S \approx 230$ K) associated to its characteristic magnetic spiral state [19]. The reported electrical polarization (P) values in the spiral phase are fairly large and reach 0.4 $\mu C/cm^2$ in polycrystalline samples [19, 46]. In addition YBCFO exhibits an extraordinary tunability of its spiral ordering temperature (T_S=T_{N2}), which can be increased far beyond room temperature (RT) by different routes including the manipulation of Cu/Fe chemical disorder in the bipyramids and substitutional doping at the AA' and BB' sites [47–49].

$YBaCuFeO_5$ was first synthesized in 1988 [43], shortly after the discovery of high-temperature superconductivity in $YBa_2Cu_3O_{6+x}$ [50], recieving modest attention from then on due to the difficulties in obtaining samples in single-crystal or thin film forms. However, in the recent years renewed interest on this material resurged in view of its unique physical properties, which are nowadays subject of intense debate and study in the field of condensed matter physics and magnetic materials [46–49, 51].

1.3.1 Magnetic phase transitions in YBCFO

Although the existence in YBCFO of two successive commensurate (CM) and incommensurate (ICM) magnetic phases upon cooling was known since 1995 [44], studies on the nature of such magnetic orders, specially the ICM one, were lacking until very recently. The first detailed neutron diffraction study on this material was published in 2015 by M. Morin *et al.* [46] with the aim of understanding the origin of the ICM magnetic order and the consequent multiferroism, reported by Kundys *et al.* [19].

Fig. 1.8(a) shows the temperature dependent neutron powder diffraction (NPD) patterns of YBCFO around the main magnetic reflections (1/2 1/2 1/2) and (1/2 1/2 3/2) from Ref. [46], as collected on the DMC diffractometer at the Swiss Neutron Source SINQ of the Paul Scherrer Institute (Villigen, Switzerland) with λ=2.45 Å. Upon cooling from 500 K two phase transitions are clearly observable. The commensurate (CM) antiferromagnetic phase [AF1, with a propagation vector $\mathbf{k}_1 = (1/2, 1/2, 1/2)$] with onset temperature $\mathrm{T_{N1}} \approx 430$ K precedes an incommensurate (ICM) spiral (cycloidal) order [AF2, with propagation vector $\mathbf{k}_2 = (1/2, 1/2, 1/2 \pm q)$] at $\mathrm{T_{N2}}$ ($\mathrm{T_{N2}} = \mathrm{T_S} \approx 200$ K) that persists down to the base temperature.

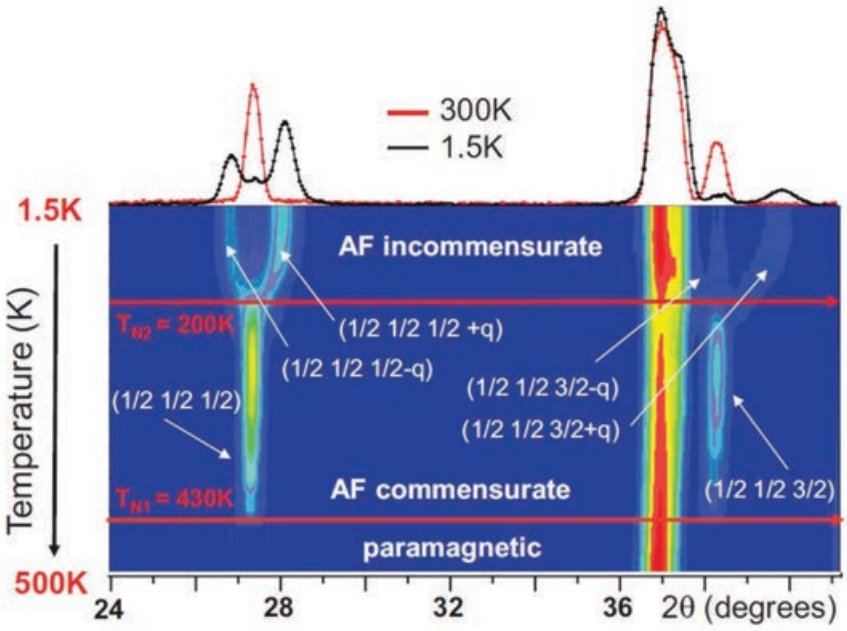

FIGURE 1.8: Magnetic transitions in YBCFO. Contour plot showing the temperature dependence of the NPD patterns for $YBaCuFeO_5$ measured on DMC diffractomrter (λ=2.45 Å). The patterns at 1.5 and 300 K are shown separately. Figure from Ref. [46].

Upon cooling below T_{N2}, the ICM modulation parameter q along the c axis appears and increases continuously with decreasing temperature until nearly saturating at base temperature, as shown in Fig. 1.9. As we can see, the onset of the ICM magnetic order coincides with a sharp anomaly in the –also shown– magnetic susceptibility and with the appearance of a net electric polarization P, indicating a direct relation between the two phenomena. In Ref. [46] the authors reported a P value of about $\sim$0.64 $\mu C/cm^2$, close to the value found by Kundys [19] ($\sim$0.4 $\mu C/cm^2$) and about ten times larger than the one reported by Kawamura [52] ($\sim$0.04 $\mu C/cm^2$).

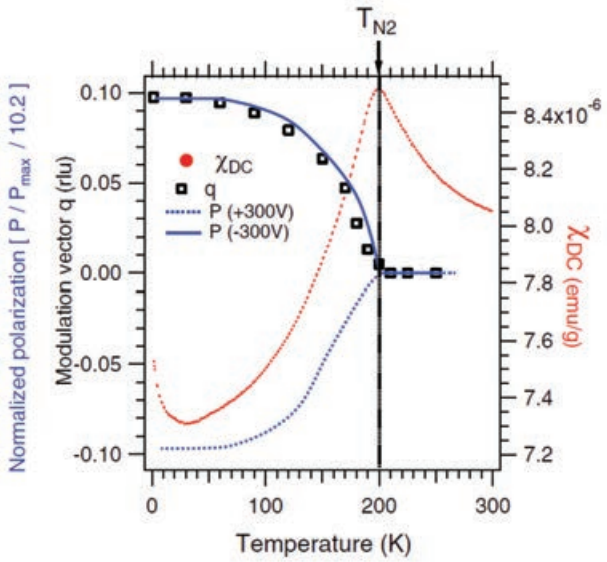

FIGURE 1.9: Red dots: DC magnetic susceptibility of YBCFO measured at 1 T by heating after cooling in zero field. Black open squares: incommensurate modulation vector q (reciprocal lattice units). Blue dotted and continuous lines: normalized electric polarization measured by applying an electric field of $\pm$300 V. In order to use the same axis as q, the polarization values are normalized to their saturation value ($\sim$0.64 $\mu C/cm^2$) and further divided by a constant value of $\sim$10.2 [46].

Magnetic structures

The CM ($\mathbf{k}_1$) and ICM ($\mathbf{k}_2$) magnetic structures in YBCFO were described for the first time in detail by M. Morin, A. Scaramucci *et al.* in Ref. [46]. From the representation analysis they found the possible magnetic moment arrangements compatible with the $P4mm$ symmetry and the $\mathbf{k}_1$ and $\mathbf{k}_2$ propagation vectors. If only one irreducible representation (*irrep*) becomes active below each of the magnetic transitions, the direction of the moments is restricted to either the ab plane or along the c axis. Instead, they found that at all temperatures the best fits to the NPD data corresponded to inclined arrangements

needing the combination of the 2 *irreps*. The best agreement found for the CM phase (T_{N2}<T<T_{N1}) corresponds to the collinear magnetic structure displayed in Fig. 1.10(a-1). Spins in the ab plane are antiferromagnetically (AFM) coupled, whereas the alignment along c alternates: it is AFM across the O-free Y planes and ferromagnetic (FM) inside of the bipyramidal blocks. The orientation of the spins in the ab plane, perpendicular to the fourfold axis, cannot be determined from NPD, and the component of the moments along c is found to be nonzero. So the, model consists of spins tilted in the ac plane forming an angle θ respect to the c axis.

For the ICM phase (T<$TN2$), M. Morin, A. Scaramucci *et al.* propose an inclined circular spiral configuration model in which the AFM collinear coupling within the unit cell is preserved but collinearity between FM coupled spins inside the bipyramids gets lost, leading to the formation of the chiral structure shown in Fig. 1.8(a-2), where the rotation of the moments propagates along the c direction. The incommensurability parameter q derived from the $k_z = 1/2 \pm q$ satellites is directly related to the rotation angle of the moments in the bipyramids (φ) as $\varphi = 2\pi q$. This model implies that the FM coupling in bipyramids are more sensitive to the external thermal changes as compared with the AFM

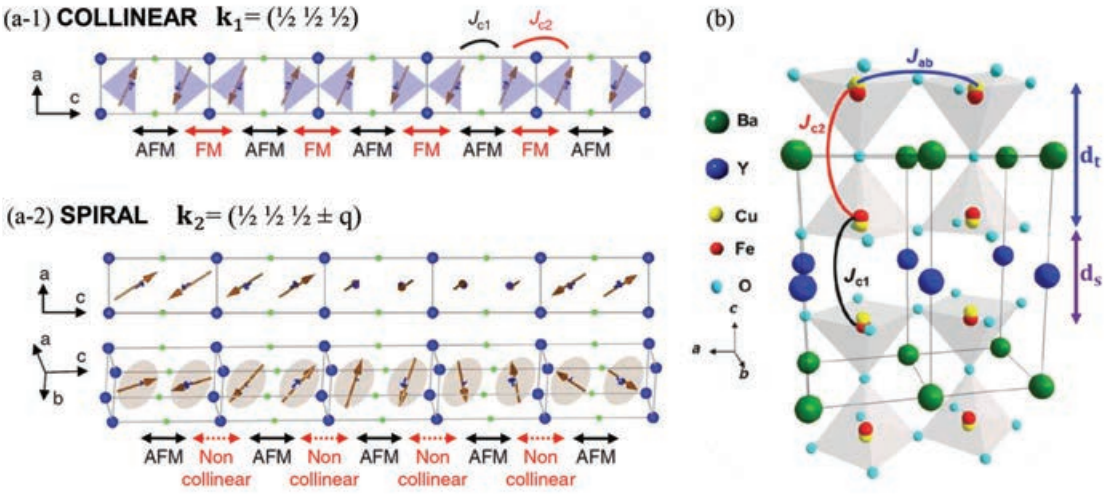

FIGURE 1.10: (a) Magnetic structures in the commensurate collinear (a-1) and incommensurate spiral phases (a-2). The rotation plane of the spiral is indicated for clarity, and the nearest-neighbour magnetic couplings along the c axis are also shown. (b) Illustration of the $YBaCuFeO_5$ crystal structure showing the nearest-neighbor (NN) antiferromagnetic (AFM) and ferromagnetic (FM) couplings, along the c axis (J_{c_1} and J_{c_2}, respectively), and the average NN AFM coupling in the ab plane (J_{ab}). Figures adapted from Refs. [47] and [48].

coupling across the Y layers. As in the case of the $\mathbf{k}_1$ collinear phase, the results in Ref. [46] indicate that the plane of the helix forms an angle θ respect to the c axis.
It is noteworthy, however, that using models based on variable-moment sinusoids and constant-moment helices, both with spins inclined with respect to the direction of the ICM modulation vector, equally good fits of the neutron powder diffraction data can be obtained. In view of the observation of electrical polarization, authors adopt the spiral solution, but direct proof of the existence of such modulated spiral order is still lacking. This further highlights the importance of disposing of YBCFO samples in single crystal form. The limitations of NPD will be further addressed in Chapter 4, and Chapters 6 and 7 will attempt to overcome those limitations by the fabrication and study of single crystals with the aim of unambiguously determining the nature of the CM and ICM phases in YBCFO.

1.3.2 Crystal structure and the relevance of B-site disorder in YBCFO

In the structure of the $YBaCuFeO_5$ (YBCFO) double perovskite A^{3+}/A'^{2+} layers alternate along the c-axis (A^{3+}=Y^{3+} or R^{3+} [rare earth] and A'^{2+}=Ba^{2+}). The layered ordering of Y^{3+} and Ba^{2+} is caused by their very different ionic radii [53]. B/B'-sites accomodate the metals forming $CuFeO_9$ bilayers of corner-sharing $Cu^{2+}O_5$ and $Fe^{3+}O_5$ square pyramids that extend parallel to the ab plane. Y^{3+} (or R^{3+}) layers accommodate the oxygen vacancies which separate the $CuFeO_9$ bilayers, and the Ba^{2+} ions are located within the bilayer spacing.

From Density-Functional Theory (DFT) calculations, Morin *et al.* [46] suggested that the small difference of the Fe^{3+} and Cu^{2+} ionic radii (0.58 Å for Fe^{3+} and 0.65 Å for Cu^{2+}, both in V coordination [53]), which lead in consequence to slightly different Fe-O and Cu-O apical distances, favour the scenario of randomly oriented Cu-Fe dimers in order to minimize microstrains along c, rather than distributions with coexisting Cu-Cu (long), Fe-Fe (short), and Cu-Fe (intermediate) bonds. In a the structural study detailed in the same reference, Morin *et al.* reported for the first the experimental observation of a particular kind of Cu/Fe chemical disorder characterized by the existence of such Cu-Fe bipyramidal dimers, demonstrating that rather than a fully disordered configuration (described by the tetragonal centrosymmetric $P4/mmm$ space group), the structure is better described by a non-centrosymmetric $P4mm$ symmetry

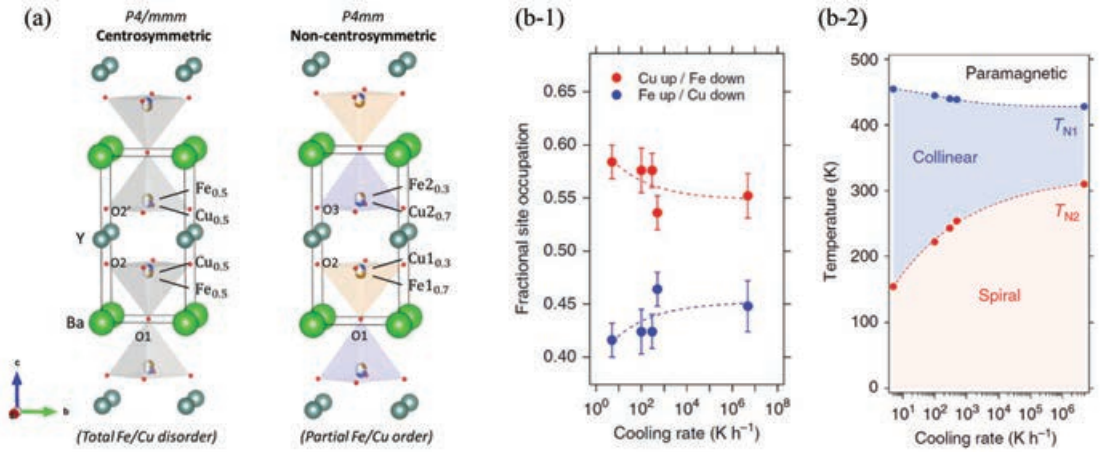

FIGURE 1.11: (a) Models for the crystal structure of $YBaCuFeO_5$. Left: fully disordered centrosymmetric ($P4/mmm$) model with Fe/Cu sites split. Right: Non-centrosymmetric ($P4mm$) model with partial Fe/Cu order. (b) Influence of the preparation method (cooling rate) on the B-site occupation (Fe/Cu disorder) in the pyramids (b-1) and stability range of the collinear and spiral phases (b-2), figure adapted from Ref. [47].

where Fe and Cu bonds prefer to adopt partially ordered arrangements. In consequence, the mirror plane containing the Y^{3+} ions is lost and there are two non-equivalent sites for B-atoms. In a formal ordered sample, Cu atoms are located at $(1/2, 1/2, z \approx 3/4)$ while Fe atoms are placed at $(1/2, 1/2, z \approx 1/4)$ position. The schematic representation of the centrosymmetric $P4/mmm$ (full Fe/Cu disorder) and non-centrosymmetric $P4mm$ (partial Fe/Cu order) models are depicted in Fig. 1.11(a).

Later on, Morin *et al.* also demonstrated that in contrast to Y^{3+} and Ba^{2+} ions, due to the smaller difference of the Fe^{3+} and Cu^{2+} ionic radii, B-site ordering (Cu^{2+}/Fe^{3+}) is strongly dependent on the preparation method and can be easily tuned by applying controlled cooling rates at the final stage of the annealing process [47]. As shown in Fig. 1.11(b) (from Ref. [47]), higher cooling rates result in higher Fe/Cu chemical disorder (parametrized by the partial Fe/Cu occupations in upper and lower pyramids in respect to a unit cell). In addition, Morin *et al.* fond that Fe/Cu cation disorder has a strong impact on the stability of the spiral phase (T_{N2}=T_S), which can be increased by more than 150 K (far beyond RT [47, 48]) by manipulating the chemical disorder in the bipyramids, as evidenced in Fig. 1.11(c). The observation Cu/Fe disorder and its correlation between with the high stability and tunability of the spiral ordering temperature in YBCFO was key for the theorization of the "*spiral order by disorder*" mechanism by Scaramucci and co-workers.

1.3.3 Magnetic interactions and the spiral order by disorder mechanism in YBCFO

The exceptional stability of the spiral magnetic order in this layered structure requires a non-conventional mechanism. Though the reference compound YBCFO is not a geometrically frustrated magnet, magnetic frustration gets present in absence of perfect B-site cation order when samples are prepared with partial Fe/Cu order in the structure (chemical disorder of the magnetic cations at the B-site). The CM phase of YBCFO exhibits three types of average magnetic couplings [46]. As illustrated in Fig. 1.10(b), between pyramids in the ab plane there is strong antiferromagnetic (AFM) interaction (J_{ab}) for any combination of neighboring atoms (Fe-Fe, Cu-Cu, Fe-Cu). Along the c axis instead, there are two different magnetic couplings. There is a weak AFM interaction (J_{c_1}) between successive bilayers across the Y-sublattice and a weak

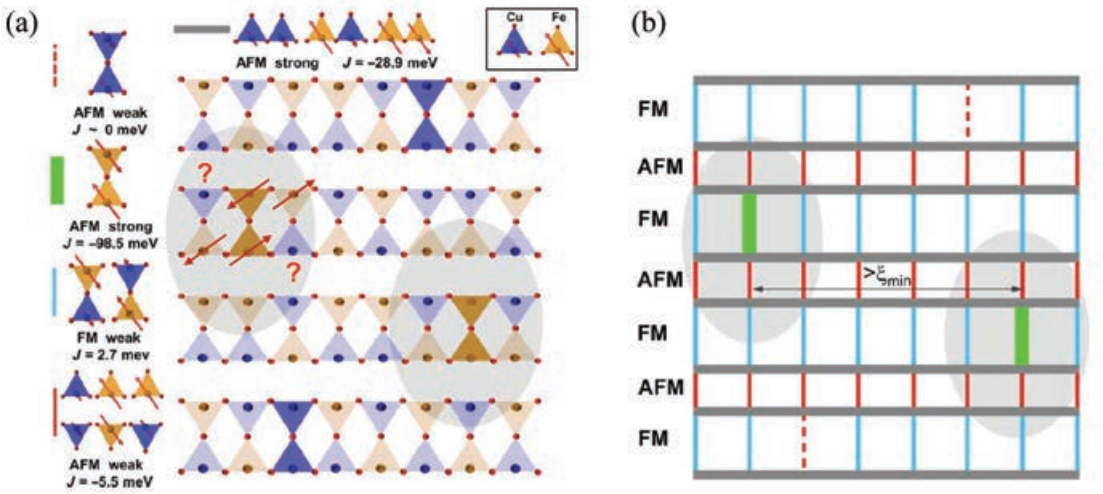

FIGURE 1.12: (a) Scheme of the correlated Cu-Fe chemical disorder in $YBaCuFeO_5$, characterized by the presence of randomly disordered Cu-Fe FM "dimers". The presence of strongly AFM Fe-Fe bonds is the source of magnetic frustration in the system, inducing the loss of collinearity in nearby Fe-Cu pairs with weaker FM coupling. The J values of the nearest-neighbor (NN) couplings along c and in the ab plane for the different the Fe-Fe, Cu-Cu and Fe-Cu pairs shown are those of Scaramucci *et al.* [54]. (b) Representation of (a) in terms of magnetic bonds. The impact of a few strong, randomly distributed AFM Fe-Fe "defects" is illustrated by the gray ellipses, which delimit the regions where the Cu-Fe spins lose their collinearity. Thinner bonds represent weak AFM or FM couplings, while thicker bonds indicate strong AFM couplings. The crosstalking of these regions eventually gives rise to a spiral if the in-plane separation of the Fe-Fe impurities is smaller than $\xi_{\min}$. Note that the same number of weakly interacting Cu-Cu "defects" is necessary to preserve the material's stoichiometry. Figure adapted from Ref. [48].

ferromagnetic (FM) coupling (J_{c_2}) within each bilayer across the apical oxygen (Cu-O1-Fe). The latter is the most affected by cation disorder [47]. The magnitude and character of the NN couplings (J values) for the Fe-Fe, Cu-Cu and Fe-Cu pairs along c and in the ab plane from Scaramucci *et al.* [54] are depicted in Fig. 1.10(a).

As mentioned, Morin *et al.* unveiled a huge impact of cation disorder on T_S, the magnetic modulation vector and the inclination of the spiral rotation plane [47]. In an effort to justify the unexpectedly high stability of the spiral order in this double perovskite, Scaramucci and co-workers theoretically addressed the foreseeable effects of frustration due to B-site disorder (Fe/Cu) in this layered structure. So, the theoretical model developed by Scaramucci *et al.* describes the formation of high-T_S spiral order in nonfrustrated lattices of classical XY ferromagnets with only nearest-neighbor interactions when an enough fraction of equally oriented ferromagnetic bonds are substituted by random impurity bonds presenting sufficiently strong antiferromagnetic coupling (J_{imp}) [54, 55]. An antiferromagnetic impurity bond would correspond to a bipyramid composed of Fe_2O_9 instead of $FeCuO_9$ in YBCFO, and its presence induces local frustration and spin canting around it. The sense of rotation of the local spin canting can mirror Ising variables. Additionally, thanks to the identical orientation of the impurity bonds (along to a single crystallographic direction, here always parallel to the c-axis), the long range correlations between the local cantings are favoured and can generate a magnetic-spiral order (a 'ferromagnetic' Ising ground state of either clockwise or counterclockwise canting of the spins). In other words, a continuous twist can be induced parallel to the direction of the antiferromagnetic impurity bonds. The model by Scaramucci *et al.* also predicts that (i) the continuous twist ground state is favoured in Bravais lattices in which neighbouring impurities are closer in the plane than along the orientation of the impurity bonds. Moreover, (ii) the transition temperature (T_S) and spiral wave vector (magnetic modulation) is (for low degree of disorder) proportional to the density of antiferromagnetic impurity bonds. The proposed novel mechanism thus entails "spiral order by disorder" and could also underlay very stable non-collinear modulated orders in other very anisotropic structures (such as, *e.g.*, some doped hexaferrites [56, 57], $(Fe,Cr)_2O_3$ [58], etc.).

1.3.4 Designing magnetic spirals far beyond room temperature

Upon cooling, several works reporting fairly large electric polarization associated to the spiral phase in these perovskites [19, 46] have raised great expectation due to the possibility to stabilize the spiral order even above room temperature. In view of this, new strategies are being investigated in order to optimize and upgrade the magnetic and magnetoelectric properties in such high-temperature spiral oxides and potential ferroelectrics. The following lines are a brief review of the research done to the date in this direction following different routes, as well as their main benefits and drawbacks:

(i) **B-site disorder modification:** In agreement with the theoretical model developed by Scaramucci and co-waarkers [54, 55], which predicts that both the spiral ordering temperature T_S and the magnetic modulation vector q should increase linearly with the presence of randomly distributed frustrating Fe/Fe bonds, in Ref. [47] it was verified that among different YBCFO samples prepared with different cooling rates, the highest spiral ordering temperature was achieved for a sample quenched in liquid nitrogen (*i.e.*, that with the largest Fe/Cu disorder) with $T_S \approx 310$ K (Fig. 1.13(a)-Left). This also suggests that the spiral ordering temperature could be further raised by increasing the Fe/Cu disorder. However, faster cooling rates are not easily achieved experimentally, and a too large disorder could lead to clustering of the Fe-Fe defects within the ab plane if they are too close.

(ii) **A-site substitutional doping:** In a recent work carried out by T. Shang *et al.* [48], it was found that the limitations in the Fe/Cu disorder route can be overcome by the application of chemical pressure. The J_{c_1} and J_{c_2} NN couplings along the c axis, which are strongly correlated, respectively, with the separation between bipyramidal layers (d_s) and the thickness of the bipyramids (d_t) [see Fig. 1.10(b)], can be modified by isovalent AA'-cation substitutions. Specifically, T. Shang *et al.* found that the replacement of Y^{3+} by rare-earths (RE^{3+}) with increasingly higher cationic sizes induce a progressive increase of the distance between the bipyramid layers and a decrease of the average bipyramid thickness. The increase in the magnetic frustration, caused principally by the effect in the J_{c_2} couplings, result in a increase of the stability range of the spiral. The $REBaCuFeO_5$ phase diagram in Fig. 1.13(a)-Middle shows an increase in the spiral ordering temperature from ∼220 K ($LuBaCuFeO_5$) up to ∼310 K ($DyBaCuFeO_5$) [48].

On the other hand, T. Shang *et al.* prepared a second series of compounds in which Ba^{2+} was partially substituted by different amounts of smaller Sr^{2+}. In this case, a similar effect in the d_s and d_t interatomic distances was achieved. The compression of the bilayers (d_t distance) in $YBa_{1-x}Sr_xCuFeO_5$ further increases the stability of the spiral by enhancing the AFM coupling inside the bipyramids, reaching $T_S \approx 375$ K in $YBa_{0.6}Sr_{0.4}CuFeO_5$ [48]. Fig. 1.13(a)-Right shows the phase diagram of $YBa_{1-x}Sr_xCuFeO_5$ (with $0 \leq x \leq 0.5$).
In the $REBaCuFeO_5$ and $YBa_{1-x}Sr_xCuFeO_5$ series studied by T. Shang *et al.* in Ref. [48], to add up the impact of both the lattice and the Cu/Fe disorder,

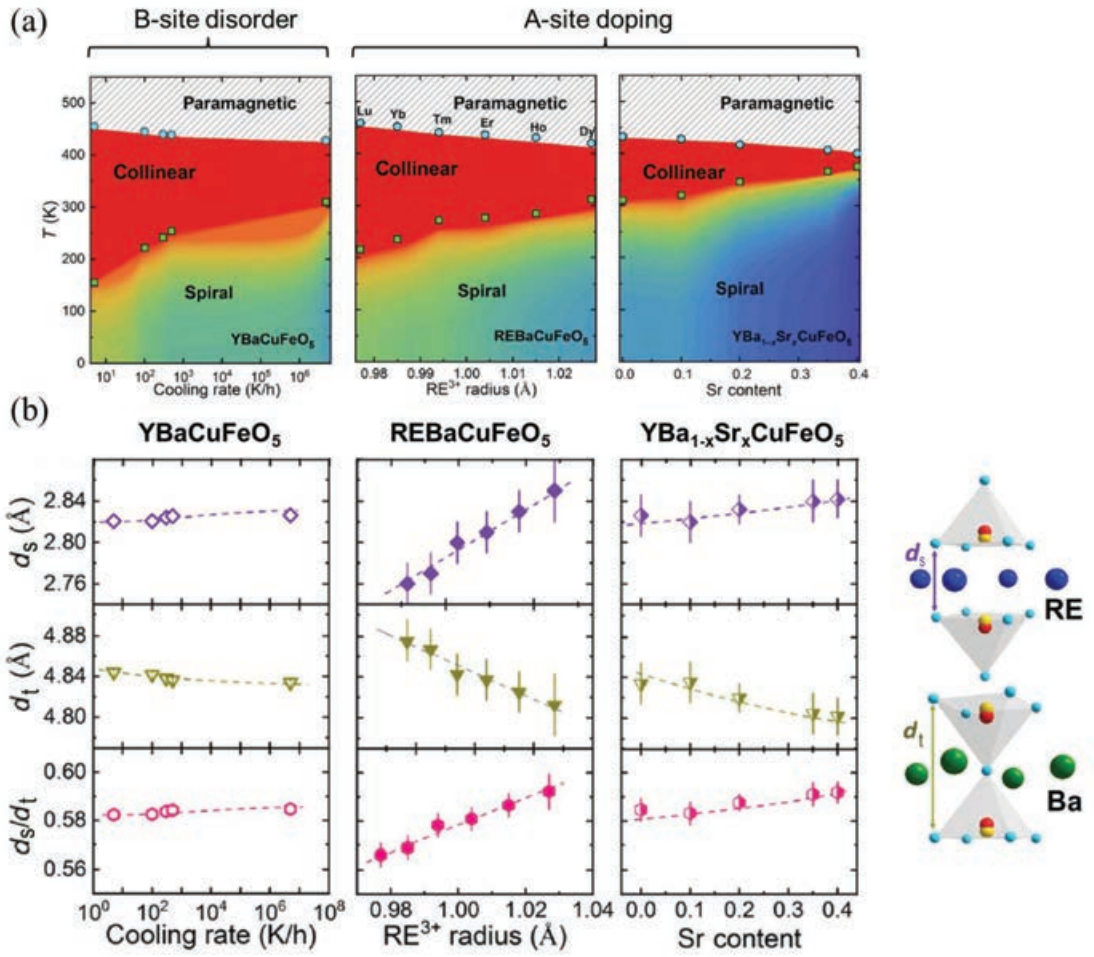

FIGURE 1.13: (a) Magnetic phase diagrams illustrating the evolution of the collinear (T_{N1}) and spiral (T_S=T_{N2}) onset temperatures using different routes for tuning the spiral phase: (Left) Modification of the B-site disorder in $YBaCuFeO_5$ samples prepared with different cooling rates (experimental points from from [47]); (Middle) Replacement of Y^{3+} by a rare-earth cation (RE^{3+}); and (Right) replacement of Ba^{2+} by Sr^{2+}. (b) Evolution in each series of the separation between bipyramids (d_s) and the thickness of the bipyramids (d_t). Figure adapted from Ref. [48].

the last parameter was maximized by quenching the samples in liquid nitrogen after the last annealing. Although the inclination of the spins in samples with the highest T_S in the two series correspond to a nearly perfect cycloid, indicating that the samples with the highest spiral ordering temperature (which exceeds 300 K) have also the potential of displaying the largest saturation polarization, the main drawback in such Y(Ba,Sr)$CuFeO_5$ samples is that the polycrystalline samples were too leaky to sustain electric polarization at room temperature (RT).

(iii) **B-site substitutional doping:** Another route that has been much less explored than the modification of chemical disorder and A-site doping above described is the substitutional doping of Fe or Cu in the B-sites by different isovalent $3d$ Transition Metals (TM). Due to the different characters of their electronic structures, TM ions exhibit different spin states. In the case of metals with non-zero magnetic moment, those substitutions can have an impact over the competing superexchange terms in the system, whose character is determined by the Goodenough-Kanamori rules. Furthermore, the fact that in some cases TM are prone to induce lattice distortions in the presence of –in this case pyramidal– crystal fields caused by the surrounding oxygen anions entails additional complexity.
To the date there is only one publication where X. Zhang *et al.* explored this route by the chemical substitution of Fe^{3+} by Mn^{3+} ions in the FeO_5 pyramids [49]. In this work, a systematic investigation of the $YBaCuFe_{1-x}Mn_xO_5$ series showed that Mn produce a progressive reorientation of the rotation plane of the magnetic spiral from nearly perpendicular to alomst parallel to the c axis, transforming a helical-type spin order into a cycloidal one, which may critically determine the ferroelectric and magnetoelectric behavior in these systems. Additionally, the increase of the spin-orbit coupling through the substitution of highly symmetric Fe^{3+} ions ($3d^5$, L=0, S=5/2) by less symmetric Mn^{3+} ions ($3d^4$, L=2, S=2) could favour the generation of spontaneous polarization according to the antysimetric DM interaction. The main problem in this strategy is the partial decrease of the stability range of the spiral phase due to the changes in the magnetic exchange couplings parallel to the c axis. Upon Mn substitution, a fraction of the Fe-Fe bonds with very strong AFM coupling, which are an essential ingredient of the model developed by Scaramucci and co-workers, are substituted by the much weaker Fe-Mn (or Mn-Mn) AFM coupling.

1.4 ε-Fe_2O_3, a high-T_C multiferroic with super-hard ferrimagnetism

1.4.1 ε-Fe_2O_3 among Fe(III) oxides

Crystalline iron(III) oxides (Fe_2O_3) constitute a very interesting kind of materials, as they can show up in a rich variety of crystal forms displaying rather large and complex structures that can lead to different interesting physical properties. Besides the amorphous Fe_2O_3, at ambient pressure the four polymorphs known to the date are: α-Fe_2O_3 (hematite), β-Fe_2O_3, γ-Fe_2O_3 (maghemite) and ε-Fe_2O_3 (luogufengite). Their unit cells are illustrated schematically in Fig. 1.14(a).

α-Fe_2O_3 and γ-Fe_2O_3 have been well examined and are employed in various applications. The latter, which is a representative soft magnet, is a ferrimagnet with a spinel structure, and hematite, which shows weak ferromagnetism due to the Dzyaloshinsky-Moriya mechanism, is the most naturally abundant phase. On the contrary, ε-Fe_2O_3 is the most elusive and one of the less studied polymorphs. This is because its formation requires the mutually exclusive

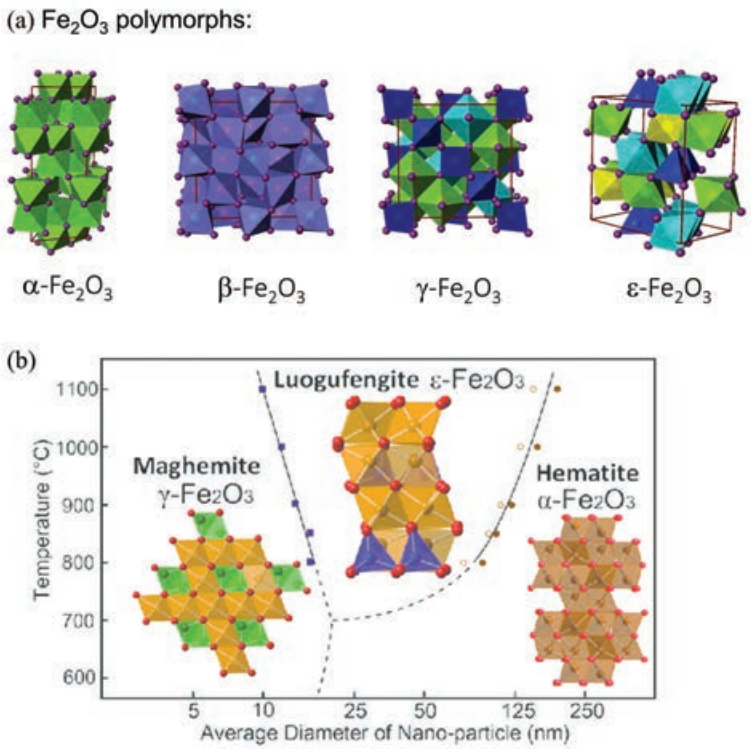

FIGURE 1.14: (a) Schematic representations of the crystal structures of Fe_2O_3 polymorphs. (b) Size-dependent phase map of nanometric iron(III) oxide. Figure adapted from Ref. [59].

conditions of high temperatures and small sizes [60], as shown by the size-dependent phase map in Fig. 1.14(b). In the last years, the interest in ε-Fe_2O_3, which remained unexplored for a long time, has recently been revived thanks to the possibility of synthesizing it in pure form [60, 61] and because of its appealing and unusual physical properties.

1.4.2 Crystal structure of ε-Fe_2O_3

Despite being known since 1934, ε-Fe_2O_3 has been much less studied than other iron(III) oxides, such as the α and γ polymorphs. This is explained because, like β-Fe_2O_3, ε-Fe_2O_3 is a rare Fe_2O_3 polymorph that exists only in the form of nanostructures and whose natural abundance is low. Its structure is isomorphous to $GaFeO_3$ and $AlFeO_3$, and stands out for its non-centrosymmetric orthorhombic structure, belonging to the $Pna2_1$ space group. Its unit cell (with lattice parameters a=5.098 Å, b=8.785 Å and c=9.468 Å at room temperature), presents four different Fe sites, three of them (Fe1, Fe2, Fe3) in octahedral coordination, and one (Fe4) in tetrahedral oxygen environment [62], as shown in Fig. 1.15. All of the FeO_x cation polyhedra exhibit a certain degree of distortion.

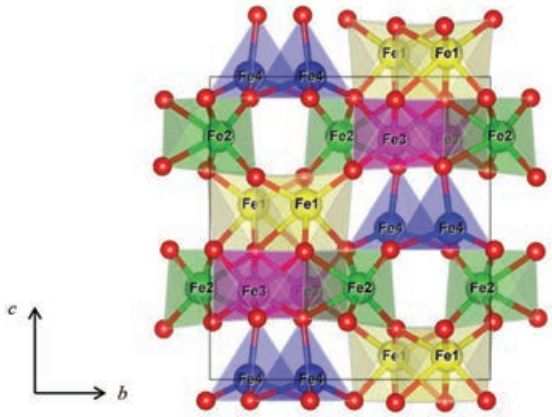

FIGURE 1.15: Orthorhombic structure of ε-Fe_2O_3. The four independent Fe sites of the cell are represented in different colors: distorted octahedral Fe1d and Fe2d in yellow and green, respectively; regular octahedral Fe3r, pink; tetrahedral Fe4t, blue. Oxygen atoms are shown in red.

1.4.3 Magnetic properties of ε-Fe_2O_3

ε-Fe_2O_3 presents unique magnetic properties among single metal oxides, probably related to the highly packed structural features specific to this polymorph, which produces a rich temperature-dependent magnetic phase diagram:

- **150 K<T<490 K**: between T_C = 500 K and T_{N2} = 150 K, ε-Fe_2O_3 exhibits a collinear ferrimagnetic structure due to the antiferromagnetic (AF) coupling (parallel to the a-axis) between dissimilar magnetic sublattices [63]. This phase is characterized by a huge coercivity, related to a marked magnetocrystalline anisotropy.
- **T<150 K**: below 150 K, this oxide presents a broad low-temperature incommensurate magnetic transition starting at 150 K, characterized by a large reduction of the coercivity, and of the remanent and the saturation magnetization. The magnetic softening, accompanied by a decrease in the dielectric constant, is associated to the onset of the commensurate-to-incommensurate magnetic transition and the concomitant decrease in the magnetocrystalline anisotropy [63].

The unexpectedly huge room temperature coercivity revealed by the magnetic studies ($H_C \sim 2$ T) [61, 64] at the collinear ferrimagnetic phase, makes the epsilon polymorph the transition metal oxide with the highest coercivity and an appealing material for the next-generation high-density magnetic recording media, high-frequency electromagnetic wave absorbers, or a building block for exchange-coupled permanent magnets [65–67]. The giant coercive field is also related to a marked magnetocrystalline anisotropy [68], a remarkable non-linear magneto-optical effect in the range of millimeter waves [66, 69] and coupled magnetoelectric features [69, 70].

Interestingly, a nonzero orbital angular momentum ($m_L \sim 0.15\ \mu_B$/Fe at RT under 40 kOe) was detected by X-ray Magnetic Circular Dichroism (XMCD) in the hard collinear ferrimagnetic phase (150 K<T<500 K), which is suppressed by the magnetostructural changes concurrent with the ferrimagnetic-to-incommensurate magnetic transition within the interval 85-150 K [71]. The nonzero orbital momentum is thought to be at the origin of the hughe RT coercivity.

Furthermore, ε-Fe_2O_3 (in the form of thin films) was discovered to be one of the few room temperature multiferroics with strong ferrimagnetism and ferroelectricity [72], although with a very small coupling between the ferroic orders. The ferroelectric switching mechanism is still not well understood [73, 74], and the possible multiferroic properties in bulk form are still a subject of debate.

1.5 Scope and objectives

The need of finding multiferroic materials for its application in electronic devices at room temperature has given great interest to the study of some materials belonging to the family of iron oxides, which constitute an exceptional family of materials that have been studied during many decades due to their fundamental interest and proved and promising applicability for new technologies based on biochemical, magnetic and catalytic properties, but especially because of their promising multiferroic properties. If we take a look at the very wide variety of materials that conform the iron oxides family we will realize that, although it is a very elusive property, a considerable number of them exhibit magnetoelectric behaviours, even some of them at high temperature. For instance, Kimura *et al.* [42] reported a room temperature ME effect originating from helimagnetism in a so-called Z-type hexaferrite $Sr_3Co_2Fe_{24}O_{41}$. A series of hexaferrite compounds which display large cells with complex magnetic couplings between Fe atoms are also good candidates for high temperature multiferroic materials [16]. Another one is the Y-type hexaferrite $Ba_2Mg_2Fe_{12}O_{22}$, or the delafossite-type $CuFeO_2$, where the screw-type spiral order drives ferroelectric polarization. Further examples of magnetoelectric iron oxides are the RT multiferroic frustrated and charge ordered $LuFe_2O_4$ films, the MF magnetite Fe_3O_4, the $RbFe(MoO_4)_2$, $GdFeO_3$, $DyFeO_3$, and so on.

The reason why iron oxides have proved to be very good candidates for high-temperature multiferroics is that in these materials the Fe-O-Fe exchange interaction (J) is very strong, propiciating very stable long-range magnetic orders able to remain activated under very high temperatures. Good examples of this type of materials are the α-Fe_2O_3 (hematite), the γ-Fe_2O_3 (maghemite) and the Fe_3O_4 (magnetite), with characteristic ordering temperatures of 950 K, 940 K and 853 K respectively [75]. As previously explained, one of the main problems found in type II multiferoics (in which long-range magnetic orders is a necessary condition for ferroelectricity), is their typically low-magnetic ordering temperatures. In such strongly correlated systems, magnetic frustration and plays an undeniable role in some non-collinear magnetic order driven multiferroics, although it produces the destabilization of the magnetic structure, causing the onset temperature of the multiferroic phase to be low. The strong Fe-O-Fe exchange interactions could contribute to revert this effect by raising the stability range of the magnetic order. In this sense, iron oxides offer a stimulating playground in the search for high temperature multiferroics.

The research carried out in this thesis revolves around two different families of oxides belonging to this promising source of high-T_c multiferroics. On the one hand, we focused on the family of $YBaFeCuO_5$ layered perovskites due to its extraordinary magnetostructural and magnetoelectric properties recently discovered. As we have seen, the role of the strong Fe-O-Fe superexchange interactions in $YBaCuFeO_5$ are an essential ingredient for the high stability of its multiferroic spiral phase. On the other hand, we have also studied the different types of magnetic orders and the magnetostructural properties of ε-Fe_2O_3, which is thought to be a type I room temperature multiferroic and diaplays outstanding properties at high temperatures. Accordingly, the results are organized in two main blocks, corresponding to '*Part II*' and '*Part III*' of this thesis. Its objectives and content and are briefly described in the following lines.

Part II. Investigating the family of spin-induced $YBaCuFeO_5$ multiferroics with high-T_c chiral magnetism

This aims to contribute in the research on the $YBaCuFeO_5$ system by addressing relevant questions not only from a fundamental point of view, but also with a perspective of finding new routes to enhance the magnetoelectric and ferroelectric properties in this promising family of oxygen-defficient perovskites.

- **Chapter 4** *(Helimagnets by disorder: its role on the high-temperature magnetic spiral in the YBCFO perovskite)*: this chapter aims to extend the previous investigations on YBCFO regarding the impact of Fe/Cu cation disorder on the noncollinear spiral order. The stability range of this magnetic phase has been extended to record temperatures by the B-site disorder route, and a detailed analysis of its effect on the evolution of the structure was carried out by means of Synchrotron X-ray Powder Diffraction (SXRPD) and by soft X-ray Absorption Spectroscopy (XAS) measurements. On the other hand, the influence of disorder on the magnetic phase diagram and the characteristics of the magnetic phases were thoroughly studied using Neutron Powder Diffraction (NPD) extending the range of previous studies.

- **Chapter 5** *(Enhancing the spiral stability in YBCFO by B-site divalent non-JT substitutions)*: In the need for developing new strategies to enhance the magnetic and magnetoelectric properties of the YBCFO family of potential multiferroics, in this chapter we propose and a new route aiming to extend the thermal stability of the spiral phase far beyond RT without the need of modifying the B-site cation disorder. This new route, based on $YBaCu_{1-x}M_xFeO_5$

isovalent cation substitutions where Cu^{2+} is partially replaced by M^{2+} = Co^{2+} and non-magnetic Zn^{2+} ions at the divalent B-sites, was validated by an exhaustive structural and magnetic investigation carried out by means of bulk magnetometry, SXRPD and NPD experiments. In the light of theoretical models we analyzed the interplay between lattice effects and magnetic frustration, as well as its impact on the magnetic phase diagram and its potential benefits on the magnetoelectric response. Finally, as nothing is known yet about the effect of external pressure on the magnetic spiral order, we also present a first angle-dispersive synchrotron XRD study up to 20 GPa to tentatively anticipate the influence pressure on the spiral stability through its structural evolution.

- **Chapter 6** *(Influence of Fe/Cu disorder on the magnetic properties of YBCFO single crystals)*: The fact that investigations on YBCFO single crystals are still very scarce due to the difficulties in obtaining samples of suitable quality and size for neutron diffraction studies motivated the growth of YBCFO single crystals by a modified Traveling Solvent Floating Zone (TSFZ) method. In this chapter growth of different single crystals is explained in detail. We also report the characterization of their structural properties and a meticulous quantification of the Fe/Cu chemical disorder by Synchrotron X-ray Powder Diffraction (SXRPD) and Single Crystal Neutron Diffraction (SCND) experiments. Furthermore, the exceptionally low values of Fe/Cu disorder found in some YBCFO crystals were correlated with the presence of unconventional magnetic properties, which were also characterized using neutron Laue and NPD techniques.

- **Chapter 7** *(Does a magnetic spiral exist in YBCFO? A single crystal investigation)*: In previous publications, the existence of the spiral order is assumed only from the observation of spontaneous polarization in some YBCFO perovskites, as in this particular case NPD is unable to distinguish between a non-collinear spiral order and a collinear variable-moment spin arrangement. Aiming to respond such fundamental question, in this chapter we disclose the results of Single Crystal Neutron Diffraction (SCND) and Spherical Neutron Polarimetry (SNP) investigations carried out using unpolarized and polarized neutron beams, respectively. In addition, within the scope of our single crystal investigations, we also studied the the anisotropic magnetic response of the spiral phase under the influence of external electric and magnetic fields: (i) the possibility of chiral magnetic domain switching applying an electric field was investigated in parallel by means of Spherical Neutron Polarimetry (SNP) and synchrotron Resonant Magnetic X-ray Scattering (RMXS), (ii) the influence of

magnetic fields was characterized by means of dc and ac susceptibility and by SCND measurements under magnetic fields.

Part III. Magnetostructural properties of ε-Fe_2O_3, a high-T_C multiferroic with super-hard ferrimagnetism

In this part we present important contributions in the understanding of the different types of magnetic orders in the exotic ε-Fe_2O_3 polymorph in the form of nanoparticles, as well as the underlying mechanisms of its outstanding magnetic properties. Investigation presented in this part was carried out in collaboration with M. Gich from the Nanoparticles and Nanocomposites Group at ICMAB-CSIC.

- **Chapter 8** *(Complex magnetism investigated in the frustrated ε-Fe_2O_3 multiferroic)*: This chapter reports a complex study in which we have combined magnetometry and NPD to unveil and characterize the existence of a high temperature "soft" ferrimagnetic order preceding the "super-hard" ferrimagnetic phase in ε-Fe_2O_3 nanoparticles. Additionally, we have investigated the low temperature incommensurate magnetic order by means of NPD, whose magnetic structure is under discussion. This investigation allowed us to rule out some of the models proposed in the litarature, based on cycloidal or amplitude-modulated spin orders [63, 76]. Instead, we propose an alternative collinear model with inversion anti-phase magnetic domains.

- **Chapter 9** *(Understanding the magnetostructural properties of ε-Fe_2O_3)*: The mechanism underlying some of the exceptional magnetic properties in this oxide (*e.g.*, its huge magnetic coercivity and anisotropy) could be linked to a non-zero orbital angular moment at the Fe atoms, as suggested by experimental evidences [71] and theoretical predictions based on first-principles and molecular orbital calculations [77]. In view of this, we used high-resolution SXRPD to investigate the magneto-structural coupling. In view of this, we used high-resolution SXRPD to investigate the magneto-structural coupling across the soft-hard magnetic transition, aiming to determine the underlying structural mechanisms driving the emergence of the ultra-hard ferrimagnetic order. Finally, neutron diffraction experiments under magnetic fields were carried out to determine the evolution of incommensurate and collinear "super-hard" magnetic phases under magnetic field, and the possible magnetostrictive mechanisms related to the exceptionally high coercivity.

Chapter 2

Synthesis of polycrystalline samples and crystal growth

Two families of iron oxides have been studied in this work: the oxygen defficient perovskite $YBaCuFeO_3$ and the iron (III) oxide polymorph ε-Fe_2O_3. Polycrystalline and single crystal samples of the first mentioned compounds were synthesized at the ceramic sample preparation and crystal growth laboratories at ICMAB-CSIC. On the other hand, the samples mentioned in second place were previously prepared and provided for its characterization in collaboration with M. Gich *et al.* from the Nanoparticles and Nanocomposites group at ICMAB-CSIC. The methods used for the synthesis of each family of samples are introduced below:

- $YBaCuFeO_5$: the main activity related with the synthesis carried out by the author of this work was focused on obtaining $YBaCuFeO_5$ samples in the form of polycrystalline sintered powdera and single crystals. A set of $YBaCuFeO_5$ polycrystalline samples with a wide range of Fe/Cu cation disorder was prepared by the solid-state reaction method. In compounds of this family, the sintering/cooling process entails determinant factors related with the Fe/Cu ordering, being altered the magnetic properties and, specifically, the onset temperature of the ferroelectric phase [47, 48]. Additionally, series of Co- and Zn-doped samples, $YBaCu_{1-x}Co_xFeO_5$ ($0 \leq x \leq 0.5$) and $YBaCu_{1-x}Zn_xFeO_5$ ($0 \leq x \leq 0.3$), were prepared in a similar way to the pristine $YBaCuFeO_5$ samples. High quality $YBaCuFeO_5$ single crystals were grown from polycrystalline seeds through

the Traveling Solvent Floating Zone (TSFZ) method using a four mirror infrared (IR) optical floating zone (OFZ) furnace. The general aspects of the mentioned synthesis techniques are explained in this chapter, although specific details about the preparation of each series of polycrystalline and single crystals samples are described in the chapters referred to the respective compounds.

- ε-Fe_2O_3: in this case, high-quality single-crystalline nanograin ceramic samples of ε-Fe_2O_3 with minimal intrusion of secondary phases, embedded in silica matrix, were produced by sol-gel chemical process. Hydrated iron (III) nitrate $Fe(NO_3)_3{\cdot}9H_2O$ was used as the Fe precursor and Tetraethyl orthosilicate (TEOS, $Si(OC_2H_5)_4$) was the metal-organic precursor for the formation of a SiO_2 matrix. The use of sol-gel methods with Si alcoxides and Fe salts makes it possible to confine Fe_2O_3 nanoparticles in a silica matrix, avoiding its agglomeration and preventing its transformation into α-Fe_2O_3 while annealed up to 1100 °C [see Fig. 2.1(a)] [78]. Afterwards, the silica support in the sample can

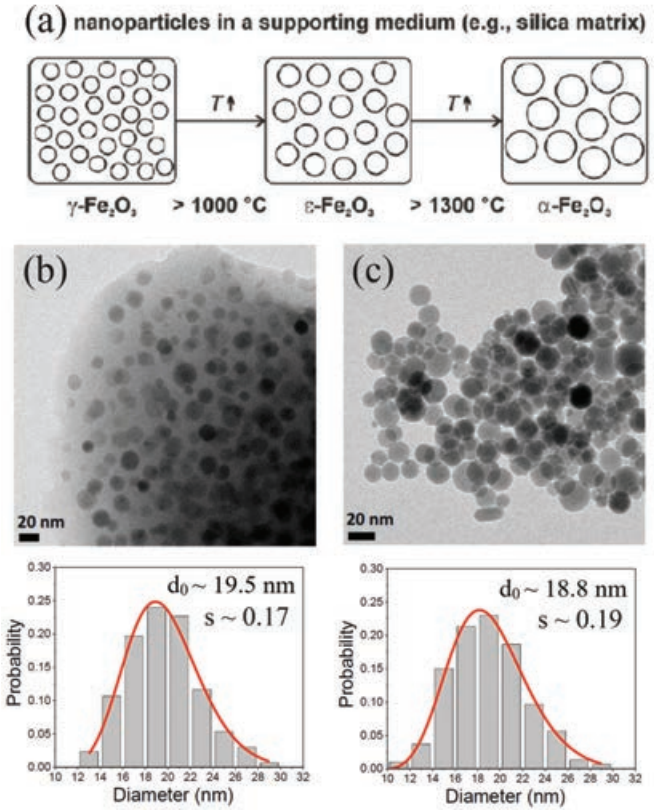

FIGURE 2.1: (a) Scheme of the mechanisms and temperature ranges of the thermally induced polymorphous transformation of ε-Fe_2O_3 in a supporting medium. TEM images of the ε-Fe_2O_3 nanoparticles embedded in the SiO_2 matrix (b), and etched ε-Fe_2O_3 nanoparticles (c). Lower panels represent the respective particle size distributions along with the fitting to the log-normal distribution (red lines). Figures adapted from Refs. [78] and [79].

be removed by etching the resulting powder into concentrated NaOH aqueous solution (12 M) at 80 °C for 48 hours. After this process nanometric ε-Fe_2O_3 samples ($\sim$19 nm), which are highly satable upon heating in air up to 940 K, are obtained. Figs. 2.1(b) and 2.1(c) show TEM images of the nanoparticles before and after the NaOH etching to remove the silica support. The reader is referred to Refs. [60, 61, 79] for further details about the synthesis of the nanoparticles. The optimisation of this preparation method by M. Gich *et al.*, obtaining for the first time virtually pure ε-Fe_2O_3, opened the door to the study of this rare polymorph.

2.1 Polycrystalline samples fabrication: the solid-state reaction method

For the preparation of $YBaCuFeO_5$ (and Co- and Zn-doped) polycrystalline samples, the solid-state reaction method was employed. This is the most conventional method used to prepare perovskite-oxide and similar materials, and the synthesis is produced due to the ionic diffusion between the different reactants assisted by thermal energy. In general, the process consists in mixing the solid reactants in the required amounts (stoichiometric mixture of the precursors) to prepare a specific solid crystalline compound and then grind to homogenize and press in pellets. Heating is a slow process in which usually high temperatures and long annealing periods are required for the complete solid state reaction to take place. Besides temperature and duration, another important parameter during the heat treatments is the use of appropriate atmospheres. For instance, during the annealing process an inert gas such as Argon may be used to prevent oxidation to a higher oxidation state, and an oxygen atmosphere can be used to promote the formation of high-oxidation states; or, conversely, a hydrogen atmosphere can be used to produce a low oxidation state [44]. Some examples are shown below:

- Reaction in a reducing atmosphere

$$V_2O_5\ (V^{5+}) \xrightarrow{H_2} VO\ (V^{2+})$$

- Reaction in a oxidizing atmosphere

$$LaNiO_{2.5}\ (Ni^{2+}) \xrightarrow{O_2} LaNiO_3\ (Ni^{3+})$$

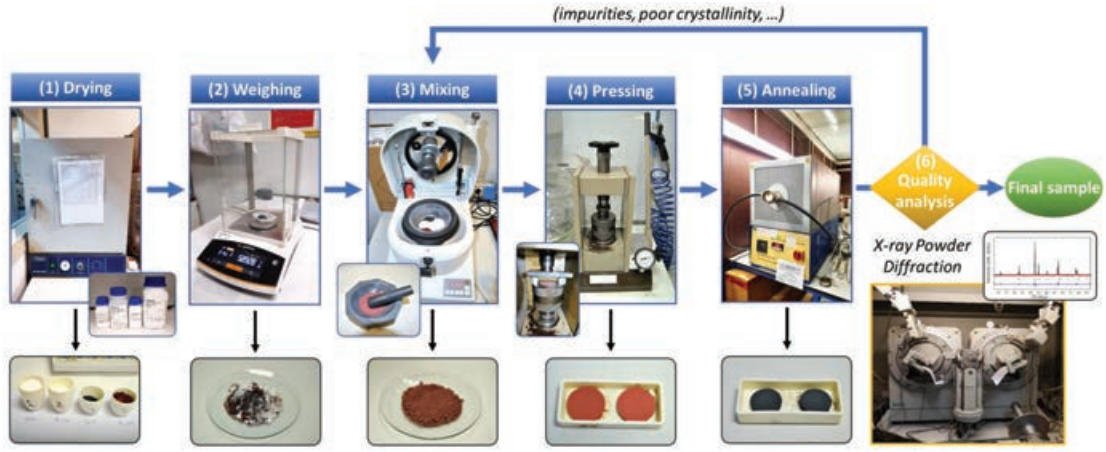

FIGURE 2.2: Scheme illustrating the polycrystalline sample synthesis workflow using the solid-state reaction method. (1) The selected precursors are dried or pre-calcinated, (2) weighed, (3) ground and mixed into fine powder, (4) pressed into pellets, and (5) annealed in a tubular furnace. Finally, X-ray powder diffraction is used to assess the quality of the samples (6). The process is repeated from step (3) if impurities or poor crystallinity are detected. The pictures were taken during the synthesis of $YBaCuFeO_5$.

To illustrate the solid-state reaction technique, the fabrication process of $YBaCuFeO_5$ samples is described here in detail. $YBaCuFeO_5$ was prepared in air following the solid-state reaction below:

$$Y_2O_3 + 2BaCO_3 + 2CuO + Fe_2O_3 \xrightarrow{air} 2YBaCuFeO_5 + 2CO_2 \tag{2.1}$$

Fig. 2.2 shows the sequential steps in the experimental process, exemplified by images taken during the preparation of $YBaCuFeO_5$:

(1) First, the precursors are dehydrated in a stove to avoid under-weighting errors due to the presence of moisture. In this case, high-purity Y_2O_3, $BaCO_3$, CuO and Fe_2O_3 commercial oxides were dehydrated at 150 °C for 48 h. A pre-annealing process at 900 °C for 10 h was also carried out on Y_2O_3 to promote the evaporation of carbonates.

(2) After dehydration and decarbonation processes, stoichiometric amounts of precursor oxides required by the reaction [eq. (2.1)] are weighed using a high-precision electronic balance.

(3) The precursor oxides are pre-ground using a manual agate mortar, and then thoroughly mixed for several hours until a very fine and homogeneous powder is obtained. For this process we disposed of an automatic laboratory agate mortar (Pulverisette 2 from Fritsch), but an agate ball

mill can be also be effective. Sometimes, the wet method of mixing can be used for reducing the mixing time and improving the homogeneity. Pure ethyl-alcohol is usually used as mixing medium.

(4) The resulting powder is placed into a steel die mold and the required pressure is applied using a laboratory hydraulic press. In this case, approximately 20 g of the mixed powder was pelletized under 12 tons of pressure using a ⌀35 mm circular mold. More pressure is not always better, since over-pressing usually results in cracking of the pellets. For difficult cases, the powder can be mixed with a very small amount of glycerol, or a few drops of 4 wt.% solution of Poly(vinyl alcohol) (PVA) in water in order to enhance the compaction. A good compaction favours the ionic diffusion in the annealing process.

(5) After pressing, the pellets are placed on alumina crucibles and annealed in air using a high-temperature tubular furnace. The furnace is programmed to follow a sequence. For $YBaCuFeO_5$, a 300 °C/h warming ramp was applied up to 1150 °C. After 50 hours at this temperature, a specific process was employed to cool the sample down to room temperature. In Chapter 4 the preparation of samples with controlled cooling rates and quenching processes by immersion into liquid nitrogen or water at the final stage of the annealing are explained with more detail.

(6) Finally, small amounts of the annealed polycrystalline samples are ground for assessing its quality by collecting laboratory X-ray diffraction patterns at RT. A Siemens D-5000 diffractometer (λ[Cu K_α] = 1.54 Å) was used to check the $YBcCuFeO_5$ samples. Too large FWHM of the diffraction peaks could indicate that the annealing process was not been sufficient for the complete crystallization of the sample. The presence of additional peaks that can not be reproduced by the expected crystalline phase indicate the presence of impurities in the sample. The quality analysis allows to evaluate if an additional annealing process is necessary. If so, the sample is re-processed from step (3). For some compounds, several annealing processes can be necessary.

2.2 Single crystal fabrication: the Floating-Zone growth method

Floating zone (FZ) growth is a zone melting technique in which the zone melting is carried out vertically for crystal growing. This technique gained popularity in the last decades for the growth of various nonconventional oxides including high temperature superconductors and new magnetic materials due to the high quality of the single crystals produced. The clear advantages over other melting techniques come from the fact that since there is no need for a container, any chemical reaction between the melt and the crucible material is avoided, and that by this technique the traveling solvent scheme needed for growing incongruently melting materials can be achieved [80].

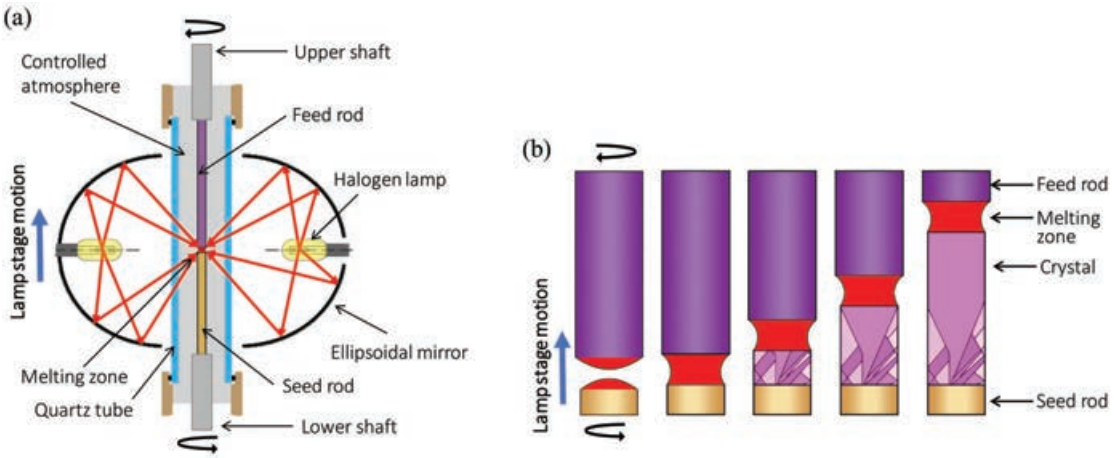

FIGURE 2.3: (a) Configuration of an infrared (IR) optical floating zone (OFZ) furnace, based on ellipsoidal mirrors. (b) Schematic illustration of the growth of congruent materials by the traveling solvent floating zone method. Figures adapted from Ref. [81].

Modern optical floating zone (OFZ) furnaces use halogen lamps and ellipsoidal mirrors as a heat source. Fig. 2.3(a) shows the scheme of an OFZ furnace. In this technique, the seed crystal is supported vertically downwards, and the polycrystalline feed rod vertically upwards. Fig. 2.3(b) illustrates the typical crystal growth scheme of congruently melting compounds. Initially, the seed and feed rods are mounted with their tips close to the focal point of the ellipsoidal mirrors. Then, the power of the halogen lamps located at the other focal points of the mirrors is increased until the tips of polycrystalline rods melt and a liquid zone is established. The melt is supported between the rods by its surface tension. The construction of the furnace with rods and mirrors mounted in separate panels allows to operate them independently. So, during the pulling

operation the molten zone travels upwards through the polycrystalline rod by moving the mirror stage up while the seed and feed are kept fixed. The driving force of the crystal growth in the FZ technique is the temperature gradient between the melt and the seed. When the hot zone moves away from the seed, the liquid cools and the material eventually crystallizes at the solid-liquid interface [see Fig. 2.3(b)]. While the melting zone travels through the feed, the crystal keeps on growing. During growth the rods rotate either in the same or in opposite directions with experimentally established rates (usually ranging from 0 to 50 rpm) with the aim of creating convection flows for mixing the materials and optimizing the shape of the solid-liquid interface.

The scheme in Fig. 2.4 summarizes in four phases the experimental activities and processes followed in this thesis regarding the growth and characterization of YBCFO single crystals. First of all, the starting polycrystalline YBCFO powders were synthesized by the solid-state reaction method. Then, the powders were shaped into compact polycrystalline rods. The optical floating zone method was then optimised to grow large single crystals from the polycrystalline rods. Finally, the quality of the grown single crystals is assessed, and the crystalographic axes of selected single-domain crystals are determined. To perform a variety of synchrotron, neutron and macroscopic properties characterization experiments, single crystals were cut into different shapes and orientations, and specific surfaces were also polished in some cases. General aspects of the experimental techniques and methodologies are exposed in the next four sections.

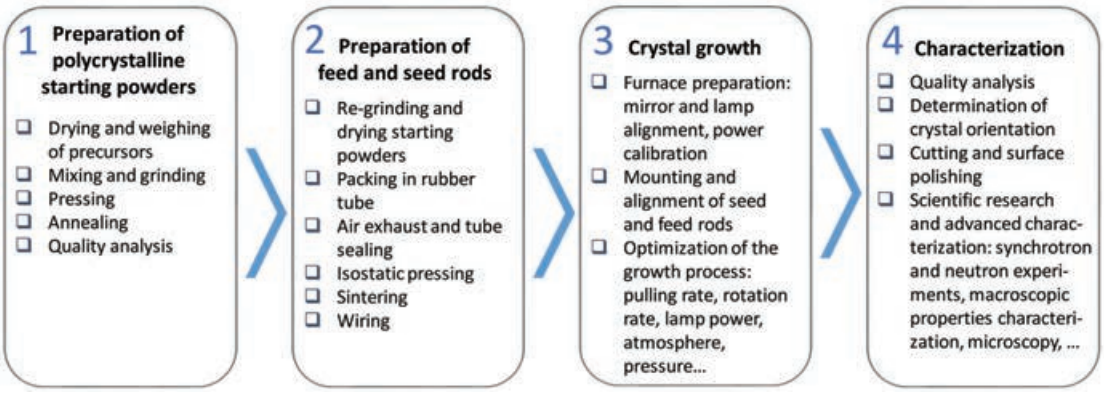

FIGURE 2.4: Experimental chart of the process followed for the fabrication of single crystals using the optical floating zone (OFZ) growth method, splitted into four phases.

2.2.1 Preparation of YBCFO polycrystalline starting powders

The starting powders used for growing YBCFO crystals were prepared following the solid-state reaction method described in Section 2.1. The drying and calcination process of the precursor oxides before weighing is of special importance here, since the composition of the starting powders has to be correct. Due to the small volume of the molten zone, an incorrect stoichiometry can lead to precipitation of impurities or segregated phases during the pulling process that can act as nucleation points obstructing the progression of the growth front or modifying the properties of the melt (melting point, viscosity, ...) leading to instability of the growth. In general, evaporation losses can also occur when volatile oxides are used and to achieve the desired stoichiometry the weights of the starting powders should reflect the mass loss of each element in the final composition, if the quantity is known.

2.2.2 Preparation of YBCFO feed and seed rods

The the qualities of the feed and seed rods are very important and have a decisive influence on the successful formation of the molten zone and the stability of the growth. Crystal growth can be started on single crystal or polycrystalline seeds. Using an oriented crystal as a seed has advantages, since it facilitates the beginning of crystallization and controls the appropriate orientation. However, since YBCFO crystal rods were not available, sintered YBCFO polycrystalline seeds with composition identical to the feed rod were used instead. When a polycrystalline rod is used as the seed, crystal growth starts from several nucleation points. In consequence, grains with different orientations are formed at the initial stage, as illustrated in Fig. 2.3(b). With growth progression, grains with favourable orientations will prevail over less favourable orientations, and the number of crystal grains will decrease gradually. Eventually, large crystal domains are formed.

For the growth of YBCFO single crystals, poycrystalline seed and feed rods of the same composition were synthesized in the form of cylindrical bars by the solid-state reaction technique. After the synthesis and quality analysis of polycrystalline YBCFO, the resulting starting powders were thoroughly ground for several hours using an automatic agate mortar to reduce as much as possible the grain size. The complete process of shaping the powders into compact polycrystalline rods is shown in Fig. 2.5.

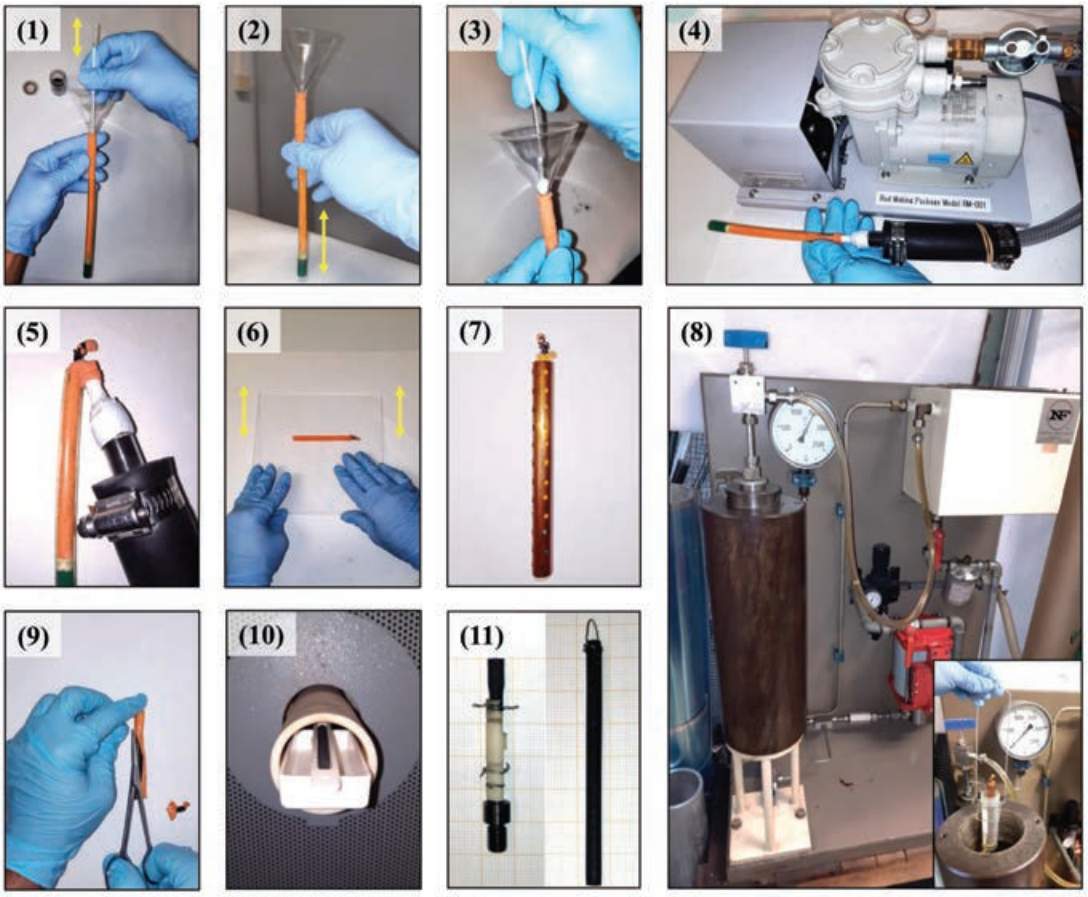

FIGURE 2.5: Steps followed for the preparation of rods. The polycrystalline powder is packed in a rubber tube, air exhausted, sealed, pressed and sintered in a tubular furnace.

First, the starting polycrystalline powder was packed into a thin rubber tube. For this, the rubber tube was introduced into a thicker flexible plastic cylinder that served as a mold to obtain better diameter and density uniformity, and to ease the manipulation of the rubber tube. The filling consisted of introducing a small amount of powder with the help of a funnel, pushing softly with a stick (1) and further compacting the powder by dropping the tube several times on a solid surface (2). Steps (1) and (2) were repeated until the tube was filled to the desired length. Then, a small piece of cotton is placed at the end side (3) to avoid the loss of powder when the air inside the tube is exhausted. The end side of the rubber tube was attached with electrical tape to a glass mouthpiece connected to vacuum pump (4). After 15 minutes, with the pump still working, a loop with the excess rubber tube was done and tied using an elastic ring to seal the tube (5). The rod was made further uniform and round by softly rolling it under a flat plastic plate (6). The packed rubber

tube was pressed by the cold isostatic press method using oil. A copper cylinder with holes drilled in it was made to keep the rod as straight as possible during the pressing (7). The rod was inserted into the oil filled vessel of the isostatic press (8). Then, oil was pumped into the vessel until reaching 1500 bar. The rod is pressed isostatically at this pressure for approximately 1 hour. After the pressing, a very fragile bar was obtained. With the help of a small precision scissors the rubber was carefully cut longitudinally, and with the help of tweezers the rubber is detached from the rod surface (9). After extracting the bar from the rubber tube, it was placed in an alumina crucible of adequate shape for sintering in a tubular furnace (10). During the sintering process the rod shrinks and the density increases, obtaining a solid and compact cylinder. It is important to mention that the pressed bars were very difficult to manipulate due to their fragility, and in most of the attempts the pressing resulted in cracked or broken bars. This problem was solved by mixing the initial powder with a very small amount of 4 wt.% solution of Poly(vinyl alcohol) (PVA) in water, obtaining more compact and solid bars thus reducing the formation of cracks or breaking during the pressing and subsequent manipulation. Finally, the wiring was done using 0.5 mm diameter Ni wire (11). A thin fissure along the rod circumference was carved using a disc saw to improve the wire grip.

During the crystal growth the seed rod is fixed to the lower shaft by means of an alumina holder, and the feed rod hangs loosely from a hook attached to the upper shaft. Since the stability of the melted zone in crystal growth depends critically on the quality of the starting rods as well as on the alignment of both the feed and the seed rods, a great deal of effort was made to create compact straight bars of uniform diameter.

2.2.3 Growth of YBCFO crystals by the Traveling Solvent Floating Zone (TSFZ) crystal growth method

An important consideration in the crystal growth of oxides containing several cations and in materials where cation substitutions are made, is whether the melting is congruent or incongruent. In a congruently melting compound the composition of ceramic rods, growing crystal and the melt is the same. In this case crystal growth will proceed easily by the direct crystallization method [Fig. 2.3(b)]. However, the congruent melting temperature is usually not exactly at the stoichiometric composition and the solidification of the melt results in a stoichiometry that is not identical to the feed. For this reason, when incongruent

melting happens, one has to use a solvent (flux) of appropriate composition to achieve the congruent melting that will lead to the desired stoichiometric composition of the grown crystal. The choice of the appropriate solvent is not always evident, and if the melting properties and phase diagrams are not known from previous works and published in the literature they must be assessed by thermoanalytical techniques as the Differential Scanning Calorimetry (DSC) or Differential Thermal Analysis (DTA). When a new material is grown and the phase diagrams are not known or the compound is complex, the so called self-flux method can work in some cases. The self-flux approach, consists of establishing the floating zone by melting the ceramic rod, and carefully adjusting the temperature and growth speed until the composition of the liquid zone stabilizes. In the case of peritectic transformation, the crystal growth starts with the precipitation of the high temperature primary phase on the seed rod.

In the case of cuprates, in which copper reacts easily with all common ceramic and metal crucible materials at high temperatures, the floating zone method is essential to obtain single crystals of cuprates. The application of both the FZ and the TSFZ methods has given succesful results in the growth of high quality single crystals of copper oxides. H. A. Dąbkowska *et al.* reported in detail the successful growth of high quality single crystals of $SrCu_2(BO)_2$ and $CuGeO_3$, as well as the $LaSrCuO_4$ and LaBaCuO high temperature superconductors by the Optical Floating Zone method [82]. The first work reporting the growth of an $YBaCuFeO_5$ crystal by an optical floating-zone method was published by Yen-Chung Lai *et al.* in 2015 [83]. For the growth of YBCFO, which melts incongruently around 1220°C, Lai *et al.* achieved the congruent melting by means of a self-adjusted flux strategy strating from a pure CuO flux.
Fig. 2.6(a) shows the pseudo-binary phase diagram of the YBCFO-CuO system based on DTA analysis reported in Ref. [83]. In the phase diagram, green arrows (temperature variation) and pink arrows (variation of melt composition) show the evolution of the melt composition along the different steps of the self-adjusted flux growth of YBCFO, also illustrated in Fig. 2.6(b) by the following steps:

- *Initial:* A CuO flux pellet is synthesized and mounted between the feed and seed rods.
- *CuO melting:* Temperature is increased until the flux pellet melts at 805°C and the rods are joined forming a pure CuO melted zone.
- *Flux self-adjustment:* At this point the crystal growth starts and the CuO melt

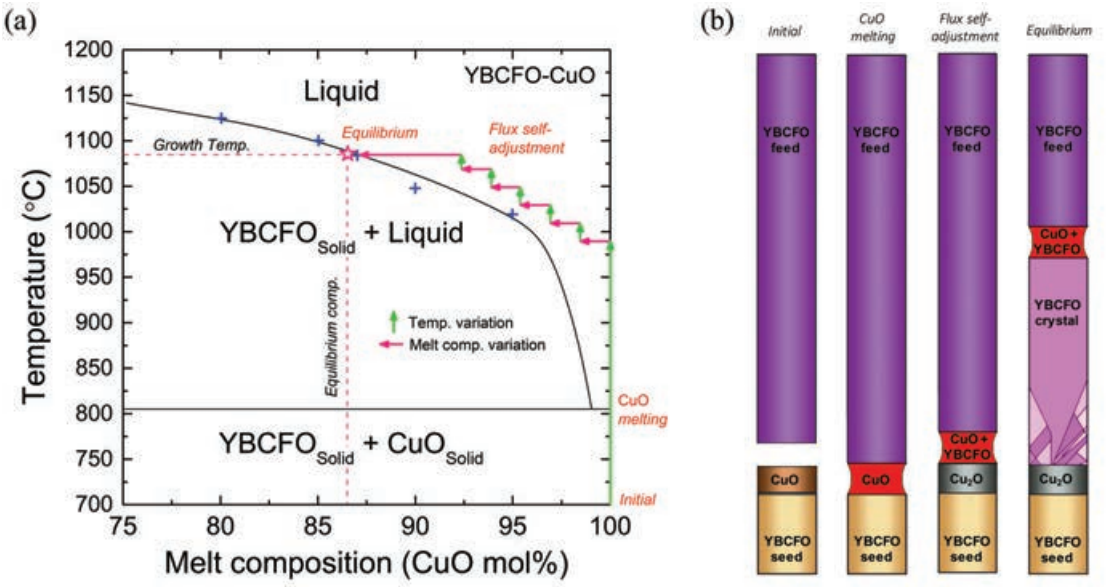

FIGURE 2.6: (a) Pseudo-binary phase diagram of YBaCuFeO5-CuO showing the eutectic temperature at 805°C and the liquidus line, adapted from Ref. [83]. The pink star represents the equilibrium composition of the melt at the growth temperature, achieved after a self-adjusted process of the initial pure CuO melt. Arrows show the evolution of the melt composition along the process. Notice that the composition of the molten zone in equilibrium depends on the temperature. (b) Scheme of the creation of self-adjusted flux for the growth of YBCFO crystals.

is continuously enriched in YBCFO from the feed rod. On the beginning of the growth a low temperature copper oxide solid phase, which is in excess, solidifies at the seed in the form of Cu_2O. During this process the temperature is carefully increased in small steps (green arrows in the phase diagram) accordingly to the growth rate until the optimal growth is achieved. During this process, the composition of the melt is self-adjusted as Cu_2O solidifies (pink arrows). The seed and feed rods are rotated at 25 rpm in opposed directions and a very slow 0.25 mm/h pulling rate are used for an optimal adjustment of the molten zone composition, and temperature homogeneity at the molten zone.

- *Equilibrium:* When supersaturation of the YBCFO phase happens, precipitation of the desired stoichiometric YBCFO single phase happens and a steady state is reached. The rotation and growth are kept, and after several days of stable growth a crystal rod is obtained.

Further details about the growth of the different YBCFO crystals studied in this thesis are given in Chapter 6.

2.2.4 Quality analisys, orientation and cutting of single crystal samples

Accurate knowledge of the quality and the orientation of single crystals is necessary to investigate the physical properties of YBCFO, since they are anisotropic and their response under external fields depend on the direction of application. Different methods were used to determine the quality of the grown YBCFO single crystals. The elemental composition of the crystals was determined with high accuracy via Inductively Coupled Plasma Optical Emission Spectroscopy (ICP-OES) and by Scanning Electron Microscopy - Energy Dispersive X-ray spectroscopy (SEM-EDX). Neutron Laue diffraction and X-ray diffraction with bidimensional detectors were used for the analysis of sample crystallinity and granularity. In combination with these crystallographic techniques, which also served to determine the orientation of the crystallographic axes, high-quality pieces of large single-domain crystals were selected and cut using high-precision diamond wire and disc saws equipped with goniometers. Two different procedures were used depending on the geometry of the pieces. The neutron Laue diffraction method was specially useful in the case of crystals with irregular shapes, while X-ray diffraction with a bidimensional detector was very efficient in the orientation of crystals where one of the crystallographic directions was known.

Orienting a crystal using neutron Laue diffraction

The Laue method, in which the single crystal is maintained fixed in an incident beam containing a wide spectral range of wavelengths, is the most convenient technique for the determination of the orientation and the symmetry of such crystals. Neutron Laue diffraction measurements on YBCFO single crystals were done at the Orient Express instrument located at the Institut Laue-Langevin (Grenoble) [84, 85]. In this case, the much larger penetration depth of neutrons compared to X-rays and the large amount of reciprocal space that can be explored using the Laue method makes it a much easier and an efficient technique compared to monochromatic single-crystal methods for the orientation and quality analysis of large crystal samples.

The Orient Express Laue neutron diffractometer and its main parts are shown in Figs. 2.7(a) and 2.7(b). In this instrument, the collimated white neutron beam is scattered by the sample, which is attached to a goniometric head fixed to the arm of a motorized table. ω is the rotation around the Z axis of the sample

table. The patterns are recorded by a two-dimensional scintillator detector in

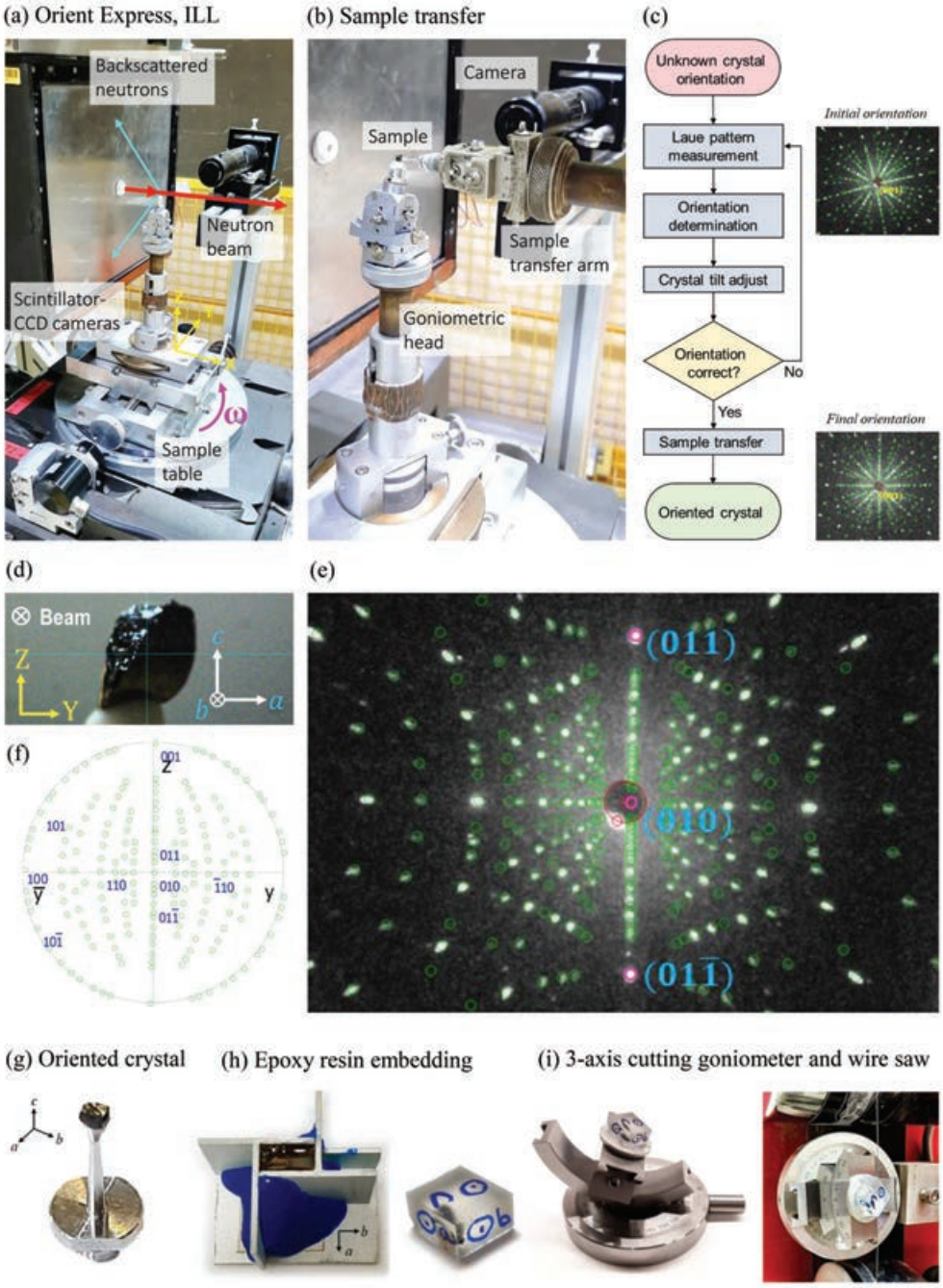

FIGURE 2.7: (a) Image of the Orient Express instrument at ILL with its main parts indicated. (b) Detail of the sample transfer arm during the transfer of an oriented crystal into a pin. (c) Schematic flow chart of the process followed to orient single crystals using the Orient Expres neutron Laue diffractometer. (d-f) Image of a single crystal with its final orientation as seen from the Orient Express camera and the corresponding Laue indexed image and stereographic projection. (g-i) Embedding of the oriented crystal in epoxy resin for cutting with a high precision diamond wire saw, in this case using a 3-axis goniometer complement.

back-reflection geometry equipped with two high-performance thermoelectrically cooled image-intensified CCD cameras. A video system facilitates the optical alignment of the crystal (XYZ translations) with respect to the incident neutron beam.

The process followed to orient single crystals using the Orient Express Laue neutron diffractometer is summarized in the scheme shown in Fig. 2.7(c). First, a Laue pattern is collected. The indexation of the diffraction peaks in the Laue image is then done using the Cologne Laue Indexation Program (Clip). By introducing the instrumental parameters, unit cell constants and symmetry, and defining spots and zones marked on the Laue photograph, Clip allows the indexing of the peaks and the refinement of the crystal orientation matrix [see Fig. 2.8]. The angles to rotate the crystal in the desired orientation are calculated using this program and then applied to the goniometric head, which allows to manipulate the crystal orientation with precision. A single neutron Laue pattern is usually enough to find the sample orientation and then rotate it to the desired orientation, but the process can be repeated to potimize the crystal orientation. Figs. 2.7(d-f) show an YBCFO crystal oriented with the b axis along X (the direction normal to the detector plane, YZ) and the corresponding indexed Laue image and stereographic YZ projection.

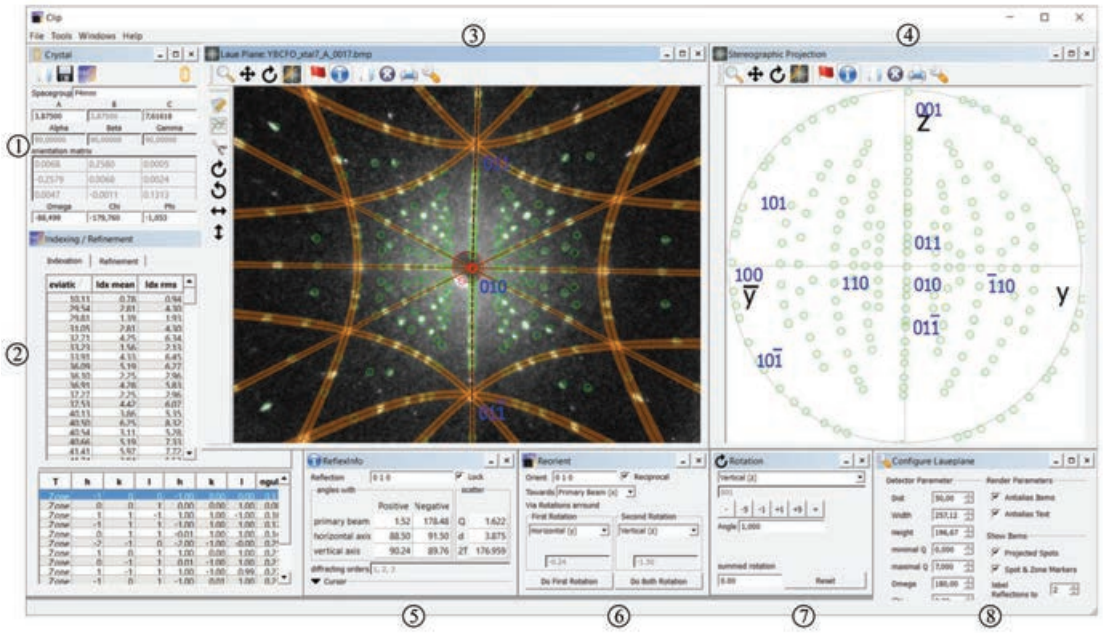

FIGURE 2.8: View of the Clip main window with different subscreens and tools: (1) crystal parameter input, (2) indexing and refinement tool window, (3) Laue plane window, (4) stereographic projection, (5) reflection information, (6-7) rotation and reorientation tools, (8) Laue instrument configuration.

Finally, the crystal with the desired orientation is glued at the tip of a pin or sample holder preserving its orientation thanks to a sample transfer arm, as shown in Fig. 2.7(b). The crystal is then ready to be cut or used for measurements on the ILL diffractometers and spectrometers. The cutting process is illustrated in Figs. 2.7(g-i). To ease the sample manipulation during the cutting, the oriented pin and samples waere embedded in epoxy resin using a mould of parallel faces and edges according to the crystallographic axes. Then, using a high precision diamond wire or disc saws, the crystals were cut leaving well defined faces to perform different types of experiments. The cutting of surfaces with more complex orientations was done using a 3-axis goniometer complement attached to a high precision diamond wire saw.

Orienting a crystal using a 4-circle X-ray diffractometer

Due to the short penetration depths of conventional X-rays produced by Cu radiation tubes, the capabilties of conventional XRD in single crystals are mostly limited to surface analysis of crystallinity, texture, epitaxial relationships and lattice parameters. Nevertheless, 4-circle X-ray diffractometers can be also used to determine the orientation of large single crystal samples. Fig. 2.9(a) shows the Bruker D8 Advance (GADDS) X-ray diffractometer equipped with a 4-circle centric Eulerian cradle, a VANTEC-500 area detector and a Cu X-ray generator (λ[Cu K_α] = 1.54 Å) used to orient YBCFO single crystals. The angle ω is the goniometer and sample stage rotation, χ is the goniometer tilt, and ϕ is the sample rotation angle. The ϕ rotation axis is always on the Z axis, typically normal to the sample surface in reflection mode diffraction. The different rotation axes and angles enable various X-ray measurement geometries.

In some cases, large pieces of YBCFO crystals are easily extracted from the grown ingot by cleaving along the ab plane, as shown in Fig. 2.9(d). Although in cleaved crystals the c axis is clearly identified as a clean, flat and bright surface, the orientation of the [100] (and [010]) directions of the tetragonal crystal lattice is unknown. Although the Laue technique allows the exploration of a large volume of reciprocal space, monochromatic XRD can only explore reciprocal space plane-by-plane at best. Even so, the measurement of pole figures in partially oriented cleaved crystals, mounted on the diffractometer with the [001] direction parallel to the sample rotation axis (Z), was found to be a very practical and efficient way to determine the orientation of the a and b axes.
The measurement of pole figures, usually used to characterize surface texture

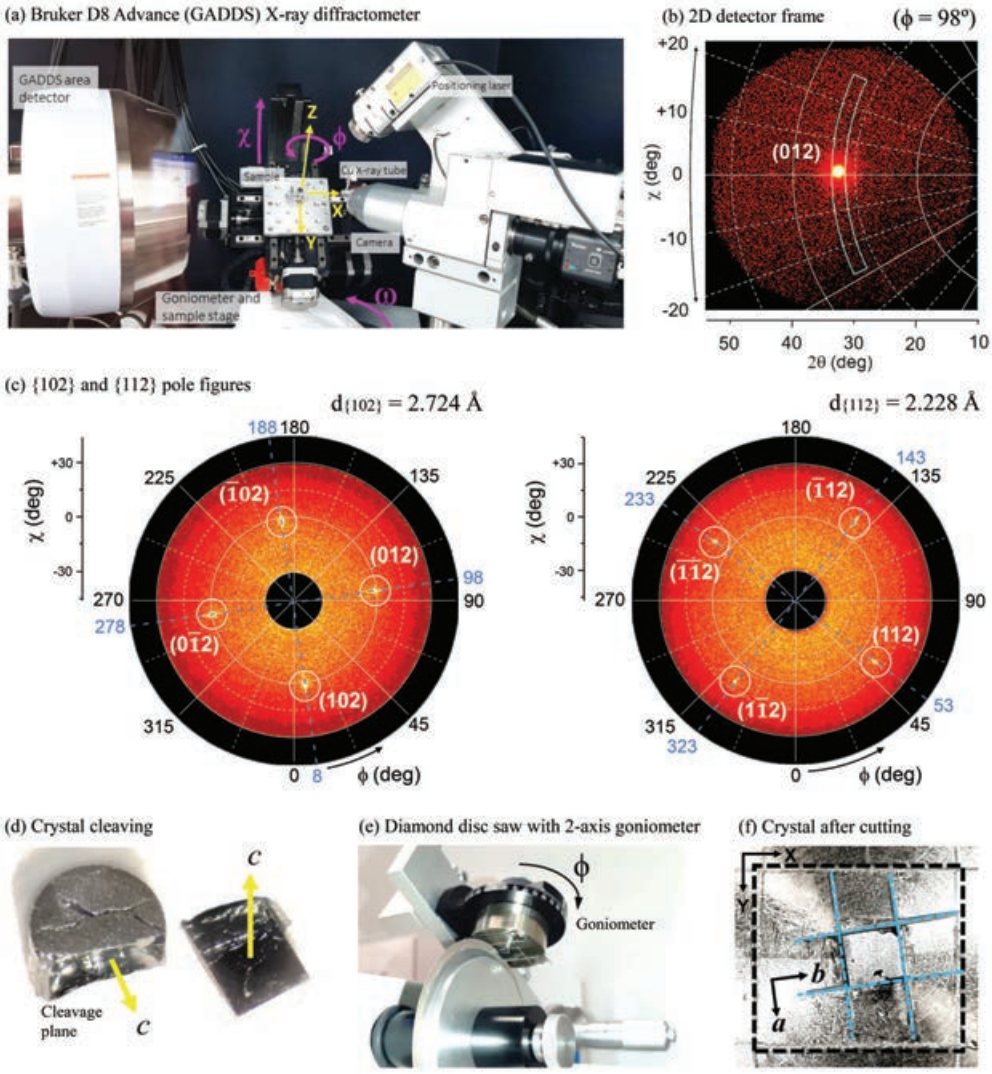

FIGURE 2.9: (a) Image of the 4-circle Bruker D8 Advance diffractometer with the GADDS area detector, showing the sample orientation angles (ω, χ, ϕ) and translation axes (XYZ) in the laboratory system. (b) GADDS 2D XRD pattern showing the (012) reflection at $\phi = 98°$. The ϕ and 2θ axes are indicated by dashed and straight white lines. The area delimited in blue shows an integration region along 2θ. (c) Pole figure scans around the YBCFO $\{102\}$ and $\{112\}$ reflections. The circles denote the reflection positions. The ϕ position values of the reflections are shown in blue. (d) YBCFO crystal samples showing the cleaved [001] surface. (e) Cutting of the oriented crystal using a high precision diamond disc saw equipped with a goniometer arm. (f) Single crystal after cutting showing the a and b crystallographic axes and the XY reference frame.

and preferred crystallite orientation, consist of setting a Bragg reflection (ω-2θ) and a tilt angle χ, collecting a series of frames varying the in-plane rotation around the center of the sample (ϕ). In the case of area detectors, the 2D frames captured at each ϕ position can be considered as the intensity distribution of the diffracted X-rays as a function of both 2θ and χ angles [86]. The 2D frames

are reduced into χ scans of constant 2θ by integrating the counts along 2θ, as shown in Fig. 2.9(b). Integrating a narrow region around a 2θ value allows to select a specific family of lattice planes (constant d spacing). The integrated χ scans are then projected into a pole figure perpendicular to the Z rotation axis. Fig. 2.9(c) presents the pole figure scans performed around the $\{102\}$ and $\{112\}$ planes for an YBCFO crystal with the c axis mounted along Z. The frames were collected from $\phi = 0^\circ$ to 360° at fine steps of 0.5° to determine with accuracy the orientation of the poles. Since YBCFO has a tetragonal symmetry, four equivalent poles separated every 90° in azimuth are observed for the $\{102\}$ and $\{112\}$ families along a complete ϕ scan.
Previous to the measurements, a reference feature of the sample (the side of the crystal or glass slide on which the crystal is attached) is set along the X or Y axis using the positioning camera of the diffractometer. Then, the positions of the $\{102\}$ poles indicate the offset angle of the perpendicular a and b axes respect to the reference feature of the sample. Finally, using a high precision diamond disc saw equipped with a goniometer arm the sides of the crystal were cut along the crystallographic axes using the measured offset angle [see Figs. 2.9(e) and 2.9(f)].

Polishing of single crystal surfaces

The lapping of oriented surfaces was done to perform measurements that require flat parallel faces for a precise application of electric or magnetic fields. A final polishing was done in the case of techniques requiring very smooth surfaces, such as Scanning Electron Microscopy or X-ray resonant magnetic scattering.

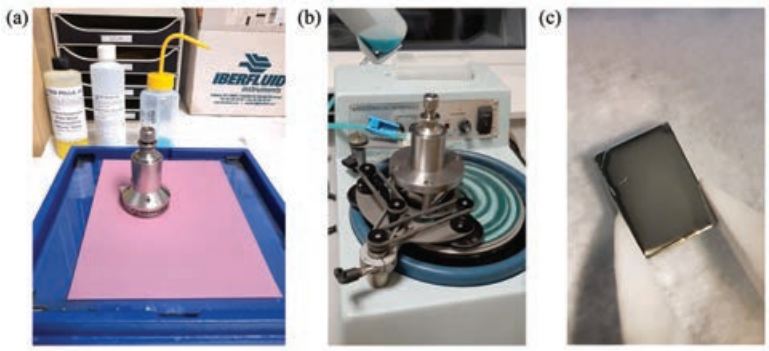

FIGURE 2.10: (a) Hand lapping process using abrasive Al oxide sheets. (b) Polishing process using small grain abrasive suspensions (< 3 μm). (c) Appearance of the sample surface after final polishing.

For the lapping process, the crystal was attached to the holder of a precision lapping fixture using mounting wax. The lapping was done by hand using abrasive 12 μm aluminium oxide sheet on top of a flat glass lapping tray [Fig. 2.10(a)]. The lapping was done by repeating by hand movements drawing a ∞ pattern until highly planar and parallel faces were obtained. The final polishing was subsequently done using small abrasive grain suspensions on a soft polishing cloth mounted in a rotating disc polisher. The polishing was done in different steps using abrasive suspensions of successively smaller grains: 3 μm diamond suspension, 1 μm diamond suspension, and 0.05 μm colloidal silica suspension. Fig. 2.10(c) shows the crystal mirror surface after the final polishing process.

Chapter 3

Characteriztion techniques and instrumentation

The results presented in this thesis were obtained by means of a variety of experimental techniques. The advanced characterization of the structural and magnetic order properties, as well as their anisotropic responses under external magnetic and electric fields was accomplished by the realization of experiments in large research facilities: elastic and inelastic scattering techniques were used in synchrotron and neutron facilities. This chapter provides a review of the main aspects of the research related with the characterization techniques, beamlines and instruments, and computational methods and programs used for the analysis of the data collected different experiments.

3.1 X-ray diffraction

X-ray diffraction (XRD) is a technique widely used for the analysis of crystalline structures. X-rays are electromagnetic waves with wavelengths ranging from ultraviolet to gamma radiation. In particular, the phenomenon of diffraction occurs when the wavelength is of the same order of magnitude as the typical distances between the atoms of the crystal, and for that reason they are so convenient. When the beam of photons goes through the material, they interact with the electronic cloud that surrounds the atoms of the crystal and as a result secondary waves are generated. These secondary waves by interfering with each other will form the transmitted beam, which consist of a diffraction pattern that analyzed properly allows the crystal structure characterization.

Diffraction conditions

Although in the majority of directions the interference will be destructive, constructive interference happend in some specific directions that satisfy certain conditions. If each point in the crystal has a certain density of electrons, and therefore each point acts as a center of dispersion, we consider two of these centers in O i O' separated by the vector $\mathbf{r}$ (Fig. 3.1). When a plane wave with vector $\mathbf{k}$ goes through the crystal, the dispersion centers are excited and become sources of emission of secondary spherical waves that will interfere between them. If we consider the resulting wave in a given direction, which will now

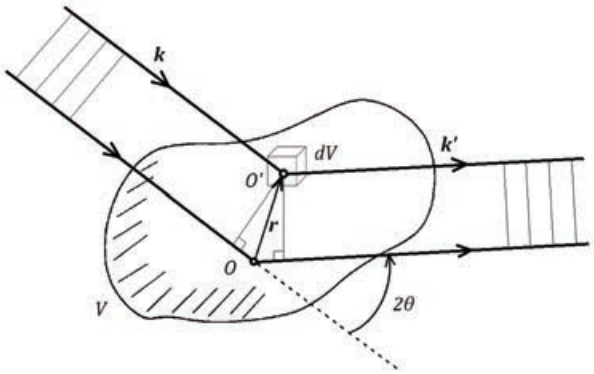

FIGURE 3.1: Scheme of the dispersion of a plane wave by two dispersion centers in O and O'.

have a vector $\mathbf{k}'$, the phase difference between the incident wave and the diffracted wave will be $(\mathbf{k}-\mathbf{k}')\cdot\mathbf{r}$, and therefore in the transmitted wave we will have a phase factor of $e^{i(\mathbf{k}-\mathbf{k}')\cdot\mathbf{r}}$. The amplitude of the transmitted wave is proportional to the number of electrons $\rho(\mathbf{r})dV$ of the point from which it was re-emitted, it is only necessary to integrate over the total volume to obtain the structure factor, which will also be proportional to the total amplitude of the diffracted wave:

$$F = \int_V \rho(\mathbf{r}) e^{-i\mathbf{k}\cdot\mathbf{r}} dV \tag{3.1}$$

where it has been defined $\mathbf{k} = \mathbf{k}' - \mathbf{k}$. Due to the periodic nature of the crystals, the electron density must verify the following condition:

$$\rho(\mathbf{r}) = \rho(\mathbf{r} + \mathbf{T}) \tag{3.2}$$

where $\mathbf{T} = n_1\mathbf{a}+n_2\mathbf{b}+n_3\mathbf{c}$ is a translation vector of the crystal lattice, $n_1, n_2, n_3 \in \mathbb{Z}$ and $\mathbf{a}, \mathbf{b}, \mathbf{c}$ are the base vectors of the lattice. In this particular case the electronic density can be decomposed into Fourier series as

$$\rho(\mathbf{r}) = \sum_{\mathbf{Q}} \rho(\mathbf{Q}) e^{i\mathbf{Q}\cdot\mathbf{r}} \tag{3.3}$$

where $\mathbf{Q} = h\mathbf{a}^* + k\mathbf{b}^* + l\mathbf{c}^*$ is the dispersion vector, $h, k, l \in \mathbb{Z}$ i $\mathbf{a}^*, \mathbf{b}^*, \mathbf{c}^*$ are the vector base of the reciprocal lattice[1]. Indeed, doing $\rho(\mathbf{r} + \mathbf{T})$ in equation (3.3), applying the definition of vectors $\mathbf{T}$ and $\mathbf{Q}$ and using the properties of the lattice vectors it can be checked that the condition of periodicity (3.2) is satisfied. Finally, replacing (3.3) in (3.1) the following expression for the structure factor is obtained:

$$F(\mathbf{Q}) = \sum_{\mathbf{Q}} \int_V \rho(\mathbf{Q}) e^{i(\mathbf{Q}-k)\cdot\mathbf{r}} dV \tag{3.4}$$

It is easy to realize that the value of F is maximum when $\mathbf{k}$ is equal to a vector of the reciprocal lattice, that is to say $\mathbf{k} = \mathbf{k}' - \mathbf{k} = \mathbf{Q}$, and instead it becomes negligible otherwise. On the other hand, since we are considering only elastic dispersion, we will have $k = k'$, that is to say that the module of the incident wave vector can not change after being diffracted[2]. Combining these two results we obtain the condition for constructive interference:

$$2\mathbf{k}\cdot\mathbf{Q} = Q^2 \tag{3.5}$$

This diffraction condition, which can be understood very intuitively from the Ewald sphere in the reciprocal space [Fig. 3.2(a)], is equivalent to the well-known Bragg's law:

$$2d_{(hkl)} \sin\theta_{(hkl)} = \lambda \tag{3.6}$$

where $d_{(hkl)}$ is the distance between consecutive (hkl) planes and $2\theta_{(hkl)}$ is the angle between the incident and the diffracted beam [Fig. 3.2(b)]. The interplanar distance of a set of planes with Miller indices (hkl) can be calculated as

$$d_{(hkl)} = \frac{2\pi}{|\mathbf{Q}|} = \frac{2\pi}{|h\mathbf{a} + k\mathbf{b} + l\mathbf{c}|} \tag{3.7}$$

[1]The conditions that a lattice with vectors $\mathbf{a}, \mathbf{b}, \mathbf{c}$ and another lattice with vectors $\mathbf{a}^*, \mathbf{b}^*, \mathbf{c}^*$ must satisfy to be reciprocal are
$\mathbf{a}\cdot\mathbf{b}^* = \mathbf{a}\cdot\mathbf{c}^* = \mathbf{b}\cdot\mathbf{a}^* = \mathbf{b}\cdot\mathbf{c}^* = \mathbf{c}\cdot\mathbf{a}^* = \mathbf{c}\cdot\mathbf{b}^* = 0$
$\mathbf{a}\cdot\mathbf{a}^* = \mathbf{b}\cdot\mathbf{b}^* = \mathbf{c}\cdot\mathbf{c}^* = 2\pi$

[2]In an elastic dispersion the energy of the dispersed photon is equal to that of the incident photon, $E = E'$. Since $E = \hbar\omega = k\hbar c$, it is clear that $k = k'$.

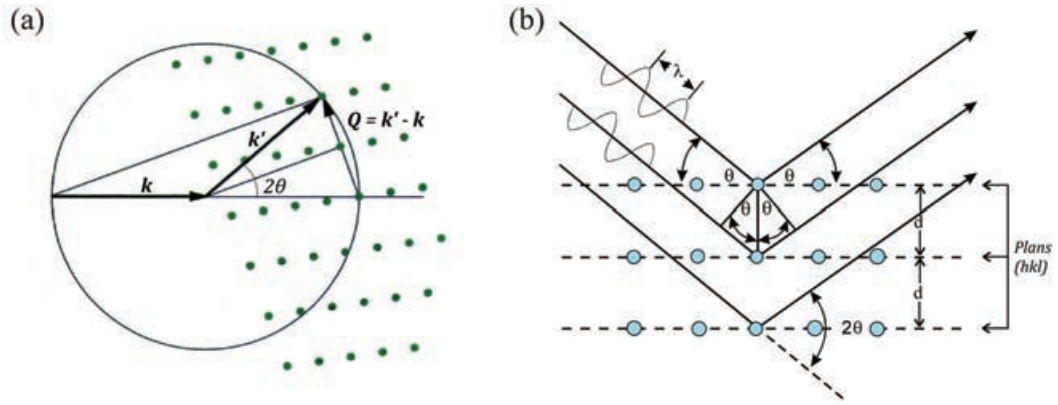

FIGURE 3.2: (a) Ewald construction in a 2D reciprocal lattice. (b) Scheme of Brag's law.

X-ray diffraction in a real crystal

To calculate the structure factor, the atomic factor $f_j(\mathbf{Q})$ of each atom in the unit cell is defined as

$$f_j(\mathbf{Q}) = \int_V \rho_j(\mathbf{Q}) e^{i\mathbf{Q}\cdot\mathbf{r}} dV \tag{3.8}$$

where $\rho_j(\mathbf{Q})$ is the electronic density of the j-atom. In general, the form factor of an atom depends on the type and characteristics of the dispersion process involved, which in turn also depends on the nature of the radiation (X-rays, neutrons or electrons). From the form factors the structure factor (3.4) can be written as

$$F(\mathbf{Q}) = \sum_{j=1}^{N} f_j(\mathbf{Q}) e^{i\mathbf{Q}\cdot\mathbf{r}_j} \tag{3.9}$$

where N is the number of atoms in the unit cell and $\mathbf{r}_j = x_j\mathbf{a} + y_j\mathbf{b} + z_j\mathbf{c}$ is the position of the j-atom inside the cell. The reality shows that atoms vibrate with respect to their equilibrium position due to thermal oscillation, making the electronic cloud more diffuse and reducing the dispersion efficiency for the larger angles. This effect can be taken into account by applying the Debye-Waller term $e^{-Bsin^2\theta/\lambda^2}$. Finally, the structure factor is:

$$F(\mathbf{Q}) = \sum_{j=1}^{N} f_j(\mathbf{Q}) e^{-B_j sin^2\theta/\lambda^2} e^{i\mathbf{Q}\cdot\mathbf{r}_j} \tag{3.10}$$

where B_j atomic temperature factor of the j-atom. It can also be expressed as a function of (hkl) as

$$F(hkl) = \sum_{j=1}^{N} f_j(hkl) e^{-B_j sin^2\theta/\lambda^2} e^{2\pi i(hx_j + ky_j + lz_j)} \tag{3.11}$$

Finally, the intensity of the diffracted wave for each crystalline plane with Miller indices (hkl), which is the measured magnitude during diffraction experiments, can be described from the structure factor as

$$I(hkl) \propto |F(hkl)|^2 \tag{3.12}$$

It is important to note that the angular position of each (hkl) reflection, and therefore of each intensity maximum, will depend only on the cell parameters (shape of the unit cell) and can be determined from Brag's law (3.6). Instead, the intensity $I(hkl)$ of each reflection will depend on the configuration and coordinates of the atoms (content of the unit cell) and can be determined from the structure factor (3.11).

X-ray powder diffraction

X-ray powder diffraction (XRPD) is one of the most widespread analytical technique for structural analysis and phase identification of crystalline materials, as it can be readily obtained from conventional laboratory diffractometers, where the radiation source is commonly an X-ray tube with a copper anode (λ[Cu K_α] = 1.54 Å). The analyzed powder sample consists of a large number of randomly oriented microcrystals, with dimensions that can be approximately 1-10 μm. The principles that describe diffraction in a single-crystal are also applied to polycrystals. In the case of polycrystalline samples, for a particular orientation of the incident beam, we will have multiple (hkl) planes (each with a different orientation of the diffracted wave) that satisfy the Bragg diffraction condition due to the random orientations of the microcrystals. Therefore, each (hkl) reflection will correspond to a diffraction cone with semi-vertical angle $2\theta_{(hkl)}$ (Fig. 3.3).

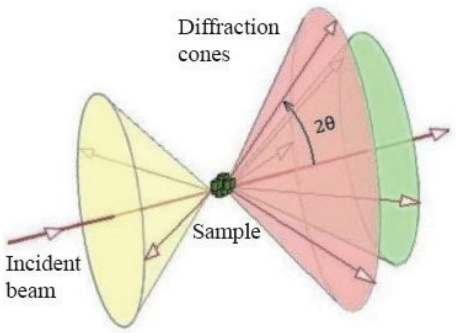

FIGURE 3.3: Debye-Scherrer cones obtained from diffraction of a monochromatic X-Ray beam by crystalline powder sample.

3.1.1 X-Ray diffraction using synchrotron radiation

Having covered the theory for X-ray powder diffraction (XRPD), we now introduce into synchrotron radiation (SR) attempting to convey the most important aspects relevant to the current study. We also list the great advantages and benefits of synchrotron X-ray powder diffraction (SXRPD) in front of conventional laboratory X-ray techniques. For a better understanding of SR theory, the reader is referred to the work of Willmott [87].

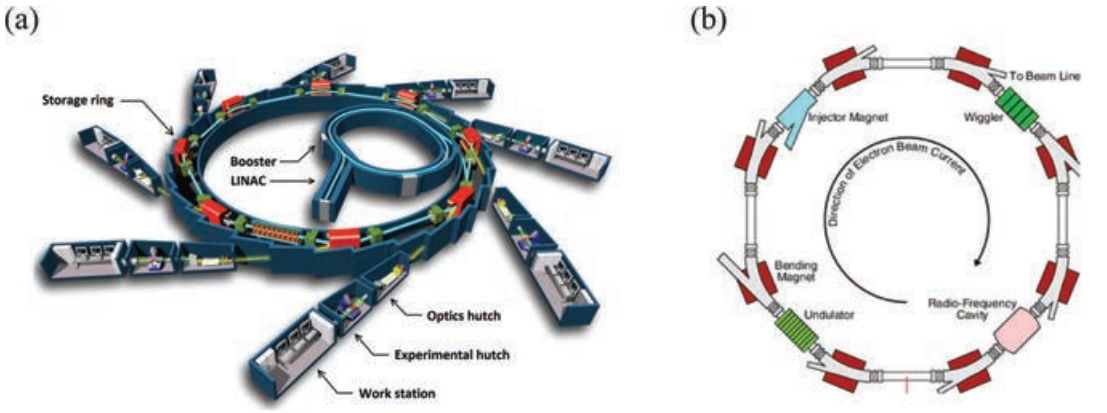

FIGURE 3.4: (a) Illustration of a synchrotron radiation facility. (b) Scheme of a storage ring.

Briefly, a typical synchrotron source consists of a linear accelerator (LINAC) that produces and pre-accelerates electrons, a booster ring where the projected electrons are further accelerated, and an evacuated electron storage ring [Fig.3.4(a)]. Synchrotron light (electromagnetic radiation) is produced within the storage ring, where the high-energy electrons circulate in a closed path at highly relativistic velocities and its trajectory is curved and modified by different types of devices distributed along the storage ring [Fig.3.4(b)] using very intense magnetic fields perpendicular to the orbital plane. The acceleration that the electrons undergo causes the emission of radiation –also called Bremsstrahlung– tangentially to the orbital trajectory. Different types of devices such as undulators, wigglers or bending magnets are used to give the radiation emitted a certain structure or polarization. The radiation is then focused and/or monochromatized using X-ray optics at the beamlines positioned tangential to the storage ring, where the experiments are performed with the selected configuration. Some of the main properties of the synchrotron radiation are the following:

- Wide and continuous spectrum energy: the electromagnetic spectrum ranges from radiofrequency to hard X-rays continuously, allowing the users to tune the wavelength required for special experiments;
- High flux and brlliance (combined with high collimation): radiation is emitted in a small angular range along the tangential path of the electron trajectory, which causes the number of photons emitted per second and steradian to be very high;
- Beam stability and size tunability;
- Polarization: the beam is naturally linear polarized in the orbital plane of the electrons, but elliptical or circular polarization is achievable by means of undulators;
- Time structure: pulsed time structure of the radiation, with pulse of the order of picoseconds or femtoseconds, allowing resolution of processes on the same time scale;
- Partially coherent radiation.

The use of synchrotron radiation in powder samples presents greater possibilities compared to conventional X-ray sources due to the exceptional properties of this radiation that allows to obtain high resolution powder diffractograms (HRPD). The main advantages are the following:

- High photon wavelength resolution ($\Delta\lambda/\lambda \sim 2 \cdot 10^{-4}$);
- Very high signal-to-noise and signal-to-background ratios;
- Ultrafast data acquisition;
- Tunable photon energy to use very wavelengths, allowing to collect data at very high angles while reducing the absorption in heavy elements;
- High angular resolution of the peaks (FWHM);
- Very high counting statistics in few seconds.

Furthermore, some experiments may require special measurement conditions, such as in situ, and controlled ambient setups including cryogenic coolers, high-temperature furnaces, and high-pressure anvil cells, which are accessible at most synchrotron-based diffraction stations, yet generally cannot be implemented in a conventional laboratory-based diffractometer. The tunability and high brilliance of synchrotron X-rays, which is related to the photon flux and the collimation of the beam (*i.e.*, how the beam diverges as it propagates), as well as the size of the source, are also essential perform X-ray diffraction measurements at very high pressures using a Diamond Anvil Cell (DAC), which usually requires a very small volume of sample.

3.1.2 BL04-MSPD beamline (Alba Synchrotron Light Facility)

The Synchrotron X-ray Powder Diffraction (SXRPD) data for the structural characterization of the materials investigated was acquired at the Materials Science and Powder Diffraction Beamline (BL04-MSPD) of the Alba Synchrotron Light Facility [88]. The BL04-MSPD beamline has two experimental end stations, one devoted to high angular resolution powder diffraction (HRPD) and the second one dedicated to high pressure and micro diffraction experiments. In this beamline, the energy of the photons can be selected in a range from 8 keV to 50 keV (wavelength from 1.56 Å to 0.25 Å). The beam, after leaving the wiggler, is filtered, collimated and monochromated by a double crystal of Si(111) refrigerated with liquid nitrogen before reaching the sample.

High angular Resolution Powder Diffraction end station

The High angular Resolution Powder Diffraction (HRPD) station of the beamline consists of a three-circle diffractometer [Fig. 3.5(a)]. The outer and middle circles support respectively the high-angular resolution Multi Analyzer Detection (MAD26) setup and the high-throughput Position Sensitive Detector (PSD) MYTHEN. The inner circle is equipped with an Eulerian Cradle on which all sample environments are mounted. An ALBA designed 4 capillaries holder can be used with either cryostream to perform measurements at low temperatures and high temperatures [Fig. 3.5(b)].

- **MAD26 high reslution detector**: the MAD26 is a detector that allows to make high resolution measurements. This detector is convenient for cases where the objective is to obtainin very exhaustive information of a sample at one or a few specific temperatures. It has 13 channels with Si(111) and Si(220) crystals with an angular separation of 1.5°. It works in a range of energies from 8 keV to 50 keV.
- **MYTHEN detector**: the MYTHEN detector consists of 6 1D Mythen modules and allows to make measurements of less resolution than the MAD26 detector, but with a much smaller data acquisition time. For this reason, this detector is convenient in cases where we a large number of patterns are collected, as in temperature-dependent experiments to obtain detailed information on the thermal evolution of the crystal structure. It works in a range of energies from 8 keV to 30 keV and covers an angular range of 40°.

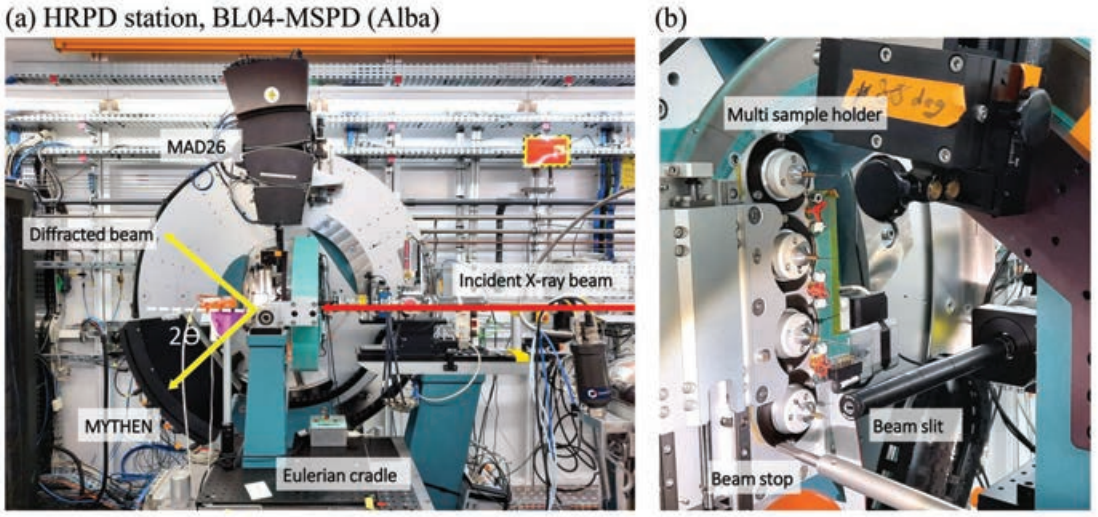

FIGURE 3.5: (a) View of the High Resolution Powder Diffraction (HRPD) station of the BL04-MSPD beamline showing the MYTHEN and MAD26 detectors and the Eulerian Cradle. (b) Detail of the multi sample holder with four sample capillaries allocated in it.

High Pressure Powder Diffraction end station

The High Pressure (HP) Powder Diffraction station, with its focused beam (microns size) is principally devoted to pressure experiments using Diamond Anvil Cells (DACs). The station consists of two stacks of linear and rotation stages [Fig. 3.6(a)]. The first stack contains the sample table, with vertical and horizontal movement stages allowing XYZ translations and a rotation stage (ω angle). The second stack contains a SX165 (Rayonix) bidimensional CCD camera.

Fig. 3.6(b) shows a scheme of the experimental setup. In our case, a membrane Diamond Anvil Cell (DAC) consisting of two diamonds faced one to each other was used [Fig. 3.6(c)]. Between them, a gasket with a hole drilled in the middle defines the cavity where the sample and the calibrant are loaded. The applied pressure is controled by the membrane of the DAC which is inflated applying force to the mobile anvil whereas the other anvil is fixed. The pressure inside the cell is determined by monitoring the cell parameters of the calibrant whose dependence of the unit cell volume with pressure (equation of state) is known.

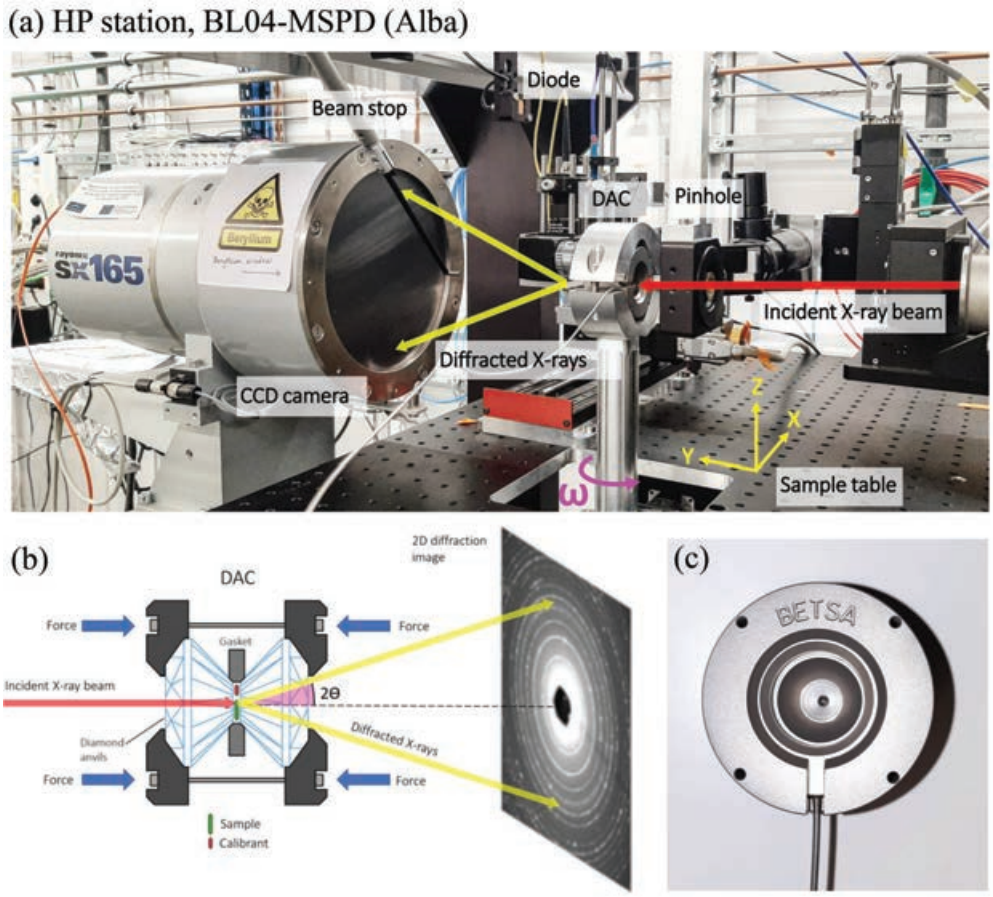

FIGURE 3.6: (a) Image of the High Pressure (HP) Powder Diffraction station of the BL04-MSPD beamline showing the sample stack with a DAC mounted and the detector stack with the bidimensional CCD camera. (b) Schematic illustration of the high-pressure synchrotron radiation setup using a diamond anvil cell (DAC). (c) Detail of the membrane DAC used in the HP diffraction measurements.

3.2 Neutron diffraction

3.2.1 Neutrons vs X-rays

Complementary to X-ray scattering, neutron scattering is another powerful tool for the characterization of the periodic nuclear and spin orders in polycrystalline materials and single crystals. The mass of neutrons in thermalized beams gives them a *de Broglie* wavelength comparable to the interatomic distances in crystalline materials, which is an essential condition for diffraction. Besides that, neutrons are neutral particles. Hence, as a difference of X-rays, which are primarily scattered at the electrons of atomic shells via electromagnetic interaction, neutrons interact with the atomic nuclei via very short-range strong nuclear interaction (nuclear scattering), as illustrated in Fig. 3.7(a). Neutrons

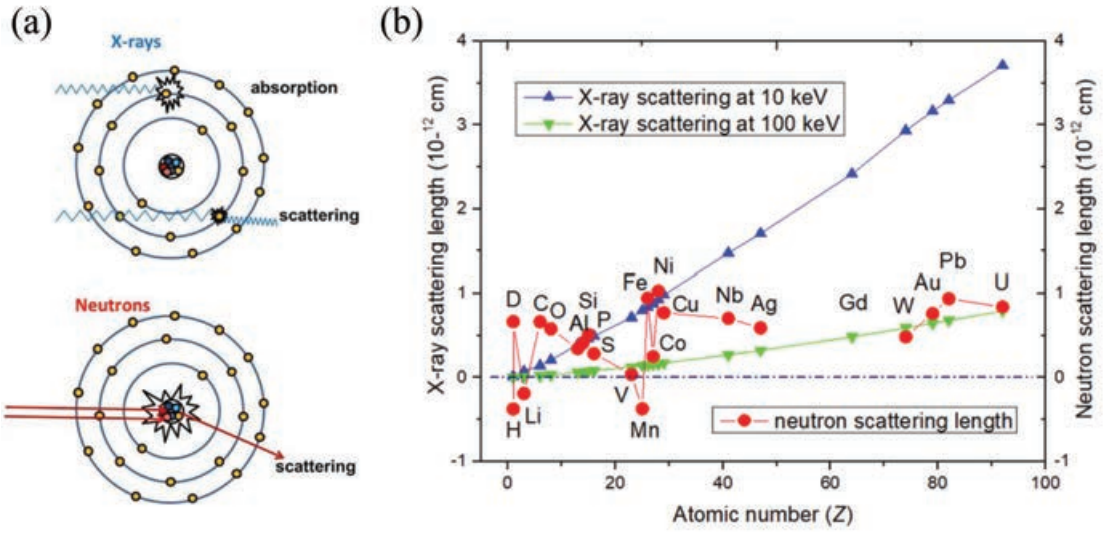

FIGURE 3.7: (a) Schematic illustration of the different nature of the scattering processes in X-rays and neutrons. (b) X-ray and neutron scattering length of some selected elements. X-ray scattering lengths at photon energy of 10 keV and 100 keV are also plotted for comparison. While scattering power of X-rays generally scales systematically with electron density and therefore with the atomic number Z of an atom, neutron scattering power from atoms is rather random, due to complicated short-range nuclear interaction between neutron and nuclei. Figure adapted from Ref. [89].

are therefore able to penetrate deeper into bulk matter without being scattered or absorbed, providing information about the whole volume of the sample, and not only about its surface. Another distinct aspect of neutrons is that they are fermionic particles carring nonzero spin S = 1/2, which interacts with the unpaired spin and orbital magnetic moments of atoms via magnetic dipole-dipole interactions (magnetic scattering). In virtue of the above mentioned properties, neutrons are a unique tool not only to study the crystal stucture of crystalline materials, but also their magnetic structure.

The measure of the strength of the neutron-nucleus interaction is represented by the neutron scattering length, which depends sensitively on the details of the nuclear interaction, and thus on the nuclear properties (isotopes, nuclear spin, energy levels, etc.) of every particular type of nucleus (*i.e.*, element and isotope). As a result, the neutron scattering length varies seemingly irregularly across the periodic table. This can be seen from Fig. 3.7(b) showing the neutron scattering length of different elements. The irregular variation of neutron scattering length means that, in contrast to X-rays, which are very transparent to light elements, neutrons are very sensitive to some light elements (namely, hydrogen, oxygen or carbon). Furthermore, in many cases, elements having

similar Z values in the periodic table can have vastly different neutron scattering lengths from one another. Because of this differing atomic sensitivities with X-rays, together with its unique magnetic sensitivity, neutron is often regarded as a complementary probe to photon-based methods. In particular, in the current study this concerns the contrast in the scattering length between Fe and Cu, which has a special relevance for the quantification of Fe/Cu cation disorder in $YBaCuFeO_5$ [see App. A].

3.2.2 Magnetic diffraction

In the case of neutrons the analysis of the theory of diffraction is similar to that made for X-rays. In this case, the structure factor due to the interaction with the nuclei of the atoms will be

$$F_N(\mathbf{Q}) = \sum_{j=1}^{N} b_j e^{i\mathbf{Q}\cdot\mathbf{r}_j} e^{-B_j sin^2\theta/\lambda^2} \tag{3.13}$$

where b_j is the scattering length, which depends on the interaction between the neutron and the atomic nuclei. In addition to purely *nuclear scattering*, the *magnetic scattering* must also be considered, and it is described as:

$$F_M(\mathbf{Q}) = \sum_{j=1}^{N'} S_{\mathbf{k}j} f_{Mj}(\mathbf{Q}) e^{i\mathbf{Q}\cdot\mathbf{r}_j} e^{-B_j sin^2\theta/\lambda^2} \tag{3.14}$$

where N' is the number of magnetic atoms in the unit cell, $f_{Mj}(\mathbf{Q})$ is the magnetic form factor of the j-atom in the unit cell, and $\mathbf{S}_{\mathbf{k}j}$ is the Fourier component associated to the propagation vector $\mathbf{k}$ of the magnetic moment distribution. Remember that the magnetic moment distribution $\mathbf{m}_{lj}$ in the crystal (referred to the atom j in the magnetic unit cell l) is a periodic function that can be Fourier expanded as:

$$\mathbf{m}_{lj} = \sum_{\mathbf{k}} \mathbf{S}_{\mathbf{k}j} e^{-2\pi i\mathbf{k}\cdot\mathbf{R}_l} \tag{3.15}$$

where the $\mathbf{S}_{\mathbf{k}j}$ Fourier coefficients satisfy the relation $\mathbf{S}_{\mathbf{k}j} = \mathbf{S}^*_{-\mathbf{k}j} \cdot \mathbf{m}_{lj}$. This expression represents the magnetic vector distribution that gives the magnitude and direction of any magnetic moment.

On the other hand, bearing in mind the expression for the magnetic interaction operator [$\mathbf{D}_\perp = \mathbf{Q} \times (\mathbf{M} \times \mathbf{Q})$] where $\mathbf{M}$ is the magnetic operator and $\mathbf{Q}$ is the scattering vector, it can be proved that the magnetic neutron scattering

is only sensitive to the perpendicular direction of the magnetic moment ($M^{\perp}$) to the scattering vector **Q** [90]. Finally, the magnetic contribution in the intensity of the diffracted beam can be determined using the general Halpern and Johnson formula:

$$I(\mathbf{Q}) \propto |F_M^{\perp}(\mathbf{Q})|^2 = |F_M(\mathbf{Q})|^2 - (\mathbf{e} \cdot F_M(\mathbf{Q}))^2 \tag{3.16}$$

where $F_M(\mathbf{Q})$ is the magnetic form factor, $F_M^{\perp}(\mathbf{Q})$ is the projection of the magnetic form factor along the perpendicular direction and e is the unit vector along the scattering vector **Q**.

3.2.3 Neutron diffraction instruments

The structural and magnetic properties of most of the compounds involved in this thesis were analyzed and characterized by Neutron Powder Diffraction (NPD) or Single Crystal Neutron Diffraction (SCND) at the high-flux reactor of the Institut Laue Langevin (Grenoble, France). The neutron scattering instruments used in this work are briefly described next:

D1B (CRG): this instrument is a high intensity two-axis powder diffractometer, useful for real time experiments and very small samples because of its high efficiency Position Sensitive Detector (PSD) [91]. A great number of experiments performed on D1B concern the determination of magnetic structures. At small angles where magnetic peaks are expected, a high spatial resolution can be achieved, the FWHM reaches 0.25° at 1.28 Å and 0.3° at 2.52 Å (for a sample of 5 mm in diameter). D1B is equipped with a $^3He/CF_4$ position sensitive detector composed of a system of multi electrodes with 1280 wires covering a 2θ range from 0.8° to 128°. Its specially designed cryostat is known for its low background crucial for some experiments with small intensity changes, the sample can be measured in the interval 1.5-300 K. A dedicated vanadium furnace achieving up to 1200 K is also available. A fast detection of phase transitions can be obtained by scanning temperature. A complete thermal variation of the diffraction patterns (1.5-300 K) can be achieved in few hours (3-5 h).

D20: this instrument is a very high intensity 2-axis diffractometer equipped with a large microstrip detector [92]. Due to the extremely high neutron flux, it opens up new possibilities for real-time experiments on very small samples. A pyrolitic graphite HOPG (002) monochromator in reflection position with fixed vertical focusing offers a wavelength of 2.4 Å at a take-off angle of 42°. A

variable vertical focusing Ge (113) monochromator gives increased resolution at higher take-off angles and several out of plane reflections are also accessible. The PSD housing of aluminium provides a detection zone about 4 m long by 0.15 m high. The major interests of the micro-strip detection system for the instrument D20 are the precise and perfectly stable geometry, resulting in a very homogeneous response and a very high stability, the possibility of achieving very high counting rates because of the small distance between the anode and cathode (170 μm), allowing a fast evacuation of the positive ions. The Data Acquisition System (DAS) has a parallel input for up to 1600 cells.

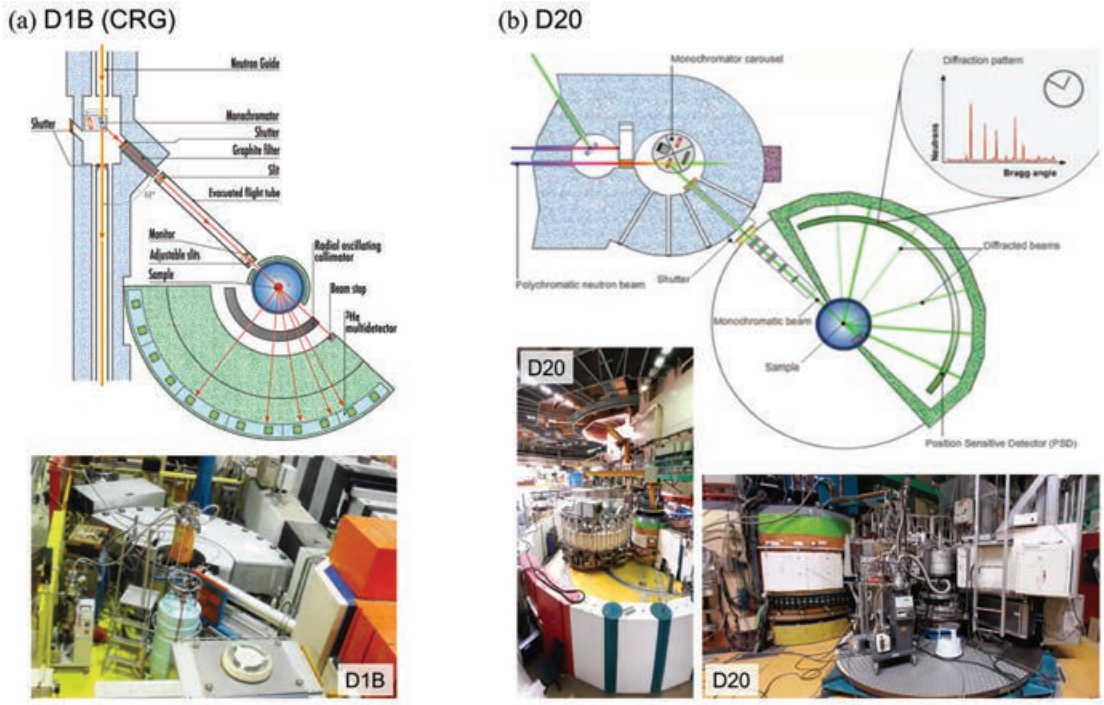

FIGURE 3.8: Layout and experimental setup on the two different high intensity 2-axis diffractometers used for NPD experiments, located at the Institut Laue Langevin (Grenoble): (a) the D1B-CRG instrument and (b) the D20 hot neutron diffractometer.

D9: it is a hot neutron four-circle diffractometer used for precise and accurate measurements of Bragg intensities up to very high momentum transfer [93]. The resolution allows routine recording of extended data sets for the detailed study of atomic disorder and atomic thermal motions. The wavelength of neutrons is among the shortest available at any reactor in the world. Among other research areas, this diffractometer is used to study structural phase transitions and magnetic structures. Because of the short neutron wavelength very small atomic displacements can be identified, accurate to typically 0.001 Å. This instrument is placed on a Tanzboden floor allowing a continuous choice

of wavelengths in the range 0.35-0.85Å. In its standard "four-circle" geometry the sample holder sits on an Eulerian cradle with offset χ-circle. D9 is equipped with a small 2D area detector which is particularly useful for rapid alignment and characterization of samples and for studies of satellites and twinning. It covers $8 \times 8^{\circ}$ in 32×32 pixels. Programs are available for intensity integration using this detector. Measurement of one Bragg reflection normally takes a few minutes, and recording of a full set of data takes a few days. If the crystal is studied as a function of temperature, pressure etc., the total measurement time is about a week.

D10: this is a single-crystal four-circle diffractometer with optional energy analysis as on three-axis spectrometers [94]. It possesses a unique four circle dilution cryostat for temperatures down to 0.1 K. Due to its good momentum resolution with relatively high flux and its low intrinsic background, D10 can be used for all kinds of conventional crystallographic studies of nuclear and magnetic structures. The automatic monochromator protection allows a continuous change of the incident wavelength. Two detectors are available in the diffraction configuration, an 80×80 mm^2 two-dimensional microstrip detector for three-dimensional resolution in reciprocal space, or a single ^{3}He detector when the highest efficiency and lowest background are required. In the four-circle mode, the offset C-shaped Eulerian cradle can be equipped with a helium-flow cryostat (1.6 K to 450 K, or 0.1 K to 10 K in dilution mode), or a hot-air furnace (up to 1000 K), both with full four-circle accessibility. In the two-axis mode, a cryomagnet can be mounted with computer control of the double-axis tilt stage to allow limited out-of-plane access.

D3: this beamline serves as a spin polarised hot neutron beam facility [95]. It is a very versatile diffractometer for magnetic structure analysis, offering several set-ups. The low-field option implement a third-generation CryoPAD (Cryogenic Polarisation Analysis Device) for precision measurement of neutron spin rotations occurring in the scattering process. This option is used to study non-collinear magnetic structures, antiferromagnetic form factors, etc. The scattered polarisation is analysed with a ^{3}He neutron spin filter hosted by Decpol. Decpol is a compact detector shielding providing the homogeneous holding-field required for long relaxation time of the ^{3}He polarisation. The diffractometer uses readily exchangeable CoFe and Heusler polarising monochromators within removable shielded cassettes in symmetric Laue geometry. Wavelength change is an automatic on-line operation, including the insertion of the appropriate resonant harmonic filter.

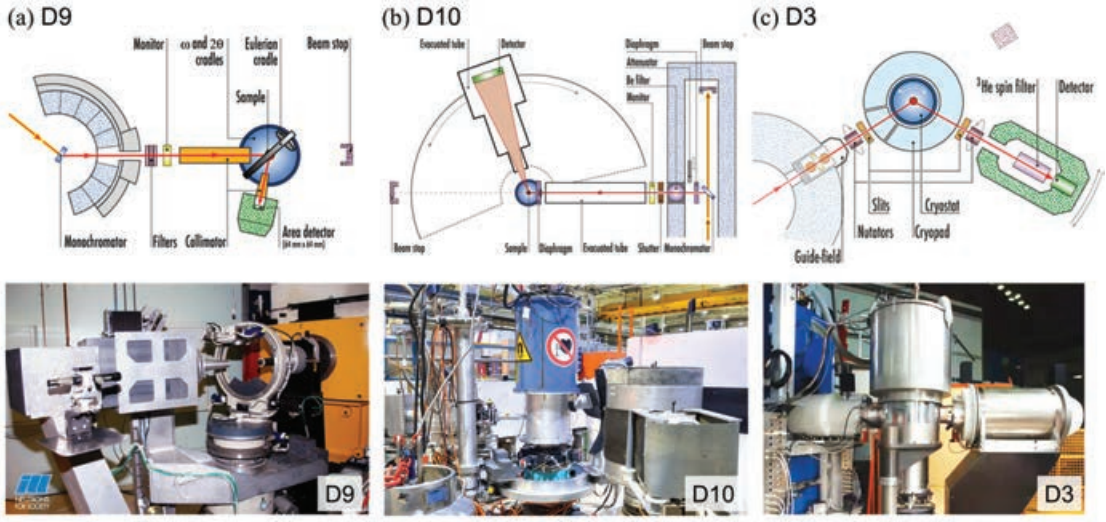

FIGURE 3.9: Layout and experimental setup on the three different single crystal neutron diffractometers used to carry out the different SCND experiments, located at the Institut Laue Langevin (Grenoble): (a) the D9 hot neutron 4-circle diffractometer, (b) the D10 4-circle diffractomete (in the picture equipped with a 6 T cryomagnet) and (c) the D3 single crystal diffractometer equipped with the CryoPAD used to perform SNP measurements on single crystals.

3.3 Synchrotron X-ray absorption spectroscopy

Synchrotron facilities provide X-rays with the characteristics necessary to perform X-ray Absorption Spectroscopy (XAS) and X-ray Magnetic Circular Dichroism (XMCD) experiments: intensity, energy tunability and resolution, polarization control and so on. The XAS and XMCD studies used to investigate the local electronic structure around $3d$ metals in the materials studied in this thesis was particularly concentrated in Fe and Cu $L_{2,3}$ edges ($2p \rightarrow 3d$ transitions), and in the O K edge ($1s \rightarrow 2p$ transitions).

Beyond elastic scattering, other main inelastic processes can occur when X-rays interact with core electrons. Very generally, when an incident photon strikes an atom and excites a core electron, the excited electron can either be promoted to an unoccupied level, or ejected from the atom. Both of these processes will create a core hole. The absorption of photons due to these inelastic scattering processes lead to the attenuation of a monochromatic X-ray beam of intensity I_0 passing through a uniform layer of material in thickness x. This effect is ruled by the Lambert-Beer law:

$$I = I_0 e^{-\mu x} \tag{3.17}$$

where μ is called the "mass-dependent absorption coefficient" and is usually expressed in units of cm^{-1}.

The probability of an interaction mechanism depend on the energy of the incident photon and on the density of the electronic states in the atoms. Therefore, as the absorption is a direct measurement of the total probability of a photon to be absorbed by any mechanism, energy dependent measurements of the absorption can provide information about the initial states of the excited electrons, and therefore on the electronic structure of the atoms in the material. Despite the derivation of the absorption coefficient (μ) is in principle a complicated quantum mechanics problem, a number of key approximations allow to simplify the expression. First of all the one-electron approximation should be invoked, which means that we consider only one photoelectron to be excited by each incoming photon while the other electrons merely act as spectators. Then, the absorption coefficient is proportional to the photoabsorption cross-section $\sigma(E)$, which is given by the Fermi's Golden Rule as the probability per unit of time ($\Gamma_{i,f}$) to excite an electron from the initial state $|\psi_i\rangle$ to a final state $|\langle\psi_f|$:

$$\mu \propto \sigma(E_f) = \sum_f \Gamma_{i,f} = \sum_f \frac{2\pi}{\hbar} |\langle\psi_f|H_{int}|\psi_i\rangle|^2 \delta(E_f - E_i - \hbar\omega) \tag{3.18}$$

where H_{int} denotes the interaction operator reflecting a time-dependent perturbation of the Hamiltonian of the atom. XAS involves the measurement of X-ray absorption cross-section at energies near and above the binding energy of core-level electrons, which correspond to the energy required to eject a core-electron into an excited empty state above the Fermi level (E_F) through the electric-dipole transition (Δl=$\pm$1), producing a photoelectron, thus producing a sudden increase of the absorption (absorption edge). The fact that binding energies are characteristic of each element allows the independent study of different elements in the material by selecting specific energy ranges. Different approaches or methods are used for measuring the absorption coefficient (μ) as a function of the energy of incident X-rays:

- *Transmission*: This method involves passing X-rays through the sample and comparing the incident and transmitted intensities. This method is normally applied for experiments involving hard X-rays, since due to the larger cross-sections using soft X-rays the beam may be totally attenuated at the absorption edge if the sample is too thick. For the same reason, soft photons have

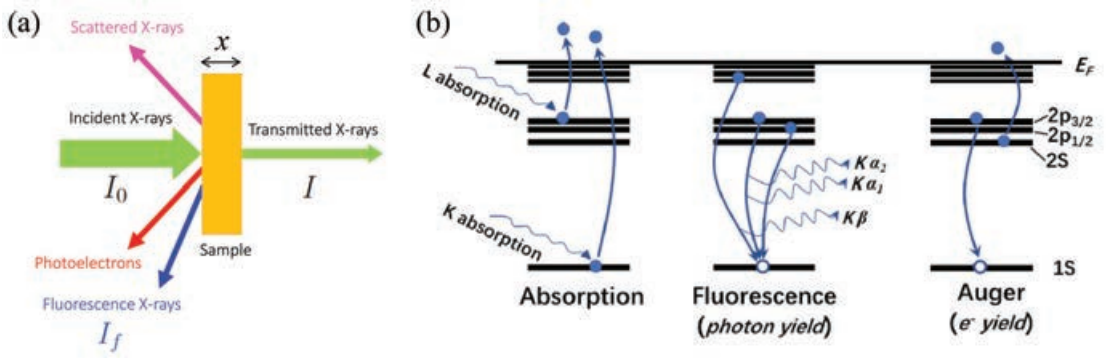

FIGURE 3.10: Schematic diagram of the absorption process and possible decay channels following it.

a large absorption cross-section in air; hence the experiments have to be performed under very good vacuum conditions.

- *Total electron yield*: The yield of electrons escaping from the surface of the sample generated by the different decay channels after the X-ray irradiation (*e.g.*, photoelectrons, Auger electrons, and secondary electrons, illustrated in Fig. 3.10) is generally proportional to the X-ray absorption intensity. Thus, the photocurrent can flow in electrically conductive matter by X-ray irradiation when it is grounded. Monitoring the sample current during X-ray energy scanning is easy using XAS, which is a Total Electron Yield (TEY) method. As the transmission method is difficult to apply to soft X-ray absorption measurements due to the strong beam attenuation, TEY is commonly used as an alternative. However, as the emitted electrons are easily absorbed in the sample, this method is mainly sensitive to surface features.

- *Fluorescence yield (FY)*: In this method, an X-ray detector is used to measure the photons created in the fluorescent decay. Unlike the TEY, the interaction of the emitted photons with matter is much lower than that of emitted electrons, and in consequence FY measurements exclude any surface effect. Fluorescence measurements are often carried out using Partial Fluorescence Yield (PFY) that rely on detectors having photon energy discrimination. This allows to improve the sensitivity and the signal-to-background ratio of the measured spectra.

3.3.1 BL29-BOREAS beamline (Alba Synchrotron Light Facility)

Synchrotron XAS measurements presented in this thesis to study the electronic structure of atoms in our materials were conducted at the BL29-BOREAS beamline of the ALBA Synchrotron Light Facility [96]. BL29-BOREAS is a soft X-ray

beamline dedicated to polarization-dependent spectroscopic investigations of advanced materials, involving those composed of 3d and 4d metals and rare earths. In our case the samples studied were in bulk form, but thin film, multilayered, powder or nanostructured materials can also be studied. The X-rays are produced by an APPLE II elliptical undulator which offers a high flux (10^{12} photons/s at 150-1000 eV), high energy resolution (ΔE$\sim$50-100 meV), and full polarization control on an extended soft X-ray regime of 80 to 4000 eV. The beam size at sample can be adjusted from approx. $< 100\times100$ μm to 1×1 mm thanks to its vertical and horizontal refocusing mirror system with adjustable in-situ mirror benders. In Fig. 3.11 the main optical components of the beamline located upstream the end-stations are shown.

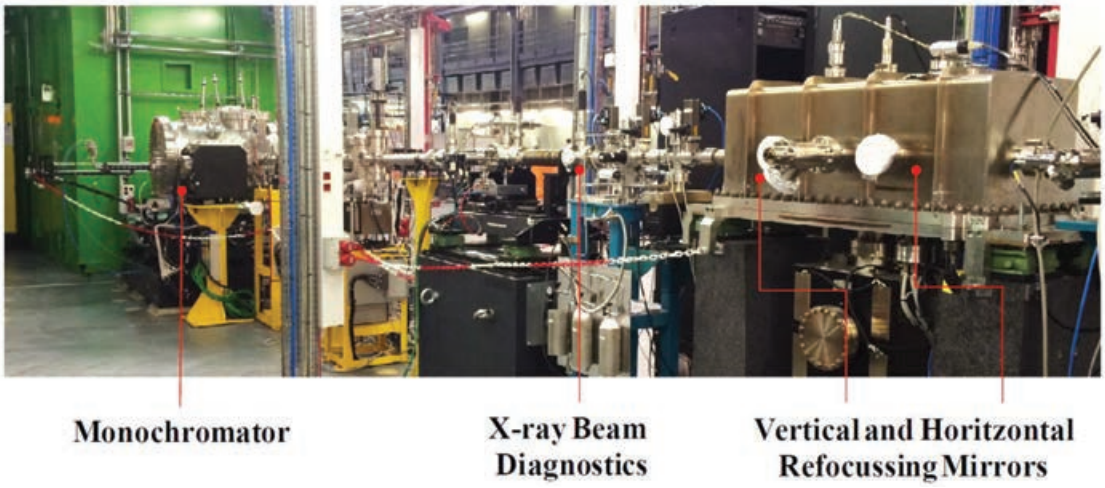

FIGURE 3.11: The main optical components of the BL29-BOREAS beamline. Image from Ref. [96].

The beamline is equipped with two state-of-the-art end stations:

(i) a High-field vector magnet (HECTOR) for soft-XAS and Dichroism techniques such as NEXAFS, XMCD or XMLD;

(ii) a UHV reflectometer (MARES) for scattering and reflection approaches including resonant soft X-ray reflectivity, resonant magnetic scattering and GISAXS.

The description will focus on the HECTOR end station, where all the XAS/XMCD measurements were performed. This end-station consists of a UHV-compatible cryomagnet (Scientific Magnetics Ltd). The magnet is composed of a set of three orthogonal superconducting split-coils allowing maximum fields of up to 6 T in the horizontal plane along the beam direction, and 2 T in the horizontal plane

perpendicular to the X-ray beam and in the vertical plane.

The samples are in a UHV environment with a base pressure of the order of $<10^{-10}$ mbar, and mount on a sample holder attached to the cold finger of a variable temperature cryostat (3 K - 350 K). The system counts on three chambers for storage and sample preparation, all operating high-to-ultra-high vacuum (UHV) conditions [Fig. 3.12(a)]: (i) the load-lock chamber, (ii) the buffer chamber, and (iii) the preparation chamber. The first one allows to introduce/change samples at ambient pressure and to reach a good vacuum in a few minutes. The buffer chamber is a transition chamber between the load-lock and the preparation chamber where UHV conditions are mandatory. Finally, the preparation chamber presents a complete range of sample preparation tools such as: a cleaver, a scraper, MBE-evaporators for metals and organic molecules, an e-beam heating stage and an ion sputtering gun.

The sintered pellet samples in our experiments were fixed onto Aluminum

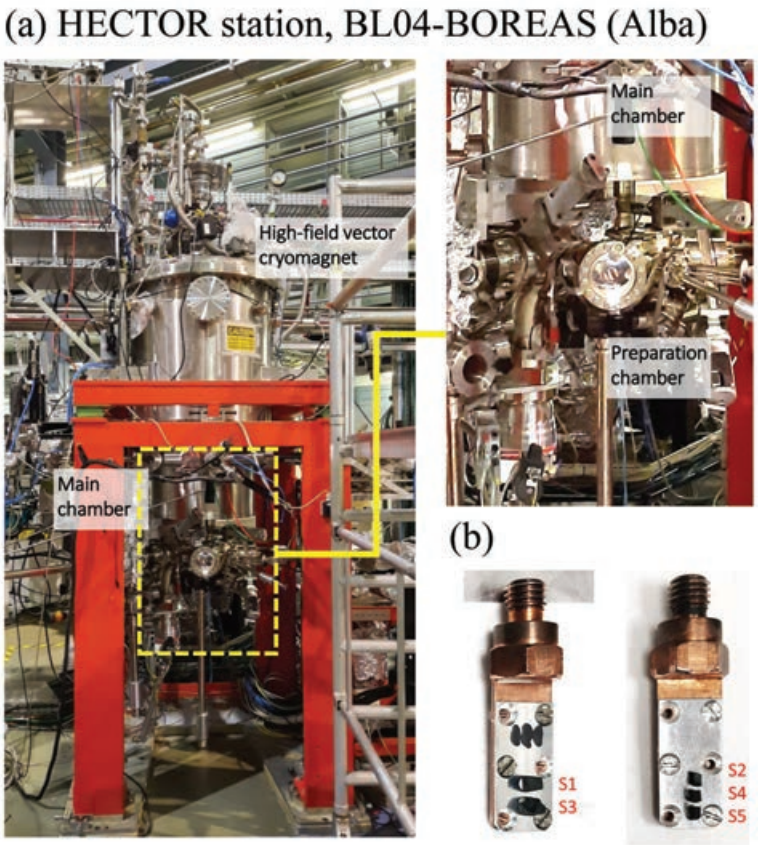

FIGURE 3.12: (a) General view of the HECTOR XAS/XMCD end station in BL29-BOREAS beamline (Alba synchrotron) and detail of the main and preparation chambers. (b) Sample holders with YBCFO pellet samples mounted on them.

plates using a strong epoxy and diluted Ag paint, and coated with a graphite solution to guarantee a good electrical conductivity of the assembly. These plates were then screwed into Cu sample holders. Fig. 3.12(b) shows the YBCFO samples studied in Chapter 4. Then, the samples were cleaved under high vacuum (in the preparation chamber) to allow the study of fresh, non oxidized surfaces.

3.4 Bulk magnetic characterization

The *magnetization* of a material (M) is defined as the magnetic moment per unit volume (or per unit mass) and the magnetic *susceptibility* (χ) is the proportionality between the magnetization induced in response to an applied magnetic field, and the intensity of this magnetic field. As we know, when a constant field (H) is applied to a sample, it gets magnetized and its state is characterized with a certain magnetization M. Then, macroscopic magnetic state of a material can be characterized from its response to a steadily applied dc magnetic field by these two magnitudes (M and χ). The dependence of the magnetic response of materials is commonly studied as a function of temperature and external magnetic fields by measuring the M(T) and M(H) curves.

In contrast, if an ac field is applied superimposed to the dc field, the magnetic response becomes time-dependent. The difference between dc and ac measurements is that the latter gives information about the slope of the magnetization curve at a certain point H. At low frequencies and small ac field amplitudes, the induced ac magnetization is given by

$$\mathrm{M}_{ac} = \frac{d\mathrm{M}}{dH} h_{ac} \cos(\omega t) \tag{3.19}$$

where h_{ac} is the amplitude of the ac field and $\omega = 2\pi f$ its frequency. Varying the dc magnetic field allows to obtain the field dependence of the slope of the M(H) curve, which corresponds to the ac susceptibility, $\chi_{ac} = d\mathrm{M}/dH$. Therefore, ac measurements are very sensitive to small variations in the magnetic response of the material. Measurements at higher frequencies allow to study the dynamic effects in the sample.

SQUID magnetometers

Both ac and dc susceptibility techniques were used to probe the macroscopic magnetic response of polycrystalline and single crystal samples as a function of the temperature and under external magnetic fields using equipments based on Superconducting QUantum Interference Device (SQUID) technology. SQUID magnetometers, which have an extremely high sensitivity (in the order of $10-7$ emu), are able to detect extremely tiny magnetic fields. This device is based on the tunneling of superconducting electrons across a Josephson junction between two superconductors. Its high sensitivity lies on the fact that it responds to changes of magnetic field associated with one flux quantum. In a SQUID, this flux is converted into a measurable electical voltage.

The SQUID measurements in the present work were carried out in a Magnetic Property Measurement System (MPMS-XL), and/or in a Physical Properties Measurement System (PPMS), both from Quantum Design, Inc (shown in Fig. 3.13). The capabilities measurements done in these two equipments are briefly described below:

- **Quantum Design MPMS-XL:** This magnetometer is based on a SQUID detector that is able to determine extremely low magnetization signals present in the material under study. The core system consists of a superconducting longitudinal solenoid able to generate mangetic fields up to 7 T. The system is able to precisely control the temperature at the sample space at any value from 2 K to 400 K. In RSO measurement mode (oscillatory motion through the pickup coils) it has a sensitivity of 10^{-7} emu. We used this setup to obtain temperature dependencies of the magnetization, M(T), and M(H) curves under dc fields up to 7 T.
- **Quantum Design PPMS:** The core system in this equipment makes possible to generate magnetic fields up to 9 T and to control the sample space temperature to any value between 2 K and 400 K. Temperature dependent M(T) curves were measured using the Vibrating Sample Magnetometer (VSM) option, which provide a fast and precise method for the determination of the DC magnetization of a material. In this option, an specially built sample holder that contains a heater allows to extend the working temperature up to 1000 K. In addition, the AC Measurement System (ACMS) provides the possibility to use the PPMS as DC extraction magnetometer (sensitivity, 10^{-5} emu) or an AC Susceptometer (sensitivity, 10^{-8} emu). Field dependent $\chi_{ac}(H)$ susceptibility curves were recorded using this hardware option under

magnetic fields up to 9 T.

FIGURE 3.13: Views of the two different magnetometers used: (a) the Magnetic Property Measurement System (MPMS-XL) and (b) the Physical Properties Measurement System (PPMS), both located at the Low Temperature and Magnetometry Lab at ICMAB.

In most cases the measurements were done with the support of the Service technician. Field dependent ac susceptibility measurements on YBCFO single crystals (presented in Chapter 7) were conducted with the help of Vassil Skumryev (ICREA Research Professor at Universitat Autònoma de Barcelona), and the magnetic study on ε-Fe_2O_3 nanoparticles (in Chapter 8) was performed in collaboration with Martí Gich (Nanoparticles and Nanocomposites Group at the ICMAB-CSIC).

3.5 Computational tools

- **FullProf**: the FullProf Suite is formed by a set of crystallographic programs (FullProf, WinPLOTR, EdPCR, GFourier, etc...) mainly developed for Rietveld analysis (structure profile refinement) of neutron (constant wavelength, time of flight, nuclear and magnetic scattering) or X-ray powder diffraction data collected at constant or variable step in scattering angle 2theta. FullProf has been used for the analysis of all the X-ray and neutron powder and single crystal data presented in this work [97].
- **Mag2Pol**: program for the analysis of single-crystal and powder diffraction data. Used to refine the magnetic structures from spherical polarimetry data and for the calculation of the polarization matrices of different magnetic models [98].

- **Esmeralda**: the Esmeralda suite is a set of applications that range from the simulation of Laue patterns to the extraction from measured Laue patterns of normalized squared structure factors ready for use for structure determination. The program was used for the data processing of the CYCLOPS neutron Laue diffractometer (ILL) [99, 100].
- **Clip**: the Cologne Laue Indexation Program is a software for the analysis of Laue patterns. It allows to determine the crystal orientation from spots and zones marked on a Laue photograph. Clip was used for the indexation of the Laue neutron patterns measured at the Orient Express Laue diffractometer (ILL) and to calculate the angles to rotate the crystal in the desired orientation.
- **Dioptas**: Python based GUI-Program for integration and exploration of two-dimensional X-ray diffraction area detector data. Used to calibrate and integrate the high pressure X-ray bidimensional diffractograms prior to the Rietveld analysis [101].
- **Bilbao Crystallographic Server**: The Bilbao Crystallographic Server is a web site with crystallographic databases and programs available online (`www.cryst.ehu.es`). The server gives access to general information related to crystallographic symmetry groups, programs for the analysis of group-subgroup relations between space groups, and software package studying specific problems of solid-state physics, structural chemistry and crystallography [102–104].
- **ISOTROPY**: The ISOTROPY software suite is a collection of software which applies group theoretical methods to the analysis of phase transitions in crystalline solids [105].
- **VESTA**: 3D visualization program for structural models, volumetric information such as electron density, and crystal morphologies [106].

3.5.1 Analysis of synchrotron and neutron diffraction data: the Rietveld method

In this work, all diffraction data has been analyzed using the Rietveld method, implemented in the FullProf set of programs. The method, developed by Hugo Rietveld in 1969, is currently the most common procedure for the analysis of X-ray and neutron powder diffraction data when the structure is approximately well-known.

Implementation of the Rietveld method

The method is based on the minimization of the weighted squared difference between the observed data and the calculated diffraction pattern using an approximate structural model. The function to be minimized is:

$$S_y = \sum_{i=1}^{N} w_i \mid y_o(2\theta_i) - y_c(2\theta_i) \mid^2 \tag{3.20}$$

where N is the number of experimental points of the pattern, $y_o(2\theta_i)$ and $y_c(2\theta_i)$ are respectively the observed and calculated intensities in each i point, and w_i is the weight for each i point. This last term is defined from the variance of the observation σ_i of each experimental value of the intensity as $w_i = 1/\sigma_i^2$. The calculated intensity for each position $2\theta_i$ of the diffraction pattern can be expressed as:

$$y_c(2\theta_i) = y_b(2\theta_i) + L_p(2\theta_i) \sum_{j=1}^{N_f} S_j \sum_{k=1}^{N_p} m_{k,j} \mid F_{k,j} \mid^2 S_j(2\theta_i - 2\theta_{k,j}) P_{k,j}(2\theta_i) \tag{3.21}$$

where N_f is the number of phases and N_p the number of reflections, $y_b(2\theta_i)$ is the background contribution, L_p contains the Lorentz and polarization correction factors, S_j is the scale factor for each j crystallographic phase, $m_{k,j}$ is the multiplicity for each k reflection, $F_{k,j}$ is the structure factor (3.11), $S_j(2\theta_i - 2\theta_{k,j})$ is the function in charge to describe the reflection's shape and $P_{k,j}(2\theta_i)$ is a factor to correct the effect of preferential orientation, absorption and extinction.

An issue that is also important is that the number of reflections is determined by the symmetry and the space group of the crystalline phase. In general, the higher the degree of symmetry the less reflections the diffraction pattern will have due to equivalent or cancelled reflections. The fact that multiple reflections can contribute to a single intensity peak is taken into account with the multiplicity factor $m_{k,j}$.

The calculated model should refine (adjust) the angular position, intensity and shape for each peak of the diffraction pattern. With this objective, the Fullprof software allows us to adjust different parameters using the Rietveld method in order to obtain a good refinement between the experimental profile and the calculated one. For this reason it is necessary to start from an approximate model of the structure, that is to say that it is necessary to introduce the space group to which it is expected that the crystal belongs and approximate

values of the structural parameters (cell parameters and atomic coordinates). The main parameters that need to be adjusted for a good refinement are detailed below:

- **Peak position**: the correct angular position of each (hkl) reflection can be computed and refined from Brag's law (3.6) by adjusting the unit cell parameters $(a, b, c, \alpha, \beta, \gamma)$ of each crystalline phase present in the specimen. It is also important the adjust of the zero shift error of the goniometer;
- **Peak intensity**: The intensity of the peaks depends on the selected structural model for each crystalline phase, thus on the composition of the unit cell, which includes the coordinates (x_j, y_j, z_j) of the atomic positions, the occupation of each atom in a given position and the temperature factors B_j. These parameters, which are implicit in the structure factor (3.11), can be refined. The scale factors S_j, which also are adjusted, and are related to the proportion x_j of each crystalline phase according to:

$$x_j = \frac{S_j z_j M_j V_j}{\sum_{i=1}^{N_f} S_j z_j M_j V_j} \tag{3.22}$$

  where z_j is the number of formula units of the specie per unit cell, M_j the molecular mass corresponding to the formula unit and V_j is the volume of the unit cell. The background, the presence of preferred orientation, absorption, extinction and other microstructural factors may also have an effect on the intensity.
- **Peak shape**: the shape of the peaks can be a complex feature to adjust, since it can depend not only on the characteristics of the sample, but also on instrumental features such as the radiation source, geometry, monochromator, and so on. The main characteristics of the peaks to be adjused are the asymmetry factors (which are more imporant for small angles), the type of function and the full width at half maximum (FWHM) of the function. These aspects are taken into account in factor $S_j(2\theta_i - 2\theta_{k,j})$. The function can be a Gaussian (G), a Lorentzian (L) or a pseudo-Voigt (pV), that is a combination of the first two and is the one used in this work. This function can be described as:

$$pV(x; H, \eta) = \eta L(x; H_L) + (1 - \eta) G(x; H_G) \tag{3.23}$$

  where $0 \leq \eta \leq 1$ is the parameter that will be refined and H_L, H_G are the FWHM of the Lorentzian and Gaussian functions respectively. Moreover, the

H parameters may have an angular dependence, described for both Lorentzian and Gaussian functions by the Caglioti relation as:

$$H_L(\theta) = X \tan\theta + Y/\cos\theta \tag{3.24}$$

$$H_G^2(\theta) = U \tan^2\theta + V \tan\theta + W \tag{3.25}$$

where X, Y, U, V, W are the refinable parameters.

Agreement R-factors

The quality of the agreement between the observed and calculated profiles can be measured by the R-factors, a set of parameters that are defined as follows:

- **Profile Factor**:

$$R_p = 100 \frac{\sum_{i=1}^{N} \mid y_o(2\theta_i) - y_c(2\theta_i) \mid}{\sum_{i=1}^{N} y_o(2\theta_i)} \tag{3.26}$$

- **Weighted Profile Factor**:

$$R_{wp} = 100 \left[\frac{\sum_{i=1}^{N} w_i \mid y_o(2\theta_i) - y_c(2\theta_i) \mid^2}{\sum_{i=1}^{N} w_i y_o^2(2\theta_i)} \right]^{1/2} \tag{3.27}$$

- **Expected Weighted Profile Factor**:

$$R_{exp} = 100 \left[\frac{N-P}{\sum_{i=1}^{N} w_i y_o^2(2\theta_i)} \right]^{1/2} \tag{3.28}$$

where P is the number of refined parameters;

- **Reduced chi-square**:

$$\chi^2 = 100 \left[\frac{R_{wp}}{R_{exp}} \right]^2 \tag{3.29}$$

- **Bragg Factor**:

$$R_B = 100 \frac{\sum_{(hkl)} \mid I_o(hkl) - I_c(hkl) \mid}{\sum_{(hkl)} I_o(hkl)} \tag{3.30}$$

Part II

Investigating the family of spin-induced $YBaCuFeO_5$ multiferroics with high-T_c chiral magnetism

Chapter 4

Helimagnets by disorder: its role on the high-temperature magnetic spiral in the YBCFO perovskite

4.1 Introduction

Despite the theoretical progresses achieved in the last years for modeling the *spiral order by disorder* mechanism [54, 55], from the experimental viewpoint more precise and exhaustive investigations are still pending. The work presented in this chapter is aimed to fill that gap, extending previous reports on the reference composition YBCFO [46, 47]. In the following we report a systematic, meticulous experimental investigation of the influence of Fe/Cu cation disorder (monitored and quantified through the improper occupancy of the Fe and Cu positions) on the evolution of the noncollinear magnetic and the structural properties in the YBCFO layered perovskite. The interplay between disorder, stability, and the features of the modulated spiral magnetic phase in YBCFO have been thoroughly and quantitatively described, and also analyzed in the light of the theoretical predictions. In YBCFO the influence of disorder (and only disorder) on the magnetic phase diagram, the structure, and the features of the modulated spiral is studied on a quantitative basis, extending the range of previous studies. Three different regimes are distinguished in the YBCFO phase diagram versus disorder, where a multicritical point has been found. A triple point driven by Fe/Cu disorder in YBCFO sets limits to the thermal stability of the helicoidal order and also to its cycloidal component (characterized by the inclination of the spin rotation plane). Magnetic and structural mechanisms activated by disorder are carefully analyzed and confronted to theory.

This approach paves the way to further progress for the optimization of multifunctional perovskites with high-T_S spiral magnetic order. Some conclusions also present interest for other noncollinear anisotropic or layered magnets in which the spiral order (cycloidal, conical,...) can form "by disorder" at normal working temperatures.

4.2 Sample praparation and experimental methods

Synthesis of polycrystalline $YBaCuFeO_5$ samples with different Fe/Cu disorder

Polycrystalline samples with identical composition $YBaCuFeO_5$ were prepared by the solid state reaction method. High-purity Y_2O_3, $BaCO_3$, CuO and Fe_2O_3 precursor oxides were dehydrated at 150 °C for 48 h. Decarbonation of Y_2O_3 oxide was achieved by a pre-annealing process at 900 °C for 10 h. Stoichiometric amounts of the oxides were then mixed, thoroughly grounded using an automatic agate mortar for several hours until a fine and homogeneous powder was obtained. The resulting powder was then pressed into pellets, which were heated for 50 h at 1150 °C in air. Finally, in order to obtain specimens with different degree of B-site cationic order, we applied dissimilar cooling processes to each sample. We will refer to them as Sn ($1 \leq n \leq 7$, where higher n values denote ascending Fe/Cu disorder). To samples S1, S2 and S3 we applied a controlled cooling rate of, respectively, 10 °C/h, 300 °C/h and 450 °C/h. Samples S4, S5, S6 and S7 were obtained by quenching into liquid nitrogen or water. The quenching process consisted on pulling the sample crucible out of the tubular furnace, turn it over to drop the sample into a wide cryogenic Dewar flask containing the quenching medium. By this process samples S4 and S5 were quenched using liquid nitrogen and water, respectively. Although it is not possible to determine quantitatively the real cooling rate of quenched samples, the time elapsed between the moments in which these samples were pulled out of the furnace and get in contact with the medium was $\sim$12 seconds. Later on, with the aim of achieving even higher cooling rates, the process of dropping the samples into the medium was modified. By decreasing as much as possible the distance between the furnace tube and the Dewar flask, and dropping directly both crucible and sample into the medium, the process could be effectively shortened

to ∼5 seconds. By this improved process samples S6 and S7 were quenched respectively into liquid nitrogen and water. The highest Fe/Cu disorder was obtained for the sample S7, where the quenching was done by fast cooling in liquid water. After this, small pieces of each sample were kept solid for the macroscopic measurements, and the rest was pulverized to perform powder diffraction experiments.

The quality of the samples was assessed by X-ray and neutron diffraction, and magnetic measurements. Laboratory X-ray diffraction patterns collected at RT using a Siemens D-5000 diffractometer (λ[Cu K_α] = 1.54 Å) showed a very good crystallinity and purity of the samples within the detection limit of the technique.

Characterization methods

- *Synchrotron X-ray powder diffraction:* for the structural study, high resolution synchrotron radiation X-ray powder diffraction patterns (SXRPD) were collected at 300 K at the BL04-MSPD beamline [107] of the ALBA Synchrotron Light Facility (Cerdanyola del Vallès, Spain). The samples were loaded in borosilicate glass capillaries (0.7 mm diameter) and kept spinning during data acquisition. A short wavelength, λ = 0.41357(3) Å was selected to reduce absorption and enlarge the q-range. The value of λ was calibrated using a NIST standard silicon. As detection system we used a high-throughput position sensitive detector MYTHEN which allows a high photon flux. The acquisition time to perform a RT full structural characterization was 90 s.
- *Neutron powder diffraction:* to characterize the magnetic order, neutron powder diffraction (NPD) measurements were carried out at the high-flux reactor of the Institut Laue Langevin (Grenoble, France), using the high-intensity, high-resolution two-axis D20 diffractometer configured with a HOPG monochromator and 42° take-off angle (λ= 2.41 Å), with excellent resolution at low-q and a high efficiency position sensitive detector covering an angular range up to 150°. Powder samples were filled into 8 mm diameter vanadium containers. For each sample, two patterns with an acquisition time of 15 min were collected at 10 K and averaged for signal-to-noise ratio optimization. To study the evolution of the magnetic order with temperature, neutron thermodiffractograms were also collected in continuous mode following temperature ramps within the range 10 to 500 K, with applied heating rate of 2 K/min and acquisition time of 2.5 min per scan. Around 100 patterns were recorded in the range 10 K

to 500 K with a resolution in temperature of 5 K between successive patterns. Finally, the end members of the series (S1, S2 and S7 samples) were also measured on D20 in the paramagnetic state (at 490 K) using a shorter wavelength (λ = 1.54 Å). The temperature range of the experiment was covered by using a dedicated helium cryofurnace.

Structural and magnetic Rietveld refinements of the X-ray synchrotron and neutron patterns were made using the Fullprof package of programs [97]. Crystallographic tools from the Bilbao Crystallographic server [102–104] and ISOTROPY Software Suite [105] were also used. The illustrations of the crystal structure were obtained using the VESTA program [106]. The cationic disorder in each sample was determined by SXRPD data analysis through the Fe/Cu occupancies at the B-sites of the perovskite. It is represented by the 'improper occupancy' parameter $\mathrm{n_d}$ (0 [full order]$<\mathrm{n_d}\leq$0.5 [full disorder]) described in next section. A second key parameter for the description of the samples is the modulation q_s of the incommensurate spiral magnetic phase, ($\mathbf{k}_2 = (1/2, 1/2, 1/2 \pm q_s)$ being the propagation vector, directly related to $\mathrm{n_d}$, which was obtained from the NPD data.

• *Synchrotron X-ray absorption spectroscopy:* soft X-ray absorption spectroscopy (XAS) and X-ray magnetic circular dichroism (XMCD) measurements at the Fe and Cu $L_{2,3}$ edges ($2p \rightarrow 3d$ transitions) were performed in the HECTOR cryomagnet endstation at the BL29-BOREAS beamline of the ALBA Synchrotron Light Facility (Barcelona, Spain). Sintered pellets of $YBaCuFeO_5$ were stuck onto Al plates using a hard bicomponent epoxy (Torrseal®) and diluted Ag paint, and coated with a graphite solution to guarantee a good electrical conductivity of the assembly. These plates were screwed into Cu sample holders while sandwiching In foil interfaces to optimize thermal and electrical conductivities. All data were recorded in a total electron yield (TEY) and partial fluorescence yield (PFY) detection modes. For the latter, a commercial Si-drift diode (SDD) built by Rayspec Ltd., UK was used. The main chamber of the cryomagnet was kept at 1×10^{-10} mbar during measurements. The XMCD spectra were recorded using alternatively left and right circularly polarized X-rays produced by an APPLE II undulator. The 6 T magnetic field along the direction of propagation of the incident photons set for the XMCD measurements was generated by a superconducting split coil setup within the cryomagnet. The total incoming radiation flux was about 5×10^{11} photons/s with an energy resolution $\Delta\mathrm{E/E}\sim10^{-4}$.

- *Magnetometry:* macroscopic magnetic measurements were performed using a vibrating sample magnetometer (VSM) in a Physical Properties Measurement System (PPMS, Quantum Design Inc) for recording the temperature dependence of the magnetization M(T) in the interval 10-500 K under an applied external magnetic field of 2 kOe.
- *Electrical characterization:* Polarization curves as a function of the applied electric field, P(E), were obtained at the Instituto de Nanociencia y Materiales de Aragón (INMA-Universidad de Zaragoza) with the collaboration of Drs. Gloria Subías and Javier Blasco. The dielectric measurements were carried out as a function of temperature between 5 and 300 K in a He cryostat employing a home-made coaxial-line inset. Sintered discs were cut and polished into flat circular pellets of about 8 mm in diameter (surface about 50 mm^2) and a thickness of about 0.5 mm. Silver paint was applied to disc surface for proper electrical contact. The complex dielectric permittivity of the samples was measured using an impedance analyzer (Wayne Kerr Electronics 6500B), applying voltages with amplitude of 1 V and a frequency range between 10 Hz and 5 MHz. Polarization versus electric-field loops were recorded using a commercial polarization analyzer (Easy Check 300 from aixACCT Systems GmbH) for frequencies up to 250 Hz, together with a high voltage amplifier (electric-field amplitude up to $\sim$20 kV/cm).

Pyroelectric current was measured with a Keithley 2635B electrometer by warming the sample at a constant rate with values ranging between 0.5 and 10 K/min. The change in the electrical polarization was obtained by integrating the pyroelectric current as a function of time. Different poling fields were tested. The electric field was applied at 150 K followed by cooling at a rate of 10 K/m down to 5 K. Then, the field was removed and the stabilization of the polarization was reached after shorting the circuit for 15 m to remove surface charges. The results are displayed in Sec. A.2 [App. *A*].

4.3 Structural evolution of YBCFO due to B-site disorder studied by SXRPD

4.3.1 B-site disorder and magnetic incommensurability

First of all, some considerations have to be done regarding the concept we are referring to as "disorder". In $YBaCuFeO_5$, non-centrosymmetric $P4mm$ models with partial Fe/Cu disorder give significantly better agreement factors than

fully ordered models with the centrosymmetric $P4/mmm$ space group, as Morin *et al.* pointed out for the first time [46]. This work further confirms that YBCFO samples are well described using the $P4mm$ symmetry, which allows to vary the chemical disorder in the layers formed by bipyramids through a distinct occupancy of the nominal Cu and Fe sites ($1b$ sites) [46–48, 108]. So, it is demonstrated that in YBCFO the "mixed" $FeCuO_9$ bipyramids are partially arranged forming Fe-rich and Cu-rich layers of pyramids that extend parallel to the ab plane. Furthermore, a second component of disorder that adds to the formerly described is the presence of "non-mixed" M_2O_9 (M=Fe or Cu) defects, which are inherent to the disordered nature of Fe and Cu at the B-sites, and were proposed by Scaramucci *et al.* to be the origin of magnetic frustration in YBCFO [54, 55]. In consequence, the refined Fe/Cu occupancies reflect the sum of these two disorder components, rather than the real density of improper Fe/Fe defects. Although it is not possible to extract this relevant quantity from the refined occupancies, both types of disorder are originated by the same mechanism during the annealing process of the samples and a relation of proportionality between them is assumed.

Figure 4.1 displays the refined SXRPD patterns for the seven YBCFO samples investigated, and Table 4.1 reports the corresponding structural parameters and agreement factors at 300 K. SXRPD patterns allowed to refine the atomic positions and the occupancies of the Cu and Fe ions in the two pyramids of the unit cell [Cu-rich is the upper (M1) and Fe-rich the lower (M2) pyramid, respectively]. For this purpose, the z-coordinates of the two positions that a given metal M (either Fe or Cu) can occupy in the cell (M1 and M2) were constrained in the form z(M1)+z(M2)=1. In Table 4.1 we denote as proper positions Cu1 (upper pyramid in the cell) and Fe2 (lower pyramid in the cell). In the ordered limit Cu1 and Fe2 sites are fully occupied, and hence the partial (improper) occupancy of the positions $Fe1^*$ and $Cu2^*$ is proportional to disorder. So, disorder is monitored by the improper occupancy n_d, defined as the fraction of Fe^{3+} [Cu^{2+}] cations that occupy $Fe1^*$ [$Cu2^*$] sites (see Table 4.1). Hereinafter the improper occupancy n_d in a sample is used to parameterize its chemical disorder (related to the density of impurity bonds in Ref. [54]).

We have studied the influence of Fe/Cu cation disorder (n_d) on the incommensuration (q_s) of the spiral magnetic phase (full details on the magnetic orders are given in Section 4.5). The values of both parameters in all the YBCFO samples investigated are listed in Table 4.4. Fig. 4.2 discloses the experimental

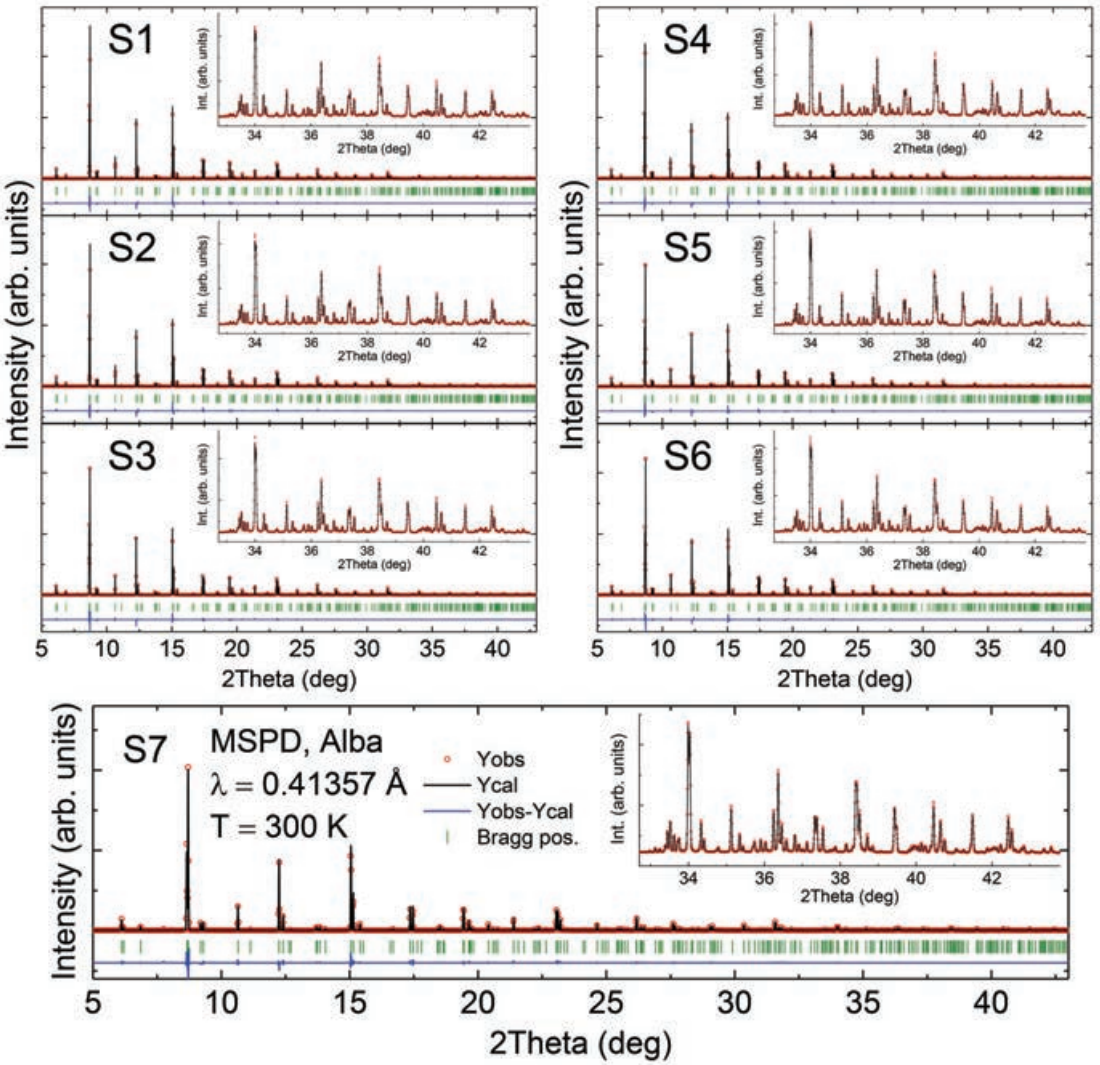

FIGURE 4.1: Rietveld refinement (black curve) of the synchrotron X-ray intensities (red circles) at 300 K (seven samples). Bottom blue line is the observed-calculated difference. Inset: Detail of the high-angles region.

relationship found between the values of the magnetic incommensurability (determined by neutron diffraction at 10 K) and the chemical disorder $\mathrm{n_d}$ in our YBCFO samples prepared with increasing disorder. The evolution shown in the figure proves a direct relationship between cation disorder ($\mathrm{n_d}$) and the magnetic incommensurability q_s. The q_s ($\mathrm{n_d}$) dependence found in our set of samples with growing disorder is satisfactorily parametrized by fitting the experimental points to a linear function (also exposed in Fig. 4.2):

$$q_s = -0.025(31) + 0.445(78) \cdot \mathrm{n_d} \tag{4.1}$$

The dashed lines in Fig. 4.2 illustrate the fitted evolution versus the *improper*

TABLE 4.1: Structural parameters at T = 300 K and agreement factors from Rietveld refinement of MSPD@ALBA synchrotron data (λ=0.413570 Å). (*: minority fraction; n_d (disorder)=Occ (Fe1*/Cu2*)). The coordinates of each metal (M: Cu or Fe) are constrained by z(M1)+z(M2)=1.

T=300 K *P4mm*		S1	S2	S3	S4	S5	S6	S7
a=b (Å)		3.87491 (2)	3.87526 (2)	3.87556 (2)	3.87566 (2)	3.87549 (1)	3.87606 (1)	3.87642 (2)
c (Å)		7.66432 (4)	7.66278 (4)	7.66236 (4)	7.66056 (4)	7.65962 (3)	7.65974 (3)	7.65917 (4)
$\Delta_T \equiv$c/2a		0.988967 (7)	0.988678 (7)	0.988548 (7)	0.988290 (7)	0.988212 (5)	0.988082 (5)	0.987918 (7)
V (Å^3)		115.0792 (13)	115.0771 (13)	115.0885 (13)	115.0675 (13)	115.0433 (10)	115.0789 (10)	115.0915 (13)
Y 1*a* (00z)	z/c	0.4948 (8)	0.4941 (8)	0.4932 (6)	0.4937 (8)	0.4942 (8)	0.4929 (5)	0.4938 (8)
	U_{iso} (Å^2)	0.00245 (10)	0.00204 (10)	0.00354 (8)	0.00177 (9)	0.00379 (9)	0.00350 (7)	0.00328 (9)
Ba 1*a* (00z)	z/c	0	0	0	0	0	0	0
	U_{11} (Å^2)	0.00689(6)	0.00666(6)	0.00750(5)	0.00666(6)	0.00768(5)	0.00765(4)	0.00764(5)
	U_{33} (Å^2)	0.0253(2)	0.0244(2)	0.02767(20)	0.0244(2)	0.0284(2)	0.02823(16)	0.0282(2)
Cu1 1*b* (½ ½ z)	z/c	0.71898 (37)	0.71894 (52)	0.72008 (45)	0.71837 (49)	0.72104 (63)	0.72072 (45)	0.72110 (68)
Fe1* 1*b* (½ ½ z)	z/c	0.74390 (50)	0.74455 (93)	0.74475 (81)	0.74578 (94)	0.74295 (93)	0.74452 (78)	0.74323 (96)
Cu2* 1*b* (½ ½ z)	z/c	0.28102 (37)	0.28106 (52)	0.27992 (45)	0.28163 (49)	0.27896 (63)	0.27928 (45)	0.27890 (68)
Fe2 1*b* (½ ½ z)	z/c	0.25610 (50)	0.25545 (93)	0.25525 (81)	0.25422 (94)	0.25705 (93)	0.25548 (78)	0.25677 (96)
	U_{iso} (Å^2)	0.00483(12)	0.00461(12)	0.00642(10)	0.00375(12)	0.00699(11)	0.00682(8)	0.00678(11)
O1 1*b* (½ ½ z)	z/c	0.0119 (13)	0.0085 (17)	0.0035 (14)	0.0045 (22)	0.0013 (28)	0.0002 (20)	0.0004 (29)
	U_{11} (Å^2)	0.00537(15)	0.00539(15)	0.00561(11)	0.00533(14)	0.00604(13)	0.00609(10)	0.00595(13)
	U_{33} (Å^2)	0.0118(6)	0.0119(6)	0.0128(4)	0.0117(6)	0.0144(5)	0.0146(4)	0.0141(5)
O2 2*c* (½ 0 z)	z/c	0.3138 (14)	0.3128 (16)	0.3131 (14)	0.3119 (17)	0.3135 (18)	0.3133 (12)	0.3131 (18)
	U_{11} (Å^2)	0.00756(15)	0.00758(15)	0.00780(11)	0.00753(14)	0.00823(13)	0.00828(10)	0.00814(13)
	U_{22} (Å^2)	0.00440(15)	0.00442(15)	0.00465(11)	0.00437(14)	0.00508(13)	0.00512(10)	0.00498(13)
	U_{33} (Å^2)	0.0055(6)	0.0055(6)	0.0064(4)	0.0053(6)	0.0081(5)	0.0083(4)	0.0077(5)
O3 2*c* (½ 0 z)	z/c	0.6809 (15)	0.6812 (17)	0.6824 (14)	0.6815 (18)	0.6820 (18)	0.6849 (11)	0.6833 (17)
	U_{11} (Å^2)	0.00756(15)	0.00758(15)	0.00780(11)	0.00753(14)	0.00823(13)	0.00828(10)	0.00814(13)
	U_{22} (Å^2)	0.00440(15)	0.00442(15)	0.00465(11)	0.00437(14)	0.00508(13)	0.00512(10)	0.00498(13)
	U_{33} (Å^2)	0.0055(6)	0.0055(6)	0.0064(4)	0.0053(6)	0.0081(5)	0.0083(4)	0.0077(5)
Occ (Cu1/Fe2)	$1-n_d$	0.706 (29)	0.684 (28)	0.628 (29)	0.613 (28)	0.563 (43)	0.594 (26)	0.560 (43)
Occ (Fe1*/Cu2*)	n_d	0.294 (29)	0.316 (28)	0.372 (29)	0.387 (28)	0.437 (43)	0.406 (26)	0.440 (43)
χ^2		*91.6*	*97.8*	*46.0*	*57.8*	*40.8*	*92.2*	*71.4*
R_B		*4.26*	*4.54*	*3.56*	*3.68*	*4.26*	*4.53*	*3.94*
R_f		*2.56*	*2.57*	*2.11*	*1.80*	*2.54*	*2.00*	*2.44*

occupancy n_d (occupation of Fe1* and Cu2* sites in Table 4.1, $0 < n_d < 0.5$) and also versus the symmetrically equivalent *proper* occupation ($[1 - n_d]$: occupation of Cu1 and Fe2 sites in Table 4.1). An improper occupation n_d=0.5 would thus correspond to a random B-site cation distribution. On the other hand, the canting angle φ determined for each sample is also shown in the right-axis of Fig. 4.2. The frequency shift q_s measures how much the spiral wave deviates from the antitranslational symmetry along **c** ($\Phi = \pi + \varphi = \pi + 2\pi q_s$). The angle Φ (see Fig. 4.2) stands for the rotation angle between the spins of equivalent pyramids in successive cells [46, 49, 109]. Therefore, Fig. 4.2 portrays a direct relationship between Fe/Cu disorder and the range of the constant twist (mean canting angle $\varphi = 2\pi q_s$) between the two spins in a bipyramid M_2O_9. Notice that, taking errors into account, Eq. (4.1) is compatible with the lack of incommensuration in absence of chemical disorder, although this point will be

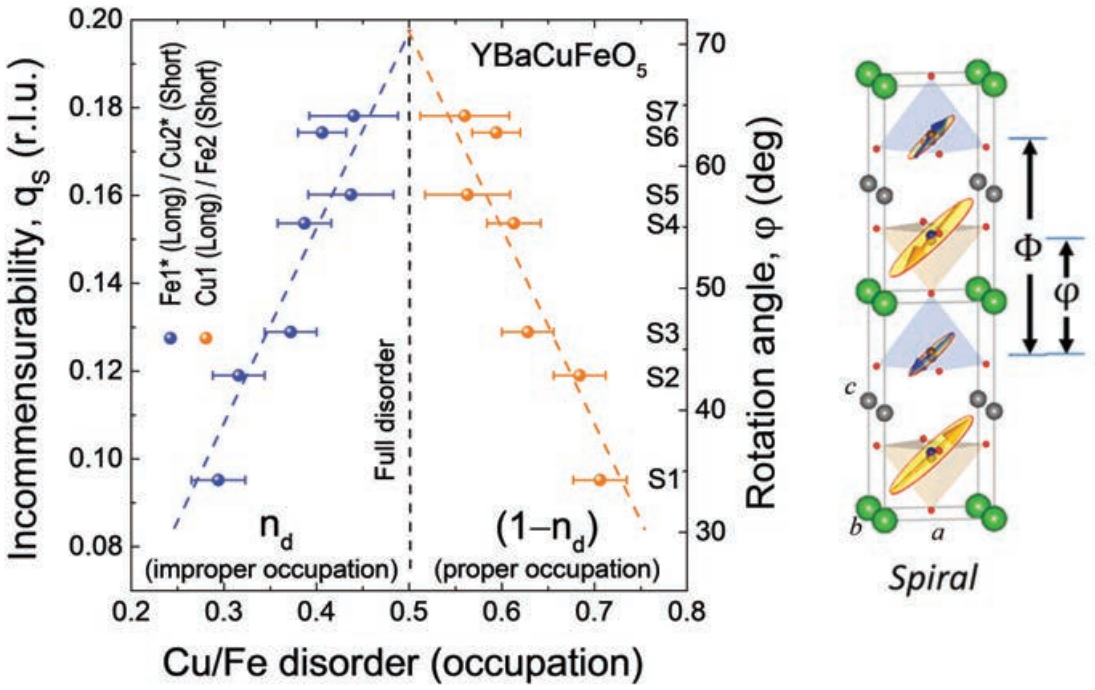

FIGURE 4.2: **Magnetic incommensurability versus B-site disorder.** Incommensurate modulation q_s of the magnetic spiral in YBCFO as a function of its fractional Fe/Cu cation disorder in the structure (described by the refined improper occupation n_d of Fe1* [Cu2*] sites in the bipyramids). Blue (brown) points represent the improper (proper) occupation of a given pyramid. A random disorder would correspond to n_d=0.5. The twist (canting) angle $\varphi = 2\pi q_s$ between the two spins in a bipyramid is shown in the right-axis, and φ is also illustrated in the sketch of the spiral order that is shown in the right side. In the structural projection the blue color stands for Cu and the brown for Fe, majority in the upper (M1) and lower (M2) pyramids, respectively. The q_s versus n_d linear fits (dashed lines) are reported in Table 4.6.

analyzed in more detail further on. As mentioned before, the key factor for the spiral phase is the fraction of c-aligned straight Fe-O-Fe superexchange bonds. The model of Scaramucci and co-workers [54, 55] predicts a linear relationship between q_s and the fraction of bipyramids with Fe-O-Fe bonds (improper Fe/Fe bonds).

In our set of YBCFO samples the Fe/Cu disorder varies in the range $0.29 \leq n_d \leq 0.44$[1]. The maximum achieved cation disorder was n_d=0.44(4) (S7 sample), very close considering errors to the extreme limit of total cation disorder at the B-site (n_{random}=0.5). Later we are discussing the impact of this large Fe/Cu disorder in more detail. Fig. 4.2 thus confirms that an excellent equivalent choice to n_d in order to quantitatively monitor the B-site chemical disorder

[1]The suitability and advantages of using SXRPD instead of NPD to determine the Fe/Cu cation disorder is discussed in Appendix A.

is to consider the experimental incommensurate modulation q_s, the shift of the magnetic wave respect to the chemical cell. Consequently, in this investigation we have extensively used the magnetic modulation value q_s as an alternative and very accurate quantification (determined by neutron diffraction) of the level of B-site chemical disorder in the samples.

4.3.2 Structural evolution due to B-site disorder

The evolution of the cell parameters and volume included in Table 4.1 have been plotted in Fig. 4.3. The expansion in the a parameter concurs with a systematic contraction of c when disorder increases, whereas the unit cell volume hardly changes. A certain evolution of the unit cell dimensions changing the cooling rate applied when preparing YBCFO was earlier observed in Ref. [47]. Figs. 4.3(a) and 4.3(b) disclose a linear correspondence between the cell parameters (a and c) and the incommensurability of the spiral phase (q_s). The influence of cation disorder on the tetragonal distortion ($\Delta_{\mathrm{T}} \equiv c/2a$) of YBCFO is shown in Fig. 4.4(a), and also reveals a linear evolution with the modulation q_s of the spiral phase. The linear fit to the experimental (Δ_{T}, q_s) points in Fig. 4.4(a) yields:

$$\Delta_{\mathrm{T}} = 0.990056(86) - 0.01153(56) \cdot q_s \tag{4.2}$$

To fully understand the influence of Fe/Cu disorder, beyond the creation of frustrating bonds, it is necessary to identify the key structural changes associated to disorder. Firstly, although the parameter a raises systematically as disorder increases, this lattice parameter mainly affects the perpendicular coupling terms gathered in J_{ab}. Remind that changes in this AFM term are much less relevant for $\mathrm{T_S}$ than changes in J_{c_2} [Fig. 4.4(b)] induced by the compression of the lattice along the c-axis. The influence of disorder on the average $\mathrm{d_t}$, $\mathrm{d_s}$ distances and the $\mathrm{d_t/d_s}$ ratio is displayed in Figs. 4.4(c,d). $\mathrm{d_t}$ stands for the thickness of the bilayers and $\mathrm{d_s}$ for their separation [Fig. 4.4(b)]. It should be stressed that the c contraction observed in Fig. 4.3(b) is caused by a systematic contraction in the thickness of the bipyramidal layers ($\mathrm{d_t}$), as shown in Fig. 4.4(c). Such contraction is not compensated by the lesser increase of the separation between bilayers ($\mathrm{d_s}$) when disorder increases. These observations agree with similar previous results reported in Ref. [48].

As Scaramucci *et al.* pointed out [54, 55], magnetic frustration is activated by the presence of AFM Fe-O-Fe c-bonds ($\mathrm{J}_{c_2'}$) inside a number of bipyramids

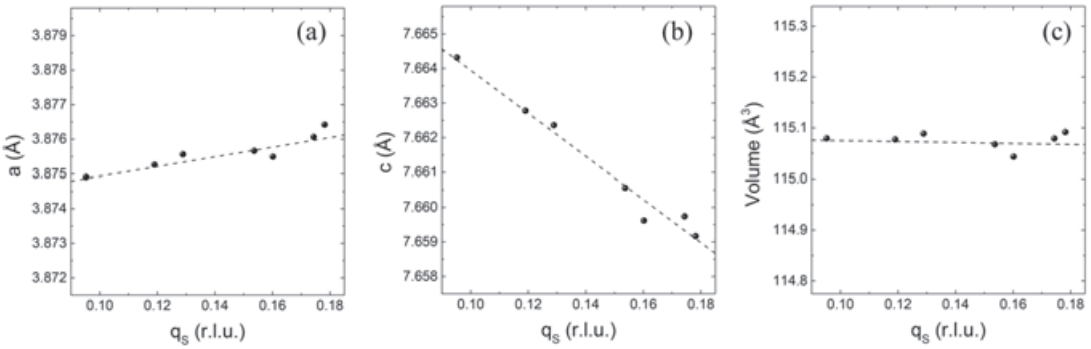

FIGURE 4.3: Evolution of the cell parameters (a, b) and (c) volume (V) at 300 K (from synchrotron data) increasing the Fe/Cu disorder in YBCFO. The incommensurability q_s in the spiral phase is used here to parametrize the disorder according to Eq. (4.1). Lines showed in the figures are linear fits described in Table 4.6.

[substituting the pristine FM Fe-O-Cu bonds, (J_{c_2})] [see Fig. 4.4(b)]. Whereas the J_{c_1} exchange between two neighbor (successive) bilayers [separated by the distance d_s along-c, Fig. 4.4(b)] is always AFM, independently of the Fe/Cu distribution. Additionally, we must bear in mind that bipyramids form layers where nearest-neighbors (NN) couplings in the ab plane are also always AFM, regardless of the Fe/Cu disorder. On one hand, disorder governs the density of Fe-O-Fe c-bonds. On the other hand, Fig. 4.4(c) discloses additional concurrent lattice effects (decrease [increase] of d_t [d_s]) that are inherent to increasing Fe/Cu randomness and (in presence of improper Fe-Fe bonds) also contribute to frustration through the tuning of the magnetic exchange couplings.

The evolution increasing disorder of z_{O1} (apical) and z_{O2} and z_{O3} (basal) coordinates is shown in Fig. 4.5, plotted as a function of q_s. From these coordinates, we can identify that the pyramids in the unit cell have different elongations. Consequently, hereinafter we'll call "*long*" pyramid (L) to that mostly occupied by Cu, and "*short*" pyramid (S) to that mostly occupied by Fe [(see Fig. 4.6(a)]. The thickness of the bipyramidal layer is given by $d_t = H_L + H_S$, the sum of the heights of the two pyramids sharing the O1 (apical) atom [see Fig. 4.4(b) and 4.6(a)]. In addition to O1 the heights depend on the z-position of the basal oxygens: O2 and O3 in, respectively, the S- and L-pyramids. From a quick glance to the atomic shifts shown in the Fig. 4.5 (plotted using the same scale range), it is apparent that the shift of the apical oxygen is the primary responsible for the changes in the heights H_L, H_S and the layer thickness d_t. In Fig. 4.5(d) we have illustrated the relative atomic shifts in the YBCFO samples investigated with increasing the structural disorder. The shifts along-z are shown for all the atoms taking the Ba position as fixed reference.

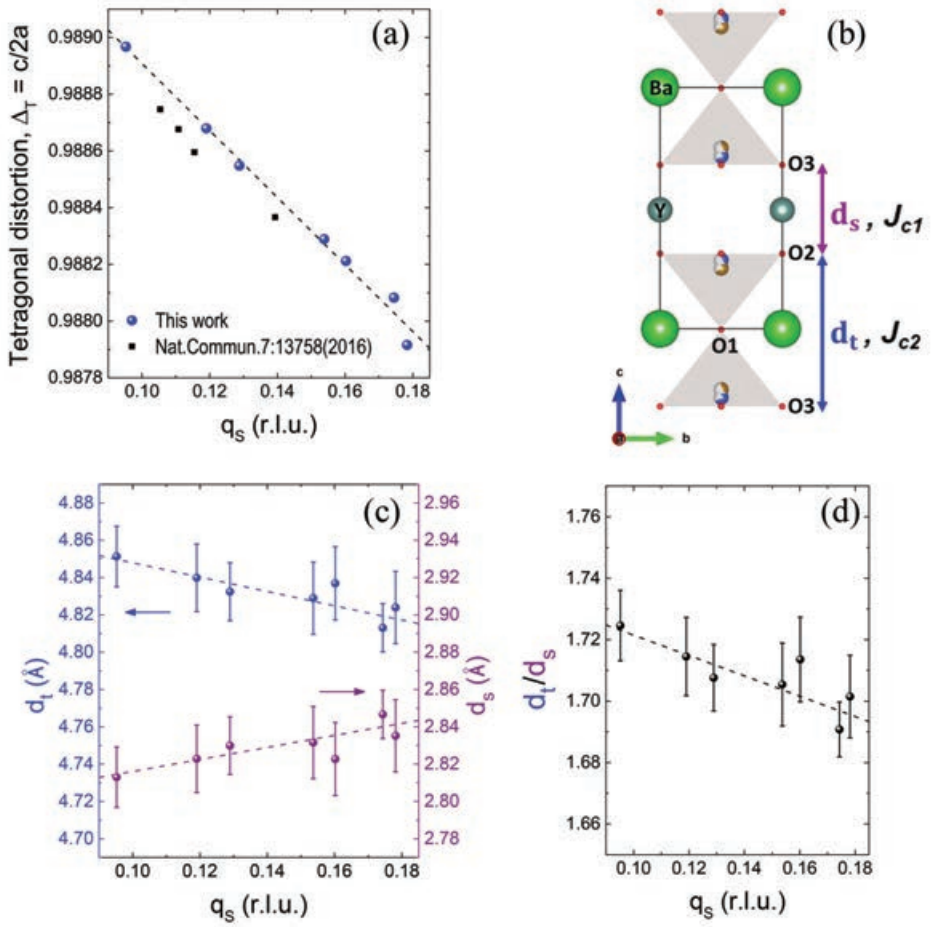

FIGURE 4.4: **Influence of disorder on the thickness and separation of the bilayers.** (a) Linear dependence of the tetragonal distortion (Δ_T=$c/2a$) on the incommensurability q_s of the spiral phase. (b) Projection of the $P4mm$ structure showing the thickness d_t of a bilayer and the separation d_s between bilayers. (c) Evolution of the thickness of the bipyramidal layer (d_t, left axis) and of the separation between bilayers (d_s, right axis). (d) The ratio d_t/d_s when increasing B-site chemical disorder in YBCFO. Dashed lines are linear fits to data points which are reported in Table 4.6.

4.3.3 Impact of the Fe/Cu disorder on the evolution of the pyramids

So, it has been found that by far the largest atomic displacement generated by increasing B-cation disorder corresponds to shifting apical O1 atoms parallel to **c**. The main consequence of such displacement is the shrinkage of the long pyramid (Cu) and the concomitant stretching of the short pyramid (Fe). For more clarity Fig. 4.6(b) displays the obtained evolution of the heights of both pyramids (H_L and H_S) as a function of the Fe/Cu disorder. Their heights in Angstroms are plotted versus the incommensurability of the spiral order (q_s) in each sample. Notice that disorder tends to make them more uniform, and

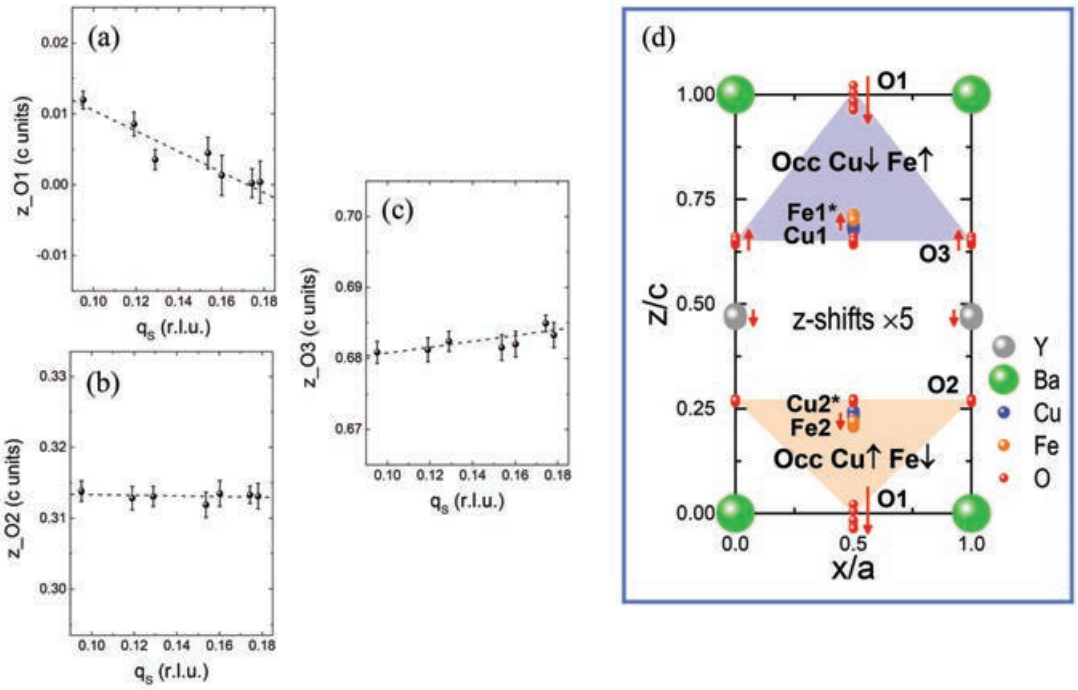

FIGURE 4.5: **Atomic shifts of apical and basal oxygens versus B-site disorder.** (a,b,c) Evolution of the z-coordinate for O1 (apical), O2 and O3 (basal) oxygens increasing Fe/Cu disorder, plotted against q_s (incommensurability). The height of the L- and S-pyramids is given by: $H_L = c \cdot (1 + z_{O1} - z_{O3})$; $H_S = c \cdot (z_{O2} - z_{O1})$. (d) Schematic projection of the YBCFO structure illustrating the magnitude and direction of the atomic shifts along the z-axis in samples with increasing B-site disorder. Dashed lines correspond to linear fits shown in Table 4.6.

so, due to the extreme level of disorder achieved, we obtained samples with average pyramids having practically identical sizes. In order to precisely understand the evolution shown in Fig. 4.6(b) it is important to pay attention to the evolution of the individual metal-to-oxygen distances in the pyramids of the compound when B-site disorder increases. Such dependence is shown in Figs. 4.6(c) and 4.6(d) as a function of q_s. Moreover, the main interatomic distances in the structure are gathered in Table 4.2. The distances displayed in Figs. 4.6(c) and 4.6(d) are the M-O bond-lengths for the majority metal in each pyramid. A look to Fig. 4.6(c) confirms severe changes in the average Jahn-Teller splitting between basal and apical distances around $Cu^{2+}(t_{2g}{}^6e_g{}^3)$. The large difference between Cu-O1 (apical) and Cu-O3 (basal) coordination distances in the Cu-rich pyramid (long one) decreases from a 15.4% down to the 9.7% in the most disordered sample. In other words, whereas the basal Cu-O3 is hardly modified, the apical Cu-O1 bond shrinks a 5% (-0.11 Å). Fig. 4.6(c) thus proves that the reduction in the average Jahn-Teller splitting around Cu is significant but nevertheless only partial. Notice that in Fig. 4.6(c) distances are taken respect to

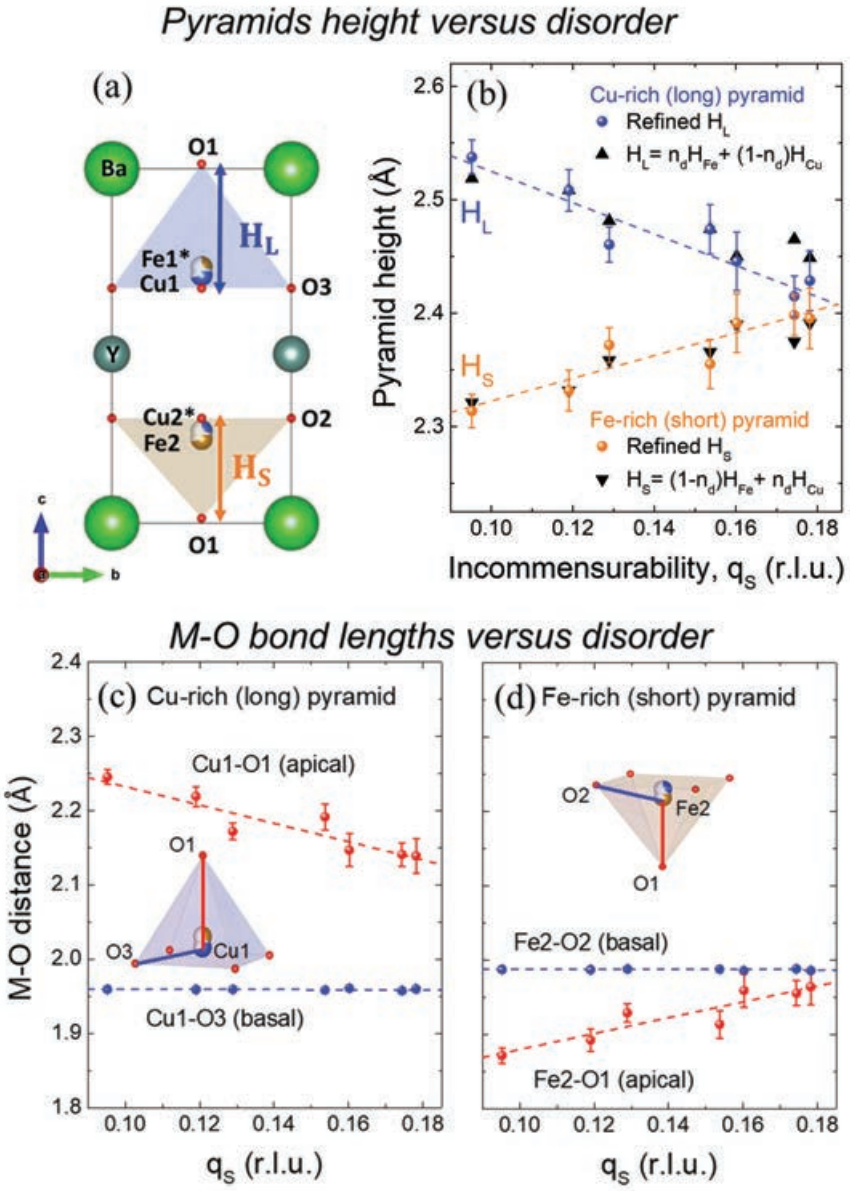

FIGURE 4.6: **Evolution of the two pyramids versus B-site disorder: H_L, H_S and the average CuO_5 Jahn-Teller splitting.** (a) Scheme of the structure illustrating the 'long' (upper, Cu-rich) and 'short' (lower, Fe-rich) average pyramids of the chemical unit cell. (b) Experimental correlation between the height of the two pyramids (at 300 K) and the incommensurability q_s of the spiral magnetic order when increasing Fe/Cu chemical disorder in YBCFO. CuO_5 pyramids are longer than FeO_5 ones in virtue of the Jahn-Teller distortion. The triangles correspond to the heights calculated from the refined fractional occupancy (n_d) using Eqs. (4.3) and (4.4). Evolution increasing the disorder of the (c) Cu-O and (d) Fe-O interatomic distances in the two pyramids. The evolution of the apical and basal (equatorial) distances in both pyramids (illustrated in the insets) is shown. Linear fits to experimental points (dashed lines) are reported in Table 4.6.

the Cu position, whereas they are taken respect to the Fe position in Fig. 4.6(d). In the short pyramid (Fe-rich) described in Fig. 4.6(d) the average apical Fe-O1

TABLE 4.2: Refined interatomic distances (in Angstroms) at 300 K in layered $YBaCuFeO_5$ from MSPD@ALBA synchrotron data (λ=0.413570 Å). (H: height of the pyramid).

T=300 K $P4mm$	**S1**	**S2**	**S3**	**S4**	**S5**	**S6**	**S7**
1-n_d=Occ(Cu1/Fe2)	0.706 (29)	0.684 (28)	0.628 (29)	0.613 (28)	0.563 (43)	0.594 (26)	0.560 (43)
n_d=Occ(Fe1*/Cu2*)	0.294 (29)	0.316 (28)	0.372 (29)	0.387 (28)	0.437 (43)	0.406 (26)	0.440 (43)
d_s (Å)	2.813 (16)	2.823 (18)	2.830 (16)	2.832 (19)	2.823 (20)	2.847 (13)	2.835 (19)
d_t (Å)	4.851 (16)	4.840 (18)	4.832 (16)	4.829 (19)	4.837 (20)	4.813 (13)	4.824 (19)
d_t/d_s	1.725 (11)	1.715 (13)	1.708 (11)	1.705 (13)	1.713 (14)	1.691 (10)	1.701 (13)
H_L (Å)	2.538 (15)	2.510 (18)	2.455 (15)	2.475 (22)	2.448 (26)	2.416 (18)	2.430 (26)
H_S (Å)	2.314 (15)	2.330 (18)	2.378 (15)	2.354 (22)	2.389 (26)	2.397 (18)	2.394 (27)
d(Cu1-O1)$_{apical}$ (Å)	2.245 (10)	2.221 (13)	2.162 (11)	2.193 (17)	2.149 (22)	2.142 (16)	2.140 (23)
d(Cu1-O3)$_{basal}$ (Å)	1.959 (3)	1.959 (2)	1.960 (1)	1.958 (1)	1.961 (1)	1.957 (1)	1.960 (1)
d(Fe2-O1)$_{apical}$ (Å)	1.871 (10)	1.890 (15)	1.943 (13)	1.912 (18)	1.956 (23)	1.954 (17)	1.963 (24)
d(Fe2-O2)$_{basal}$ (Å)	1.987 (4)	1.987 (4)	1.986 (2)	1.988 (2)	1.985 (2)	1.988 (1)	1.986 (2)

Comment: distances metal to Oa [= O1 (apical)] and Ob [= O2, O3 (basal)] correspond to the majority cation in upper (Cu-rich) and lower (Fe-rich) pyramids.

distance remains always shorter than the basal one (Fe-O2), but increases with disorder from -6% up to ∼-1% (+0.10 Å). In the most disordered sample (S7), apical and basal Fe-O bonds in the short pyramid are closely similar, and the heights H_L and H_S fully comparable ($H_L \approx H_S$).

To interpret correctly the diffraction results, it is important to emphasize that in the present case the refined information presents some limitations due to the disordered nature of YBCFO. The refined structural models don't reflect the real crystallographic unit cell, but an average of the local structural configurations. In consequence, the observed evolution of the pyramid heights (H_L and H_S) can be understood as the sum of two contributions: (i) the reduction (increase) of the long (short) pyramids due to the average of Cu and Fe pyramid heights (hereinafter called H_{Cu} and H_{Fe}) weighted by the fractional occupancy (n_d), and (ii) a reduction in the Jahn-Teller splitting at Cu pyramids caused by local distortions due to the increase of chemical disorder at the B-sites. In the case that the environments of Cu and Fe (in particular the Jahn-Teller character of Cu pyramids) are preserved regardless of the disorder, the latter component is neglectable and the observed pyramid heights as a function of disorder (n_d) can be approached as

$$H_L \approx n_d \cdot H_{Fe} + (1 - n_d) \cdot H_{Cu} \tag{4.3}$$

for the Cu-dominant (upper) pyramid, and

$$H_S \approx (1 - n_d) \cdot H_{Fe} + n_d \cdot H_{Cu} \tag{4.4}$$

for the Fe-dominant (lower) pyramid. Under this approach, using the refined values of n_d the best fit between the experimental H_L and H_S pyramid heights and those calculated using Eqs. (4.3) and (4.4) yields to $H_{Cu} \approx 2.66$ Å and $H_{Fe} \approx 2.18$ Å. The calculated pyramid heights are also plotted in Fig. 4.6(b). Bear in mind that this values are only an estimation of the real Cu and Fe pyramid heights under the virtual situation in which all Cu/Fe pyramids always have the same distortion regardless of the amount of disorder. According to this, Cu pyramids are up to ∼0.48 Å longer than Fe pyramids.

4.3.4 Effect of B-site disorder on the magnetic interaction paths

To explore the lattice impact in the different magnetic exchanges along the c axis and in the ab plane [J_{c_1}, J_{c_2} and J_{ab} in 4.7(a)], we have plotted the evolution of different relevant distances and angles. Notice that the Cu1-Fe1* (and Fe2-Cu2*) splitting distance (also shown in Table 4.3), deduced from their refined positions, does not change within errors for the different values of disorder. For this reason, to reduce statistical and experimental variations and to simplify the discussion we only plotted the average values of the interatomic distances and bond angles calculated respect to the centroid between the splitted M1 (Fe1*/Cu1) and M2 (Cu2*/Fe2) positions at the upper and lower pyramids, although Table 4.3 reports the complete set of distances and angles respect to each metal.

For the nearest-neighbor (NN) magnetic interactions along the c axis, the distances M1-O1-M2 (J_{c_2}) and M1-M2 (J_{c_1}) of the exchange interaction paths along the c axis reflect a similar behavior as the intra- and inter-layer separations (d_t and d_s) obtained from oxygen coordinates. As previously discussed, the c contraction is the net result of a decrease of the bipyramidal layers thickness (d_t) and a smaller increase of their separation (d_s) as a consequence of increasing disorder. The average M1-O1-M2 and M1-M2 distances [see Fig. 4.7(b)] evolve accordingly to the observed d_t and d_s evolutions. The decrease observed in the M1-O1-M2 distance is of special relevance, since it means that beyond the creation of Fe/Fe defects, the increase of disorder leads to a strenghtening of the AF coupling in the Fe_2O_9 improper bipyramids ($J_{c_2'}$) that further favours the stability of the frustrated noncollinear magnetic order (T_S).

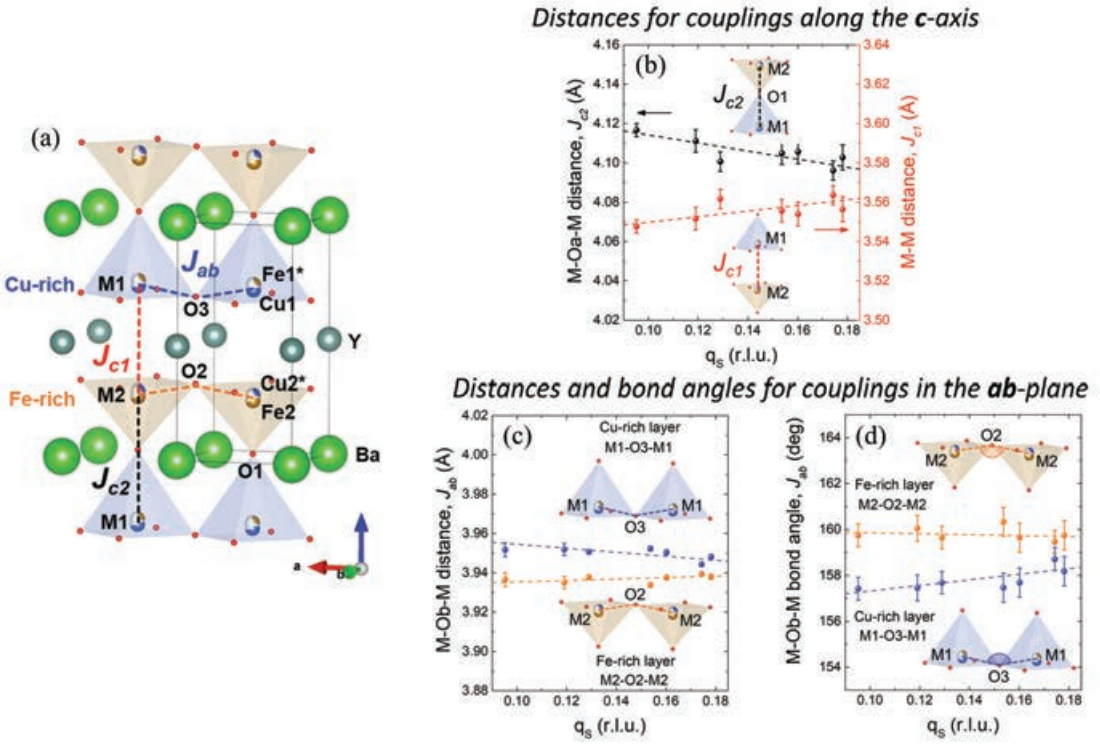

FIGURE 4.7: (a) Three-dimensional view of the $P4mm$ crystal structure of YBCFO showing the average nearest-neighbor (NN) magnetic interactions: J_{c_1} is assigned to the M1-M2 AFM couplings between bipyramidal layers and J_{c_2} to the M1-Oa-M2 (Oa=O1) FM couplings within bipyramids. J_{ab} describes the M-Ob-M AFM couplings between pyramids in the ab plane. M1-O3-M1 corresponds to the upper (Cu-rich) pyramids and M2-O2-M2 to the lower (Fe-rich) pyramids. (b) Effect of Fe/Cu disorder on the magnetic exchange paths along the c axis: M1-Oa-M2 distance (left axis, black points) and M1-M2 distance (right axis, red points). (c) Evolution with disorder of the in-plane interatomic distances and bond angles. Blue (brown) points correspond to Cu-rich (Fe-rich) average pyramid layers.

Due to the marked directionality of Jahn-Teller distortions around Cu^{2+} cations along the pyramid apical oxygens, the in-plane lattice variations caused by increasing Fe/Cu disorder values are much less marked than those along the c direcion. In consequence, smaller changes are observed in the evolution of the interatomic distances and angles in the ab plane. The distances and bond angles for the AFM ab couplings (J_{ab}) in the Cu-rich (upper) and Fe-rich (lower) pyramid layers are plotted in Figs. 4.7(c) and 4.7(d). The average M2-O2-M2 distance and superexchange angle is nearly constant in the Fe-Rich layers. In the case of Cu-rich layers, due to the positive shift in O3 z-coordinate, the M1-O3-M1 distance decreases slightly and the superexchange bond angle increases ($\sim$+1 deg). In any case we should bear in mind that changes in the J_{ab} AFM term are much less relevant for T_S than changes in J_{c_2}.

TABLE 4.3: Refined interatomic distances (in Angstroms) for the magnetic coupling paths (J_{c_1}, J_{c_2} and J_{ab}) and bond angles (in deg) for the magnetic couplings in the **ab**-plane (J_{ab}) at 300 K in layered YBCFO from MSPD@ALBA synchrotron data (λ=0.413570 Å).

T=300 K *P4mm*	**S1**	**S2**	**S3**	**S4**	**S5**	**S6**	**S7**
	M-M distances along the **c**-axis: inter-bowtie couplings (J_{c_1})						
d(Fe1*-Fe2) (Å)	3.7387 (54)	3.7479 (97)	3.7507 (88)	3.7656 (98)	3.7218 (97)	3.7459 (84)	3.7259 (99)
d(Cu1-Cu2*) (Å)	3.3567 (40)	3.3554 (56)	3.3727 (49)	3.3457 (53)	3.3862 (68)	3.3813 (49)	3.3869 (74)
d(M1-M2) (Å)	3.5477 (34)	3.5516 (58)	3.5617 (50)	3.5557 (57)	3.5540 (61)	3.5636 (49)	3.5564 (64)
	M-Oa-M distances along the **c**-axis: intra-bowtie couplings (J_{c_2})						
d(Fe2-O1-Fe1*) (Å)	3.9257 (54)	3.9149 (99)	3.9116 (88)	3.8949 (97)	3.9378 (99)	3.9138 (85)	3.9333 (98)
d(Cu2*-O1-Cu1) (Å)	4.3077 (40)	4.3074 (56)	4.2897 (49)	4.3149 (53)	4.2735 (68)	4.2784 (49)	4.2723 (74)
d(M2-O1-M1) (Å)	4.1167 (34)	4.1112 (58)	4.1007 (50)	4.1049 (57)	4.1056 (61)	4.0961 (49)	4.1028 (64)
	M-Ob-M distances for couplings in the **ab**-plane (J_{ab}): Cu-rich layer						
d(Fe1*-O3-Fe1*) (Å)	3.9936 (57)	3.9950 (57)	3.9916 (21)	3.9987 (23)	3.9864 (23)	3.9820 (17)	3.9837 (24)
d(Cu1-O3-Cu1) (Å)	3.9187 (42)	3.9181 (28)	3.9183 (13)	3.9165 (14)	3.9213 (14)	3.9146 (10)	3.9195 (14)
d(M1-O3-M1) (Å)	3.9517 (35)	3.9519 (31)	3.9506 (12)	3.9523 (13)	3.9504 (13)	3.9443 (10)	3.9481 (14)
	M-Ob-M distances for couplings in the **ab**-plane (J_{ab}): Fe-rich layer						
d(Fe2-O2-Fe2) (Å)	3.9747 (57)	3.9738 (57)	3.9756 (21)	3.9751 (23)	3.9708 (23)	3.9760 (17)	3.9714 (24)
d(Cu2*-O2-Cu2*) (Å)	3.9074 (42)	3.9057 (25)	3.9087 (11)	3.9033 (11)	3.9114 (12)	3.9110 (10)	3.9117 (13)
d(M2-O2-M2) (Å)	3.9365 (35)	3.9350 (31)	3.9378 (12)	3.9338 (13)	3.9376 (13)	3.9394 (10)	3.9380 (14)
	M-Ob-M angles for couplings in the **ab**-plane (J_{ab}): Cu-rich layer						
Fe1*-O3-Fe1* (deg)	152.0 (7)	151.9 (8)	152.3 (7)	151.5 (9)	152.9 (9)	153.5 (7)	153.3 (9)
Cu1-O3-Cu1 (deg)	162.8 (7)	163.0 (8)	163.1 (7)	163.4 (9)	162.5 (9)	163.9 (7)	163.0 (9)
M1-O3-M1 (deg)	157.4 (5)	157.5 (6)	157.7 (5)	157.5 (6)	157.7 (6)	158.7 (5)	158.2 (6)
	M-Ob-M angles for couplings in the **ab**-plane (J_{ab}): Fe-rich layer						
Fe2-O2-Fe2 (deg)	154.3 (7)	154.4 (8)	154.2 (7)	154.3 (9)	154.8 (9)	154.2 (7)	154.9 (9)
Cu2*-O2-Cu2* (deg)	165.2 (7)	165.7 (8)	165.1 (7)	166.4 (9)	164.5 (9)	164.7 (7)	164.6 (9)
M2-O2-M2 (deg)	159.7 (5)	160.1 (6)	159.7 (5)	160.3 (6)	159.7 (6)	159.5 (5)	159.7 (6)
Fe-Cu splitting distance, **d(Cu1-Fe1*)=d(Fe2-Cu2*) (Å)**	0.191 (5)	0.196 (8)	0.189 (7)	0.210 (8)	0.168 (9)	0.182 (7)	0.170 (9)

Comment: for simplicity and to reduce statistical and experimental variations, the averages of interatomic distances and bond angles have also been calculated respect to the centroid between the splitted Fe and Cu positions at the pyramids: $\mathrm{z\_M1(avg)} = (\mathrm{z\_Fe1^* + z\_Cu1})/2$ and $\mathrm{z\_M2(avg)} = (\mathrm{z\_Cu2^* + z\_Fe2})/2$.

4.4 XAS study of the B-site electronic structure and stoichiometry versus disorder

The partial ordering of Fe and Cu, described and parametrized in the previous sections from the refined improper occupation $\mathrm{n_d}$ of Fe1* [Cu2*] sites in the bipyramids (Fig. 4.2), is controlled by the cooling process during the preparation of YBCFO samples and shows up jointly with the presence of "non-mixed" M_2O_9 (M=Fe or Cu) bipyramids, which are at the origin of magnetic frustration in YBCFO [54, 55]. Although as previously mentioned the real density of non-mixed bipyramids can't be directly derived from the improper occupation and could be rather small, it is assumed that the density of M_2O_9 bipyramids increases along with chemical disorder, while the number of "ordered" $FeCuO_9$ bipyramids is in consequence reduced [54].

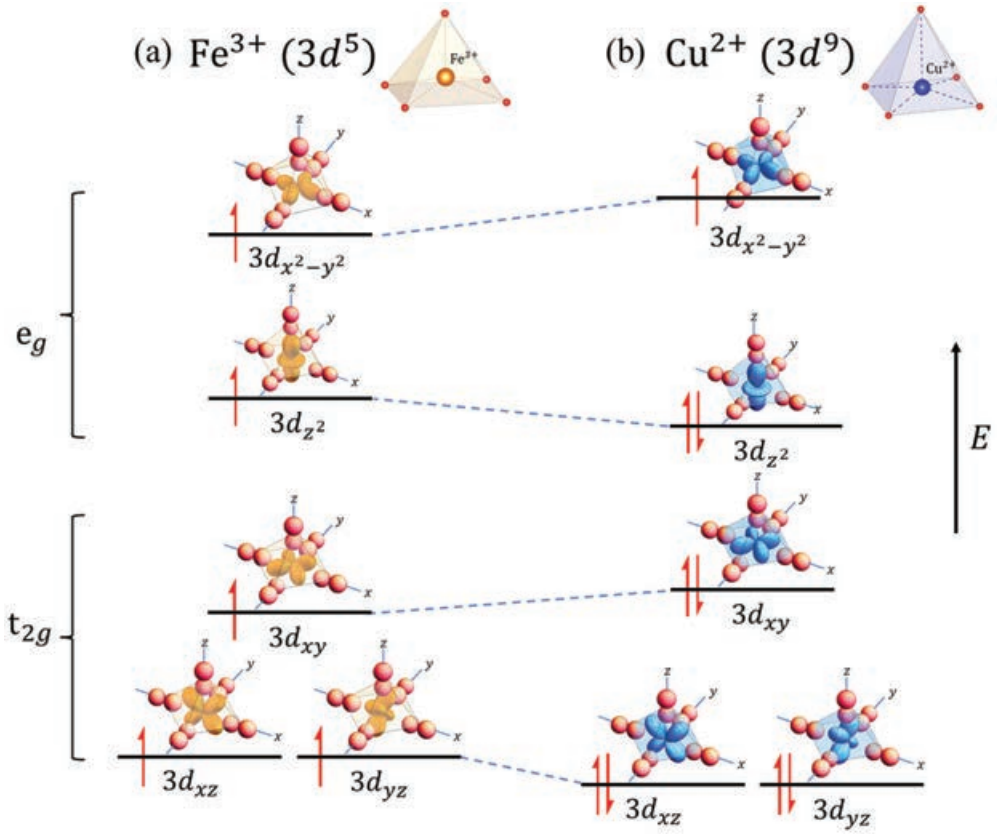

FIGURE 4.8: Schematic diagram of the $3d$ orbital splittings in pyramidal crystal fields. (a) Fe^{3+} in the High Spin (HS) state ($t_{2g}^3 e_g^2$) has a half-filled $3d^5$ shell. Fe is not susceptible of Jahn-Teller distortions and is out of the O_4 pyramid basal plane. (b) Cu^{2+} ($t_{2g}^6 e_g^3$) has an almost-filled $3d$ shell with a hole that makes it susceptible of undergoing Jahn-Teller distortions, leading to an elongated pyramid in the z direction and Cu very close to the O_4 pyramid basal plane. Red arrows represent the occupancy of orbitals by electrons. Oxygen $2p$ orbitals are depicted in red, and $3d$ orbitals of Fe^{3+}(Cu^{2+}) are shown in brown (blue) color.

The impact on the structutre of increasing Fe/Cu disorder, as well as the density of improper Fe/Fe bipyramids, has been addressed in the previous sections from SXRPD data. The average distortions observed around the Fe-rich and Cu-rich sites evidence that Fe and Cu adopt different pyramidal distorions. From the average Fe-Oa and Cu-Oa distances and from the heights of Fe-rich and Cu-rich pyramids, it is clear that the pyramidal crystal fields around Fe are compressed, while in the case of Cu they are elongated. In $3d$ transition metals in pyramidal crystal fields, the t_{2g} orbitals become split into two degenerated orbitals: the d_{xz}/d_{yz} and the d_{xy}. The higher energy e_g orbitals are likewise split into the d_{z^2} orbital, which points towards the $2p$ orbital of the apical oxygen, and the highest energy $d_{x^2-y^2}$ orbital, which is directed towards the four basal

oxygen $2p$ orbitals. Fig. 4.8 illustrates schematically the splitting of the $3d$ orbitals in a pyramidal crystal field for the two metallic ions involved in YBCFO. Fe^{3+}, with a half-filled $3d^5$ shell [see Fig. 4.8(a)], adopts a high-spin configuration with all the orbitals occupied ($t_{2g}^3 e_g^2$) and therefore is not susceptible of Jahn-Teller distortions. In contrast, Cu^{2+} has an almost-filled $3d^9$ shell with a hole [see Fig. 4.8(b)]. X-ray Linear Dichroism (XLD) measurements in a YBCFO single crystal reported by Srivastava *et al.* show evidence that Cu $3d$ e_g holes are located at the in-plane $3d_{x^2-y^2}$ orbital, while the $3d_{z^2}$ electrons extend along c leading to the Jahn-Teller elongation of the CuO_5 pyramid in the [001] direction [110], in accordance with our SXRPD observations.

Still, as exposed in Section 4.3.3, due to the disordered nature of YBCFO the diffraction results present some limitations when it comes to clarify how relevant is the effect of increasing disorder and the presence of non-mixed M_2O_9 bipyramids on the local Fe/Cu crystal fields. It is a matter of interest the accomodation of Cu_2O_9 bipyramids in the structure. Whereas the mixed $FeCuO_9$ bipyramids are formed by one regular and one distorted pyramid, the concurrence of two distorted Cu pyramids with large Jahn-Teller distortions can be problematic. In $YBaCuFe_xMn_{1-x}CuFeO_5$ samples investigated in Ref. [49], Fe^{3+} is substituted by potential Jahn-Teller active Mn^{3+} ions ($t_{2g}^3 e_g^1$) at the B-sites. In this series it is observed that the Jahn-Teller splitting of copper (average Cu-Oa distance) is not affected upon increasing the presence of Mn^{3+} at the bipyramids, while the average (Fe/Mn)-Oa distance is reduced, suggesting that the concurrence of Cu^{2+} and Mn^{3+} ions with the $3d_{z^2}$ orbitals pointing towards the apical oxygen along c in the same bipyramid ($Cu^{2+}Mn^{3+}O_9$) results in a too high energy penalty and the e_g electron in Mn^{3+} occupies the in-plane $3d_{x^2-y^2}$ orbital [49]. This draws questions on what can be expected in the case of non-doped YBCFO samples with cation disorder, where two Cu^{2+} ions with very stable Jahn-Teller splitting converge in a bipyramid. Both a compression of Cu bipyramids or a suppression of the Jahn-Teller splitting in a fraction of Cu pyramids are compatible with the observed decrease of the average Cu-Oa distance when Fe/Cu disorder increases. Although Fig. 4.6 could also indicate that locally Cu pyramids are not modify by the presence of disorder.

While diffraction provides average information on the independent crystallographic sites (Fe-rich and Cu-rich pyramids), element-selective X-ray Absorption Spectroscopy (XAS) techniques may help overcoming this limitations providing insight on the local crystal fields surrounding Fe and Cu separately.

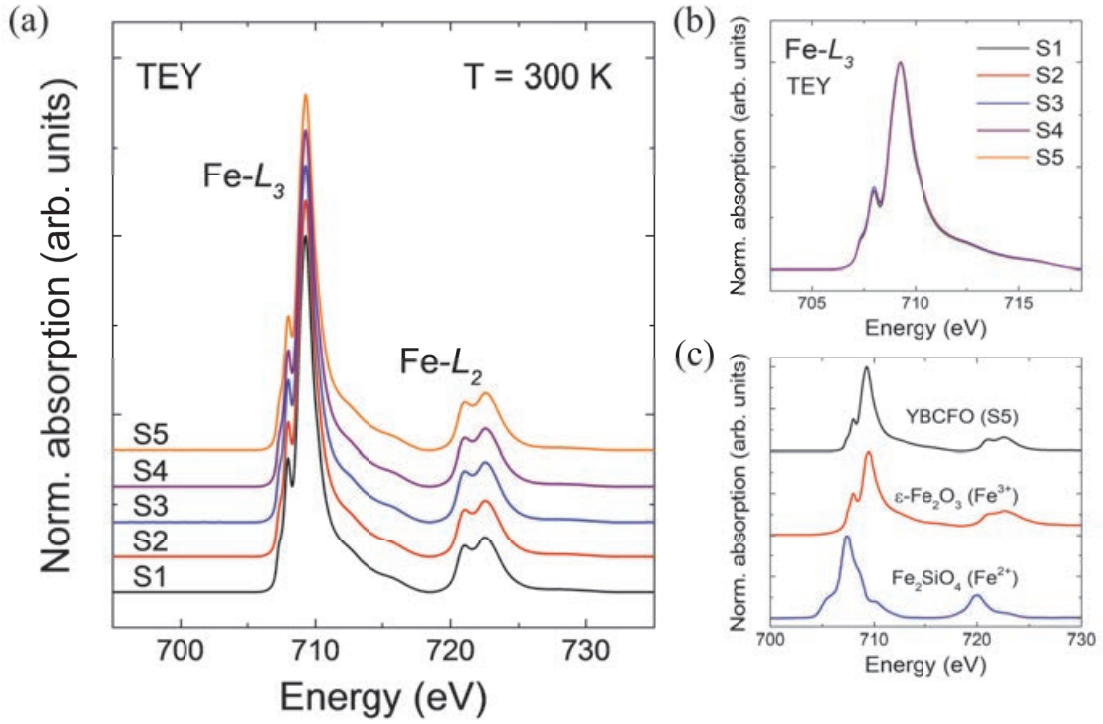

FIGURE 4.9: (a) Experimental TEY XAS spectra at Fe $L_{2,3}$ edges for YBCFO samples with different Fe/Cu disorder at 300 K. (b) Details of the Fe L_3 edge evidence no variation of spectra with Fe/Cu disorder. (c) Fe $L_{2,3}$ edges at 300 K: the black line corresponds to the measured spectrum in YBCFO sample S5. Red an blue lines are XAS reference spectra of Fe^{3+} and Fe^{2+} iron in ε-Fe_2O_3 and Fe_2SiO_4 [111], respectively.

Thus, with the purpose of assessing the electronic states of the metals at the YBCFO B-sites and, in particular, the stability of their electronic structure as a function of Fe/Cu disorder, a soft XAS study was conducted at room temperature focusing on Fe and Cu $L_{2,3}$ edges for samples prepared under increasingly higher cooling rates. The experimetal XAS spectra across the Fe and Cu $L_{2,3}$ region for YBCFO samples S1 to S5 are presented in Figs. 4.9 and 4.10, respectively. The highest absorption peak, corresponding to the Fe (Cu) L_3 edge, is found at 709.26 (929.67) eV, and the L_2 edge appears around 722.22 (949.42) eV. In general, the $L_{2,3}$ edges in Fe (Cu) are primarily associated with the $2p \rightarrow 3d$ transitions, and depend strongly on the multiplet structures, which are related to the Fe (Cu) $3d$-$3d$ and $2p$-$3d$ Coulomb and exchange interactions, the local crystal field and the hybridization between Fe (Cu) $3d$ and O $2p$ states [110].

Fig. 4.9(c) displays the XAS reference spectra of Fe in compounds with well-known formal oxidation states: ε-Fe_2O_3 (Fe^{3+}) and Fe_2SiO_4 (Fe^{2+})[112]. By comparison with the reference spectra, it can be easily observed that the experimental Fe XAS spectra in all YBCFO samples [plotted in Fig. 4.9(a)] display the

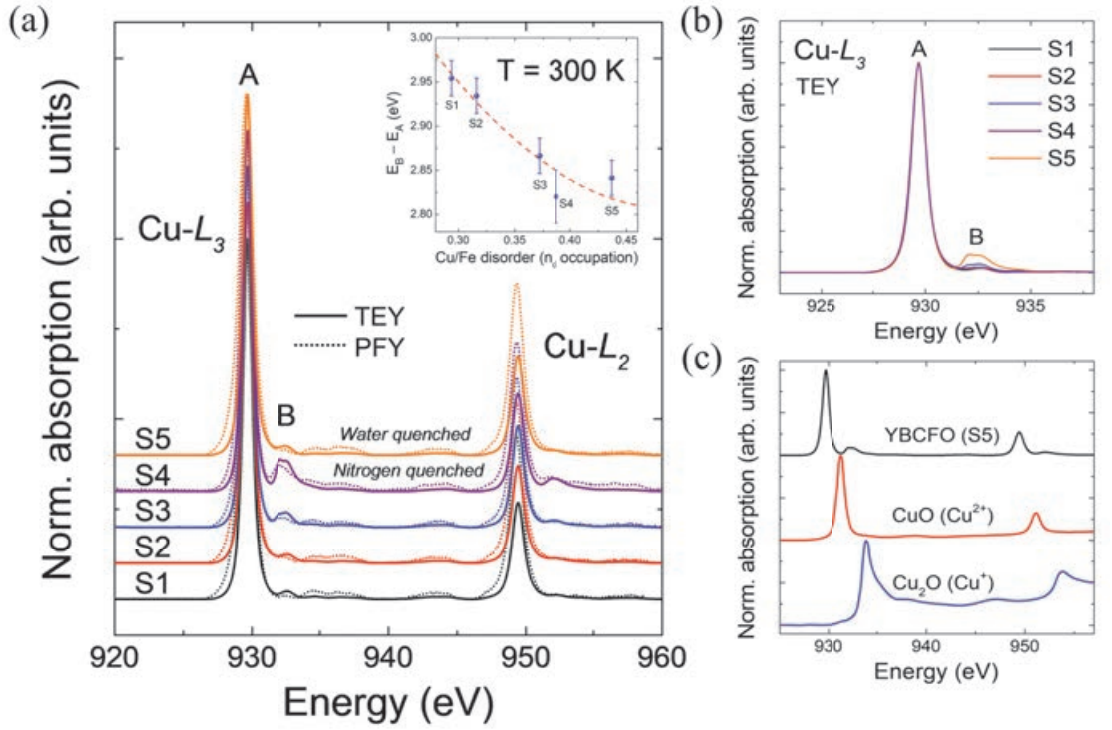

FIGURE 4.10: (a) Experimental Cu $L_{2,3}$ XAS spectra at 300 K for YBCFO samples with different chemical disorder. Labels A and B mark features discussed in the text. Solid lines correspond to the TEY measurements and dotted lines to PFY data. [Inset: energy separation between A and B peaks in the TEY spectra as a function of the Fe/Cu disorder (n_d) of the samples] (b) Cu L_3 region showing the A and B features in more detail. (c) Cu $L_{2,3}$ edges at 300 K: the black curve is the experimental data in sample S5. The red an blue lines are provided as XAS references of divalent and monovalent copper in CuO and Cu_2O single crystals, respectively, from Ref. [111].

well-known fingerprint of a high spin (S=5/2) and trivalent electronic state of Fe [110, 113, 114]. A closer look at the Fe L_3 region, shown in Fig. 4.9(b), evidences the resilience of the valence and crystal field structure around Fe upon Fe/Cu disorder increase, since no variations in the width and energy position of the absorption peaks is observed at all.

For the case of Cu, Fig. 4.10(a) displays the set of XAS spectra taken at the $L_{2,3}$ region. At first sight, the measurements show two well defined peaks of Lorentzian shape at 929.67 eV (L_3) and 949.42 eV (L_2), the former labeled as A in the figures. These structures can be attributed to the expected $3d^9$ configuration of Cu^{2+}. For comparison, the spectral shapes of typical divalent and monovalent copper (from CuO and Cu_2O single crystals, respectively) obtained from Ref. [111] are shown in Fig. 4.10(c). Notice that in the compounds studied, the excitation to the empty Cu s, d states are at lower energy than in the reference CuO shown in Fig. 4.10(c). The difference in energy observed between YBCFO

and CuO is related to the different crystal fields around Cu. While Cu^{2+} ions are found at the center of an oxygen rectangle in CuO [115], in YBCFO they are surrounded by five oxygens with pyramidal symmetry. That said, as in the case of Fe, the invariance in the energy position and width of the A peak in Cu spectra measured on the different YBCFO samples [see Fig. 4.10(b)] seems to indicate that the crystal field around Cu^{2+} ions are probably not modified by the increase of Fe/Cu disorder.

On top of this, in the L_3 region it is evident the presence in all of the YBCFO samples of an asymmetric satellite structure above the Cu L_3 edge at ∼933 eV, labeled as B in Figs. 4.10(a) and 4.10(b) . It is known that Cu displays enhanced affinity for highly polarizable anions like oxygen and a marked tendency to covalency. As a consequence of this character, the sharing of electrons between metal and ligand cations usually leads to nonintegral values for the number of electrons on the metal [116]. For this reason, it is common in copper oxides that Cu appears in mixed ionic states. Van der Laan *et al.* adscribed similar structures observed in Cu_2O and Cu_2S to monovalent (Cu^+) ionic states [117]. Also, Mostovshchikova *et al.* reported similar features on CuO nanoceramics [111]. In the latter case, the peaks are associated to a reduction of Cu^{2+} into Cu^+ ions at the surface. In this sense, it is not surprising to observe the formation of Cu^+ in our TEY measurements, which are highly surface sensitive. If samples are not cleaved in vacuum before exposing them to the beam, then a clear Cu^+ peak is usually visible. So, a CuO dead layer is likely present at the surface of samples left in air, although we do not know how fast is the reduction process and in consequence it is not possible to establish a relation between the variation of the A peak intensity and intrinsic parameters of the sample. This is confirmed by bulk sensitive partial fluorescence yield (PFY) spectra collected in parallel, which also showed the presence (to a lesser extent) of the Cu^+ peak. For this, we also assume that certain amount of monovalent copper is intrinsic of the sample preparation process, which involve factors such as the quenching medium or cooling rates applied. Notice that S4, which was cooled rapidly by quenching in liquid nitrogen, is the sample with higher presence of monovalent copper as observed from both TEY and PFY measurements [Fig. 4.10(a)]. This remarkably higher presence of monovalent copper is likely related to the abrupt quenching process, in which the sample was cooled from very high temperatures (1150 °C) surrounded by a non-oxidizing nitrogen atmosphere. A similar effect is observed in $YBa_2Cu_3O_{7+\delta}$ ceramics, for which a

decrease of the oxygen content (δ) was reported in samples quenched from successively higher temperatures in a inert atmosphere (in this case Ar) [118]. In our case, oxygen vacancies provoked by quenching in liquid nitrogen could explain the higher presence of monovalent copper in sample S4. It should be also stressed that no bad crystallization or extra phases in the YBCFO samples were detected from high-resolution SXRPD data [Fig. 4.1 in Section 4.3.1].

Interestingly, whereas the energy values of the A peak for the different samples is rather constant at 929.7 eV, the position of the B peak associated to monovalent copper varies. In addition, the energy separation between A $2p^5 3d^{10}$ (A) and $2p^5 3d^{10} 4s^1$ (B) peaks seems to be correlated with the chemical disorder, ranging from 932.65 eV for the more ordered sample (S1) to 932.52 eV for the sample with higher disorder (S5). C. de Nadaï *et al.* [119] suggest that the energy separation between A and B peaks [of initial states (prior to photoionization) $2p^6 3d^9$ and $2p^6 3d^{10}$, respectively] is related to the ionization potential of the ligands. Based on this, in our compounds the variation of the energy separation (from 2.95 eV for the more ordered sample to 2.82 eV for the sample with higher disorder) could be attributed to local structural distortions and strain effects on the local environment of Cu^+ ions as a consequence of the increase of non-mixed M_2O_9 bipyramids as the chemical disorder increases. It is important to notice that this effect is not observed on the absorption peaks of Cu^{2+} and Fe^{2+} with fully occupied d shell due to the pure d nature of their absorption.

4.5 Magnetic phase diagram versus Fe/Cu chemical disorder in YBCFO

4.5.1 Magnetic transitions

The magnetic transition temperatures were identified by susceptibility and neutron diffraction measurements. The magnetic susceptibility curves $\chi(\mathrm{T})$ are shown in Fig. 4.11, from 5 K to 500 K, as obtained in field-cooling (FC) conditions using a dc magnetic field of 2 kOe. Two local maxima in $\chi(\mathrm{T})$ identify the two separated transitions. The commensurate ($\mathrm{T_{N1}}$) and incommensurate ($\mathrm{T_{N2}} = \mathrm{T_S}$) magnetic orders were comparatively investigated by neutron diffraction within the 10 K-500 K range to elucidate the influence of increasing the level of Fe/Cu disorder in YBCFO.

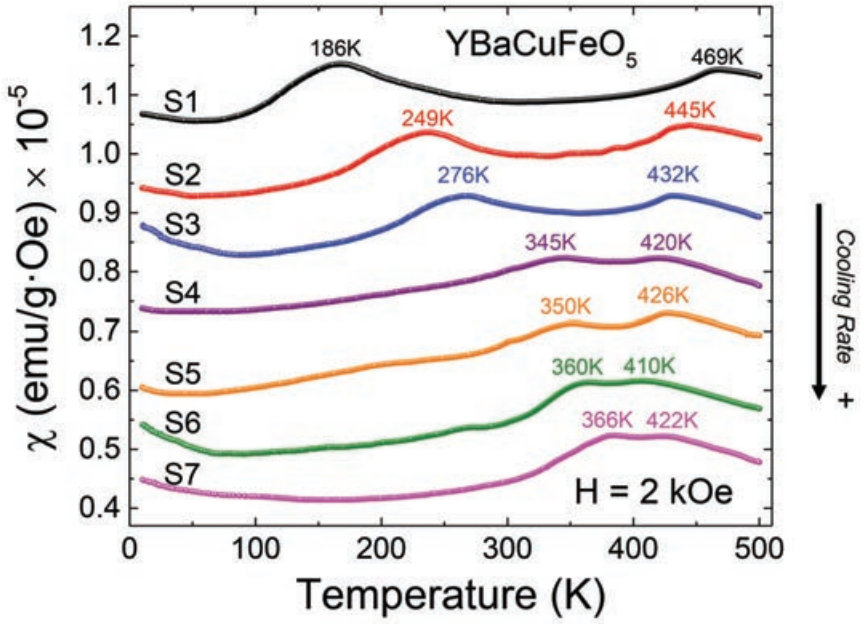

FIGURE 4.11: Evolution of the magnetic susceptibility curves (measured in FC, 2 kOe) for YBCFO samples with increasing Fe/Cu cation disorder. Successive curves were shifted by $+10^{-6}$ emu $\cdot$ g^{-1} $\cdot$ Oe^{-1} for clarity. The higher transition signals the onset of the collinear order (T_{N1}, $\mathbf{k}_1$); the lower corresponds to the non-collinear spiral transition ($T_{N2} = T_S$, $\mathbf{k}_2$).

Figure 4.12(a) shows the T-Q projections of the NPD intensities collected between 10 K and 500 K. The figure focuses on a Q-range around the (1/2 1/2 1/2) peak that covers the main magnetic reflections. The onset and evolution of the two magnetic phases is also shown from the evolution of the magnetic integrated intensities [Fig. 4.12(b)]. Upon cooling from 500 K, first peaks indexed as (h/2 k/2 l/2) appear at T_{N1} (T_{N1}>400 K in all the samples). The propagation vector $\mathbf{k}_1 = (1/2, 1/2, 1/2)$ of the collinear phase sites at the A-point of the Brillouin Zone. T_S is easily identified in all the samples by the apparition of a new set of magnetic Bragg reflections (satellites) with propagation vector $\mathbf{k}_2 = (1/2, 1/2, 1/2 \pm q)$. Throughout this dissertation, this phase is referred to as "spiral phase", although further on we will point out certain limitations of the neutron diffraction data obtained from powder samples. In all the samples a spiral order emerges at T_{N2} (T_S) and persists down to the base temperature [Figs. 4.12(a) and 4.12(d)].

The Rietveld analysis of magnetic intensities in the NPD patterns as a function of the temperature was done using the sequential refinement tool in FullProf. The fitted magnetic reflections were generated by defining different phases

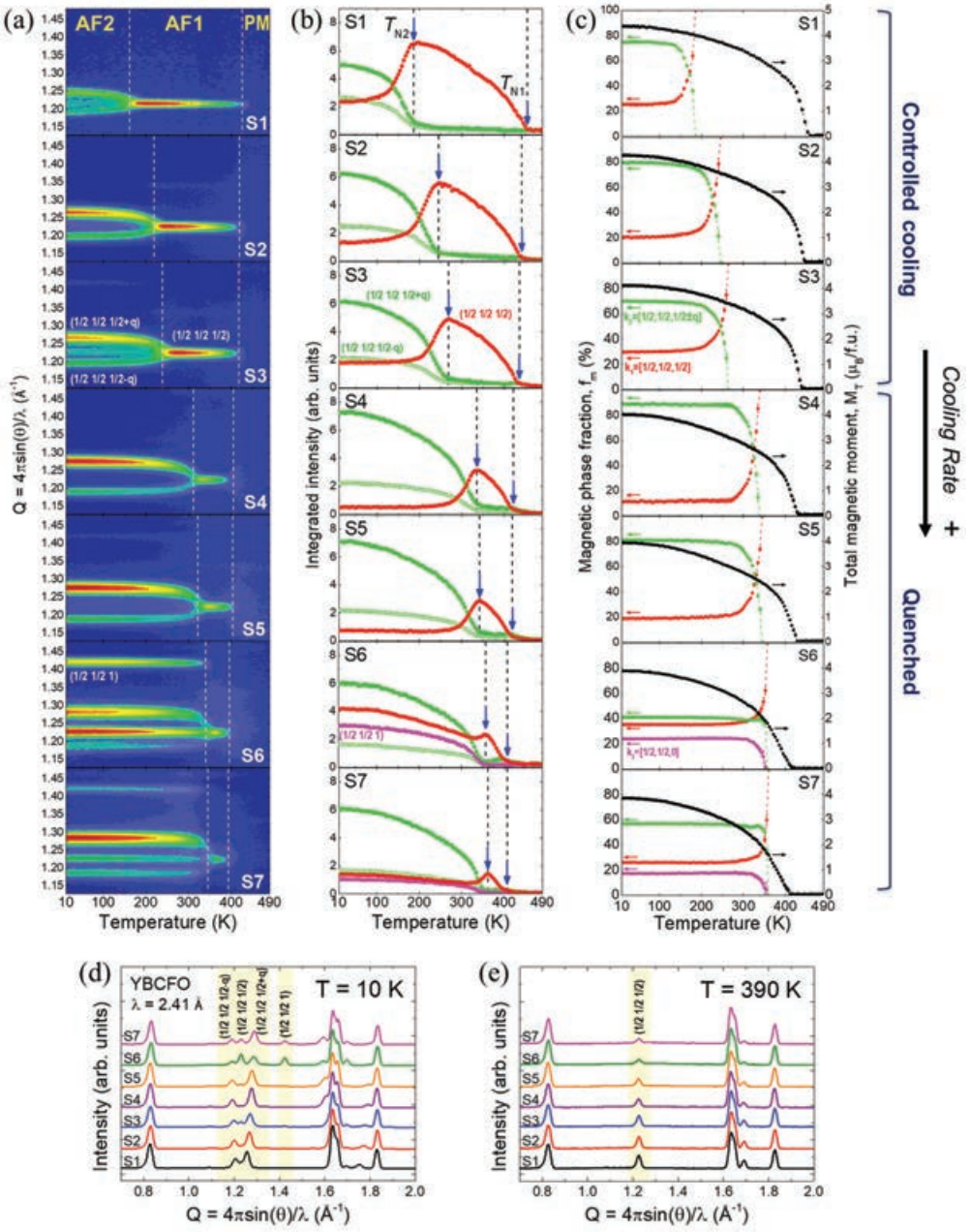

FIGURE 4.12: (a) Contour maps showing the T-Q projection of the temperature dependence for the neutron-diffracted intensities around the (1/2 1/2 1/2) magnetic reflection (D20@ILL). The neutron intensities illustrate the emergence of the commensurate and incommensurate (spiral) magnetic phases. (b) Thermal variation of the integrated intensities of the selected magnetic Bragg reflections and satellites, which correspond to the propagation vectors $\mathbf{k}_1 = (1/2, 1/2, 1/2)$ (red), $\mathbf{k}_2 = (1/2, 1/2, 1/2 \pm \mathrm{q})$ (green), and $\mathbf{k}_3 = (1/2, 1/2, 0)$ (pink). (c) Ordered magnetic moment per formula unit (right axis, in μ_B/f.u.) and fraction (left axis, in %) of the spiral and collinear magnetic phases with propagation vectors $\mathbf{k}_1$ (green), $\mathbf{k}_2$ (red), and $\mathbf{k}_3$ (pink), refined from the NPD data as a function of temperature. (d) Low Q region of the neutron diffraction patterns recorded at 10 K and (e) at 390 K. Evolution increasing the Fe/Cu disorder.

of given magnetic translational symmetries described by the propagation vector $\mathbf{k}_i$ (with $i = 1, 2, 3$). In order to have better control of the orientation and amplitude of the magnetic moments, the real and imaginary components of the Fourier coefficients were defined for each magnetic atom using spherical coordinates; the magnetic symmetry operations were introduced manually using the P-1 Space Group. The scale factors of the crystallographic and magnetic parts were related by the following constraint:

$$\mathrm{S_n} = \sum_i \mathrm{S_m}(\mathbf{k_i}) \tag{4.5}$$

where $\mathbf{S_n}$ is the scale factor of the nuclear phase and $\mathrm{S_m}(\mathbf{k_i})$ ($i = 1, 2, 3$) are the magnetic scale factors of the different magnetic phases. In order to get correct magnetic moment values, the occupancies (Occ) of the atomic positions in the nuclear phase were defined as Occ = (Multiplicity of special position)/(General multiplicity of the Space Group). The occupation numbers in the magnetic part are related to the number of symmetry operators given and the centrosymmetry (or not) of the magnetic structure. With these requirements satisfied, the scale factors can be related as described in Eq. (4.5). The magnetic phase fractions $\mathrm{f_m}$ (in $\%$) are then derived from the refined scale factors as

$$\mathrm{f_m}(\mathbf{k_i}) = 100 \cdot \frac{\mathrm{S_m}(\mathbf{k_i})}{\sum_j \mathrm{S_m}(\mathbf{k_j})} \tag{4.6}$$

We should bear in mind that from NPD it is not possible to distinguish between single phase and segregated phase scenarios, and that in the latter case it is not possible to distinguish the real ordered moment in a magnetic phase from its fraction relative to the total volume of the sample. In our refinements, the phase fractions were determined from the scale factors assuming that the ordered magnetic moment is the same for the different coexisting magnetic phases, which might not be true in the reality if the different magnetic orderings occur in separated regions of the crystal grains. The relative magnetic phase fractions and refined average magnetic moments at 10 K are reported in Table 4.5. The evolution with temperature of the total magnetic moment per formula unit (in $\mu_\mathbf{B}/\mathbf{f.u.}$) and the relative magnetic phase fractions $\mathrm{f_m}(\mathbf{k}_i)$ (in $\%$) derived from the scale factors using Eq. (4.6) are shown in Fig. 4.12(c). For the sake of comparison, the ordered magnetic moments are plotted together in Fig. 4.13(a). Beyond the typical thermal variation of the ordered moment, an important and worthy of attention observation is the systematic decrease of the

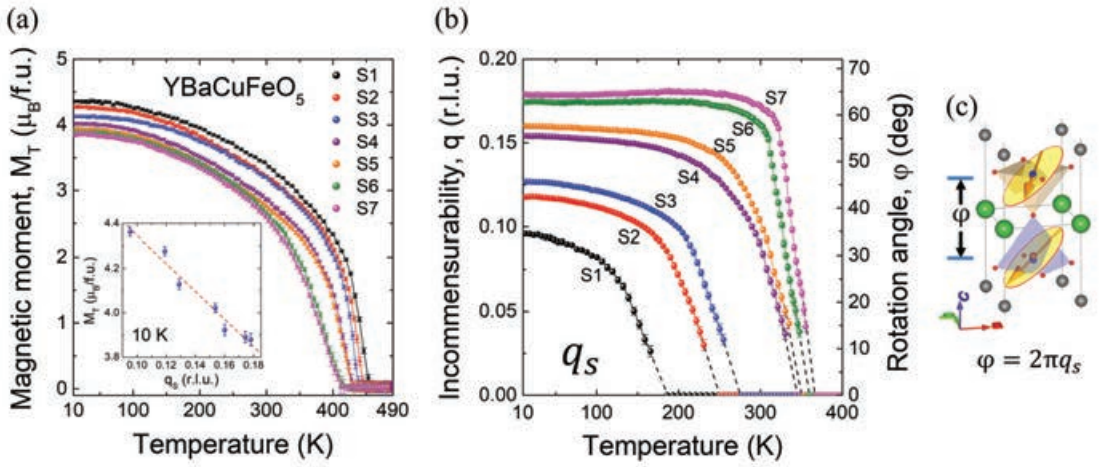

FIGURE 4.13: (a) Temperature dependence of the average ordered magnetic moment M_T per formula unit in YBCFO. The inset shows the magnetic moment values at 10 K plotted versus the ICM modulation q_s of the samples. Notice the linear decrease of M_T as q_s (*i.e.* the Fe/Cu cation disorder, n_d) increases. (b) Influence of chemical disorder on the incommensuration q_s of the spiral phase and its temperature dependence. The dashed lines are linear extrapolations used to identify the spiral transition temperatures. (c) Illustration of the twist angle φ (canting) formed by the two spins of a bipyramid in the spiral phase ($\varphi = 2\pi q_s$).

average magnetic moment as Fe/Cu disorder increases. The inset in Fig. 4.13(a) shows a nearly linear dependence between the average ordered magnetic moment at 10 K and the incommensurability q_s, with a decrease $\Delta m_T \approx -0.5$ $\mu_B/f.u.$ between the more ordered sample (S1) and the sample with highest disorder (S7). We attribute this effect to the increase of magnetic frustration in the system associated to the higher presence of frustrating AFM Fe/Fe bonds as B-site disorder increases.

The temperature evolution of the spiral modulation q_s(T) was obtained for all the samples and it is exposed in Fig. 4.13(b), where the influence of disorder is immediately appreciable. The smooth decreasing evolution of q_s(T) approaching T_S in the more ordered samples (low n_d) strongly contrasts with a very rapid downfall at the collinear-to-spiral transition in the most disordered YBCFO specimens. The observed change is consistent with an evolution of the transition from second to first order when the triple point approaches. At the triple point this collinear-spiral transition meets the second-order paramagnetic-collinear ordering. In the A-site substituted $YBa_{1-x}Sr_xCuFeO_5$ family quenched in liquid nitrogen [48] a similar abrupt q_s(T) evolution approaching T_S was reported in the sample with Sr content x=0.40, with higher T_S and q_s=0.175. The model of Scaramucci *et al.*, based on orientationally correlated Fe-O-Fe bonds, is

compatible with a critical value $n_{crit} \lesssim 0.50$ above which the transition becomes of first-order [55]. Our neutron results and the q_s(T) evolutions depicted in Fig. 4.13(b) suggest a first-order collinear-to-spiral transition in YBCFO samples approaching the triple point for a chemical disorder $n_d \gtrsim 0.44$ ($q_s \gtrsim 0.17$ r.l.u.). In contrast, the evolution exposed in Fig. 4.13(b) for more ordered samples rather suggests a continuous (second-order) transition. Discerning whether n_{crit} is indeed reached before the triple point or coincides with the merging of the two transitions into a single direct transition (paramagnetic-spiral) is out of the scope of this work. It would require a specific study using additional techniques and more compositions near the triple point (with controlled homogeneous disorder).

Fig. 4.14 discloses a complete T-n_d magnetic phase diagram for the YBCFO system. In the horizontal axis we have represented the B-site disorder n_d obtained by Rietveld refinement in our samples. As in the preceding sections, aside aside from the disorder n_d and given that the chemical composition is not varied, the incommensuration q_s of the spiral is also used to typify the increasing cationic disorder in B sites (upper horizontal axis). It is worth noting that in practice the experimental accuracy for assessing q_s is greater than the accessible accuracy for the occupation n_d. For the sake of comparison, in Fig. 4.14 we show together the experimental (q_s,T_S) points of this work (in red color) and those from the YBCFO samples (in black color) reported earlier in Ref. [48]. The overall picture is thus consistent with previous studies reporting a positive variation of T_S and a negative slope of T_{N1} when the cooling rate of the prepared YBCFO samples is increased [47, 48]. In the light of this phase diagram shown in Fig. 4.14 it is important to underline several noteworthy issues:

(i) As expected, the Néel temperature associated with the collinear commensurate order decreases in YBCFO when magnetic frustration increases, but the downward slope is quite smooth compared to the upward slope for T_S. The $T_S(q_s)$ and $T_{N1}(q_s)$ dependencies are parametrized by linear fits to T_{N1} and T_S experimental values, respectively:

$$T_{N1} = 517.2(15.7) - 590.9(106.5) \cdot q_s \tag{4.7}$$

$$T_S = T_{N2} = -61.7(9.9) + 2610.1(78.6) \cdot q_s \tag{4.8}$$

The fits are also detailed in Table 4.6 and shown as dashed lines in Fig. 4.14. The points taken from Ref. [48] match well our results.

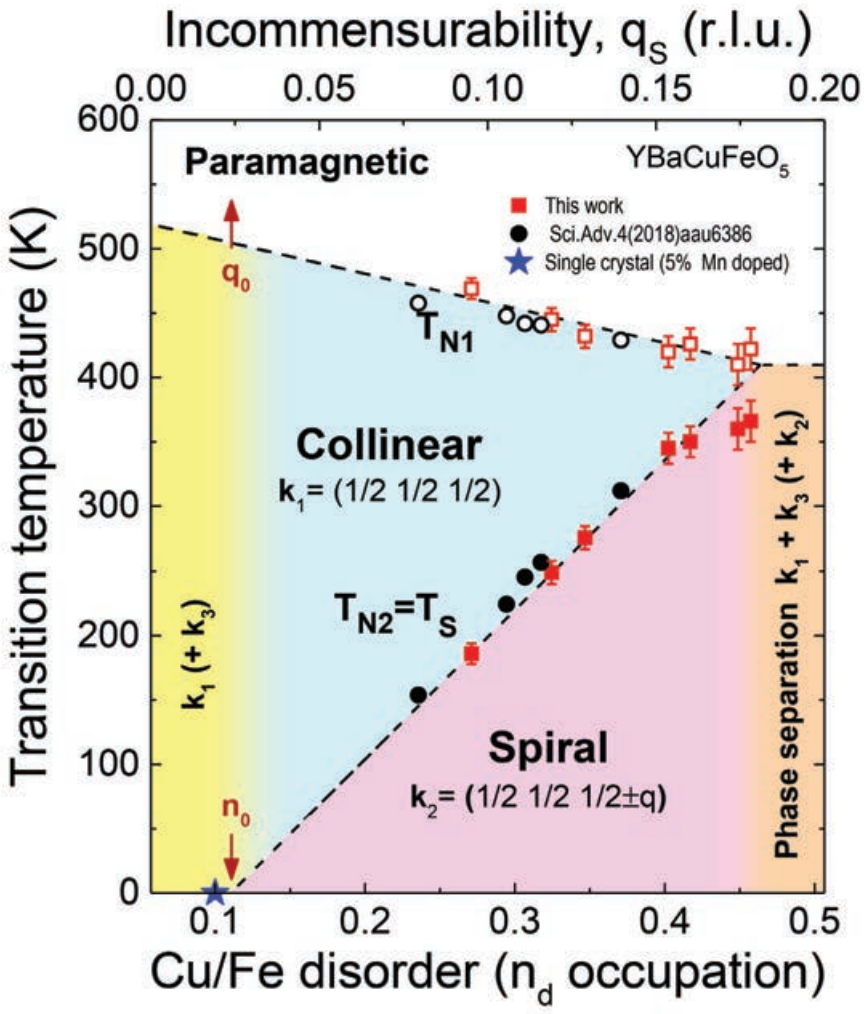

FIGURE 4.14: **Magnetic phase diagram versus Fe/Cu chemical disorder for $YBaCuFeO_5$.** q_s-T and n_d-T magnetic phase diagram for YBCFO. The phase boundaries describe the onset of the magnetic phases according to neutron diffraction data. For the sake of comparison, black points correspond to q_s-T values from samples reported in Ref. [48]. Empty and filled symbols correspond to T_{N1} and T_{N2}=T_S, respectively.

(ii) Our fit of the experimental (q_s, T_S) points confirms the linear relationship predicted in the theory, in which the incommensurate wave vector and the spiral temperature are both proportional to the concentration of improper Fe/Fe bonds [48]. However, an interesting feature is the intersection point with the x axis. It is noteworthy from Fig. 4.14 that the linear extrapolation does not go through the origin (q_s=0, T_S=0), in contrast with the usual assumption in previous reports. Remarkably, the horizontal axis (T_S=0) is cut at a point q_0 (and at n_0), both related by Eq. (4.1) clearly separated from the origin: q_0 = 0.025 r.l.u. and $n_0 \approx 0.112$. It is worth mentioning here that the additional point at

[n_d = 0.10(3), T_S = 0] shown in Fig. 4.14 is taken from Ref. [120], which reports a highly ordered YBCFO single crystal (with 5% Mn doping) presenting $\mathbf{k}_1$ and $\mathbf{k}_3$ phase coexistence and lack of spiral order. Consequently in this structure there is a critical threshold of disorder (n_0) or minimum frustration level, below which a long-range spiral magnetic state cannot be formed. Such critical disorder tells us that if the concentration of straight Fe-O-Fe bonds is too low and they are too far apart, the dipolar interaction (mediated by spin waves) between individual canted spins in the vicinity of the separated Fe/Fe bonds decay without forming a coherent spiral. From the obtained q_0 critical value an estimation of the associated minimum canting angle yields $\varphi_0 \approx 9^\circ$ ($\varphi_0 = 2\pi q_0$).

(iii) The critical threshold n_0 to achieve a spiral ground state entails the existence of a inhomogeneous region in the phase diagram when disorder is too low [$0<n_d<n_0$ in Fig. 4.14]. In this antiferromagnetic perovskite the ferromagnetic J_{c_2} exchange between Fe^{3+}/Cu^{2+} ions within "ordered" $FeCuO_9$ bipyramids leads to the antitranslation k_z = 1/2. The perfectly ordered YBCFO system ($n_d = 0$) is thus expected to be of $\mathbf{k}_1$–type. Conversely, when the order is not totally perfect but it approaches, then there is a minority fraction of non-mixed M_2O_9 bipyramids (M=Fe or M=Cu), in which the M-O-M exchange is antiferromagnetic. If that fraction is still too small to form spiral ordering, phase segregation can occur, favored but with the presence of short-ranged minority regions with tendency to k_z = 0 (non-mixed AM_2O_9 bipyramids with internal antiferromagnetic coupling). So, in the region with just incipient disorder, dominant $\mathbf{k}_1 = (1/2, 1/2, 1/2)$ magnetic regions with high-T_{N1} values could coexist at lower temperatures with a small fraction of short-ranged $\mathbf{k}_3 = (1/2, 1/2, 0)$ magnetic clusters (AF3 collinear phase). These could exhibit a dynamic nature before eventually freezing out when cooling down. Recently, segregated $\mathbf{k}_3$-type collinear domains (AF3) were observed in highly ordered single crystals (with absence of spiral order) dominated by $\mathbf{k}_1$-type collinear ordering [120]. Thus, an inhomogeneous regime is anticipated in the phase diagram of Fig. 4.14 when disorder is still incipient ($n_d \to 0$ and $n_d<n_0$) and the cross talking between (too far apart) AFM Fe-Fe "defects" cannot stabilize a magnetic spiral.

(iv) From the slope of the linear evolution described by Eq. (4.8) in the YBCFO perovskite we obtain $T_{spi}/|q_s| \approx 71(3)$ meV, in very good agreement with the estimation of 68 meV made in the model by Scaramucci *et al.* in Ref. [55].

(v) Of utmost importance is the presence of seemingly a paramagnetic-collinear-spiral triple-critical point in the phase diagram of Fig. 4.14. The triple point marks a stability limit for the spiral phase, where the collinear and spiral lines intersect and fluctuation phenomena give way to another regime. It unveils that the critical incommensurability for YBCFO is given by $q_s^c \approx 0.18$ r.l.u. and the critical propagation vector $\mathbf{k}_2^c = (1/2, 1/2, 1/2 \pm q_s^c)$. The maximum incommensuration previously reported in YBCFO was q_s = 0.14 r.l.u. in a quenched sample (T_S = 310 K) [47], although a triple point in AA'$CuFeO_5$ was first proposed by Shang *et al.* in $YBa_{1-x}Sr_xCuFeO_5$ samples quenched into liquid nitrogen. The stability range of the spiral was further extended by the application of chemical pressure instead of Fe/Cu disorder, reaching $T_S \approx 375$ K and $q_s \approx 0.175$ r.l.u. in the $YBa_{0.6}Sr_{0.4}CuFeO_5$ solid solution [48]. Given that divalent A-cations are located within the bilayer spacing, smaller Sr^{2+} ions (respect to Ba^{2+}) produce a compression of the bilayers in $YBa_{1-x}Sr_xCuFeO_5$, reducing d_t and increasing T_S by enhancing the AFM coupling ($J_{c_2'}$) inside the Fe_2O_9 bipyramidal units (impurity bonds). Our exhaustive study of the YBCFO perovskite unveils that a triple point can be attained in this layered structure without increasing the number of divalent or trivalent chemical species in the structure. Later on we will come back to the triple point in YBCFO.

Next, we will describe how to control relevant details of the magnetic anisotropy and the magnetic spirals through the degree of B-site chemical order in our layered (AA')(BB')O_5 perovskites, keeping invariant their chemical composition in both, the A and the B sites.

4.5.2 Influence of B-site disorder on the magnetic easy axis

We have investigated the impact of disorder on the magnetic anisotropy of YBCFO by means of neutron diffraction. Henceforth we call the orientation of the collinear magnetic moments in the commensurate phase "magnetic easy axis". As shown in Fig. 4.17(b), it is defined by the inclination angle θ that the moments (or the spiral plane in the incommensurate case) form with the c axis. Notice that due to the tetragonal symmetry of the parent cell, it is not possible from NPD to distinguish the orientation of the magnetic easy axis component parallel to the ab plane. Any orientation of that component does not produce changes in NPD intensities. With the aim of studying the influence of chemical disorder on the magnetic easy axis, the collinear spin order in the $2a \times 2a \times 2c$

magnetic cell was refined in all the samples at 390 K. Table 4.4 reports the θ_C values obtained in the collinear regime, as well as the refined magnetic moments. Given that the theoretical ratio m(Fe^{3+})/m(Cu^{2+}) of their respective unpaired spins is 5, we imposed in the neutron refinement that the ratio r between the ordered moments at the two pyramids should be

$$r \equiv \frac{m_L}{m_S} = \frac{1 + 4 \cdot n_d}{5 - 4 \cdot n_d}, \tag{4.9}$$

where n_d stands for the improper occupation factor (associated to the migrated cations) and m_L, m_S are the ordered magnetic moments refined at the long (Cu-rich) and short (Fe-rich) pyramids, respectively. We found that disorder has no influence on the orientation of the easy axis in the AFM collinear phase (k_1). The spin orientation is found at $\theta_C \approx 50°$ in all the samples, no matter the level of disorder. We observed in addition that the orientation θ_C of the magnetic easy axis was temperature-independent in the collinear regime (see also Ref. [49]). To illustrate this, in Fig. 4.17(c) we show as an example the thermal evolution of the inclination angle θ(T) for sample S2 for the two magnetic regimes (θ_C and θ_S). The inclination of the spiral rotation plane (θ_S) is very similar (although slightly lower) and equally remains very stable below T_S. Contrasting with the collinear easy axis, in next section we will explore and describe a very different response to disorder of the characteristic spin rotation plane of the spiral phase.

4.5.3 Influence of B-site disorder on the anisotropy of the spiral phase

Limitations of the neutron powder diffraction

In a powder diffraction pattern all the reciprocal space is projected onto one dimension, as a function of *2Theta*. Therefore, all reflections located at the same *2Theta* angle contribute to a unique peak of the pattern, whose intensity results from all those peaks. In contrast to single crystal diffraction measurements, where each single reflection is collected individually, the averaging inherent to NPD entails limitations that in the case of cycloidal or helicoidal orders may prevent its complete description. In the case of magnetic structures, in addition to projecting onto a single dimension, only the perpendicular component of the magnetic structure factor to the scattering vector contributes to the intensity of each reflection. A more detailed example about the limitations of NPD to fully characterize incommensurate spiral orders can be found in Ref. [121]. NPD

data collected in our set of YBCFO samples are compatible with an incommensurate spiral phase below T_S, described in the form:

$$\mathbf{m}_{lj}(\mathbf{k}) = M_R \mathbf{u}_j \cos 2\pi\left(\mathbf{k}\cdot\mathbf{R}_l + \Phi_j\right) + M_I \mathbf{v}_j \sin 2\pi\left(\mathbf{k}\cdot\mathbf{R}_l + \Phi_j\right) \tag{4.10}$$

where $\mathbf{m}_{lj}$ is the magnetic moment of the atom j in the unit cell l, $\mathbf{R}_l$ is the vector joining the arbitrary origin to the origin of unit cell l, and Φ_j is a magnetic phase. $\mathbf{u}_j$ and $\mathbf{v}_j$ designate the orientation of the two perpendicular unitary vectors that define the plane of the helix, where M_R (real) and M_I (imaginary) amplitudes fix the dimensions of the elliptical envelope described by the rotating magnetic moments.

In these powder samples (due to the intrinsic limitations mentioned above) it is not possible to independently refine (i) the real and imaginary amplitudes (M_R and M_I) or (ii) the two magnetic moments in the bipyramidal units, forcing us to fix their ratios using constraints. Hence the neutron patterns were refined constraining the two ordered moments (at the long and short pyramids) according to the ratio r ($r \equiv m_L/m_S$) deduced from the refined occupations (disorder) for each sample [see Eq. (4.9)] and listed in Table 4.4. Moreover, the two moments of a bipyramid were restricted to the same inclination angle θ in the neutron refinements. Additionally, the phase difference between the magnetic moments at the two pyramids separated by the Y layer in the chemical cell was fixed to 180° as found in Refs. [19, 46, 47, 109] (during the data analysis we confirmed that any deviation from 180° when comparing the different samples should be lower than 2-3°).

It is necessary to stress that the most relevant drawback of studying powder samples of this layered structure probably is the inability to refine the real and imaginary amplitudes (M_R and M_I) of the elliptical spiral order. In other words, identical agreement factors are obtained regardless of the chosen M_I/M_R ratio. So, we decided to extend the study of the incommensurate magnetic order to include the two opposite limits of (i) very large ($M_R \gg M_I$) and (ii) null eccentricity ($M_R = M_I$). The latter picture has been the one adopted in the majority of earlier works and agrees well with the tetragonal symmetry of the paramagnetic structure. In Fig. 4.15 we show how the two models: (i) *a variable-moment sinusoid* [Fig. 4.15(a)] and (ii) *a spiral magnetic order* [Fig. 4.15(a)], can give account of/reproduce very well the incommensurate phase of the neutron powder diffraction patterns from YBCFO. Fig. 4.15 illustrates the need to

conclusively study the incommensurate order in YBCFO by single crystal neutron diffraction experiments. The spiral solution was assumed from powder samples to explain the ferroelectricity but its existence has not been yet unambiguously attested.

Neutron powder diffraction refinements at 10 K

In Table 4.4 we list the refined magnetic moments (m_L,m_S), modulation vectors (q_s) and tilting angles θ_S of the rotating plane of the spins (easy plane) for the incommensurate magnetic phase obtained from NPD data at 10 K. This table exposes the information of the incommensurate magnetic phase in YBCFO samples with increasing magnetic frustration induced by rising the level of Fe/Cu disorder (quantified through n_d and q_s). The two opposite extremes or limits mentioned before were considered and are shown in the table: $M_R \gg M_I$ (*model 1*) and $M_R = M_I$ (*model 2*). The former limit draws a collinear sinusoidal order ($M_I = 0$) and the second one describes a circular spiral. Keep in mind that intermediate eccentricities ($0<M_I/M_R<1$) between the two extremes are also compatible with recorded NPD patterns. A study of the possible changes in the eccentricity induced by disorder would require single crystals. In order to minimize the uncertainty in the refined θ_S values, first we used the $M_R \gg M_I$

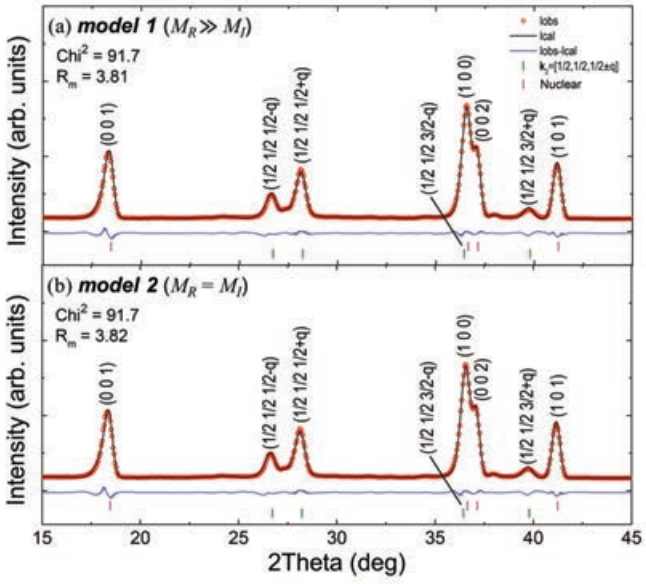

FIGURE 4.15: **Sinusoidal versus spiral NPD fit in a polycrystalline YBCFO sample**. Rietveld refinement (black curve) of the neutron diffraction data (red circles) collected at 10 K on the two-axis D20@ILL diffractometer for a powder $YBaCuFeO_5$ sample (S2). (a) Variable-moment collinear sinusoid model ($M_R \gg M_I$). (b) Spiral model ($M_R = M_I$). Rows of bars are indicated in the inset of the bottom panel.

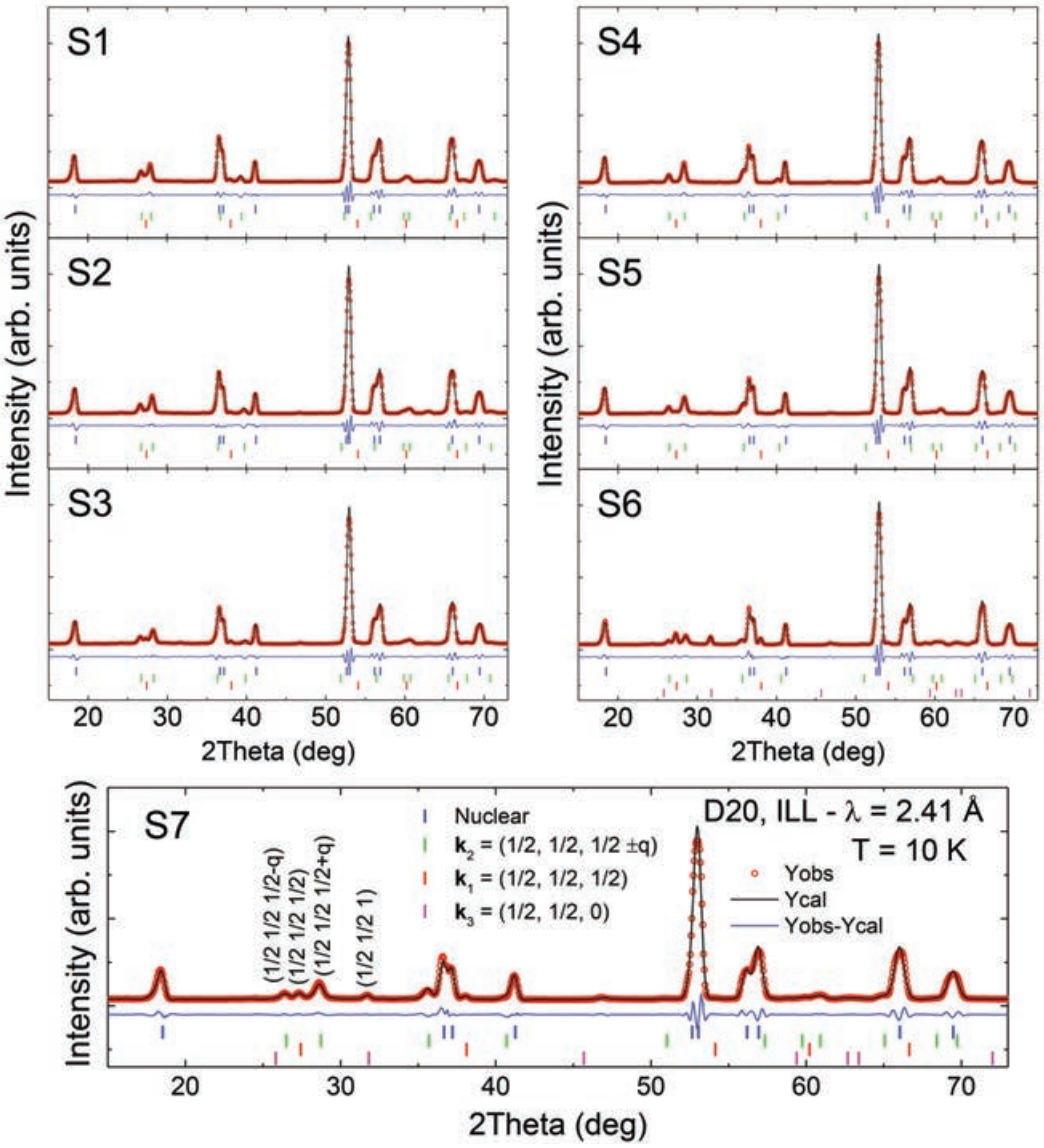

FIGURE 4.16: Rietveld refinement (black curve) of the D20 neutron diffraction patterns (red circles) at 10 K ($M_R = M_I$) for the $YBaCuFeO_5$ samples with increasing B-site disorder. Rows of bars are indicated in the inset of the bottom panel. Low-temperature neutron refinements of samples S6 and S7 (most disordered) were done including the additional $\mathbf{k}_3 = (1/2, 1/2, 0)$ phase (see Table 4.5 for additional information).

limit for obtaining this tilting angle below T_S. Then, this refined θ_S value was used in the magnetic refinement of the circular spiral (*model 2*). This allows to maximize accuracy, minimizing the errors in the determination of θ_S. The full neutron Rietveld refinements (at 10 K, using *model 2*) for all our YBCFO samples are exposed in Fig. 4.16 and the extracted magnetic information is listed in Table 4.5.

TABLE 4.4: Refined magnetic parameters for the spiral (10 K) and collinear (390 K) orders in $YBaCuFeO_5$ as a function of the Fe/Cu chemical disorder at the B-sites of the perovskite. See explanation in the text (theta angle of the ICM phase (θ_S) in *model-2* was fixed to its refined value in *model-1*).

	S1	**S2**	**S3**	**S4**	**S5**	**S6**	**S7**
$\mathbf{q_s}$ **(r.l.u.)**	0.09522 (29)	0.11901 (29)	0.12890 (29)	0.15366 (29)	0.16018 (29)	0.17432 (29)	0.17813 (29)
$\mathbf{n_d}$	0.294 (29)	0.316 (28)	0.372 (29)	0.387 (28)	0.437 (43)	0.406 (26)	0.440 (43)
$\mathbf{r = m_L/m_S}$	0.569 (48)	0.606 (48)	0.708 (56)	0.738 (56)	0.845 (98)	0.777 (55)	0.852 (98)
$\mathbf{T_{N1}}$ **(K)**	469 (8)	445 (9)	432 (9)	420 (12)	426 (12)	410 (16)	422 (16)
$\mathbf{T_{N2} = T_S}$ **(K)**	186 (8)	249 (9)	276 (9)	345 (12)	350 (12)	360 (16)	366 (16)
			Spiral order	**10 K**	**(AF2-ICM)**		
Model 1 ($M_I \sim 0$)							
m_S (μ_B)	3.480 (32)	3.287 (35)	2.760 (32)	3.175 (28)	2.693 (27)	2.002 (38)	2.409 (31)
$m_L = r \cdot m_S$ (μ_B)	1.985 (18)	2.002 (21)	1.954 (24)	2.343 (20)	2.260 (23)	1.563 (30)	2.049 (26)
θ_S (deg)	47.3 (5.3)	41.9 (5.1)	35.5 (5.2)	36.1 (3.7)	30.3 (4.3)	32.7 (6.0)	28.7 (5.8)
Model 2 ($M_R = M_I$)							
m_S (μ_B)	2.549 (23)	2.418 (25)	2.042 (23)	2.325 (21)	1.973 (20)	1.450 (28)	1.755 (23)
$m_L = r \cdot m_S$ (μ_B)	1.455 (13)	1.473 (15)	1.446 (17)	1.715 (15)	1.656 (16)	1.132 (22)	1.493 (19)
θ_S (deg)	47.3	41.9	35.5	36.1	30.3	32.7	28.7
χ^2	*31.18*	*40.76*	*54.67*	*31.61*	*34.30*	*60.05*	*52.04*
R_B	*2.03*	*4.05*	*4.97*	*2.67*	*2.84*	*2.23*	*2.63*
R_f	*1.11*	*2.14*	*2.41*	*1.58*	*1.43*	*1.52*	*1.52*
R_m	*6.62*	*8.58*	*9.85*	*9.54*	*8.30*	*10.8*	*8.50*
			Collinear order	**390 K**	**(AF1-CM)**		
m_S (μ_B)	3.34 (23)	3.08 (24)	2.80 (21)	2.39 (20)	2.10 (21)	1.66 (27)	1.60 (27)
$m_L = r \cdot m_S$ (μ_B)	1.91 (13)	1.88 (15)	1.98 (16)	1.77 (14)	1.76 (18)	1.29 (21)	1.36 (23)
θ_C (deg)	52.7 (7.6)	52.4 (7.5)	52.0 (7.4)	49.7 (5.9)	50.6 (6.9)	51.8 (8.6)	49.6 (7.9)
χ^2	*30.82*	*37.67*	*46.98*	*30.84*	*32.79*	*58.41*	*48.77*
R_B	*2.04*	*2.78*	*3.66*	*3.19*	*1.84*	*2.45*	*2.68*
R_f	*1.20*	*1.75*	*1.90*	*1.74*	*1.14*	*1.63*	*1.66*
R_m	*8.46*	*11.2*	*11.4*	*16.5*	*14.6*	*17.7*	*18.0*

Influence of chemical disorder on the inclination of the magnetic spiral plane

As mentioned before, we use the angle θ to describe the angular distance (inclination) between the direction of the spins and the c axis, in the collinear and noncollinear phases. In the former the magnetic easy axis is given by the collinear spins direction $\mathbf{u}$ (CM phase). In the spiral ICM phase at $T<T_S$, θ_S describes the tilting of the rotation plane of the helix [$\mathbf{uv}$ plane; see Eq. (8.1) and Fig. 4.17(b)]. The tetragonal symmetry prevents specifying the orientation of the moments in the ab plane. For simplicity, the director vector $\mathbf{u}$ can be taken as within the ac plane, $\mathbf{v}$ being thus parallel to the b axis. θ_S values close to zero means the magnetic easy axis is close to the c axis, whereas $\theta_S \approx 90^\circ$ implies that the easy axis is parallel to the ab plane. Morin *et al.* were the first to report changes in the inclination angle in YBCFO samples prepared changing the cooling rate. Only for $\theta_S = 0^\circ$ or 90° do all the active magnetic modes describing the magnetic arrangement belong to the same magnetic irreducible representation [46].

Fig. 4.17(a) plots the experimental (q_s, θ_S) points obtained from neutrons

TABLE 4.5: Magnetic parameters of the coexistent magnetic phases at T = 10 K with propagation vectors $\mathbf{k}_1 = (1/2, 1/2, 1/2)$, $\mathbf{k}_2 = (1/2, 1/2, 1/2 \pm \mathrm{q})$ and $\mathbf{k}_3 = (1/2, 1/2, 0)$ derived from the Rietveld refinements of the neutron powder diffraction data of the $YBaCuFeO_5$ samples with different Fe/Cu cation disorder. Refined average magnetic moments $\mathrm{m_L}$ and $\mathrm{m_S}$ at the respective Cu-rich and Fe-rich pyramid sites were obtained imposing $\mathrm{m_L} = \mathrm{r} \cdot \mathrm{m_S}$, with the ratio r calculated according to the refined Fe/Cu cation disorder.

T = 10 K	S1	S2	S3	S4	S5	S6	S7
$\mathbf{n_d}$	0.294 (29)	0.316 (28)	0.372 (29)	0.387 (28)	0.437 (43)	0.406 (26)	0.440 (43)
$\mathbf{r = m_L/m_S}$	0.569 (48)	0.606 (48)	0.708 (56)	0.738 (56)	0.845 (98)	0.777 (55)	0.852 (98)
COLLINEAR (AF1)							
$\mathrm{f_m}(\mathbf{k}_1)$ (%)	25.26 (79)	20.7 (1.1)	30.17 (77)	10.3 (2.0)	18.2 (1.2)	35.29 (56)	25.69 (78)
θ_C (deg)	52.7	52.4	52.0	49.7	50.6	51.8	49.6
SPIRAL (AF2)							
$\mathrm{f_m}(\mathbf{k}_2)$ (%)	74.74 (83)	79.3 (1.1)	69.83 (86)	89.7 (1.9)	81.8 (1.2)	40.12 (65)	56.41 (81)
θ_S (deg)	47.3 (5.3)	41.9 (5.1)	35.5 (5.2)	36.1 (3.7)	30.3 (4.3)	32.7 (6.0)	28.7 (5.8)
q_s (r.l.u.)	0.09522 (29)	0.11901 (29)	0.12890 (29)	0.15366 (29)	0.16018 (29)	0.17432 (29)	0.17813 (29)
COLLINEAR (AF3)							
$\mathrm{f_m}(\mathbf{k}_3)$ (%)	-	-	-	-	-	24.60 (48)	17.91 (67)
θ_C (deg)	-	-	-	-	-	51.8	49.6
$\mathrm{m_S}$ (μ_B)	2.780 (23)	2.664 (25)	2.417 (23)	2.314 (21)	2.126 (20)	2.190 (28)	2.094 (23)
$\mathrm{m_L} = \mathrm{r} \cdot \mathrm{m_S}$ (μ_B)	1.582 (13)	1.614 (15)	1.712 (17)	1.708 (15)	1.797 (16)	1.701 (22)	1.785 (19)
χ^2	*31.18*	*40.76*	*54.67*	*31.61*	*34.30*	*60.05*	*52.04*
R_B	*2.03*	*4.05*	*4.97*	*2.67*	*2.84*	*2.23*	*2.63*
R_f	*1.11*	*2.14*	*2.41*	*1.58*	*1.43*	*1.52*	*1.52*
R_m ($\mathbf{k}_1$)	*11.5*	*22.7*	*18.2*	*54.2*	*30.7*	*5.74*	*12.1*
R_m ($\mathbf{k}_2$)	*6.62*	*8.58*	*9.85*	*9.54*	*8.30*	*10.8*	*8.50*
R_m ($\mathbf{k}_3$)	-	-	-	-	-	*10.2*	*16.1*

at 10 K. Fig. 4.17(a) illustrates the systematic decrease of θ_S (within the range ~50°-30°) in YBCFO samples with increasing disorder [q_s or $\mathrm{n_d}$; the ($\mathrm{n_d}$, θ_S) plot is also shown]. The observed $\theta_\mathrm{S}(q_s)$ evolution is satisfactorily described by a parabolic fit. We should call to mind that the orientation of the plane of the helix respect to the c axis (axis of the magnetic modulation, with k_z orientation) determines if the spiral order resembles more a cycloid ($\theta_\mathrm{S} \rightarrow 0°$) or a helix $\theta_\mathrm{S} \rightarrow 90°$). The observed reorientation of the spiral plane agrees with earlier works reporting a greater misalignment respect to the tetragonal plane in samples prepared by fast cooling (more disordered) [47, 48]. Keep in mind that in the presence of spin-orbit coupling and effective DM terms (or spin-current mechanism triggering magnetoelectric coupling), the expected dependence of the electrical polarization magnitude P with the orientation of the helix is of the type $\mathrm{P} \propto \mathrm{Q}\cos(\theta_\mathrm{S})$ ($\mathbf{Q} = \mathbf{S}_i \times \mathbf{S}_j$ is the spin-chirality, different from zero in the non-collinear phase). Hence, in this scenario, a cycloidal order ($\mathbf{Q} \perp \mathbf{q}_S$) should be more favorable to ferroelectricity than a pure helix ($\mathbf{Q} \parallel \mathbf{q}_S$).

Additionally, we wanted to examine the dependence of the tilting (θ_S) on –directly– the Fe/Cu disorder monitored by the occupation $\mathrm{n_d}$. This is plotted

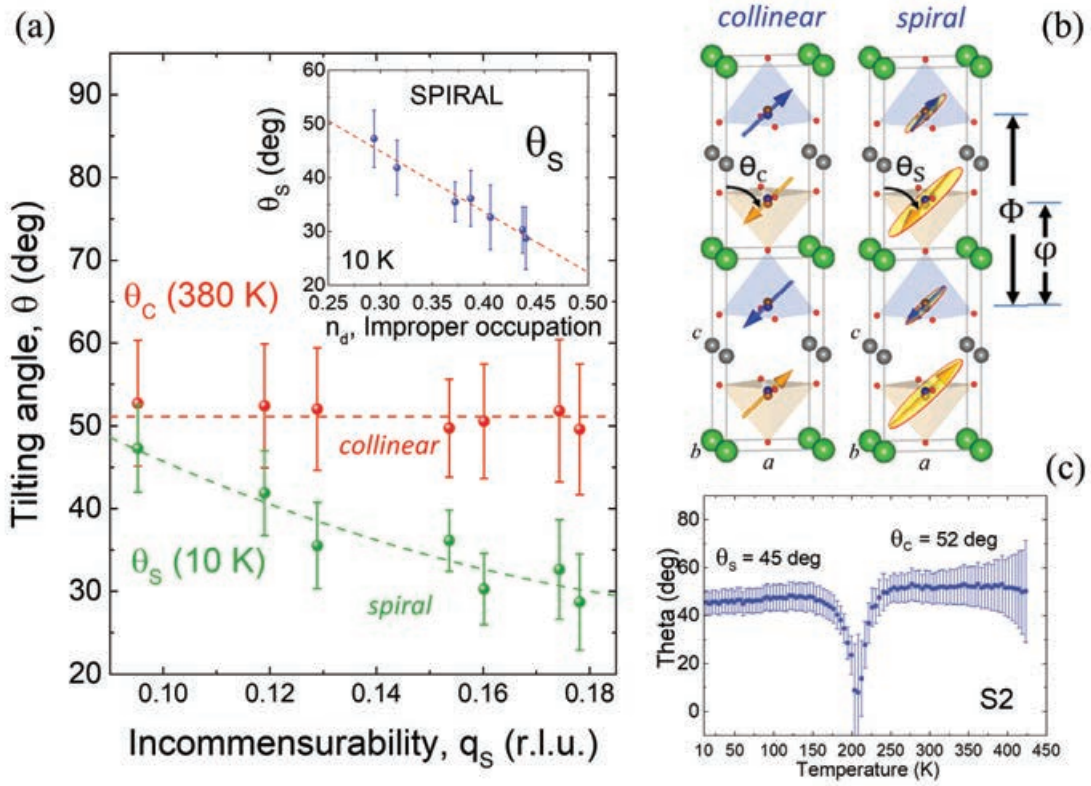

FIGURE 4.17: (a) Influence of the improper Fe/Cu occupation (n_d, chemical disorder) in YBCFO on the inclination angle θ_S of the spiral rotation plane determined at 10 K (green symbols). The flat dependence of the inclination θ_C of the collinear spins in the CM phase (at 390 K) is also shown (red symbols). The dashed lines are linear fits to the experimental points (data from Table 4.4). In the inset the spiral inclination θ_S is plotted versus the ICM modulation q_s of the samples. Notice the linear dependence of $\theta_S(n_d)$. (b) Projections showing of the inclination angles θ_C and θ_S of the collinear spins and the rotation plane of the spiral, respectively. (c) Example of the T-dependence of the inclination angle of the collinear spins ($T_S<T<T_{N1}$) and of the spiral rotation plane ($T<T_S$) (sample S2, the slope $d\theta_S/dT \gg 0.025\ ^\circ/K$).

as an inset in Fig. 4.17(a). This plot unveils a noteworthy finding. Interestingly, we reveal a linear relationship between the spiral's tilting angle and the level of Fe/Cu cation disorder in these layered perovskites, parametrized by the improper occupation n_d. So, the linear fit of all experimental (n_d, θ_S) points is shown in the inset of Fig. 4.17(a). It shows that the linear relationship is very well suited and the linear parameters found are given in Table 4.6 [2].

Figure 4.18(a) displays the projection of the incommensurate magnetic structures described in Table 4.4, refined at 10 K using the circular spiral model ($M_R = M_I$). Two complementary projections are plotted for each sample, which

[2] In Fig. 4.2 [q_s versus n_d] we used a linear regression fit for the sake of simplicity.

TABLE 4.6: Regression slopes and intercepts obtained from linear least squares regression fits to key structural and magnetic parameters in the layered $YBaCuFeO_5$ structure obtained from Rietveld refinement of X-ray and neutron powder diffraction data as function of the incommensurability q_s. The goodness of the regression model R^2 and standard error of the intercept and slope (A and B, respectively) are shown. In the case of θ_S as function of q_s, a regression model with an additional quadratic coefficient C was used.

Equation	A	B	R^2
$a = A + B \cdot q_s$	3.87354 (60)	0.0139 (38)	0.8247
$c = A + B \cdot q_s$	7.67016 (83)	-0.0621 (55)	0.9750
$V = A + B \cdot q_s$	115.084 (47)	-0.09 (31)	0.0152
$\Delta_T \equiv c/2a = A + B \cdot q_s$	0.990056 (86)	-0.01153 (56)	0.9908
$q_s = A + B \cdot n_d$	-0.025 (31)	0.445 (78)	0.8435
$d_t = A + B \cdot q_s$	4.886 (13)	-0.383 (87)	0.7481
$d_s = A + B \cdot q_s$	2.784 (13)	0.322 (91)	0.6446
$d_t/d_s = A + B \cdot q_s$	1.755 (13)	-0.331 (86)	0.6888
$H_L = A + B \cdot q_s$	2.663 (32)	-1.38 (23)	0.8795
$H_S = A + B \cdot q_s$	2.222 (27)	1.00 (19)	0.8394
$z_{O1} = A + B \cdot q_s$	0.0250 (32)	-0.145 (24)	0.8902
$z_{O2} = A + B \cdot q_s$	0.3138 (11)	-0.0045 (77)	0.0564
$z_{O3} = A + B \cdot q_s$	0.6766 (21)	0.041 (14)	0.5769
$d(Cu1 - O_1)_{apical} = A + B \cdot q_s$	2.35581 (93)	-1.2362 (67)	0.8507
$d(Cu1 - O_3)_{basal} = A + B \cdot q_s$	1.9612 (40)	-0.016 (25)	0.0209
$d(Fe2 - O_1)_{apical} = A + B \cdot q_s$	1.773 (25)	1.07 (19)	0.8438
$d(Fe2 - O_2)_{basal} = A + B \cdot q_s$	1.9888 (35)	-0.011 (22)	0.1015
$T_{N1} = A + B \cdot q_s$	517.2 (15.7)	-590.9 (106.5)	0.8602
$T_{N2} = T_S = A + B \cdot q_s$	-61.7 (9.9)	2610.1 (78.6)	0.9961
$\theta_C = A + B \cdot n_d$	58.1 (2.4)	-17.7 (6.3)	0.5298
$\theta_S = A + B \cdot n_d$	78.8 (3.1)	-112.8 (8.1)	0.9776
$\theta_S = A + B \cdot q_s + C \cdot q_s^2$	A = 84.1 (30.6); B = -488.4 (457.9); C = 1044.0 (1663.6)		0.8949

help to illustrate the inclination of the spiral plane in each of the seven YBCFO specimens with gradually larger disorder n_d. The progressive reorientation of the rotation plane of the spins is schematically illustrated in Figure 4.18(b). Regarding samples S1 and S7, the most distant in terms of disorder, there is between them a reorientation $\Delta\theta_S$ of the spiral plane of $\approx -20°$. In Figure 4.18(a) the arrows represent the average ordered moment in each pyramid according to the values gathered in Table 4.4. The blue (brown) color applies to CuO_5 (FeO_5) pyramids. The degree of Fe/Cu disorder in each pyramid is represented by mixing both colors according to the improper occupation n_d in that site. For that reason the colors of the two pyramids in the cell become increasingly similar in Fig. 4.18(a), and finally end up being almost indistinguishable from each other in the most disordered samples [$n_d \sim 0.44(4)$ in sample S7].

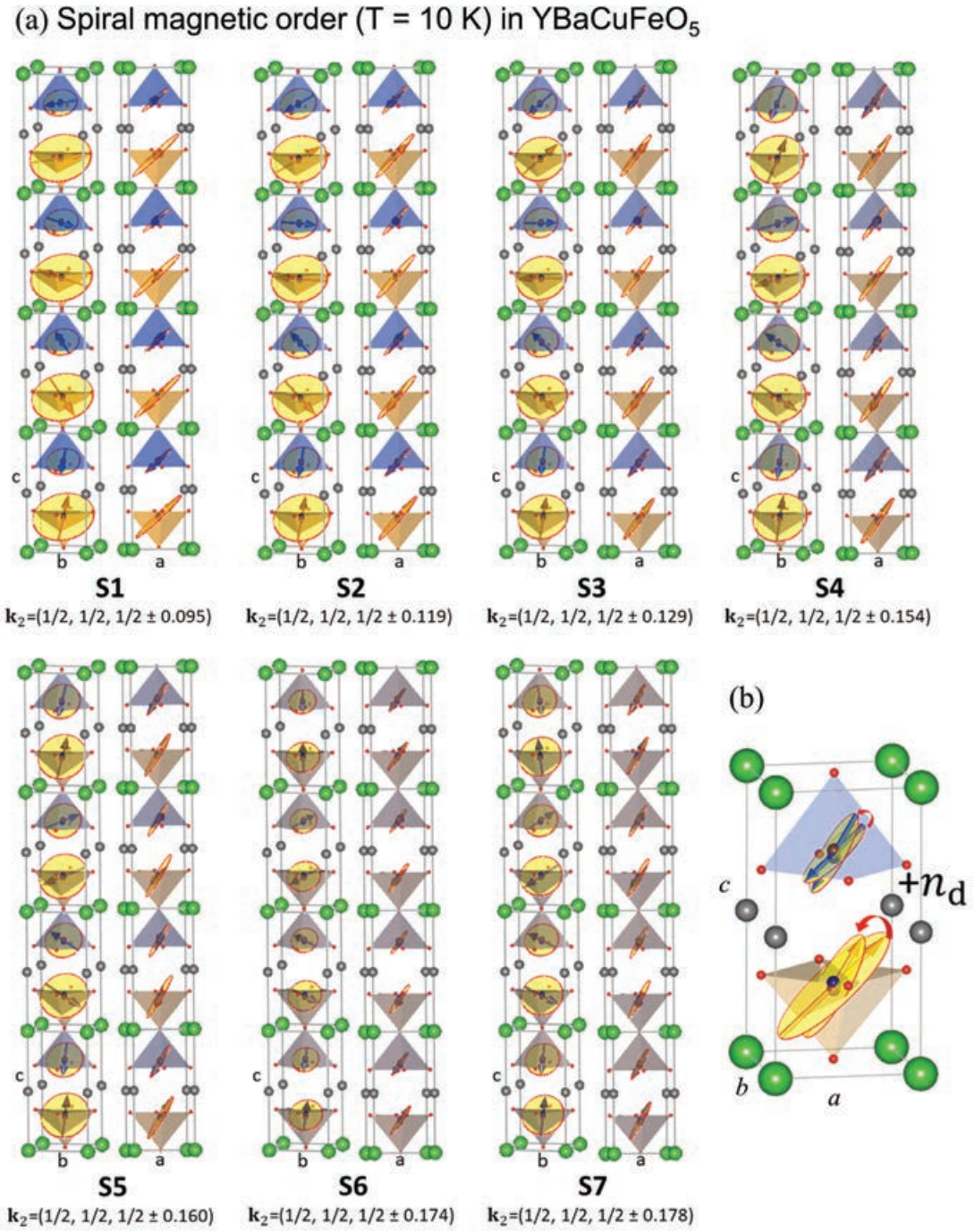

FIGURE 4.18: (a) Two projections of the refined circular spiral order at 10 K in YBCFO samples with increasing Fe/Cu disorder (*model-2* described in Table 4.4). The incommensurate magnetic propagation vector determined in each sample is indicated. (b) Sketch of the evolution of the orientation of the spiral rotation plane when increasing disorder (n_d). For clarity, the average magnetic moment is depicted in each pyramid. The colors of the moments and pyramids reflect the fraction of Fe/Cu ions (brown/blue) at each site.

4.5.4 The magnetic "phase separation" region: beyond the triple point in $YBaCuFeO_5$

A magnetic triple point was initially proposed for $YBa_{1-x}Sr_xCuFeO_5$ samples quenched into liquid nitrogen in Ref. [48]. Here we have shown that the convergence of T_{N1} and T_S, which imposes the limit for the highest spiral temperature, can be attained in samples with identical composition ($YBaCuFeO_5$). Without the need to increase the number of dissimilar divalent cations in the A site of the structure. A noteworthy experimental conclusion is that in bulk samples the triple point represents a critical end point for the incommensurate spiral phase. The stability of the modulated order cannot overcome the stability of the collinear order. At least in absence of external perturbations and fields, the *spiral order by disorder* mechanism requires and cannot avoid a commensurate collinear phase preceding the spiral incommensurate magnetic order. This relevant observation confirms that the orientationally aligned frustrated bonds in YBCFO cannot generate a paramagnetic-spiral phase boundary of finite size. The energy terms deciding the magnetic configuration to adopt at a given temperature below the Néel point were analyzed in Refs. [46, 47, 54, 55]. Moreover, given the concurrence of disordered and ordered spin configurations, the latter undergoing a transition between spatially uniform (commensurate) and spatially modulated (incommensurate) magnetic orders, the triple point in YBCFO seems a good candidate to a possible Lifshitz multicritical point [122–124].

In addition, notice that the phase diagram in Fig. 4.14 is not strictly equivalent to that reported by Shang *et al.* in the vicinity of the triple point [48]. In that one the driving force approaching the triple point ($YBa_{1-x}Sr_xCuFeO_5$ samples with increasing Sr-content) are structural effects produced by A-site cationic substitutions with little or no change in the Fe/Cu disorder. For that reason the slope dT_S/dq_s is clearly dissimilar when comparing the $YBaCuFeO_5$ (B-site disorder) and the $YBa_{1-x}Sr_xCuFeO_5$ (Sr-content) series of samples. In the phase diagram of Fig. 4.14 composition does not change. Keep in mind that, by comparing the ICM transition temperatures, the maximum Fe/Cu disorder of YBCFO in Ref. [48] is significantly lower than in our sample S4 (being $T_S \approx 310$ K in Ref. [48], its disorder should be between the present samples S3 and S4). The driving force along the x axis in the phase diagram of Fig. 4.14 is strictly the Fe/Cu chemical disorder, which extends T_S up to ≈ 366 K (sample S7). On another hand, from the magnetic phase diagram [Fig. 4.14] we can also identify the critical values at the intersection (triple) point. For this one can combine the

linear relationships listed in Table 4.6 for the pairs T_{N1}-q_s and T_{N2}-q_s, and imposing T_{N1}=T_{N2} one gets: q_s^c=0.186(13) r.l.u. and T_S^c=407(16) K (T_{N1}^c=T_S^c). Here, q_s^c and T_S^c stand for the "extrapolated" critical values at the triple point. In the same way, the corresponding critical disorder results n_d^c=0.47(3), below but very close to the maximum possible disorder n_d=0.5.

What happens then when in this structure the Fe/Cu disorder acquires values greater than n_d^c? The answer is that the system enters in another regime that we have named *the phase-separated region* [see Fig. 4.14]. Ideally, the phase-separated region corresponds to samples with a degree of Fe/Cu disorder within the interval n_d^c<n_d<0.5, and it is characterized by the presence of magnetic phase segregation. We expect this region to be characterized by the competition of emergent collinear AF3 and declining AF1 regions, whereas spiral order rapidly vanishes [48]. The AF3 configuration is favored in front of the AF1 and AF2 ones when the competition between FM and AFM tendencies inside the bipyramids gets unbalanced by an excessive number of strongly AFM Fe/Fe bipyramids. In our most disordered samples (real, not ideal, materials) the phase coexistence includes the magnetic propagation vectors $\mathbf{k}_1 = (1/2, 1/2, 1/2)$, $\mathbf{k}_2 = (1/2, 1/2, 1/2 \pm q)$ and $\mathbf{k}_3 = (1/2, 1/2, 0)$. Here, we want to stress the fact that in real samples (powders or crystals), beyond the average disorder n_d, local fluctuations in the distribution of Fe/Cu atoms very likely play also a role. Namely, the variance $\sigma^2[n_d]$ and its spatial distribution can also favor magnetic phase-separation. On one hand, inhomogeneous disorder (very dependent on the preparation) explains the possibility of preparing samples with the same apparent magnetic modulation and transition temperature but different residual amount of collinear phase at low temperature [as occurs in our sample S3, Fig. 4.12(c)]. On the other hand, another consequence of certain inhomogeneous disorder is that it smears out the boundary separating the spiral and the phase-separated regions [as exposed in Fig. 4.14]. So, a certain degree of inhomogeneous disorder can explain the presence of the three magnetic phases (the emergent collinear AF3 [$\mathbf{k}_3$], the AF1 one [$\mathbf{k}_1$], and also the spiral) in the two most disordered YBCFO samples (S6 and S7). However, it is important to stress that spiral order with q_s larger than $q_s^c \approx 0.18$ r.l.u. has never been observed.

In Fig. 4.12(c) the coexisting magnetic phases characteristic of the phase-separation region are apparent in samples S6 and S7. To get a closer view of this region of disorder, the evolution of the magnetic phase fractions for sample

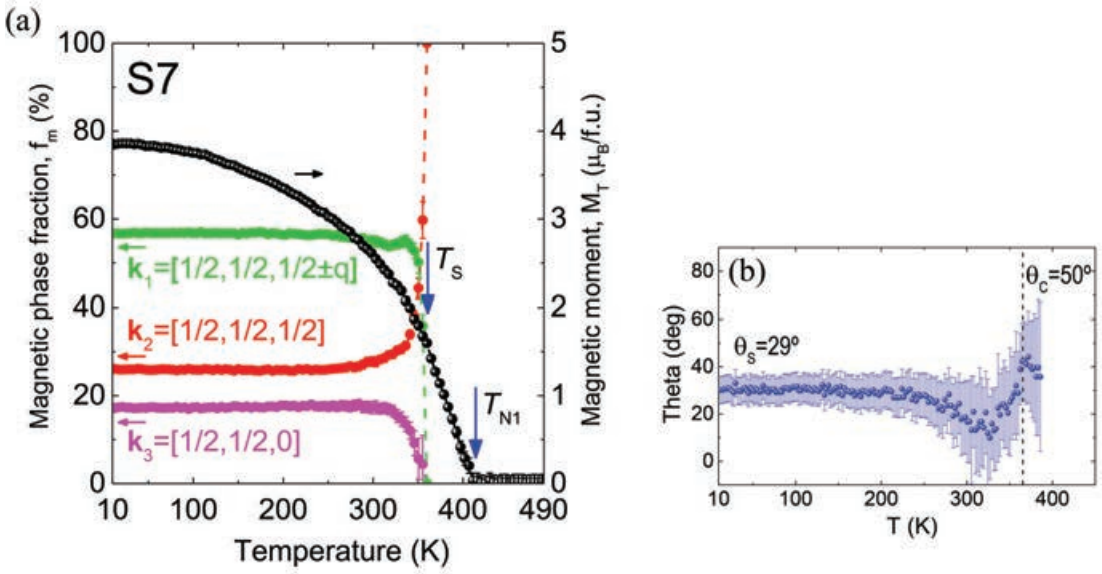

FIGURE 4.19: Phase-separation regime. Sample S7 [highest disorder level, n_d=0.44(4)]. (a) Temperature dependence of the magnetic phase fractions associated to the different propagation vectors in the phase-separation regime (f_m, left axis) and total ordered magnetic moment (m_T, right axis). (b) Evolution of the inclination angle θ of the magnetic easy axis in the collinear (T_S<T<T_{N1}) and spiral orders (T<T_S).

S7, the less ordered sample, is displayed in Fig. 4.19(a). This figure allows us to extract several conclusions on the phase separation beyond the triple point. (i) The first is that when disorder exceeds n_d^c, a multidomain magnetic texture is favored where the coexisting magnetic orders ($\mathbf{k}_1$, $\mathbf{k}_2$, and $\mathbf{k}_3$) share (k_x, k_y)=$(1/2, 1/2)$ but differ in their translational symmetry parallel to the improper bonds along the c-axis (k_z = 1/2, 1/2$\pm q$ and 0). (ii) Second, the collinear $\mathbf{k}_1 = (1/2, 1/2, 1/2)$ magnetic domains start to develop prior to the ICM spiral order in all the cases. Moreover, when cooling from the paramagnetic state, $\mathbf{k}_1$ always emerges before $\mathbf{k}_3$-type domains. (iii) Third, the additional CM magnetic domains characteristic of the phase-separation regime [$\mathbf{k}_3 = (1/2, 1/2, 0)$] develop simultaneously to the ICM $\mathbf{k}_2 = (1/2, 1/2, 1/2 \pm q)$ order. As an example, we show in Fig. 4.19(a) the simultaneous appearence of $(1/2, 1/2, 0)$ $\mathbf{k}_3$ and spiral $\mathbf{k}_2$ magnetic intensity in sample S7, coinciding with the partial collapse of the $(1/2, 1/2, 1/2)$ order. This third observation can be interpreted as a consequence of the limitations included in the model, some of which relate to the density of improper bonds. The required conditions to stabilize the spiral were analyzed in Refs. [54, 55] and some concern the distribution of improper Fe/Fe bonds in the structure. In particular, the spiral order is not favored in those regions where neighbouring Fe/Fe bonds are closer along the c axis (the

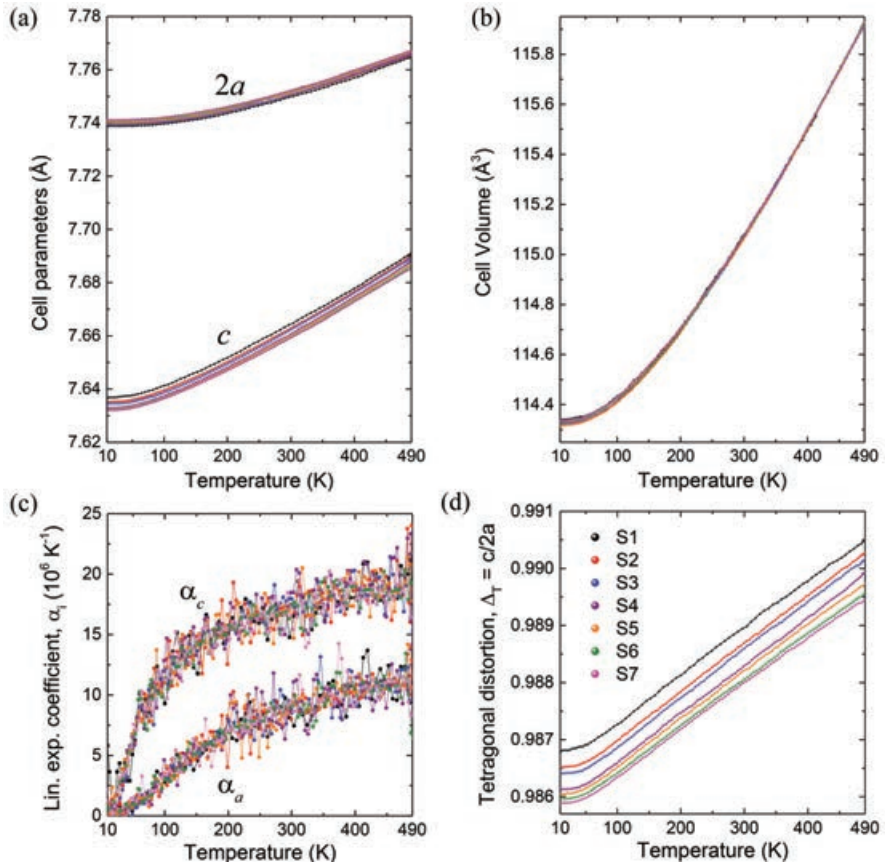

FIGURE 4.20: (a) Thermal evolution of the pseudo-cubic lattice parameters ($2a$ and c), and (b) unit cell volume of the tetragonal lattice obtained from neutron thermodiffractograms of the S1-S7 YBCFO samples. (c) Temperature dependence for the linear thermal expansion coefficient α_i derived from Eq. (4.11) along the a and c directions: α_a (circles) and α_c (squares). (d) Temperature dependence of the tetragonal distortion ($\Delta_T \equiv c/2a$).

orientation of the impurity bonds) than within the bilayer (ab plane). Predictably, when chemical disorder is too high, unsatisfied conditions in certain parts of the volume would explain the appearance of additional competing translational orders and the phase-separation regime.

4.6 Probing magnetostructural coupling in YBCFO

The existence of exchange striction (magnetostructural coupling) at the paramagnetic-to-collinear (T_{N1}) and collinear-to-spiral (T_{N2}=T_S) antiferromagnetic transitions in YBCFO samples with different Fe/Cu disorder was investigated from NPD patterns collected in D20 (λ=2.41 Å) between 10 K and 490 K. The

thermal evolution of the tetragonal lattice parameters and unit cell volume obtained from the Rietveld refinements are plotted in Figs. 4.20(a-b). In the YBCFO perovskite with $P4mm$ symmetry the unit cell is related to the pseudocubic symmetry as $c \approx 2a$. Hence, the quantities $2a(\mathrm{T})$ and $c(\mathrm{T})$ are plotted in the same graph for the sake of comparison (Fig. 4.20(a)). We observe that the thermal contraction on cooling is bigger along the c parameter than in the a and b directions, and that the relation c<$2a$ is satisfied along the temperature range studied. This is also evident from the linear thermal expansion coefficients (α) along the a and c directions deduced from Eq. (4.11), displayed in Fig. 4.20(c):

$$\alpha_i(T) = \frac{1}{l_{i0}} \frac{dl_i}{dT} \tag{4.11}$$

where l_{i0} is the value of the l_i parameter (size of the unit cell along l_i: a, b, c) at RT. From the evolution of α_a and α_c we have not detected apparent anomalies at the entering of the AF1 collinear phase, nor on going from the AF1 to the AF2 spiral phase (below $\mathrm{T_{N2}}$=$\mathrm{T_S}$). The thermal evolutions of the linear expansion coefficients are nearly identical for samples S1 to S7. The evolution of the tetragonal distortion (δ_T=$c/2a$) increases linearly with the temperature above T > 70 K, neither of the samples studied showing evidence of anomalies along the magnetic transitions.

The absence of strong magnetostructural coupling along the successive magnetic transitions is as expected for the YBCFO samples studied, although the limitations of NPD data used for this analysis should be taken into account. A more exhaustive study of the lattice thermal evolution would be better addressed from SXRPD measurements.

4.7 Summary

Frustrated magnets displaying spiral magnetic orders (conical screw, cycloidal, helimagnetic, etc.) at ambient temperatures are intrinsically rare. In nongeometrically frustrated structures (such as YBCFO) this typically requires competing nearest-neighbors and next-nearest-neighbors interactions of similar strength and both strong, which is highly unlikely. This bottleneck can be avoided if frustration is generated by chemical disorder. The exceptional stability of the spiral magnetic order in the layered perovskite structure investigated here entails a nonconventional mechanism that, as proposed by Scaramucci and

co-workers, relies on the presence of random strongly frustrating antiferromagnetic bonds introduced along a single crystallographic direction [54, 55]. As a credible realization of this model, we have methodically investigated and described the influence of tuning frustration in YBCFO through B-site cation disorder, covering practically the full interval between total order and random disorder. Our understanding of these layered perovskites is disclosing a radical mechanism for stabilization of cycloidal (spiral) orders in which frustration has no geometrical or electronic origins but it is essentially based on chemical disorder. The quantitative and thorough description of the interplay between disorder (frustration) and the magnetic and structural features illustrates in this reference composition the avenue *spiral order by disorder* to supply noncollinear functional magnets at normal working temperatures. It can help to define or inspire design strategies in these and other anisotropic functional magnets able to adopt phases with magnetic chirality at high temperatures.

Chapter 5

Enhancing the spiral stability in YBCFO by B-site divalent non-JT substitutions

5.1 Introduction

There is presently a need for developing new strategies that are capable to optimise and upgrade the magnetic and magnetoelectric properties of high-temperature spiral oxides and potential multiferroics. In the previous chapter, we have studied in detail how by applying different cooling rates in the synthesis process of $YBaCuFeO_5$ the Fe/Cu cation ordering can be tuned, resulting in a modification of the density of non-mixed Fe_2O_9 bipyramids and a modification of the interatomic distances. In this study, the maximum spiral ordering temperature was $\sim$366 K, achieved by quenching in water. Although the YBCFO maximum spiral ordering temperature was significantly increased respect to previous works ($\sim$310 K in Ref. [47]), the B-site disorder strategy presents prominent experimental and fundamental limitations. First, faster cooling rates are not easily achieved experimentally. Second, an excessive number of strongly AFM Fe/Fe bipyramids produces an unbalance of the FM and AFM competing interactions inside the bipyramids, which ultimately leads to the phase-separated region above the critical disorder value $n_d^c \approx 0.47$, where AF1 and AF2 phases coexist with emerging collinear AF3 magnetic regions [with $\mathbf{k}_3 = (1/2, 1/2, 0)$ translational symmetry] and the spiral is rapidly weakened. Third, the lossy dielectric behavior of the polycrystalline samples difficulted the study of electrical polarization and limits the effective range of temperatures of the potential multiferroic properties.

In view of these limitations, design strategies based on chemical substitutions have been proposed to tune the properties of this interesting multiferroic candidate $YBaCuFeO_5$ with perovskite structure AA'BB'O_5. By means of cationic substitutions in the AA'-site of this perovskite, in previous reports it was demostrated that in the Y(Ba,Sr)$CuFeO_5$ system and R$BaCuFeO_5$ oxides (R: rare-earth or Y), the interatomic distances between the magnetic transition metal atoms (M) are modified with respect to YBCFO [48]. Of great importance are the changes in the distances parallel to c as they can tune the magnitude of the competing interactions in that direction [54, 55]. A shrinkage in the height of the bipyramids (d_t distance, *e.g.* by partially substituting Ba^{2+} by the smaller Sr^{2+}) or an increase of the separation between bipyramids (d_s distance, *e.g.* by substituting Y^{3+} by a bigger trivalent R^{3+} rare-earth) produce the rise of the spiral transition temperature [48]. Although a notable raise of the spiral ordering temperature up to ∼375(3) K was achieved by Ba^{2+}/Sr^{2+} A-site substitution, spontaneous polarization was not observed in these perovskites [48]. The lack of FE in Sr-doped YBCFO was atrributed to a negligible DM energy term due to a configuration of the helical spin rotation plane parallel to the ab plane [109, 125]. In R$BaCuFeO_5$ the magnetic properties can also be favorably tuned by using larger rare-earths [48], but this strategy ends up by generating defects in the orderly stacking of R^{3+} and Ba^{2+} layers, when the size of both cations gets closer.

As an alternative strategy to upgrade the properties of YBCFO, X. Zhang and co-workers presented a selective investigation on the BB'-site doped $YBaCuFe_{1-x}Mn_xO_5$ series [49]. The isovalent cationic substitution of highly symmetric Fe^{3+} ions ($3d^5$, L=0, S=5/2) by less symmetric Mn^{3+} ions ($3d^4$, L=2, S=2) at the trivalent B'-site was aimed to favor the spin-orbit coupling and the magnetoelectric response through the antysimmetric Dzyaloshinskii–Moriya (DM) interaction, thanks to the highly non-spherical charge distribution in the isovalent Mn^{3+} ion. In this work, although it was proved that the presence of Mn produced a progressive reorientation of the plane of the magnetic spiral in the ICM phase, transforming the helical magnetic order into a cycloidal one (which might critically determine the ferroelectric and magnetielectric behavior), a systematic reduction in the spiral ordering temperature was also found when increasing Mn content [49].

Motivated by the above described works, along the lines of this chapter we present an investigation on two BB'-site doped $YBaCu_{1-x}M_xFeO_5$ series where

Cu^{2+} is partially substituted by M^{2+} = Co^{2+} and Zn^{2+} transition metals. We have comprehensively investigated the effects of Cu/Co and Cu/Zn substitutions in the YBCFO perovskite and explored its influence on the structure and magnetic properties. Three relevant aspects in our B-site substitution strategy are described below:

(1) *The lattice effect*: The strategy considers the steric (chemical internal pressure) effects induced from B-sites. As we know, the basic structure of YBCFO is formed by [$CuFeO_9$] bipyramids of corner-sharing $Cu^{2+}O_5$ and $Fe^{3+}O_5$ units. In contrast to the $Fe^{3+}O_5$ flattened square pyramids, $Cu^{2+}O_5$ pyramids are notably elongated along the c axis due to the Jahn-Teller (JT) distortion around Cu^{2+} ($3d^9$: $t_{2g}^6e_g^3$), which shows a large difference between the interatomic distances of Cu to apical and basal oxygens. The divalent Co^{2+} ($3d^7$: $t_{2g}^5e_g^2$) ion present a high spin (HS) state in most of cobalt oxides, and is a non JT ion. Similarly, Zn^{2+} ($3d^{10}$: $t_{2g}^6e_g^4$) is also a non JT ion, since it presents a totally filled $3d$ shell. In consequence, Cu/Co and Cu/Zn divalent B-site substitutions are expected to have a sizeable effect on the lattice, specially on the interatomic distances along c, which have a strong influence on the two opposite nearest-neighbor (NN) couplings along c (the FM J_{c_2} and the AFM J_{c_1}).

(2) *Nature of the magnetic interactions*: In contrast to trivalent B'-site Mn substitutions ($YBaCu_{1-x}M_xFeO_5$ studied in Ref. [49]), in Cu/Co and Cu/Zn divalent substitutions the occupation of trivalent B'-site by Fe^{3+} is preserved, which is key for the strong AFM ($J_{c_2'}$) coupling of Fe-O-Fe bonds to induce magnetic frustration. On the other hand, the substitution of Cu^{2+} by Co^{2+} or Zn^{2+}, which have very different spin configurations, are expected to induce distinct changes on the magnetic properties of the compounds. Whereas substitution of Cu^{2+} by low concentrations of non-magnetic Zn^{2+} ($3d^{10}$: $t_{2g}^6e_g^4$, S=0) is not expected to have a strong influence on the magnetic frustration, the presence of HS Co^{2+} ($3d^7$: $t_{2g}^5e_g^2$, S=3/2) can have relevant effects over the competing superexchage terms in the system.

(3) *Spin-orbit coupling*: One important consideration in our strategy to improve the properties of the spiral phase by isovalent TM substitutions is to aim for an enhancement of spin-orbit coupling. In many cobaltites the (high spin) ground state configuration of $3d^7$ Co^{2+} cations if surrounded by six oxygen anions creating a local O_h cubic symmetry is $t_{2g}^5e_g^2$, as shown in Fig. 5.1(a). Such state may be split under a local symmetry lowering, *e.g.* by a tetragonal or orthorhombic distortion. The degeneracy in the t_{2g} subshell, will be thus lifted.

This can be seen from the total energy-level diagram shown in the Fig. 5.1(b). When the $3d$ spin-orbit interaction is not considered ($\xi = 0$ case), we find three low-lying quartets within the first 0.1 eV. In electron language, each of them would correspond to the hole occupying one of the three t_{2g} orbitals. The importance of the lifted degeneracy is that the orbital occupation will no longer be isotropic, *i.e.*, the Co-ion charge distribution will be highly nonspherical. If we enable a non-zero spin-orbit coupling ($\xi \neq 0$ case), the energy level diagram reveals that there is indeed a large amount of mixing due to spin-orbit interaction. So, N. Hollmann, Z. Hu *et al.* [126] found that the $3d$ spin-orbit interaction has a major influence on the energies and nature of the low-lying states of the $CoWO_4$ system. As in the case of Mn^{3+}, Co^{2+} atoms contain both a spin and an appreciable orbital component (close to 1 μ_B). This results in a strong coupling of the magnetic moment direction to the crystal structure, which is responsible for the large single- permits to estimate the single-ion anisotropy in Co^{2+} ions. Over

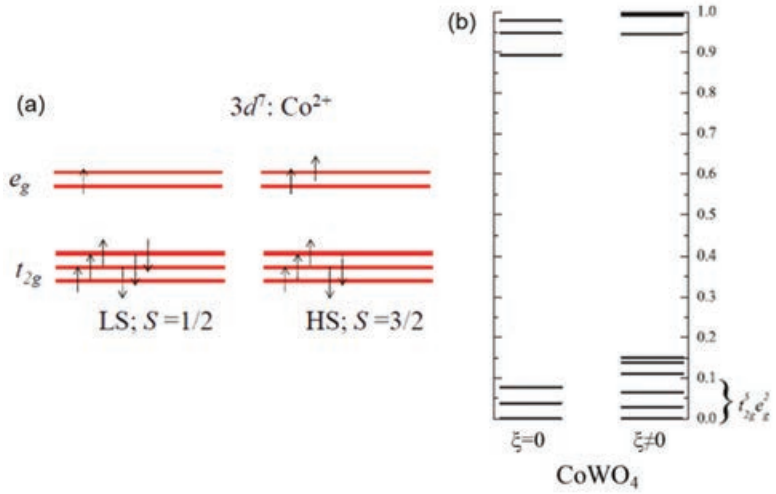

FIGURE 5.1: (a) The electronic configuration of the $3d^7$: Co^{2+} ion with low spin (LS) and high spin (HS) state. (b) The energy-level diagram for Co^{2+} ion, excluding and including the $3d$ spin-orbit coupling ξ. Only the states up to 1 eV are shown. Figure adapted from Ref. [126].

the past decades, there were many works done on the structural and magnetic properties of transition metal oxide containing Co^{2+} related to its spin-orbit coupling and single-ion magnetic anisotropy natures [127–132]. Thus, in this work, the substitution of Cu by Co was supposed to help increasing the magnetic anisotropy and the spin-lattice coupling thanks to the significant orbital moment contribution from Co^{2+} ions. This should have a direct incidence over the characteristics and stability of the spiral.

In this chapter we will also present a first synchrotron diffraction study on the evolution of YBCFO crystal lattice under pressure. Based on our research and previous works, we will use the rules governing the interplay between chemical pressure lattice effects and magnetic frustration to infer the influence of external pressure on the magnetic spiral order.

5.2 Sample praparation and experimental methods

Synthesis of polycrystalline YBa(Cu,M)FeO_5 samples (M = Cu, Zn)

The fabrication of YBa(Cu,M)FeO_5 samples with M = Cu,Zn chemical doping at the B-site was performed by the solid-state reaction method. Two sets of samples were prepared: (1) the $YBaCu_{1-x}Co_xFeO_5$ series with Co doping amounts x = 0, 0.01, 0.03, 0.04, 0.05, 0.06, 0.065, 0.075, 0.08, 0.10, 0.125, 0.15, 0.20 and 0.25; and (2) the $YBaCu_{1-x}Zn_xFeO_5$ series with Zn doping values x = 0, 0.02, 0.05, 0.075, 0.1, 0.125 and 0.15. In both cases the synthesis process was conducted in a similar way to the one described in the experimental section of Chapter 4 for non-doped $YBaCuFeO_5$ samples. First of all, the Y_2O_3, $BaCO_3$, CuO, Fe_2O_3, Co_3O_4 and ZnO high-purity precursors were dehydrated at 150 °C

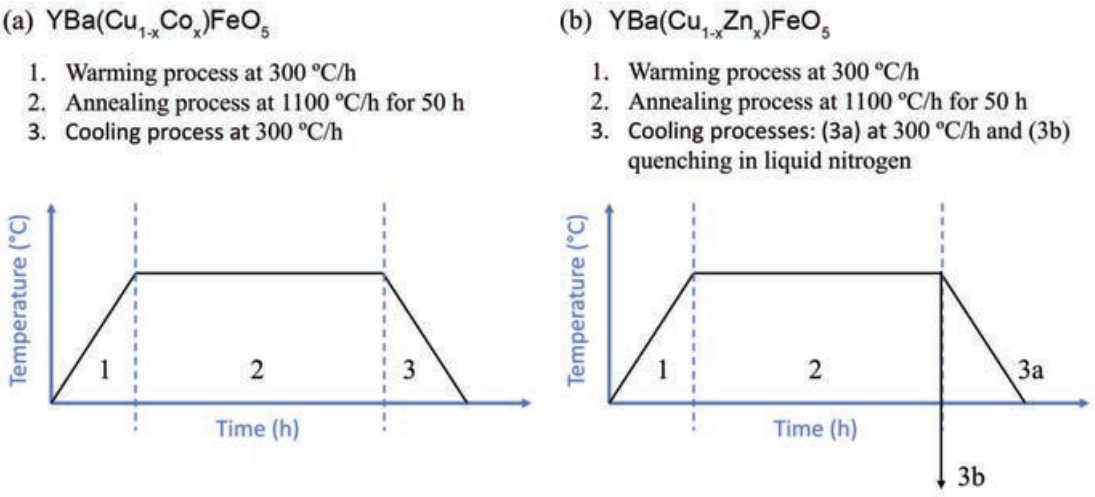

FIGURE 5.2: Scheme of the thermal process used for the synthesis of ceramic YBCFO samples doped with increasingly higher amounts of Co and Zn at the B-site: (a) $YBaCu_{1-x}Co_xFeO_5$ and (b) $YBaCu_{1-x}Zn_xFeO_5$.

for 48 h, and a pre-annealing process at 900 °C for 10 h was done on Y_2O_3 to promote decarbonation. To prepare the YBa(Cu,Co)FeO_5[YBa(Cu,Zn)FeO_5] series of samples with different Co[Zn] doping amount, Co_3O_4[ZnO] oxide was combined stoichiometrically with the Y_2O_3, $BaCO_3$, CuO and Fe_2O_3 precursors. The starting materials were then mixed and thoroughly grounded using an automatic agate mortar for several hours until obtaining fine and completely homogeneous powders, which were subsequently pressed into pellets. Thermal processes were then performed on the resulting pellets using tubular furnaces in air atmosphere. In both YBa(Cu,Co)FeO_5 and YBa(Cu,Co)FeO_5 series a heating rate of 300 °C/h was appied to increase the temperature up to 1100 °C. The samples were annealed at this temperature for 50 h. Finally, different cooling processes were applied as illustrated in Fig. 5.2. For the YBa(Cu,Co)FeO_5 series, a controlled cooling rate of 300 °C/h was used to cool the samples down to room temperature. An identical process was applied to the YBa(Cu,Zn)FeO_5 series of samples. In the case of YBa(Cu,Zn)FeO_5 series of samples, for each specimen we made two identical pellets using the same powder which were annealed in the same conditions as the Co-doped ones (at 1100 °C in air for 50 h). The two sets of Zn-doped samples were then cooled following two different processes: (1) a controlled cooling rate of 300 °C/h and (2) a quenching into liquid nitrogen with the aim of optimizing the ordering temperatures and properties of the spiral phase. After this, small pieces of each sample were kept solid for the macroscopic measurements, and the rest was pulverized to perform powder diffraction experiments.

The quality of the as prepared samples was checked from laboratory X-ray diffraction patterns collected at RT using a Siemens D-5000 diffractometer (λ[Cu K_α] = 1.54 Å) showing no secondary phases within the detection limit of the technique. Synchrotron and neutron diffraction measurements further confirmed the good crystallinity and purity of the samples. A detailed structural and sample quality analysis on the Co-doped series was performed by X. Zhang based on synchrotron SXRPD and XAS measurements, reported in Ref. [133]. From X-ray absorption spectroscopy (XAS) measurements done using the HECTOR cryomagnet endstation at the BL29-BOREAS beamline of the Alba Synchrotron Light Facility across the Fe and Cu $L_{2,3}$ edges it was found that the oxidation states of Fe^{3+} ($3d^5$) and Cu^{2+} ($3d^9$) ions were well preserved during the preparation process of all samples. The XAS spectra across the Co $L_{2,3}$ edges for $YBaCu_{1-x}Co_xFeO_5$ compounds with $x = 0.01$, 0.05, 0.1 and 0.25

are plotted in Fig. 5.3(a). The inset shows that the Co L_3 edge is clearly distinguished above the Ba M_5 edge tail, whose much higher intensity is due to the larger absorption cross section of the Ba $M_{4,5}$ transitions and a higher relative concentration of Ba in the samples. The XAS energy positions and structure of the Co L_3 edge match well with those found in a prototypical Co^{2+}-based compound like CoO [see Fig. 5.3(b)], verifying that the Co^{2+} by Cu^{2+} chemical substitution was isovalent up to $x = 0.25$, and that cobalt ions indeed adopted the divalent HS Co^{2+} electronic configuration ($3d^7$: $t_{2g}^5 e_g^2$).

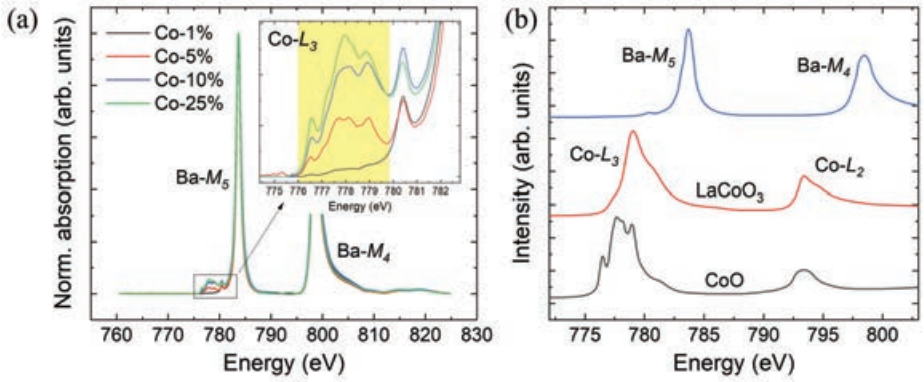

FIGURE 5.3: (a) XAS spectra across the Co $L_{2,3}$ edges for $YBaCu_{1-x}Co_xFeO_5$ samples with $x = 0.01$, 0.05, 0.10 and 0.25. The inset in panel (a) focuses on the Co L_3 edge. (b) XAS spectra provided as references across the Co $L_{2,3}$ and the Ba $M_{4,5}$ edges of the compounds CoO (Co^{2+}), $LaCoO_3$ (Co^{3+}) and $Ba_{1.60}Ce_{0.20}Na_{0.20}Ca(BO_3)_2$ (Ba^{2+}). Figure from Ref. [133].

Characterization methods

- *Synchrotron X-ray powder diffraction:* the structural study of the two series of samples was done by collecting high resolution synchrotron radiation X-ray powder diffraction patterns (SXRPD) at 300 K. Measurements were conducted at the BL04-MSPD beamline [107] of the Alba Synchrotron Light Facility (Cerdanyola del Vallès, Spain). The samples were loaded in borosilicate glass capillaries (0.7 mm diameter) and kept spinning during data acquisition. A short wavelength, λ = 0.413378(4) Å was selected to reduce absorption and enlarge the q-range. The value of λ was calibrated by measuring a NIST standard silicon. As detection system we used a high-throughput position sensitive detector MYTHEN which allows a high photon flux. The acquisition time to perform a RT full structural characterization was 90 s.

Structural Rietveld refinements of the SXRPD patterns, made using the Fullprof package of programs [97], allowed for the determination of the cationic

disorder (n_d) and the evolution of the different relevant interatomic distances in the samples as a function of B-site chemical doping, as it will be described in the following section. Illustrations of the crystal structure were obtained using the VESTA program [106].

- *Neutron powder diffraction:* to study the magnetic order, neutron powder diffraction (NPD) experiments were conducted at the high-flux reactor of the Institut Laue Langevin (Grenoble, France) on D1B and D20 powder diffractometers using similar wavelengths. The measurements performed on Co- and Zn-doped samples are described below:

(1) For the YBa(Cu,Co)FeO_5 series NPD data was obtained at the high-intensity D1B powder diffractometer using a highly oriented pyrolytic graphite (HOPG) monochromator and a take-off angle of 44.22° towards the sample position. In this configuration the calibrated wavelength was λ= 2.52 Å. A Radial Oscillating Collimator (ROC) is implemented in D1B to eliminate parasitic diffraction beams from sample environment devices. For the characterization of the low temperature magnetic order of the samples two patterns with an acquisition time of 10 min were collected at 10 K and averaged for signal-to-noise ratio optimization. In addition, neutron diffraction patterns were also recorded in a continuous mode following temperature ramps in the temperature range between 10 and 500 K, with heating rates of 3 K/min.

(2) In the case of the YBa(Cu,Zn)FeO_5 series measurements were performed using the high-intensity, high-resolution two-axis D20 diffractometer configured with a HOPG monochromator and 42° take-off angle, which provided a λ= 2.41 Åwavelength, with excellent resolution at low-q and a high efficiency position sensitive detector covering an angular range up to 150°. For each sample, two 15 min patterns were collected at 10 K, which were averaged for signal optimization. The evolution of the magnetic order with temperature was also studied in $x = 0.05$, 0.1 and 0.15 Zn doped samples by collecting neutron thermodiffractograms in continuous mode following temperature ramps within the range 10 to 500 K, with applied heating rate of 2 K/min and acquisition time of 2.5 min per scan. Around 100 patterns were recorded in the range 10 K to 500 K with a resolution in temperature of 5 K between successive patterns.

In all cases powder samples were filled into 8 mm diameter vanadium containers, and the temperature range of the experiments were covered using dedicated He cryofurnaces. For the sake of comparison, NPD patterns collected on both instruments are plotted as a function of the $Q = 4\pi \sin(\theta)/\lambda$ parameter.

Rietveld analysis of the NPD patterns was made using the Fullprof package of programs [97] allowing for the characterization of the different magnetic phases and its evolution with temperature, focusing on the properties of the spiral order such as the inclination of the rotation plane of the spins and the magnitude of its ordered magnetic moment. Another key parameter for the description of the samples is the modulation q_s of the incommensurate spiral magnetic phase, ($\mathbf{k}_2 = (1/2, 1/2, 1/2 \pm q_s)$), which is illustrative of the magnetic frustration in the samples as it is directly related to the canting angle $\varphi = 2\pi q_s$ between the two spins in a bipyramid.

• *Angle-dispersive synchrotron XRD under pressure:* High pressure (HP) SXRPD measurements were carried out at the high pressure powder diffraction end station of the BL04-MSPD beamline at the Alba Synchrotron Light Facility. The wavelength and detector position parameters were obtained using lanthanum hexaboride (LaB6) as a calibrant. The calibrated wavelength was 0.4246 Å and the distance to the detector was ∼200.15 mm.

For this experiment, a piece of polycrystalline YBCFO sample was thoroughly ground in pure ethanol for several hours using an automatic mortar. Then, the smallest grains were selected by sieving successively the powder with ethanol through 10 μm and 5 μm mesh size sieves, obtaining a fine powder with <5 μm grain size. Each sample was loaded at the High-Pressure laboratory at ALBA into a Membrane Diamond Anvil Cell (MDAC) equipped with 400 μm-cullet diamond anvils. Samples were loaded with methanol-ethanol-water (MEW) as pressure transmitting medium (PTM) in 20 μμm hole drilled in Inconel gasket pre-indented to a thickness of 40-45 μm. For each sample HP-XRD measurements were done increasing pressure gradually up to ∼20 GPa at ambient temperature. The membrane pressure step between collected patterns was 1 bar in the range where the pressure inside the MDAC increases linearly with membrane pressure, and it was reduced to 0.8 bar in the exponential regime (approx. > 47 bar). The DAC was re-aligned each 5 GPa. As pressure calibrant a small amount of Cu metal powder was loaded along with the sample.

For the measurements, a highly collimated beam was used in front of a bidimensional SX165 (Rayonix) CCD camera to obtain 2D images of the diffracted rings. The indented area of the gasket was initially mapped to select the regions with optimal amount of Cu and sample for pressure calibration and Rietveld analysis of the sample, respectively, as far as possible aiming also for non-grainy diffraction rings which would lead to preferred orientation effects. Collecting time was also adjusted to avoid saturating the detector.

The Dioptas program [101] was employed to calibrate and integrate the raw data and to mask the saturated regions of the detector when necessary, and the Rietveld analysis of the integrated *2Theta* diffraction patterns was carried out using the FullProf suite [97].

- *Magnetometry:* macroscopic magnetic susceptibility curves as a function of the temperature χ(T) were recorded in the interval 10-500 K under an applied external magnetic field of 2 kOe in FC conditions using a vibrating sample magnetometer (VSM) in a Physical Properties Measurement System (PPMS, Quantum Design Inc). Samples in the form of small solid pellets were used for the measurements.

5.3 Structural evolution versus Cu/Co and Cu/Zn B-site substitutions

The structural characterization of the $YBaCu_{1-x}Co_xFeO_5$ and $YBaCu_{1-x}Zn_xFeO_5$ series was done from the analysis of SXRPD patterns collected at the BL04-MSPD beamline of the ALBA Synchrotron Light Facility. The structural study on the Co-doped series was conducted in collaboration with X. Zhang. The reader is referred to Ref. [133] for further details on the characterization of this series of compounds. The refined SXRPD profiles and structural parameters as a function of Co doping (12 $YBaCu_{1-x}Co_xFeO_5$ samples with doping amounts ranging between $x = 0$ to 0.25) are summarized in Fig. B.1 and Table B.1 [App. B]. As for the Zn-doped samples investigated in this work, Fig. B.2 [App. B] displays the refined SXRPD patterns, and Table B.2 [App. B] reports the corresponding structural parameters and agreement factors at 300 K as a function of Zn content (7 $YBaCu_{1-x}Zn_xFeO_5$ samples with doping values ranging from $x = 0$ to 0.15). In all cases the Rietveld analysis procedure was done using the same symmetry (non-centrosymmetric $P4mm$ space group) and parameter constraints as reported in Chapter 4 for non-doped YBCFO samples. For simplicity, only two split positions were considered: the Fe one, and the (Cu,M) position where Cu is substituted by M = Co, Zn transition metals (the z-coordinates of M metals were constrained to be the same as Cu). The two transition metal positions and their respective Fe/(Cu,M) fractional occupancy were refined in the upper (M1, blue) and lower (M2, brown) pyramids within the unit cell [see Fig. 5.4(c)]. To refine the positions and fractions of the metals in the two M1 and M2 pyramids, the z-coordinates of the two positions that a given metal [either Fe

or (Cu,M)] occupy in the cell were refined using the constraint z(M1)+z(M2)=1.

5.3.1 Effect of Cu-site substitutions on cation disorder

First of all, we have studied the effect of Cu/Co and Cu/Zn doping on the B-site disorder, which as previously discussed plays an utterly important role on the magnetic frustration and exchange interactions between the different metals in the structure. As in the previous chapter, chemical disorder is parametrized by the improper occupancy n_d, which is defined as the fractional occupancy of the minority ions in the upper and lower pyramids [*i.e.*, n_d = Occ Fe1*/(Cu,M)2*]. The refined Fe/(M,Cu) fractional occupancies at the M1 and M2 pyramids for YBa(Cu,M)FeO_5 series with M = Co and Zn plotted in Figs. 5.4(a) and 5.4(b) [and reported in Tables 5.1(a) and 5.1(b)] show that there is no dependency on the Co and Zn content within errors, being the B-site disorder preserved up to the maximum doping amounts studied ($x = 0.25$ in the case of Cu/Co and $x = 0.15$ for Zn/Co). A similar behavior is found in Cu/Mg substituted samples, as shown by X. Zhang in Ref. [133]. However, this invariance of the chemical disorder upon B-site Cu/Co, Cu/Zn substitutions strongly contrasts with the evolution of disorder in YBaCu(Fe,Mn)O_5 doped samples. In these compounds, the introduction of a third metal like Mn^{3+} occupying the Fe^{3+} sites progressively increases the disorder at the B-sites [49].

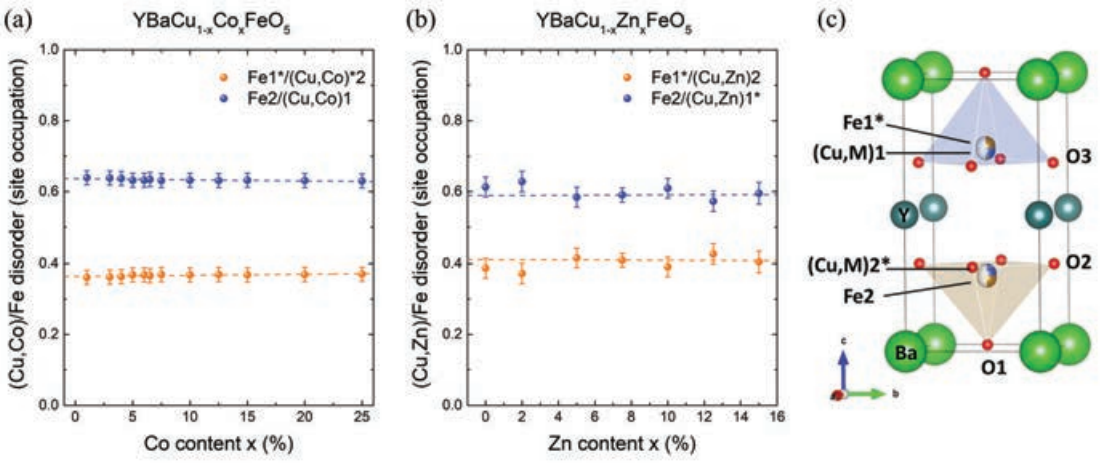

FIGURE 5.4: Dependence of B-site chemical disorder in $YBaCu_{1-x}M_xFeO_5$ versus M = Co and Zn B-metal substitutions. (a) Refined Fe/(Cu,Co) occupations for the $YBaCu_{1-x}Co_xFeO_5$ series. (b) Fe/(Cu,Zn) occupations in $YBaCu_{1-x}Zn_xFeO_5$ samples. (c) Scheme of the YBCFO unit cell. In the structure, Fe1* and (Cu,M)1 are accomodated in the upper pyramid, and Fe2 and (Cu,M)2* occupy the lower one (* indicates the minority fraction site).

Finally, the different average disorder values observed in the two series [n_d(Cu/Co)$\sim$37% and n_d(Cu/Zn)$\sim$42%] are a direct consequence of the distinct synthesis processes used. A controlled cooling rate of 300 °C/h was performed on the former, while for the Zn-doped series samples were cooled rapidly by quenching into liquid nitrogen. The disorder values observed are well correlated (within errors) with those reported for S2 and S6 samples of reference $YBaCuFeO_5$ composition cooled in similar conditions (see Table 4.2 in Chapter 4).

5.3.2 Impact of B-site doping on the structure

The refined cell parameters, tetragonal distortion ($\Delta_T \equiv c/2a$) and volume as a function of Co and Zn content (also included in Tables B.1 and B.2 [App. B]) are plotted in Figs. 5.5(a) and 5.5(b). From these plots similar behaviors can be identified upon increasing concentrations of Co and Zn doping metals. While the cell parameter a increases, c displays a larger contraction, which is even more marked in the Co-doped series.

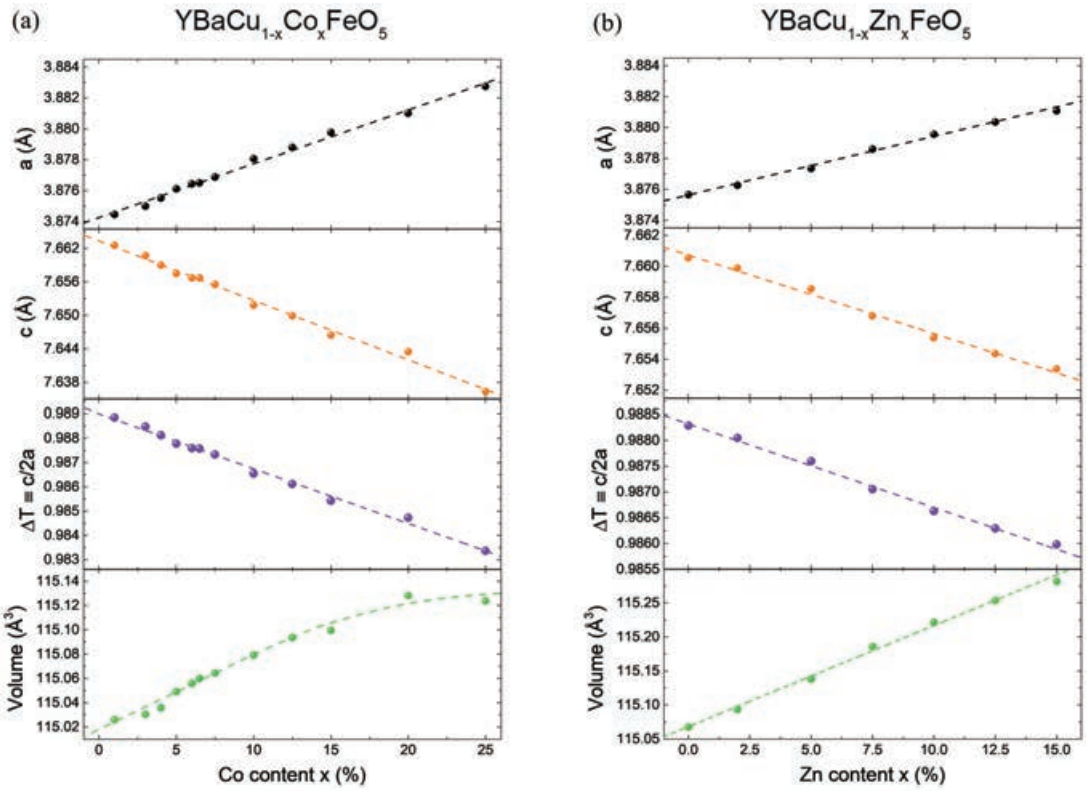

FIGURE 5.5: Evolution of the cell parameters (a=b and c), tetragonal distortion ($\Delta_T = c/2a$) and volume (V) at 300 K as a function of the doping metal content in (a) $YBaCu_xCo_{1-x}FeO_5$ and (b) $YBaCu_xZn_{1-x}FeO_5$ series.

TABLE 5.1: Refined interatomic distances (in Angstroms) at 300 K using the $P4mm$ S.G. of B-site doped YBa(Cu,M)FeO_5 samples with different M = Co and Zn content (x) from MSPD@ALBA synchrotron data (λ=0.413378 Å). (H: height of the pyramid). (a) $YBaCu_{1-x}Co_xFeO_5$ (prepared with 300 °C/h cooling rate). (b) $YBaCu_{1-x}Zn_xFeO_5$ (quenched in liquid nitrogen).

(a) $YBaCu_{1-x}Co_xFeO_5$ (300 °C/h cooling)	**Co-1%**	**Co-3%**	**Co-4%**	**Co-5%**	**Co-6%**	**Co-6.5%**	**Co-7.5%**	**Co-10%**	**Co-12.5%**	**Co-15%**	**Co-20%**	**Co-25%**
1-n_d = **Occ (Cu,Co)1/Fe2**	0.639 (20)	0.638 (20)	0.637 (20)	0.632 (20)	0.632 (20)	0.634 (20)	0.631 (20)	0.632 (20)	0.631 (20)	0.632 (20)	0.631 (20)	0.630 (20)
n_d = **Occ Fe1*/(Cu,Co)2*)**	0.361 (20)	0.362 (20)	0.363 (20)	0.368 (20)	0.368 (20)	0.366 (20)	0.369 (20)	0.368 (20)	0.369 (20)	0.368 (20)	0.369 (20)	0.370 (20)
d_s (Å)	2.826 (10)	2.827 (10)	2.827 (13)	2.828 (11)	2.828 (14)	2.831 (13)	2.830 (11)	2.834 (12)	2.836 (13)	2.841 (13)	2.847 (12)	2.851 (12)
d_t (Å)	4.837 (10)	4.834 (10)	4.832 (13)	4.829 (11)	4.828 (14)	4.826 (13)	4.826 (11)	4.818 (12)	4.814 (13)	4.806 (13)	4.796 (12)	4.785 (12)
d_t/d_s	1.7117 (71)	1.7103 (73)	1.7093 (88)	1.7078 (77)	1.7072 (01)	1.7048 (91)	1.7053 (76)	1.6997 (83)	1.6973 (88)	1.6918 (90)	1.6847 (86)	1.6780 (85)
H_L (Å)	2.474 (19)	2.469 (20)	2.467 (20)	2.462 (23)	2.459 (22)	2.454 (22)	2.454 (21)	2.444 (21)	2.439 (22)	2.429 (22)	2.417 (22)	2.401 (19)
H_S (Å)	2.362 (19)	2.365 (20)	2.365 (20)	2.367 (23)	2.369 (22)	2.371 (22)	2.371 (21)	2.373 (21)	2.375 (22)	2.377 (22)	2.379 (22)	2.384 (19)
d((Cu,Co)1-O1)$_{apical}$ (Å)	2.158 (18)	2.155 (19)	2.154 (18)	2.151 (21)	2.146 (20)	2.144 (20)	2.139 (20)	2.139 (20)	2.134 (20)	2.131 (20)	2.128 (21)	2.119 (17)
d((Cu,Co)1-O3)$_{basal}$ (Å)	1.963 (3)	1.963 (3)	1.963 (2)	1.962 (3)	1.963 (3)	1.962 (3)	1.964 (4)	1.963 (3)	1.963 (4)	1.963 (4)	1.962 (4)	1.962 (2)
d(Fe2-O1)$_{apical}$ (Å)	1.903 (18)	1.906 (19)	1.907 (19)	1.910 (22)	1.913 (21)	1.915 (21)	1.919 (20)	1.918 (20)	1.924 (21)	1.922 (21)	1.924 (21)	1.928 (17)
d(Fe2-O2)$_{basal}$ (Å)	1.903 (18)	1.906 (19)	1.907 (19)	1.910 (22)	1.913 (21)	1.915 (21)	1.919 (20)	1.918 (20)	1.924 (21)	1.922 (21)	1.924 (21)	1.928 (17)

(b) $YBaCu_{1-x}Zn_xFeO_5$ (quenched)	**Zn-2%**	**Zn-5%**	**Zn-7.5%**	**Zn-10%**	**Zn-12.5%**	**Zn-15%**
1-n_d=**Occ(Cu1/Fe2)**	0.628 (29)	0.584 (28)	0.590 (20)	0.609 (28)	0.573 (29)	0.595 (31)
n_d=**Occ(Fe1*/Cu2*)**	0.372 (29)	0.416 (28)	0.410 (20)	0.391 (28)	0.427 (29)	0.405 (31)
d_s (Å)	2.830 (9)	2.845 (8)	2.848 (10)	2.847 (10)	2.857 (6)	2.855 (10)
d_t (Å)	4.830 (9)	4.814 (8)	4.809 (10)	4.808 (10)	4.798 (6)	4.798 (10)
d_t/d_s	1.7064 (63)	1.6921 (54)	1.6888 (67)	1.6887 (68)	1.6796 (44)	1.6803 (66)
H_L (Å)	2.473 (14)	2.469 (12)	2.450 (16)	2.464 (18)	2.447 (12)	2.451 (16)
H_S (Å)	2.357 (8)	2.345 (8)	2.359 (11)	2.345 (13)	2.351 (9)	2.347 (10)
d((Cu,Zn)1-O1)$_{apical}$ (Å)	2.191 (11)	2.149 (11)	2.128 (17)	2.104 (22)	2.084 (16)	2.085 (16)
d((Cu,Zn)1-O3)$_{basal}$ (Å)	1.957 (2)	1.958 (4)	1.964 (3)	1.963 (3)	1.964 (4)	1.966 (3)
d(Fe2-O1)$_{apical}$ (Å)	1.926 (12)	1.945 (12)	1.951 (18)	1.969 (23)	1.972 (17)	1.949 (17)
d(Fe2-O2)$_{basal}$ (Å)	1.988 (4)	1.992 (2)	1.988 (2)	1.992 (2)	1.997 (1)	1.999 (2)

Comment: distances metal to Oa [= O1 (apical)] and Ob [= O2, O3 (basal)] correspond to the majority cation in upper (Cu-rich) and lower (Fe-rich) pyramids.

In all cases cell parameters disclose a linear correspondence with the doping metal content (x) as shown by the linear fits to the experimental points (dashed lines in Fig. 5.5). Moreover, a linear reduction of the tetragonal distortion ($\Delta_T = c/2a$) was observed in both series accompanying a small expansion of the unit cell volume. This volume expansion, which is ultimately caused by the expansion of the a(and b) parameters, is probably linked to the slightly larger ionic effective radius of Co^{2+} and Zn^{2+} (Co^{2+}: 0.67 Å (HS) and Zn^{2+}: 0.68 Å in V coordination [53]) as compared to Cu^{2+} (Cu^{2+}: 0.65 Å in V coordination [53]). However, this is at odds with the contraction observed in the c parameter. A look into Fig. 5.6, which shows the evolution of $\mathrm{d_s}$ and $\mathrm{d_t}$ average interatomic distances along c [also reported in Tables 5.1(a) and 5.1(b)], provides further insight on this question.

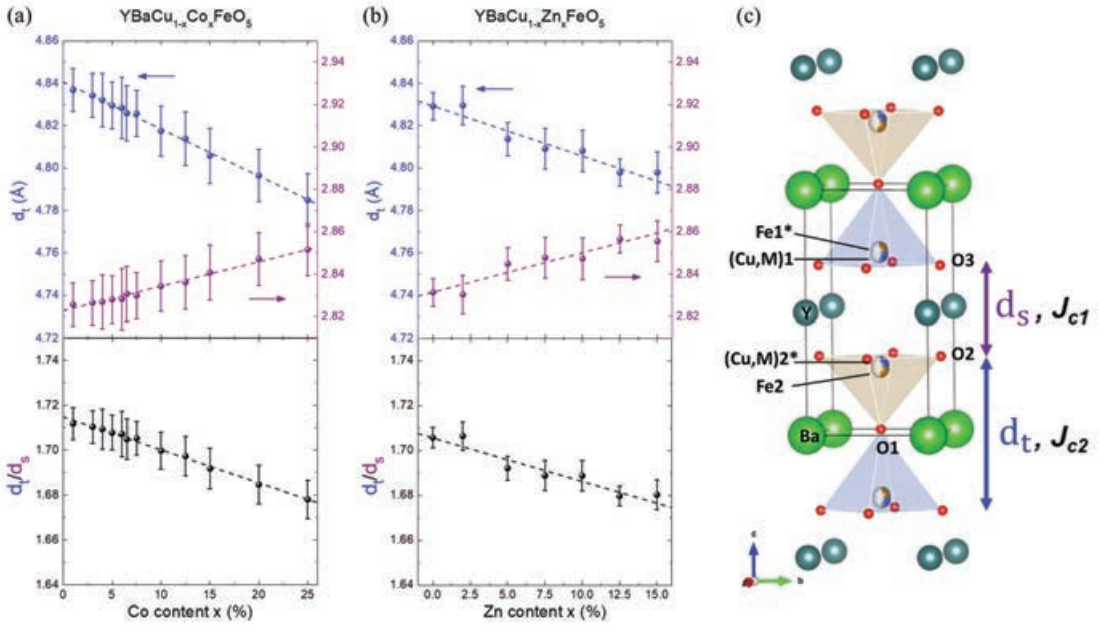

FIGURE 5.6: **Influence of Cu/Co and Cu/Zn B-metal substitutions on the thickness and separation of the bilayers**. Evolution of the thickness of the biliramidal layer ($\mathbf{d_t}$, left axis) and of the separation between bilayers ($\mathbf{d_s}$, right axis) as a function of B-site doping in (a) the $YBaCu_{1-x}Co_xFeO_5$ and (b) the $YBaCu_{1-x}Zn_xFeO_5$ series. (c) Projection of the YBCFO structure showing two successive bipyramids along c showing the thickness $\mathbf{d_t}$ of a bilayer and the separation $\mathbf{d_s}$ between bilayers.

For increasing concentration of M = Co and Zn metals in the pyramids, a systematic contraction of the thickness of the pyramid bilayers ($\mathrm{d_t}$) was observed, accompanied by a lesser increase in the separation between pyramid bilayers ($\mathrm{d_s}$). The contraction of c results then from the overall decompensation between both evolutions (remember that $c = \mathrm{d_t}+\mathrm{d_s}$). Comparing the distance variations in both series up to $x = 0.15$ doping amounts of Co[Zn], we found

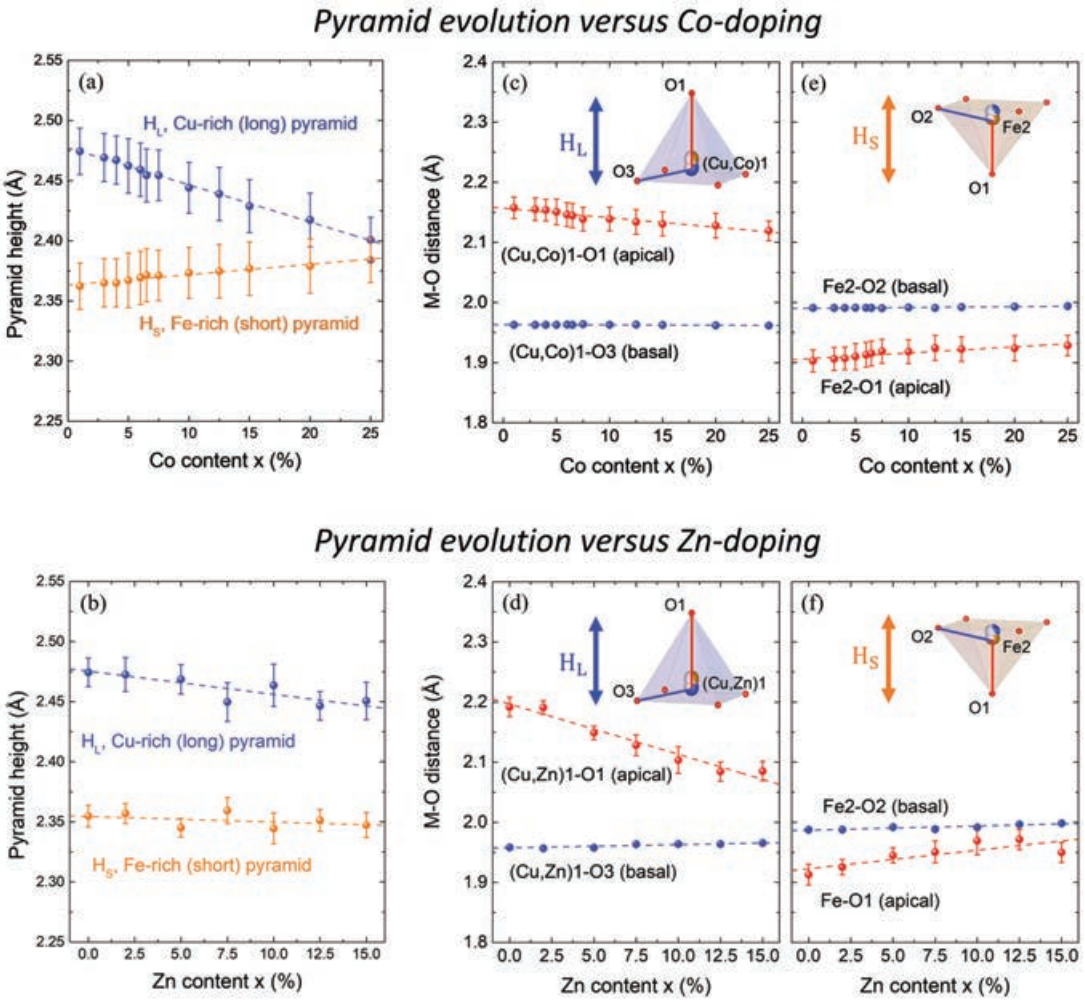

FIGURE 5.7: **Evolution of the two pyramids versus Cu/Co and Cu/Zn B-metal substitutions: H_L, H_S and the average (Cu,M)O_5 Jahn-Teller splitting**. (a,b) Average heights of the 'long' (upper, Cu-rich) and 'short' (lower, Fe-rich) pyramids (at 300 K) within the chemical unit cell versus Co and Zn content (x). (Cu,M)O_5 pyramids are longer than FeO_5 ones as a consequence of the Jahn-Teller character of Cu^{2+} ions. Evolution increasing the concentration of M = Co, Zn metals at the B-sites of the (c,d) (Cu,M)-O and (e,f) Fe-O interatomic distances in the two pyramids. The (Cu,Co)-O1 and (Cu,Zn)-O1 apical distances shrink as the concentration of dopant metals (x) increases in virtue of the non Jahn-Teller character of Co^{2+} and Zn^{2+} ions in contrast with Cu^{2+} ones.

a decrease in the bipyramid layer thickness of d_t ≈-0.032 Å[-0.035 Å] and an increase of the separation d_s ≈+0.017 Å[+0.025 Å]. The evolution of the d_t/d_s ratio, which shows a linear increase with x, is also plotted in Fig. 5.6.

The effects of B-site doping on the pyramid distortions and metal-to-oxygen distances within them [summarized in Tables 5.1(a) and 5.1(b)] are also rather appealing. The evolution of the average height of the upper and lower pyramids (H_L and H_S) in both series, plotted in Figs. 5.7(a,b), show that the average

Cu-rich pyramids (H_L) undergo a shrinkage as the concentration of Co and Zn metals in them increase, concomitant with a stretching of the average Fe-rich pyramid sites (H_S). To understand this evolution it is necessary to dissect the individual metal-to-oxygen distances in the pyramids. M-O bond lengths for the majority metal in each pyramid are disclosed in Figs. 5.7(c,e) for the Co-doped series and in Figs. 5.7(d,f) for the Zn-doped samples. As in the case of pristine YBCFO compositions, the Jahn-Teller (JT) splitting between (Cu,M)-O1 (apical) and (Cu,M)-O3 (basal) distances around Cu^{2+} ($t_{2g}^6e_g^3$) is evident along the whole Co- and Zn- doped series. The average pyramid heights (H_L and H_S) confirm, as expected, that this effect is specially relevant in the case of Cu-rich pyramids (upper site, represented in blue color). Furthermore, under the addition of Co^{2+} ($t_{2g}^5e_g^2$, HS) and Zn^{2+} ($t_{2g}^6e_g^4$), Cu^{2+} gets progressively replaced by the former, which are non Jahn-Teller ions. The consequence of this is a shrinkage of the apical (Cu,M)-O1 bond lengths, which indicate that the average JT effect in (Cu,M)O_5 gets progressively tamed as Cu is substituted by non JT Co and Zn ions. Ultimately, this produces the reduction of the crystal lattice along the [001] direction, overcoming the fact that the ionic sizes of Co^{2+} and Zn^{2+} are slightly larger than that of Cu^{2+}. Finally, we see that the two basal distances (Cu,M)-O3 and Fe-O2 remain nearly unchanged upon increasing Co and Zn doping levels.

In summary, we have demonstrated that the nearest-neighbor (NN) magnetic interaction paths along the c axis [J_{c_1} and J_{c_2} couplings, shown in Fig. 5.6(c)], whose relevance was discussed in the previous chapter, can also be modified by means of B-site chemical doping through similar structural modifications as in the case of A-site doping (reduction of d_t and increase of d_s distances in the $RBaCuFeO_5$ and $YBa_{1-x}Sr_xCuFeO_5$ series, reported by T. Shang *et al.* in Ref. [48]). Substituting Cu^{2+} by JT inactive ions such as Co^{2+} and Zn^{2+} reduces the incidence of Cu^{2+} Jahn-Teller pyramid elongation on the pyramid bilayer thickness (d_t). In addition, Cu/M substitutions are more advantageous than Fe/M substitutions, since the latter inevitably reduces the density of AFM Fe/Fe pair defects, leading to a weakening of magnetic frustration, as observed in the case of YBaCu(Fe,Mn)O_5, where the onset of the spiral magnetic order (T_S) is shifted to lower temperatures upon Fe/Mn doping (see Ref. [49]). The benefits and drawbacks of Cu/M substitutions with regard to the spiral phase will be disclosed in the next sections.

5.4 Magnetic phase diagram versus Cu/Co and Cu/Zn B-site substitutions

5.4.1 Magnetic phases and transitions

The magnetic transition temperatures in the two series were identified by macroscopic susceptibility and neutron powder diffraction measurements. Its values are summarized in Table 5.4. The magnetic susceptibility curves χ(T) obtained in field-cooling (FC) conditions under an external dc magnetic field of 2 kOe are displayed for all the samples in Fig. 5.8 within the temperature range 10 K-500 K.

A first look on the susceptibility curves of $YBaCu_{1-x}Co_xFeO_5$ samples (cooled at 300 °C/h), shown in Fig. 5.8(a), allows to identify two maxima (indicated

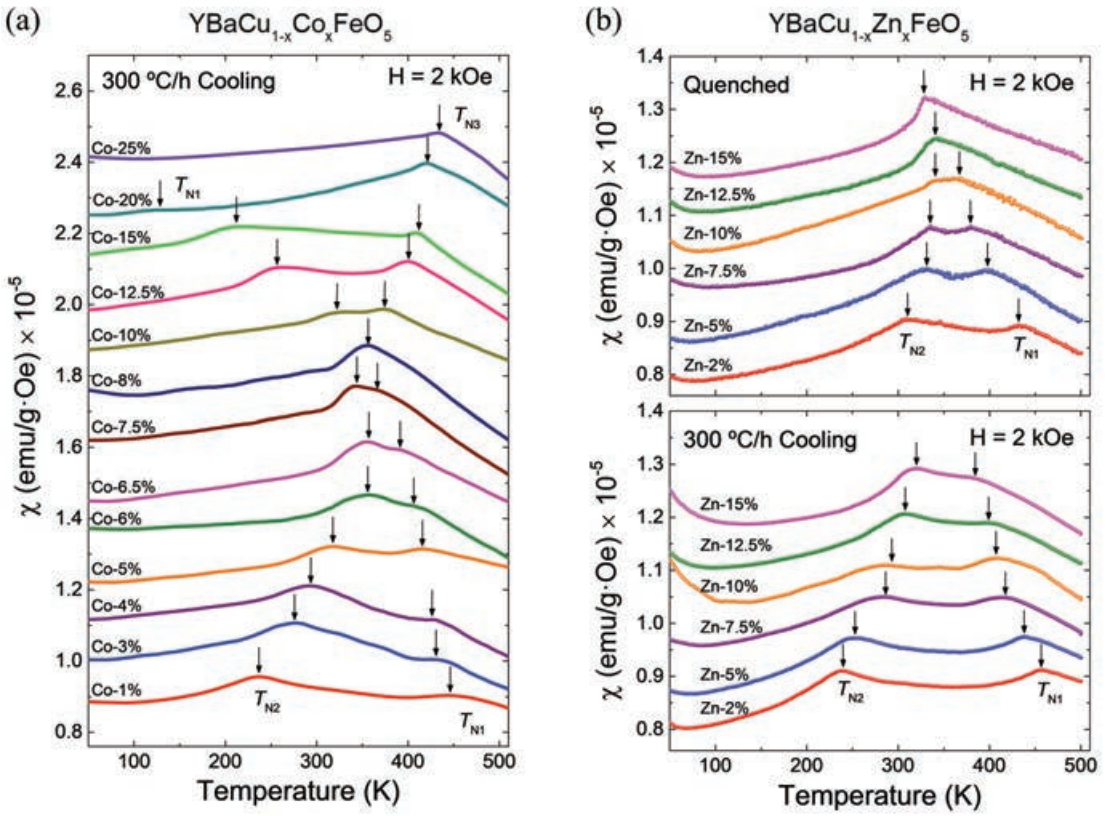

FIGURE 5.8: Evolution of the mass magnetic susceptibility curves (measured in FC, 2 kOe) for (a) $YBaCu_{1-x}Co_xFeO_5$ samples (with $0\% < x \leq 25\%$) prepared under 300 °C/h cooling rate, and (b) $YBaCu_{1-x}Zn_xFeO_5$ (with $0\% < x \leq 15\%$) prepared by quenching in liquid nitrogen (top panel) and under 300 °C/h cooling (bottom panel). For clarity successive curves were shifted by $\sim+10^{-6}$ emu·g^{-1}·Oe^{-1}.

by black arrows), which indicate the presence of two separated magnetic transitions. In the Co-doping range studied, two distinct regimes were identified in this series regarding the characteristics of the different magnetic phases: (1) the low Co-doping range between $0\% \leq x \leq 6.5\%$, and (2) the high Co-doping range within the interval $6.5\% < x \leq 25\%$.

In the former, a comparative investigation using neutron diffraction within the 10 K-500 K range showed that, as in the case of $YBaCuFeO_5$ reference compositions, the two local maxima in χ(T) observed in the low Cu/Co doping range ($0\% \leq x \leq 6.5\%$) identify (upon cooling) the two separated magnetic transitions at T_{N1} and T_{N2}=T_S, which correspond respectively to the onsets of the AF1 collinear phase [with $\mathbf{k}_1 = (1/2, 1/2, 1/2)$ propagation vector] and the AF2 spiral order [with incommensurate vector $\mathbf{k}_2 = (1/2, 1/2, 1/2 \pm q)$]. This was confirmed by the T-Q projections of the NPD intensities [shown in Fig. 5.11(a)], where the ($h/2$ $k/2$ $l/2 \pm q$) magnetic Bragg reflections (satellites) characteristic of the spiral order with $\mathbf{k}_2$ propagation vector emerge at T_{N2} (=T_S) and persist down to the base temperature. It should be pointed out that in this transition, the AF1 phase isn't completely transformed into the AF2 spiral order, and certain amount of the CM ($\mathbf{k}_1$) phase remains below T_{N2} accompanying the ICM ($\mathbf{k}_2$) magnetic satellites down to the base temperature.

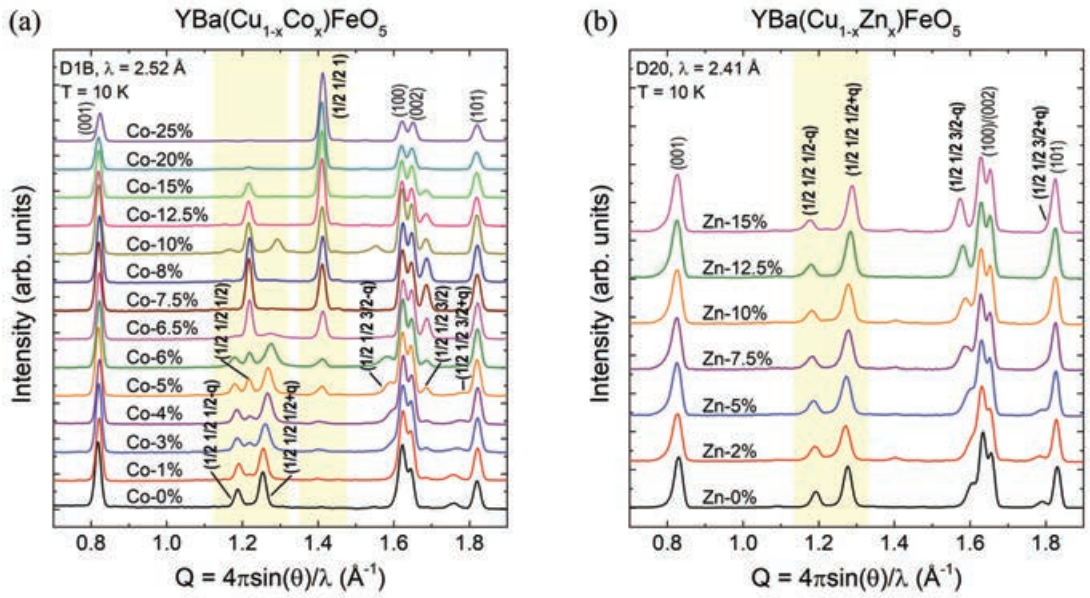

FIGURE 5.9: Low-angle region of the neutron powder diffraction (NPD) patterns recorded at 10 K for the two series of B-site doped samples. (a) $YBaCu_{1-x}Co_xFeO_5$ samples ($0\% \leq x \leq 25\%$) prepared under 300 °C/h cooling rate (D1B@ILL, $\lambda = 2.52$ Å), and (b) $YBaCu_{1-x}Zn_xFeO_5$ ($0\% \leq x \leq 15\%$) quenched in liquid nitrogen (D20@ILL, $\lambda = 2.41$ Å). For comparison, NPD patterns are plotted as a function of $Q = 4\pi \sin(\theta)/\lambda$.

According to susceptibility and NPD measurements, a remarkable raise of the spiral order temperature was observed upon increasing Co amounts (x), being T_{N2} increased by more than 120 K from $x = 0\%$ (∼230 K) to $x = 6.5\%$ (∼355 K), well above room temperature. However, in this doping range, a systematic decrease of the ICM magnetic satellite intensities is also observed, indicating that that the spiral order is progressively suppressed upon Cu/Co substitution, being $x = 6.5\%$ the maximum concentration of Co that the spiral order is able to tolerate.

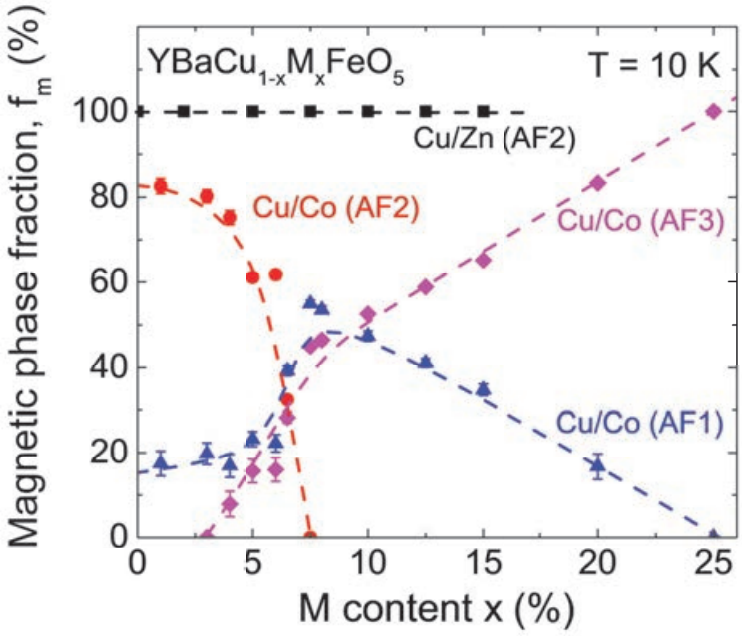

FIGURE 5.10: Magnetic phase fractions at T = 10 K in YBa(Cu,M)FeO_5 samples (M = Co, Zn) versus the concentration (x) of M metals in Cu/M B-sites. Black squares correspond to $f_m(\mathbf{k_2})$ single phase in Cu/Zn doped series. Blue triangles, red circles and purple diamonds correspond respectively to $f_m(\mathbf{k_1})$, $f_m(\mathbf{k_2})$ and $f_m(\mathbf{k_3})$ in the Cu/Co doped series. The values, refined from NPD data, are also reported in Table 5.4.

The nature and evolution of the magnetic phases as a function of Cu/Co doping is well illustrated by the low-angle region of the NPD diffraction patterns recorded at 10 K, shown in Fig. 5.9(a). In this plot we observe that the (h/2,k/2,l/2±q) incommensurate AF2 magnetic satellites progressively decrease at expenses of an increase of of the (h/2,k/2,l/2) commensurate AF1 magnetic reflections, and both orders coexist along the low Co-doping range until the spiral order vanishes for $x \geq 7.5$. Interestingly, Fig. 5.9(a) also discloses that a second commensurate phase AF3 with translational symmetry $\mathbf{k}_3 = (1/2, 1/2, 0)$ emerges as a consequence of Cu/Co doping. The intensity of its associated (1/2,1/2,1) magnetic reflection is favored upon Co-doping,

getting increasingly higher along the high Co-doping range ($6.5\% < x \leq 25\%$), and becoming dominant to the point that AF1 ($\mathbf{k}_1$) reflections decline until it gets entirely replaced by the new AF3 ($\mathbf{k}_3$) phase in the $x = 25\%$ sample. This unconventional behavior is also quantitatively disclosed in Fig. 5.10 from the magnetic phase fractions [$f_m(\mathbf{k}_i)$, with $i = 1, 2, 3$] obtained from the Rietveld fits of NPD patterns at 10 K (also summarized in Table 5.4). The intense competition between the AF3 ($\mathbf{k}_3$) and the ICM AF2 ($\mathbf{k}_2$) magnetic phases is a novel phenomenon which will be discussed later on in this chapter.
Accordingly to the strenghtening(weakening) of the AF3(AF1) magnetic phases, an increase(decrease) of the T_{N3}(T_{N1}) ordering temperature is observed as shown by the T-Q projections of the NPD intensities for samples with $x \geq 5\%$ [see Figs. 5.11(a,b)]. By comparison with T-Q neutron thermodiffractograms, the onset of the AF3 transition (T_{N3}) is associated to the first maxima observed (upon cooling) in the magnetic susceptibility curves for $6.5\% < x \leq 25\%$ samples [Fig. 5.8(a)].

The magnetic behavior upon Cu/Zn substitution strongly contrasts with the effect of Cu/Co doping. Magnetic susceptibility curves χ(T) for the two $YBaCu_{1-x}Zn_xFeO_5$ sets of samples quenched in liquid nitrogen and prepared under 300 C/h cooling rate [Fig. 5.8(b)] show two maxima at the Néel temperatures of two separated AFM transitions. Upon cooling, the first transition (T_{N1}) corresponds to the onset of the AF1 [$\mathbf{k}_2 = (1/2, 1/2, 1/2)$] collinear phase, and the second one (T_{N2}=T_S) to the ordering of the ICM AF2 [$\mathbf{k}_2 = (1/2, 1/2, 1/2 \pm q)$] spiral order, as confirmed by temperature dependent NPD measurements done in x= 5, 10 and 15% quenched samples [see Figs. 5.12(a-c)]. On the other hand, it should be highlighted the relevance of the fact that in Zn-doped samples the spiral order shows up as a single magnetic phase along the whole temperature range below T_{N2}, getting this transition temperature stabilized up to a maximum of ∼340 K in the quenched Zn-doped series (∼320 K in the 300 °C/h cooled series). Furthermore, in contrast to Co-doped samples, NPD diffraction patterns recorded at 10 K [Fig. 5.9(b)] show no signs of spiral order weakening, nor magnetic phase segregation as no traces of secondary $\mathbf{k}_1$ or $\mathbf{k}_3$ phases were observed below T_{N2} in any of the Zn-doped compounds studied ($x \leq 15\%$).

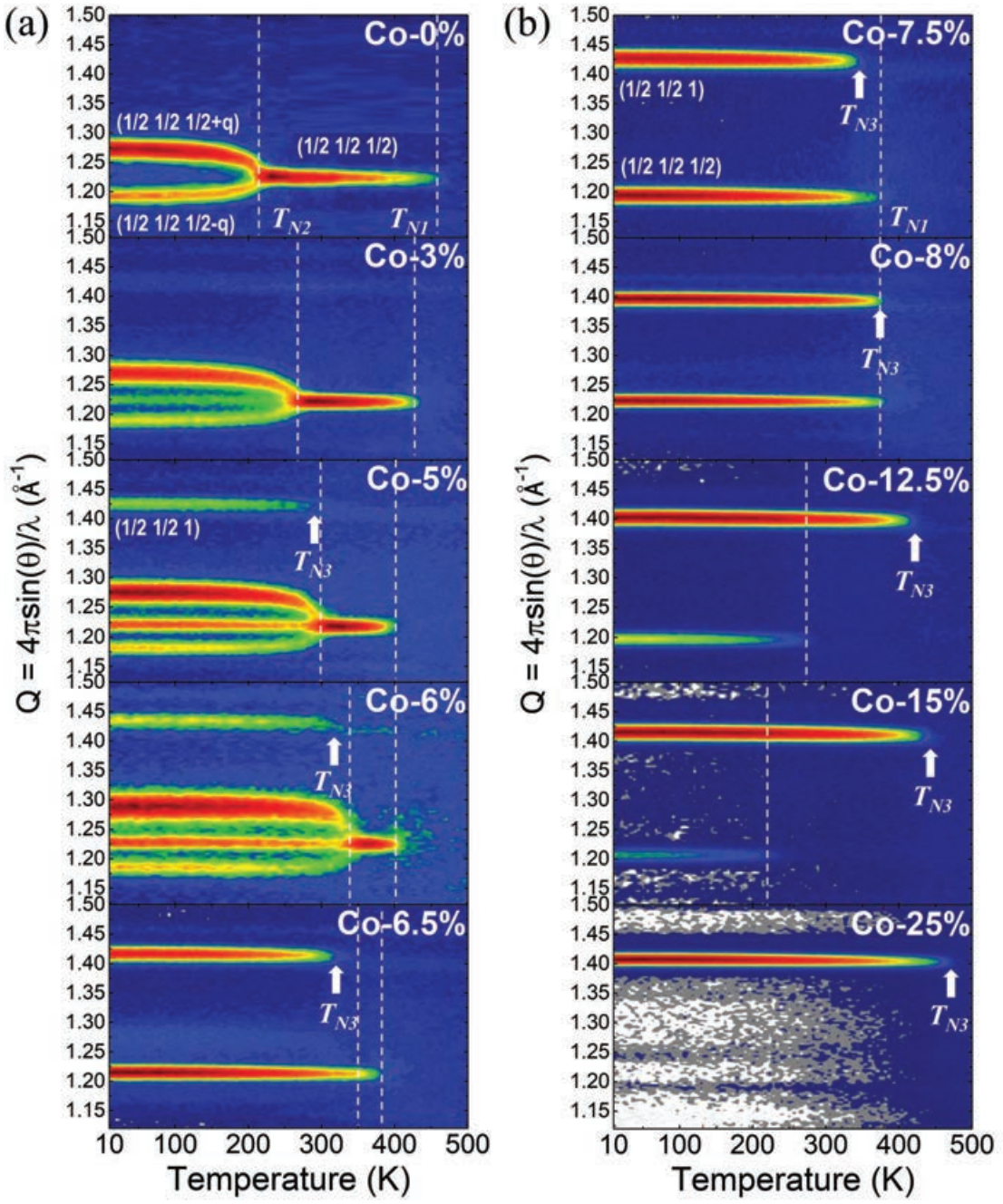

FIGURE 5.11: Contour maps showing the T-Q projection of the temperature dependence for the neutron-diffracted intensities (D1B@ILL, $\lambda = 2.52$ Å). The low Q region shows the thermal evolution of magnetic reflections (1/2 1/2 1/2) ($\mathbf{k}_1$), (1/2 1/2 1/2$\pm q$) ($\mathbf{k}_2$) and (1/2 1/2 0) ($\mathbf{k}_3$) in $YBaCu_{1-x}Co_xFeO_5$ samples. (a) Low Co-doping range ($0\% \leq x \leq 6.5\%$), with presence of the spiral order (AF3) coexisting with increasingly higher AF1 and AF3 reflections, and (b) high Co-doping range ($6.5\% < x \leq 25\%$) where the AF1 and AF3 phases dominate and the spiral order has been suppressed. Vertical dashed lines indicate the onset of AF1 (T_{N1}) and AF2 (T_{N2}) phases, and white arrows signal the emergence of the AF3 (T_{N3}) phase.

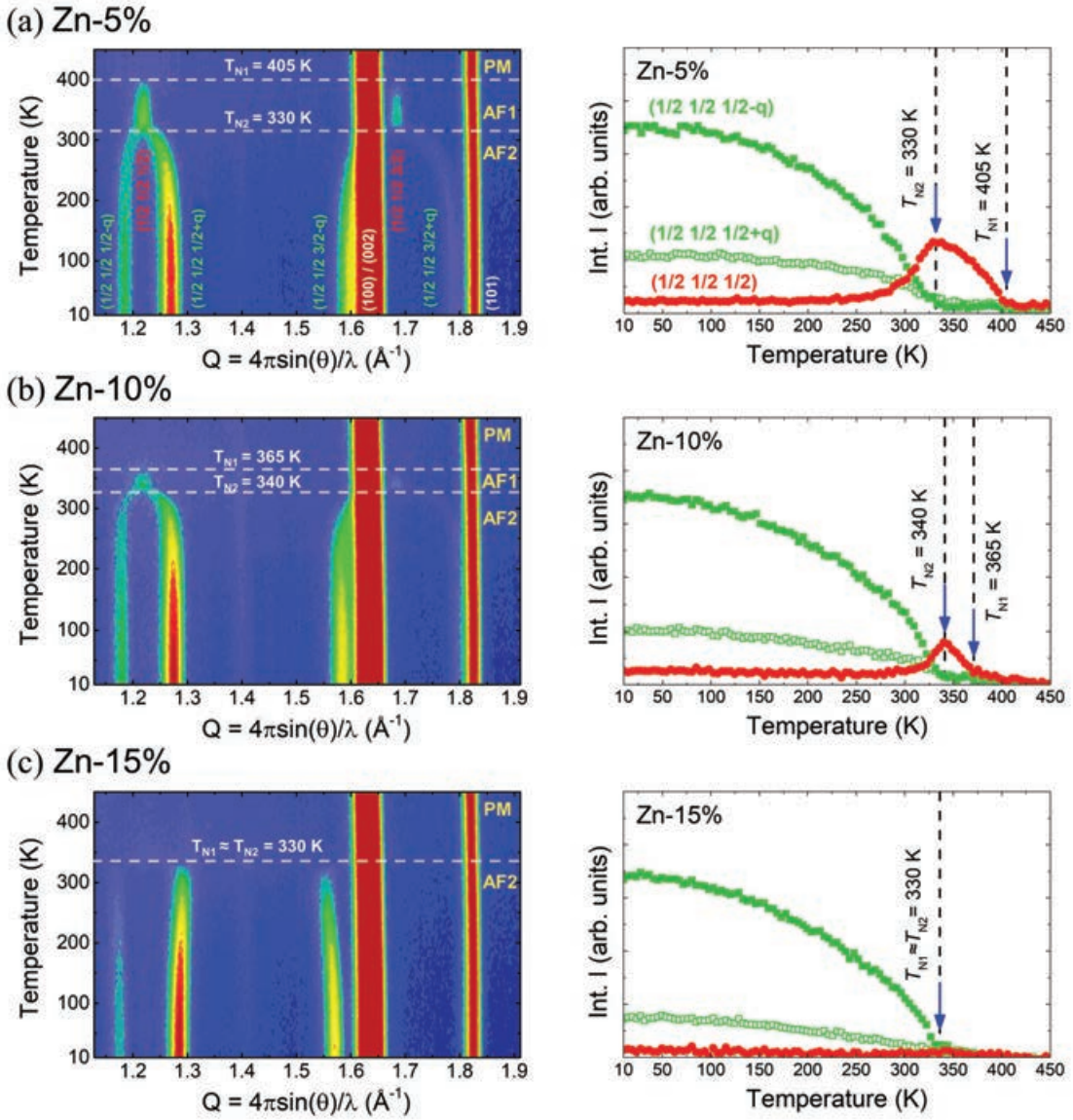

FIGURE 5.12: Contour maps showing the T-Q projection of the temperature dependence for the neutron-diffracted intensities (D20@ILL, $\lambda = 2.41$ Å). The low Q region shows the thermal evolution of magnetic reflections $(h/2\ k/2\ l/2)$ ($\mathbf{k}_1$), and $(h/2\ k/2\ l/2 \pm q)$ ($\mathbf{k}_2$) in $YBaCu_{1-x}Zn_xFeO_5$ quenched samples with (a) $x = 5\%$, (b) $x = 10\%$ and (c) $x = 15\%$. Horizontal dashed lines indicate the onset of AF1 (T_{N1}) and AF2 (T_{N2}) phases. No traces of AF3 ($\mathbf{k}_3$) reflections were observed. Right panels show the thermal variation of the integrated intensities of selected Bragg reflections and satellites, which correspond to the propagation vectors $\mathbf{k}_1 = (1/2, 1/2, 1/2)$ (red) and $\mathbf{k}_2 = (1/2, 1/2, 1/2 \pm \mathrm{q})$ (green).

The compositional dependence of the $\mathbf{k}_2$ spiral magnetic incommensurability (q_s), was parametrized by the q_s ground state saturation values, refined from NPD patterns (10 K) [see Table 5.4]. Its evolution as a function of the M = Co, Zn content (x) in the $YBaCu_{1-x}M_xFeO_5$ perovskites, plotted in Fig. 5.13(a), shows

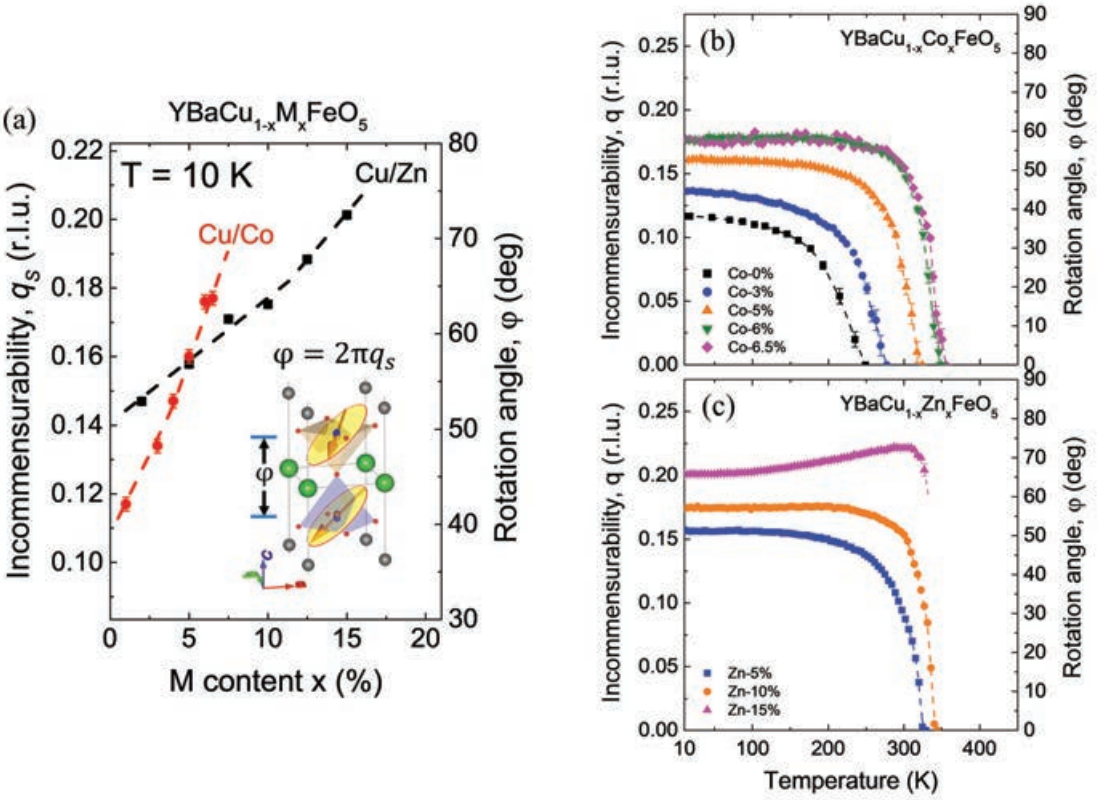

FIGURE 5.13: **Compositional B-site doping dependence of the magnetic spiral incommensurability and its temperature evolution**. (a) Influence of Cu/Co and Cu/Zn B-site doping (parametrized by the M = Co, Zn content x in $YBaCu_{1-x}M_xFeO_5$) on the ICM modulation q_s of the AF2 spiral phase, obtained from NPD refinements at T = 10 K. The inset shows an illustration of the the twist angle φ (canting) formed by the two spins of a bipyramid in the spiral phase ($\varphi = 2\pi q_s$). Temperature dependence of q_s obtained from neutron thermodiffractograms measured in (a) Co-doped samples with x[Co]= 0, 3, 5, 6, 6.5% and (b) quenched Zn-doped samples with x[Zn]= 5, 10, 15%.

a gradual strengthening upon increasing concentrations of Co and Zn. Remind that for the spiral wave propagating along **c**, the frequency shift q_s measures the constant twist ($\varphi = 2\pi q_s$) between the two spins in a bipyramid M_2O_9. For the two series of samples studied, the obtained q_s values yield maximum twist angles φ=63.72(72)° for x[Co]$= 6.5\%$ and φ=72.47(5)° for x[Zn]$= 15\%$. It should be emphasized that although the slopes of q_s and T_S versus M metal substitution (x) were larger for M = Co than in M = Zn substitutions, the spiral order was suppressed in the former for compositions with $x > 6.5\%$. In contrast with its interruption in the Co-doped series, the spiral phase abides higher concentrations of Zn, thus allowing to reach remarkably high q_s and T_S values without significant weakening of the magnetic spiral nor signs of phase segregation. In addition, the maximum spiral magnetic phase amplitude $q_s = 0.20130(13)$ r.l.u.

obtained for the $YBaCu_{0.85}Zn_{0.15}FeO_5$ quenched compound is to our knowledge the largest incommensurability value reported to the date in this kind of perovskites.

Finally, the temperature evolution of the spiral modulation q_s(T) was obtained for some samples from the Rietveld analysis of T-Q neutron thermodiffractograms. In Fig. 5.13(b), q_s(T) curves for compounds with x[Co] = 0, 3, 5, 6, 6.5% doping amounts show a smooth, continuous $q_s \rightarrow 0$ evolution on warming, characteristic of a second-order phase transition. This decrease becomes progressively steeper for $x \lessapprox 6.5\%$ samples with higher T_S transition temperatures, but a continuous collapse of q_s is still observed. Discerning whether T_{N1} and T_{N2} transitions merge into a single direct transition (paramagnetic-spiral) before the total interruption of the spiral order is difficult due to the abrupt decrease of the ICM satellite intensities. A more detailed study on this subject is out of the scope of this work.
On the other hand, Fig. 5.13(c) plots the q_s(T) evolution for quenched samples with x[Zn] = 5, 10, 15% doping amounts. As complementarily shown by χ(T) susceptibility curves [Fig. 5.8(b) (top panel)], for x[Zn]$\lessapprox 15\%$, $T_{N1} \approx T_{N2}$ transitions are merged and only a single paramagnetic-spiral transition can be distinguished, as confirmed by NPD temperature dependent measurements shown in Fig. 5.12(c). For x[Zn] = 5, 10% samples an abrupt, still continuous decrease of q_s was observed on warming. However, the evolution in x[Zn] = 15% compound displays an interesting behavior. In this sample the two ICM branches show an anomalous evolution, getting slightly but steadily distanced (increase of q_s) before a sharp collapse, nearly or apparently displaying a single direct paramagnetic-spiral transition.

5.4.2 Magnetic phase diagrams

From the magnetic transition temperatures and phase characteristics studied by susceptibility and neutron diffraction measurements described in the preceding sections, the x-T magnetic phase diagrams shown in Fig. 5.14 were built up for the Cu/Co and Cu/Zn doped series within the temperature range 10 K-500 K. In the horizontal axis we have represented the amount of M = Co and Zn in the $YBaCu_{1-x}M_xFeO_5$ samples, parametrized by x[Co] and x[Zn] (in %). In order to understand the evolution of the spiral order and the dissimilar magnetic behaviors of of these Co- and Zn- doped compounds with regard to the AF3 phase,

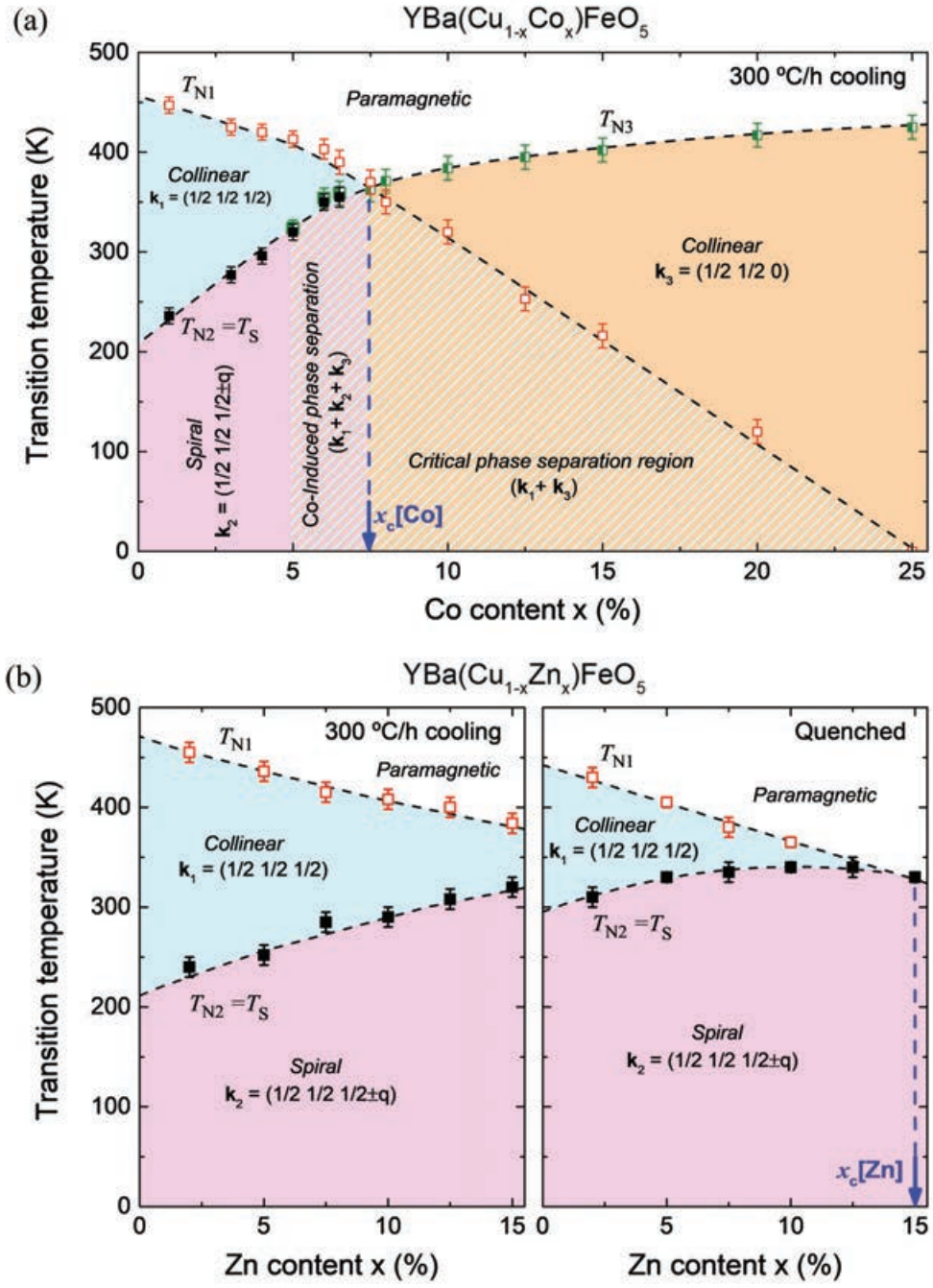

FIGURE 5.14: **Magnetic phase diagram versus Cu/Co and Cu/Zn B-site doping**. (a) x[Co]-T magnetic phase diagram for $YBaCu_{1-x}Co_xFeO_5$ (with $0\% < x \leq 25\%$) prepared under 300 °C/h cooling rate. (b) x[Zn]-T magnetic phase diagrams for $YBaCu_{1-x}Zn_xFeO_5$ (with $0\% < x \leq 15\%$) series prepared under 300 °C/h cooling (left panel) and by quenching in liquid nitrogen (right panel). The phase boundaries describe the onset of the magnetic phases according to magnetic susceptibility and neutron diffraction data. Empty red squares correspond to T_{N1}, black squares correspond to $T_{N2} = T_S$ and green half-filled squares refer to T_{N3}.

first it is necessary to understand the implications on the magnetic exchange interactions entailed by (1) the structural changes induced by the substitution of Cu^{2+} by Co^{2+} and Zn^{2+} metals, and (2) the magnetic exchange between divalent (Cu^{2+}, Co^{2+}, Zn^{2+}) and trivalent (Fe^{3+}) BB' ions, whose magnetic exchange constants are modified due to the spin configurations of Co^{2+} and Zn^{2+}. In the following sections these two points are discussed in the light of the detailed structural study and magnetic phase diagrams disclosed in Fig. 5.14.

Raising the spiral ordering temperature by Cu/Co and Cu/Zn substitution

The x-T magnetic phase diagrams in Figs. 5.14(a,b) portray a strong variation of the Néel temperatures associated with the AF1 (T_{N1}) and AF2 (T_{N2}=T_S) magnetic transitions, summarized in Table 5.2. Upon raising Co and Zn contents, the former displays a negative slope, while a positive variation is observed for the incommensurate spiral order (T_S). A noteworthy finding is the remarkably high maximum T_S values achieved: (x[Co],T_S)$_{300°C/h}$=(6.5%, 355 K) in the Co-doped series; (x[Zn],T_S)$_{300°C/h}$=(15%, 320 K) and (x[Zn],T_S)$_{quenched}$=(12.5%, 340 K) in the two Zn-doped series.

The stability of the different magnetic phases in YBCFO is specially sensitive to the average magnetic frustration. As we know from previous works, in this kind of perovskites an increase of magnetic frustration comes associated to a negative variation of T_{N1}, while an increase of T_S is favored [47, 48]. In accordance, the T_{N1} and T_S evolutions observed in our YBa(Cu,M)FeO_5 series are compatible with an increase of magnetic frustration upon Cu/Co and Cu/Zn substitions. To elucidate the mechanisms by which Co and Zn substitutions trigger such raise of the spiral ordering temperature, we should consider in the first place the effect of BB'-site cation disorder. As previously explained, the dilute presence of strongly AFM Fe/Fe bipyramids is at the origin of magnetic frustration, and an increase of the density of these frustrating Fe-O1-Fe improper bonds can shift the onset of the spiral phase (T_S) towards higher temperatures [47]. As it was shown in Figs. 5.4(a,b), cation disorder in YBa(Cu,M)FeO_5 samples (related to the density of Fe/Fe bonds) showed no variations within errors caused by M = Co and Zn substitutions that could potentially favor a raise of T_S (see Table 5.2). Hence, the evolutions observed in T_{N1} and T_{N2} (=T_S) can be safely attributed to crystal lattice steric effects (chemical internal pressure) induced by B-site cation substitutions, and probably also to the concomitant variations of magnetic NN exchange interactions caused by the introduction of Co and Zn in Cu sites. Although it is true that a weakening of the average

FM couplings inside the bipyramids is produced when Cu/Fe pairs are substituted by AFM Co/Fe or decoupled Zn/Fe spins (remind the non-magnetic nature of Zn^{2+}), the relatively low concentrations of Co and Zn are expected to have a second-order incidence on the transition temperatures in front of the strong lattice effects caused by such substitutions. In addition, in contrast to trivalent B'-site doping (Fe^{3+}/M^{3+} substitutions), Cu^{2+}/M^{2+} substitutions in the divalent B-site have a priori no direct effect on the density of randomly distributed Fe/Fe AFM dimers, which are the primary source of magnetic frustration. In the next section we will discuss the effects derived of Co^{2+} magnetic properties, whose substitution in the bipyramids has striking consequences for increasingly higher concentrations.

At this point it is important to recall the work of T. Shang *et al.* [48], which described the impact on the spiral properties of the lattice effects induced by isovalent A-site substitutions. In $RBaCuFeO_5$ and $YBa_{1-x}Sr_xCuFeO_5$ perovskites, the replacement of Y^{3+} by rare-earths (R^{3+}) with increasingly higher cationic sizes, and the partial substitution of Ba^{2+} by smaller Sr^{2+} cations, resulted in

TABLE 5.2: Correlation between magnetic transition temperatures (T_{N1} and T_{N2}=T_S) and some relevant structural parameters at 300 K [chemical disorder (n_d) and d_s, d_t interatomic distances (in Angstroms)] for B-site doped YBa(Cu,M)FeO_5 samples with different M = Co and Zn content (x) prepared by different cooling processes.

(a) $YBaCu_{1-x}Co_xFeO_5$ (300 °C/h cooling)

x[Co] (%)	T_{N1} (K)	T_S (K)	n_d	d_s (Å)	d_t (Å)
1	447 (8)	236 (8)	0.361 (20)	2.826 (10)	4.837 (10)
3	425 (8)	277 (8)	0.362 (20)	2.827 (10)	4.834 (10)
4	420 (8)	296 (8)	0.363 (20)	2.827 (13)	4.832 (13)
5	413 (8)	320 (8)	0.368 (20)	2.828 (11)	4.829 (11)
6	403 (10)	350 (8)	0.368 (20)	2.828 (14)	4.828 (14)
6.5	390 (12)	355 (10)	0.366 (20)	2.831 (13)	4.826 (13)
$\sim \Delta$	-60 K	+120 K	0	+0.005 Å	-0.011 Å

(b) $YBaCu_{1-x}Zn_xFeO_5$ (quenched)

x[Zn] (%)	T_{N1} (K)	T_S (K)	n_d	d_s (Å)	d_t (Å)
2	430 (10)	310 (10)	0.372 (29)	2.830 (9)	4.830 (9)
5	405 (5)	330 (5)	0.416 (28)	2.845 (8)	4.814 (8)
7.5	380 (10)	335 (10)	0.410 (20)	2.848 (10)	4.809 (10)
10	365 (5)	340 (5)	0.391 (28)	2.847 (10)	4.808 (10)
12.5	340 (10)	340 (10)	0.427 (29)	2.857 (6)	4.798 (6)
15	330 (5)	330 (5)	0.405 (31)	2.855 (10)	4.798 (10)
$\sim \Delta$	-100 K	+30 K	0	+0.025 Å	-0.032 Å

(c) $YBaCu_{1-x}Zn_xFeO_5$ (300 °C/h cooling)

x[Zn] (%)	T_{N1} (K)	T_S (K)
2	455 (10)	240 (10)
5	436 (10)	252 (10)
7.5	415 (10)	285 (10)
10	408 (10)	290 (10)
12.5	400 (10)	308 (10)
15	384 (10)	320 (10)
	-30 K	+80 K

Comment: the $\sim \Delta$ parameter in the last row is the approximate variation of the parameters between the maximum and minimum doping values shown in this table.

a compression of the bilayers (of thickness $\mathrm{d_t}$) and in a increase of the separation between pyramid bilayers ($\mathrm{d_s}$ distance). A raise of magnetic frustration was favored by these structural modifications, principally due to the compression of $CuFeO_9$ bipyramids, resulting in a huge increase of the stability range of the spiral (up to $\mathrm{T_S} \approx 375(3)$ K in $\mathrm{YBa_{0.6}Sr_{0.4}CuFeO_5}$) [48]. From the theoretical model developed by A. Scaramucci and co-workers [54, 55], we know that magnetic order depends (apart from the AFM coupling within the ab plane) on the two opposite nearest-neighbour (NN) interactions (J_{c_1} and J_{c_2}) along the c axis [shown in Fig. 5.6(c)]. Their sign and strength depend principally on the spatial distribution of Fe^{3+} and Cu^{2+} ions (chemical disorder) and on the M-M' and M-O1-M' bond lengths for the different magnetic exchange paths along c. The AFM J_{c_1} direct exchange acts between successive bipyramids, which are separated by the characteristic distance $\mathrm{d_s}$. This interaction coexists with the J_{c_2} exchange within the $FeCuO_9$ bipyramids (Fe-O1-Cu). In the presence of disorder (*i.e.*, in presence of improper Fe_2O_9 bipyramids), the shrinking of the $MM'O_9$ bipyramids ($\mathrm{d_t}$ distance) has the most relevant effect on the increase of magnetic frustration, since this contraction implies the shortening of the strongly AFM Fe-O1-Fe c-bonds, further strengthening $\mathrm{J}_{c_2'}$ in the improper Fe_2O_9 bonds, which competes with the FM J_{c_2} Fe-O1-Cu bonds in mixed $FeCuO_9$ bipyramids. The increase of $\mathrm{d_s}$ only produce a secondary weakening of the AFM J_{c_1} direct exchange between successive bilayers.

Then, a remarkable achievement in the new B-site substitution strategies presented in this chapter is that a novel way (respect to the A-site substitutions in $RBaCuFeO_5$ and $YBa_{1_x}Sr_xCuFeO_5$ perovskites) of generating chemical pressure and appropiate structural changes has been effectively proved that is based on the disruption of the JT distortion in nominally CuO_5 pyramids. In our structural study (disclosed in Sec. 5.3.2), we quantified the disturbance of JT distortion produced by the insertion of divalent non JT Co^{2+} and Zn^{2+} ions in Cu^{2+} sites. The correlation between the stability of the AF1 and AF2 phases ($\mathrm{T_{N1}}$ and $\mathrm{T_S}$) and some structural parameters relevant for the magnetic couplings ($\mathrm{d_s}$, $\mathrm{d_t}$ and the $\mathrm{n_d}$ improper occupancy) are summarized in Table 5.2 for the Co- and Zn-doped series. Notice that for the Cu/Co series this table shows information within the doping range with presence of the spiral phase (x[Co]$\leq 6.5\%$). The structural evolution between the two extreme doping values shown in Table 5.2 (formerly presented in Sec. 5.3.2, see Fig. 5.6) showed that upon Co[Zn] doping the separation between pyramid bilayers was increased by $\Delta \mathrm{d_s} \approx$ +0.005Å[+0.025Å], whereas the bipyramids were shrunk by

$\Delta d_t \approx$ -0.011Å[-0.032Å]. For the Co-doped samples the variation in the thickness (d_t) is almost two times the variarion in the space between bilayers (d_s), while in the Zn-doped (quenched) samples the variation of d_t is also larger, but more similar to that of d_s. These structural evolutions are fully compatible with the huge raise of the spiral transition temperatures observed (T_S), being caused as a consequence of increasing the $3d$-$2p$ orbital overlap across the M-O1-M' superexchange path.

The highest increase of the spiral ordering temperature T_S (=T_{N2}) was observed for the Cu/Co doped compounds. In the $YBaCu_{1-x}Co_xFeO_5$ series, the variation of T_S is of a striking $\sim +120$ K up to x[Co]=6.5%. For Cu/Zn substituted compounds, the spiral transition (T_S) undergoes an increase upon Zn substitution in the two sets of $YBaCu_{1-x}Zn_xFeO_5$ samples prepared by two different cooling processes. For the controlled 300 °C/h cooling rate samples [5.14(b) (left panel)], this variation is of a remarkable ∼+80 K up to $x = 0.15$; meanwhile, for the quenched samples [5.14(b) (right panel)], T_S gets just lifted by $\sim +30$ K. We have to stress that in the quenched Zn-doped series, the observed values of T_S result from the combined effects associated to (a) the modification of d_t and d_s distances (specially the contraction of bipyramid thickness) within the crystal lattice by Zn B-site substitution and (b) the higher (but constant along the series) degree of B-site cation disorder induced by the fast sample cooling process. This confirms that in addition to the tuning of the lattice by Cu/Zn doping, the properties of the spiral phase can be efficiently optimized by further adding the effect of B-site chemical disorder.

Influence of B-site substitutions on the magnetic "phase separation"

From the T-x[Co] magnetic phase diagram shown in Fig. 5.14(a), two doping regimes are clearly differentiated regarding the magnetic properties of the $YBaCu_{1-x}Co_xFeO_5$ compounds: (1) the low Co-doping range ($0\% \leq x \leq 6.5\%$) is characterized by the presence of the ICM AF2 [$\mathbf{k}_1 = (1/2, 1/2, 1/2 \pm q)$] spiral phase coexisting with CM AF1 [$\mathbf{k}_1 = (1/2, 1/2, 1/2)$] domains, and (2) the high Co-doping region (which extends within $6.5\% < x \leq 25\%$), where the the spiral has been suppressed and a novel CM magnetic phase AF3 [$\mathbf{k}_3 = (1/2, 1/2, 0)$] coexists and competes with AF1 regions. The CM AF3 phase, which 'separates' from the main AF1 ($\mathbf{k}_1$) and AF2 ($\mathbf{k}_2$) phases, shows up in progressively higher fractions along the series upon increasing amounts of Co ions in the Cu sites. In contrast, Zn substitutions produce magnetic phase diagrams where the spiral

order was more resilient to suppression. In the following lines we comment on some issues and observations that help to understand better the x-T magnetic phase diagram and the phase separation region in YBa(Cu,Co)FeO_5 and YBa(Cu,Zn)FeO_5 compounds:

(i) The '*spiral order by disorder*' mechanism in the studied perovskites requires and cannot avoid a commensurate collinear phase preceding the chiral incommensurate order. A paramagnetic/spiral phase boundary of finite size is not possible. In consequence, beyond the so-called tri-critical point, where the continuous evolution of the collinear-to-spiral phase transition intersects the paramagnetic-to-collinear transition line, the spiral can no longer exist. Further this point, the disappearance of the spiral should be adscribed to the fact that the strong AFM couplings between Fe-Fe bonds become so large that the FM coupling of the bipyramids can no longer compete. This causes the suppression of the spiral order in favor of AF3 collinear magnetic regions where all NN couplings are AFM, favoring the previously described magnetic phase with $\mathbf{k}_3$ wave vector. Hereinafter we will refer to this magnetic regime above the tri-critical point as the '*critical phase separation region*'. In YBCFO samples where magnetic frustration is increased by modifying the amount of Fe/Cu cation disorder, this *critical phase separation region* is settled within a very narrow disorder range between $\mathrm{n_d^c} = 0.47(3)$ (the tri-critical point) and $\mathrm{n_d} = 0.5$ (the maximum possible disorder), hence difficulting investigating its properties. Instead, the critical boundary was loosely reached in our B-site Co and Zn substitution strategies keeping invariant the density of AFM Fe/Fe bonds by further strengthening the frustrating AFM Fe/Fe interactions due to the reduction of the $\mathrm{d_t}$ average thickness. The vertical dashed line and arrows in Figs. 5.14(a) and 5.14(b) (right panel) indicate the expected *critical phase separation* boundary at $x_\mathrm{c}[\mathrm{Co}] \approx 7.5\%$ and $x_\mathrm{c}[\mathrm{Zn}] \approx 15\%$, respectively.

(ii) As described in the previous point, in the Co-doped series the interruption of the $\mathbf{k}_2$ spiral order due to the '*critical phase separation*' is observed above $x_\mathrm{c}[\mathrm{Co}] \approx 7.5\%$. However, incipient regions with the AF3 commensurate phase with $\mathbf{k}_3 = (1/2, 1/2, 0)$ wave vector can be observed in compounds with much lower Co concentrations, which gradually replace the AF2 spiral regions accordingly to Co substitution [see the relative increase/decrease of $\mathrm{f_m}(\mathbf{k}_3)/\mathrm{f_m}(\mathbf{k}_2)$ magnetic phase fractions plotted in Fig. 5.10]. This evolution

indicates that cobalt substitution induces the magnetic phase separation in concentrations $x \ll x_c[\mathrm{Co}]$. We will refer to this effect as the '*induced phase separation*' (induced by cobalt). In the magnetic phase diagram this effect leds to a zone characterized by a transient coexistence of the three types of competing AFM domains with k_z = 1/2, 1/2$\pm q$ and 0 translational symmetries [dashed $\mathbf{k}_1$+$\mathbf{k}_2$+$\mathbf{k}_3$ region in Fig. 5.14(a)].

This new phenomena can be explained as a consequence of inhomogeneities in the sign and strength of exchange magnetic couplings between the different cation pairs in the bipyramids caused by the Cu/Co substitution. To understand the origin of the CM AF3 ($\mathbf{k}_3$) regions, first we need to figure out these effects over the competing superexchage terms in the system caused by the substitution of Cu^{2+} by magnetic HS Co^{2+} ($3d^7$: $t_{2g}^5e_g^2$, S=3/2) cations in the bipyramids. The sign and strength of exchange magnetic couplings between the different cation pairs in the bipyramids are governed by the Goodenough-Kanamori-Anderson (GKA) rules [134][135][136]. These rules, applied to the inter-pyramidal M-O1-M' paths in a bipyramid occupied by a Co^{2+}/Fe^{3+} pair or even Co^{2+}/Cu^{2+} pair (instead of Cu^{2+}/Fe^{2+}), state that the superexchange interaction is AFM (instead of FM). This AFM inter-pyramidal coupling favors k_z = 0 instead of k_z = 1/2, and therefore Cu/Co substitution progressively favors the emerging magnetic phase with wave vector $\mathbf{k}_3 = (1/2, 1/2, 0)$ [see the AF3 magnetic structure, illustrated in Fig. 5.16(c)].

Summarizing, in $YBaCu_{1-x}Co_xFeO_5$ compounds two main factors add up to progressively enhance the AFM coupling inside bipyramids: (1) bringing metals closer in Fe_2O_9 and (2) promoting AFM Fe/Co and Cu/Co pairs in M_2O_9 centers. (3) In addition, we should not discard the possible effects due to local spatial inhomogeneities in the distribution of Cu/Fe and Co/Fe atoms, which could also favor magnetic phase separation.

(iii) Finally, in the quenched $YBaCu_{1-x}Zn_xFeO_5$ series, the intersection of T_{N1} and T_S temperatures was also found, in this case at a critical zinc doping fraction of about $x_c[\mathrm{Zn}] \approx 15\%$ [see Fig. 5.14(b) (right panel)]. Although we did not observe the spiral order interruption as in Co-doped compounds, the *critical phase separation* is expected for Zn substitutions exceeding $x_c[\mathrm{Zn}] \approx 15\%$. This study needs to be completed by further extending the Zn doping range. Nevertheless, the presented results unveil a very remarkable finding. In contrast with the YBa(Cu,Co)FeO_5 series, in YBa(Cu,Zn)FeO_5 quenched compounds with higher degree of disorder no traces of the AF3 phase, nor signs

of AF1 regions coexisting with the AF2 spiral phase below T_{N2} (=T_S) were detected below the tri-critical point. In other words, the '*induced phase separation*' is avoided in samples where Cu is substituted by non-magnetic Zn. Unlike Co doping, Zn doping does not enhance/favor AFM exchange coupling within bipyramids. The formation of a single magnetic spiral phase below T_S in these compounds is clearly a favourable difference with respect to B-site cation disorder and Cu/Co B-site substitution strategies.

The linear relationship between T_S and q_s

Another interesting observation in the $YBaCu_{1-x}M_xFeO_5$ (M = Co, Zn) families studied in this chapter is the linear relationship between the spiral ordering temperature (T_S) and the magnetic modulation (q_s). For the sake of comparison, taking advantage from the fact that in this kind of layered perovskites the amplitude q_s of the magnetic disconmensuration is an intrinsic feature of the spiral ground state, we have simultaneously plotted in Fig. 5.15 the experimental (q_s, T_S) points for all the series investigated so far, including the compositions reported in Refs. [48, 133]. This overall picture shows certain consistency among the different spiral tuning routes, which comprise the modification of B-site cation disorder and the lattice tuning strategies by means of A-site and B-site cation substitutions. All series shown in Fig. 5.15 disclose a positive slope of T_S versus q_s. The linear fits to T_S the experimental (q_s, T_S) values are shown in Fig. 5.15 as dashed lines. The slopes and intercepts in the $T_S = A + B \cdot q_s$ linear regressions are summarized in Table 5.3. The q_s-T_S linear relationship, theoretically anticipated in the model by Scaramucci *et al.* in

TABLE 5.3: Regression slopes and intercepts obtained from linear least squares regression fits to (q_s,T_S) experimental points along different series of layered perovskites in the different strategies applied to tentatively rise the spiral phase stability. The strategy followed (variation of B-site disorder or AA'- and BB'-site substitutions), the cooling process applied to the samples in the fabrication process are indicated. R^2 is the goodness of the regression model. The last column reports the $T_{spi}/|q_s|$ parameter (in meV) obtained from the linear evolutions.

$T_S = A + B \cdot q_s$						
Compound	**Strategy**	**Cooling process**	**A**	**B**	**R^2**	$T_{spi}/\|q_s\|$ (meV)
$YBaCuFeO_5$	B-site disorder	Variable parameter	-61.7	2610.1	0.9961	71 (3)
$RBaCuFeO_5$ [48]	A-site substitution (Y^{3+}/R^{3+})	Quenched	87.5	1651.5	0.9751	54 (5)
$YBa_{1-x}Sr_xCuFeO_5$ [48]	A'-site substitution (Ba^{2+}/Sr^{2+})	Quenched	26.9	1965.9	0.9582	45 (4)
$YBaCu_{1-x}Co_xFeO_5$	B-site substitution (Cu^{2+}/Co^{2+})	300°C/h cooling	16.1	1907.4	0.9945	52 (2)
$YBaCu_{1-x}Zn_xFeO_5$	B-site substitution (Zn^{2+}/Co^{2+})	Quenched	216.8	675.6	0.7378	19 (5)
$YBaCu_{1-x}Mg_xFeO_5$ [133]	B-site substitution (Cu^{2+}/Mg^{2+})	Quenched	178.7	853.9	0.9721	23 (2)

Comment: The $T_{spi}/|q_s|$ is defined as the slope of the $k_B T_S$ versus $|Q| = \pi q_s$ linear regression fit. $k_B = 0.08617$ meV/K is the Boltzmann constant.

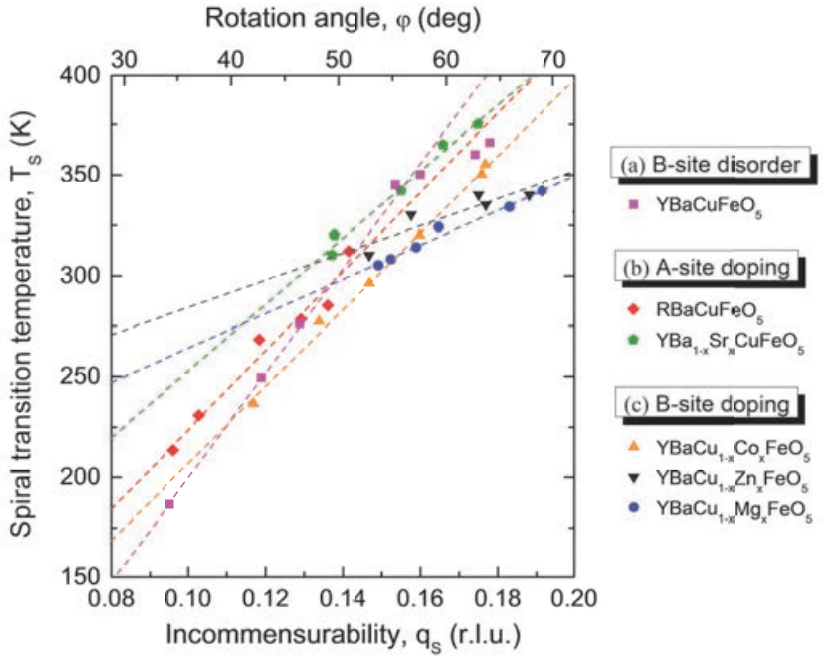

FIGURE 5.15: Linear relationship between the thermal stability (T_S) of the magnetic spiral phase and its ground-state modulation q_s along different series of layered YBCFO perovskites where magnetic frustration is increased by different routes based on (a) the variation of B-site disorder in $YBaCuFeO_5$ (experimental points from Chapter 4), (b) the substitution of AA'-site cations in the $YBa_{1-x}Sr_xCuFeO_5$ and $YBaCu_{1-x}Co_xFeO_5$ series (from Ref. [48]), and (c) the substitution BB'-site metals in the series $YBaCu_{1-x}Co_xFeO_5$, $YBaCu_{1-x}Zn_xFeO_5$ (studied in this work) and $YBaCu_{1-x}Mg_xFeO_5$ (in Ref. [133]). The linear extrapolations corresponding to the linear regressions (shown in Table 5.3) disclose a variability in the slopes for the different series. The twist angle ($\varphi = 2\pi q_s$) is also indicated in the upper horizontal axis.

Ref. [55] for $YBaCuFeO_5$ compounds where frustration is only originated by B-site cation disorder (spiral order by disorder mechanism), was experimentally verified by several works, including the study presented in Chapter 4. However, wheras the reported $T_{spi}/|q_s| \approx 71(3)$ meV is in very good agreement with the theoretical estimation of 68 meV [55], the experimental $T_{spi}/|q_s| \approx$ quantities derived from the (q_s, T_S) linear evolutions for the different families of perovskites (shown in Table 5.3) show a noticeable variability with respect to the above mentioned reference value. This important observation unveils that the q_s-T_S relation, which discloses the interplay between the stabilization of cycloidal (spiral) orders and magnetic frustration (remember that q_s measures the twist in the FM $CuFeO_9$ bipyramids, $\varphi = 2\pi q_s$), is not universal within all the different families of YBCFO-type layered perovskites. Indeed, this interplay is strongly dependent on the specific routes applied with the aim of strengthening the magnetic frustration in the system.

5.5 Influence of B-site doping on the easy axis and magnetic anisotropy

In this section we have investigated the impact of Cu^{2+} by Co^{2+} and Zn^{2+} B-site cation substitutions on the magnetic anisotropy of YBCFO by means of neutron powder diffraction. To this end, a similar Rietveld analysis methodology as in Chapter 4 was followed to refine the parameters of the AF2 incommensurate spiral phase. In Co-doped compounds, collinear order models were also used to refine independently the magnetic parameters of AF1 and AF3 phases by fitting the magnetic reflections associated to commensurate propagation vectors $\mathbf{k}_1$ and $\mathbf{k}_3$. The phase difference between magnetic moments at the two sites was fixed to 180° as found in earlier Refs. [46, 109, 137]. Magnetic structure models for the AF2, AF1 and AF3 phases used to fit the $\mathbf{k}_2$, $\mathbf{k}_1$ and $\mathbf{k}_3$ reflections in the NPD patterns are depicted in Fig. 5.16(a-c), where the the different magnetic couplings giving raise to k_z = 1/2±q, 1/2 and 0 translational symmetries along c are illustrated along three successive unit cells. Notice that for the AF3 collinear phase, the suppression of the magnetic anti-translation for successive cells along c ($k_z = 0$) is a consequence of the AFM character of coupled spin pairs at the bipyramids. This is in contrast with the AF1 order, where these pairs are ferromagnetically coupled in virtue of the FM Fe^{3+}-O-Cu^{2+} exchange interaction.

The inclination angle of the magnetic easy axis is defined by the θ polar angle, which measures the angular distance between the direction of magnetic spins and the c axis, namely (i) the collinear magnetic spin direction $\mathbf{u}$ in the CM AF1 and AF3 phases and (ii) the rotation plane of the spins in the spiral ICM AF2 magnetic phase ($\mathbf{uv}$ plane). The θ_S, θ_{C1} and θ_{C2} inclination angles the AF2, AF1 and AF3 magnetic structures are also indicated in Fig. 5.16(a-c).
It should be recalled that due to the tetragonal symmetry of the parent cell, it is not possible from NPD to determine the orientation of the easy axis component parallel to the ab plane. Hence, following the same procedure as in Chapter 4, for simplicity, the director vector $\mathbf{u}$ was taken as within the ac plane and $\mathbf{v}$ was constrained to be parallel to the b axis. A θ value $\approx 0°$ mean an easy axis nearly parallel to the c axis, whereas $\approx 90°$ would correspond to an easy axis within the tetragonal ab plane. In the $P4mm$ structure, when θ adopts intermediate values (different to 0° or 90°), the magnetic arrangement according to $\mathbf{k}_i$ ($i = 1, 2, 3$) translational symmetries requires the concurrent activation of magnetic modes belonging to distinct irreducible representations (magnetic *irreps*) [46].

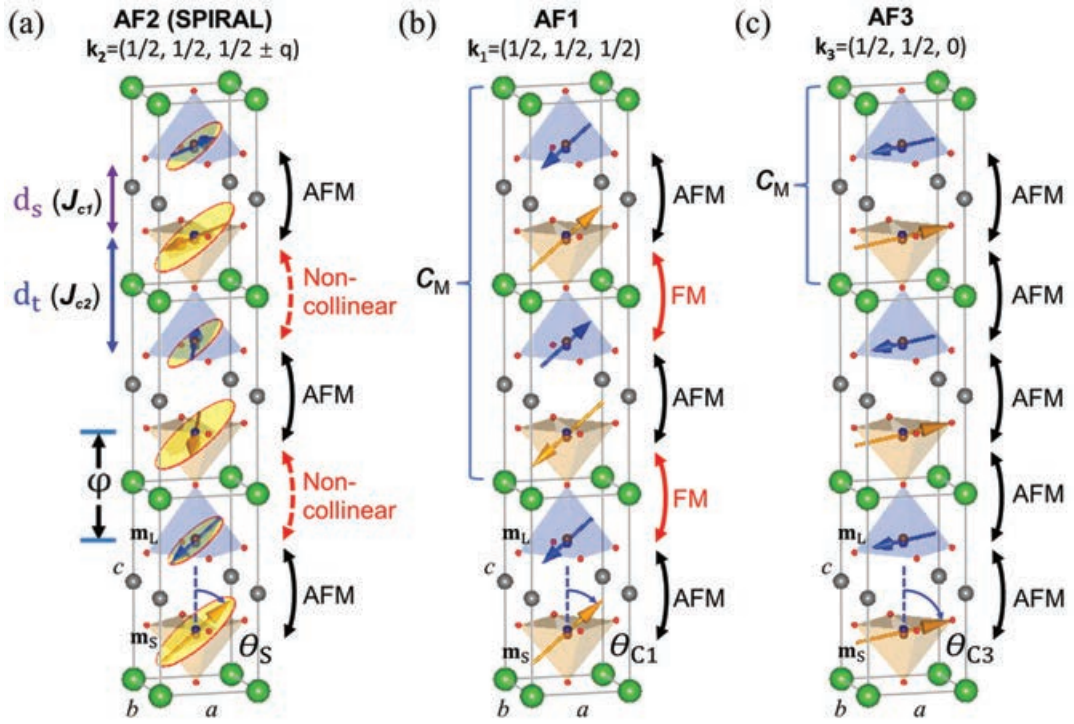

FIGURE 5.16: Projections of the magnetic structures in the incommensurate AF2 spiral phase (a), and in the commensurate collinear AF1 (b) and AF3 (c) phases along three successive crystallographic cells along c. The average nearest-neighbor (NN) competing magnetic couplings for the inter-layer (J_{c_1}) and intra-layer (J_{c_2}) exchange paths along the c crystal axis are also shown. While the always AFM J_{ab} interactions within the ab plane preserve the same (k_x,k_y)=(1/2, 1/2) in the $\mathbf{k}_1$, $\mathbf{k}_2$ and $\mathbf{k}_3$ phases, the sign of J_{c_2} gives raise to the different k_z = 1/2$\pm q$, 1/2 and 0 translational symmetries along c. For the moments and pyramids, blue(brown) colors reflect the predominance of Cu(Fe) at the upper(lower) pyramids, with average ordered magnetic moments $m_L(m_S)$.

With the aim of thoroughly investigating the impact of Co and Zn doping on the features of the spiral order, we have carefully refined the neutron patterns at 10 K. The full neutron Rietveld refinements for $YBaCu_{1-x}Co_xFeO_5$ samples with x[Co] = 1, 3, 4, 5, 6, 6.5% are exposed in Fig. 5.17, and refinements of the neutron patterns for $YBaCu_{1-x}Zn_xFeO_5$ quenched samples with x[Zn] = 2, 5, 7.5, 10, 12.5, 15% are shown in Fig. 5.18. The extracted magnetic parameters for the AF1, AF2 and AF3 phases are listed in Table 5.4. As an approximation, the amplitudes of the ordered magnetic moments at the nominally Fe and Cu sites (m_L and m_S) were refined imposing $m_L = r \cdot m_S$, with the ratio r calculated using Eq. (4.9) according to the refined Fe/Cu cation disorder exposed in Table 5.1. Notice that since NPD cannot distinguish between the real amplitudes of the ordered magnetic moments in the different AF1, AF2 and AF3 phases, which might not be identical, the refined magnetic phase fractions shown in this table were referred to the total volume of sample imposing

the same $\mathrm{m_L}$ and $\mathrm{m_S}$ moment amplitudes in the different coexisting magnetic phases. It should be also mentioned that as in the similar NPD magnetic analysis presented in Chapter 4, the ICM phase was refined using a circular spiral model ($\mathrm{M_R}$=$\mathrm{M_I}$) in which the theta angle (θ_S) was fixed from its refined value using a sinusoidal model ($\mathrm{M_I} \sim 0$) to minimize errors.

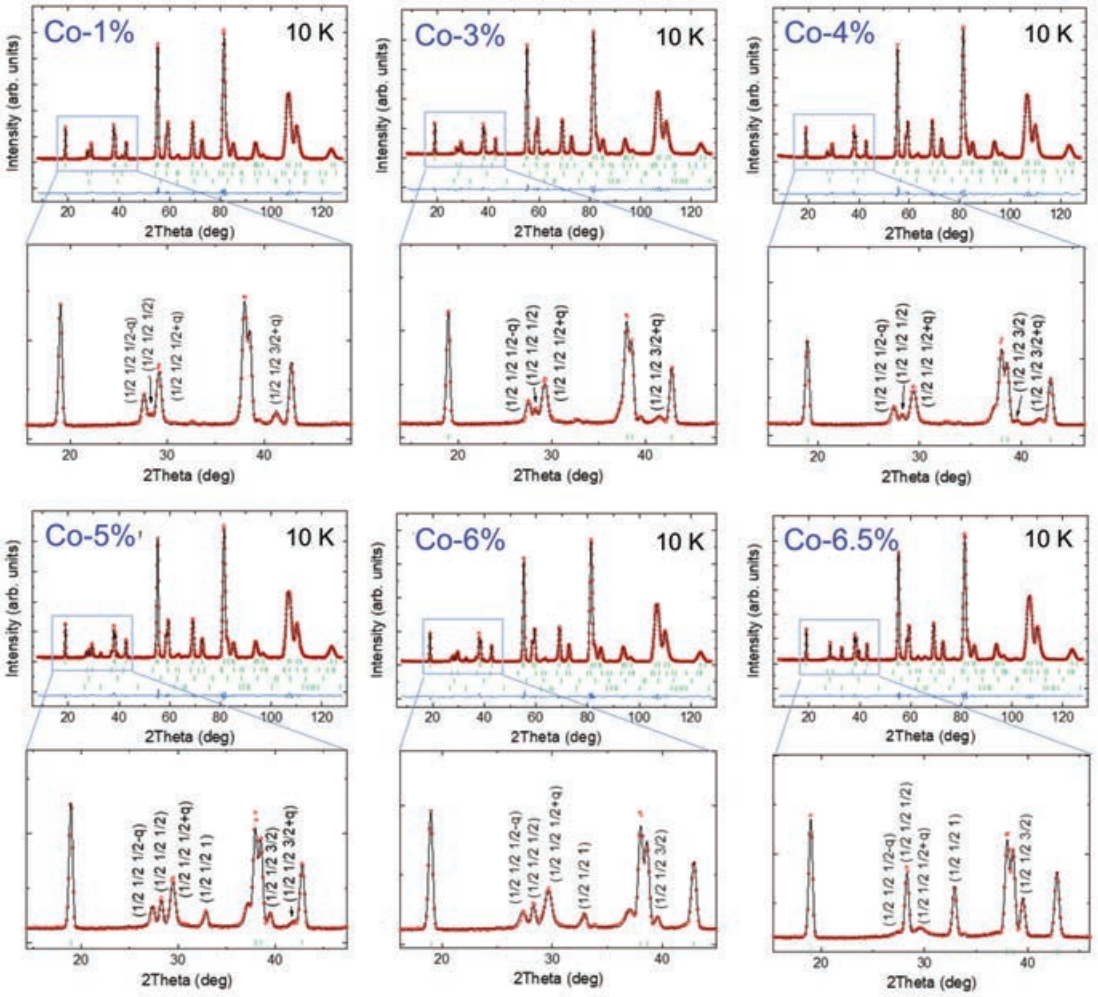

FIGURE 5.17: Rietveld refinement (black curve) of the D1B@ILL ($\lambda = 2.52$ Å) neutron diffraction patterns (red circles) at 10 K ($\mathrm{M_R} = \mathrm{M_I}$) for the $YBaCu_{1-x}Co_xFeO_5$ samples ($1\% \leq x \leq 6.5\%$) prepared under 300°C/h with increasing B-site cobalt substitution (x[Co]). Rows of bars indicate indicate, from upper to lower, the allowed Bragg reflections for the structural, ICM (AF2) and CM (AF1, AF3) phases. The bottom panel insets zoom in the low-angle region in each sample's full pattern to show the agreement in the fit of the main magnetic reflections. Magnetic parameters obtained from the fits are reported in Table 5.4(a). Agreement factors: Co-1% (χ^2: 10.2, R_B: 1.16, R_f: 0.658, R_m: 9.44); Co-3% (χ^2: 8.63, R_B: 0.923, R_f: 0.551, R_m: 8.71); Co-4% (χ^2: 12.1, R_B: 1.82, R_f: 1.10, R_m: 11.7); Co-5% (χ^2: 9.48, R_B: 0.918, R_f: 0.576, R_m: 9.83); Co-6% (χ^2: 8.40, R_B: 1.35, R_f: 0.866, R_m: 9.84); Co-6.5% (χ^2: 8.48, R_B: 0.720, R_f: 0.440, R_m: 11.3).

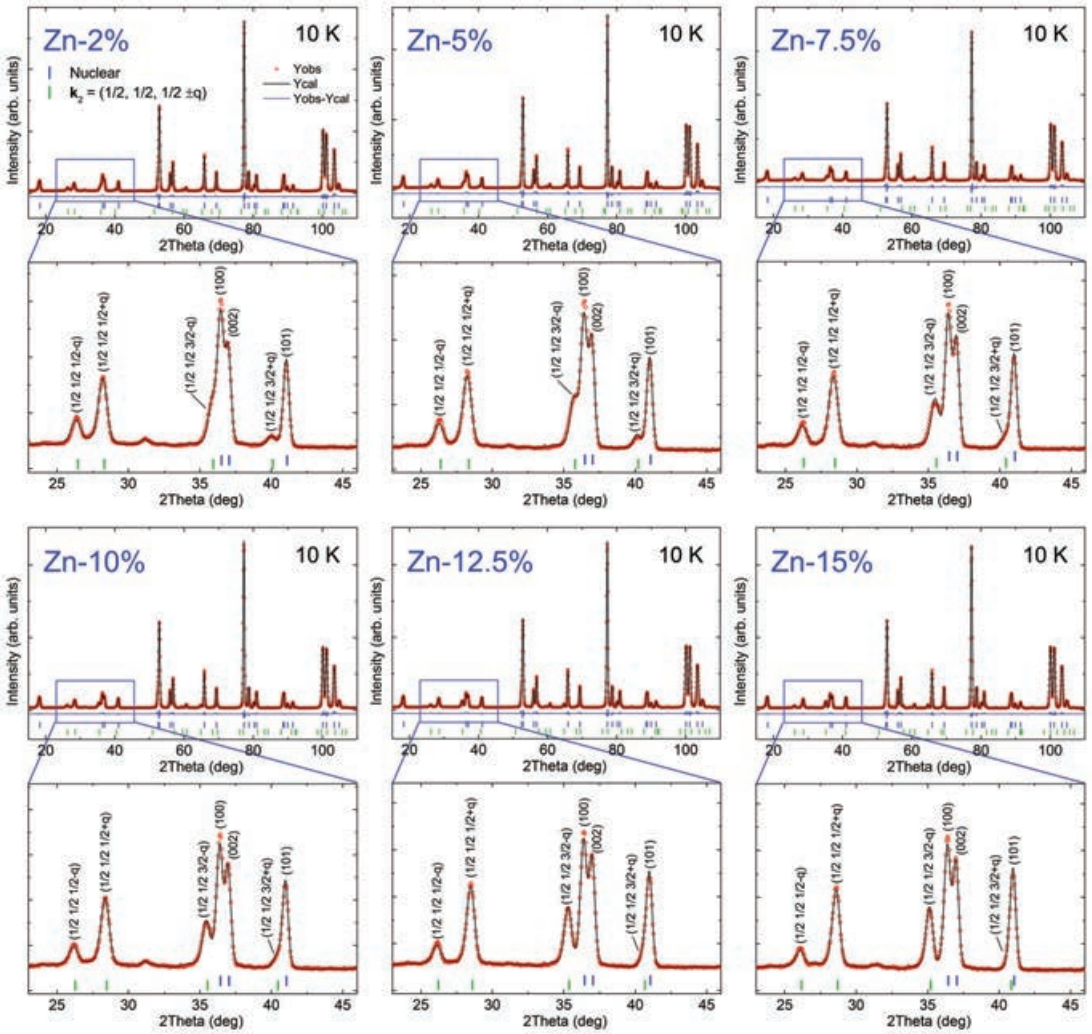

FIGURE 5.18: Rietveld refinement (black curve) of the D20@ILL ($\lambda = 2.41$ Å) neutron diffraction patterns (red circles) at 10 K ($\mathrm{M_R} = \mathrm{M_I}$) for the $YBaCu_{1-x}Zn_xFeO_5$ samples ($2\% \leq x \leq 15\%$) quenched in liquid nitrogen with increasing B-site zinc substitution (x[Zn]). Rows of bars indicate indicate, from upper to lower, the allowed Bragg reflections for the structural and the ICM (AF2) phases. The bottom panel insets zoom in the low-angle region in each sample's full pattern to show the agreement in the fit of the main magnetic reflections. Magnetic parameters obtained from the fits are reported in Table 5.4(b). Agreement factors: Zn-2% (χ^2: 15.3, R_B: 1.75, R_f: 1.09, R_m: 2.54); Zn-5% (χ^2: 16.7, R_B: 2.00, R_f: 1.25, R_m: 3.83); Zn-7.5% (χ^2: 11.3, R_B: 1.06, R_f: 1.79, R_m: 2.75); Zn-10% (χ^2: 12.6, R_B: 1.42, R_f: 0.873, R_m: 2.80); Zn-12.5% (χ^2: 11.2, R_B: 1.13, R_f: 0.704, R_m: 2.73); Zn-15% (χ^2: 14.9, R_B: 1.25, R_f: 0.814, R_m: 3.04).

TABLE 5.4: Magnetic parameters for the different magnetic phases at T = 10 K with propagation vectors $\mathbf{k}_1 = (1/2, 1/2, 1/2)$ (AF1), $\mathbf{k}_2 = (1/2, 1/2, 1/2 \pm \mathrm{q})$ (AF2) and $\mathbf{k}_3 = (1/2, 1/2, 0)$ (AF3) obtained from Rietveld refinements of the neutron powder diffraction data of (a) the $YBaCu_{1-x}Co_x$ samples (prepared with 300 °C/h cooling rate) and (b) the $YBaCu_{1-x}Zn_x$ series (quenched in liquid nitrogen) as a function of Co and Zn content (x) at the B-sites of the perovskite. Refined average magnetic moments $\mathrm{m_L}$ and $\mathrm{m_S}$ at the respective Cu-rich and Fe-rich pyramid sites were obtained imposing $\mathrm{m_L} = \mathrm{r} \cdot \mathrm{m_S}$, with the ratio r calculated according to the refined Fe/Cu cation disorder exposed in Table 5.1. The ICM phase was refined using a circular spiral model ($\mathrm{M_R}$=$\mathrm{M_I}$) in which the theta angle (θ_S) was fixed from its refined value using a sinusoidal model ($\mathrm{M_I} \sim 0$).

(a) $YBaCu_{1-x}Co_xFeO_5$ (300 °C/h cooling)	**Co-1**%	**Co-3**%	**Co-4**%	**Co-5**%	**Co-6**%	**Co-6.5**%	**Co-7.5**%	**Co-8**%	**Co-10**%	**Co-12.5**%	**Co-15**%	**Co-20**%	**Co-25**%
T_{N1} (K)	447 (8)	425 (8)	420 (8)	413 (8)	403 (10)	390 (12)	370 (12)	350 (12)	320 (12)	253 (12)	216 (12)	120 (12)	0
$T_{N2} = T_S$ (K)	236 (8)	277 (8)	296 (8)	320 (8)	350 (8)	355 (10)	-	-	-	-	-	-	-
T_{N3} (K)	-	-	-	320 (8)	350 (10)	355 (12)	362 (12)	371 (12)	384 (12)	395 (12)	402 (12)	417 (12)	425 (12)
COLLINEAR (AF1)													
$f_m(\mathbf{k}_1)$ (%)	17.4 (3.0)	19.8 (2.6)	16.9 (2.7)	23.2 (1.7)	22.3 (2.0)	39.3 (1.2)	55.0 (0.8)	53.5 (0.9)	47.4 (1.2)	41.1 (1.0)	34.8 (1.4)	16.7 (3.0)	0
θ_{C1} (deg)	42 (9)	45 (6)	51 (10)	44 (3)	40 (4)	56 (2)	52 (2)	54 (1)	47 (2)	52 (2)	52 (2)	53 (3)	-
SPIRAL (AF2)													
$f_m(\mathbf{k}_2)$ (%)	82.6 (1.7)	80.2 (1.5)	75.2 (1.6)	61.1 (1.0)	61.8 (1.1)	32.4 (0.6)	0	0	0	0	0	0	0
θ_S (deg)	43 (3)	38 (3)	31 (5)	26 (3)	16 (5)	13 (6)	-	-	-	-	-	-	-
q_s (r.l.u.)	0.117 (2)	0.134 (2)	0.147 (2)	0.160 (2)	0.176 (2)	0.177 (2)	-	-	-	-	-	-	-
COLLINEAR (AF3)													
$f_m(\mathbf{k}_3)$ (%)	0	0	7.9 (3.0)	15.7 (2.8)	16.0 (2.8)	28.3 (1.3)	45.0 (0.9)	46.5 (1.0)	52.6 (0.8)	58.9 (0.6)	65.2 (0.6)	83.3 (0.5)	100
θ_{C3} (deg)	-	-	66 (96)	94 (60)	94 (60)	77 (8)	78 (6)	77 (6)	84 (14)	82 (6)	80 (3)	80 (3)	78 (3)
$\mathbf{r = m_L/m_S}$	0.687 (52)	0.689 (52)	0.691 (51)	0.701 (49)	0.701 (49)	0.697 (50)	0.703 (49)	0.701 (49)	0.701 (49)	0.703 (49)	0.701 (49)	0.703 (49)	0.705 (48)
m_S (μ_B)	2.532 (56)	2.569 (50)	2.684 (61)	3.109 (45)	2.873 (46)	2.958 (33)	2.369 (21)	2.268 (20)	2.030 (19)	2.462 (19)	2.357 (20)	2.213 (20)	1.982 (10)
$m_L = r \cdot m_S$ (μ_B)	1.741 (50)	1.770 (44)	1.855 (55)	2.178 (40)	2.013 (40)	2.061 (27)	1.664 (15)	1.589 (15)	1.422 (14)	1.730 (14)	1.651 (14)	1.555 (14)	1.396 (5)

(b) $YBaCu_{1-x}Zn_xFeO_5$ (quenched)	**Zn-2**%	**Zn-5**%	**Zn-7.5**%	**Zn-10**%	**Zn-12.5**%	**Zn-15**%
T_{N1} (K)	430 (10)	405 (5)	380 (10)	365 (5)	340 (10)	330 (5)
$T_{N2} = T_S$ (K)	310 (10)	330 (5)	335 (10)	340 (5)	340 (10)	330 (5)
SPIRAL (AF2)						
$f_m(\mathbf{k}_2)$ (%)	100	100	100	100	100	100
θ_S (deg)	35.2 (2.7)	39.7 (2.6)	39.3 (2.7)	43.5 (2.8)	52.2 (2.7)	57.8 (2.7)
q_s (r.l.u.)	0.14694 (23)	0.15779 (16)	0.17709 (17)	0.17525 (17)	0.18835 (15)	0.20130 (13)
$\mathbf{r = m_L/m_S}$	0.708 (56)	0.799 (60)	0.786 (43)	0.746 (57)	0.823 (64)	0.775 (65)
m_S (μ_B)	2.369 (15)	2.236 (20)	2.234 (22)	2.273 (21)	2.184 (33)	2.186 (24)
$m_L = r \cdot m_S$ (μ_B)	1.679 (11)	1.786 (10)	1.756 (13)	1.697 (10)	1.796 (12)	1.694 (10)

5.5.1 Tuning the inclination of the magnetic spiral plane: opposite tilts by Co and Zn

As mentioned before, we use the angle θ_S to describe the angular inclination between the c axis and the rotation plane of the helix [**uv** plane; see Eq. (8.1) and Fig. 5.16(a)]. Fig. 5.19(a) plots the experimental (x[M],θ_S) points obtained from neutron diffraction at 10 K for the Cu/Co and Cu/Zn doped $YBaCu_{1-x}M_xFeO_5$ series, reported in Table 5.4. This graph unveils a noteworthy finding. We can observe that a systematic modification of the spiral tilting takes place upon raising the fraction of M = Co and Zn in the Cu sites. Interestingly, the θ_S angle evolves in opposite directions in the two series. Such evolution is also illustrated by the sketches shown as insets in Fig. 5.19(a),

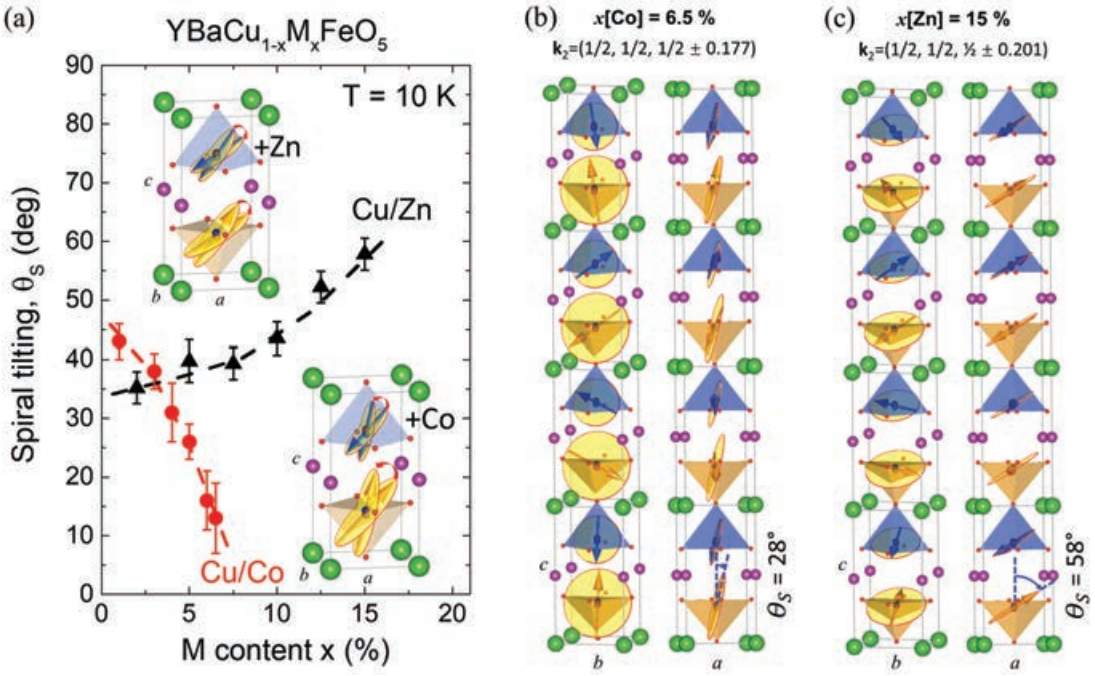

FIGURE 5.19: **Impact of Cu/Co and Cu/Zn B-site substitutions on the inclination of the magnetic spiral plane**. (a) Evolution of the inclination angle θ_S of the ICM spiral rotation plane determined at 10 K in the $YBaCu_{1-x}M_xFeO_5$ series as a function of the B-site doping amount (x) for M = Co (red circles) and M = Zn (black triangles). Dashed lines are guides to the eye. Sketches of the evolution of the spiral rotation plane orientation increasing Cu/Co and Cu/Zn substitutions are shown as insets. In the right panels, projections of the refined circular spiral magnetic structures at 10 K are shown for (b) the x[Co]=6.5% sample with the minimum inclination [θ_S =13(6)°] and (c) the x[Zn]=6.5% sample with maximum tilting [θ_S =58(3)°] (described in Table 5.4). The incommensurate magnetic propagation vector determined in each sample is indicated. The colors of upper/lower average moments and pyramids reflect the majority fraction of Cu/Fe ions (brown/blue) at each site.

which helps visualizing the reorientation process of the magnetic spiral plane triggered by increasing the presence of Co and Zn B-site cations. The largest modification was encountered for $YBaCu_{1-x}Co_xFeO_5$ compounds, where a remarkable $\Delta\theta_S \approx$ -30° reorientation towards the c axis determined that a nearly cycloidal configuration of the spiral structure is achieved at x[Co]=6.5%, which has the minimum spiral tilting value along the Co-doped series, namely, θ_S =13(6)°. In contrast, the evolution of θ_S shown in Fig. 5.19(a) for the $YBaCu_{1-x}Zn_xFeO_5$ compounds, unveiled that the substitution of Cu by Zn tuned the rotation plane of the spins in the spiral phase towards the tetragonal ab plane, accounting for a lower, but still sizeable reorientation $\Delta\theta_S \approx$ +23°, being θ_S =58(3)° the maximum inclination across the Zn-doped series achieved in x[Zn]=15%. Figs. 5.19(b,c) show two complementary projections of the incommensurate magnetic structures for x[Co]=6.5% and x[Zn]=15% samples described in Table 5.4, refined at 10 K using the circular spiral model ($M_R = M_I$). This figure illustrates the large difference between the minimum(maximum) spiral tilting angle reached in the Co(Zn) doped series.

We should bring to mind that in the presence of spin-orbit coupling and effective Dzyaloshinskii–Moriya (DM) antisymmetric exchange terms (or spin-current mechanism triggering magnetoelectric coupling), chirality ($\mathbf{Q}$) and polarization ($\mathbf{P}$) both change their sign under space reversal but transform differently under time inversion. In terms of invariance, 'helical spins' and 'cycloidal spins' behave similarly to chirality and polarization, respectively. According to the DM interaction theory, electrical polarization $\mathbf{P}$ could be described as $P \propto \mathbf{r}_{ij} \times (\mathbf{S}_i \times \mathbf{S}_j)$, being $\mathbf{r}_{ij}$ the translation vector along c connecting two consecutive magnetic atoms with non-collinear spins $\mathbf{S}_i$ and $\mathbf{S}_j$ along the axis of the magnetic modulation ($\mathbf{q}_S$) [20, 21]. So, in order to elucidate multiferroic behavior in non-collinear chiral magnets, it is very helpful to distinguish cycloidal ($\mathbf{Q} \perp \mathbf{q}_S$) from helical ($\mathbf{Q} /\!\!/ \mathbf{q}_S$) spin orders. Applied to our case, the above described DM interaction leads to $P \propto Q\cos(\theta_S)$, where $\mathbf{Q} = \mathbf{S}_i \times \mathbf{S}_j$ is the spin-chirality, different from zero in the non-collinear phase. The magnitude of the resulting electrical polarization (P) in the spiral phase is then strongly sensitive to the θ_S orientation of the plane of rotation of the spins respect to the c axis (axis of the magnetic modulation, with k_z orientation), being maximal for a cycloidal magnetic order ($\theta_S \to 0°$), and zero in the case of pure helical order ($\theta_S \to 90°$). Having that in mind, the evolution from an inclined helix-type towards a nearly cycloidal-type spiral configuration achieved in the Co-doped series should be highly favorable to ferroelectricity. Conversely, Zn-doped compounds display

remarkably higher tilting angles, although the inclined helix-type spiral order is still far from a purely helical configuration, for which the DM interaction mechanism predicts null electrical polarization. Summarizing, we have proved the possibility of manipulating the orientation of the helicoidal order by B-site divalent substitutions in this family of high-temperature chiral magnets. Showing that the manipulation can be performed indistinctly in opposite directions.

5.6 Structural evolution under external pressure investigated by angle-dispersive synchrotron XRD

In coherence with our investigation on the steric effects produced by chemical substitutions, the following question arises naturally: can the influence of hydrostatic pressure stabilize further the spiral order in YBCFO? We have demonstrated in this chapter the strong influence of "chemical pressure" effects on the spiral stability. We have also rationalised such influence through the evolution of key interatomic distances that have strong influence on the magnetic exchange and the magnetic frustration in the material. Hence, we are naturally led to suggest that probably external pressure effects have a big impact on these high-temperature spiral magnets. This fact opens the door to new possible strategies to engineer their properties by acting on the lattice dimensions (both, in bulk and films samples). So, the application of external pressure (as demonstrated in the family of low-T_c cycloidal MFs $Mn_{1-x}Co_xWO_4$ [138]), could enhance T_S and/or produce pronounced effects on the FE and magnetoelectric responses. We expect that decreasing the ratio $R_d = d_t/d_s$ ($R_d \ll 1$) should bring about a more stable spiral phase. No previous reports were found in the literature concerning the effect of external pressure on this relevant parameter. Hence, in this section we present an angle-dispersive synchrotron X-ray diffraction study on the evolution under pressure on the $P4mm$ structure. Diffraction measurements under pressure were performed at ambient temperature at the Micro-powder Diffraction end station of BL04-MSPD beamline of ALBA, using a Diamond Anvil Cell (DAC). Measurements were carried out on a YBCFO powder sample prepared under a controlled cooling rate of 10 °C/h (the one labelled as S1 in Chapter 4), whose determined distance ratio at ambient conditions of temperature and pressure was $R_d \approx 1.72$, and $T_S \approx 186$ K.

In order to assure hydrostatic conditions, measurements were performed (at ambient temperature) in compressed $YBaCuFeO_5$ powder using methanol-ethanol-water (MEW) as pressure transmitting medium. For the data collection, the beam was centered on a carefully selected point within the indented area of the gasket aiming to ensure the best possible statistics and data reliability. The pressure inside the DAC was accurately determined from the cubic cell volume (a^3) of a metallic copper calibrant, refined from the reflections present in the

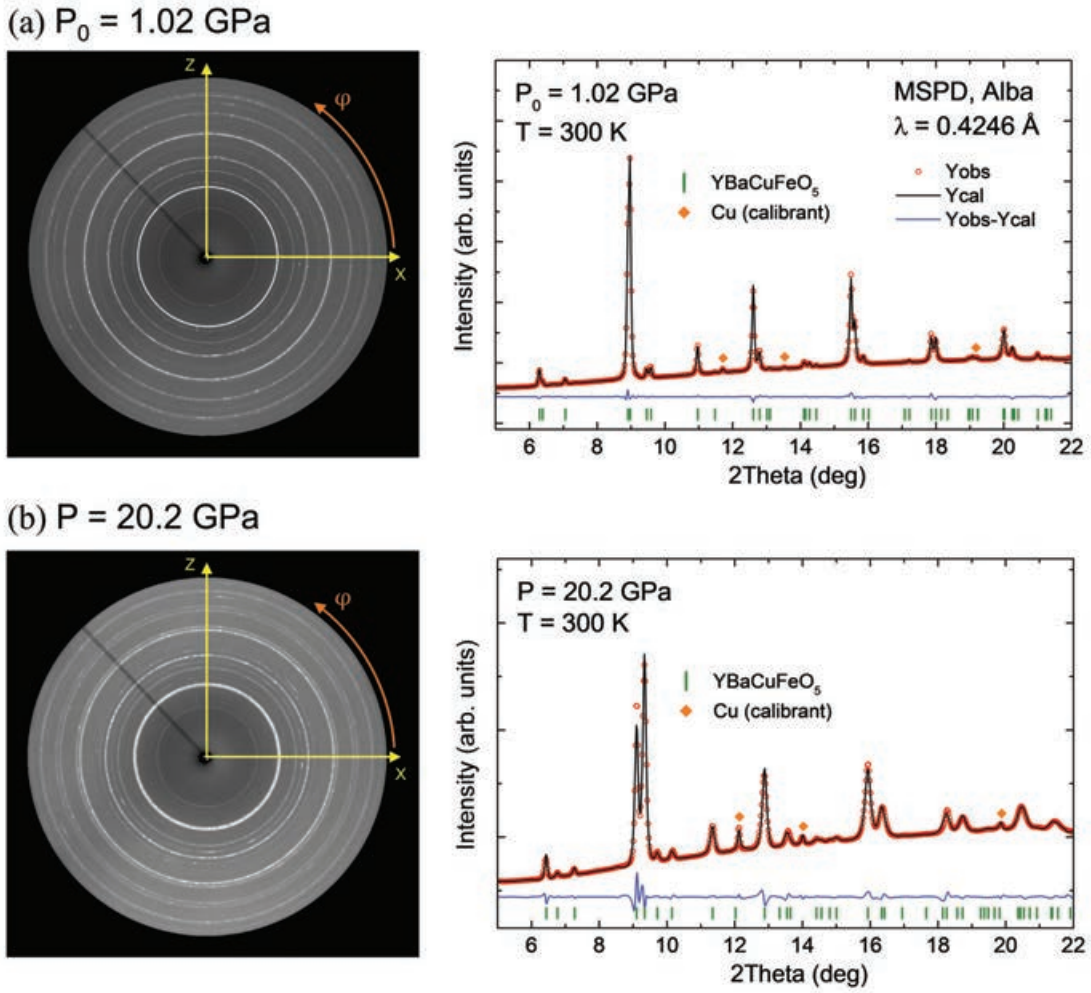

FIGURE 5.20: Synchrotron XRPD measurements at RT for the YBCFO sample under pressure applied by means of a membrane DAC. (a) Initial pressure (P_0 = 1.02 GPa) and (b) maximum pressure applied (P = 20.2 GPa). Left panels: bidimensional diffraction patterns showing the Debye-Scherrer diffraction rings. The *2Theta* intensity profiles are obtained by integrating the intensity along φ in the calibrated 2D frames. Right panels: Rietveld fits of the XRD profiles (black line: calculated pattern, red circles: experimental points, blue line: observed-calculated difference, position markers of the X-ray Bragg reflections are shown as green bars for YBCFO sample, and orange diamonds correspond to the Cu calibrant). Agreement factors: P_0 = 1.02 GPa (R_B: 1.69, R_f: 1.46, χ^2: 199); P = 20.2 GPa (R_B: 0.806, R_f: 0.937, χ^2: 575).

diffraction patterns. The P(V) equation of state (EoS) for Cu from A. Dewaele *et al.* [139] allowed to calibrate the sample pressure. Fig. 5.20 shows two selected XRD patterns at the initial pressure (P_0 ≈1.02 GPa) and at the maximum pressure reached (P ≈20.2 GPa). The quality of the diffraction patterns allowed performing Rietveld refinements up to 20.2 GPa keeping free the z-coordinates of the different atoms within the $P4mm$ unit cell. To reduce the number of free parameters, the partial occupancy at Fe/Cu sites ($n_d \approx 0.29$) and atomic displacement parameters were fixed to its values at ambient conditions obtained by high-resolution SXRPD (reported in Tab. 4.1), and an overall Debye–Waller temperature factor (DWF) was refined to account for the average atomic motion variation due to compression. Right panels in Fig. 5.20 show examples of the Rietveld refinement quality at two different pressures, where no traces of additional phases were found out of Cu calibrant reflections. It should be mentioned that whereas the quality of the collected patterns was exceptionally good, the reliability of the atomic z-coordinates was affected in pressures approx. > 10 GPa by the attenuation of the diffracted intensities and a severe widening of the Lorentzian peaks. This was specially aggravated in the case of oxygen coordinates (from which d_t and d_s lengths are calculated) due to the short X-ray cross-sections of oxygen atoms.

The lattice evolution under pressure [volume, cell parameters and the tetragonal distortion, shown in Fig. 5.21(a)] exhibit a smooth tendency. The absence of anomalies in the observed crystal lattice lengths confirm the stability of the tetragonal $P4mm$ symmetry in the YBCFO layered perovskite up to 20.2 GPa. The (P,V) experimental points were analyzed through a fit to a third-order Birch–Murnaghan equation:

$$P(V) = \frac{3B_0}{2}\left[\left(\frac{V_0}{V}\right)^{7/3} - \left(\frac{V_0}{V}\right)^{5/3}\right]\left\{1 + \frac{3}{4}(B_0' - 4)\left[\left(\frac{V_0}{V}\right)^{2/3} - 1\right]\right\} \quad (5.1)$$

where V_0 is the reference volume, B_0 is the bulk modulus, and B_0' is the derivative of the bulk modulus with respect to pressure. The fit to the (P,V) experimental points using Eq. (5.1), shown as solid lines in Fig. 5.21(a) (top panel), allowed us to determine the third-order Birch-Murnaghan isothermal EoS parameters for $YBaCuFeO_5$ (at RT): V_0 = 115.241 (34) Å^3, B_0 = 107.8 (1.8) GPa and B_0' = 9.95 (35). While those values correspond to the reference YBCFO compound, we should bear in mind that they can be different in isostructural compounds, with different cationic disorder or cation substitutions.

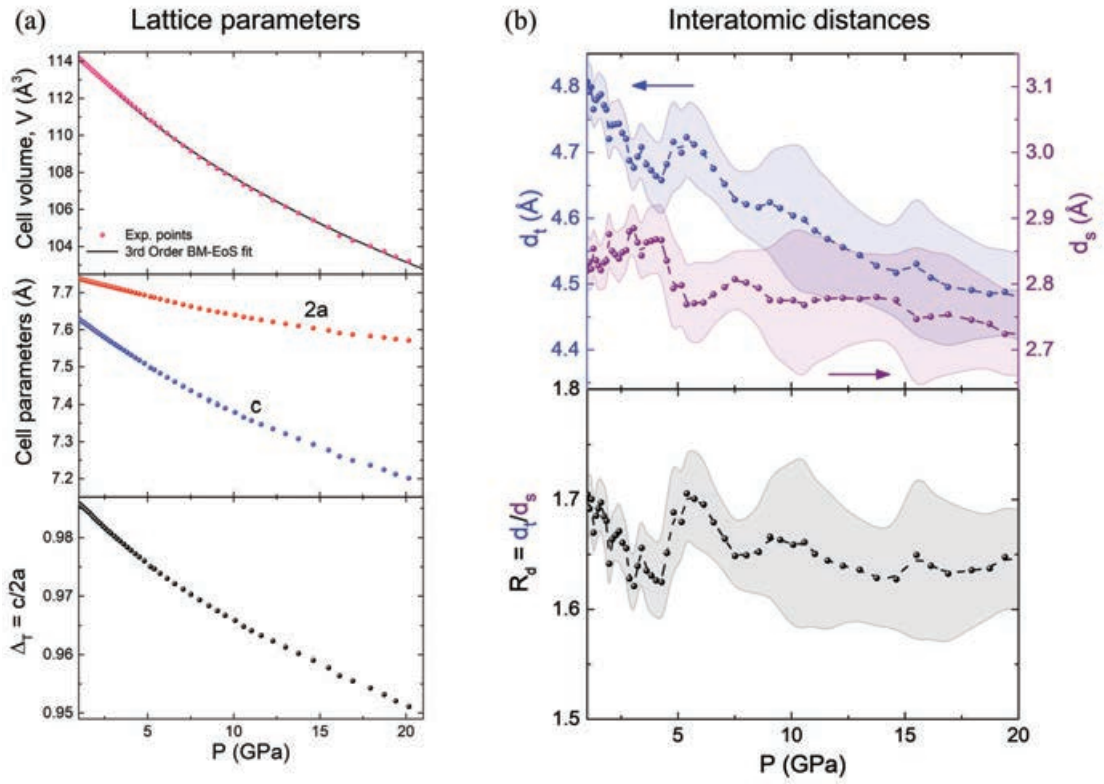

FIGURE 5.21: **Evolution of the YBCFO structure under pressure: lattice parameters and interatomic $\mathbf{d_t}$, $\mathbf{d_s}$ distances**. (a) Top: evolution of the unit cell volume V (pink symbols) under compression. Solid line corresponds to the fit to 3rd order Birch–Murnaghan EoS according to Eq. (5.1). Middle: evolution with pressure of the pseudo-cubic lattice parameters $2a$ (red symbols) and c (blue symbols) versus pressure. Bottom: evolution of the tetragonal distortion (black symbols). (b) Top: pressure dependence of the interatomic intra-bowtie distance ($\mathrm{d_t}$, left axis) and the inter-bowtie separation ($\mathrm{d_s}$, right axis) up to 20.2 GPa calculated from the refined atomic z-coordinates. Bottom: evolution of the distance ratio $\mathrm{R_d} = \mathrm{d_t}/\mathrm{d_s}$. The error bars are represented as shadowed envelopes around the experimental values.

Regarding the influence of pressure on the interatomic distances, as T. Shang and co-workers pointed out in Ref. [48], a priori one does not expect that the compressibility will be the same for $\mathbf{d_t}$ and $\mathbf{d_s}$. Considering that, in general, bonds involving cations with high coordination or low valence expand or compress faster than those with cations in low coordination or high valence, it is expected that the distance $\mathbf{d_s}$, which involves 8 (Y^{3+}-O^{2-}) bonds, will be less compressible than $\mathbf{d_t}$, which involves 12 (Ba^{2+}-O^{2-}) bonds [48]. Our HP-XRD results on the relative variations of $\mathrm{d_t}$ and $\mathrm{d_s}$ under pressure appear to settle this hypothesis. In Fig. 5.21(b) we see that while distance $\mathrm{d_s}$ is rather uncompressible, displaying a small variation within the whole pressure range ($\Delta \mathrm{d_s} \approx$ -4 %),

the distance $\mathrm{d_t}$ shows a much higher compressibility. Up to 20.2 GPa, the bipyramids got shrunk by $\Delta \mathrm{d_t} \approx$ -6 %. From this evolution, a decreasing tendency of the $\mathrm{R_d} = \mathrm{d_t}/\mathrm{d_s}$ ratio is also deduced. As this is the first experimental study validating the possibility of further stabilizing the spiral order by the effect of external pressure, we would like to underline the importance of this result.
Additionally, in this chapter we have proved that the modification of the average JT splitting associated to elongated CuO_5 pyramids in the structure can play a major role on $\mathrm{d_t}$. For that reason, further efforts are necessary to elucidate the evolution of the JT splitting in the elongated CuO_5 pyramids under pressure. Possible modifications of the JT splitting at Cu sites favored by pressure could cause sizeable anomalies in the bipiramid thickness $\mathrm{d_t}$ and a big impact on the magnetic order. In this regard, further work is required to discern between real intringuing features from fit artifacts as those observed in Fig. 5.21(b).

5.7 Summary

In this chapter we have methodically investigated and described a new strategy addressed to enhance the properties of the high-$\mathrm{T_S}$ chiral magnetic order in the proposed multiferroic YBCFO family of layered perovskites. The new route, based on the generation of internal chemical pressure in the YBCFO structure by appropriate cationic substitutions at the divalent B-site, takes advantage of the combination of chemical disorder and the lattice tuning of the relevant magnetic exchanges along c to stabilize the spiral magnetic order up to temperatures significantly above room temperature.
Our structural study has experimentally proved that the partial substitution of JT Cu^{2+} by non JT Co^{2+}/Zn^{2+} ions, which preserve (do not modify) the degree of B-site cation disorder, severely reduce the strong average JT splitting between basal and apical distances characteristic of Cu^{2+} sites. Despite the slightly larger ionic size of Co^{2+}/Zn^{2+} as compared to Cu^{2+}, this effect produce a strong compression of the bipyramid layers and a lower increase of the separation between successive bipyramid layers, accounting for the average shrinkage of the lattice along c.

The impact of Cu/Co and Cu/Zn B-site doping on the magnetic phase diagram was extensively investigated by combining magnetometry and neutron techniques. We have revealed qualitative significant differences when comparing their corresponding phase diagrams. A huge increase of the stability range

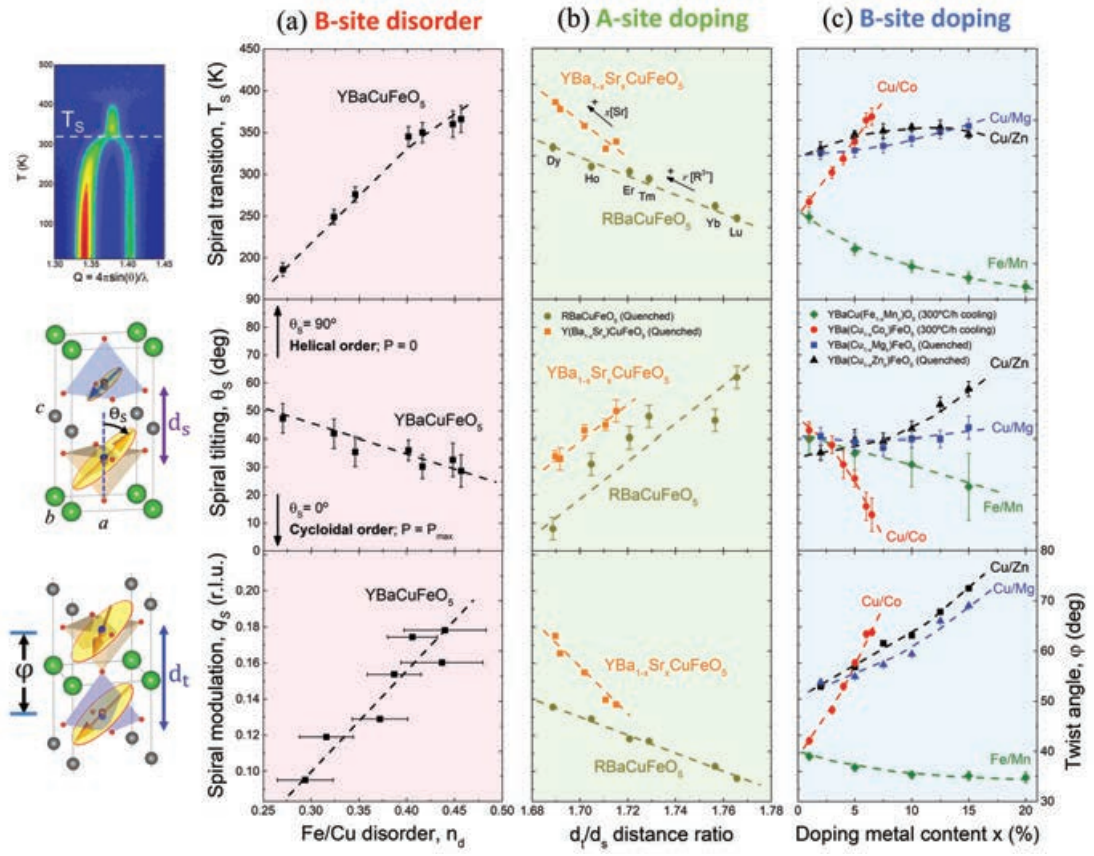

FIGURE 5.22: General picture summarizing the impact of the different tuning strategies on three relevant attributes of the spiral magnetic order studied in this thesis: the thermal stability (T_S, top panels), the tilting of the spin's rotation plane (θ_S, middle panels) and the magnetic modulation (q_S, bottom panels). These parameters are plotted for the different families of YBCFO series in three columns according to the spiral tuning strategy: (a) the variation of B-site disorder in $YBaCuFeO_5$ (experimental points from Chapter 4), (b) the substitution of AA'-site cations in the $YBa_{1-x}Sr_xCuFeO_5$ and $YBaCu_{1-x}Co_xFeO_5$ series (from Ref. [48]), and (c) the substitution BB'-site metals in the series $YBaCu_{1-x}Co_xFeO_5$, $YBaCu_{1-x}Zn_xFeO_5$ (studied in this work), $YBaCu_{1-x}Mg_xFeO_5$ (in Ref. [133]) and $YBaCuFe_{1-x}Mn_xO_5$ (in Ref. [49]). Correspondingly, in the horizontal axis of each column characteristic parameters of the magnetic frustration driving mechanism are used to typify the evolution of the magnetic properties.

of the spiral up to $T_S \sim 355$ K (comfortably far beyond RT) was found in low-doped Co samples presenting relatively low cation disorder (samples from 300 °C/h cooling). In agreement with previous works [47, 48], this striking rise of T_S could be mainly attributed to an increase of magnetic frustration, triggered by the further strengthening of the strong Fe/Fe intra-layer AFM exchange couplings along c as a consequence of the shortening of M-O-M' superexchange paths within $MM'O_9$ bipyramids. A tri-critical point was achieved in Co and Zn doped series (with different level of disorder) confirming the effectiveness

of our new strategy to tune or enhance the frustration in the material, based on acting over the average JT splitting at the "nominal" Cu sites. In addition to the phase separation into AF1 and AF3 domains beyond the tricritical point in $YBaCu_{1-x}Co_xFeO_5$, Co ions favors the presence of a proportional fraction of AF3 domains that compete with the spiral phase even before the tri-critical point (Co induced phase separation). The replacement of FM Cu^{2+}/Fe^{2+} pairs by AFM Co^{2+}/Fe^{2+} (and Co^{2+}/Cu^{2+}) dimers (in $CoMO_9$ bipyramids) favors the emergence of collinear AFM regions with k_z = 0 translational symmetry (AF3). Remarkably this induced phase separation was avoided by using the non-JT Zn^{2+} cation (instead of Co). Additionally, in Zn substituted samples prepared using different cooling methods we have extended the incommensurate modulation (q_s) achieving the largest magnetic discommensuration never seen in this family of compounds (q_s = 0.201, giving a twist angle $\varphi = 72.47(5)^\circ$ in the spiral). Such extension was possible thanks to the non-JT and non-magnetic nature of Zn^{2+} ions. The later (lack of Zn moments) slightly reduces the spiral temperature at the tri-critical point in the Zn-doped series.

In the light of earlier works, Fig. 5.22 sums up in a comprehensive way the results exposed in Chapters 4 and 5. Our contributions to this picture were focused on investigating the magnetic frustration driven mechanisms taking place as a consequence of BB'-site cation disorder and the substitution of BB'-cations by isovalent transition metals. Our understanding of the diverse results produced by Cu^{2+}/Co^{2+} and Cu^{2+}/Zn^{2+} substitution strategies provides further insight toward setting the rules for the manipulation of the magnetic spiral characteristics that influence the ME response. Furthermore, through the application of such rules this work is expected to encourage new research lines based on the combination of the reported strategies for the design of functional high-temperature chiral magnets and multiferroic perovskites. In addition, it could also open the door toward the design of high-temperature multiferroic thin-films, in which the spiral order stability and properties could be potentially tuned by inducing tensile or compressive internal lattice strains.

Chapter 6

Influence of Fe/Cu disorder on the magnetic properties of YBCFO single crystals

6.1 Introduction

Many physical properties of materials in solid-state physics, such as magnetic susceptibility, electrical resistivity or electrical polarization, are usually anisotropic, and their characterization by advanced neutron and synchrotron scattering techniques (such as single-crystal neutron diffraction, spherical neutron polarimetry and X-ray resonant magnetic scattering, among others) require of high-quality oriented single crystals. In this chapter we present the growth and a detailed structural characterization of different YBCFO single crystals, as well as the determination of their magnetic properties. As will be shown, the complexity of the Traveling Solvent Floating-Zone (TSFZ) crystal growth technique, used to prepare YBCFO single crystals, makes intrinsically diffcult to obtain the desired distribution of Fe/Cu cations in the bipyramids together with good crystallinity and suitable crystal size for neutron experiments. So much so that from the several growth experiments carried out in our Crystal Growth Laboratory at ICMAB, the most of them resulted in polycrystals, or in high quality crystals where the incommensurate satellites characteristic of the spiral phase, $\mathbf{k}_2 = (1/2, 1/2, 1/2 \pm q_s)$, were absent and replaced by the commensurate translational symmetry $\mathbf{k}_3 = (1/2, 1/2, 0)$ in the range where the emergence of the ICM phase is expected. Only after many efforts we were able to find the good conditions for the appearance of the incommensurate ($\mathbf{k}_2$) magnetic ordering transition, with a spiral ordering transition (T_S=T_{N2}) at 195 K, the highest T_S reported for a crystal to date. On the other hand, the fabrication of

crystals in which the ICM magnetic order ($\mathbf{k}_2$) is replaced by the $\mathbf{k}_3$ commensurate phase raises interesting questions from the fundamental point of view. The growth and characterization of YBCFO single crystals presented in this chapter aims to go further in our understanding of their physical properties and phase diagram, particularly extending the investigation to the regime of low Fe/Cu disorder.

6.2 Characterization methods

- *Synchrotron X-ray powder diffraction:* for the structural study, high resolution synchrotron radiation X-ray powder diffraction patterns (SXRPD) were collected at 300 K at the BL04-MSPD beamline [107] of the ALBA Synchrotron Light Facility (Cerdanyola del Vallès, Spain). The samples were loaded in borosilicate glass capillaries (0.7 mm diameter) and kept spinning during data acquisition. A short wavelength, λ = 0.41357(3) Å was selected to reduce absorption and enlarge the q-range. The value of λ was calibrated using a NIST standard silicon. As detection system we used a high-throughput position sensitive detector MYTHEN which allows a high photon flux. The acquisition time to perform a RT full structural characterization was 90 s.
- *Neutron powder diffraction:* For the characterization of the magnetic order in powdered single crystal samples, neutron powder diffraction (NPD) measurements were carried out at the high-flux reactor of the Institut Laue Langevin (Grenoble, France), using the high-intensity, high-resolution two-axis D20 diffractometer configured with a HOPG monochromator and 42° take-off angle (λ= 2.41 Å), with excellent resolution at low-q and a high efficiency position sensitive detector covering an angular range up to 150°. Powder samples were filled into 8 mm diameter vanadium containers. For each sample, two patterns with an acquisition time of 15 min were collected at 10 K and averaged for signal-to-noise ratio optimization. To study the evolution of the magnetic order with temperature, neutron thermodiffractograms were also collected in continuous mode following temperature ramps within the range 10 to 500 K, with applied heating rate of 2 K/min and acquisition time of 2.5 min per scan. Around 100 patterns were recorded in the range 10 K to 500 K with a resolution in temperature of 5 K between successive patterns. The temperature range of the experiment was covered by using a dedicated helium cryofurnace.

The structural and magnetic Rietveld refinements of the X-ray synchrotron and neutron patterns were made using the Fullprof package of programs [97]. The

illustrations of the crystal structures were obtained using the VESTA program [106].

- *Neutron Laue diffraction:* With the aim of characterizing the quality and orientation of YBCFO single crystals, neutron Laue back-scattering images were obtained using the Orient Express (OE) instrument at the ILL (Grenoble) [84, 85]. The indexation and determination of the crystal orientations was done using the Clip program.

Further temperature dependent reciprocal space maps were recorded between 50 and 300 K on selected high-quality crystals using the CYCLOPS (CYlindrical Ccd Laue Octagonal Photo Scintillator) neutron Laue single-crystal diffractometer [140] located upstream in the same neutron guide as OE. The Esmeralda suite[99, 100] was used to correct the Laue images for the CYCLOPS instrumental geomety, for the indexing of peaks and the refinement of the sample orientation, the determination of the magnetic propagation vector components and the integration of Bragg peaks.

- *Single crystal neutron diffraction:* Single-crystal neutron diffraction data presented in this chapter was collected at the hot-neutrons four-circle diffractometer D9 (λ=0.837 Å) (ILL, Grenoble, France). For the measurements, crystals were wrapped in thin aluminum foil to improve its adherence to the dedicated refractory cement used to glue the samples to pin. The pin was then mounted on the four-circle diffractometer. A self-dedicated closed shell furnace was used for the structural characterization at high temperature, and a closed-cycle cryostat was used to cover the low temperature range and to collect q-scans along specific directions to assess the presence of the different propagation vectors. Before the measurements, the orientational UB matrix describing the crystal orientation respect to the diffractometer angles was calculated from selected well-centered Bragg reflections.

A large set of 537 nuclear Bragg reflections (295 independent) were collected for each crystal sample at 450 K, above the paramagnetic transition (T_{N1}), to obtain a good structural model that allowed us to determine the Fe/Cu cationic order and interatomic distances. A small two-dimensional (2D) area detector of 6×6 cm^2 (32×32 pixels) allows reciprocal space survey and a more accurate optimization of the peak positions. The program RACER was used to integrate the omega- and omega-2theta-scans and to correct them for the Lorentz factor. DataRED program was used to read the list of measured reflections and reduce it to a single crystal diffraction pattern consisting of a unique set of independent

reflections, which was then used to refine the crystal structure. Neutron refinements were carried out using the FullProf set of programs [97] by least square minimization of the integrated intensities and extinction corrections were applied following the Becker-Coppens model.

- *Chemical analysis:* The elemental composition of YBCFO single crystal samples was determined at the Chemical Analysis Service (SAQ) at UAB via Inductively Coupled Plasma Optical Emission Spectroscopy (ICP-OES). For the determination, a high-throughput optical emission spectrometer (Agilent, model 5900) and a Mettler Toledo MX5 microbalance were used. To this end, approximately 1 mg of each single crystal specimen (SC1, SC2 and SC3) was thoroughly ground and dissolved in 10% (v/v) HCl (Merck; p.a.). The above solutions were then diluted in 1% (v/v) HCl before being injected. The content of Y, Ba, Cu and Fe in the measurement solutions was then determined by ICP-OES.
- *Electron microscopy:* Backscattered electron images (BEI) and energy- dispersive X-ray analysis (EDAX) was performed on previously polished sample surfaces using a QUANTA FEI 200 FEG-ESEM model Scanning Electron Microscope (SEM), equipped with a field emission gun (FEG) for optimal spatial resolution and an EDX detector for chemical analysis. The microscope was operated in high vacuum (HV) condition with 10-mm working distance and an accelerating voltage of 30 kV.

6.3 Growth of $YBaCuFeO_5$ single crystals

The YBCFO oxygen-deficient double-perovskite was grown in the form of single-crystals using an OFZ furnace (model: FZ-T-P1200_H-I-S-PC from Crystal System Corporation) at the new Single-crystal growth Laboratory of the of the CMEOS group in the ICMAB-CSIC [Fig. 6.1(a)]. The successful growth of a quality YBCFO crystal was reported for the first time by Yen-Chung Lai *et al.* [83] using a self-adjusted Traveling Solvent Floating Zone (TSFZ) approach starting from a pure CuO melt. However, its characterization was partial and incomplete ($T_{N1} \approx 465$ K and $T_{N2} \approx 170$ K), and did not include single-crystal neutron diffraction measurements. Details about the principles of the TSFZ growth technique and the self-flux method are described in Chapter 2 (Sec. 2.2.3). For further knowledge of the crystal growth technique the reader is referred to Refs. [80–82].

The crystal growth process starts with the preparation of the polycrystalline YBCFO seed and feed rods. The starting YBCFO powders were prepared

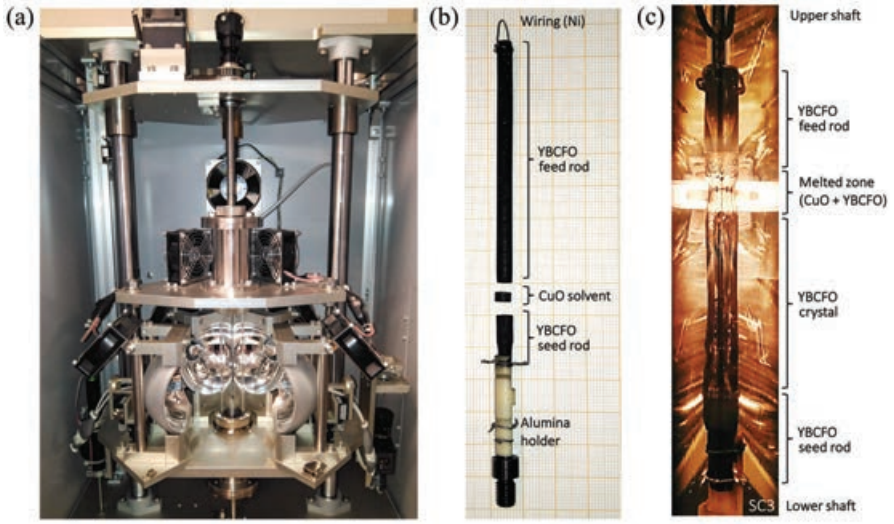

FIGURE 6.1: (a) Detail of the four ellipsoidal mirrors inside the optical floating furnace that are used to focus the light from four halogen lamps (400 W power rated) onto a vertically held rod sample. (b) The YBCFO seed and feed rods and the CuO solvent chip before being mounted on the OFZ furnace. (c) Ongoing growth of the incongruently melting YBCFO in the OFZ furnace after 8 days of stable pulling (48 mm). The image correspond to the growth of SC3 crystal sample.

through the conventional solid-state reaction method described in Chapter 2 (Sec. 2.1). Stoichiometric amounts of Y_2O_3, $BaCO_3$, CuO and Fe_2O_3 were dried and weighed. A decarbonation process was performed on the Y_2O_3 oxide at 900 °C for 20 h. All precursors were thoroughly mixed, grounded and pressed into pellets, and then sintered in a tubular furnace at 1150 °C for 50 h in air. Finally, the sample was cooled down to room temperature at a controlled rate of 300 °C/h. The sample quality was assessed by X-ray powder diffraction using a Siemens D-5000 diffractometer (λ[Cu K_α] = 1.54 Å).

The polycrystalline YBCFO was then thoroughly re-ground into a very fine powder and mixed with a few drops of 4 wt.% solution of Poly(vinyl alcohol) (PVA) in water to enhance the compaction of the rods. Subsequently, the powder was loaded into a rubber tube and the air inside was exhausted with a vacuum pump. The sealed rubber tube was pressed by means of a cold isostatic oil press under 1500 bars of pressure for approximately 1 h. After pressing, the rubber tube was removed and the rod was further compacted by sintering at 1150 °C/h for 20 h in air. A slow heating rate of 100 °C/h was used to allow for a slow evaporation of the PVA. See Chapter 2 (Sec. 2.2.2) for a detailed description of the process followed to obtain very straight, homogeneous and compact YBCFO rods of about 7.5 cm in length. Feed rods of diameters ranging between 4.5 mm, 5 mm and 6 mm were prepared using different rubber tube sizes. The

average density of the feed rods after the sinterization process was approximately 5.3 g/cm^3 (86.2% of crystallographic density of the material). The seed consisted of a shorter piece (normally 1.5 cm) of identical composition and diameter as the YBCFO feed. For the solvent, a rod consisting of CuO with 2 wt.% B_2O_3 added to increase the viscosity of the melt was prepared in a similar way. The CuO solvent rod was annealed for 20 h at 900 °C, and a chip-like piece of a volume similar to the melted zone (∼5 mm high and diameter according to the seed/feed rods) was cut.

A proper preparation of the optical furnace and mounting of the rods is essential for a successful growth. Using a bubble level the furnace was leveled, and the alignment of the mirrors as well as the positioning of the lamp filaments at the focal points of the mirrors were verified and adjusted to ensure an optimal temperature gradient and an homogeneous temperature distribution within the melted zone. Ni wire (0.5 mm) was used for the wiring of the rods. The feed rod was hanged loosely from a hook attached to the upper shaft, and the seed was wired to an alumina holder fixed to the lower shaft [see Figs. 6.1(b) and 6.1(c)]. The seed and feed rods were mounted so as to be perfectly aligned, and the chip-like solvent was put on top of the seed rod. The rods were enclosed inside the quartz tube to protect the sample and to control the atmosphere during the growth process. During the growth of YBCFO crystals, a constant air flow of 120 cm^3/min was kept constant to renew the atmosphere and to reduce the darkening of the inner walls of the tube caused by evaporation of the oxides.

In Fig. 6.2(a) a sequence of images were taken at the relevant steps and phases along the complete growth process of an YBCFO single crystal. The schematic illustration of the process in Fig. 6.2(b) complements the images. In the first growth attempts a problem was found at the moment of melting the solvent to create a stable CuO melt due to excessive wetting of the porous seed and feed rods at the sides in contact with the liquid. In view that the addition of B_2O_3 to increase the viscosity of the melt was not sufficient to avoid the soaking, an initial pre-melting process of the feed and seed rods without the solvent worked well to avoid the penetration of the molten CuO at the solid-liquid interfaces. In Fig. 6.2(a) (1-2) show the pre-melting of seed and feed rods. After this, the CuO solvent chip is placed on top of the seed (3) and the power of the lamps is increased slowly until pre-melting of the upper surface of the solvent is observed (4). The upper shaft is then lowered until the tip of the feed is in contact with the pre-melted chip (5). The power of the lamps is immediately decreased so that the solvent solidifies and gets attached to the feed (6). At this point,

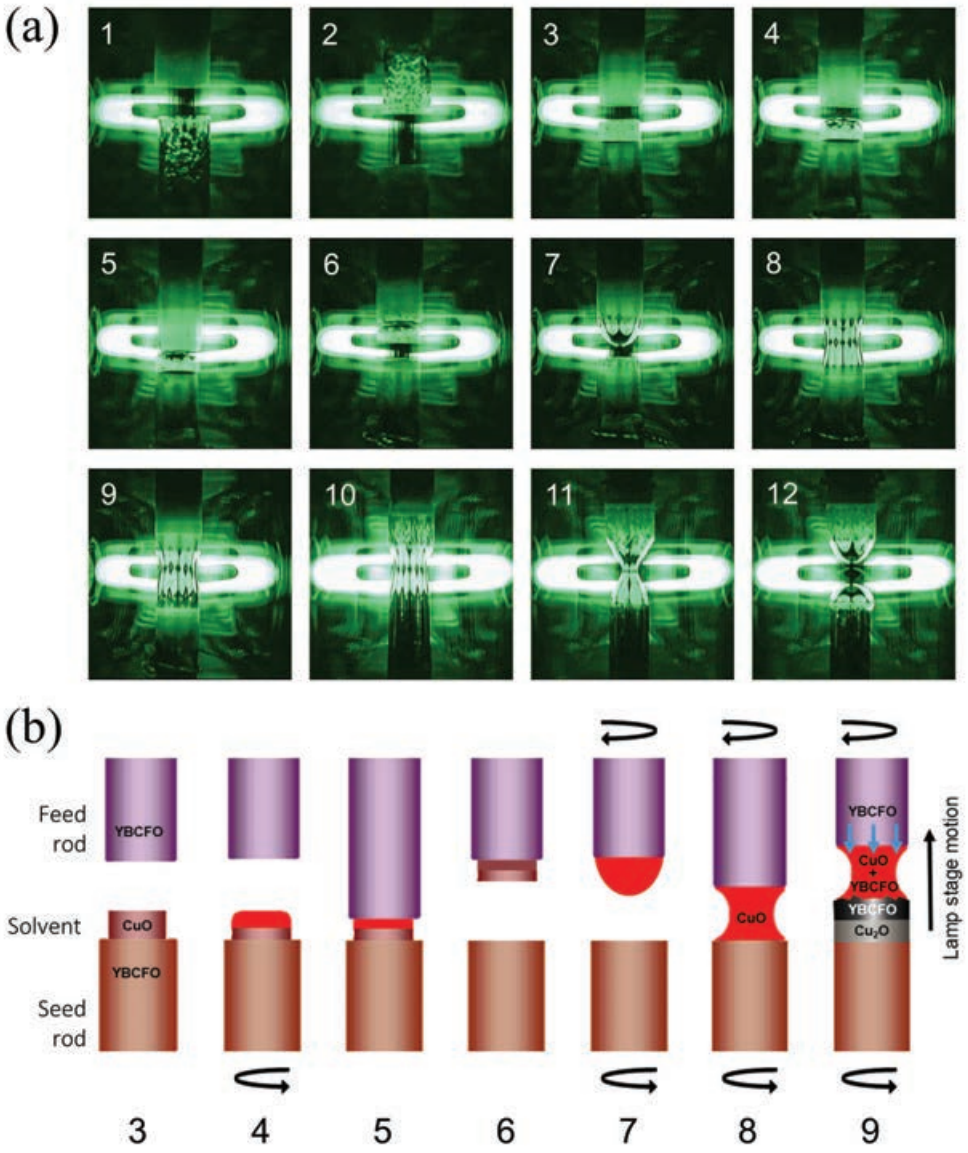

FIGURE 6.2: (a) Sequence of images and (b) scheme showing the self-adjusted TSFZ growth of YBCFO using an OFZ furnace: (1-2) pre-melting, (3-8) incorporation of the CuO solvent, (9-10) stabilization and growth, (11-12) termination. The captures correspond to the growth of SC3 crystal sample.

the rotation is activated at 25 rpm to get a uniform heating in the molten zone and to avoid local density fluctuations. The sample rod is continuously rotated clockwise, while the seed rod is rotated counterclockwise. Then, the solvent can be melted in a controlled way by increasing the power until the solvent is completely melted and stays suspended on the top rod (7). The upper shaft is lowered carefully until the melt contacts the seed and a pure CuO melted zone is established (8). After adjusting the separation between the rods to have a nearly straight meniscus the growth starts by moving the lamp panel upwards.

A slow pulling rate of 0.25 mm/h allows a to keep the liquid composition homogeneous as YBCFO is dissolved in it. To obtain stoichiometric $YBaCuFeO_5$ it is necessary to increase the temperature of the melt containing excess CuO accordingly to the feeding rate. During the initial stage of growth the excess of CuO solvent will become depleted in Cu_2O as YBCFO feed is dissolved into the CuO rich melt (9). Eventually, the melt will get saturated of YBCFO and stoichiometric YBCFO single phase will start to precipitate. Once the melt reaches the compositional equilibrium, the growth is kept at a constant pulling rate and power for about 12 days (10). Finally, the crystal growth is terminated by slowly separating the upper rod while decreasing accordingly the lamp power. The tip of as-grown crystal is left in the hot zone during the cooling process to reduce the thermal shock (11-12).

Three crystal growth processes were conducted successfully using feed rods of different diameters, obtaining in consequence three YBCFO grown ingots of approximately 4 mm, 4.5 mm and 6 mm of diameter. Henceforth the three crystals will be referred to as SC1, SC2 and SC3, respectively. The as-grown rods present a regular appearance with black and shiny surfaces. Fig. 6.3(a) shows the SC3 crystal after about 12 days of stable pulling. The initial part of growth was cut longitudinally and polished for its examination by optical and scanning electron microscopy (SEM) methods. The initial evolution of the grain boundaries is clearly observed in the optical macrophotograph of the axial cross section [Fig. 6.3(a)]. Nucleation begins at the ceramic seed rod and crystal grains with different orientations are formed at the initial stage. With growth progression domains with more favourable orientations grow faster and prevail over less favorable orientations. In the cross sections perpendicular to the rod axis it is also well appreciated how along the growth the number of crystal grains decreases gradually, and a multigrain crystal evolves into a single crystal. Notice the nearly parallel grain boundaries in the cross sections indicating the presence of crystal facets perpendicular to the c axis (cleavage planes).

From the SEM images of the initial section different interfaces are identified with different porosity, morphology and size of the crystallites, as well as zones and inclusions of distinct chemical composition [see Figs. 6.3(c) and 6.3(d)]. Remember that in backscattered electron images (BEI) brighter zones correspond to compositions with elements of higher atomic number, while darker zones correspond to lighter element compositions. Energy-dispersive X-ray analysis (EDAX) was performed on some selected points in order to determine the atomic percent (At%) of Y, Ba, Cu, Fe, and O. In zone Z2 [Fig. 6.3(d)]

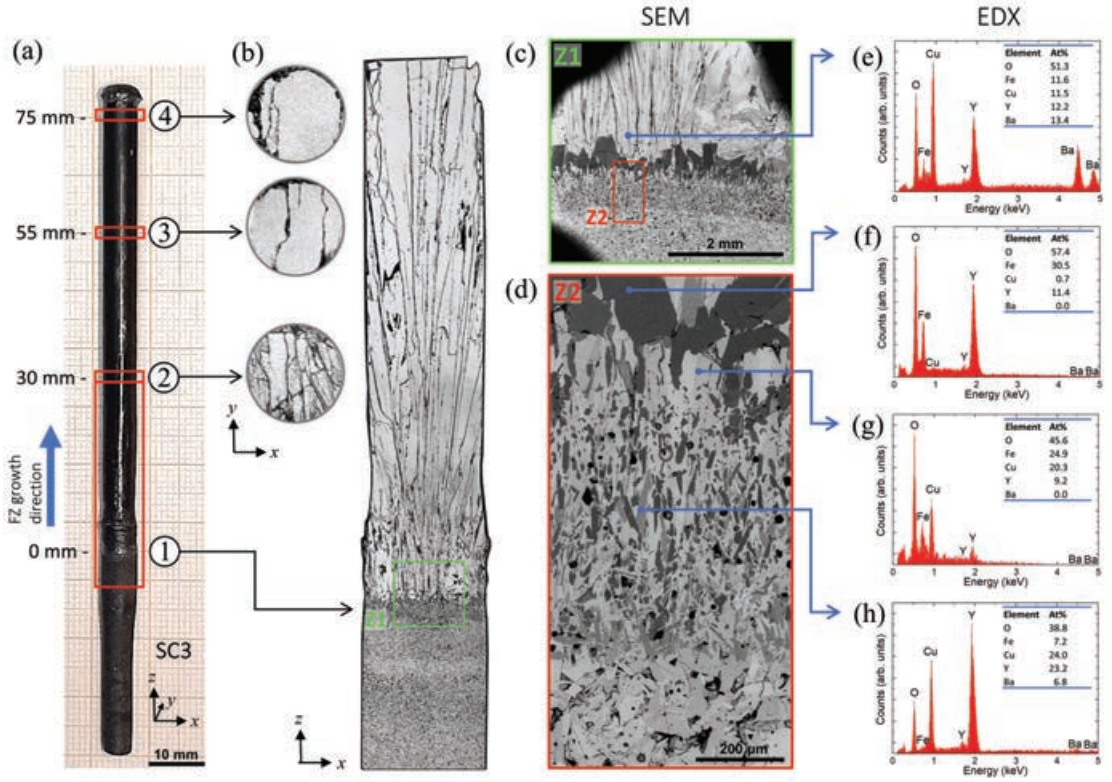

FIGURE 6.3: (a) Image of the as-grown YBCFO single crystal. The z direction corresponds to the FZ growth direction. (b) Optical macrophotographs of the axial cross section of the initial region, and cross sections perpendicular to the FZ growth direction (z) showing the evolution of crystal grains after 30 mm, 55 mm and 75 mm of growth. (c) Low magnification SEM image of the Z1 stabilization zone, and (b) the Z2 zone showing in detail the different interphases prior to the precipitation of YBCFO. (e-h) EDX spectra measured at the indicated points.

a region with dark and light small crystallites elongated in the growth direction and diversity of chemical compositions [Figs. 6.3(g) and 6.3(h)] precedes another zone with larger crystal precipitations principally composed of Y and Fe [Fig. 6.3(f)]. The EDX spectra in Fig. 6.3(e) confirms the precipitation of the stoichiometric $YBaCuFeO_5$ single phase after the composition of the melt is stabilized.

The SEM analysis of the polished section reveals that in this case the stabilization of the flux proceeded in a different way to the reported by Yen-Chung Lai *et al.* [83], in which the CuO in excess is initially depleted at the seed in the form of crystalline Cu_2O until the melt supersaturation is reached and the stoichiometric YBCFO phase starts to precipitate. In our growth process, the single Cu_2O phase did not form. This is possibly a result of starting the growth with an insufficient volume of CuO solvent. In consequence, to achieve the equilibrium composition the melt is enriched in Cu as YBCFO is dissolved in it at the

expense of precipitating Y, Ba and Fe rich phases.

6.3.1 Quality analysis and crystal growth direction

For the three crystal rods prepared (SC1, SC2 and SC3) large high quality single domain crystals were obtained, as confirmed by the chemical analysis and neutron diffraction. The elemental composition of YBCFO single crystals was determined via Inductively Coupled Plasma Optical Emission Spectroscopy (ICP-OES). The results presented in Table 6.1 show that the mass fractions of the different cations in $YBaCuFeO_5$ obtained for the three crystal samples (SC1, SC2 and SC3) are in agreement with the expected for the ideal composition (Y: 20.9 wt%, Ba: 32.3 wt%, Cu: 14.9 wt%, Fe: 13.1 wt%). Therefore, no deviations from the ideal molar ratio (Y:Ba:Cu:Fe = 1:1:1:1) outside the errors are observed. The stoichiometry was further verified from the single crystal neutron diffraction experiments, in which the refinement of a large set of structural reflections collected at D9 showed no deviations of the stoichiometric $YBaCuFeO_5$ composition and no presence of extra oxygen at the Y layers [the 1*b*: (1/2, 1/2, z) position] was observed within the detection capabilities of this technique.

Neutron Laue diffraction provides an excellent confirmation of the total crystal quality because all the substantial grains present in the crystal sample can be detected. To perform single crystal neutron diffraction experiments at ILL three large high-quality crystal pieces were selected from each ingot. The neutron Laue images collected at the Orient Express instrument (ILL) confirmed the quality of the single-domain crystals and provided information about the orientation along the growth direction. Fig. 6.4 (middle and bottom panels)

TABLE 6.1: Analytical results obtained from ICP-OES for the different cations in $YBaCuFeO_5$. Mass fractions (respect to the total mass of the sample, m_tot) and relative molar fractions (atomic ratios respect to Y) in SC1, SC2 and SC3 crystal samples are listed.

Mass fraction (wt%)	**m_Y/m_tot**	**m_Ba/m_tot**	**m_Cu/m_tot**	**m_Fe/m_tot**
$YBaCuFeO_5$ *(ideal)*	*20.9*	*32.3*	*14.9*	*13.1*
SC1	20.8 (1.0)	32.3 (0.9)	14.9 (1.1)	13.3 (1.1)
SC2	20.4 (0.9)	31.8 (0.9)	14.3 (1.0)	13.3 (1.0)
SC3	20.4 (0.2)	31.5 (0.2)	14.7 (0.4)	12.9 (0.4)
Atomic ratio	**n_Y/n_Y**	**n_Ba/n_Y**	**n_Cu/n_Y**	**n_Fe/n_Y**
$YBaCuFeO_5$ *(ideal)*	*1*	*1*	*1*	*1*
SC1	1.000 (68)	1.005 (56)	1.002 (88)	1.018 (96)
SC2	1.000 (64)	1.009 (54)	0.981 (86)	1.038 (88)
SC3	1.000 (14)	1.000 (12)	1.008 (29)	1.007 (33)

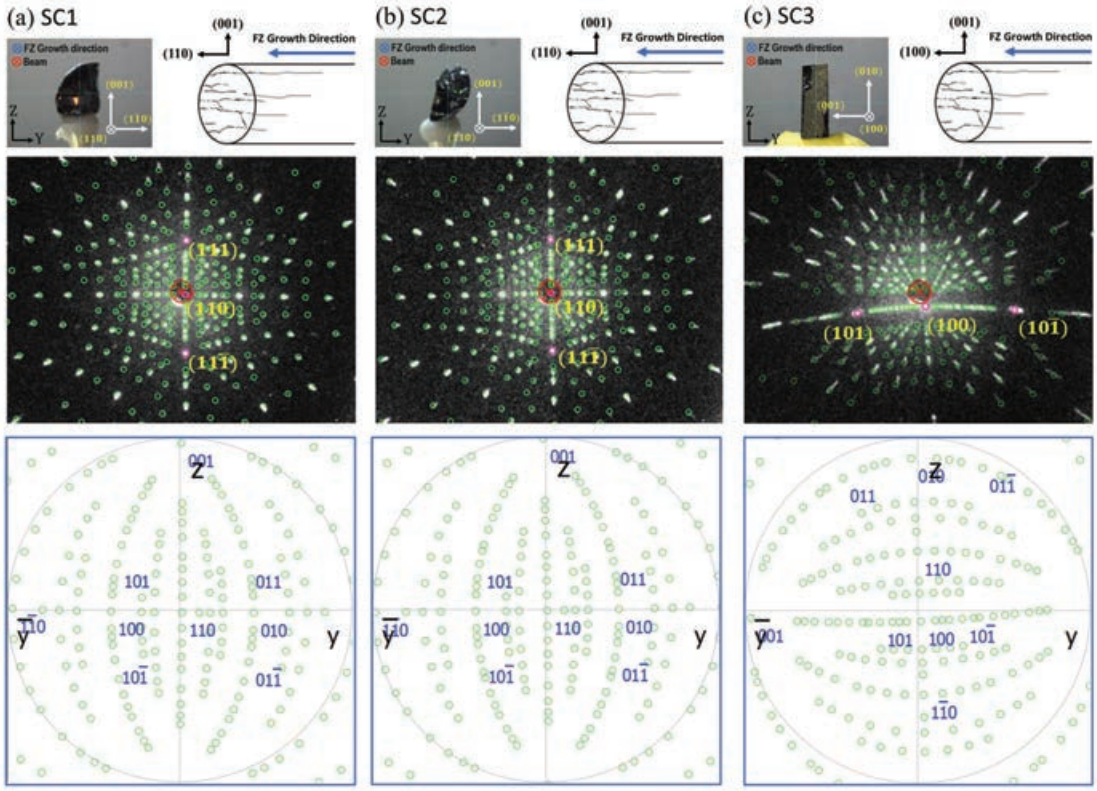

FIGURE 6.4: Neutron Laue analysis of the quality and orientation along the FZ crystal growth direction of (a) SC1, (b) SC2 and (c) SC3 single crystals. Top: Image of the single crystal as seen from the Orient Express camera and scheme of the crystal rod with the (001) direction perpendicular to the rod axis and different directions along the growth direction. The FZ growth direction of the crystals is indicated as blue arrows and markers in the images, and the direction of the white neutron beam is indicated by red markers. Middle: indexed neutron Laue images obtained with the growth direction perpendicular to the backscattering Laue plane. Bottom: stereographic projections of the Laue plane.

shows the indexed Laue images and corresponding stereographic projections obtained with the backscattering Laue plane perpendicular to the FZ growth direction of the crystals. As illustrated in Fig. 6.4 (top panels), in all cases the (001) direction was perpendicular to the rod axis. For SC1 and SC2 crystals the orientation along the growth direction correspond to the (110) direction, while for SC3 a growth direction in the (100) direction was found. Probably, the advance of the growth front in a tilted (110) orientation is more favourable in the case of smaller rod diameters (4 mm and 4.5 mm for SC1 and SC2), while thicker rods (6 mm for SC3) favour the growth along the (100) direction. In Ref. [83] the growth an YBCFO crystal of 5 mm in diameter is reported along the (100) direction.

6.4 Structural characterization

6.4.1 B-site disorder in YBCFO single crystal samples

While in the case of sintered polycrystalline YBCFO samples higher (or lower) Fe/Cu cation disorder can be achieved by applying faster (or slower) cooling rates during the solid-state reaction process, the complex TSFZ technique used to prepare YBCFO single crystals, in which the very slow pulling rates favours the ordering of the different cations, entails evident difficulties to control the resulting distribution of Fe/Cu in the bipyramids. As discussed in Chapter 4, the presence of strongly frustrating antiferromagnetic Fe/Fe defects and how

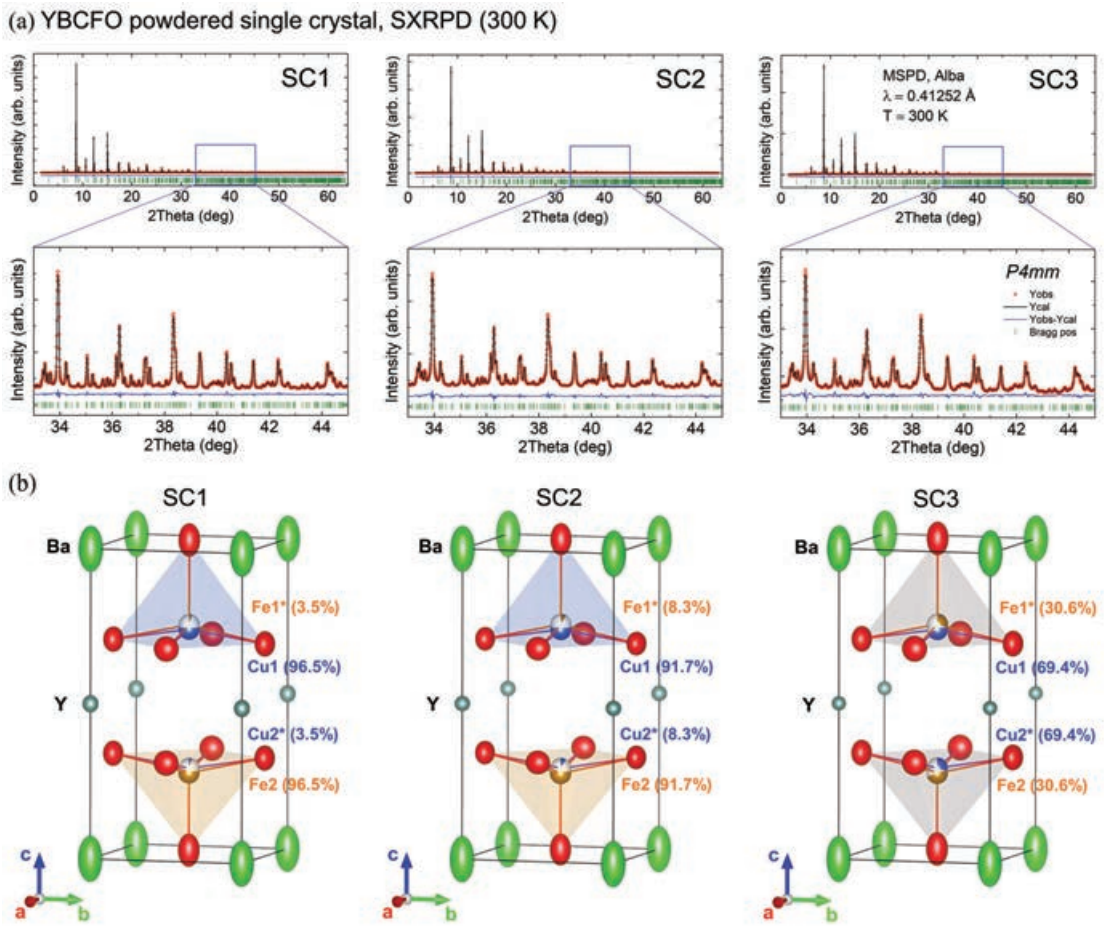

FIGURE 6.5: Rietveld refinement (black curve) of the synchrotron X-ray intensities (red circles) at 300 K (SC1, SC2 and SC3 powdered YBCFO single crystal samples). Bottom blue line is the observed-calculated difference. Lower panel: detail of the high-angles region. (b) Scheme of the refined $P4mm$ unit cell of SC1, SC2 and SC3 YBCFO crystals showing the refined amount of Fe/Cu disorder and the thermal anisotropic displacement ellipsoids of the atoms. The color of each pyramid reflects the fraction of Fe/Cu ions in it (blue: Cu; brown: Fe).

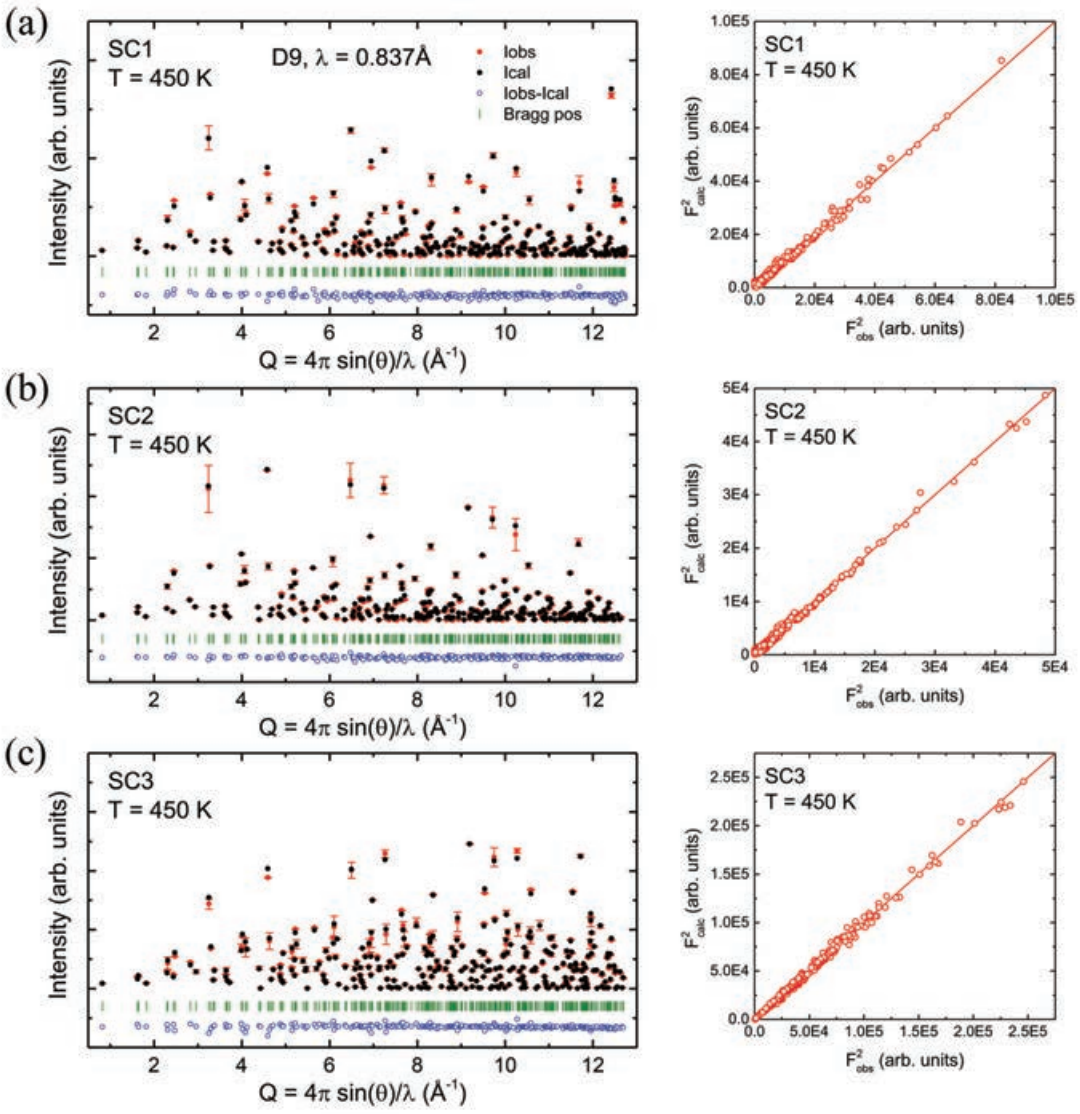

FIGURE 6.6: Refinement of the integrated single-crystal neutron reflections collected in D9 at the paramagnetic phase (450 K) on (a) SC1, (b) SC2 and (c) SC3 YBCFO single crystals. In left panels the observed and calculated integrated intensities of the refections are plotted as a function of Q = 4πsin(θ)/λ (red points: observed; black points: calculated; blue points: difference). Right panels show the agreement plots of the nuclear structure refinements. The calculated structure factors are plotted against the experimental ones.

densely they are distributed in the material (related to the average disorder of Fe and Cu ions at the B-sites) plays a leading role in the spiral stabilization mechanism. The determination of the Fe/Cu occupancy in the single crystals we have grown is therefore essential to understand the nature of their magnetic behavior.

The atomic positions and partial Cu/Fe occupancies in the two pyramids of the unit cell [1*b* (½ ½ z) sites] were obtained from Rietveld refinements of high

resolution SXRPD data measured on powdered samples of the SC1, SC2 and SC3 crystals. The non-centrosymmetric $P4mm$ refinements of the SXRPD patterns at 300 K are shown in Fig. 6.5(a), and Table 6.2 reports the corresponding structural parameters and agreement factors. Projections of the YBCFO unit cell showing the refined Fe/Cu occupancies and the anisotropic atomic displacement ellipsoids for the different crystals are also plotted in Fig. 6.5(b). Additionally, the crystal structure was also studied by means of unpolarized single crystal neutron diffraction. Fig. 6.6 (a-c) (left panels) displays the observed and calculated squared structure factors for the nuclear structure of the YBCFO crystals, refined in the paramagnetic phase (450 K) from 537 nuclear reflections (295 independent) collected on D9 using the closed shell furnace. The agreement plot of the nuclear structure refinement at 450 K is shown in Fig. 6.6 (a-c) (right panels).

In the refinements, the z-coordinates of a same metal M in upper (1, blue) and lower (2, red) pyramids were constrained by z(M1)+z(M2)=1. The rest of the symmetry-inequivalent atoms were refined independently. The detailed structural information obtained in the crystals obtained from both high resolution SXRPD and single crystal neutron diffraction is summarized in Table 6.2. Fe/Cu disorder, which as mentioned is a key feature in these perovskites because it determines the level of frustration and has a strong influence on the magnetic features and transition temperatures, is described by the refined improper occupation n_d: the fraction of Fe at the Cu pyramid (1) (Fe1* site) or the fraction of Cu at the Fe pyramid (2) (Cu2* site). So, a B-site random disorder would correspond to n_d= 0.5, and n_d= 0 describes a fully ordered Fe/Cu structure. We carefully refined the partial occupations, finding consistency in the results obtained from SXRPD and single-crystal experiments. The refined Fe/Cu occupancies (reported in Tab. 6.2) reveal that in the case of SC1 and SC2 the growth process resulted in highly ordered YBCFO crystals. The improper occupancy in these crystals ($n_d \lessapprox 0.1$) is exceptionally close to zero. It is important noticing that the lowest disorder values reported in Chapter 4 for sintered YBCFO samples prepared under very slow cooling rates (n_d= 0.29(3) for the S1 sample cooled at 10 °C/h) are still considerably higher than those obtained in SC1 and SC2 single crystals. In contrast, SC3 single crystal displays a higher degree of disorder, n_d= 0.31(5), similar to the values obtained in sintered samples S1 and S2 ($n_d \approx 0.3$). This implies that $\approx 32\%$ of nominal Cu pyramids are occupied by Fe in the SC3 crystal, and vice versa. Remarkably, although chemical disorder is in the SC3 crystal lower than in powder samples prepared under

TABLE 6.2: Crystal structure of the YBCFO single crystals (SC1, SC2, SC3) and agreement factors from Rietveld refinement of (i) MSPD@ALBA synchrotron data (λ=0.413570 Å) at 300 K, and (ii) D9@ILL single crystal neutron intensities (λ=0.837 Å) at 450 K (paramagnetic phase). (*: minority fraction; n_d (disorder)=Occ (Fe1*/Cu2*)). The coordinates of each metal (M: Cu or Fe) are constrained by z(M1)+z(M2)=1.

		(i) SXRPD, MSPD (300 K)				(ii) SC-neutron diffraction, D9 (450 K)		
		SC1	**SC2**	**SC3**		**SC1**	**SC2**	**SC3**
a=b (Å)		3.87654 (1)	3.87563 (1)	3.87511 (1)		3.8756 (6)	3.8815 (6)	3.8810 (6)
c (Å)		7.66407 (2)	7.66296 (2)	7.66332 (3)		7.6630 (10)	7.6839 (10)	7.6843 (10)
$\Delta_T \equiv$c/2a		0.988519 (4)	0.988608 (4)	0.988790 (5)		0.98862 (20)	0.98981 (15)	0.98999 (20)
V (Å^3)		115.1723 (7)	115.1016 (7)	115.0761 (7)		115.100 (39)	115.766 (36)	115.742 (39)
Y $1a$ (00z)	z/c	0.49999 (42)	0.50114 (48)	0.50324 (56)		0.5013 (15)	0.4979 (25)	0.4991 (36)
	U_{iso} (Å^2)	0.00352 (7)	0.00311 (10)	0.00261(11)		0.0086 (9)	0.0088 (11)	0.0062 (6)
Ba $1a$ (00z)	z/c	0	0	0		0	0	0
	U_{11} (Å^2)	0.00770 (4)	0.00774 (6)	0.00765 (6)		0.0092 (8)	0.0092 (11)	0.0071 (6)
	U_{33} (Å^2)	0.02847 (17)	0.0286 (2)	0.02830 (20)		0.027 (4)	0.026 (5)	0.026 (3)
Cu1 $1b$ (½ ½ z)	z/c	0.72418 (41)	0.72345 (42)	0.72290 (48)		0.72129 (27)	0.72211 (33)	0.72341 (23)
Fe1* $1b$ (½ ½ z)	z/c	0.73915 (52)	0.74070 (55)	0.74086 (62)		0.74319 (27)	0.74301 (33)	0.74131 (23)
Cu2* $1b$ (½ ½ z)	z/c	0.27582 (41)	0.27655 (42)	0.27709 (48)		0.27871 (27)	0.27789 (33)	0.27659 (23)
Fe2 $1b$ (½ ½ z)	z/c	0.26085 (52)	0.25930 (55)	0.25914 (62)		0.25681 (27)	0.25699 (33)	0.25869 (23)
	U_{iso} (Å^2)	0.00714 (12)	0.00650 (15)	0.00619 (16)		0.0080 (3)	0.0080 (4)	0.0071 (2)
O1 $1b$ (½ ½ z)	z/c	0.01770 (56)	0.01958 (65)	0.01631 (99)		0.00198 (96)	0.00191 (77)	0.00119 (160)
	U_{11} (Å^2)	0.00616 (10)	0.00586 (13)	0.00621 (13)		0.0136 (8)	0.0143 (10)	0.0108 (5)
	U_{33} (Å^2)	0.0149 (4)	0.0137 (5)	0.0151 (5)		0.023 (4)	0.018 (4)	0.015 (4)
O2 $2c$ (½ 0 z)	z/c	0.31543 (107)	0.31769 (123)	0.31925 (145)		0.31406 (58)	0.31494 (58)	0.31555 (86)
	U_{11} (Å^2)	0.00835 (10)	0.00805 (13)	0.00840 (13)		0.0094 (5)	0.0100 (6)	0.0077 (3)
	U_{22} (Å^2)	0.00519 (10)	0.00489 (13)	0.00525 (13)		0.0070 (5)	0.0071 (6)	0.0050 (3)
	U_{33} (Å^2)	0.0085 (4)	0.0074 (5)	0.0088 (5)		0.0213 (11)	0.0187 (15)	0.0121 (11)
O3 $2c$ (½ 0 z)	z/c	0.68300 (114)	0.68411 (131)	0.68581 (155)		0.68337 (68)	0.68138 (69)	0.68349 (97)
	U_{11} (Å^2)	0.00835 (10)	0.00805 (13)	0.00840 (13)		0.0094 (5)	0.0100 (6)	0.0077 (3)
	U_{22} (Å^2)	0.00519 (10)	0.00489 (13)	0.00525 (13)		0.0070 (5)	0.0071 (6)	0.0050 (3)
	U_{33} (Å^2)	0.0085 (4)	0.0074 (5)	0.0088 (5)		0.0213 (11)	0.0187 (15)	0.0121 (11)
Occ (Cu1/Fe2)	$1-n_d$	0.965 (34)	0.917 (36)	0.694 (48)		0.991 (20)	0.980 (22)	0.701 (17)
Occ (Fe1*/Cu2*)	n_d	0.035 (34)	0.083 (36)	0.306 (48)		0.009 (20)	0.020 (22)	0.299 (17)
	χ^2	*31.93*	*41.11*	*22.2*	χ^2	*2.27*	*0.417*	*1.57*
	R_B	*2.21*	*2.28*	*2.48*	R_F	*7.83*	*7.40*	*5.70*
	R_f	*2.53*	*2.13*	*2.23*	R_F^2	*8.32*	*6.88*	*7.69*

fast cooling that yield T_S above RT, we will show in the next sections that this disorder is enough to stabilize the incommensurate magnetic order close to $\approx$ 200 K, whereas in the case of SC1 and SC2 the Fe/Cu disorder is insufficient for the formation of the spiral. For consistency throughout this manuscript, the discussions that will follow related to Fe/Cu disorder (n_d) will be referred to the values refined from SXRPD, which are in very good agreement with the single crystal neutron diffraction results.

As single crystals were grown in similar conditions of temperature and identical pulling rates, the different amount of disorder could be associated to the direction of the crystallization front in the pulling process. The progression of the

crystallization front in a tilted (110) direction in smaller diameter SC1 and SC2 crystals probably favoured a higher ordering of Fe and Cu within the bipyramid layers compared to SC3 crystal, which grew along the (100) direction. However, more experiments are necessary to draw solid conclusions on this matter.

6.4.2 Interatomic distances in YBCFO single crystals

Different relevant interatomic distances derived from the refined coordinates at 300 K are reported in Table 6.3. As expected, the obtained results put in evidence the effect of B-site cation disorder on the bilayer thickness (d_t) and separation between bilayers (d_s), as well as on the average height of Cu-rich (H_L) and Fe-rich (H_S) pyramids. Due to the Jahn-Teller splitting between basal and apical distances around Cu^{2+}, the average pyramid height at the Cu-rich site (H_L, upper pyramid) is a $\sim 1.5\%$ ($\sim$0.04 Å) longer in the highly ordered SC1 and SC2 crystals compared to the SC3 crystal with higher degree of Fe/Cu disorder. Inversely, for the sites where Fe is the majority the average pyramid height (H_S, lower pyramid) is a $\sim 1.6\%$ ($\sim$0.04 Å) shorter.

A look to Figs. 6.7 (b-d), where the interatomic distances and pyramid heights are plotted together with the values obtained for the polycrystalline samples (S1-S7 in Chapter 4) as a function of the disorder (parametrized by the refined n_d occupancy), provides a wider view and confirms the consistency between

TABLE 6.3: Interatomic distances (in Angstroms) at 300 K in $YBaCuFeO_5$ single crystals (SC1, SC2, SC3) derived from the structures refined from MSPD@ALBA synchrotron data (λ=0.413570 Å). (H: height of the pyramid).

T=300 K *P4mm*	**SC1**	**SC2**	**SC3**
1-n_d=Occ(Cu1/Fe2)	0.965 (34)	0.917 (36)	0.694 (48)
n_d=Occ(Fe1*/Cu2*)	0.035 (34)	0.083 (36)	0.306 (48)
d_s (Å)	2.817 (12)	2.808 (14)	2.809 (17)
d_t (Å)	4.847 (12)	4.855 (14)	4.854 (17)
d_t/d_s	1.7206 (85)	1.7291 (98)	1.7281 (99)
H_L (Å)	2.565 (10)	2.571 (11)	2.533 (15)
H_S (Å)	2.282 (10)	2.284 (11)	2.322 (13)
d(Cu1-O1)$_{apical}$ (Å)	2.2496 (53)	2.2692 (59)	2.2485 (84)
d(Cu1-O3)$_{basal}$ (Å)	1.9638 (20)	1.9611 (30)	1.9583 (33)
d(Fe2-O1)$_{apical}$ (Å)	1.8635 (59)	1.8370 (65)	1.8609 (90)
d(Fe2-O2)$_{basal}$ (Å)	1.9829 (40)	1.9888 (40)	1.9916 (52)

Comment: distances metal to Oa (apical) and Ob (basal) correspond to the majority cation in upper (Cu-rich) and lower (Fe-rich) pyramids.

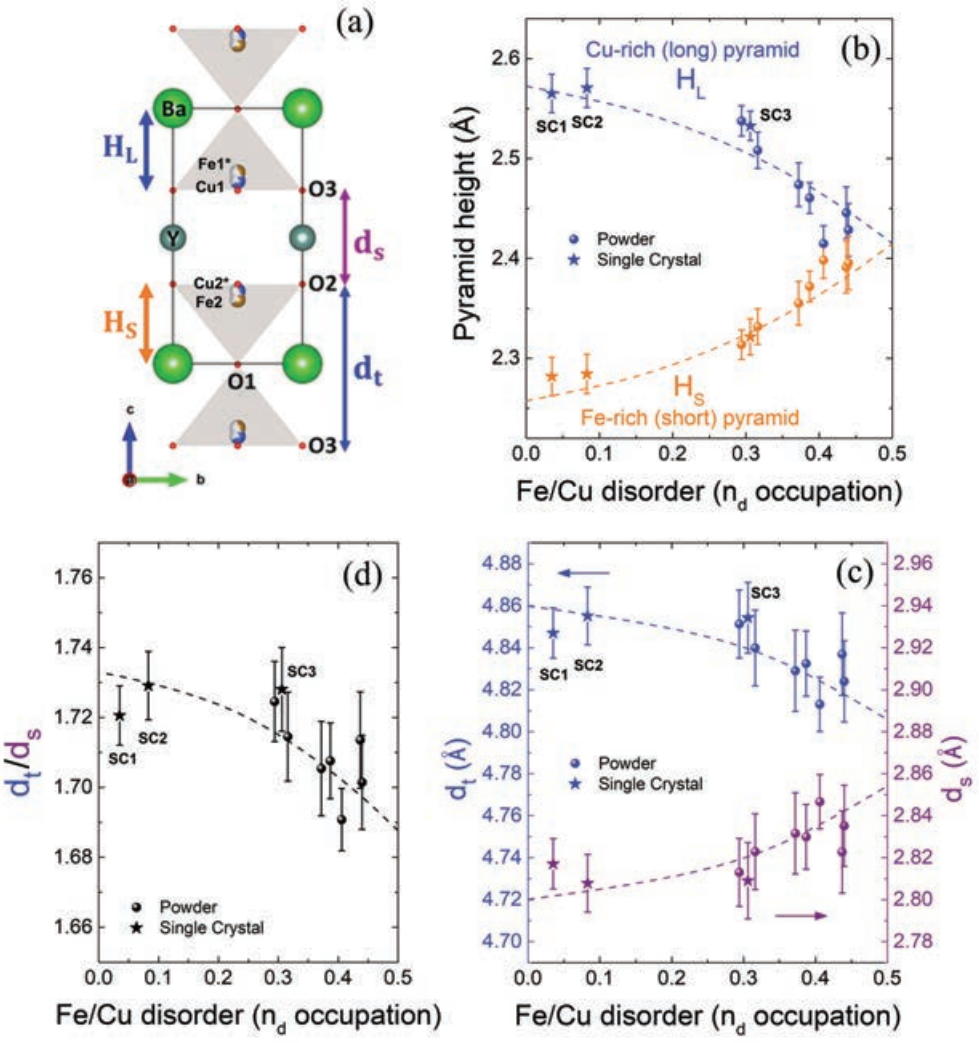

FIGURE 6.7: (a) Projection of the $P4mm$ structure of YBCFO showing the d_t and d_s intra- and inter-layer distances, and the H_L (upper, Cu-rich) and H_S (lower, Fe-rich) pyramid heights. Their values at 300 K for SC1, SC2 and SC3 crystals are plotted together with the values in polycrystalline YBCFO samples (S1-S7) a function of disorder (n_d): (b) height of the two pyramids, (c) thickness of the bipyramidal layer (d_t, left axis) and separation between bilayers (d_s, right axis); (d) The ratio d_t/d_s. Dashed lines (second order polynomial fits to the experimental data) are guides to the eye.

the structural results and its correlation with the B-site cation disorder in both sintered and single crystal YBCFO samples.

6.5 Magnetic characterization

6.5.1 Neutron Laue diffraction

Temperature dependent neutron diffraction measurements were performed using the CYCLOPS Laue diffractometer at ILL, which allowed to identify the magnetic phases in the YBCFO single crystals. The indexation of magnetic reflections at 50 K in SC3 revealed a behavior analogous to the observed in polycrystalline samples of the same composition and similar Fe/Cu disorder. The presence of magnetic phases with propagation vectors $\mathbf{k}_1 = (1/2, 1/2, 1/2)$ and $\mathbf{k}_2 = (1/2, 1/2, 1/2 \pm q_s)$ is depicted in red and green colors in the indexed Laue pattern at 50 K [see Fig. 6.8(c)]. The 2D contour plot of the temperature dependent integrated intensities of SC3 evidences the emergence of $\mathbf{k}_2$ magnetic satellites characteristic of the modulated magnetic phase at $\lessapprox 200$ K (T_{N2}). The incommensurate magnetic order in SC3 is further confirmed by the Q_L scan collected at 10 K in D9 along the (0.5, 0.5, L) line (in the range 0.2<L<1.2). The value of the incommensurability determined at 10 K is $q_s = 0.104$ r.l.u.

On the other hand, neutron measurements revealed a non-conventional magnetic behavior in the highly ordered single crystals SC1 and SC2. Remarkably, in these crystals the ICM satellites characteristic of the spiral phase have been suppressed and replaced by a new translational symmetry with $\mathbf{k}_3 = (1/2, 1/2, 0)$ propagation vector. In the indexed Laue patterns at 150 K [see Figs. 6.8(a) and 6.8(b)], magnetic reflections of translational symmetry $\mathbf{k}_3$ are depicted in yellow, and $\mathbf{k}_2$ reflections in red. Furthermore, magnetic phases with translational symmetries $k_z = 1/2$ and $k_z = 0$ coexist below the ordering temperature of the $\mathbf{k}_3$ phase (henceforth denoted as T_{N3}). This is further evidenced by the 2D contour plots of the temperature dependent profiles integrated along selected regions of the Laue images. In SC1, magnetic reflections associated to $\mathbf{k}_1$ and $\mathbf{k}_3$ propagation vectors appear almost simultaneously and coexist below $T_{N1} \approx T_{N3} \approx 400$ K. Magnetic reflections (1/2 1/2 1/2) and (1/2 1/2 1) in the Q_L scan in Fig. 6.8(b) evidences the coexistence of the $\mathbf{k}_1$ and $\mathbf{k}_3$ magnetic phases with $k_z = 1/2$ and $k_z = 0$ at 300 K. Differently, in SC2 the $\mathbf{k}_3$ magnetic reflections appear only below $T_{N3} \approx 290$ K.

In the following sections of this chapter the discussion is focused on SC1 and SC2 ordered crystals with $\mathbf{k}_1$ and $\mathbf{k}_3$ commensurate (CM) phases, whereas a detailed study of the magnetic transitions and the nature of the $\mathbf{k}_1$ and the incommensurate $\mathbf{k}_2$ magnetic orders in SC3, for which advanced neutron and X-ray scattering techniques were used, is addressed more extensively in Chapter 7.

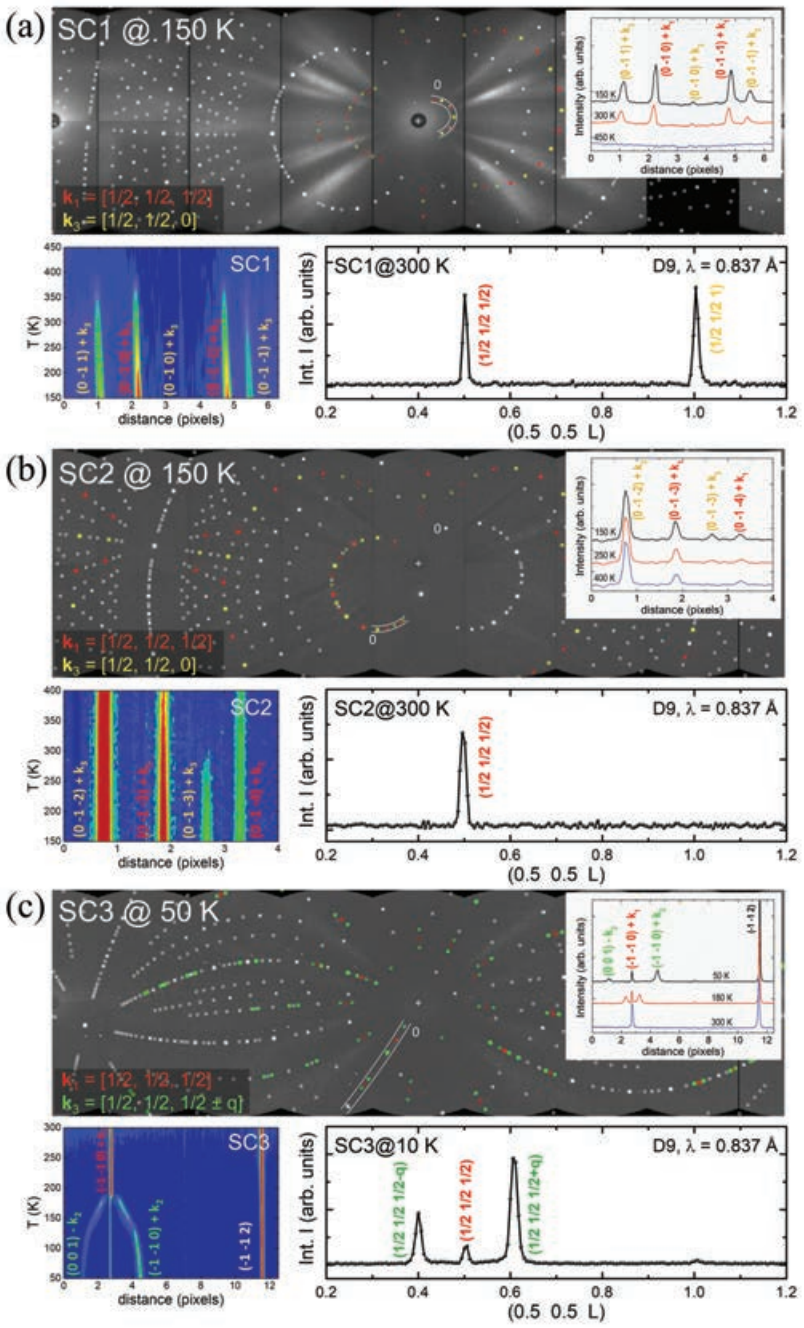

FIGURE 6.8: Identification of the magnetic phases in YBCFO single crystals: (a) SC1, (b) SC2 and (c) SC3. The CYCLOPS neutron Laue images at low temperature show the indexation of nuclear reflections (in white) and the magnetic ones with $\mathbf{k}_1 = (1/2, 1/2, 1/2)$, $\mathbf{k}_2 = (1/2, 1/2, 1/2 \pm q)$ and $\mathbf{k}_3 = (1/2, 1/2, 0)$ propagation vectors (in red, green and yellow, respectively; some magnetic reflections have also nuclear contribution). Intensity integrations along selected regions of the area detectors (indicated in the Laue images) are represented in the form of 2D contour maps to show its evolution with temperature. Q_L scans collected in the D9 single crystal diffractometer show the magnetic phases along the (0.5, 0.5, L) line (range 0.2<L<1.2) for the three single crystals.

6.5.2 Characterization of the AF1 and AF3 magnetic phases in highly ordered YBCFO crystals

Magnetic transitions

The properties of the magnetic phases in highly ordered SC1 and SC2 crystals and its evolution with temperature were assessed by means of neutron powder diffraction measurements on powdered single crystal samples, carried out in the high-intensity, high-resolution two-axis D20 diffractometer (λ= 2.41 Å). The

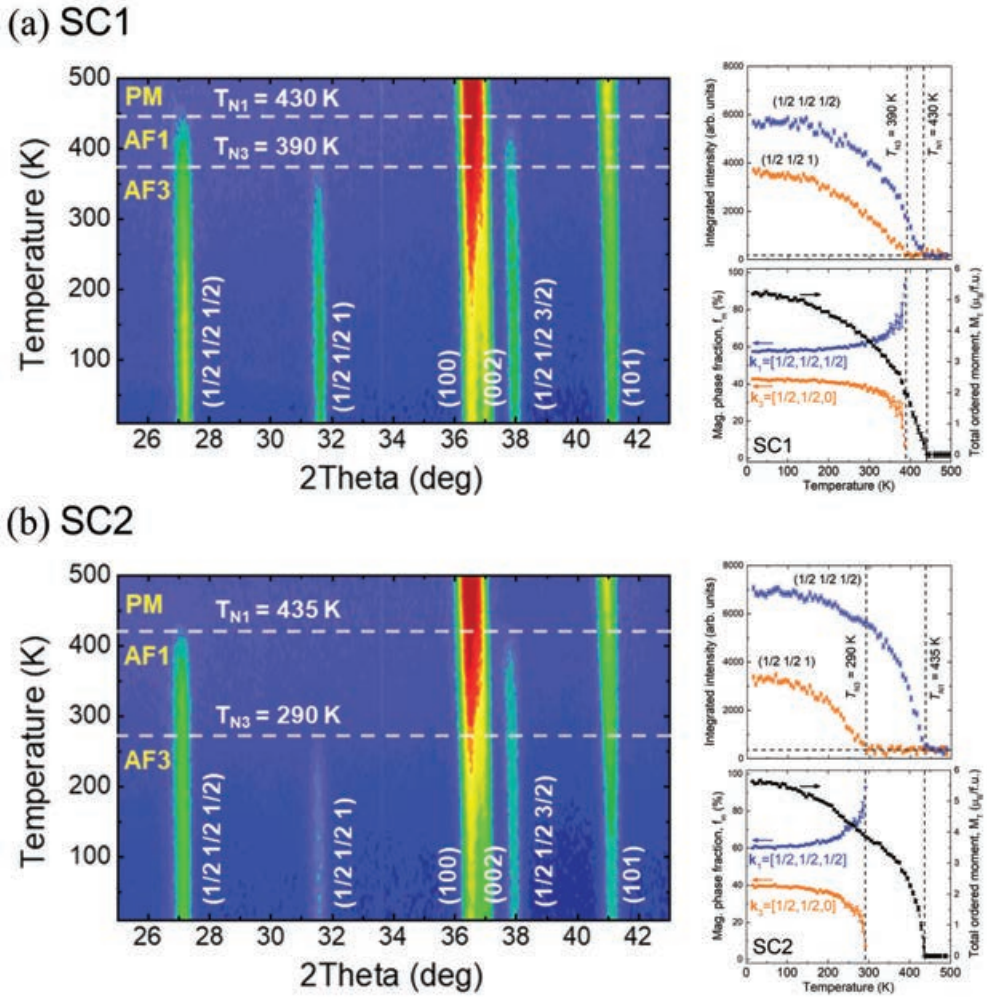

FIGURE 6.9: Evolution of the magnetic order in highly ordered single crystals (a) SC1 and (b) SC2 from neutron diffraction (D20@ILL). Left panels: contour maps showing the $2Theta$-T projection pf the temperature dependence for the NPD intensities at the low Q-range showing the main magnetic reflections. Right panels: thermal evolution of the integrated intensities of the (1/2 1/2 1/2) and (1/2 1/2 1) magnetic peaks (top); Ordered average magnetic moment per formula unit (right axis, in μ_B/f.u.) and phase fractions (left axis, in %) of the AF1 and AF3 magnetic phases (bottom). Blue squares refer to $\mathbf{k}_1 = (1/2, 1/2, 1/2)$ propagation vector, and orange circles to $\mathbf{k}_3 = (1/2, 1/2, 0)$.

$2Theta$-T contour graphs of the NPD intensities between 10 K and 500 K for SC1 and SC2 are plotted in Figs. 6.9(a) and 6.9(b), focusing on a Q-range that covers the main magnetic reflections. From the temperature dependent NPD results shown in Fig. 6.9, three noteworthy observations can be made:

(i) In agreement with the single crystal neutron Laue measurements, NPD confirms that the two transitions observed correspond to (1) the CM phase which appears at the onset temperature T_{N1}, with propagation vector $\mathbf{k}_1 = (1/2, 1/2, 1/2)$, and (2) the CM phase with propagation vector $\mathbf{k}_3 = (1/2, 1/2, 0)$, showing up at T_{N3}. The transition temperatures, reported in Tab. 6.4, were determined from the evolution of the integrated intensities of magnetic reflections (1/2 1/2 1/2) and (1/2 1/2 0), characteristic of the $\mathbf{k}_1$ and $\mathbf{k}_3$ propagation vectors [see Figs. 6.9(a) and 6.9(b), right panels].

(ii) The magnetic evolutions disclosed in Fig. 6.9 suggest that the two magnetic phases very likely develop in distinct regions of the crystal. Notice in that figure that the evolution of the $\mathbf{k}_1$-type magnetic intensity does not show any anomaly or influence upon warming across the T_{N3} transition temperature, ruling out a mutual transformation between $\mathbf{k}_1$ and $\mathbf{k}_3$ phases, in contrast with what is observed between the $\mathbf{k}_1$ and $\mathbf{k}_2$ YBCFO sintered samples discussed in Chapter 4 [see the magnetic phase diagram in Fig. 4.20(b)].

(iii) Although a similar magnetic behavior is observed in SC1 and SC2 crystals, it is evident from the evolution of neutron-diffraction intensities that SC1 and SC2 have very different ordering temperatures. While the collinear AF1 phase emerge at very similar temperatures in SC1 and SC2 (T_{N1} = 430 K and 435 K, respectively), the two samples display remarkably different onset temperatures for the AF3 phase. In SC1 (T_{N3} = 390 K), the ordering temperature of AF3 is 100 K higher than in SC1 (T_{N3} = 290 K). Although this difference in the ordering temperature of the AF3 phase is not well understood, we believe that it might be related to the higher presence of Fe-O-Fe bonds in SC2. Despite in both crystals the presence of AFM Fe-O-Fe bonds is insufficient to stabilize the ICM spiral order, the higher presence of them in SC2 increases the magnetic frustration at the AF3 regions reducing in consequence its ordering temperature (T_{N3}). Bear in mind that the level of Fe/Cu disorder in SC2 ($n_d \approx 0.08$) is closer to the minimum disorder necessary for the formation of the spiral order ($n_0 \approx 0.112$, as reported in Sec. 4.5 of Chapter 4) than in SC1 ($n_d \approx 0.04$).

Magnetic structures

The spin configuration and orientation of the spins with respect to the tetragonal unit cell for the two coexisting CM phases at 10 K in SC1 and SC2 YBCFO crystals was determined by means of neutron powder diffraction (D20, ILL). For the refinement of the diffraction patterns, collinear order models were used to fit the magnetic reflections associated to each propagation vector ($\mathbf{k}_1$ and $\mathbf{k}_3$). The phase difference between magnetic moments at the two sites was fixed to 180° as found in earlier Refs. [46, 109, 137]. The angular distance of the spins to the c axis is measured by the θ polar angle. For the AF1 and AF3 phases, corresponding θ_{C1} and θ_{C3} inclination angles were refined independently. Although due to the inherent limitations of the neutron powder diffraction it is not possible to determine the orientation of the moments in the tetragonal ab plane, this question is covered in Ref. [120] from single crystal neutron diffraction studies in a Mn-doped $YBaCuFe_{0.95}Mn_{0.05}O_5$ single crystal with very similar properties as in SC1 and SC2 pristine crystals. In the here presented NPD study the in-plane direction of the moments was constrained parallel to the a axis. The amplitudes of the ordered magnetic moments at the nominally Fe and Cu sites ($\mathrm{m_L}$ and $\mathrm{m_S}$) were refined without constraints and independently in the AF1 and AF3 phases. The ratio $\mathrm{m_L}/\mathrm{m_S}$ in each phase could thus inform on fluctuations in the spatial distribution of cation disorder. For this reason the scale factors of the magnetic phases were constrained to be equal to the nuclear scale factor, and the values of the moments are referred to the total volume of sample.
Fig. 6.11(a) shows a schematic projection of the AF1 and AF3 magnetic phases embracing four unit cells to illustrate their different translational symmetry along c. Notice that for the AF3 collinear phase the magnetic anti-translation for successive cells along c is suppressed ($k_z = 0$), meaning that the coupling between spins at the bipyramids is antiferromagnetic. This is in contrast with the AF1 order, where the spins sharing a bipyramid are ferromagnetically coupled in virtue of the FM Fe^{3+}-O-Cu^{2+} exchange interaction along c. In minority regions presenting higher chemical disorder the FM Fe-O-Cu bond has been substituted by the strong Fe-O-Fe AFM pair. The magnetic refinements unambiguously converged to the same solution independently of the proposed initial values.

The full neutron Rietveld refinements at 10 K for SC1 and SC2 samples are exposed in Figs. 6.10(a) and 6.10(b). The refined magnetic parameters at 10 K

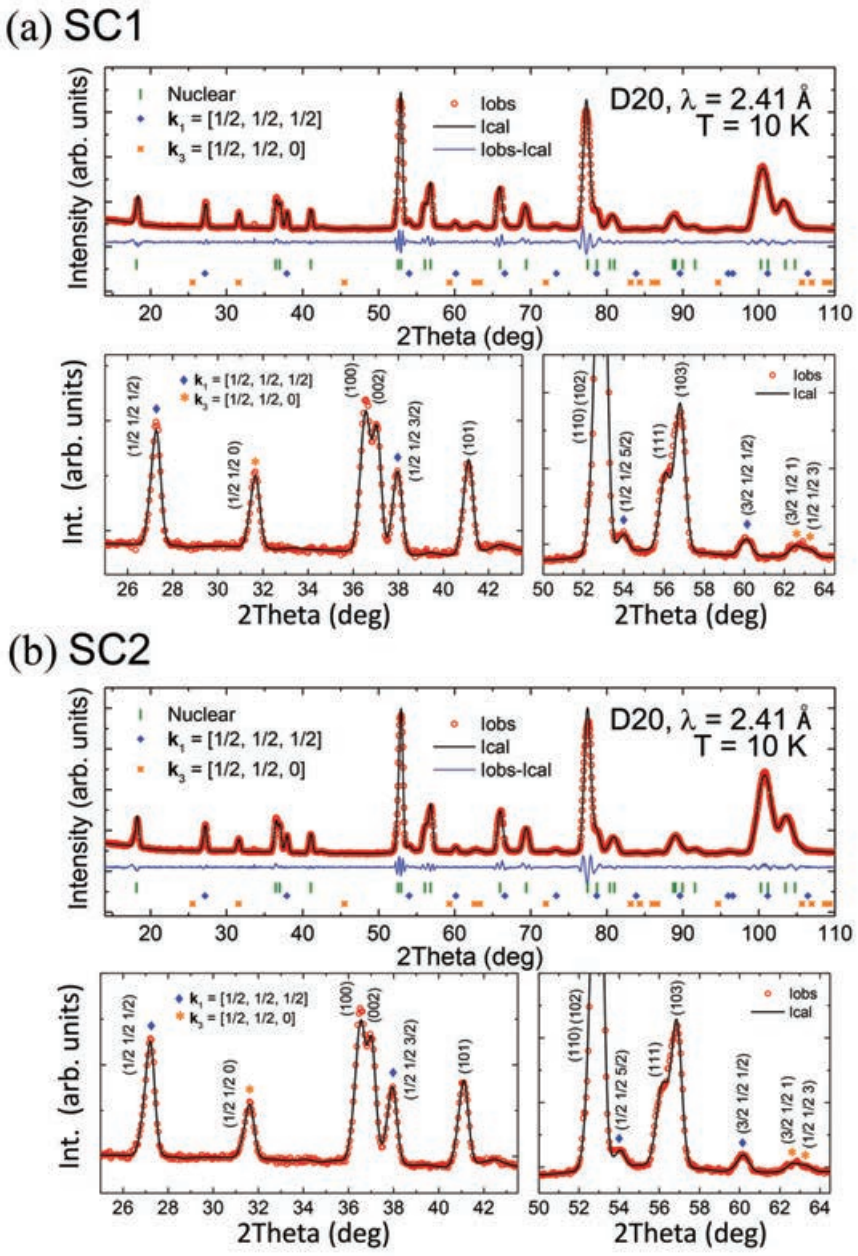

FIGURE 6.10: Rietveld refinement (black curve) of the D20@ILL (λ=2.41 Å) neutron diffraction patterns (red circles) at 10 K for the (a) SC1 and (b) SC2 powdered YBCFO crystals with high Fe/Cu order. Green bars indicate the positions of nuclear Bragg reflections. Blue diamond markers and orange stars correspond to magnetic Bragg peaks associated to the $\mathbf{k}_1 = (1/2, 1/2, 1/2)$ and $\mathbf{k}_3 = (1/2, 1/2, 0)$ propagation vectors, respectively.

for the AF1 and AF3 phases are reported in Table 6.4, corresponding respectively to the propagation vectors $\mathbf{k}_1 = (1/2, 1/2, 1/2)$ and $\mathbf{k}_3 = (1/2, 1/2, 0)$. Notice that the specific volume fraction occupied by each phase is unknown, and the magnetic phase fractions ($\mathrm{f_m}$) measure the total ordered moment ($\mathrm{m_T}$ = $\mathrm{m_L}$

TABLE 6.4: Magnetic parameters at T = 10 K of the coexistent magnetic phases AF1 and AF3 with propagation vectors $\mathbf{k}_1 = (1/2, 1/2, 1/2)$ and $\mathbf{k}_3 = (1/2, 1/2, 0)$, respectively, derived from the Rietveld refinements of the NPD data of the powdered SC1 and SC2 $YBaCuFeO_5$ crystals with very low Fe/Cu cation disorder (n_d). Average magnetic moments m_L and m_S at the respective Cu-rich and Fe-rich pyramid sites, and the tilting angles Θ_C were refined independently for each phase. The expected ratio between average moments at the two pyramids ($r = m_L/m_S$) was calculated from experimental values of n_d using Eq. (4.9).

T = 10 K	**SC1**	**SC2**
$\mathbf{n_d}$	0.035 (34)	0.083 (36)
$\mathbf{r = m_L/m_S}$ (expected)	0.235 (35)	0.285 (40)
COLLINEAR (AF1)		
T_{N1} (K)	430 (5)	435 (5)
Phase fraction, $f_m(\mathbf{k}_1)$ (%)	57.0 (1.4)	60.3 (1.6)
m_L (μ_B)	0.316 (43)	0.388 (62)
m_S (μ_B)	2.654 (29)	2.807 (31)
$r = m_L/m_S$	0.119 (16)	0.138 (22)
θ_{C1} (deg)	79 (7)	72 (4)
COLLINEAR (AF3)		
T_{N3} (K)	390 (5)	290 (5)
Phase fraction, $f_m(\mathbf{k}_3)$ (%)	43.0 (1.6)	39.7 (1.2)
m_L (μ_B)	1.132 (53)	1.062 (38)
m_S (μ_B)	1.106 (53)	1.045 (38)
$r = m_L/m_S$	1.024 (69)	1.016 (52)
θ_{C3} (deg)	88 (19)	94 (17)
χ^2	*4.63*	*4.96*
R_B	*1.59*	*1.90*
R_f	*0.929*	*0.932*
R_m ($\mathbf{k}_1$)	*4.35*	*5.37*
R_m ($\mathbf{k}_3$)	*5.06*	*4.04*

+ m_S) of a magnetic phase respect to the total ordered magnetic moment in the crystallographic unit cell, m_T(AF1) + m_T(AF2).

For the AF1 collinear phase the average ordered magnetic moments obtained at the two sites [m_L at the long (Cu-rich) pyramid and m_S at the short (Fe-rich) pyramid] are rather different. This contrasts with the moments in the AF3 phase, which are nearly identical. This result is very clear if we look at the $r = m_S/m_L$ ratios calculated from the experimental refined moments at the two phases (see Tab. 6.4), and provides strong evidence that the secondary $\mathbf{k}_3$-type collinear phase (AF3) observed in these highly ordered YBCFO single crystals, where Fe/Cu disorder is too small to form spiral ordering, come from the minoritary presence of non-mixed M_2O_9 bipyramids with internal AFM coupling, which favour short-ranged minority clusters with tendency to $k_z = 0$. Differently, regions dominated by mixed $FeCuO_9$ bipyramids with FM coupling

lead to $\mathbf{k}_1$-type magnetic regions with high-T_{N1} values. The smaller fractions obtained for the AF3 phase as compared to the AF1 one are compatible with this statement, suggesting that the former occupies a smaller fraction of the crystal.

Regarding the tilt angle (θ) of the spins respect to the c axis, in the AF1 phase their values [$\theta_{C1} = 79(7)^\circ$ in SC1 and $\theta_{C1} = 72(4)^\circ$ in SC2] indicate that the moments are closer to the ab plane compared to polycrystalline YBCFO samples of the same composition [$\theta_{C1} = 53(8)^\circ$ for the more ordered sample, S1]. In relation to the AF3 phase, despite the higher experimental error of the refined θ angles [$\theta_{C3} = 88(19)^\circ$ in SC1 and $\theta_{C3} = 94(17)^\circ$ in SC2] its values are compatible with spins contained or very close to the ab plane. The tilting of the magnetic moments respect to the c axis in the AF1 and AF3 phases, as well as the relative

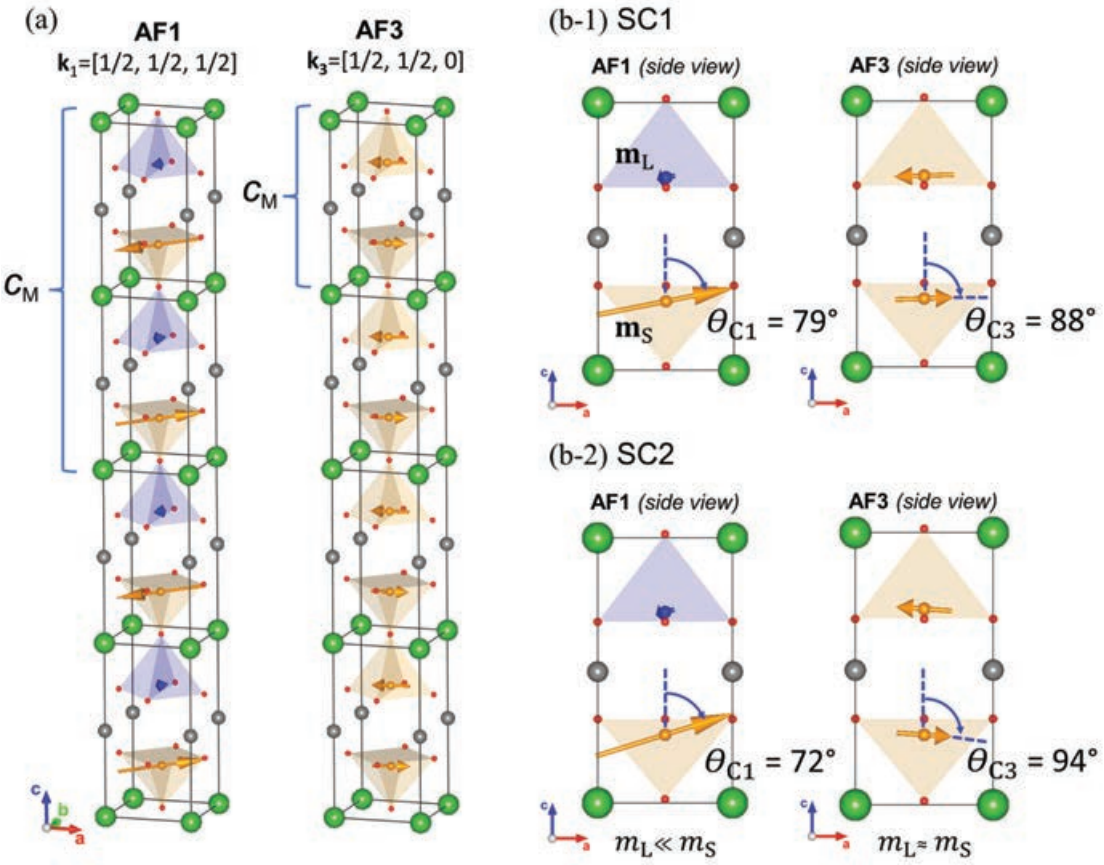

FIGURE 6.11: Projections of the refined AF1 (left) and AF3 (right) collinear magnetic phases including four unit cells to illustrate the different translational symmetries along the c direction. In the unit cell, only the majoritary atoms are shown in the puramids (blue: Cu; brown: Fe). (b) Projections of the chemical unit cell illustrating the inclination angles θ_{C1} and θ_{C3} of the collinear spins in the AF1 and AF3 phases for the SC1 (b-1) and SC2 (b-2) single crystals.

amplitudes of the magnetic moments (m_L and m_S) at the two phases phase are shown in Figs. 6.11(b-1) and 6.11(b-2) for SC1 and SC2.

6.5.3 Extending the magnetic phase diagram of YBCFO towards the low disorder regime

The information obtained from the study of polycrystalline YBCFO samples, from which the linear extrapolation of the experimental (q_s,T_S) points suggested a critical threshold of disorder at $n_0 \approx 0.112$ below which a long-range

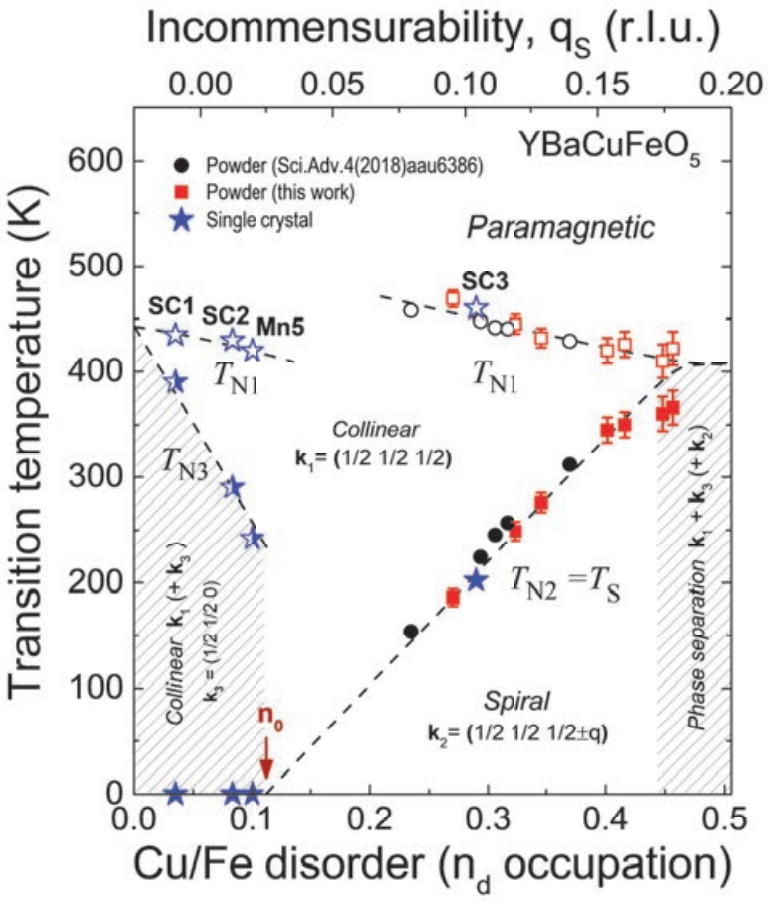

FIGURE 6.12: YBCFO magnetic phase diagram versus Fe/Cu cation disorder including the n_d-T points in SC1, SC2 and SC3 single crystals. Dashed lines in the $0<n_d<n_0$ range of disorder describe temptatively the phase boundaries from the onset of the magnetic phases according to neutron diffraction data. Blue stars and red points correspond respectively to YBCFO single crystals and polycrystalline samples studied in this work. For the sake of comparison black points refer to q_s-T values from samples reported in Ref. [48]. Empty and filled symbols correspond to T_{N1} and T_{N2}=T_S, respectively, and half-filled points correspond to T_{N3}.

spiral magnetic state cannot be formed, is based on samples with disorder values quite above n_0 [S1 to S7 in Chapter 4, whose disorder ranges from n_d = 0.29 to 0.44]. In view of this weakness and the difficulty to obtain YBCFO samples with Fe/Cu disorder near or below n_0 by conventional solid-state reaction methods, the unintended fabrication of highly ordered YBCFO single crystals by the TSFZ growth method offered a chance to explore this regime in more detail. So, taking advantage of the information obtained from YBCFO crystals, Fig. 6.12 discloses the n_d-T (and q_s-T) magnetic phase diagram including the experimental n_d-T points of SC1, SC2 and SC3 YBCFO single crystals. The (n_d,T_{N1}) and (n_d,T_S) points for the SC3 crystal with the ICM spiral phase are in perfect agreement with the PM-AF1 and AF1-AF2 transition temperatures in polycrystalline YBCFO samples. The fact that in all of the samples falling in the $0<n_d<n_0$ range of disorder the spiral order is suppressed (represented in the phase diagram as $T_S = 0$) constitutes a solid proof of the existence of the $\mathbf{k}_1$ ($+\mathbf{k}_3$) inhomogeneous regime anticipated in Chapter 4, where disorder is still too low ($n_d \rightarrow 0$ and $n_d<n_0$) and the AFM Fe/Fe defects are too far apart to stabilize a magnetic spiral.

6.6 Summary

Crystal growth experiments were successfully conducted by a modified Traveling Solvent Floating Zone (TSFZ) technique to obtain $YBaCuFeO_5$ single crystals of suitable quality and sizes for neutron experiments, using unpolarized and also polarized neutron beams (as will be shown in next chapter). Structural characterization consisting in the analysis of high resolution SXRPD data on powdered samples and complementary single crystal neutron diffraction measurements allowed to quantify the B-site disorder in three different YBCFO crystals. The Fe/Cu chemical disorder obtained (n_d = 0.035 in SC1, 0.083 in SC2, and 0.306 in SC3) revealed that the TSFZ method used to grow the single crystals resulted in perovskites with much higher level of Fe/Cu cationic order than in powder samples of the same composition. From magnetic neutron diffraction we have shown that this fact has deep implications on the magnetic properties of the system. Out of the three crystals studied only one of them had large enough Fe/Cu disorder for the formation of the incommensurate spiral phase, while in the other two the disorder was too small for the stabilization of the spiral order. The sample with Fe/Cu disorder above $n_0 \approx 0.112$ (SC3) was the only one adopting a spiral phase below $T_S \approx 200$ K [$\mathbf{k}_2 = (1/2, 1/2, 1/2 \pm q)$

with $q = 0.104$ (r.l.u)], whereas the modulated spiral order lacks in the other two crystals with n_d<n_0 (SC1 and SC2). In these crystals neutron diffraction reveals that on cooling, the ordering of the collinear phase with propagation vector $\mathbf{k}_1 = (1/2, 1/2, 1/2)$ at T_{N1} is followed by the ordering of a second collinear phase with $\mathbf{k}_3 = (1/2, 1/2, 0)$ which develops below T_{N3}. The two collinear magnetic structures were determined at 10 K from NPD. In both crystals inclinations of the AF1 and AF3 magnetic easy axis respect to c were found to be similar and close to 90°. Noteworthily, the refined moments at the two pyramids ($m_L \ll m_S$ in AF1 and $m_L \approx m_S$ in AF3) evidenced that the AF3 phase comes from regions in the crystal with higher cationic disorder where the Fe-Cu ferromagnetic coupling between spins sharing a bipyramid becomes antiferromagnetic due to disorder.

The results presented in this chapter are mostly in agreement with the theoretical works developed in the last years to model the new avenue based on the '*spiral order by disorder*' mechanism [55]. However, theoretical models have paid little attention to the existence of a minimum disorder threshold for the spiral order formation. We have further established and described such a low-disorder region in the phase diagram, and have associated the observed phase segregation with intrinsic spatial fluctuations in the degree of cation disorder. Additionally our results will contribute to the understanding of this mechanism near the low disorder boundary and further highlight the influence of the preparation method on the potential chiral or multiferroic properties of this family of compounds.

Chapter 7

Does a magnetic spiral exist in YBCFO? A single crystal investigation

7.1 Introduction

Among the properties realized in chiral magnetic systems the multiferroicity and the magnetoelectricity are two of the most attractive. Ordered spiral phases are particularly promising because the noncollinear spiral magnetic order breaks space-inversion symmetry and can induce spontaneous polarization through inverse Dzyaloshinsky-Moriya or spin-current mechanisms [30]. So, a common origin of polarization and spiral order guarantees a substantial coupling "*by construction*" in cycloidal multiferroic materials. The spiral phase in YBCFO has raised great expectation making the $LnBaCuFeO_5$ family of layered perovskites one of the most promising spin-driven multiferroic candidates. The extraordinary behavior of YBCFO lies on its unique capacity to tune the spiral transition temperature in a very wide interval, from 150 K to 360 K [47], simply by enhancing chemical disorder. The exceptional stability of the presumed chiral magnetic order in this layered structure has been attributed to a non-conventional mechanism that produces "*spiral order by disorder*" , according to the theoretical model developed by Scaramucci *et al.* based on equally oriented ferromagnetic bonds that are substituted by random impurity bonds presenting a sufficiently strong antiferromagnetic coupling [54].

Several works have reported fairly large electric polarization (reaching 0.4 $\mu C/cm^2$) in polycrystalline samples of YBCFO [19, 46, 52], but not yet on single crystals where investigations are practically non-existent or still very scarce. Results on the ferroelectric response of YBCFO in its incommensurate phase

are contradictory, and have opened up a lively debate. In addition, the direction of P in YBCFO also remains a matter of debate. Although Kundys *et al.* [19] justified a polarization parallel to c due to the formation of dipole moments in the bipyramids, most of reports suggest a cycloidal induced polarization perpendicular to c, the direction of the incommensurate magnetic modulation.

In the previous works reporting spontaneous polarization, that was justified assuming the spiral solution from powder samples. A critical issue is that there are two types of spin configurations that can account for the magnetic intensities observed in the neutron powder diffraction patterns associated to the incommensurate phase of these materials. One solution is (i) a collinear modulated order (sinusoidal order), and the other (ii) a spiral (or helical) spin arrangement. In view of that both, spin modulated and spiral orders are compatible with the neutron magnetic intensities from polycrystalline samples, it is essential to investigate the incommensurate order in YBCFO by single crystal neutron diffraction. Such a study is still lacking and this work is aimed to fill that gap. Lai *et al.* [83] reported the growth of the first known YBCFO single crystal, which presented two magnetic transitions at 455 K and 170 K. By making partial maps by neutron diffraction and some linear scans of the crystal along particular directions, in 2017 [109] they were able to show the successive commensurate and incommensurate spin order transitions, and the total transformation of the first into the second at $T_{N2} \approx 170$ K. However, a more detailed study of the two magnetic structures in the crystal was not done by single-crystal neutron diffraction, and instead they used a crushed crystal to obtain neutron powder diffraction patterns (NPD) of the two magnetic phases. In Ref. [109] they attributed the absence of polarization in their crystal used for the neutron study to a spiral in the crystal without cycloidal component (ab plane), that does not satisfy the criterion for producing ferroelectric polarization in the framework of the Dzyaloshinskii-Moriya interaction. In particular we have intended to give a definitive conclusive answer to the following questions: (i) Which is the nature of the incommensurate spin order in LnBaCuFeO$_5$ perovskites? (ii) Is a chiral magnetic phase able to persist well above RT in this layered structure? (iii) Which evidences can conclusively discern between an incommensurate order caused by non-collinear magnetism and/or other caused by a collinear variable-moment spin arrangement? (iv) Can this structure host a cycloidal order? The answers to these four questions will have a major impact on the potential this exceptional family of frustrated magnets.

The limitations of neutron powder diffraction to discern between complex magnetic orders are well known (see *e.g.* Ref. [121] for an example analyzed in detail). Unlike single crystal neutron diffraction, where each single reflection is collected individually, the averaging inherent to neutron powder diffraction entails limitations that in the case of cycloidal or helicoidal orders may prevent its complete description. In a powder diffraction pattern all the reciprocal space is projected onto one dimension, as a function of *2Theta*. So, all reflections located at the same *2Theta* angle contribute to a unique peak of the powder pattern, whose intensity results from different contributing reflections. In the case of magnetic structures, in addition to projecting onto a single dimension, only the perpendicular component of the magnetic structure factor to the scattering vector contributes to the intensity of each reflection. As already said, it has been unambiguously recognized in previous works (*e.g.* [46, 48]) that for the $RBaCuFeO_5$ layered perovskites two very different magnetic models perfectly reproduce the experimental NPD patterns of the incommensurate phase recorded on powder samples: (i) a sinusoidal collinear order and (ii) a spiral magnetic order. As an example, this is illustrated in Fig. 4.15 (Sec. 4.5.3 of Chapter 4).

7.2 Crystal growth and experimental methods

Sample preparation

In this chapter all measurements were done on single crystalline samples of the layered perovskite YBCFO. The YBCFO single crystal studied in this chapter is the one referred to as SC3 in Chapter 6. The fabrication process of this crystal was done using the traveling solvent floating zone (TSFZ) method. First, polycrystalline YBCFO was prepared through the conventional solid-state reaction method. The powder was loaded, packed with cylindrical shape, compacted under 1500 bar and sintered. A solvent consisting of CuO with 2 wt% B_2O_3 was used for the crystal growth by the TSFZ method using a four-mirror optical furnace. The elemental composition of the crystal was determined by Inductively Coupled Plasma Optical Emission Spectroscopy (ICP-OES). The relative molar fractions of the cations are in agreement with the ideal composition. For the details of the growth technique and a detailed description of the fabrication process, as well as its structural and preliminary magnetic characterization, the reader is referred to Chapter 2 (*Sample synthesis: polycrystalline and single crystal*

fabrication) and Chapter 6 (*Influence of Fe/Cu disorder on the magnetic properties of YBCFO single-crystals*). For the different measurements done on this single crystal, a large piece was carefully oriented and cut with sides parallel to the three perpendicular crystallographic directions. This crystal was then cut in two pieces to perform in parallel single crystal neutron and synchrotron experiments, among other measurements.

Characterization methods

- *Unpolarized single-crystal neutron diffraction:* Single crystal neutron diffraction experiments with unpolarized neutrons were conducted at the high-flux reactor of the Institut Laue Langevin (Grenoble, France). First, Single Crystal Neutron Diffraction (SCND) measurements were carried out at the hot-neutrons four-circle diffractometer D9 (λ=0.837 Å). Large sets of 537 nuclear Bragg reflections (295 independent) were collected at 450 K and 10 K using a closed-shell furnace and a closed-cycle cryostat, respectively, to obtain a good structural model that allowed us to determine the crystal structure (Fe/Cu cationic order and interatomic distances). A small two-dimensional (2D) area detector of 6×6 cm^2 (32×32 pixels) allows reciprocal space survey and a more accurate optimization of the peak positions. Additionally q-scans were collected along specific directions to assess the presence of the different propagation vectors. The temperature dependence of particular peaks was monitored between 10 K and RT using a displex cryostat.

For the characterization of the AF1 and AF2 magnetic structures, SCND measurements with unpolarized neutrons of wavelength λ=2.36 Å were performed on the four-circle diffractometer D10. The scattered neutrons were recorded on a 94×94 mm^2 area detector. The data collected consisted of 326 incommensurate reflections (130 independent) measured at T = 10 K, and 129 commensurate reflections (61 independent) obtained at 200 K. For the Rietveld analysis of AF1 and AF2 magnetic intensities measured respectively at 200 K and 10 K, the scale factor and extinction parameters were fixed to the values obtained from a set of nuclear reflections (113 in total, 45 independent) collected in parallel at both temperatures. This allowed to determine accurately the ordered magnetic moment values. For the SCND study under magnetic field, q-scans were recorded also on D10 using a 6T cryomagnet. The crystal was mounted with the b axis along the vertical direction, parallel to the direction of the magnetic field. Several q-scans were recorded along [0T,6T] cycles, using a 0.5 T step, at different

selected temperatures within the stability range of the spiral. Before each magnetic field cycle, the sample was warmed up to the collinear phase and cooled in ZF conditions to the target temperature.
Integrated magnetic intensities and the incommensurate magnetic propagation vector versus temperature and magnetic field were extracted from the corresponding q-scans by fitting the peaks using a Gaussian function. To analyze the SCND intensities, in all cases the program RACER was used to integrate the omega- and omega-2theta-scans and to correct them for the Lorentz factor. Structural and magnetic refinements were carried out using the FullProf set of programs [97]. Neutron refinements were done by least square minimization of the integrated intensities and extinction corrections were applied following the Becker-Coppens model. The illustrations of the crystal structure were obtained using the VESTA program [106].

- *Spherical neutron polarimetry:* Spherical neutron polarimetry (SNP) experiments were conducted on the hot neutron diffractometer D3 (ILL, Grenoble). The same sample as in D10 experiments was used. Measurements were carried out using the CryoPAD equipment (operated at λ=0.832 Å) after zero-field cooling through the two magnetic transitions. The sample was mounted onto a sample stick allowing up to 10 kV high voltage by a potential difference between two parallel horizontal aluminum plates. The crystal (of dimensions 2.1 mm$\parallel a$, 3.4 mm$\parallel b$ and 1.7 mm$\parallel c$) was fixed to the lower plate by silver epoxy, and the upper plate was positioned at ∼4.4 mm above the lower plate [Fig. 7.4(a)]. With the crystal b axis vertically aligned no magnetic reflections modulated with the incommensurate propagation vector $\mathbf{k}_2 = (1/2, 1/2, 1/2 \pm q_s)$ were accessible. The crystal was then mounted in a different geometry, where the (001) and (111) axes aligned parallel to the horizontal xy plane [see the scheme in Fig. 7.4(b)] gave access to a series of magnetic reflections in the horizontal scattering plane such as those of type $(00l) + \mathbf{k}$. We investigated the polarization matrices associated to them in the AF1 and AF2 phases by taking their corresponding **k**-vector. We used the Mag2Pol program [98] for analyzing and fitting the spherical neutron polarimetry data.

- *Synchrotron Resonant Magnetic X-ray Scattering:* Resonant Magnetic X-ray Scattering (RMXS) measurements were done on the I16 beamline (Diamond Light Source, UK). With the pulsed tube cryostat in horizontal geometry, we mounted the YBCFO single crystal (of dimensions 3.4 mm$\parallel a$, 1.5 mm $\parallel b$ and 1.7 mm $\parallel c$) onto the 6-circles diffractometer sandwiched in between the plates

of a dedicated sample holder for electric field experiments. Silver paint was applied to the plate surfaces for a proper electrical contact. The shortest sides of the crystal, corresponding to the b (or a) crystallographic axis of the crystal, and the longest sides, corresponding to the a (or b) axis, were stuck parallel to the sample holder plates [see Fig. 7.12(a)]. The crystal surface normal to a vector parallel to the c axis was finely polished before the measurements to optimize the RMXS signal. Measurements in the AF1 and AF2 magnetic phases were carried out in a temperature range between 300 and 50 K using a closed cycle cryocooler. The experiments were focused on the study of the AF2 incommensurate phase below $\mathrm{T_{N2}} = 195$ K, for which we used both linear and circularly polarized incident X-rays with energies around the Fe K edge. The analysis of the diffracted X-rays polarization was done using a Cu (220) crystal analyzer in front of an FMB Oxford Avalanche photodiode (APD) detector. The beam was focused down to a spot of approximately 50 by 200 $\mu\mathrm{m}$.

- *Magnetometry:* The magnetic characterization, using dc and ac magnetic fields, was performed with the help of Vassil Skumryev (ICREA Research Professor at Universitat Autònoma de Barcelona).Two commercial instruments from Quantum Design, Superconducting Quantum Interference Device (SQUID) and Physical Properties Measurement System (PPMS), were used to measure macroscopic magnetic characteristics in single crystals, namely dc susceptibility and magnetization and ac susceptibility. For the temperature dependence of the magnetization M(T) in the interval 10-520 K under an applied external magnetic field of 2 kOe parallel to the b- and c-axes, we used the SQUID system in the range of temperatures below RT. Measurements above RT were measured using a vibrating sample magnetometer (VSM) in the PPMS.

For the magnetic field-dependent measurements, $M(H)$ magnetization curves under dc magnetic fields up to 6 T along the principal crystallographic directions was measured using the SQUID setup, and the ac measurement system (ACMS) option of the PPMS was used to record the ac susceptibility as a function of dc magnetic fields up to 9 T, superimposed in the same direction as an ac field of amplitude $H_{ac} = 10$ Oe and frequency $f = 333$ Hz.

7.3 Magnetometry

The dc magnetic mass susceptibility (χ) of the crystal, measured in field-cooling conditions (FC) between 10 to 520 K is shown in Fig. 7.1. The temperature scans of dc magnetization measured parallel to the c- [χ_c(T)] and the b-axis [χ_b(T)] show different trends. Whereas clear anomalies are not visible in the evolution of χ_c(T) ($H /\!\!/ c$), which shows a nearly paramagnetic behavior, for the case on in-plane magnetization (with $H /\!\!/ b$) we observe two magnetic transitions. Upon cooling, the first (paramagnetic) transition is found at $T_{N1} \approx 460$ K. A marked decrease in χ_b(T) takes place below this temperature. A clear kink is then observed at $T_{N2} \approx 195$ K. A further decrease of χ_b(T) takes place below the kink associated to T_{N2}, which is not observed in χ_c(T). At low temperatures the magnetization measured along-b is smaller than that perpendicular to the plane ($\chi_b \ll \chi_c$). As we will show in the following lines, neutron scattering confirmed that the anomaly at 195 K denotes the emergence of the incommensurate magnetic order.

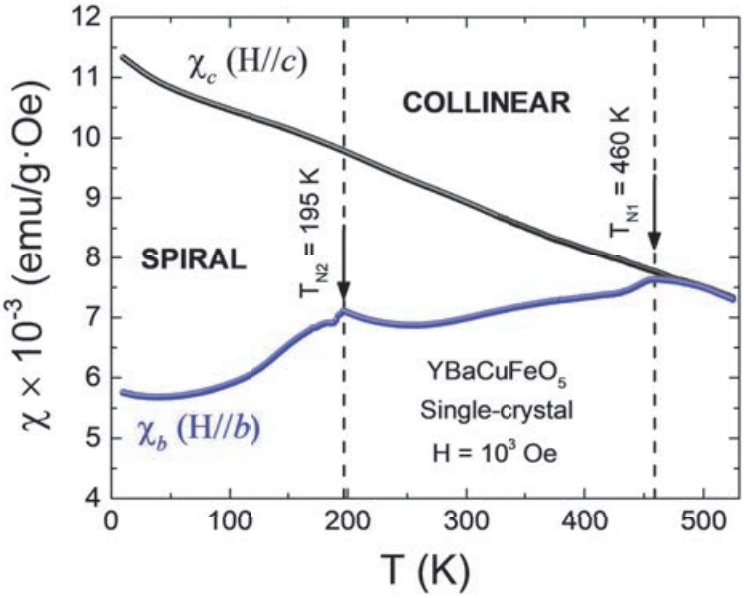

FIGURE 7.1: Temperature dependent dc magnetic mass susceptibility of the YBCFO single crystal measured in FC with the magnetic field applied along b and c axes ($H =$ 1 kOe). The two anomalies associated to the onset of the antiferromagnetic orders are shown at $T_{N1} = 460$ K and $T_{N2} = 195$ K.

7.4 Single-crystal neutron diffraction: crystal structure and temperature dependence

7.4.1 Crystal structure

In order to determine the crystal structure and to quantify the Fe/Cu chemical disorder in the YBCFO single crystal a large set of 537 nuclear reflections (295 independent) were collected at the paramagnetic phase (450 K) on D9 using a closed shell furnace. Identical measurements were conducted at low temperature (10 K) using a closed-cycle cryostat to assess the possible structural variations between both temperatures. Fig. 7.2 displays the observed and calculated squared structure factors for the nuclear structure of the YBCFO crystal, refined in the paramagnetic phase [450 K, Fig. 7.2(a)] and at low temperature

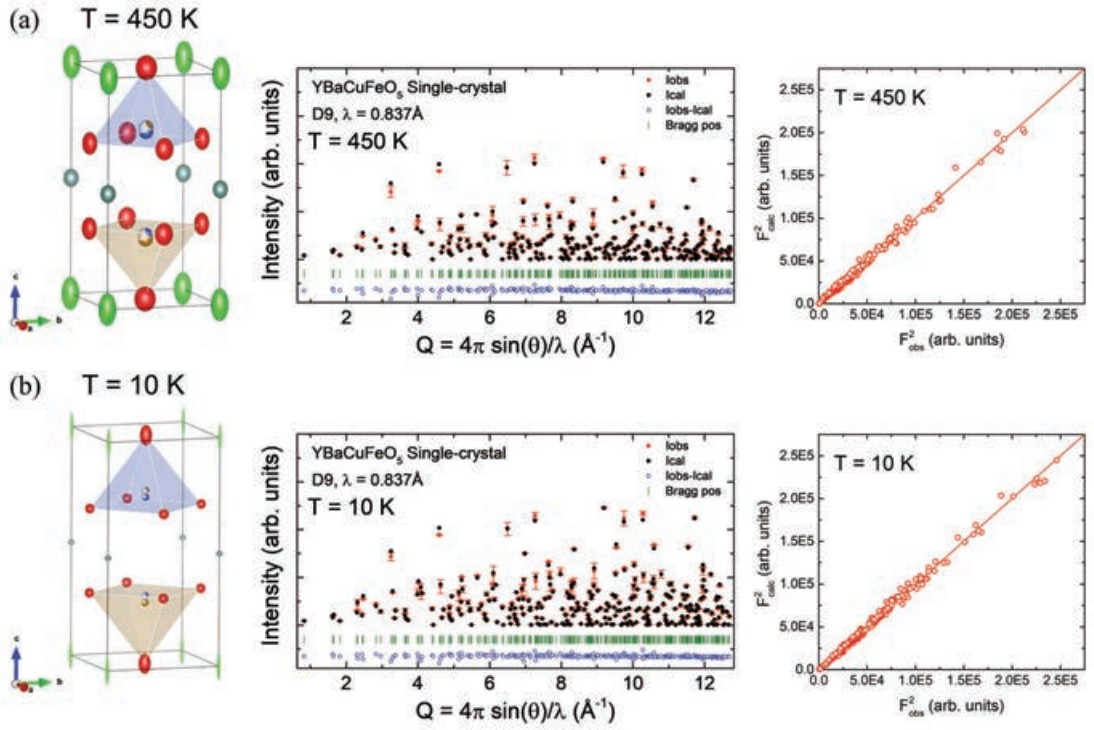

FIGURE 7.2: Structure and refinements of YBCFO single crystal nuclear intensities measured in D9@ILL (λ=0.837 Å) at (a) 450 K and (b) 10 K. Left: $P4mm$ structure showing the refined unit cell and anisotropic displacement ellipsoids. The color of each pyramid corresponds to that of the dominant cation in it (blue: Cu; brown: Fe). Middle: observed and calculated integrated intensities of the nuclear refections plotted as a function of Q = $4\pi\sin(\theta)/\lambda$ (red points: observed; black points: calculated; blue points: difference). Right: agreement plots of the nuclear structure refinements. The calculated structure factors are plotted against the experimental ones.

[10 K, Fig. 7.2(b)]. Right panels show the agreement plots of the nuclear structure refinements at 450 K (χ^2: 1.57, R_F: 5.70, R_F^2: 7.69) and at 10 K (χ^2: 0.838, R_F: 3.72, R_F^2: 5.26). Table 7.1 gathers all the refined parameters for the nuclear structure obtained in the crystal at 450 K and 10 K. The atomic positions and the Cu/Fe occupancies in the two pyramids of the unit cell were refined using the $P4mm$ symmetry. The z-coordinates of a same metal M in upper (1, blue) and lower (2, red) pyramids were constrained by z(M1)+z(M2)=1. The rest of

TABLE 7.1: Crystal structure and agreement factors for the nuclear intensities collected at 450 K and 10 K on D9 hot neutron four-circle diffractometer (λ=0.837 Å). (*: minority fraction; n_d (disorder)=Occ (Fe1*/Cu2*)). The coordinates of each metal (M: Cu or Fe) are constrained by z(M1)+ z(M2)=1.

$YBaCuFeO_5$ Single Crystal $P4mm$		**T = 450 K**	**T = 10 K**
a=b (Å)		3.8810 (6)	3.8665 (6)
c (Å)		7.6843 (10)	7.6268 (10)
Y $1a$ (00z)	z/c	0.4991 (36)	0.4995 (37)
	U_{iso} (Å^2)	0.0062(6)	0.0009 (5)
Ba $1a$ (00z)	z/c	0	0
	U_{11} (Å^2)	0.0071(6)	0.0004 (3)
	U_{33} (Å^2)	0.026(3)	0.018 (2)
Cu1 $1b$ (½ ½ z)	z/c	0.72341 (23)	0.72271 (16)
Fe1* $1b$ (½ ½ z)	z/c	0.74131 (23)	0.74061 (16)
Cu2* $1b$ (½ ½ z)	z/c	0.27659 (23)	0.27729 (16)
Fe2 $1b$ (½ ½ z)	z/c	0.25869 (23)	0.25939 (16)
	U_{iso} (Å^2)	0.0071(2)	0.0005 (2)
O1 $1b$ (½ ½ z)	z/c	0.00119 (160)	-0.00070 (192)
	U_{11} (Å^2)	0.0108(5)	0.0035 (3)
	U_{33} (Å^2)	0.015(4)	0.012 (2)
O2 $2c$ (½ 0 z)	z/c	0.31555 (86)	0.31491 (92)
	U_{11} (Å^2)	0.0077(3)	0.0025 (2)
	U_{22} (Å^2)	0.0050(3)	0.0021 (2)
	U_{33} (Å^2)	0.0121(11)	0.0026 (6)
O3 $2c$ (½ 0 z)	z/c	0.68349 (97)	0.68372 (99)
	U_{11} (Å^2)	0.0077(3)	0.0025 (2)
	U_{22} (Å^2)	0.0050(3)	0.0021 (2)
	U_{33} (Å^2)	0.0121(11)	0.0026 (6)
Occ (Cu1/Fe2)	$1 - n_d$	0.701 (17)	0.683 (19)
Occ (Fe1*/Cu2*)	n_d	0.299 (17)	0.317 (19)
	χ^2	*1.57*	*0.838*
	R_F	*5.70*	*3.72*
	R_F^2	*7.69*	*5.26*

the symmetry-inequivalent atoms were refined independently. A key feature in these perovskites is the Fe/Cu chemical disorder, because it determines the level of frustration and has a strong influence on the magnetic features and transition temperatures. Fe/Cu disorder is described by the refined improper occupation n_d: the fraction of Fe at the Cu pyramid (1) (Fe1 site) or the fraction of Cu at the Fe pyramid (2) (Cu2 site). So, a B-site random disorder would correspond to $n_d = 0.5$, and $n_d = 0$ describes a fully ordered Fe/Cu structure. From single crystal neutron measurements we carefully refined the partial occupations finding $n_d = 0.30(2)$ at 450 K. As expected, the same value (within errors) is found at 10 K. Remarkably, although chemical disorder is in the crystal lower than in powder samples prepared under fast cooling (that yield T_S above RT), we will show next that this disorder is enough to stabilize the incommensurate magnetic order at ∼200 K.
On the other hand, no significant variations in the structure are detected between 450 K and 10 K (within the experimental errors) beyond the expected decrease at low temperature of the atomic displacement parameters, related to the lower thermal agitation of the atoms. A look at the anisotropic displacement ellipsoids schematically depicted in Fig. 7.2 (left panels) evidence their variation between 450 K and 10 K.

7.4.2 Temperature dependence

In Chapter 6, from temperature-dependent neutron diffraction measurements performed using the Cyclops Laue diffractometer we showed the existence in the SC3 single crystal of the seeked modulated magnetic phase below ≈195 K (T_{N2}), and allowed indexing the commensurate [$\mathbf{k}_1 = (1/2, 1/2, 1/2)$] and incommensurate [$\mathbf{k}_2 = (1/2, 1/2, 1/2 \pm q)$] magnetic propagation vectors [see Fig. 6.8(c)]. Only these two magnetic wave vectors were observed in the crystal by varying temperature. This was further corroborated by multiple Q_L-scans performed on D9 in the 10-300 K range, using a 5 K step. Q_L-scans were collected along the (0.5, 0.5, L) line (in the range 0.2<L<1.2), with the purpose of tracing the possible magnetic reflections as a function of temperature. A Q_L-scan collected at 10 K is shown in Fig. 7.3(a). This figure also exposes a neutron contour map for the crystal showing the T-Q_L projection of the neutron-diffracted (0.5, 0.5, L) intensities collected as a function of temperature. Fig. 7.3(b) was obtained by adding up the multiple Q_L-scans recorded under a T-step of 5 K.
The temperature dependence of the representative magnetic peaks was also monitored using a displex cryostat. Fig. 7.3(c) plots their integrated intensity

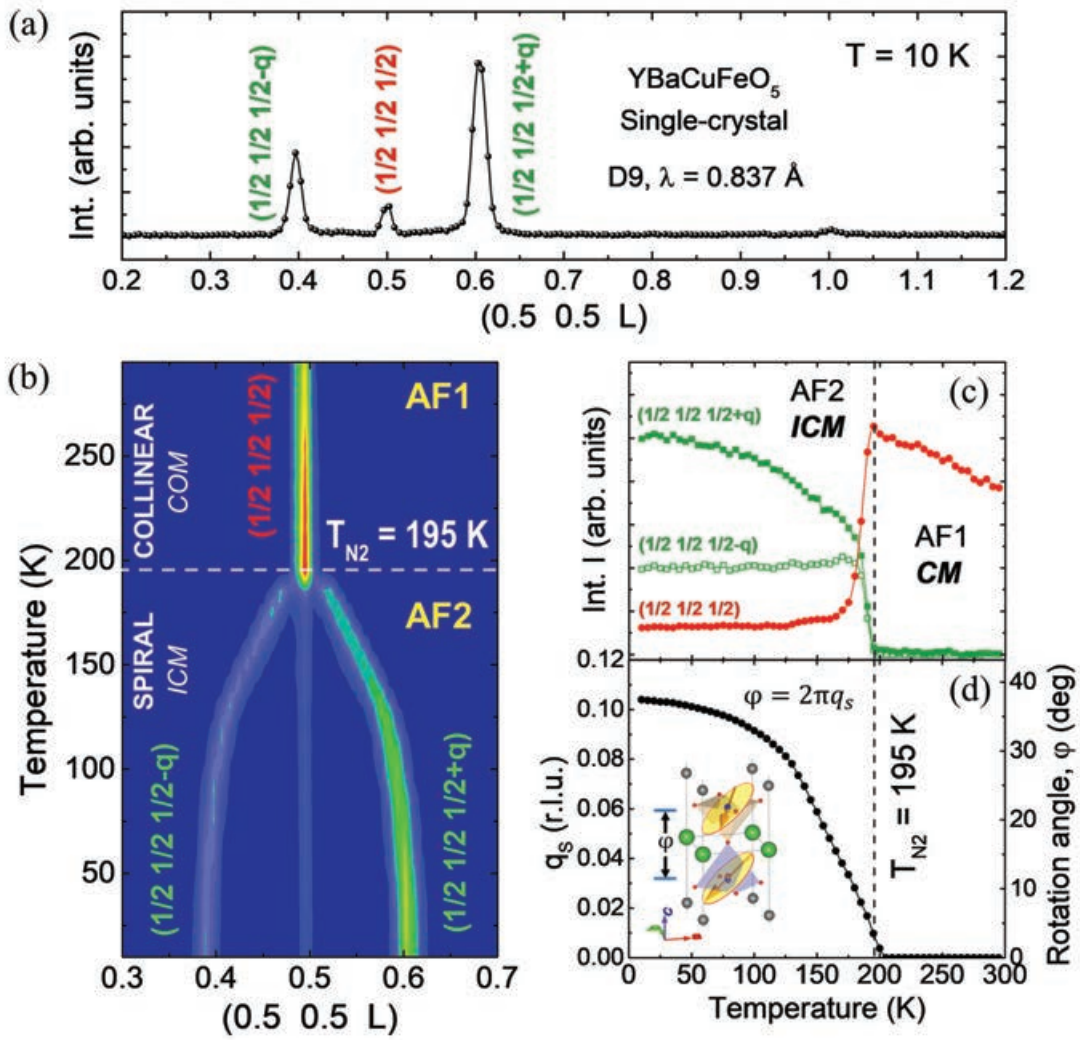

FIGURE 7.3: Single crystal neutron diffraction (q-scans using D9). (a) Q_L-scan along the (0.5, 0.5, L) line (range 0.2<L<1.2) obtained at 10 K. (b) T-Q_L projection of the temperature dependence of magnetic intensities along the (0.5, 0.5, L) line centered around the (½ ½ ½) position for the single crystal. (c) Temperature dependence of the neutron integrated intensities of CM (1/2, 1/2, 1/2) [$\mathbf{k}_1$] and ICM (1/2, 1/2, 1/2±q) [$\mathbf{k}_2$] magnetic reflections. (d) Evolution with temperature of the discommensuration q_s of the spiral phase. The twist angle φ (canting) formed by the two spins of a bipyramid in the spiral phase is also shown ($\varphi = 2\pi q_s$).

recorded on D9 across the transition exposed in the susceptibility around 200 K. Only $\mathbf{k}_1$-type collinear magnetic domains are detected above T_{N2}. Fig. 7.3(c) confirms that a mutual transformation between the commensurate $\mathbf{k}_1 = (1/2, 1/2, 1/2)$ and incommensurate $\mathbf{k}_2 = (1/2, 1/2, 1/2 \pm q)$ phases takes place at T_{N2} (T_S). Under cooling, the magnetic phase with $\mathbf{k}_1$ translational symmetry nearly completely transforms into the spin modulated $\mathbf{k}_2$ phase. Only a tiny residual amount of the high-temperature collinear phase is still observed

below the transition. 195 K is the highest T_S reported for a YBCFO crystal. Below that temperature, the discommensuration is described by the non-null modulation factor q (hereinafter referred to as q_s). The evolution of the magnetic modulation q_s(T) in the crystal was determined from the neutron scans and it is exposed in Fig. 7.3(d). The magnetic modulation appears at T_{N2}(=T_S) and progressively develops to reach its maximum amplitude. The observed evolution is compatible with a second-order type transition. We recall at this point that an evolution from second- to first-order CM-ICM transition is suggested in previous reports on powder samples when T_{N2} approaches T_{N1} (highly disordered samples). The value of the incommensurability as determined at 10 K is $q_s = 0.104$ r.l.u. This value is appreciably lower than the maximum discommensuration previously reported in YBCFO ($q_s^c \approx 0.18$ r.l.u. at the triple point, see Chapter 4).

In the theory, the incommensurate wave vector and the spiral onset temperature are both proportional to the concentration of improper Fe/Fe bonds, predicting a linear relationship between q_s and T_S. From the linear fit to the experimental (q_s,T_S) points reported in powder samples [Eq. (4.8)], a temperature $T_S \approx 210$ K would be expected. The Néel temperature associated to the collinear commensurate order decreases in YBCFO when magnetic frustration increases, but the downward slope is quite smooth compared to the upward slope for T_S. The points from our crystal match well the phase diagram varying Fe/Cu disorder (see the phase diagram in Chapter 6, Fig. 6.12).

7.5 Spherical Neutron Polarimetry

A detailed description of the SNP technique can be found in [141, 142]. The Blume-Maleyev equations [143, 144] describe the scattering of polarized neutrons. According to them the final neutron spin $\mathbf{P}_f$ is related to the initial one $\mathbf{P}_i$ by:

$$\mathbf{P}_f = \mathcal{P}\mathbf{P}_i + \mathbf{P}' \tag{7.1}$$

Where $\mathcal{P}$ is the rotation matrix acting on the initial neutron spin and $\mathbf{P}'$ is the polarization created (or annihilated). Using the orthogonal right-handed axes with x parallel to the scattering vector $\mathbf{Q}$ and z vertical, and the initial polarization along the directions x, y, or z, the final polarization can be determined by nine measurements represented in a pseudomatrix known as the polarization

matrix ($\mathbf{P}_{fi}$). The polarization matrix combines the rotation and the created polarization and each row corresponds to the final polarization when the initial polarization is along x, y and z. For reflections that are purely magnetic (as the ones measured in YBCFO) the scattered intensities depending on the initial neutron polarization are $I_x = M^2 + p_0 J_{yz}$, $I_y = I_z = M^2$, and the matrix reduces to:

$$\mathbf{P}_{fi} = \begin{bmatrix} \frac{-p_0 M^2 - Jyz}{I_x} & -\frac{J_{yz}}{I_y} & -\frac{J_{yz}}{I_z} \\ 0 & \frac{p_0(M^2_{\perp y} - M^2_{\perp z})}{I_y} & \frac{p_0 R_{yz}}{I_z} \\ 0 & \frac{p_0 R_{yz}}{I_y} & \frac{p_0(-M^2_{\perp y} + M^2_{\perp z})}{I_z} \end{bmatrix} \tag{7.2}$$

where $M^2 = \mathbf{M}_\perp \mathbf{M}^*_\perp$, $M^2_{\perp y} = M_{\perp y} M^*_{\perp y}$, and $M^2_{\perp z} = M_{\perp z} M^*_{\perp z}$. p_0 is the polarization of the incoming beam. The so-called magnetic interaction vector $\mathbf{M}_\perp$ lies in the yz plane, $\mathbf{M}_\perp(\mathbf{Q}) = (0, M_{\perp y}, M_{\perp z})$. The off-diagonal components of $\mathbf{P}$ [$R_{yz} = 2\mathrm{Re}(M_{\perp y} M^*_{\perp z})$ and $J_{yz} = 2\mathrm{Im}(M_{\perp y} M^*_{\perp z})$] generate components in the scattered polarization along directions which are not parallel to the incident neutron polarization. Hence they produce the rotation of the neutron polarization in the scattering process. The matrix can also be rewritten as

$$\mathbf{P}_{fi} = \begin{bmatrix} -1 & \frac{2\mathrm{Im}(M_{\perp y} M^*_{\perp z})}{M^2_\perp} & \frac{2\mathrm{Im}(M_{\perp y} M^*_{\perp z})}{M^2_\perp} \\ 0 & -\frac{(M^2_{\perp z} - M^2_{\perp y})}{M^2_\perp} & \frac{2\mathrm{Re}(M_{\perp y} M^*_{\perp z})}{M^2_\perp} \\ 0 & \frac{2\mathrm{Re}(M_{\perp y} M^*_{\perp z})}{M^2_\perp} & \frac{(M^2_{\perp z} - M^2_{\perp y})}{M^2_\perp} \end{bmatrix} \tag{7.3}$$

The chiral vector is $\mathbf{T} = i(\mathbf{M}^* \times \mathbf{M}) = (T_x, 0, 0) = i(M_y M^*_z - M^*_y M_z, 0, 0) = -2(\mathrm{Im}(M_y M^*_z), 0, 0)$. Thus, the so-called "chiral" terms are the off-diagonal elements P_{xy} and P_{xz}, where $J_{yz} = 2\mathrm{Im}(M_{\perp y} M^*_{\perp z})$ in the polarization matrix results from chiral scattering and can only be non-null if the magnetic structure is non-collinear. The chiral vector $\mathbf{T}$ is a real vector that directly contributes to the creation of polarization parallel to x (or $\mathbf{Q}$) when $\mathbf{M}_\perp \times \mathbf{M}^*_\perp$ (or J_{yz}) is nonzero. In the presence of domains with opposite magnetic chirality the contribution of each chiral domain to J_{yz} has the sign inverted respect to each other.

Zero-field neutron polarimetry measurements were conducted at 200 K, 100 K and 10 K using CryoPAD. The incident neutron polarization ($\mathbf{P}_i$) was selected by a cryoflipper and maintained by guide fields. The scattered polarization was analysed with a ^{3}He neutron spin filter. The efficiency of the polarization at all temperatures was corrected from several measurements of P_{zz} on the (111) nuclear reflection.

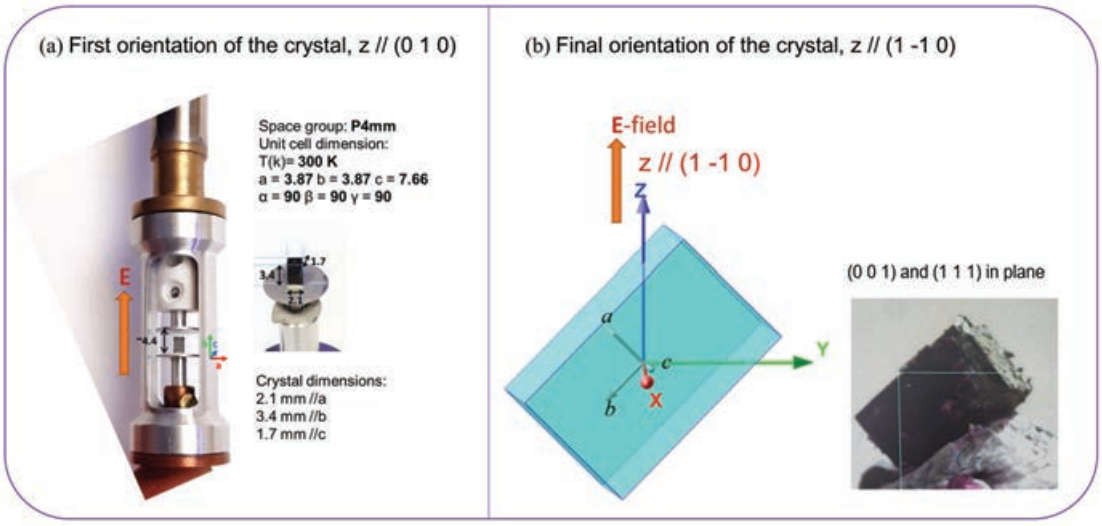

FIGURE 7.4: Crystal mounted for the spherical neutron polarimetry (SNP) measurements on the hot neutron diffractometer D3 (ILL, Grenoble) using the CryoPAD device. (a) Sample stick with the crystal mounted with the (010) axis in the vertical direction (z, parallel to the electric field applied between the two parallel horizontal aluminum plates). With this configuration no magnetic reflections were accessible. (b) Scheme showing the sample configuration during the SNP measurements. To access magnetic reflections of the type $(00l) + \mathbf{k}$ the crystal was mounted with the (001) and (111) axis parallel to the xy plane (*i.e.* with the electric field applied along the (1-1 0) direction).

7.6 The commensurate collinear AF1 phase

7.6.1 Unpolarized magnetic neutron diffraction in the AF1 phase

When the AF1 collinear phase is regarded as a single domain the calculated integrated intensities do not match the experimental ones recorded at 200 K [$\chi^2 = 28.4$, Fig. 7.5(a)]. Only when twinning domains are considered, refinements can satisfactorily reproduce the magnetic single crystal data in the AF1 state [$\chi^2 = 2.87$, Fig. 7.5(b)]. The tetragonal symmetry is broken by the spin ordering at T_{N1}, giving rise to two types of magnetic domains, related by the tetragonal axis $4^+(0,0,z)$ lost at the transition. Only the magnetic domains D1 $= (x,y,z)$ (1) and D2 $= (-y,x,z)$ (4^+) were included in the magnetic refinement of Fig. 7.5(b). The best solution found for the commensurate collinear phase is described in Table 7.2(a). The refined fraction of D1 domains from D10 data was 53.7(1.6)%, versus a 46.3% of D2 type. The refined magnetic order in each type of domain is shown in Fig. 7.5(c). θ_C is the inclination angle that spins form with the c axis in the AF1 phase. ϕ_C is the azimuthal angle that their projection onto the ab plane forms with the a axis. In Fig. 7.6 we show how the

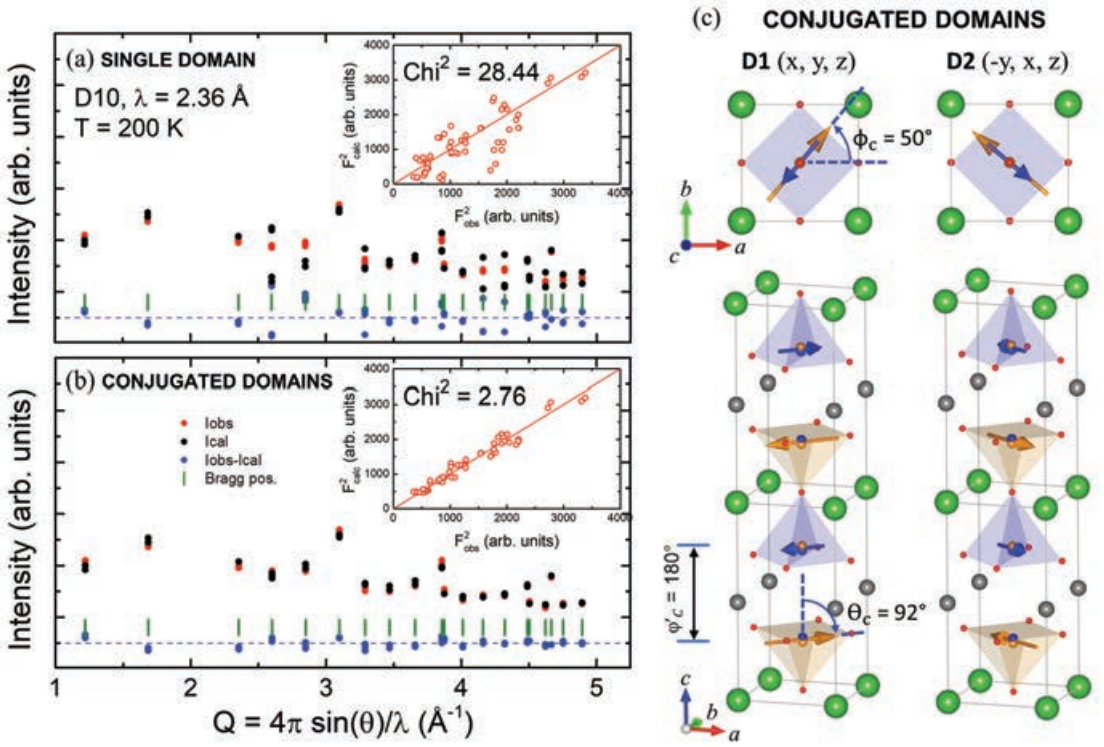

FIGURE 7.5: **Commensurate magnetic order (AF1) from integrated intensities** (200 K, D10@ILL data). Final magnetic refinements (black points) of the experimental integrated magnetic intensities (red points) at 200 K [$\mathbf{k}_1 = (1/2, 1/2, 1/2)$]. (a) For a single magnetic domain. (b) For twin magnetic domains of the type 1 and 4^+. Bottom blue points are the observed-calculated difference. Insets: calculated magnetic structure factors plotted against the experimental ones. (c) Projections of the refined collinear magnetic order for D1 $= (x, y, z)$ and D2 $= (-y, x, z)$ domains in the crystal at 200 K.

resulting agreement factors vary with the value of θ_C, ϕ_C and φ'_C (as referred to D1 domains). The best agreement found corresponds to $\theta_C = \pm\pi/2$, $\phi_C = \pi/4$ ($3\pi/4$) and $\varphi'_C = \pi$. The two first angles imply collinear moments parallel to the ab plane ($\theta_C = 90°$) aligned along the diagonal axis $[1, \pm1, 0]$ of the tetragonal cell ($\varphi_C = \pm45°$, minus signs refer to D2). Notice however in the χ^2-scale of Fig. 7.6(b) that the variations due to ϕ_C are little ($\Delta\chi^2 < 1$). Nevertheless, we will show below that SNP unambiguously confirms the diagonal direction of the moments in the AF1 state.

7.6.2 Spherical neutron polarimetry in the AF1 phase

The SNP measurements at 200 K are in excellent agreement with the calculated matrix elements for the "diagonal" collinear magnetic model (provided that the two conjugated domains are taken into account). Table 7.4 reports the

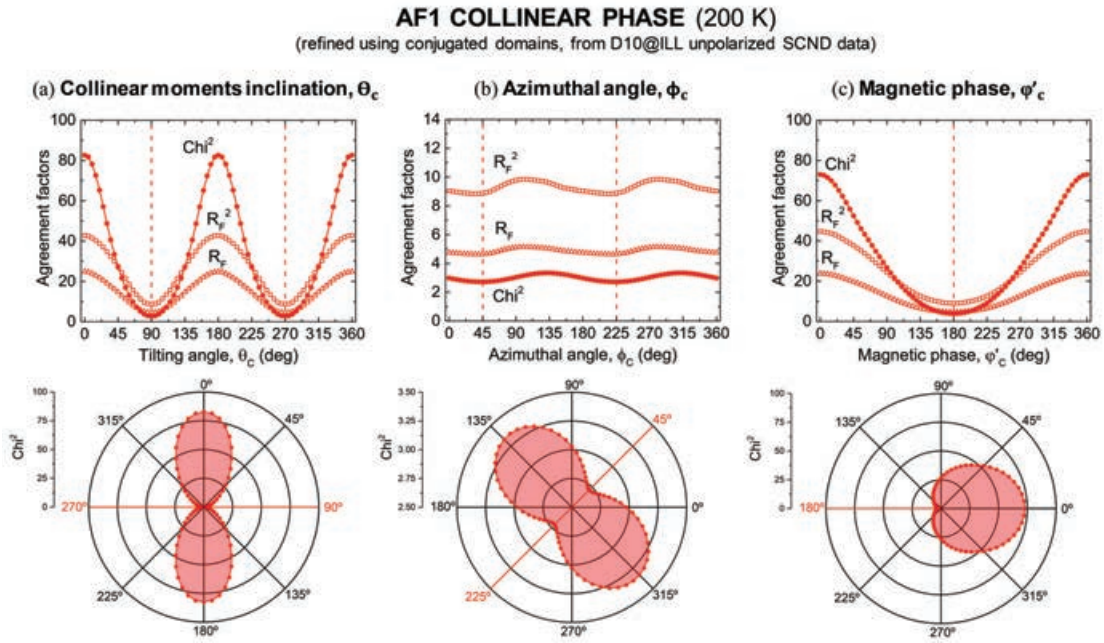

FIGURE 7.6: **Easy axis and magnetic anisotropy in the AF1 phase** (200 K, D10@ILL). Variation of χ^2 (Chi^2) as a function of (a) the inclination angle θ_C and (b) the azimuthal orientation ϕ_C (projected in the ab plane) of the spins direction in AF1. (c) Dependence with the value of the phase φ'_C between $\mathbf{m}_1$ and $\mathbf{m}_2$ moments in the chemical cell. Refinements were performed including twin domains. Best agreement corresponds to $\theta_C = \pm 90°$ (spins in the ab plane), $\phi_C = 45°/225°$ and $\varphi'_C = 180°$ ($\mathbf{m}_2$ antiparallel to $\mathbf{m}_1$).

P_{if} polarization terms for the $(00l)+\mathbf{k}$ reflections measured at 200 K in the commensurate AF1 phase with $\mathbf{k}_1 = (0.5, 0.5, 0.5)$. The calculated values from the fits of the SNP matrices calculated using Mag2Pol are shown for comparison. In the case of perfect twinning (50-50) all the off-diagonal matrix elements are null (calculations are shown in Fig. C.1 [App. C] for different spin orientations in the ab plane and domain populations). In the single domain scenario Table 7.4 shows that the P_{if} off-diagonal matrix elements that do not cancel have the two neutron polarization components (P_i, P_f) perpendicular to the collinear spins in the domain. Hence, the experimental observation of non-null off-diagonal elements in the polarization matrix (*e.g.* P_{yz}, P_{zy}) is a signature of a certain imbalance in the population of D1 and D2 collinear domains. The domain population and the spin orientation in the commensurate AF1 phase at 200 K were refined to the SNP data using Mag2Pol [98]. A domain population D1/D2 = 53.1/46.9(0.5) % was determined by SNP, in good agreement with D10 results. Unequivocally, only the diagonal solution in the presence of conjugated domains satisfactorily reproduces the elements of the full polarization

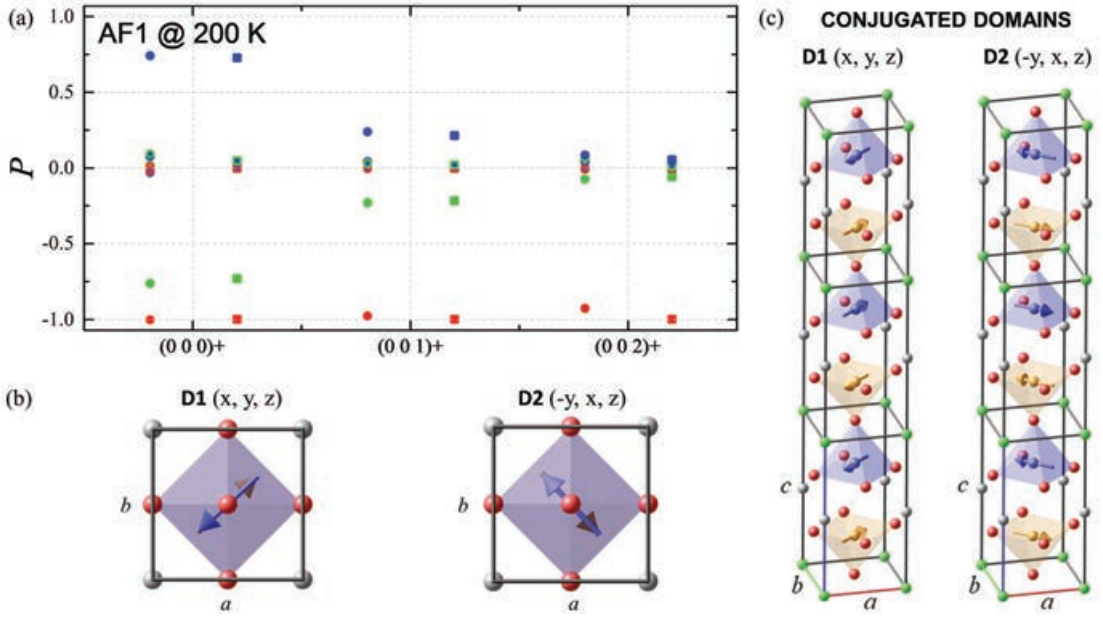

FIGURE 7.7: **Refinement to the spherical neutron polarimetry data of the commensurate AF1 phase** (200 K, D3@ILL). Observed (squares) and calculated (circles) polarization values P_{if} for incident neutrons polarized along P_i (inner symbol color) and polarization analysis along P_f (symbol edge color) for the three directions x (red symbols), y (green symbols), and z (blue symbols) in the local coordination system (x parallel to the scattering vector **Q** and z vertical). The best fit is obtained for a collinear $\mathbf{k}_1$ model with conjugated magnetic domains (D1, D2) along the ab diagonal.

matrices measured in three magnetic reflections at 200 K. The best simultaneous refinement ($\chi^2_r = 3.22$) determined the spin orientation shown in Table 7.2(b) [$\theta_C = 90.8(1)$, $\phi_C = 43(8)$]. The preferred diagonal azimuthal orientation [$\mathbf{m} /\!/ (1, \pm 1, 0)$] of the spins suggested by the magnetic integrated intensities (D10) was thus definitely confirmed by the SNP measurements. The agreement between observed and calculated elements of the polarization matrices at 200 K is shown in Fig. 7.7(a) and Table 7.4. Fig. 7.7(b-c) also exhibits the collinear magnetic structure in each domain.

To summarize the AF1 state in the crystal, polarized and unpolarized neutron results unveils the coexistence of (x, y, z) (D1) and $(-y, x, z)$ (D2) collinear AF1 domains, with volume fractions D1/D2 = 53/47(0.5) % and the spins aligned parallel to the ab plane, along the diagonals of the tetragonal cell.

TABLE 7.2: **Refined AF1 commensurate magnetic structure from SCND (D10@ILL) and SNP (D3@ILL) data at 200 K.** The two independent results correspond to the fitting of the (a) neutron integrated magnetic intensities collected in D10 (unpolarized neutrons) and (b) the fitting of the neutron polarization matrices (SNP) measured in D3. The spherical neutron polarization matrices are more sensitive than the integrated intensities to the orientation of the spins in the ab plane. The refined domain population is also shown.

AF1 collinear phase with conjugated magnetic domains (D1, D2)							
T	m_1 (μ_B)	m_2 (μ_B)	θ_C (deg)	ϕ_C (deg)	φ'_C (deg)	Dom. pop. D1/D2 (%)	Agreement factors
(a) Unpolarized neutrons (D10@ILL)							
200 K	1.284 (3)	2.188 (7)	91.8 (8)	50 (19)	179.8 (6)	53.7/46.3 (1.6)	$\chi^2 = 2.87$; $R_F = 4.82$; $R_F^2 = 9.25$
(b) Spherical Neutron Polarimetry (D3@ILL)							
200 K	-	-	90.8 (1)	43 (8)	180	53.1/46.9 (0.5)	$\chi^2 = 77.35$; $\chi_r^2 = 3.22$

7.7 The incommensurate magnetic order

7.7.1 Unpolarized magnetic neutron diffraction in the AF2 phase

The nature of the incommensurate magnetic structure was thoroughly investigated by unpolarized and polarized single crystal neutron diffraction. An incommensurate spiral phase can be described in the form:

$$\mathbf{m}_{lj}(\mathbf{k}) = M_R \mathbf{u}_j \cos 2\pi \left(\mathbf{k} \cdot \mathbf{R}_l + \Phi_j\right) + M_I \mathbf{v}_j \sin 2\pi \left(\mathbf{k} \cdot \mathbf{R}_l + \Phi_j\right) \qquad (7.4)$$

where $\mathbf{m}_{lj}$ is the magnetic moment of the atom j in the unit cell l, $\mathbf{R}_l$ is the vector joining the arbitrary origin to the origin of unit cell l, and Φ_j is a magnetic phase. In YBCFO $j = 1, 2$ (the two metal sites in the unit cell). $\mathbf{u}_j$ and $\mathbf{v}_j$ designate the orientation of the two perpendicular unitary vectors that define the plane of the helix, where M_R (real) and M_I (imaginary) amplitudes fix the dimensions of the elliptical envelope described by the rotating magnetic moments.

In powder samples of the YBCFO structural family it is not possible to independently refine (i) the real and imaginary amplitudes (M_R and M_I) or (ii) the two magnetic moments in the bipyramidal units. The inability to refine the real and imaginary amplitudes is the most relevant drawback of neutron powder diffraction to study this layered structure because it does not allow to discriminate between collinear (sinusoidal) and non-collinear (spiral) spin order. The

sinusoidal (modulated) model corresponds to the limit $M_I = 0$ (very large eccentricity: $M_R \gg M_I$) and the opposed limit is a circular spiral (null eccentricity: $M_R = M_I$). The circular spiral model was adopted to refine NPD data in earlier works, but it should be recognized that a sinusoidal collinear model perfectly reproduces the NPD patterns below T_S. The limitations of NPD were further discussed in Sec. 4.5.3 of Chapter 4. In Fig. 4.15 we illustrated how the two models: (i) *a variable-moment sinusoid* and (ii) *a spiral magnetic order*, can account for the incommensurate phase of the neutron powder diffraction patterns from an YBCFO polycrystalline sample, evidencing the need to conclusively study the incommensurate order in YBCFO by single crystal neutron diffraction studies.

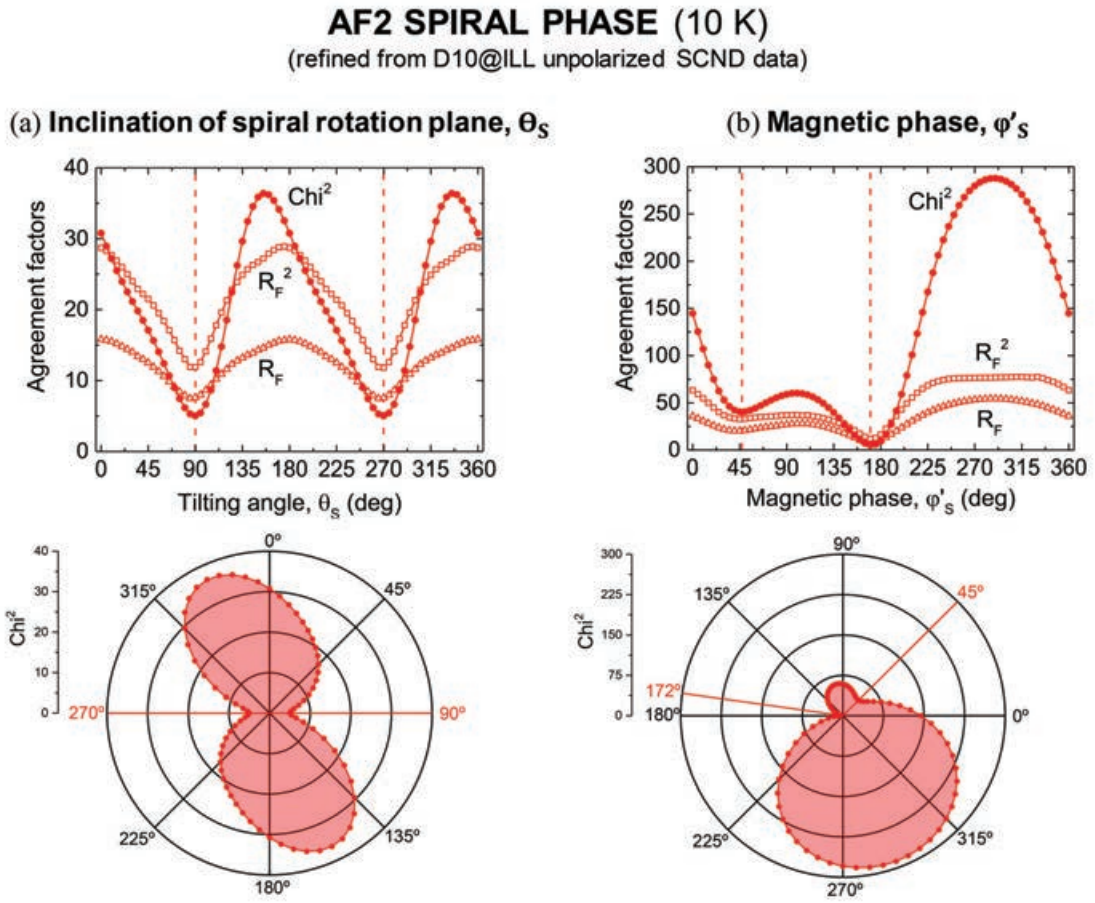

FIGURE 7.8: **Easy plane and magnetic phase in the AF2 phase** (10 K, D10@ILL). Variation of χ^2 (Chi^2) as a function of (a) the inclination angle θ_S and (b) the magnetic phase φ'_S between $\mathbf{m}_1$ and $\mathbf{m}_2$ moments in the chemical cell. Refinements were performed including chiral domains. Best agreement corresponds to $\theta_S = \pm 90°$ (spins in the ab plane) and $\varphi'_S = 172°$.

The incommensurate magnetic order in YBCFO has been investigated at 10 K first by unpolarized Single Crystal Neutron Diffraction. Large nuclear (113 reflections) and magnetic (326 incommensurate reflections) data collections were made using D10. For the magnetic data treatment the scale factor was fixed to the value obtained by refining the nuclear structure. The average magnetic moments at the two pyramids were refined independently. Given that the theoretical ratio m(Fe^{3+})/m(Cu^{2+}) of their respective unpaired spins is 5, we also performed refinements constraining the two average ordered moments (in pyramids 1 and 2) according to the ratio r [$\mathrm{r} \equiv \mathrm{m_1/m_2} = (1 + 4 \cdot \mathrm{n_d})/(5 - 4 \cdot \mathrm{n_d})$] deduced from the refined Fe and Cu occupations [being $\mathrm{n_d} = 0.30(2)$ the refined improper occupation or Fe/Cu disorder]. Within the errors both approximations gave the same results for the ordered moments.

A central feature is the inclination of the spin rotation plane in the crystal. The angle θ describes the angular distance (inclination) between the direction of the spins and the c axis. In the spiral phase θ_{S} stands for the tilting of the rotation plane of the helix [**uv** plane in Eq. (7.4)]. Fig. 7.8(a) exposes the goodness of the fit parameters (χ^2, R_F^2 and R_F) as a function of the tilting angle θ_{S} in the refinement of the spiral configuration. Two marked minima are apparent in the SCND refinements corresponding to $\theta_{\mathrm{S}} = \pm 90^{\circ}$. They confirm that the spin rotation plane in the crystal is parallel to the tetragonal ab plane. The incommensurate magnetic order, therefore, would correspond to an helicoidal rather than cycloidal configuration.

Assuming a single type of domain the sinusoidal model cannot reproduce the experimental intensities, whereas a circular spiral model with the spin rotation plane perpendicular to c (helicoidal order) fits well the observed magnetic intensities. This is illustrated in Fig. 7.9, where we show the evolution, in the single-domain picture, of the agreement factors and refined values for selected magnetic parameters as a function of the eccentricity of the elliptical envelope represented by the M_I/M_R ratio. In this picture we also display the SCND refinements of the AF2 ICM phase at 10 K corresponding to the magnetic order models with extreme values of the ellipsoid eccentricity, which correspond to a sinusoidal order when $M_I/M_R = 0$ [Fig. 7.9(a)] and to the spiral when $M_I/M_R = 1$ [Fig. 7.9(b)]. Projections of the two refined magnetic structures are also shown. Using a single-domain model the integrated neutron intensities at 10 K were well reproduced with $M_I/M_R = 1$. The best magnetic refinement

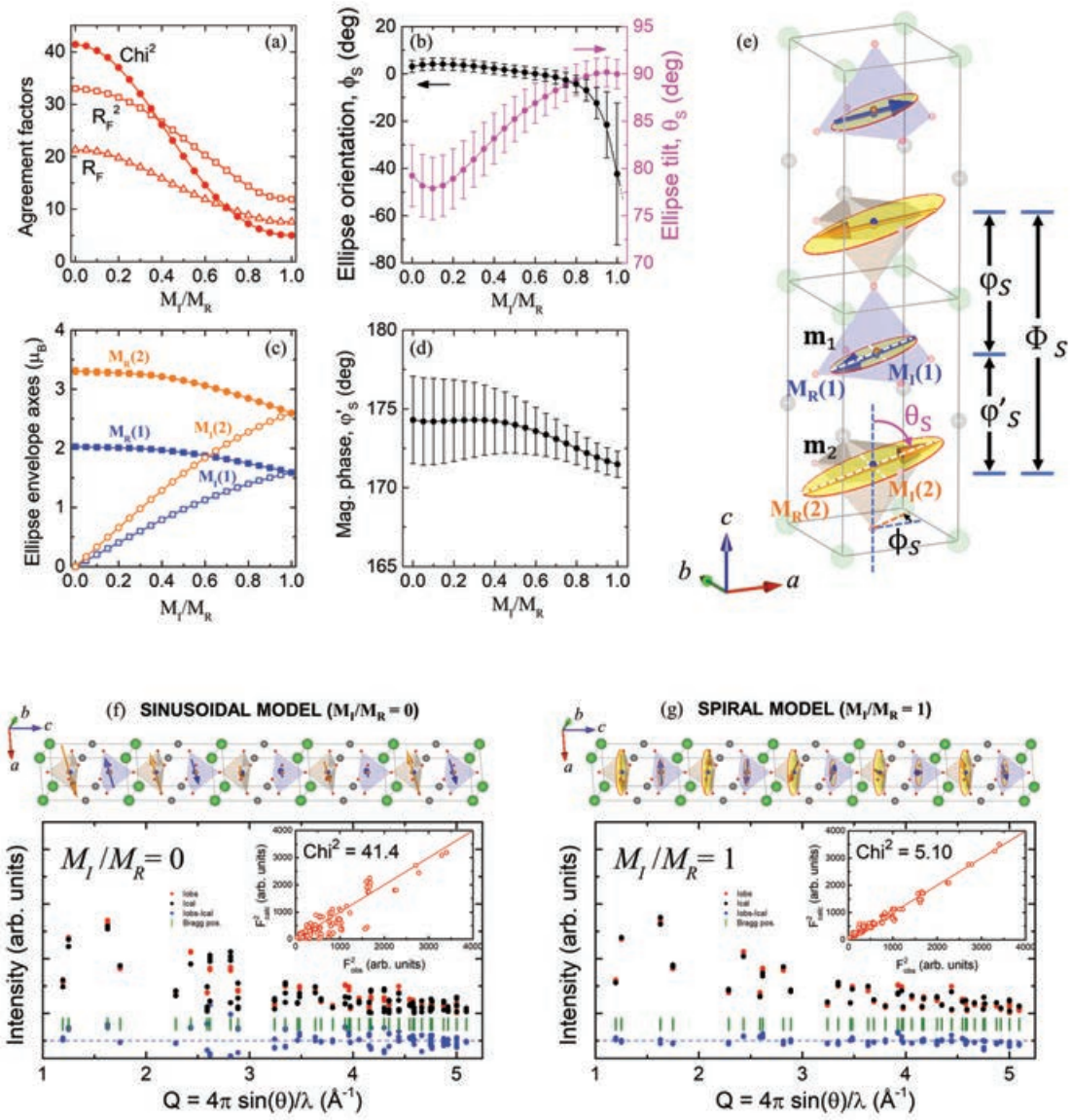

FIGURE 7.9: **Single-domain SCND refinements of the AF2 incommensurate magnetic order** (10 K, D10@ILL). (a) Evolution in the single-domain picture of the agreement factors of the AF1 refined magnetic structure from is shown as a function of the eccentricity of the elliptical envelope, represented by the M_I/M_R ratio. Refined values for selected magnetic parameters: (b) azimuthal angle φ'_S (left axis) and tilting angle θ_S (right axis), (c) the real and imaginary amplitudes of the elliptical envelope, and (d) the φ'_S phase. The real and imaginary amplitudes (M_R and M_I) of the elliptical envelopes for $\mathbf{m}_1$ and $\mathbf{m}_2$ and the different angles are illustrated in (e). Lower panels show the comparison of SCND refinements using magnetic order models with extreme values of the elliptical envelope eccentricity: (f) sinusoidal ($M_I/M_R = 0$) and (g) spiral ($M_I/M_R = 1$).

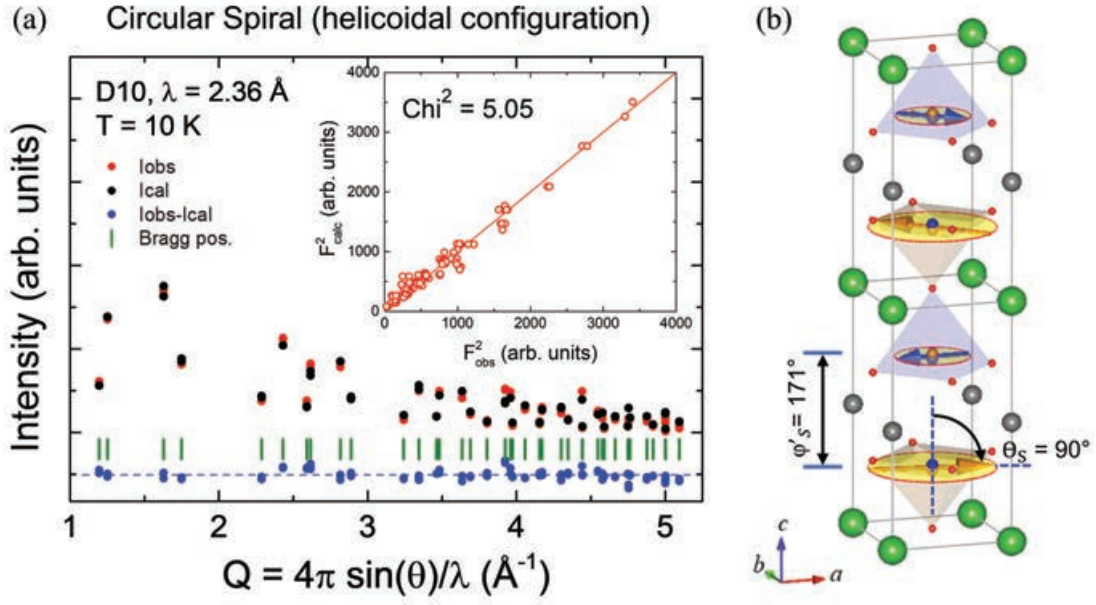

FIGURE 7.10: Neutron refinement at 10 K (four-cycles D10@ILL neutron diffractometer) of the incommensurate integrated intensities from the YBCFO crystal using the circular spiral model described in Table 7.3(b). Best fit corresponds to a helicoidal configuration (null cycloidal component).

(χ^2=5.05; R_F^2=11.8; R_F=7.55) is shown in more detail in Fig. 7.10(a). The obtained magnetic structure corresponds to the circular spiral described in Table 7.3(b) [*Unpolarized neutrons (D10)*] and plotted in Fig. 7.10(b).
The frequency shift q_s measures how much the magnetic wave deviates from the antitranslational symmetry along c ($\Phi = \pi + 2\pi q_s = \varphi + \varphi'$). The angle Φ [see Fig. 7.9(e)] stands for the rotation angle between the spins of equivalent pyramids in successive cells. The twist angle φ is the canting between the two spins of a bipyramid in the spiral phase, whereas φ' [see Fig. 7.9(e)] stands for the phase between the average magnetic moments at the two magnetic sites in the chemical cell ($\mathbf{m}_1$ and $\mathbf{m}_2$). In powder samples it has been generally assumed that φ'[cell]=π and then φ[bipyramid]=$2\pi q_s$. We carefully refined the value of φ' and Fig. 7.8(b) discloses the evolution of the goodness parameter χ^2 and other agreement factors obtained in the fits varying the value of the phase φ' between $\mathbf{m}_1$ and $\mathbf{m}_2$ moments in the chemical cell. SCND refinements unveil an absolute minimum at $\varphi'_{min} = 172(1)^\circ$ close but somewhat deviating from 180°.

A deeper analysis needs to consider configuration domains (twin domains D1/D2) in the sinusoidal model and chirality domains (C1/C2) in the spin helix configuration. Using polarized neutrons, the SNP analysis including domains

TABLE 7.3: Refined AF2 incommensurate magnetic structure at 10 K and 100 K. Independent results corresponding to the fitting of unpolarized SCND (D10@ILL) and SNP (D3@ILL) data are shown. (a) The sinusoidal model with conjugated magnetic domains (D1/D2) and (b) the circular spiral model with chiral domains (C1/C2) are compared. Agreement factors are shown. The spiral model affords the best agreement to polarimetry results.

(a)	**Sinusoidal model ($M_I \sim 0$) with conjugated magnetic domains (D1, D2)**						
T	m_1 (μ_B)	m_2 (μ_B)	θ_S (deg)	ϕ_S (deg)	φ'_S (deg)	Dom. pop. D1/D2 (%)	Agreement factors
Unpolarized neutrons (D10@ILL)							
10 K	2.187 (5)	3.732 (11)	89.4 (6)	37 (59)	171.4 (5)	49.2/50.8 (1.3)	$\chi^2 = 5.06$; $R_F = 7.54$; $R_F^2 = 11.8$
Spherical Neutron Polarimetry (D3@ILL)							
10 K	-	-	92.5 (7)	50 (9)	-	48.9/51.1 (0.9)	$\chi^2 = 110.46$; $\chi_r^2 = 1.84$
100 K	-	-	92.7 (2)	48 (4)	-	47.6/52.4 (0.5)	$\chi^2 = 105.29$; $\chi_r^2 = 1.73$
(b)	**Circular spiral model ($M_R = M_I$) with chiral magnetic domains (C1, C2)**						
T	m_1 (μ_B)	m_2 (μ_B)	θ_S (deg)	ϕ_S (deg)	φ'_S (deg)	Dom. pop. C1/C2 (%)	Agreement factors
Unpolarized neutrons (D10@ILL)							
10 K	1.547 (7)	2.638 (14)	89.5 (1.7)	0	171.4 (9)	-	$\chi^2 = 5.05$; $R_F = 7.55$; $R_F^2 = 11.8$
Spherical Neutron Polarimetry (D3@ILL)							
10 K	-	-	93.27 (43)	-61 (8)	-	49.9/50.1 (0.4)	$\chi^2 = 105.22$; $\chi_r^2 = 1.75$
100 K	-	-	92.55 (38)	-39 (6)	-	50.0/50.0 (0.3)	$\chi^2 = 91.61$; $\chi_r^2 = 1.50$

will be presented later on. Unpolarized neutrons cannot discern between inverted chirality domains and hence the results are independent of the C1/C2 ratio. The unpolarized neutron data collected in D10 at 10 K have been also analyzed considering two types of sinusoidal magnetic domains with orthogonal spin directions [D1 $= (x, y, z)$ and D2 $= (-y, x, z)$, the conjugated twin domains]. In such a case, the D10 magnetic intensities can be reproduced if the population of these two types of collinear sinusoidal domains is included in the refinement. As expected, the result of combining orthogonal modulations is equivalent to the circular spiral model when the domain fraction approaches the 50%. The values refined were 49.2/50.8(1.43). The rest of magnetic parameters and goodness factors are listed in Table 7.3(a), being identical to the single-domain spiral model. The magnetic moments are related by a $\sqrt{2}$ factor. Therefore, using unpolarized neutrons we confirmed the presence of two orthogonal magnetic modulations, as it occurs in the spiral magnetic configuration. A simple incommensurate helix with circular envelope and the spins rotating parallel to the ab

plane of the crystal satisfactorily reproduces the measurements using unpolarized neutrons. It should be noticed from Table 7.3 that the φ'_S phase that separates the orientation of the two magnetic moments in the cell ($\mathbf{m}_1$ and $\mathbf{m}_2$) is found to be $\varphi'_S = 171.4(9)^\circ$. Although the two moments are strictly inverted in the collinear AF1 phase [$\varphi'_C = 180(1)^\circ$, Table 7.2], the phase between them deviates slightly from π in the incommensurate phase. In the following paragraphs the validity and robustness of the circular spiral model is further investigated using polarized neutrons.

7.7.2 Spherical neutron polarimetry in the incommensurate magnetic phase

To further corroborate the validity of our results on the nature of the magnetic order and the domain population in the incommensurate magnetic phase, previous measurements in D9 and D10 were complemented with a SNP study below the incommensurate transition. To this end the crystal was cooled down from the paramagnetic state to 100 K and 10 K in E-field conditions (+8 kV along the z-direction). Up to 5 incommensurate reflections were investigated with polarized neutrons: $(000)+\mathbf{k}$, $(001)+\mathbf{k}$, $(002)+\mathbf{k}$, $(112)-\mathbf{k}$ and $(114)-\mathbf{k}$. For the last two, the polarization elements P_{if} were measured first with positive incident polarization ($P_i > 0$), and then additionally also with negative (inverted) incident polarization ($P_i < 0$). The measured polarization elements (P_{if}) are shown in Figs. 7.11(a) and 7.11(b) (at 100 and 10 K, respectively). Table 7.4 gathers the P_{if} polarization elements for $(00l)+\mathbf{k}$ reflections [$\mathbf{k}_2 = (0.5, 0.5, 0.6)$] at 10 K. For comparison, we have also added the fits to the SNP matrices using different magnetic order models. The full set of measurements done in the AF2 phase (10 K and 100 K) and the fitted values of the polarization matrices using the sinusoidal and spiral models are shown in Table C.1 [App. C].

The two magnetic models evaluated with unpolarized neutrons ($M_R \gg M_I$ [sinusoidal] and $M_R = M_I$ [spiral]) were carefully confronted to the experimental polarization matrices. For both models the inclusion of two types of magnetic domains (twin domains in the sinusoidal and chiral domains in the spiral models) was crucial. The fit of the polarimetry data obtained in the CryoPAD device at D3 was performed using Mag2Pol [98]. The best refinement to the polarimetry data (at 10 K and 100 K) was obtained for the circular spiral model. The fit yields the magnetic structure described in Table 7.3(b) giving validity and robustness to the helicoidal description obtained from the unpolarized neutron experiments. The results of the refinement to the SNP data at 10 K and 100 K are summarized in Fig. 7.11 and Table 7.4.

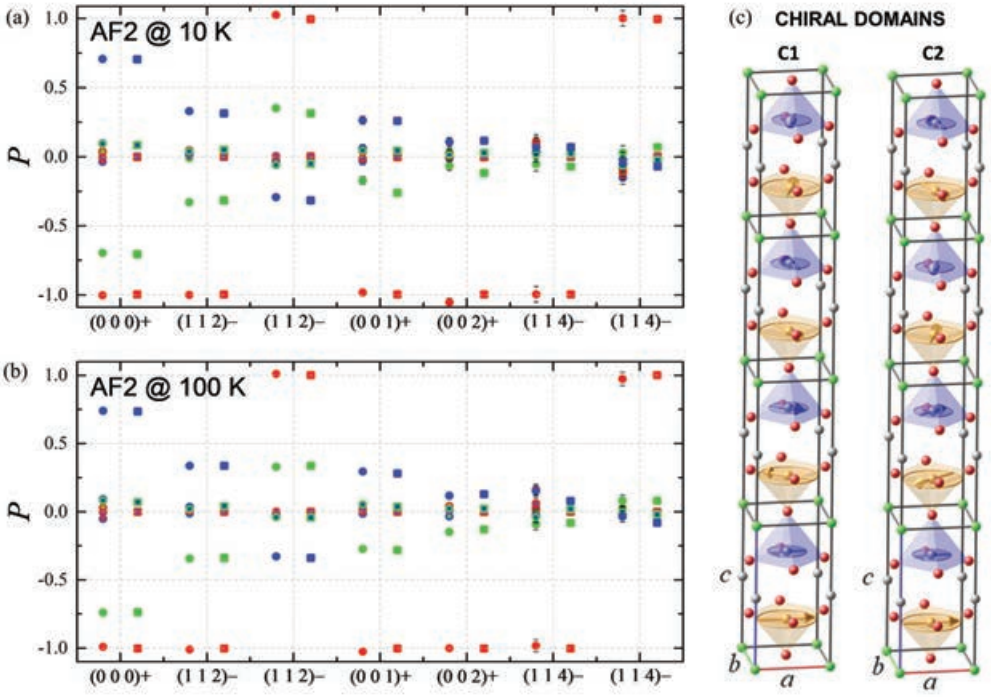

FIGURE 7.11: **Refinement to the spherical neutron polarimetry data of a circular spiral model with chiral domains** (Incommensurate AF2 phase at 10K and 100K, D3@ILL). Observed (squares) and calculated (circles) polarization values P_{if} for incident neutrons polarized along P_i (inner symbol color) and polarization analysis along P_f (symbol edge color) for the three directions x (red symbols), y (green symbols), and z (blue symbols) in the local coordination system (x parallel to the scattering vector $\mathbf{Q}$ and z vertical). For the reflections that appear twice, in the second one the incident neutron polarization was inverted respect to the first. The best fit corresponds to a helix, with spins rotating in the ab plane ($\mathbf{Q} /\!\!/ \mathbf{k}_{c2}$) and coexisting ($50/50\%$) chiral domains.

TABLE 7.4: Best fits of the SNP matrices measured at 200 K (AF1 commensurate phase) and 10 K (AF2 incommensurate phase). Magnetic models were refined using Mag2Pol including two types of magnetic domains (twin or chiral domains, depending on the model). The observed and calculated P_{if} terms are compared for some of the $(00l) + \mathbf{k}$. The complete set of reflections is shown in Table C.1 [App. C].

		AF1 (COM), $\mathbf{k}_1 = (0.5, 0.5, 0.5)$			AF2 (ICM), $\mathbf{k}_2 = (0.5, 0.5, 0.6)$				
		200 K	**Collinear model** D1/D2 = 53.1/46.9 (0.5) χ^2=77.35; χ^2_r=3.22		10 K	**Sinusoidal model ($\mathbf{M_I} \sim 0$)** D1/D2 = 48.9/51.1 (0.9) χ^2=110.46; χ^2_r=1.84		**Spiral model ($\mathbf{M_R} = \mathbf{M_I}$)** C1/C2 = 49.9/50.1 (0.4) χ^2=105.22; χ^2_r=1.75	
(hkl)	$\mathbf{P}_{fi}$	**obs**	**cal**	**obs-cal**	**obs**	**cal**	**obs-cal**	**cal**	**obs-cal**
$(000) + \mathbf{k}$	P_{xx}	-1.004 (10)	-1.000	-0.004	-1.006 (15)	-1.000	-0.006	-1.000	-0.006
	P_{xy}	0.022 (12)	0.000	0.022	0.020 (18)	0.000	0.020	0.000	0.020
	P_{xz}	-0.029 (12)	0.000	-0.030	-0.036 (18)	0.000	-0.036	0.000	-0.036
	P_{yx}	0.011 (12)	0.000	0.011	0.039 (18)	0.000	0.039	-0.002	0.041
	P_{yy}	-0.764 (11)	-0.730	-0.035	-0.699 (17)	-0.693	-0.006	-0.708	0.009
	P_{yz}	0.078 (12)	0.052	0.026	0.096 (19)	0.068	0.028	0.085	0.011
	P_{zx}	-0.014 (12)	0.000	-0.014	-0.005 (18)	0.000	-0.005	-0.002	-0.003
	P_{zy}	0.095 (12)	0.052	0.043	0.093 (18)	0.068	0.025	0.085	0.008
	P_{zz}	0.746 (11)	0.730	0.016	0.711 (17)	0.693	0.018	0.708	0.003
$(001) + \mathbf{k}$	P_{xx}	-0.979 (10)	-1.000	0.021	-0.986 (26)	-1.000	0.014	-1.000	0.014
	P_{xy}	-0.004 (10)	0.000	-0.004	0.038 (29)	0.000	0.038	0.000	0.038
	P_{xz}	-0.001 (10)	0.000	-0.001	-0.030 (28)	0.000	-0.030	0.000	-0.030
	P_{yx}	0.037 (10)	0.000	0.037	0.040 (27)	0.000	0.040	-0.003	0.043
	P_{yy}	-0.229 (10)	-0.214	-0.014	-0.173 (28)	-0.259	0.087	-0.261	0.089
	P_{yz}	0.043 (10)	0.024	0.019	0.061 (29)	0.035	0.026	0.045	0.016
	P_{zx}	-0.003 (10)	0.000	-0.003	-0.011 (28)	0.000	-0.011	-0.003	-0.008
	P_{zy}	0.033 (10)	0.024	0.009	0.045 (28)	0.035	0.010	0.045	0.000
	P_{zz}	0.241 (10)	0.214	0.027	0.266 (29)	0.259	0.006	0.261	0.004
$(002) + \mathbf{k}$	P_{xx}	-0.929 (20)	-1.000	0.071	-1.058 (30)	-1.000	-0.058	-1.000	-0.05
	P_{xy}	-0.008 (22)	0.000	-0.008	0.033 (32)	0.000	0.033	0.000	0.033
	P_{xz}	0.000 (22)	0.000	0.000	-0.010 (30)	0.000	-0.010	0.000	-0.010
	P_{yx}	0.042 (22)	0.000	0.042	0.020 (32)	0.000	0.020	-0.003	0.023
	P_{yy}	-0.074 (23)	-0.054	-0.019	-0.066 (33)	-0.121	0.055	-0.117	0.050
	P_{yz}	0.045 (22)	0.013	0.031	0.000 (33)	0.022	-0.022	0.029	-0.028
	P_{zx}	-0.007 (22)	0.000	-0.007	0.001 (32)	0.000	0.001	-0.003	0.004
	P_{zy}	0.070 (22)	0.013	0.057	0.013 (31)	0.022	-0.009	0.029	-0.016
	P_{zz}	0.087 (23)	0.054	0.033	0.108 (32)	0.121	-0.014	0.117	-0.009

7.8 Magnetoelectric response of the spiral phase in the YBCFO single crystal

7.8.1 Exploring the magnetoelectric response with SNP

At 100 K we also explored possible changes in the magnetic configuration and the proportion of the two chiral domains under application of an electrical field E parallel to z, namely along the (1-1 0) axis of the crystal (diagonal of the ab plane). The crystal was cooled down from the paramagnetic state to 100 K under an E-field of ≈+18.2 kV/cm. We performed neutron polarization measurements to determine the elements of the polarization matrix for the $\mathbf{k}_2$-type reflection (1/2 1/2 1.4), corresponding to $(112) - \mathbf{k}$.[1] The neutron polarization measurements were repeated switching the E-field from +18.2 kV/cm to 0

[1] At 100 K, the $\mathbf{k}_2 = (1/2, 1/2, 1/2 - q)$ vector of the spiral displays a $q_s \approx 0.10$ r.l.u. modulation.

TABLE 7.5: Evolution of the neutron polarization (cross) terms for the $(112) - \mathbf{k}$ reflection (D3@ILL) in the AF2 incommensurate magnetic order (100 K) under applied electric fields [$E \parallel$ (1 -1 0)].

AF2 T = 100 K		E-field $\parallel$(1 -1 0)		
(hkl)	P_{if}	+18.2 kV	0 kV/cm	-14.8 kV/cm
$(112) - \mathbf{k}$	P_{xx}	-1.007 (10)	-	-0.996 (14)
	P_{xy}	-0.012 (12)	-0.031 (17)	-0.005 (17)
	P_{xz}	-0.009 (12)	-	0.005 (18)
	P_{yx}	0.026 (12)	0.033 (17)	0.044 (17)
	P_{yy}	-0.342 (12)	-	-0.333 (18)
	P_{yz}	0.036 (12)	-	0.029 (17)
	P_{zx}	0.008 (12)	0.003 (17)	0.014 (18)
	P_{zy}	0.020 (12)	-	0.038 (17)
	P_{zz}	0.337 (11)	-	0.324 (16)

kV/cm and finally to approx. -14.8 kV (the full matrix was determined at +18.2 and -14.8 kV/cm; at 0 kV/cm only P_{xy}, P_{yx} and P_{zx} terms were measured). The SNP measurements are disclosed in Table 7.5.

At these voltages, in the configuration described, we did not detect changes in the off-diagonal terms of the polarization matrix (nor in the diagonals) for the (1/2 1/2 1.4) magnetic reflection. Off-diagonal terms were found close to zero and the variations registered varying E were not meaningful according to experimental errors [σ]. While no changes are expected in the case of sinusoidal magnetic order, for a spiral a variation in the population of magnetic chiral domains would be reflected in changes of the P_{yx} and P_{zx} terms of the neutron polarization matrix P_{if}. As it can be observed from the simulations in Fig. C.1, for YBCFO multiferroic an inversion of the sign of the P_{yx} and P_{zx} terms could be expected due to an inversion of the population of chiral domains in the case of switchable electric polarization. Since there is no variation after inverting the polarity of the voltage, it can be concluded that the applied electric field has no effect on the non-collinear spins parallel to the ab plane. The absence of magnetoelectric response is in agreement with the DM mechanism in multiferroics when there is a pure helix, with the spiral rotation plane (ab plane) perpendicular to the incommensurate wave vector (q_z). This is the case of the spiral configuration in the present crystal.

We did simulations of the P_{if} terms of the neutron polarization matrix in the incommensurate phase for the $(112) - \mathbf{k}$ magnetic reflection varying the magnetic domain populations in different models. They are shown in Fig. C.1 for three different cases: (a) the circular spiral model with chiral magnetic domains (C1, C2) and spins in the ab plane; (b) the sinusoidal model along the a

axis with conjugated magnetic domains (D1, D2); and (c) the sinusoidal model parallel to the ab diagonal axis, with magnetic conjugated domains. The expected non-null polarization matrix terms (P_{ij}) and their dependence with the domain population are shown for the three models. Notice that in the three magnetic models all off-diagonal terms are expected to be null as long as the domain population is ∼50%-50%.

7.8.2 Exploring the magnetoelectric response by Synchrotron Resonant Magnetic X-ray Scattering (RMXS)

In parallel to spherical neutron polarimetry experiments, we conducted Resonant Magnetic X-ray Scattering (RMXS) measurements at the I16 beamline (Diamond Light Source, UK) with the aim of studying the magnetoelectric response of the spiral phase in the YBCFO single crystal. Fig. 7.12 shows the experimental setup for the RMXS experiment with applied electric fields. In our configuration [horizontal geometry, see Fig. 7.12(b)], the incident beam (**k**) generated by a planar undulator is linearly polarized parallel to the horizontal scattering plane (π-polarized). In this situation, the polarization factor tells us that in the diffracted beam (**k**′) the charge scattered photons will maintain the

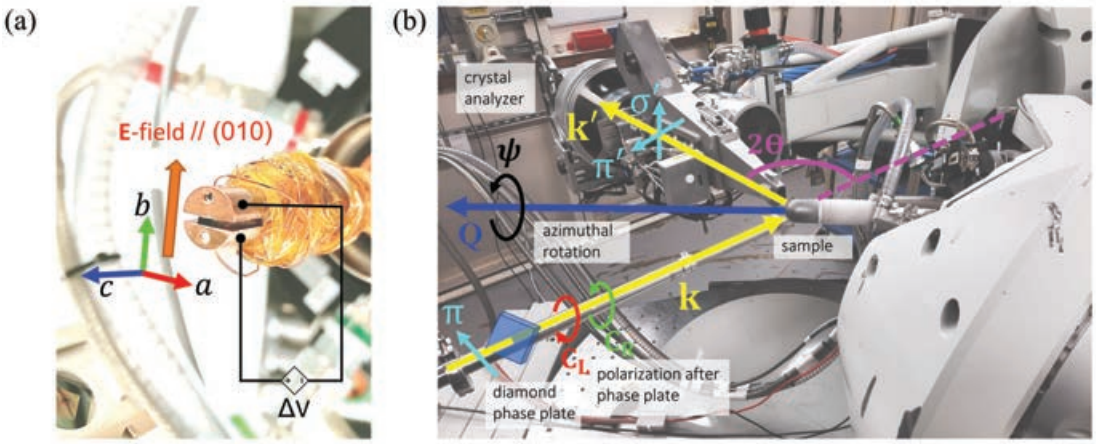

FIGURE 7.12: Experimental setup for the synchrotron Resonant Magnetic X-ray Scattering (RMXS) measurements on the I16 beamline (Diamond Light Source, UK) using linear and circularly polarized light. (a) Crystal mounted on the sample holder to apply an electric field along the b axis. (b) View of the 6-circles kappa diffractometer operating in horizontal scattering geometry. The incident X-ray beam (**k**) has linear polarization parallel to the scattering plane (π-polarized), and the scattered polarization can be analyzed in π-π' and π-σ' polarization channels using the crystal analyzer. The incident π-polarized X-rays can be turned into circular left (CL) and circular right (CR) polarizations using a diamond phase plate retarder.

same direction of the polarization (π'-polarization), in contrast to the resonant magnetic scattering, which is able to rotate the plane of linear polarization. In consequence, the analysis of the rotated σ' direction provides information exclusively related to magnetic scattering. In our case, the scattered polarization in the π-π' and π-σ' polarization channels were separated using a Cu (220) crystal analyzer, which acts as a polarization filter and reduces the fluorescence background in front of the Avalanche photodiode (APD) detector used.

First of all, using π-polarized incident X-rays and the crystal analyzer in the π-π' channel, we located charge reflections to refine the orientational UB matrix. Then, in the same polarization channel magnetic reflections characteristic of the AF1 and AF2 phases [with propagation vectors $\mathbf{k}_1 = (1/2, 1/2, 1/2)$ and $\mathbf{k}_2 = (1/2, 1/2, 1/2 \pm q)$, respectively] were found at the Fe K absorption edge. It is worth underlining that the magnitude of the RMXS intensity, which was found to be several orders of magnitude ($\sim 10^7$) weaker than that of charge scattering reflections, made the location of magnetic reflections very challenging. Ensuring an accurate determination of the orientation matrix helped in the location of those extremely weak peaks.

The intensity of magnetic reflections in the π-π' channel was measured versus the incident photon energy across the Fe K edge. To maintain the **Q** reflections fixed over the energy dependent measurements, the theta positions were automatically recalculated and corrected for each energy value. Fig. 7.13(b) shows two energy scans measured at 300 K (AF1) and 10 K (AF2) on magnetic reflections (3.5 0.5 3.5) and (3.5 0.5 3.6), respectively. In these energy scans, Fe K pre-peak intensities at ≈ 7.113 keV are due to Fe $1s \rightarrow 3d$ (Fe) quadrupolar or $1s \rightarrow$ O $2p$ dipole-allowed transitions. The two well defined features in a narrow energy range, peaking at E = 7.125 and 7.128 keV above the Fe K pre-edge are attributed to RMXS. For the measurement of magnetic reflections the incident energy was fixed to E = 7.128 keV [indicated by the dashed vertical line in the energy scans of Fig. 7.13(b)]. The RMXS origin of this intensity was confirmed by its temperature dependence. Fig. 7.13(c) shows the evolution of the (0.5 0.5 3.5) magnetic reflection in the AF1 commensurate phase recorded under cooling. As expected from susceptibility and neutron measurements, the magnetic peak was missing below $\mathrm{T_S} = 195$ K. The magnetic origin of the reflections was further corroborated by $\mathrm{Q_L}$-scans collected along the (0.5, 0.5, L) line (in the range 3.4<L<3.6) [see Fig. 7.13(d)], where we can see that the AF1 (0.5 0.5 3.5) reflection is split into the two (0.5 0.5 3.5$\pm q$) incommensurate satellites characteristic of the AF2 phase.

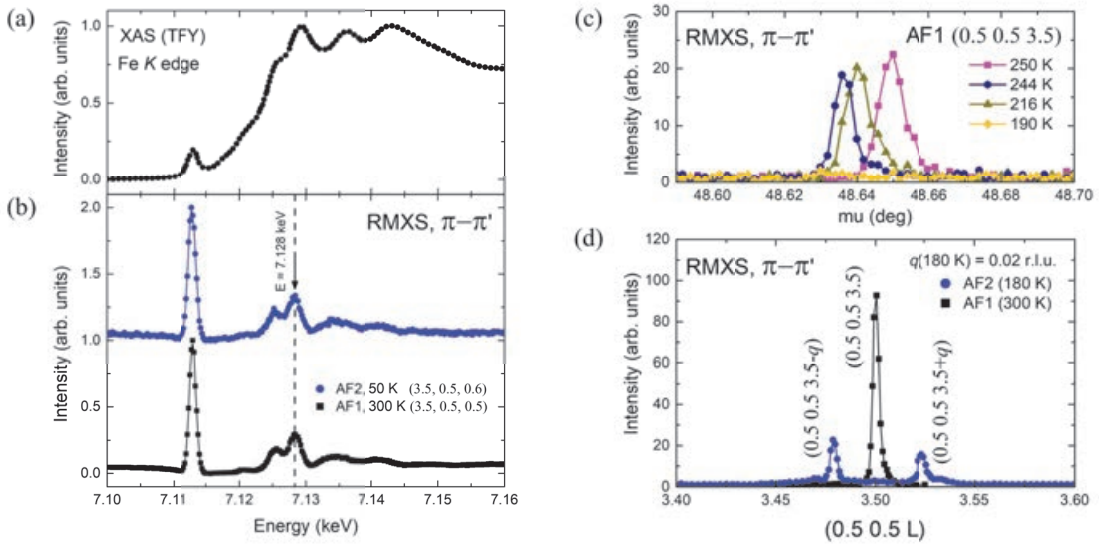

FIGURE 7.13: (a) XAS spectra measured by TFY in the YBCFO single crystal across the Fe K edge. (b) Energy dependence of the RMXS signal, filtered in the π-π' channel, measured on the forbidden lattice reflections (3.5 0.5 0.6) at 50 K (AF2 incommensurate phase, blue circles) and the (3.5 0.5 0.5) reflection at 300 K (AF1 commensurate phase, black squares). The spectra were normalized to the maximum intensity values. Blue points curve was vertically shifted for the sake of clarity (ΔInt=+1). The dashed vertical line indicates the incident energy used for the RMXS measurements. (c) Temperature dependence of AF1's (0.5 0.5 3.5) magnetic reflection at the Fe K edge (π-π' channel). (d) Q_L scans around the (0.5, 0.5, L) line (range 3.4<L<3.6) obtained at both "sides" of the spiral transition ($T_S = 195$ K). Black circles (300 K) show a single magnetic reflection at (0.5 0.5 3.5), and blue circles (180 K) display the (0.5 0.5 3.5$\pm q$) satellites characteristic of the incommensurate phase.

As mentioned, the main goal of the here reported RMXS study was to probe the magnetoelectric response of the spiral phase in our YBCFO single crystal. According to the DM antisimmetric exchange mechanism, at zero field the electrical polarization in the case of $\mathbf{k}_2 = (1/2, 1/2, 1/2 \pm q)$ propagation vector is expected to develop along the b (or a) directions, whereas its magnitude is related to the inclination of the rotation plane of the spins, being maximal for a cycloidal magnetic order, and zero in the case of pure helical order. A key feature of chiral multiferroic compounds is the possibility to control the electrical polarization by modifying the population of magnetic chiral domains (defined by the handedness of the spirals) by the application of electric fields. The direction of the electrical polarization, then, could be switched by reversing the population of chiral domains. The use of resonant magnetic scattering by circularly polarized X-rays with linear polarimetry analisis of the scattered beam offers a strong sensitivity to the imbalance in the chiral domain populations, since the handedness of the circular polarisation naturally couples to the sense

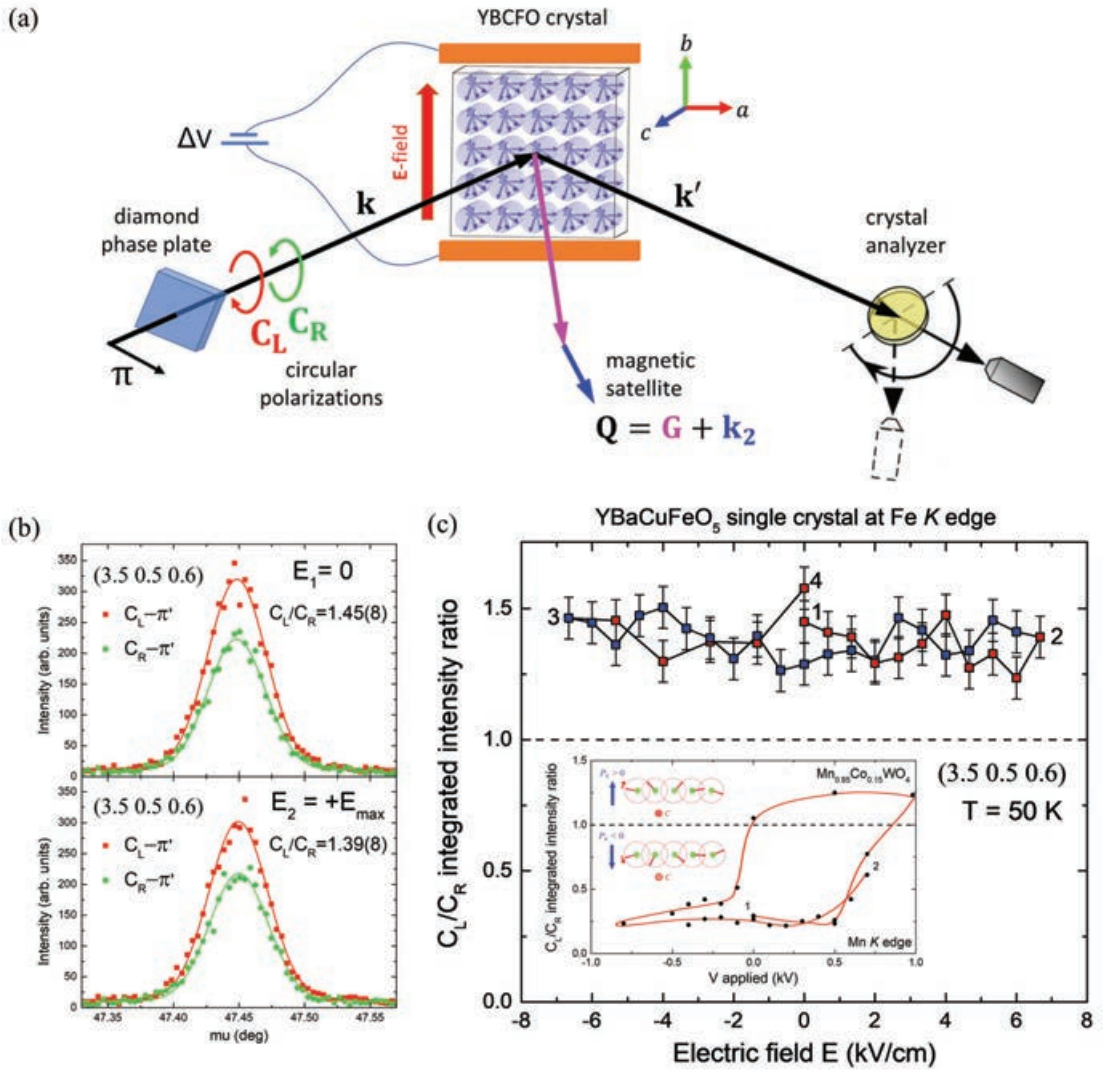

FIGURE 7.14: (a) Experimental setup used to measure the magnetic satellites in YBCFO using circularly polarized incident X-rays and electric fields applied along the b direction of the crystal. (b) π'-polarization channel analysis of the $(3.50.53.6)$ magnetic satellite for $\mathrm{C_L}$ (red squares) and $\mathrm{C_R}$ (green circles) incident polarizations, recorded at zero electric field ($\mathrm{E_1} = 0$) and at the maximum positive electric field applied ($\mathrm{E_{max}} \approx 6.67$ kV/cm). (c) Evolution at 50 K of the oriented magnetic chiral domains parametrized by the $\mathrm{C_L/C_R}$ ratio of the $(3.50.53.6)$ integrated intensity along a complete [-$\mathrm{E_{max}}$,+$\mathrm{E_{max}}$] cycle, being $|\mathrm{E_{max}}| \approx 6.67$ kV/cm. From 1 to 4, red(blue) points indicate measurements increasing(decreasing) E-field. Inset for comparison: Ratio of magnetic domains with positive/negative helicity spirals in ME AF2 phase of $\mathrm{Mn_{0.85}Co_{0.15}WO_4}$ single crystal (Mn K edge at 7.5 K) along a complete E-field cycle (E$\parallel b$ axis).

of rotation of the magnetic moments, bringing to an accurate description of the domain state.

The magnetoelectric coupling in YBCFO was studied applying electric fields parallel to the (010) direction [see Fig. 7.12(a)]. For this end the RMXS response

in the (0.5 0.5 3.6) incommensurate reflection at 50 K was measured as a function of the chirality of circularly polarized incident X-rays in the Fe K edge. Fig. 7.14(a) illustrates the experiment conducted in the I16@DLS beamline to study the chiral domain distribution as a function of poling E-fields along b. Incident circular left ($\mathrm{C_L}$) and circular right ($\mathrm{C_R}$) polarizations were generated from the initially π-polarized photons using a diamond quarter-wave phase plate retarder. Aiming for signal-to-noise ratio minimization the azimuthal rotation (ψ) on the (3.5 0.5 3.6) reflection was optimized and an harmonic rejection mirror was set up. The $\mathrm{C_L}$-π' and $\mathrm{C_R}$-π' magnetic intensities of this reflection were recorded at several values of bias V applied across the sample ranging from -$\mathrm{V_{max}}$ to +$\mathrm{V_{max}}$, being $|\mathrm{V_{max}}| = 1$ kV (separation between holder plates was $\sim$1.5 mm). Fig. 7.14(b) shows the (3.5 0.5 3.6) magnetic satellite at zero field (E=0 kV) and at the maximum electric field ($\mathrm{E_{max}} \approx 6.67$ kV/cm) that could be applied safely to avoid sample damage due to dielectric breakdown. The population of chiral magnetic domains was parametrized by the ratio between integrated intensities of the (3.5 0.5 3.6) reflection measured under $\mathrm{C_L}$ and $\mathrm{C_R}$ incident polarizations. Henceforth this parameter will be denoted as $\mathrm{C_L/C_R}$. A zone equally populated with left- and right- handed chiral domains would correspond to a $\mathrm{C_L/C_R} = 1$ ratio, whereas ratios $\mathrm{C_L/C_R} > 1$ or $\mathrm{C_L/C_R} < 1$ are indicative of predominance of one type of chiral domain. In Fig. 7.14(b) we can see that $\mathrm{C_L}$-π' and $\mathrm{C_R}$-π' measurements display remarkably different intensities, indicating a magnetic domain decompensation in the area illuminted by the beam. However, the evolution of the $\mathrm{C_L/C_R}$ ratio measured along a complete [-$\mathrm{E_{max}}$,+$\mathrm{E_{max}}$] cycle with maximum electric field $|\mathrm{E_{max}}| \approx 6.67$ kV/cm, disclosed in Fig. 7.14(c), shows no significant deviation within errors from the initial $\mathrm{C_L/C_R} \approx 1.45$ ratio, let alone a chiral domain population reversal. This behavior is far from the expected in spiral magnetic order multiferroics, where spin orbit coupling is at the origin of the interplay between an external electric field and the magnetic chiral domain state. In such materials, according to the DM antisymmetric exchange mechanism, the switching of electrical polarization is achieved by reversing the chirality of magnetic spiral domains as a consequence of the application of an external electric field. As an example, the inset in Fig. 7.14(c) shows as a reference case the magnetoelectric response measured in I16@DLS beamline on a single crystal of the $Mn_{0.85}Co_{0.15}WO_4$ wolframite, which displays cycloidal magnetic order in a narrow temperature range (AF2 phase, 6 K$< \mathrm{T_{N2}} <$10 K) with propagation vector $\mathbf{k} = (-0.214, 1/2, 0.457)$ (unpublished data ontained from internal communications, complementary to Ref.

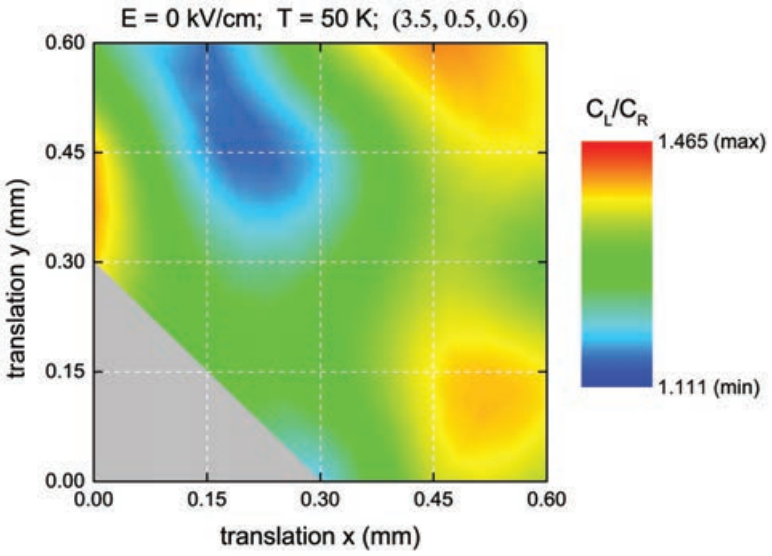

FIGURE 7.15: Topographic map of the C_L/C_R intensity ratio at 50 K and zero electric field obtained by circularly polarized incident X-rays at the Fe K edge. Measurements were done on the magnetic satellite reflection (3.5 0.5 0.6) in π' polarization channel. A 5×5 array of measurements were done along the crystal surface as represented by the white dashed lines covering a 0.6×0.6 mm^2 surface area with $\Delta x = 0.15$ mm and $\Delta y = 0.15$ mm tanslations. The colours represent zones with different C_L/C_R ratio, and the gray area at the bottom left corner corresponds to a sample edge.

[132]). The shown C_L/C_R intensity ratio, which was measured at the I16 beamline at the Mn K edge at 7.5 K nominal temperature, shows that in this material the ratio of magnetic domains with positive/negative helicity spirals can be reversed under in-situ application of an E-field (E$\parallel b$ axis), and that the ME response is generated exclusively by Mn spins order.

Finally, a real space map of the C_L/C_R intensity ratio was measured at 50 K in zero electric field conditions along the YBCFO crystal surface covering a 0.6×0.6 mm^2 area. The 2D surface map shown in Fig. 7.15 allowed to resolve inhomogeneities in the domain populations, as evidenced by the variation of the C_L/C_R ratio (represented by a color scale). The $C_L/C_R > 1$ ratios observed suggest the dominance of one type of chiral domain in the area analyzed. Remember that from neutron measurements, which provide averaged information on the full crystal volume, we proved that nearly identical amounts of left- and right- handed chiral domains were present in similar electric field and temperature conditions. Hence, the existence of zones with $C_L/C_R < 1$ is also expected. Further work is necessary to confirm this.

In summary, the results obtained from RMXS are fully compatible with the single crystal neutron diffraction and neutron polarimetry observations. The

$C_L/C_R > 1$ RMXS intensity ratios support the existence of the noncollinear spiral order, which displays an inhomogeneous distribution of chiral domains as suggested by the surface mapping. In addition, the absence of magnetoelectric coupling is in agreement with a purely helical magnetic spiral as observed from neutron experiments.

7.9 Probing the anisotropy of the magnetic spiral response to magnetic fields

In the case of spiral magnetic order it is clear that the orientation of the rotation plane of the spiral plays a very important role in the presence of electric polarization, as well as on its direction and magnitude. In this sense, as observed in the $Mn_{1-x}Co_xWO_4$ family of multiferroic compounds [129], the application of magnetic fields could induce modifications on relevant characteristics of the spiral such as its eccentricity or the direction of the magnetic easy-axis. This has a great relevance in the case of the YBCFO single crystal studied in this chapter, where the absence of magnetoelectric response in the ICM phase could attributed to the purely helical configuration of the spins and the generation of a cycloidal component would be beneficial in virtue of the DM interaction. Very little is known about the response of the spiral to magnetic fields. Moreover, J. Lyu *et al.* [51] have very recently reported the observation of weak ferromagnetism (WFM) linked to the high-temperature spiral phase when the sample is cooled under magnetic field (3×10^{-4} μ_B/f.u. at 7 T, not detectable using neutrons). Although this finding needs to be corroborated and the existence of coupling between the orientation of the spiral and the WFM component is not proved yet, this could open the way to a magnetic field-driven modification of the spiral orientation, directly related to the polarization direction. Disposing of quality spiral single crystals allows investigating the anisotropic response to magnetic fields.

In our magnetometry measurements, the M(H) curves shown in Fig. 7.16(a) disclose very different responses under dc fields applied along the principal crystallographic directions. For H parallel to the in-plane direction ($H \parallel b$, top panel), we observe field-induced transitions at relatively low fields (1-7 T range, according to the maxima in the $\delta M/\delta H$ derivative), and the noticeable presence of hysteresis indicating a first-order transition. In contrast, for H applied along the perpendicular direction ($H \parallel c$, bottom panel), M(H) evolutions show no

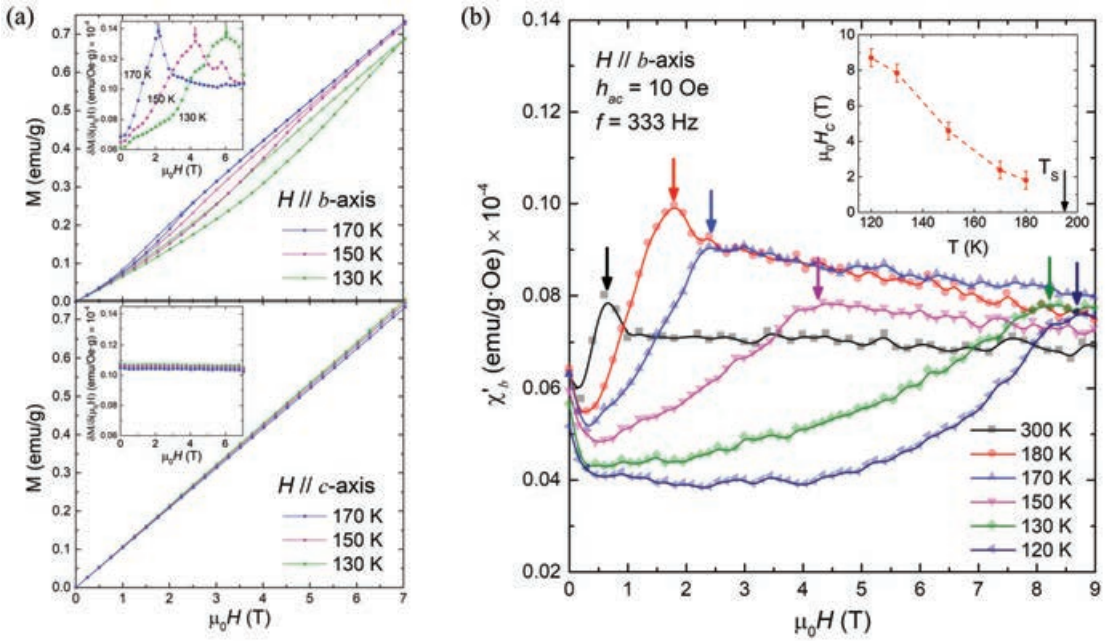

FIGURE 7.16: (a) Isothermal magnetization curves along the principal crystallographic directions versus dc magnetic field measured at different temperatures (170 K, 150 K, 130 K) below T_S =195 K (top panel: $H /\!\!/ b$, bottom panel: $H /\!\!/ c$). Insets: first order derivative of the magnetization with respect to the applied field. (b) Real component of the ac susceptibility versus superimposed dc field amplitudes along the b axis (χ'_b), measured at different temperatures (300 K, 180 K, 170 K, 150 K, 130 K and 120 K). The sample was heated to the collinear phase (above T_S) and cooled in ZF before recording complete [0T,9T] magnetic field cycles at each fixed temperature. For clarity reasons only curves increasing H are plotted, the complete curves are shown in Fig. C.2 [App. C].

signs of field-induced transitions, at least up to 7 T (notice the flat $\delta M/\delta H$ evolution). This anisotropic magnetic response is explained by the orientation of the magnetic easy-plane in this crystal. In accordance with our neutron studies, the spins in the helical magnetic spiral are not being modified by the influence of a perpendicular magnetic field (namely, parallel to the chirality vector of the spiral $\mathbf{Q} = \mathbf{S}_i \times \mathbf{S}_j$).

To better monitor the above described field-induced departure from the linear variation of magnetization with field applied along the b direction, we studied the ac susceptibility at fixed temperatures as a function of the dc field, superimposed in the same direction as the ac field. The in-phase component of the susceptibility χ'_b illustrated on Fig. 7.16(b) shows that the transition becomes more defined as we approach to the spiral-to-collinear transition at $T_S = 195$ K. In addition, the critical field H_c for the field-induced transition (defined as the maximum in the χ'_b susceptibility, which should correspond to the maximum

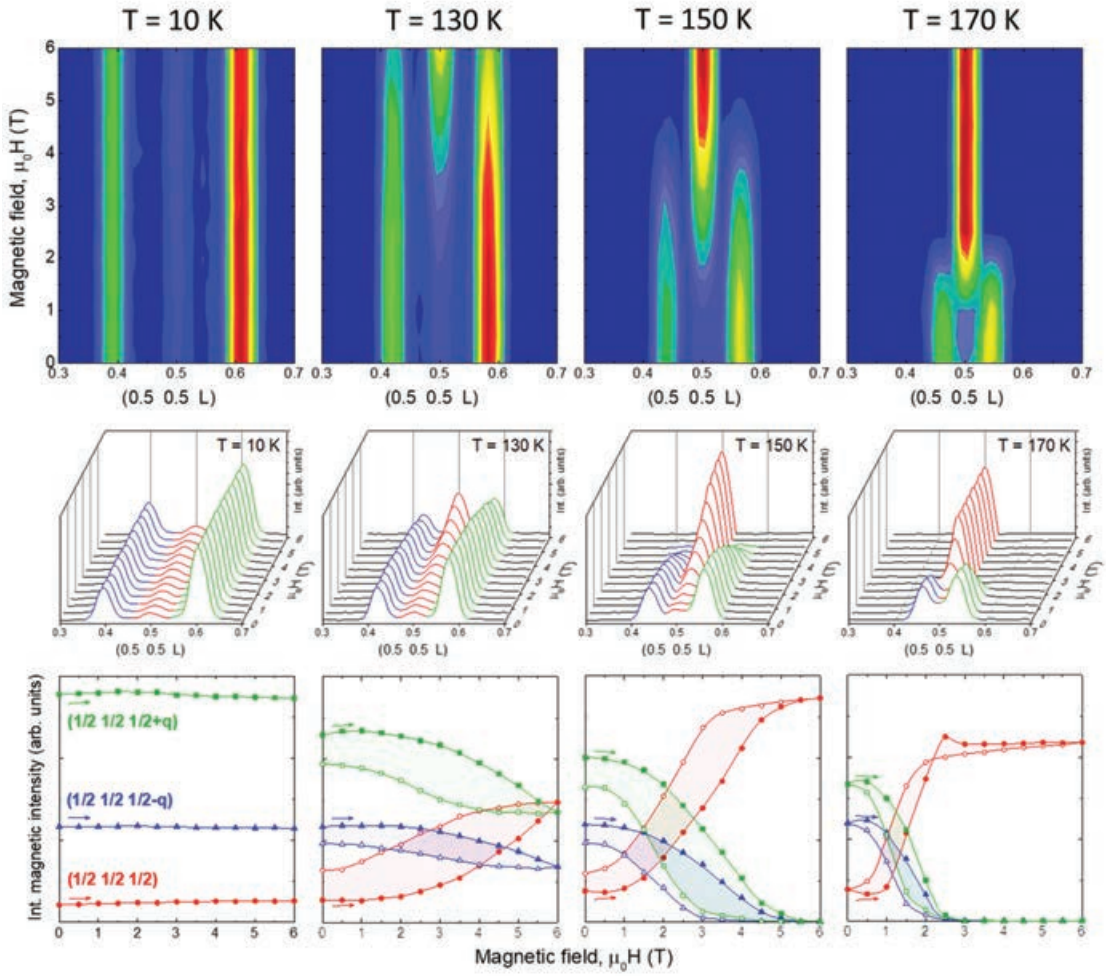

FIGURE 7.17: Single crystal neutron diffraction under magnetic fields applied parallel to the b axis (q-scans using D10). H-Q_L 2D projections and contour maps showing the isothermal magnetic field dependence (up to 6 T) of the Q_L scans along the (0.5, 0.5, L) line centered around the (½ ½ ½) position (range 0.3<L<0.7), measured at selected temperatures below $T_S = 195$ K. The integrated intensities of the (0.5 0.5 0.5) and (0.5 0.5 0.5±q) magnetic Bragg reflections associated to the $\mathbf{k}_1$ and $\mathbf{k}_2$ propagation vectors are also plotted upon increasing and decreasing magnetic fields (represented by filled and empty symbols, respectively).

slope in the dc magnetization curves), decreases down to fields as low as 1.8 T at 180 K [the evolution of H_c is plotted in the inset of Fig. 7.16(a)]. Interestingly, at 300 K a susceptibility peak shows up at ≈ 0.6 T, indicating the existence of a field-induced process also in the collinear phase.

In order to get insight on the nature of these field-induced magnetic transitions, multiple Q_L-scans along the (0.5, 0.5, L) line (range 0.3<L<0.7) were recorded on the D10 single crystal neutron diffractometer using a 6T cryomagnet. In particular, the magnetic evolution of the circular spiral phase contained in the

ab plane was characterized at fixed temperatures $\mathrm{T} < \mathrm{T_S}$ under magnetic fields applied along the b axis. The H-$\mathrm{Q_L}$ projections in Fig. 7.17 display in a visual way the impact of magnetic field in the spiral. At 10 K, the (0.5, 0.5, 0.5$\pm q$) incommensurate satellites are invariant for fields up to 6 T, denoting a strong stability of the spiral phase at low temperature. According to magnetometry, this stability range of the spiral should be maintained up to ∼130 K, where the critical field becomes low enough ($\mathrm{H_C}$<6 T) and the magnetic phase starts to display a strong response to magnetic fields. The evolutions obtained on temperatures above 130 K show that the spiral order is gradually suppressed in favour of a commensurate (CM) magnetic phase with $k_z = 1/2$ translational symmetry. This is very clear from the evolution of the integrated (0.5 0.5 0.5) and (0.5 0.5 0.5$\pm q$) magnetic intensities. In measurements done at 130 K, the transition is not completed up to the highest applied field of 6 T, and complete transition are observed at 150 K and 170 K. Despite the impact of magnetic field on the spiral is similar to that of temperature, we should highlight two remarkable differences: (i) the transition is characterized by the coexistence of the two phases along a finite range of magnetic field, which becomes narrower for temperatures closer to $\mathrm{T_S}$, in agreement with the susceptibility; (ii) along the transition, the magnetic field produces an insignificant effect on the separation between the two (0.5 0.5 0.5$\pm q$) satellites, as confirmed by the $q_s(H)$ evolutions (plotted in Fig. C.3 [App. C]). Whereas more investigations are necessary to elucidate which is the mechanism leading to the destruction of the spiral, and to determine the new stabilized CM structure, a remarkable finding is that the transition is not caused by a continuous reduction of the twist angle (canting) formed by the two spins in the bipyramids, which would eventually produce the CM collinear order. Another interesting observation is the persistence of certain amount of CM phase when the magnetic field is retreated after reaching the magnetic transition. The fraction of remanent CM phase increases as temperature decreases. Hence, the hystheresis observed in the magnetometry curves is explained by the competition of the two magnetic phases.

The intensity of selected nuclear reflections was also monitored to asses the possible emergence of ferromagnetic phases with $\mathbf{k}$ =(0,0,0) propagation vector. From the evolution under field of the (100) and (001) integrated intensities at 150 K and 10 K, shown in Fig. C.4 [App. C], we did not observe any signature of the field-induced WFM reported in Ref. [51] for YBCFO powder samples. This is not surprising, as WFM requires a FC process, and in our NPD measurements the crystal was cooled in zero field (ZFC). Furthermore, according to the

extremely small value of the net magnetization reported in [51] (3×10^{-4} μ_B/f.u. at 7 T), the WFM signal under FC would be far below the detection limit of our data. In this regard, it should be also mentioned that the signature of a ferromagnetic phase was neither observed in the SQUID magnetization curves, as no net remanence was detected after decreasing the magnetic field from 7 T. In any case, to demonstrate the presence of WFM in our crystal would require a specific study using special measurement routines such as the so-called PUND (positive-up negative-down) protocol, used in Ref. [51] to measure the WFM hystheresis cycles in powder samples.

7.10 Summary

The realization of "*spiral order by disorder*" has been thoroughly investigated in a single crystal of YBCFO with a cationic disorder level of $n_d = 0.31(2)$, grown by a modified version of the traveling solvent floating zone technique. The crystal exhibits a modulation $q_S = 0.104$ r.l.u. and a commensurate-to-incommensurate transition at $T_S = 195$ K, higher than in most known spiral-induced multiferroic type-II materials.

The limitations of NPD forced us to investigate the real magnetic nature of the "so-called" spiral magnetic phase of YBCFO by means of (i) unpolarized single-crystal neutron diffraction (SCND), (ii) spherical neutron polarimetry (SNP) and (iii) synchrotron resonant magnetic X-ray scattering (RMXS). This unavoidable study was necessary to remove the ambiguities that persisted in the literature about this important family of perovskites, mainly due to the lack of single-crystals.

Collinear modulated and non-collinear spiral models, including the analysis of magnetic and chiral domains, were confronted to the experiments on crystals using these quantum-beam techniques. In the crystal studied the emerging picture requires the combination of two perpendicular modulations to give a non-collinear circular helicoidal order below $T_S = 195$ K, in which the interplay of the modulation and the transition temperature matches the prediction of the Scaramucci model. Equally populated ±1 magnetic chiral domains were found in crystals of macroscopic size using neutrons, although RMXS allowed to resolve spatial inhomogeneities in the chiral domain populations of the helicoidal phase.

In the AF1 ordering of the crystal, collinear moments were found parallel to the ab plane and aligned along the diagonal axis. The volume fractions of the

conjugated (twin) domains [D1/D2 = 53/47(0.5) $\%$] in AF1 were close but more decompensated than the fractions of chiral domains found in AF2. This suggests that a given type of collinear AF1 domain generates below $\mathrm{T_S}$ any of the two types of chiral domains, indistinctly.
Spherical neutron polarimetry results validate and give robustness to the helicoidal description obtained from unpolarized neutron experiments on the single crystal. We disclosed a deviation of the magnetic phase φ' between $\mathbf{m}_1$ and $\mathbf{m}_2$ moments in the chemical cell when enters the helicoidal order not predicted in the model. Instead of perfectly antiparallel, in the spiral configuration Fe and Cu spins in the unit cell form $\varphi'_{\mathrm{S}} = 172(1)^{\circ}$.
Application of electrical fields parallel to (1-1 0) (SNP) and to (0 1 0) direction (RMXS by circularly polarized x-rays with linear polarimetry analysis) did not modify the population of chiral domains, where the spin rotation plane of the circular helix was parallel to the ab plane. The absence of magnetoelectric coupling is in agreement with a purely helical magnetic spiral.

First, this work confirms the ability of this family of compounds to stabilize a high-temperature magnetic spiral. Second, the work evidences the need to develop efficient strategies to fabricate YBCFO-type perovskites as single crystals, epitaxial films or heterostructures where the chiral spiral order may be formed with predominant cycloidal configuration. If Dzyaloshinskii-Moriya interaction turns out to be too small to facilitate cycloidal spiral in our crystal, it is of importance to pursue the exploration of strategies able to enhance the DM coupling or facilitate non-null cycloidal components. Some recent works seem to indicate that a higher B-site disorder, some selected partial cationic substitutions or stress-based strategies in films through appropriate selection of the substrates could locally modify the tetragonal symmetry and/or favor an easy-magnetic plane not orthogonal to the c axis, the direction of the ICM magnetic modulation.

Part III

Magnetostructural properties of ε-Fe_2O_3, a high-T_C multiferroic with super-hard ferrimagnetism

Chapter 8

Complex magnetism investigated in the frustrated ε-Fe_2O_3 multiferroic

8.1 Introduction

Iron oxides constitute an exceptional family of materials that have been studied for many decades, because they present fundamental interest and proved and promising applicability for new technologies based on biochemical, magnetic, catalytic or multiferroic properties [72, 145–147]. Apart from the amorphous Fe_2O_3, Iron (III) oxide shows four known polymorph crystal structures: α-Fe_2O_3 (hematite), β-Fe_2O_3 and γ-Fe_2O_3 (maghemite) and ε-Fe_2O_3 [75]. While hematite is the most common phase, ε-Fe_2O_3 is the most elusive and one of the less studied polymorphs. This is because its formation requires the mutually exclusive conditions of high temperatures and small sizes [60, 62, 148]. The use of sol-gel methods with Si alcoxides and Fe salts made it possible to confine Fe_2O_3 nanoparticles in a silica matrix to prevent their growth while annealed above 1000 °C, allowing, for the first time, to obtain virtually pure ε-Fe_2O_3, opening the door to the study of this rare polymorph [61, 64, 149]. The structural characterization evidenced a complex non-centrosymmetric $Pna2_1$ structure isomorphous to the multiferroic $GaFeO_3$, with four Fe sites in the asymmetrical unit: three in octahedral and one in tetrahedral environments [62]. The coordination octahedra $Fe1O_6$ and $Fe2O_6$ are largely distorted, $Fe3O_6$ is a regular octahedron and $Fe4O_4$ is the tetrahedron. For clarity we will use the Fe1d, Fe2d, Fe3r, Fe4t atomic labels where "d", "r" and "t" refer to "*distorted*", "*regular*" and "*tetrahedral*" polyhedral coordination, respectively. The structural characteristics of ε-Fe_2O_3 will be further addressed in detail in Chapter

9. The magnetic studies revealed an unexpected huge room temperature coercivity: 20 kOe, making it the transition metal oxide with the highest coercivity and an appealing material for the next-generation high-density magnetic recording media, high-frequency electromagnetic wave absorbers or a building block for exchange coupled permanent magnets [65–67]. Moreover, other important functionalities of ε-Fe_2O_3 are related with its magnetoelectric[70] and multiferroic properties [72]. These properties, quite unique among single metal oxides, stem from the structural features specific to this polymorph, in spite of being considered a structural intermediate between α-Fe_2O_3 and γ-Fe_2O_3. Its structure produces a rich temperature-dependent diagram of magnetic phases. Between T_C = 500 K and T_{N2} = 150 K, ε-Fe_2O_3 exhibits a collinear ferrimagnetic structure due to the antiferromagnetic (AF) coupling (parallel to the a-axis) between dissimilar magnetic sublattices. This oxide then presents a broad low-temperature incommensurate magnetic transition starting at 150 K (ICM) [63, 68], characterized by a large reduction of the coercivity, the remanent and the saturation magnetization [68]. Under further cooling, below ∼85 K, the ground magnetic order is stabilized [66]. Noticeable anomalies in the dielectric permittivity were reported in conjunction with these two successive transitions [70]. In addition, significant magnetostriction effects were observed in the interval 85-150 K where magnetic changes take place and spin-lattice coupling brings about atomic shifts within the orthorhombic cell and a non-monotonous evolution of the Fe-O bonds [71]. A nonzero orbital magnetic moment (m_L ∼ 0.15 μ_B/Fe at RT under 40 kOe) was detected by X-ray magnetic circular dichroism (XMCD) in the super-hard collinear ferrimagnetic phase (150 K < T < 490 K), which is suppressed by the magnetostructural changes concurrent with the magnetic transitions within the 85-150 K interval. On cooling, the coercive field drops in that interval from 20 kOe to 0.8 kOe, and then increases again under further cooling in the low-temperature magnetic phase (ICM), below 85 K [67]. Likewise, a reentrant behavior of the orbital moment was also monitored by XMCD in the low temperature magnetic phase [67]. The concurrent magnetostructural changes in the coordination polyhedra around Fe^{3+} sites and the reentrant evolution of the orbital moment should be seen as the signature of a relevant spin-orbit coupling in this magnetoelectric compound. Finally, the RT coexistence of ferrimagnetism and ferroelectricity, albeit with a small magnetocapacitance response, in thin epitaxial films of ε-Fe_2O_3 further highlights the relevance of magnetoelastic couplings in this system, for which possible multiferroic properties in bulk form are still a subject of debate. Importantly,

although the Curie temperature of ε-Fe_2O_3 has been postulated as $T_C \sim 500$ K [61, 147, 150, 151] no systematic studies of the magnetic properties above this temperature can be found in the literature. The geometrical spin frustration and Spin-Orbit Coupling effects (SOC) provides a rich magnetic phase diagram with at least four different magnetic states in zero field (PM/FM1/FM2/ICM), which we have investigated in the present chapter. Some of them were previously unknown.

8.2 Sample preparation and experimental methods

Synthesis of ε-Fe_2O_3 nanoparticles

Polycrystalline ε-Fe_2O_3 was obtained thanks to the collaboration with Martí Gich (ICMAB-CSIC) who prepared a silica gel containing 28 wt% Fe_2O_3 from an hidroethanolic sol of tetraethyl orthosilicate (TEOS) of molar composition TEOS:Ethanol:water=1:5:6 containing dissolved iron nitrate nonahydrate. First, 5.4 ml of milliQ water and 26 ml of absolut ethanol (Panreac) were added to a 100 ml beaker and stirred for 5 min. Then, the 10.60 g of iron nitrate (Aldrich) were dissolved and the solution which attained a pH ∼0.35. Finally 20 ml of TEOS (Aldrich) were added dropwise to the solution under stirring (∼200 rpm). The stirring, with the beaker covered, was maintained for 20 minutes after adding the TEOS. The sol was then distributed in 6 cm diameter petri dishes, attaining a level of 2-4 mm, which were placed in a plastic box, closed with its cover but not hermetically sealed, and placed in chemical hood at 23 °C. Gelation took place in about two weeks. The gels were removed from the petri dishes, allowed to dry and subsequently grinded in a ceramic mortar to be further dried at 60 °C in a stove. Then the xerogels were placed in an alumina boat and treated in a tubular furnace in air atmosphere at 200 °C/h to 450 °C and then to 1100 °C at 80 °C/h, and were held for 3 h at this temperature before being cooled to room temperature at 350 °C/h. About 7.5 g of SiO_2/ε-Fe_2O_3 composite were obtained. The resulting material consisted of single crystalline ε-F2O_3 nanoparticles embedded in a silica matrix with an average diameter of around 20 nm as observed by transmission electron microscopy. The silica was etched in hot (80 °C) concentrated NaOH aqueous solution (12 M). For this purpose a round bottomed flask was filled with 180 ml of distilled water in which 76 g NaOH were dissolved, then about 5 g of SiO_2/ε-Fe_2O_3 composite were

added to it and stirred overnight in a hot plate set at 80 °C using a water refrigerated condenser to avoid evaporation of water and a silicone oil bath to maintain an homogeneous temperature around the flask. Then the suspension was centrifuged at 6000 rpm for 2 min and the supernatant was discarded. The collected solid was re-dispersed in water and the centrifugation was repeated twice. Finally the tubes used for centrifugation were placed in a stove at 60 °C and about 1.5 g of ε-Fe_2O_3 nanoparticles were collected after drying. The quality of the samples was assessed by transmission electron microscopy, magnetic measurements and X-ray diffraction [60, 68].

Characterization methods

- *Magnetometry:* The magnetic characterization, using dc and ac magnetic fields, was performed in collaboration with Martí Gich. He measured the as-prepared ε-Fe_2O_3 nanoparticles embedded in SiO_2 using a Superconducting Quantum Interferometer Device (SQUID) and a Vibrating Sample Magnetometer (VSM) in a Physical Properties Measuring System (PPMS) both from Quantum Design. For the VSM measurements the ε-Fe_2O_3/SiO_2 material was mixed with a high-temperature alumina cement. The use of ε-Fe_2O_3/SiO_2 composite instead of ε-Fe_2O_3 was necessary to avoid the transformation of ε-Fe_2O_3 to magnetite due to high temperatures and the vacuum environment during the measurements. The ac-susceptibility measurements were performed at 30 Hz and 1 kHz with a magnetic field amplitude of 4 Oe from 300 K to 750 K. The temperature dependence of the magnetization, M, was studied after zero field cooled (ZFC) and FC conditions under a dc field of 1 kOe from 300 to 900 K. Hysteresis loops were obtained between 900K and 300 K with a maximum applied magnetic field of 70 kOe.
- *Neutron powder diffraction:* Neutron diffraction experiments were conducted at the high-flux reactor of the Institut Laue Langevin (Grenoble, France) on D2B and D1B powder diffractometers. For the characterization of the high-temperature magnetic orders, NPD patterns were collected using the high-intensity, high-resolution D2B diffractometer of the Institute Laue-Langevin (ILL, Grenoble), between room temperature (RT) and 850 K (λ = 1.594 Å). For the magnetic characterization of the nanoparticles at low temperature, high quality neutron diffractograms were obtained at the high-intensity D1B powder diffractometer (λ = 2.52 Å) at fixed temperatures betewwn 1.5 K and 150 K, each one with an acquisition time of 30 min. Structural and magnetic Rietveld refinements were carried out using the Fullprof program [97]. Crystallographic

tools from the Bilbao Crystallographic server [102–104] and ISOTROPY Software Suite [105] were also used.

8.3 Unveiling successive high-temperature ferrimagnetic orderings in ε-Fe_2O_3

Initially, using diffraction and magnetometry techniques, I have investigated the magnetic and magnetostructural properties of ε-Fe_2O_3 nanoparticles at high temperatures (300 K < T < 900 K). In this section I will show that, contrary to the earlier accepted scenario, ε-Fe_2O_3 remains ferrimagnetic up to at least T = 850 K, although with a reduced magnetization and a moderate coercivity.

8.3.1 Magnetic characterization: beyond the ultra-hard ferrimagnetic phase

The temperature dependence of the ZFC and FC magnetization of the ε-Fe_2O_3 particles embedded in SiO_2 is plotted in Fig. 8.1(a). Two ferrimagnetic regimes with very different magnetic behavior can be clearly distinguished below and above ∼500 K (denoted FM2 and FM1 respectively). Remarkably, contrary to the scenario assumed in previous reports, the ferrimagnetic FM2 phase (previously reported to display super-hard ferrimagnetic response, with "gigantic" coercivity values exceeding 20 kOe) does not become paramagnetic above 500 K. The M(T) evolution in Fig. 8.1 reveals a second phase transition, evidencing the existence of a new ferrimagnetic state (FM1) between 500 K and ∼850 K. The transition temperature between FM1 and FM2 can be established at T_{N2} = 480 K by the lambda-shaped peak in the ac susceptibility vs temperature curve presented in the inset of Fig. 8.1(a). From the hysteresis loops at T > 500 K it can be clearly seen that FM1 presents a ferromagnetic behavior with finite net magnetic moment and coercivity, H_C.

However, as can be seen in Fig. 8.1(b) there is a drastic collapse of the large H_C (characteristic of FM2) and M[50 kOe] at T_{N2} = 480 K [see Figs. 8.1(b,c)]. Moreover, upon heating, M[50 kOe] undergoes a Brillouin-type monotonic decrease up to 550 K, although the coercivity (and remanence, M_r) sharply drop well before this temperature, having practically vanished around ∼480 K. Nevertheless, although H_C shrinks by more than a factor 10 from $H_C \sim 16$ kOe at RT, it remains moderate (∼400 Oe) even at T ≫ 500K (T_{N2}) [see Fig. 8.1(d)].

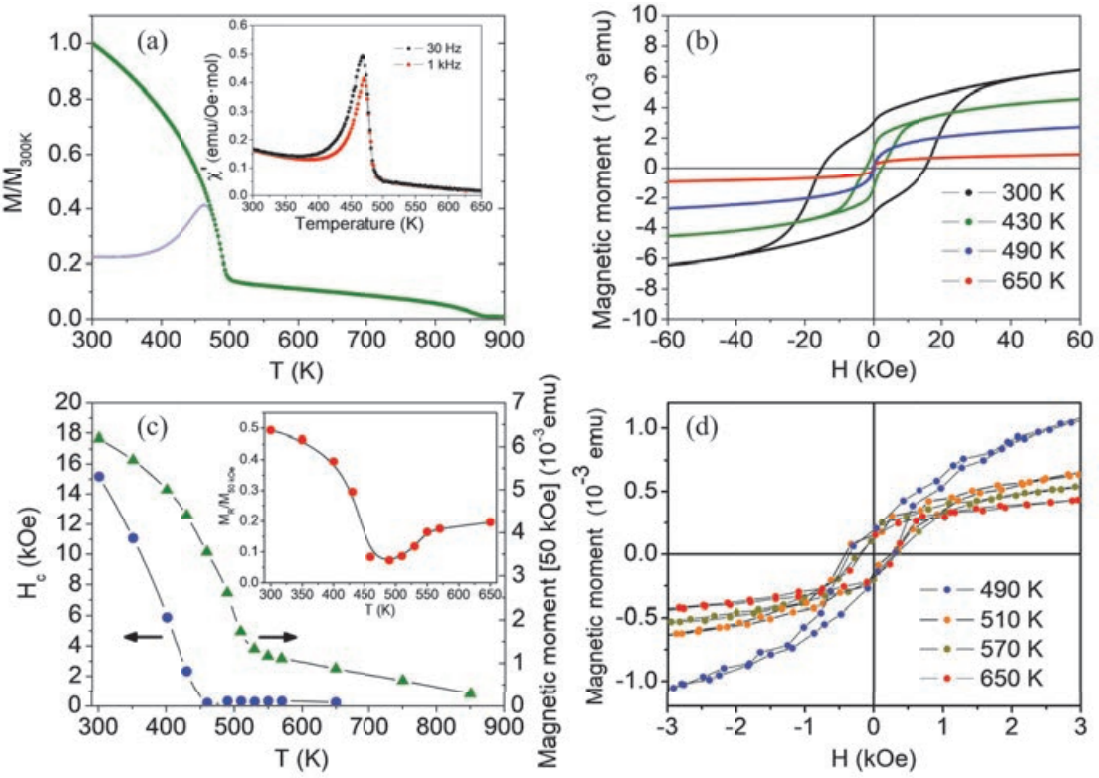

FIGURE 8.1: (a) FC (green) and ZFC (blue) dc magnetization curves (1 kOe) of the ε-Fe_2O_3 nanoparticles embedded in SiO_2 between 300 and 900 K. Inset: real part of the ac-susceptibility (h_{ac} = 4 Oe). (b) Temperature evolution of the coercive field (H_C; left axis) and net magnetic moment at 50 kOe (M[5 kOe]; right axis). Inset: dependence of the M_r/M[50 kOe] ratio. Hysteresis loops characteristic of (c) the FM2 phase and (d) the FM1 phase (note the different x- and y-scales in both figures, and the loops at 490 K and 650 K included in both panels for the sake of comparison).

Importantly, from the evolution of the magnetic properties it can be established that the critical temperature of the FM1 phase is about $T_{N1} \sim 850$ K. Hence, although there is a drastic breakdown of the super-hard ferrimagnetic state at T_{N2} = 480 K, it does not give rise to a paramagnetic phase, but it is transformed into a new softer ferrimagnetic state.

8.3.2 Neutron diffraction study of successive ferrimagnetic phases

To better understand the nature of the very high-temperature ferrimagnetic phase a systematic NPD study was performed. As can be seen in Fig. 8.2(a), the intensity of the magnetic peaks (011) and (002) progressively decreases as the temperature is increased from RT to 850 K. In agreement with the magnetization results, the intensity of the magnetic peaks remains finite even far above

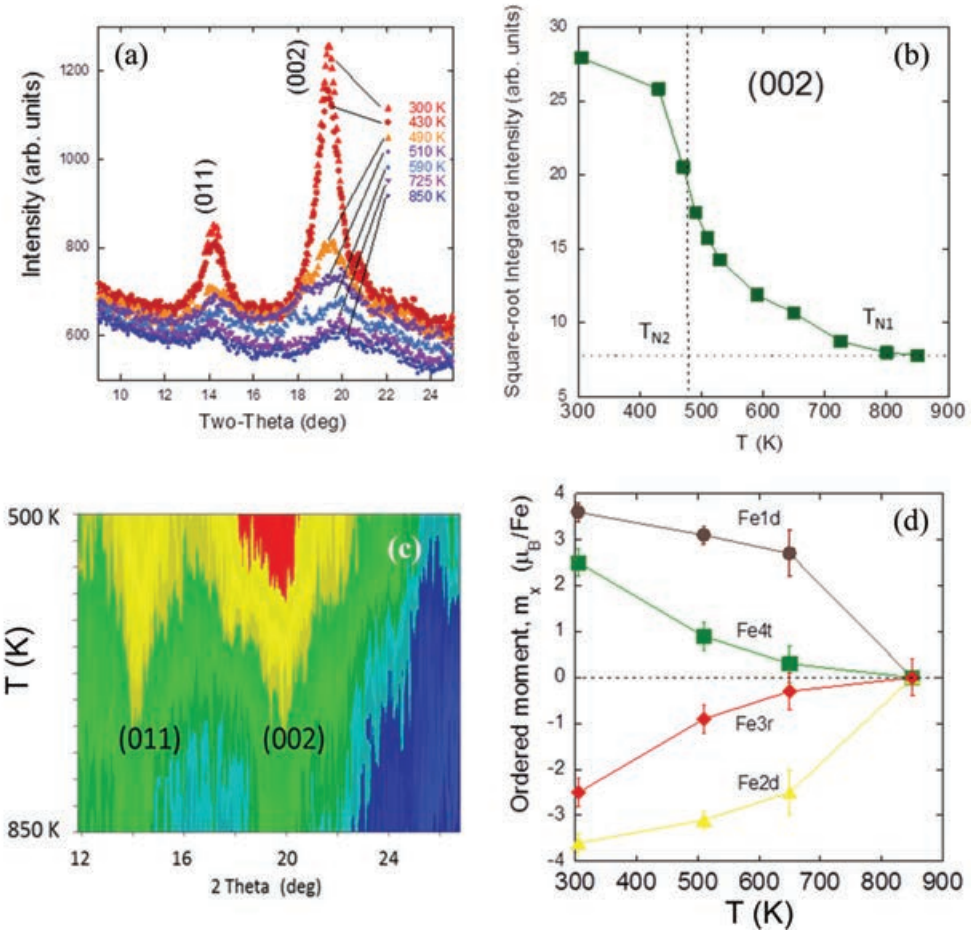

FIGURE 8.2: (a) Neutron patterns at selected temperatures in the range comprising the main magnetic peaks (011) and (002). (b) Square-root of the neutron integrated intensity of the strongest magnetic reflection (002). (c) Evolution of the neutron diffraction intensities above T_{N2} for the characteristic magnetic reflections. (d) Evolution of the ordered magnetic moments refined at Fe1d (brown), Fe2d (yellow), Fe3r (red) and Fe4t (green) sites in the structure.

T_{N2}. However, the temperature dependence of the squared root of the integrated intensity of the (002) peak (proportional to the ordered moment), shown in Fig. 8.2(b), strongly differs from a Brillouin-type evolution and exhibits the shape of a long magnetic tail that persists far beyond T_{N2}.

The magnetic structures and atomic ordered moments were fully analyzed using the neutron diffraction patterns at the two selected temperatures 305 K and 510 K. The former being representative of the ferrimagnetic phase FM2, and the second (above but close to T_{N2} = 480 K) of the new ferrimagnetic phase FM1. Note that the magnetic reflections detected between T_{N2}(= 480 K) and T_{N1}(∼850 K) do not indicate changes in the extinction conditions or the translational symmetry.

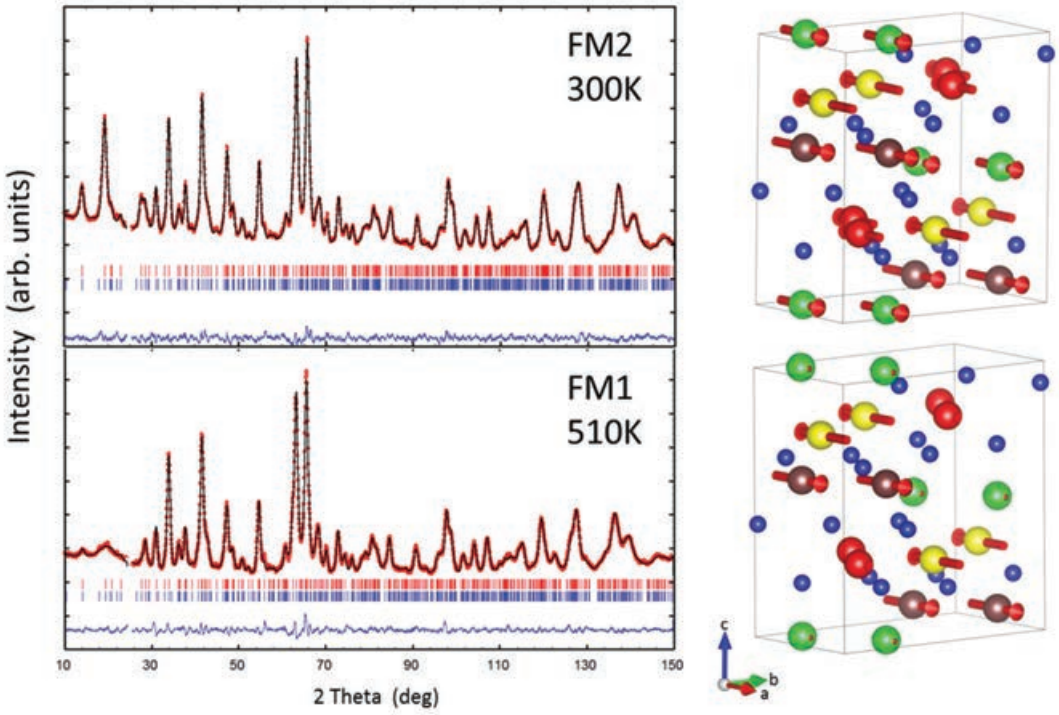

FIGURE 8.3: Neutron Rietveld refinement (black line) of the NPD patterns for ε-Fe_2O_3 obtained at 305 K ($T < T_{N2}$, FM2 ordering) and 510 K ($T_{N2} < T < T_{N1}$, FM1 ordering) (D2B, red circles: experimental points; bottom blue line: difference). Upper row of reflections correspond to the $Pna2_1$ structure, the lower one to the magnetic ordered phase ($Pna'2'_1$). Goodness factors at 305 K (510K): R_B = 2.48 (1.8), R_f = 1.55 (1.1), R_m = 2.92 (1.2), χ^2 = 0.31 (3.5). (Right) Schematic view of the FM1 (bottom) and FM2 (top) magnetic ordering at the same temperatures. Fe1d (brown), Fe2d (yellow), Fe3r (red) and Fe4t (green), O (dark blue).

Possible magnetic or Shubnikov space groups compatible with the $Pna2_1$ symmetry and null magnetic propagation vector $\mathbf{k} = (0,0,0)$ were considered. It was found that the magnetic ordering adopts the same magnetic space group (MSG) in the two ferrimagnetic phases, $Pna'2'_1$ [n. 33.147, transformation to standard settings: (**a**, **b**, **c**; 0, 0, 0)] [97, 102, 104]. The Rietveld refinement of neutron patterns at 305 K (FM2 magnetic phase) and 510 K (FM1 magnetic phase) are plotted in Fig. 8.3 and the results are summarized in Table 9.2.

Interestingly, despite the abrupt drop in the displayed by magnetization at T_{N2}, there are ordered magnetic moments with very large mx components that steadily persist in the interval T_{N2}(=480 K) < T < T_{N1}(=850 K) (m, magnetic moment). Nevertheless, they are found selectively in Fe1d and Fe2d octahedral sites. These two Fe positions are magnetically robust and persist antiferromagnetically coupled above T_{N2}. Their antiparallel ordered moments as refined at intermediate temperatures have been plotted in Fig. 8.2(d). Remarkably, the

main difference detected between FM2 and FM1 orders concerns the high degree of magnetic disorder at the Fe3rO_6 and Fe4tO_4 sites. Neutron data did not allow us discern ordered moments at Fe3r and Fe4t sites independently, and their moments were kept (above T_{N2}) identical and antiparallel, forcing m_x[Fe3r]= -m_x[Fe4t], in the neutron refinements. The refined m_x moments at these positions are also displayed in the Fig.8.2(d), which shows the evolution of the ordered moments (m_x) refined for the four Fe sites. In the high temperature phase the difference between the moments in one antiparallel pair (*e.g.* Fe3r/Fe4t) is smaller than our experimental error. At RT (305 K) the resultant net uncompensated moment ~0.2 μ_B/Fe (*i.e.* 14 emu/g) is in agreement with M_s values (net ferromagnetic signal) previously reported [64, 68]. Therefore, at

TABLE 8.1: Magnetic groups and refined magnetic moments in the ferrimagnetic FM1 (T_{N1}) and FM2 (T_{N2}) phases. The d, r and t labels of the four iron sites refer to distorted, regular and tetrahedral polyhedra, respectively). The goodness factors are given in Fig. 8.3.

Temperature	**300 K**	**510 K**
Magnetic Space Group	**Pna′2′$_1$** (n. 33.147)	**Pna′2′$_1$** (n. 33.147)
Transformation to standard setting	(**a**, **b**, **c**; 0, 0, 0)	
Fe atoms in the asymmetric unit	Coordinates Expressed in parent Ort. setting: Fe1d ≈ (0.193,0.149, 0.581) Fe2d ≈ (0.682,0.031, 0.792) Fe3r ≈ (0.809,0.158, 0.307) Fe4t ≈ (0.181, 0.153, 0.000)	
Magnetic phase	**FM2**	**FM1**
Refined moments	m_x[**Fe1d**] = 3.6 (1) μ_B/Fe m_x[**Fe2d**] = -3.6 (1) μ_B/Fe m_x[**Fe3r**] = -2.7 (1) μ_B/Fe m_x[**Fe4t**] = 2.5 (3) μ_B/Fe	m_x[**Fe1d**] = 3.1 (1) μ_B/Fe m_x[**Fe2d**] = -3.1 (1) μ_B/Fe m_x[**Fe3r**] = -0.9 (2) μ_B/Fe m_x[**Fe4t**] = 0.9 (3) μ_B/Fe
Magnetic structure	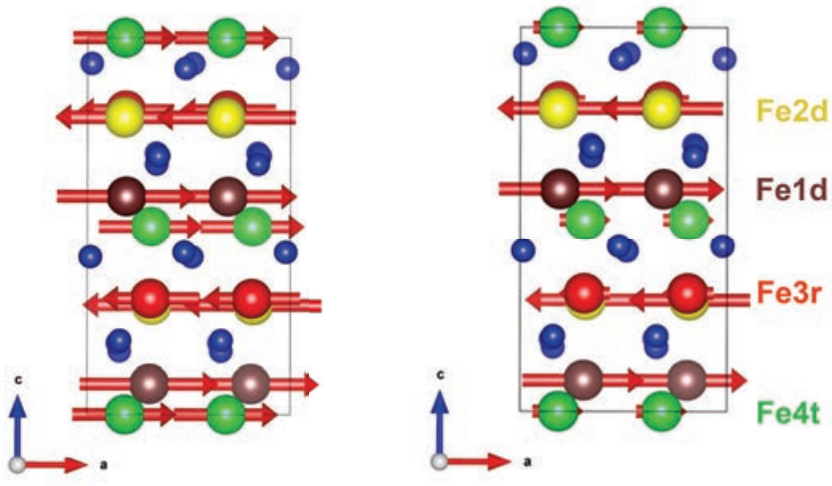	

the FM2/FM1 (hard/soft) ferrimagnetic phase boundary, there is a clear disruption of the magnetic order of the iron spins occupying the tetrahedral Fe4t and the undistorted octahedral Fe3r sites. The small moment values refined at 510 K indicate that Fe3r and Fe4t sublattices are practically disordered above T_{N2}. Likewise, the onset of magnetic ordering near 850 K is essentially driven by the AFM coupling of Fe spins in the more distorted octahedral positions (Fe1d and Fe2d). Fig. 8.2(d) clearly illustrates the anomalous evolution of the ordered moments at Fe3r/Fe4t sites. Most likely this evolution is the result of strong frustration effects between sublattices, which can be identified by the broad magnetic reflections at high temperatures.

Using a molecular-field model, the appearance of spontaneous magnetization in the FM2 phase of ε-Fe_2O_3 has been associated with the lower superexchange $Z_{ij}J_{ij}$ values of the tetrahedral site, compared to those of octahedral sites [150]. As can be seen in Fig. 8.2(d) the ordered moments at the Fe1d and Fe2d sites are larger than in the Fe4t tetragonal site in the whole range above room temperature, in concordance with the theoretical predictions. On another hand, our neutron diffraction results establish that the abrupt enhancement of the magnetization below T_{N2} takes place concurrently with the long-range ordering of Fe4t magnetic atoms occupying the tetrahedral site.

Interestingly, the new ferrimagnetic-paramagnetic boundary is shifted towards the upper characteristic ordering temperatures of ferrimagnetic iron oxides, 950 K for α-Fe_2O_3, 940 K for γ-Fe_2O_3 and 853 K for Fe_2O_3, indicating that ε-Fe_2O_3 presents comparable magnetic coupling strengths. Notably, the NPD analysis unambiguously demonstrates that the ordered magnetic components are associated to ε-Fe_2O_3, ruling out the possibility that the magnetic response above 480 K might be due to impurities of the ferrimagnetic oxides mentioned above, which present a completely different set of magnetic reflections [see Figs. D.1(a,b) in App. D.1]. Additionally, the fact that some of the magnetic peaks, although very broad, remain finite at 850 K may indicate the possible existence of a frustrated (with no long-range order) ferrimagnetic phase even above T_{N1}, similar to other oxide systems [152].

8.4 The incommensurate magnetic ground state in ε-Fe_2O_3

The large contrast between the magnetic properties of the successive phases in ε-Fe_2O_3 is illustrated in Fig. 8.4 from the temperature dependence of the magnetization and the coercive field between 10 K and 920 K. In the previous sections we have shown that above the ultra-hard ferrimagnetic (FM1) phase there is a soft ferrimagnetic order (FM1) where Fe3r and Fe4t moments are disordered. The soft FM1 phase displays a much smaller ferromagnetic component and vanishes above 850 K, where we find the PM state. This section will focus on the magnetic evolution below the ultra-hard ferrimagnetic phase (FM1) (T < 150 K), in which notable anomalies in the dielectric permittivity and a sheer reduction of the coercivity (from 20 kOe to 0.8 kOe) have been observed between 150 K and 100 K under cooling [see Fig. 8.4] associated to the onset of a commensurate-incommensurate transition (FIM2-ICM) [63, 68].

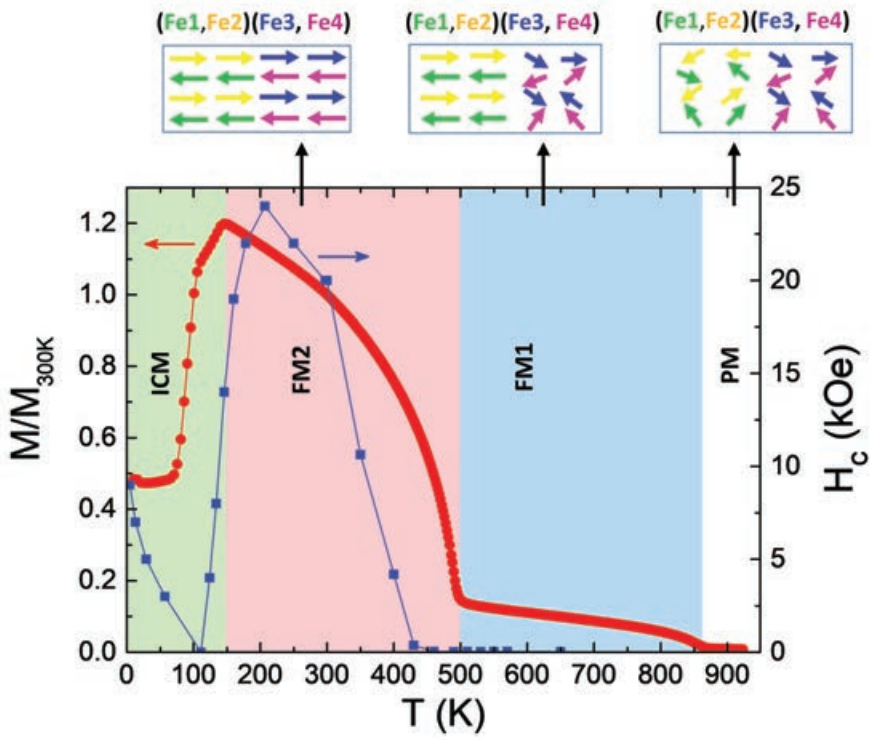

FIGURE 8.4: Successive magnetic phase transitions in ε-Fe_2O_3 shown from the temperature evolution of the FC dc M/M_{300K} normalized magnetization curves (red points; left axis) and the coercive field H_C (blue points; right axis). The sketches on top of the figure illustrate, from right to left, the paramagnetic phase (PM) and the successive soft (FM1) and ultra-hard (FM2) high-temperature ferrimagnetic orders.

Although the existence of an incommensurate magnetic phase below 150 K is well known and has been reported in previous works, its microscopic structure is still under debate. Different attempts to give an answer to this relevant question have been carried out by means of different techniques, which include Mössbauer spectroscopy [63, 153], neutron diffraction [63, 68] and Nuclear Forward Scattering (NFS) [76].
In the NPD study carried out by M. Gich *et al.* [63], it is mentioned that the helical or spiral magnetic structures (of constant m modulus) that could account for the narrow Mössbauer lines in the LT phase are inconsistent with the NPD fits, which were better explained using a collinear magnetic order model with sinusoidally modulated m amplitudes along the a axis. To make compatible the Mössbauer and NPD results, they proposed a possible solution consisting of a square-wave modulated structure (with constant m modulus), *i.e.* the superposition of a series of sinusoidally modulated structures whose propagation vectors are the harmonics of $\mathbf{k}_{\mathrm{ICM}}$. Although neutron diffraction data was thoroughly analyzed in Ref. [63], it didn't accomplish the quality necessary to unambiguously discern between the different proposed models.
On the other hand, Knyazev and co-workers reported that a non-collinear magnetic structure with the magnetic spiral as the ground state of the system could be compatible with the results obtained in a synchrotron NFS study [76]. In that work, in order to observe any transformation of the magnetic structure during the magnetic transition, a 4 T magnetic field was applied aimed to align the magnetic moments in the particles, hence promoting a measurable anisotropic NFS response. The main weakness of this work lies on assuming that the magnetic order is not significantly influenced by an external magnetic field. As it will demonstrated in this thesis, the ICM order is destroyed as a consequence of applying relatively low magnetic fields, which could indicate that the conclusions obtained in Ref. [76] are the result of a misinterpretation of the NFS data. Furthermore, ignoring what has been said, the magnetic properties of those ε-Fe_2O_3 nanoparticles could differ from ours due the notably smaller diameter (8 nm, closer to the superparamagnetic limit).

8.4.1 Neutron diffraction study of the incommensurate magnetic ground state

A detailed analysis of the ground magnetic order in ε-Fe_2O_3 using magnetic diffraction is still lacking. In order to fulfill this purpose, we extended our neutron

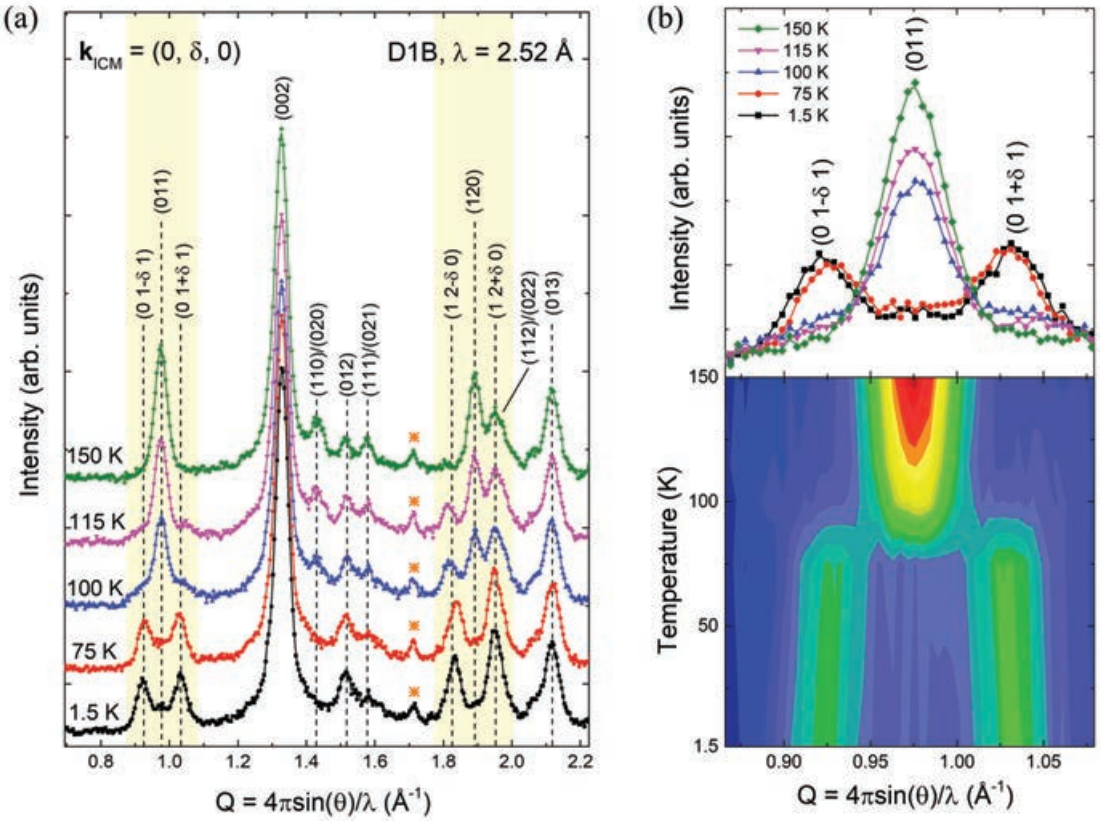

FIGURE 8.5: (a) Neutron powder diffraction (NPD) patterns (D1B@ILL, λ=2.52 Å) of the ε-Fe_2O_3 nanoparticles measured at 1.5, 75, 100, 115, and 150 K. The vertical dashed lines indicate the indexing of the most relevant nuclear and magnetic reflections. The asterisk signals the (012) structural reflection of the secondary α-Fe_2O_3 phase. (b) Profiles and contour map showing the T-Q projection of the temperature dependence for the neutron-diffracted intensities around the (011) reflection. The neutron intensities illustrate the emergence of the (0 1$\pm\delta$ 1) satellites characteristic of the ICM phase below $T_{ICM} \sim 150$ K with propagation vector $\mathbf{k}_{ICM} = (0, \delta, 0)$.

diffraction study to the low temperature range (T < 150 K) by collecting in the D1B diffractometer (λ = 2.52 Å) neutron patterns over a wider Q-range than in previous NPD studies. Fig. 8.5(a) shows the low Q region of the NPD patterns measured at five selected temperatures between 1.5 K and 150 K. From these measurements, we observe that the intensity of (011), (110), (111) and (120) commensurate magnetic reflections, characteristic of the super-hard ferrimagnetic phase (FM2) with null propagation vector, start to decrease, signaling the onset of the FM2-ICM transition. This agrees with the sharp kink observed in the M(T) curve at approximately $T_{ICM} \sim 150$ K (see Fig. 8.4). The reduction of the commensurate FM2 magnetic peaks is accompained by the emergence of new satellites near these reflections, which can be indexed with an incommensurate propagation vector $\mathbf{k}_{ICM} = (0, \delta, 0)$. The value of the incommensurability

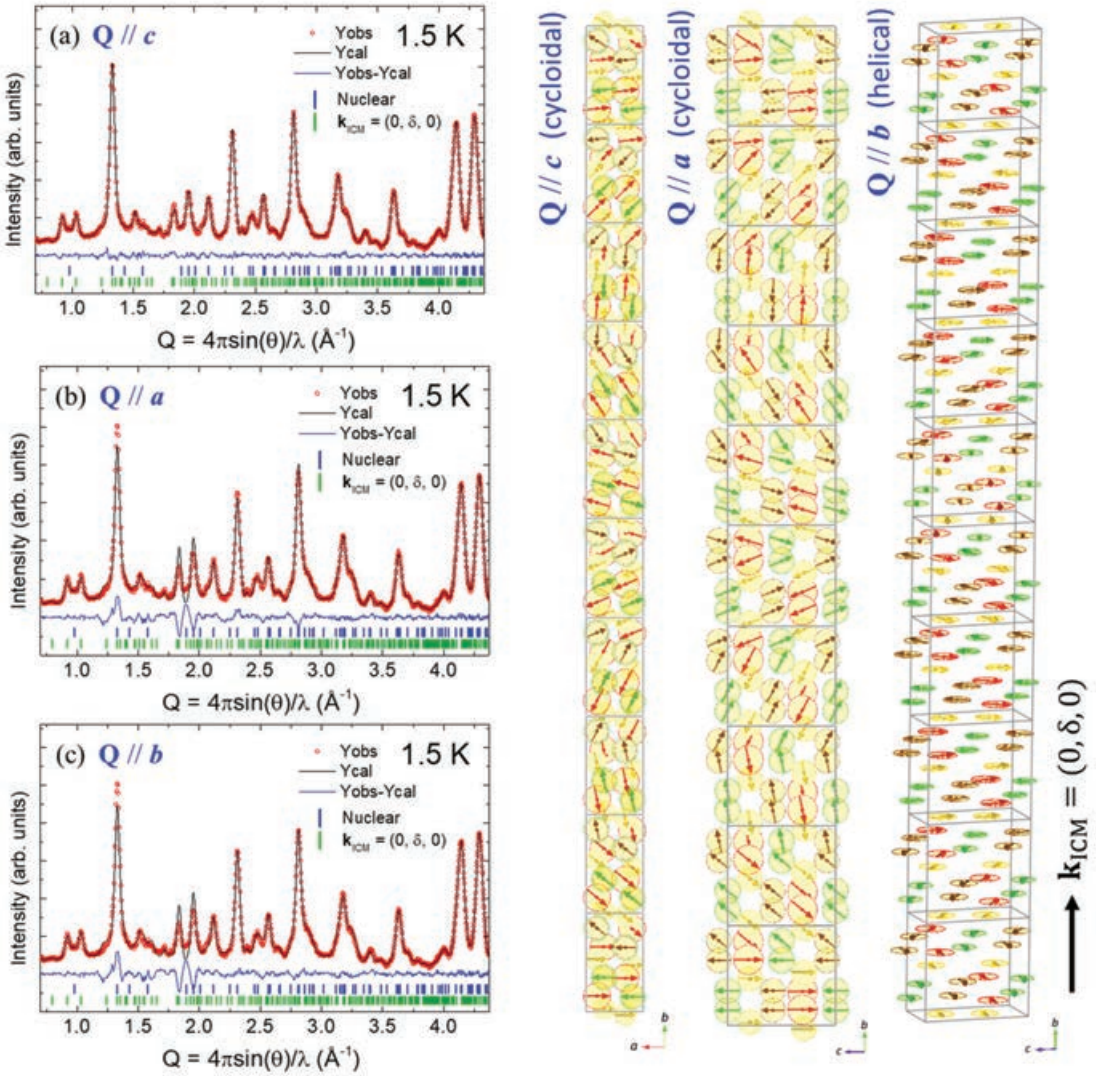

FIGURE 8.6: Rietveld refinement (black curve) of the D1B neutron diffraction pattern (red circles) at 1.5 K for different circular spiral configurations ($M_R = M_I$): (a) cycloidal model with spins rotating in the ab plane ($\mathbf{Q}/\!/\mathbf{c}$), (b) cycloidal model with spins rotating in the bc plane ($\mathbf{Q}/\!/\mathbf{a}$) and (c) helical model with spins rotating in the ac plane ($\mathbf{Q}/\!/\mathbf{b}$). (Chirality, $\mathbf{Q} \sim \mathbf{S}_i \times \mathbf{S}_j$) (Right) Projections of the three spiral magnetic orders along 10 successive unit cells along b, the direction of propagation of the spin rotations, defined by the $\mathbf{k}_{\mathrm{ICM}} = (0, \delta, 0)$ wave vector ($\delta \sim 0.11$ r.l.u.). Fe1d (brown), Fe2d (yellow), Fe3r (red) and Fe4t (green). The rotation plane of the spiral is indicated for clarity.

at 1.5 K is $\delta = 0.1091(3)$ r.l.u. (reciprocal lattice units). The phase transition is more clearly illustrated from the T-Q contour map in Fig. 8.5(b), which shows in detail the thermal evolution of the magnetic reflections (011) and (0 1$\pm\delta$ 1). In addition, the observation of higher order (1 2$\pm\delta$ 0) satellites reasserts the incommensurate nature of the ground magnetic state.

To fully elucidate the exact incommensurate ground magnetic structure in

ε-Fe_2O_3, we have carefully analyzed the neutron diffractogram at the lowest temperature (1.5 K), where the FM2 ferrimagnetic order has completely transformed and the ICM magnetic order is stable. First of all, we have probed the agreement of the Rierveld fits using three different circular helimagnetic and cycloidal structures (with constant m modulus, $\mathrm{M_R} = \mathrm{M_I}$). Remember that as in similar chiral structures previously studied in this thesis, the incommensurate magnetic structure can be described as

$$\mathbf{m}_{lj}(\mathbf{k}) = M_R \mathbf{u}_j \cos 2\pi \left(\mathbf{k}\cdot\mathbf{R}_l + \Phi_j\right) + M_I \mathbf{v}_j \sin 2\pi \left(\mathbf{k}\cdot\mathbf{R}_l + \Phi_j\right) \qquad (8.1)$$

where $\mathbf{m}_{lj}$ is the magnetic moment of the atom j in the unit cell l, $\mathbf{R}_l$ is the vector joining the arbitrary origin to the origin of unit cell l, and Φ_j is a magnetic phase. $\mathbf{u}_j$ and $\mathbf{v}_j$ are the perpendicular unitary vectors defining the spin rotation plane and M_R and M_I are the amplitudes of the elliptical envelope of the rotation plane of the moments. In particular, we have tested the three configurations where the chirality vector of the spiral (*i.e.* the vector perpendicular to the plane of rotation of the spins, $\mathbf{Q} = \mathbf{S}_i \times \mathbf{S}_j$) is parallel to the three crystallographic directions. For simplicity, in our refinements we have considered that the symmetry relations between magnetic moments at the four Fe sublattices in the preceding FM1 phase are preserved in the low temperature magnetic order. The neutron fits are shown in Fig. 8.6(a-c), where projections of the three magnetic structures embracing 10 unit cells are shown to illustrate the translational symmetry along the b axis. According to the incommensurability of the propagation vector ($\delta \sim 0.11$ r.l.u.), after $1/\delta \sim$10 unit cells the spins have roughly completed a full rotation cycle. The refined moments and agreement parameters corresponding to these fits are summarized in Table 8.2(a-c). Out of these three chiral order models, the best agreement was found for the cycloidal case where the rotation plane of the spins (easy plane) lies in the ab plane [the $\mathbf{Q}/\!/\mathbf{c}$ case in Tab. 8.2(a)].

Another possible magnetic configuration could be the collinear structure where the amplitudes of the ordered moments m along the a direction are sinusoidally modulated along b. As shown in Table 8.2(d), this model resulted in significantly better agreement factors than the cyclodal structure. However, the simple sine wave model yields non-physical magnetic moments in the four Fe sublattices, clearly above the maximum possible values (5 μ_B for high-spin Fe^{3+}

cations). This observation is in agreement with the previous neutron study carried out by M. Gich *et al.* [63]. In addition, as previously mentioned, the Mössbauer components at the ground magnetic order (below ∼90 K) reported in Ref. [63] display narrow hyperfine field distributions for all the sites, as opposite to what one would expect in a sine-modulated magnetic structure with a periodicity of ∼10 unit cells, where the amplitude of the moments range between zero and the maximum amplitude. A square wave collinear model with constant amplitudes arises as an alternative to the spiral and sinusoidal models.

TABLE 8.2: Refined magnetic moments and agreement factors in the ICM magnetic order (1.5 K) using different models. (Upper panel) Chiral magnetic models (spiral order with constant m modulus, $\mathrm{M_R} = \mathrm{M_I}$) with three different orientations of the rotation plane of the spins (normal to the chirality $\mathbf{Q} = \mathbf{S}_i \times \mathbf{S}_j$): (a) $\mathbf{Q}/\!/\mathbf{c}$, (b) $\mathbf{Q}/\!/\mathbf{a}$ and (c) $\mathbf{Q}/\!/\mathbf{b}$. (Lower panel) Collinear order models ($\mathbf{Q} = 0$) with spins oriented along the a axis, where the amplitudes of the moments are described as: (a) a sinusoidally modulated spin wave ($\mathrm{M_I} = 0$) and (b) a square-wave modulated structure with an antitranslation (1′ | 0, 1/2, 0). Colors in magnetic structure projections: Fe1d (brown), Fe2d (yellow), Fe3r (red) and Fe4t (green), O (dark blue).

CHIRAL MODELS ($\mathbf{Q} \neq 0$, $\mathrm{M_R} = \mathrm{M_I}$)	(a) Q∥c (cycloidal)	(b) Q∥a (cycloidal)	(c) Q∥b (helical)
Refined moments	m_x[**Fe1d**] = 3.685 (67) μ_B/Fe m_x[**Fe2d**] = -3.685 (67) μ_B/Fe m_x[**Fe3r**] = -4.66 (12) μ_B/Fe m_x[**Fe4t**] = 4.37 (24) μ_B/Fe	m_x[**Fe1d**] = 5.84 (12) μ_B/Fe m_x[**Fe2d**] = -5.84 (12) μ_B/Fe m_x[**Fe3r**] = -6.24 (17) μ_B/Fe m_x[**Fe4t**] = 4.89 (30) μ_B/Fe	m_x[**Fe1d**] = 6.15 (12) μ_B/Fe m_x[**Fe2d**] = -6.15 (12) μ_B/Fe m_x[**Fe3r**] = -4.81 (13) μ_B/Fe m_x[**Fe4t**] = 4.44 (28) μ_B/Fe
Agreement factors	χ^2 = 2.17 R_B = 0.415 R_f = 0.310 R_m = 1.5	χ^2 = 9.21 R_B = 1.45 R_f = 0.843 R_m = 4.66	χ^2 = 9.34 R_B = 0.963 R_f = 0.724 R_m = 4.79
Magnetic structure	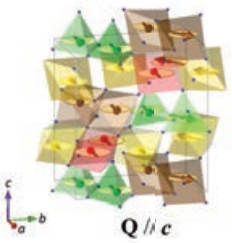	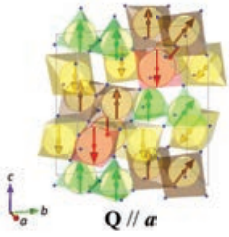	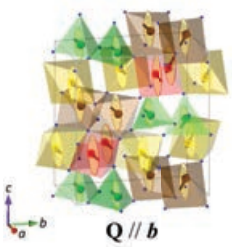

COLLINEAR MODELS ($\mathbf{Q} = 0$)	(d) Sinusoidal model ($\mathrm{M_I} = 0$)	(e) Anti-phase boundary model
Refined moments	m_x[**Fe1d**] = 5.72 (11) μ_B/Fe m_x[**Fe2d**] = -5.72 (11) μ_B/Fe m_x[**Fe3r**] = -6.71 (18) μ_B/Fe m_x[**Fe4t**] = 6.20 (31) μ_B/Fe	m_x[**Fe1d**] = 4.410 (93) μ_B/Fe m_x[**Fe2d**] = -4.410 (93) μ_B/Fe m_x[**Fe3r**] = -4.718 (92) μ_B/Fe m_x[**Fe4t**] = 4.702 (98) μ_B/Fe
Agreement factors	χ^2 = 2.04 R_B = 0.356 R_f = 0.271 R_m = 0.973	χ^2 = 3.68 R_B = 0.716 R_f = 0.455 R_m = 2.55
Magnetic structure	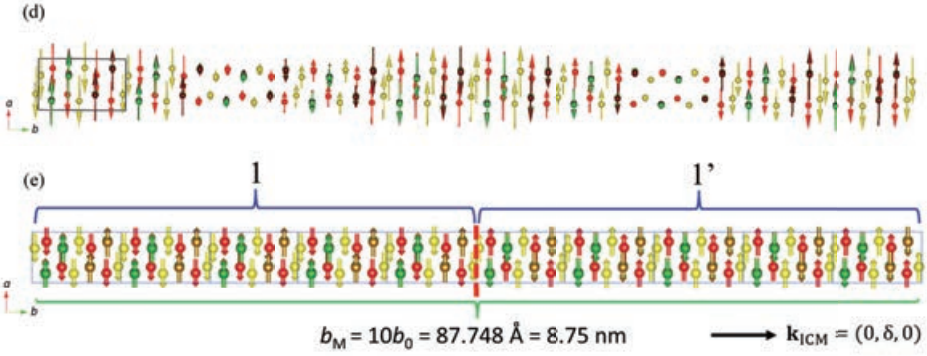	

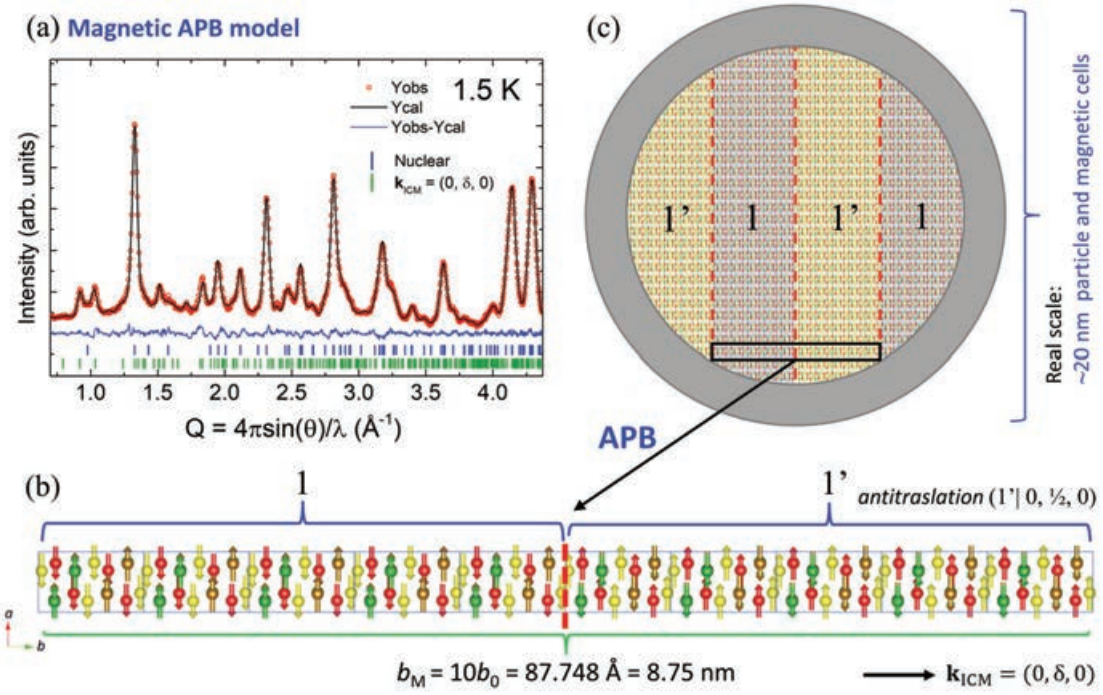

FIGURE 8.7: (a) Refinement (black curve) of the diffracted neutron intensities at 1.5 K (red circles) using a model for the ICM order based on magnetic anti-phase boundaries (APB). (b) Schematic view of the collinear magnetic ordering, where the magnetic unit cell ($b_M \approx 8.75$ nm long) consists of an antitranslation (1′| 0, 1/2, 0) of five successive unit cells along b. (c) Real scale illustration of the AP magnetic domains within a ε-Fe_2O_3 nanoparticle (∼20 nm in diameter). Vertical dashed lines (in red) indicate the magnetic anti-phase boundaries (APB) separating the AP magnetic domains.

In this work I have proved that the magnetic intensities in the NPD patterns at 1.5 K are perfectly compatible with this model. Fig. 8.7(a) shows the Rietveld fit, for which a magnetic cell of dimensions $a_0 \times 5b_0 \times c_0$ [with $a_0 = 5.0744$ (3) Å, $b_0 = 8.7748$ (4) Å, $c_0 = 9.4629$ (3) Å] was defined, containing in total 80 Fe atoms[1] with collinear moments laying along the a axis as in the commensurate ferrimagnetic phase (FM2). The successive anti-phase (AP) magnetic domains along b are generated by approximately an antitranslation symmetry operation (1′| 0, 1/2, 0), which leads to the 10 unit cell periodicity of the ICM magnetic order [see Fig. 8.7(b)]. The results of the fit are summarized in Table 8.2(e). In contrast with the sine wave model, the square wave model approach led to physically consistent magnetic moments: m_x[Fe1d]=-m_x[Fe2d] = 4.410 (93) μ_B/Fe, m_x[Fe3r] = -4.718 (92) μ_B/Fe and m_x[Fe4t] = 4.702 (98) μ_B/Fe.

Bearing in mind that the size of the ε-Fe_2O_3 nanoparticles studied was ∼20

[1]Each one of the four Fe_i sublattices generates 20 positions in that cell due to the $Pna2_1$ space group of the structure, which has a single Wyckoff position of fourfold symmetry.

nm (determined by TEM), it is interesting to notice that the length of the magnetic cell ($b_M = 10b_0 = 8.75$ nm) would only allow to accomodate up to approximately four magnetic antiphase (AP) domains. This is illustrated in Fig. 8.7(c), where a possible distribution of the AP magnetic domains is shown in an oversimplified way to give a better appreciation of the magnetic periodicity in relation with the size of the monocrystalline nanoparticles. In this figure the magnetic anti-phase boundaries (APB) separating the AP magnetic domains are indicated by the vertical dashed lines (in red), although its real distribution might entail more complexity.

Besides the NPD results, there are strong arguments in favour of postulating this model as a most ptobable candidate for the ground magnetic order of ε-Fe_2O_3. On the one hand, a ground magnetic phase preserving the collinear arrangement of the AF2 phase seems more consistent than a non-collinear order given the strong magnetic anisotropy of the system. On the other hand, it allows to understand the AF2-ICM magnetic transition in terms of formation of anti-phase "*defects*". In this respect, the unstability region observed between 150 K and 90 K, before the ground magnetic order is stabilized, could be related to the formation and/or redistribution of such magnetic AP boundaries. According to the Mössbauer study in [63], the sextet linewidth broadening in the the spectra in this temperature range seems to indicate the appearance of some disorder at the different crystallographic sites. Moreover, the AF2-ICM transition (*i.e.* the capability of the system to minimize its energy by creating anti-phase magnetic domains) is probably triggered by the underlying collapse of the orbital moment of some Fe atoms in the same temperature range, reported in Ref. [71] from synchrotron XMCD measurements. As we will see in the next chapter, the existence of a sizeable nonzero orbital moment above 150 K is thought to be at the origin of the huge magnetic coercivity and magnetocrystalline anisotropy in ε-Fe_2O_3, as the switching of the magnetization could necessarily involve atomic shifts in virtue of the spin-orbit coupling.

8.5 Summary

Summarizing, in the preceding sections we have investigated the complex magnetism in ε-Fe_2O_3 in the high- and low- temperature ranges beyond the superhard ferrimagnetic order. Contrary to the scenario proposed in the literature, magnetic order in this magnetoelectric Iron (III) polymorph does not disappear at the super-hard-ferrimagnetic transition near 480 K. We have shown that

a second ferrimagnetic phase (FM1) persists up to much higher temperatures (near 850 K). The super-hard ferrimagnetic FM2 phase (holding giant coercivity) is transformed to a different ferrimagnet state, FM1, with a much smaller ferromagnetic component and coercivity. Both magnetic orders adopt the magnetic space group $Pna'2'_1$ (n. 33.147), where the main difference between them is the disruption of the magnetic order associated to the Fe3r and Fe4t magnetic atoms. Above 480 K, the iron spins at the sublattices that occupy the regular octahedra $Fe3O_6$ and $Fe4O_4$ tetrahedra can hardly keep their antiparallel magnetizations and become rapidly disordered. Consequently, the spontaneous FM magnetization that was sustained by the different magnetic moments in these antiparallel sublattices in FM2 quickly vanishes in FM1. Thus, the small FM component persisting up to $\mathrm{T_{N1}} \approx 850$ K results from a slightly dissimilar magnetization at the antiparallel Fe1d and Fe2d sublattices. Hence, we have demonstrated that the ferrimagnetic-paramagnetic phase boundary in ε-Fe_2O_3 is $\mathrm{T_{N1}} \sim 850$ K. This temperature is similar to the Curie point in other iron oxides, confirming comparable magnetic coupling strengths. This may open the door to further expand the working range of this multifunctional iron oxide. In fact, these new findings may be an indication that the presumed multiferrroic properties of ε-Fe_2O_3 at room temperature actually could persist and extend also into the new ferrimagnetic FM1 phase.

On the other hand, we have also revisited the magnetic order emerging below the super-hard FM2 phase by means of high-resolution neutron diffraction, verifying the emergence of magnetic satellites around the different commensurate magnetic reflections below the expected temperature ($\mathrm{T_{ICM}} \sim 150$ K). The incommensurate reflections are successfully indexed using a wave vector $\mathbf{k}_{\mathrm{ICM}} = (0, \delta, 0)$, with $\delta \approx 0.11$ r.l.u at 1.5 K. The comparative analysis of the neutron diffraction data in the ground magnetic state of ε-Fe_2O_3, conducted using different chiral and collinear models, confirms that the magnetic intensities are compatible with a magnetic ordering with periodic anti-phase domains. The stabilization of this magnetic order is subsequent to the collapse of the orbital moment in Fe atoms within the 85-150 K interval, and is probably linked to some magnetostructural effects during the wide FM2-ICM transition under cooling. Very likely some local structural changes persist into the ICM phase. They are very likely associated to the narrow regions separating two antiphase magnetic domains. Indeed, I expect that, locally, an inversion center could develop at the APBs. Hence the local symmetry of Fe atoms (particularly the Fe4t)

that are in the APBs would differ from the known symmetry inside each AP domain ($Pna'2'_1$).

Chapter 9

Understanding the magnetostructural properties of ε-Fe_2O_3

9.1 Introduction

The $Pna2_1$ structure of ε-Fe_2O_3 is geometrically frustrated, and exhibits magnetically frustrated triangular exchange paths. A key feature is the spin frustration between tetrahedral-site Fe4t spins that can have a strong effect on the magnetic order. The transformation between the high temperature and the low temperature ICM magnetic structures, which is accompanied by a magnetic softening, has been attributed to second order lattice distortions involving changes in the coordination of some of the Fe sites, leading to a weakening of the spin-orbit interactions [71]. The nonzero orbital moment in ε-Fe_2O_3 is presumed to result from Fe $3d$-O $2p$ mixing and O $2p$ to Fe $3d$ charge transfer in the strongly distorted Fe^{3+} coordination polyhedra [71, 77]. However, the mechanisms that trigger the high-temperature ferrimagnetic transition studied and described in the previous chapter have not yet been deciphered.

Regarding the room temperature multiferroicity of ε-Fe_2O_3, the origin of its ferroelectricity is still uncertain, as well as the microscopic basis of the exceptional super-hard ferrimagnetic properties or the mechanism to explain the reported switching of the ferroelectric polarization, which are all being subject of debate. So far, in absence of single-crystals, experiments have confirmed reversible ferroelectric switching at room temperature only in films [72]. Using in situ scanning transmission electron microscopy (STEM) on ε-Fe_2O_3 films, partial switching of the domains was observed at small electric fields, disclosing that inside domain walls the real structure is close to the nonpolar $Pbcn$ symmetry [73] [see Fig. 9.1].

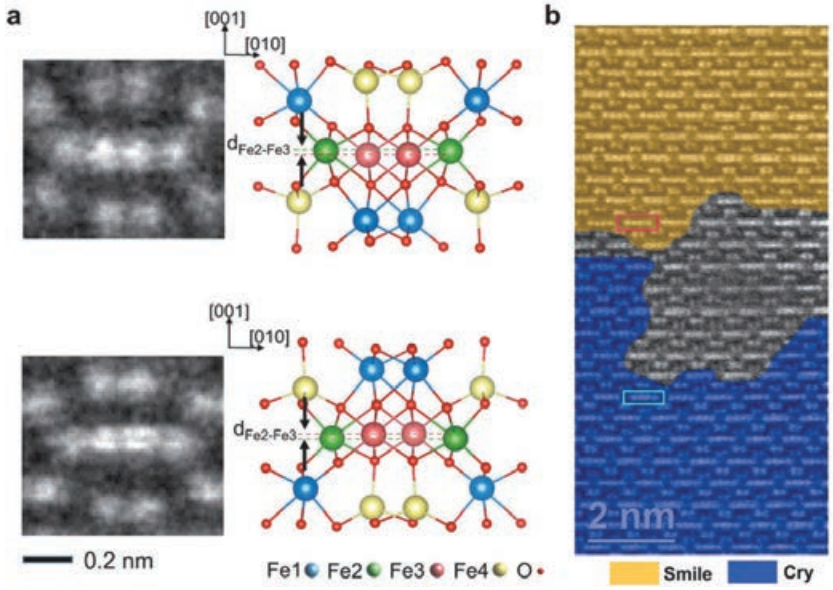

FIGURE 9.1: The ferroelectric domain structure in ε-Fe_2O_3. (a) Scanning transmission electron microscopy (STEM) images along the [100] zone axis of the ε-Fe_2O_3 film showing a smile (upper panel) and cry (lower panel) alignment of the Fe2 and Fe3 ions. The corresponding structural models are shown on the right. (b) Image of two polar domains (yellow and blue areas) separated by a non-polar boundary (grey area). Figure obtained from Ref. [73].

The results presented in this chapter will gather several clues that point very clearly to a magnetostriction-based mechanism as the responsible for the huge coercivity in the super-hard phase of ε-Fe_2O_3. Using synchrotron X-rays (SXRPD) we have observed and identified outstanding subtle atomic shifts across the hard/soft (FM2/FM1) ferrimagnetic transition at 500 K, which are coupled to changes in some frustrated Fe-O-Fe magnetic bonds. Additionally, a NPD study under magnetic fields on the super-hard and the incommensurate magnetic order gives further insight on the possible magnetostrictive mechanisms behind the unconventional properties of this exceptional Iron(III) polymorph.

9.2 Experimental methods

- *Synchrotron and neutron diffraction:* Synchrotron X-ray powder diffraction patterns (SXRPD) were collected at the BL04-MSPD beamline [107] of the ALBA Synchrotron Light Facility (Barcelona, Spain) using λ = 0.41284(6) Å in the temperature range between 100 K and 925 K. Above 300 K the sample was heated at a rate of 3 K/min using a Cyberstar-FMB Oxford hot air blower with acquisition times of 100 s per pattern. Below 300 K the heating rate (using an Oxford Cryostream) was 5 K/min, with an acquisition time of 50 s per pattern. Patterns

were continuously recorded by the MYTHEN position sensitive detector while warming the sample. Structural Rietveld refinements of the SXRPD were carried out using the sequential refinement tool implemented in the Fullprof set of programs [97].

- *Neutron powder diffraction under magnetic field:* The neutron powder diffraction (NPD) study under magnetic fields was carried out at the high-flux reactor of the Institut Laue Langevin (Grenoble, France), using the high-intensity, high-resolution two-axis D20 diffractometer. Measurements were made on ε-Fe_2O_3 samples between 10 K and 300 K using a cryomagnet providing magnetic fields up to 6 T. A wavelength 1.54 and 2.41 Å were employed, the former providing excellent resolution of the magnetic reflections at low q, and the latter a wider q-range for structural study. For the isothermal H-field loops, 40 min patterns were collected at different magnetic field values using the scanning detector mode, in which a total of 40 patterns of 60 sec collected along a Theta-scan (-8<θ_0<-6, step 0.05°) were merged for signal-to-noise ratio enhancement. In the case of variable-temperature measurements, 10 min simple acquisitions using the fixed detector mode were collected in dynamic mode by means of temperature ramps with heating rates of 0.75 K/min.

Due to the nanoparticle powder nature of the samples, it was necessary to overcome the possible appearance of preferred orientation caused by the reorientation of the powder grains under the application of magnetic fields. It is very important to avoid this effect in order to obtain reliable data from which we aim detecting magnetostrictive effects by Rietveld refinement of the nuclear intensities. With this purpose, for the measurements within the low temperature range (10 K to 130 K), the ε-Fe_2O_3 sample was immersed into deuterated isopropanol (2-Propanol-d_8 99.5 atom % D, Sigma-Aldrich) which was frozen on cooling, in order to prevent reorientation of the nanoparticles under the application of magnetic fields. To avoid crystallization of the isopropanol, which freezes around T $\sim$ 115 K in a glassy state, the liquid solution was loaded into a cylindrical vanadium holder, mounted on the stick, and rapidly cooled at zero field inside the cryomagnet. For the measurements at temperatures above the freezing point of deuterated isopropanol, we prepared a second sample in which the ε-Fe_2O_3 nanoparticles were embedded in an amorphous silica matrix. In this sample, each grain contains hundreds of randomly oriented ε-Fe_2O_3 nanoparticles, thus reducing a lot the possibility of preferred orientation effects due to magnetic field application. Additionally, a cadmium cylinder (opaque to neutrons) was used to keep the powder tight inside the vanadium container.

9.3 Structural characterization: the non-centrosymmetric $Pna2_1$ structure

First it is worth emphasizing that the orthorhombic $Pna2_1$ structure was stable up to the highest temperature reached (923 K). Namely, no transition to other more stable iron oxides (*e.g.*, α-Fe_2O_3 or γ-Fe_2O_3) has been observed up to that temperature. The structural parameters of ε-Fe_2O_3 and agreement factors from the refinement of SXRPD patterns obtained at 305 K and 510 K can be seen in Table 9.1. Figure 9.2(a) displays a projection of the ε-Fe_2O_3 non-centrosymmetric $Pna2_1$ structure, composed of four different Fe sites in the asymmetrical unit cell, three octahedral and one tetrahedral environments. The coordination octahedra $Fe1O_6$ and $Fe2O_6$ are largely distorted, $Fe3O_6$ is a regular octahedron and $Fe4O_4$ is the tetrahedron. For clarity we will use the Fe1d, Fe2d, Fe3r, Fe4t atomic labels where "d", "r" and "t" refer to "*distorted*", "*regular*" and "*tetrahedral*" polyhedral coordination, respectively.

The presence of very minority impurities was carefully explored by a detailed examination of high intensity synchrotron patterns. We detected a 2.3(9) % in weight of α-Fe_2O_3 (hematite) as impurity phase in our nanograin ceramic samples of ε-Fe_2O_3 [corresponding to the bottom row of bars in the refined synchrotron pattern shown in Fig. 9.2(b)]. This corresponds to a 0.7 wt.% in the SiO_2/Fe_2O_3 composite used for magnetic measurements.

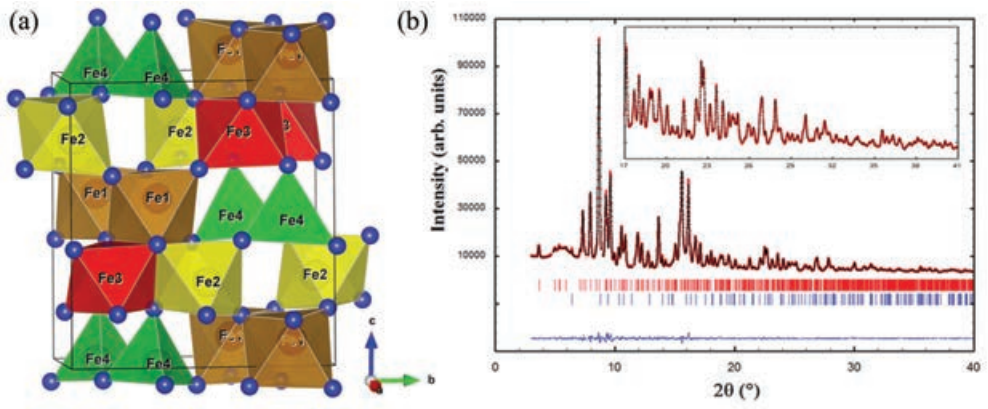

FIGURE 9.2: (a) Crystallographic projection of ε-Fe_2O_3. The four crystallographically independent Fe sites are shown with different colors in the structure (Fe1, brown; Fe2, yellow; Fe3, red; Fe4, green). O atoms are represented in dark blue. (b) Rietveld refinement (black solid line) of the synchrotron X-ray pattern of ε-Fe_2O_3 collected at 300 K (red circles: experimental points; bottom blue line: difference). The top row of bars (in red) corresponds to ε-Fe_2O_3, while the bottom row (in blue) is for hematite (α-Fe_2O_3, 2.3(9) % weight). The inset shows an enlarged view of the high-angle region.

TABLE 9.1: Lattice parameters and atomic coordinates ε-Fe_2O_3 obtained from SXRPD at 300 K and 510 K using the $Pna2_1$ space group.

T=300 K				T=510 K			
Atom	**x/a**	**y/b**	**z/c**	**Atom**	**x/a**	**y/b**	**z/c**
Fe1	0.1947 (5)	0.1497 (3)	0.5806 (2)	Fe1	0.1928 (6)	0.1499 (4)	0.5813 (2)
Fe2	0.6828 (3)	0.0323 (2)	0.7921 (3)	Fe2	0.6823 (4)	0.0314 (2)	0.7918 (3)
Fe3	0.8083 (3)	0.1592 (2)	0.3062 (2)	Fe3	0.8105 (4)	0.1583 (2)	0.3079 (2)
Fe4	0.1816 (5)	0.1538 (3)	0	Fe4	0.1819 (6)	0.1542 (4)	0
O1	0.9754 (13)	0.3276 (5)	0.4340 (5)	O1	0.9739 (14)	0.3281 (6)	0.4345 (6)
O2	0.5112 (13)	0.4933 (8)	0.4187 (9)	O2	0.5030 (14)	0.4907 (9)	0.4227 (13)
O3	0.6537 (15)	1.0011 (7)	0.1895 (5)	O3	0.6533 (18)	0.9990 (8)	0.1859 (5)
O4	0.1624 (14)	0.1622 (8)	0.1956 (4)	O4	0.1614 (16)	0.1608 (8)	0.1959 (4)
O5	0.8449 (15)	0.1657 (8)	0.6680 (5)	O5	0.8450 (17)	0.1669 (10)	0.6698 (5)
O6	0.5286 (13)	0.1590 (9)	0.9375 (6)	O6	0.5386 (14)	0.1654 (10)	0.9366 (7)
	$a = 5.0967(2)$	$b = 8.7953(3)$	$c = 9.4770(3)$		$a = 5.1133(2)$	$b = 8.8163(4)$	$c = 9.4822(4)$

Agreement factors for SXRPD pattern at 300 K (510 K): R_B = 1.35 (1.31), R_f = 1.04 (1.01), R_m = 4.45 (4.48), χ^2 = 4.6 (4.8).

9.4 Magneto-structural coupling at the ferrimagnetic transitions: synchrotron X-ray diffraction study

Magnetic ordering at high temperatures in ε-Fe_2O_3 concurs with significant magnetostructural and thermal expansion anomalies, as shown by the evolution of the orthorhombic cell obtained from SXRPD (Fig. 9.3). The cell volume reveals an abrupt contraction (≈-0.1 %) at about 500 K upon cooling from high temperature [Fig. 9.3(a)] with the appearance of the super-hard FM2 phase. The anomaly is also visible in the evolution of all three a(T), b(T) and c(T) cell parameters [Fig. 9.3(b)]: a and b abruptly contract and c expands when Fe3r and Fe4t spins become long-range ordered (T_{N2}).

In Fig. 9.3(c) we plot the linear thermal expansion coefficients α_i, deduced from l_i(T) as α_i=$1/l_{i0} \times dl_i/dT$ (l_i: a, b, c), where l_{i0} is the value of the l_i parameter (size of the unit cell along i: a, b, c) at 305 K. No change in the crystal system is observed in the range of temperatures studied. Solid curves are fits of the function $l(\mathrm{T}) = A + B\Theta\mathrm{coth}(\Theta_s/\mathrm{T})$, where A and B are coefficients of the fit and Θ_s is a saturation temperature that results in zero slope as T→0 K. Θ_s was set at 300 K to give flattening of the curves below ∼150 K. The function was fitted to data in the interval 598–803 K, well above T_{N1}, and extrapolated to the whole temperature range to make clear the deviations from the expected evolution.

Interestingly, there are anomalous contributions to the lattice evolution which are concurrent with the magnetic transitions. On the one hand, the most

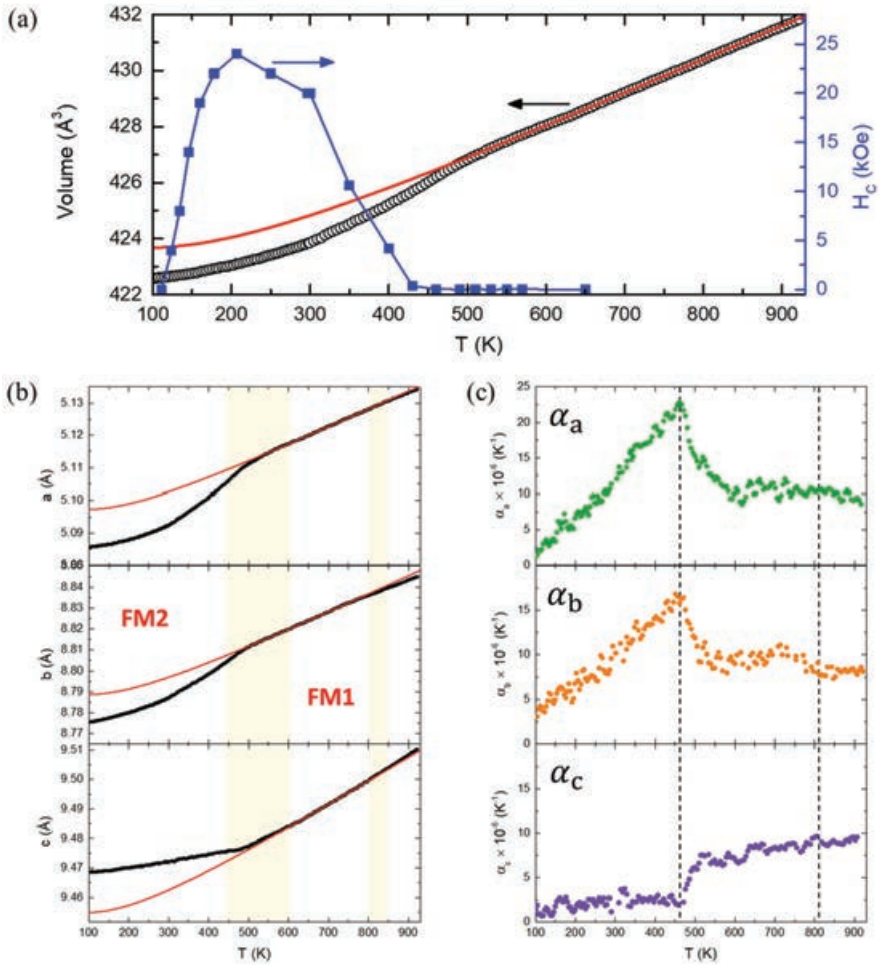

FIGURE 9.3: (a) Evolution of the unit-cell volume along the transition from the soft FM1 phase to the ultra-hard FM2 ferrimagnetic phase on cooling below ∼500 K. The evolution of the magnetic coercivity H_C is also plotted (right axis). (b) Temperature dependence of the orthorhombic cell parameters in the 100-925 K range showing magnetostructural anomalies associated to the emergence of the FM1 and FM2 ferrimagnetic orders. The solid curves (in red) are baselines obtained by fitting the coth function, $l(T) = A + B\Theta_s \coth(\Theta_s/T)$, to data between 598 k and 803 K, with the value of $_s$ fixed at 300 K. (c) The linear thermal expansion coefficient α_i (i = a, b and c) derived from SXRPD data and l_i(T) as α_i=$1/l_{i0} \times dl_i/dT$. The temperature dependence of the coefficients α_a(T), α_b(T) and α_c(T) are shown on the top, middle and bottom panels, respectively.

prominent exchange-striction effects come up accompanying the hard/soft ferrimagnetic phase boundary [see the evolution of H_C in Fig. 9.3(a)]. The strength of magnetostructural coupling associated with the ordering transition at $T_{N2} \approx$ 500 K is strongly anisotropic in a manner that it is close to uniaxial, *i.e.* elongation along the crystallographic c-direction with more or less uniform contraction in the ab-plane. The largest contraction occurs along the a-direction, *i.e.* the magnetic easy axis along which the magnetic moment at Fe3r and Fe4t sites

become ordered upon cooling. Similarly, the evolution of α_b(T) in Fig. 9.3(c) also shows a significant anomaly in the range 700-825 K which could be caused by the appearance of magnetic order at Fe1d and Fe2d sites in the FM1 phase, which is in concordance with the small deviation observed in b(T) near ∼800 K [Fig. 9.3(b)]. Note that the exchange-striction effect at T_{N1} provides further evidence that the magnetic properties between 480 K and 850 K do not originate from impurities, but from the FM1 phase of ε-Fe_2O_3. In this way, although both ferrimagnetic phases exhibit the same magnetic space group [$Pna'2'_1$ (n. 33.147)] and moment orientation (parallel to a), the observed magnetostructural response is very different in both transitions. The origin of these differences should correlate with the dissimilar character of each of the phases (*i.e.*, fully ordered FM2 vs partially frustrated FM1). Finally, there is no obvious anomalous lattice evolution nor break in any of the the α_i slopes within ∼100-150 K, where the AF2-ICM magnetic transition occurs.

9.4.1 Evolution of the interatomic distances along the successive ferrimagnetic orderings in ε-Fe_2O_3

Besides the relevant exchange-striction effects above described, originated by the ordering of the Fe3r and Fe4t sublattices which leads to a the highly anisotropic ultra-hard ferrimagnetic phase, the evolution of the cell parameters don't tell much about the possible existence of underlying variations in the interatomic distances and bond angles. Hence, the X-ray diffraction data was thoroughly analyzed so as to obtain the evolution of the atomic positions in the coordination polyhedra around Fe^{3+} sites.

In view of the difficulty entailed by the complexity of the ε-Fe_2O_3 structure, a great deal of effort was done to obtain reliable results. The required accuracy was accomplished thanks to the outstanding quality of the SXRPD data collected at the MSPD beamline of the Alba synchrotron and the quality and purity of the ε-Fe_2O_3 sample studied, which allowed to detect tiny varitions with a resolution down to ∼0.01 Å. The Rietveld analysis of the thermodiffractometry data, carried out using the FullProf suite [97], allowed to determine the evolution of the coordinates for the atoms sitting at the 10 nonequivalent fourfold symmetry Wycoff positions (4 occupied by iron and 6 by the oxygen anions). For each of the approximately 180 patterns analyzed, the refinements of the structural parameters (30 independent atomic coordinates and the atomic displacement parameters) converged to a unequivocally to a unique solution. Fig. 9.4(a) shows

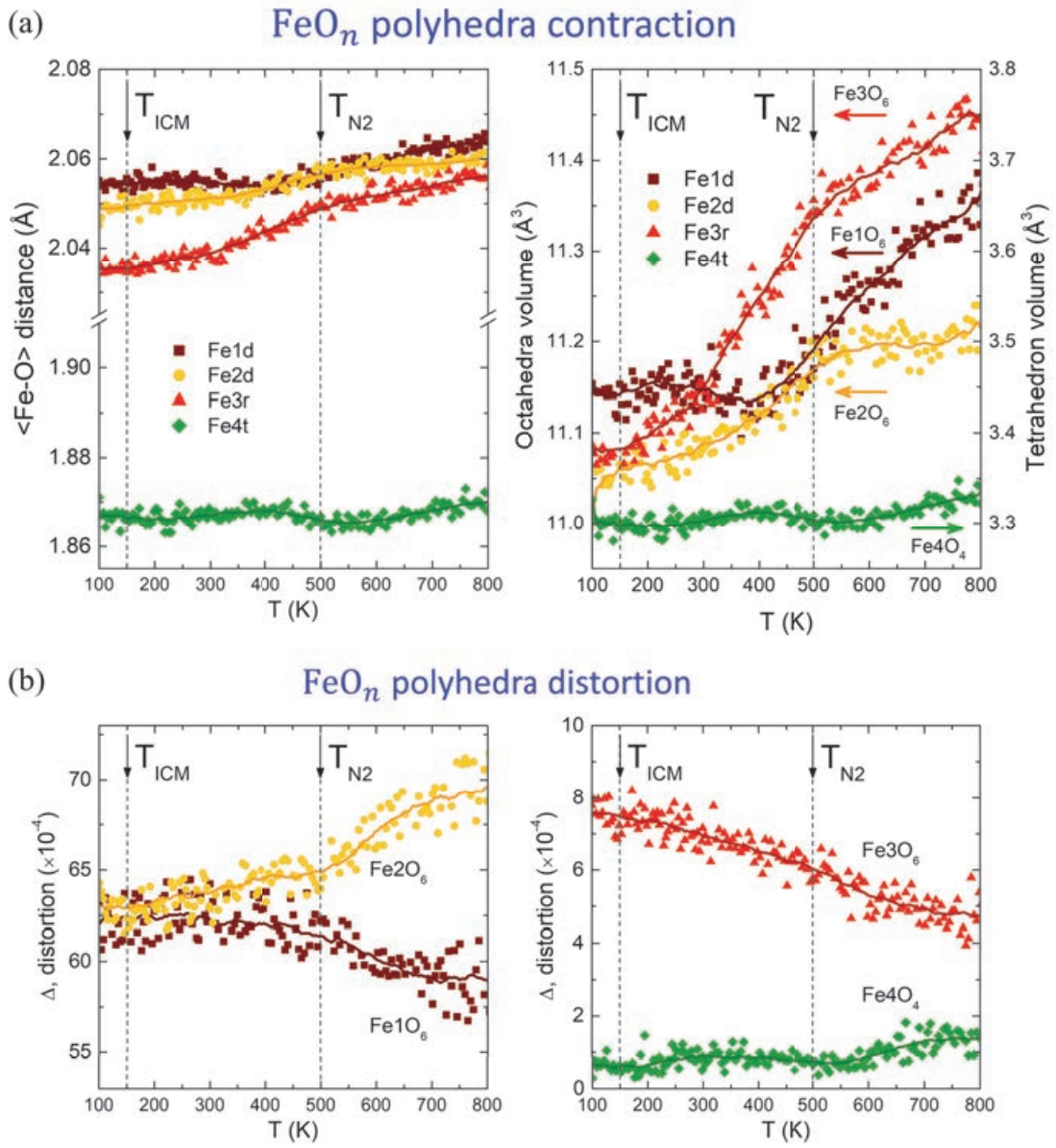

FIGURE 9.4: Temperature dependence of the coordination polyhedra around the four nonequivalent Fe^{3+} sites in the ε-Fe_2O_3 structure (Fe1d, brown; Fe2d, yellow; Fe3r, red; Fe4t, green) along the transition from the soft FM1 phase to the ultra-hard FM2 ferrimagnetic phase. (a) Contraction upon cooling of the different FeO_n polyhedra parametrized by the $\langle Fe-O \rangle$ average interatomic distance (left panel) and the volume of the polyhedra (right panel). (b) Evolution of the polyhedral distortion Δ, calculated according to its definition in Eq. (9.1) for the strongly distorted octahedra around Fe1d and Fe2d (left panel) and for the regular coordinarions surrounding Fe3r and Fe4t.

the overall thermal evolution of the four FeO_n coordinated polyhedra around the four nonequivalent Fe sites, parametrized by the average $\langle Fe-O \rangle$ bond length between the oxygens and the central Fe^{3+} cations and by the volume enclosed by the polyhedra, obtained from the refined atomic coordinates. The

evolution of these two parameters disclose that while in the three octahedrally coordinated sites ($Fe1O_6$, $Fe2O_6$ and $Fe3O_6$) the oxygens tend to get closer to the central metal under cooling, the average size of the lower coordination one ($Fe4O_4$) remains nearly constant. This is not surprising considering that the Coulomb interactions are stronger in the lower coordination tetrahedron due to its remarkably shorter Fe-O distaces. Moreover, the average octahedra contractions are not monotonous. Anomalies observed in the evolution of the average $\langle \mathrm{Fe-O} \rangle$ distance and the polyhedra volumes can be clearly identified in the range of temperatures where the ordering of magnetic moments at the F3r and Fe4t sites gives way to the super-hard ferrimagnetic regime (FM2). Another indicator of the occurring structural changes is the distortion Δ of the FeO_n polyhedra shown in Fig. 9.4(a), which is defined as:

$$\Delta = \frac{\sqrt{\sum_{i=1}^{n} (d_i - \langle d \rangle)^2}}{\langle d \rangle} \tag{9.1}$$

where $\langle d \rangle = (\sum_{i=1}^{n} d_i)/n$ is the average $\langle \mathrm{Fe-O} \rangle$ distance. A distortion $\Delta = 0$ would correspond to a regular polyhedron, and larger values indicate larger deviation from the regular case. Interestingly, the two strongly distorted Fe1d and Fe2d octahedra display opposite evolutions of Δ, which nearly stabilize under cooling below $\mathrm{T_{N2}} \sim 450$ K, where the their distortion become similar. The low distortion value in the Fe3r octahedra increases constantly along the whole temperature range. For the Fe4t tetrahedra the distortion remains always very close to zero displaying small variations.

Figure 9.5 shows the evolution of the nearest Fe-O bond lengths at the four Fe sublattices where the atomic displacements are evident near $\mathrm{T_{N2}} \approx 500$ K. The largest and the shortest Fe-O distances are both found in the $Fe2dO_6$ octahedra, which as seen in Fig. 9.4(b) presents the largest distortion among the four Fe sites. In a first principles theoretical analysis of the electronic structure of ε-Fe_2O_3, Yoshikiyo *et al.* [77] proposed that one of the possible origins of the huge coercive field could be the spin-orbit interaction arising from the single-ion magnetocrystalline anisotropy. From the calculations it was proposed that nonzero orbital angular momentum L could originate from a Fe3d-O2p hybridization between Fe and O. However, the Fe2-O5 and Fe4-O5 distances, corresponding to oxygen atoms with closest proximity to Fe^{3+}, increase across the magnetic transition, while atomic shifts with the opposite tendency would be expected if the large coercivity arised only as a consequence of an electron transfer between Fe and O.

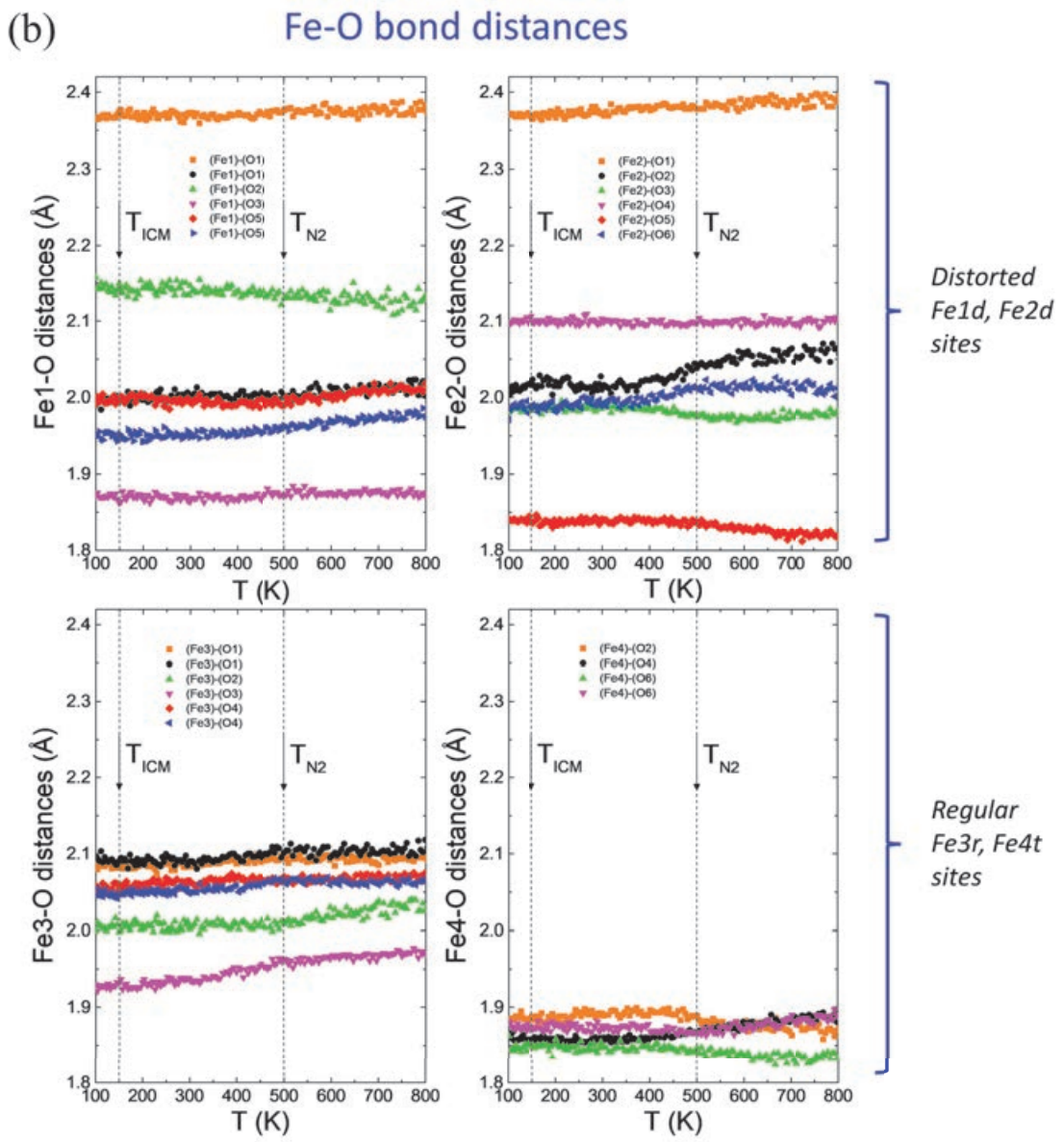

FIGURE 9.5: Evolution as a function of the temperature of the individual Fe-O bond lengths plotted separate panels for the four FeO_n polyhedra in ε-Fe_2O_3. Vertical dashed lines indicate the AF1-AF2 and the AF2-ICM magnetic transitions at $T_{N2} \approx 500$ K and $T_{ICM} \approx 150$ K, respectively.

In order to explore other possibilities related to the structural evolution, we have calculated the bond angles and distances for some selected Fe-O-Fe superexchange paths. However, the low symmetry of the $\varepsilon-Fe_2O_3$ structure makes the spin interactions rather complicated. Considering only the Nearest Neighbors between Fe-Fe pairs involving Fe-O bond lengths that do not exceed 2.4 Å, the J_i superexchange interactions involve 57 Fe-O-Fe paths. The magnitudes of all of the superexchange interactions were studied by means of density-functional-theory (DFT) calculations in Ref. [154], where it was found

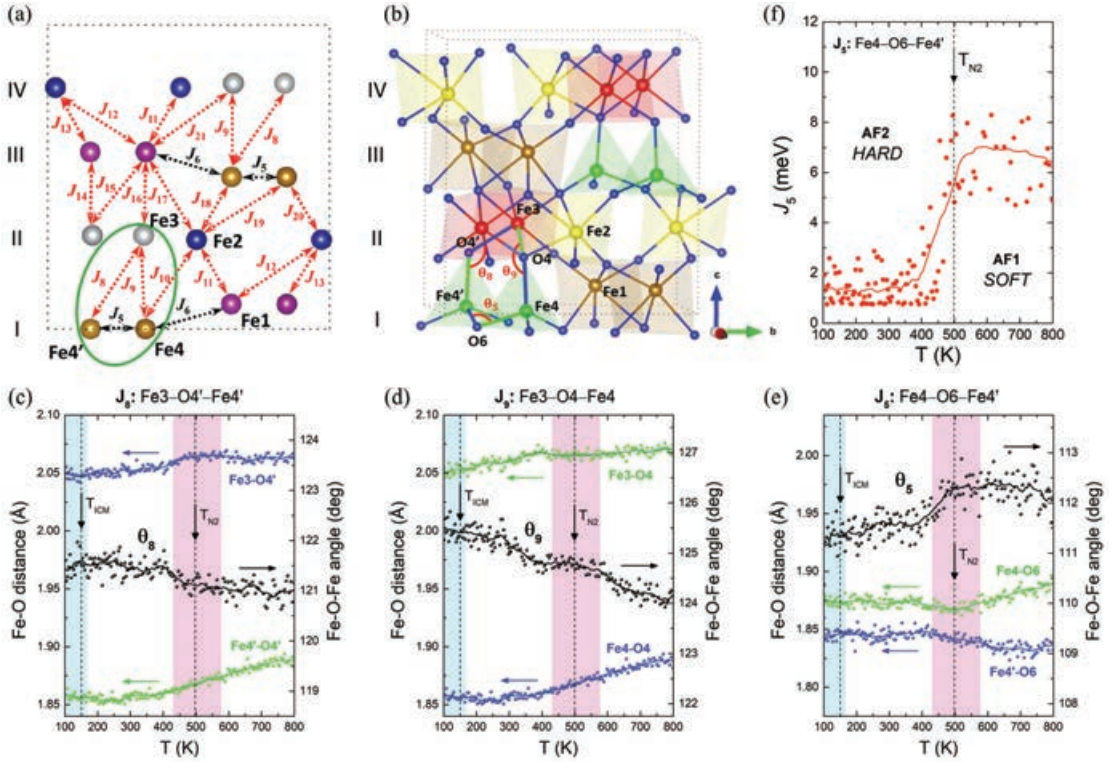

FIGURE 9.6: (a) Scheme of the strongest AFM spin superexchange interactions in ε-Fe_2O_3. Intra-layer and inter-layer interactions are shown in black and red, respectively. The strong J_5 interaction is the origin of spin frustration in the J_5, J_8, and J_9 triangle involving the regular Fe3r and Fe4t sites. Figure adapted from Ref. [154]. (b) Projection of the $Pna2_1$ structure showing the Fe-O-Fe superexchange paths studied at the J_5, J_8 and J_9 frustrated triangle. (c-e) Evolution of the Fe-O bond lengths (left axis) and the Fe-O-Fe bond angles (right axis) for the J_5, J_8 and J_9 AFM couplings, calculated from the refined atomic coordinates as a function of the temperature. (f) Evolution of the J_5 coupling parameter in the strong J_5: Fe4-O6-Fe4' superexchange path, calculated from the refined bond angle θ_5 using Eq. (9.2).

that all of them are of the AFM nature. A diagram showing the most relevant the super-exchange interactions between Fe-Fe pairs is shown in Fig. 9.5(a), where the inter-layer J_8 to J_{21} are indicated by red arrows and J_5, J_6 intra-layer couplings are shown in black. From the calculations in [154], the following issues are specially relevant for our discussion: (i) the intra-layer exchange interactions are weaker than the inter-layer exchange interactions, meaning that the magnetic structure is mainly determined and might be disturbed by the latter. (ii) The strongest intra-sheet interaction is found between the tetrahedral Fe4-Fe4 sites within sheet I (J_5: Fe4-O6-Fe4'), which is smaller but still not negligible when compared with the strongest inter-sheet interaction (J_{11}: Fe1-O5-Fe2) between layers I-II. (iii) A strong spin frustration arises as a consequence of the strong intra-layer Fe4-Fe4 exchange interaction (J_5), which can be easily

seen from the frustrated triangle composed by the AFM J_5, J_8, and J_9 interactions in Fig. 9.5(a).

With these considerations, we are now ready to discuss the possible effects of the structural evolution on the magnetic order through the evolution of the superexchange Fe-O-Fe paths. In particular, we have analyzed the evolution of the bond angles and distances in the frustrated J_5, J_8, and J_9 triangle [illustrated in Fig. 9.5(b)]. The temperature evolution of the corresponding Fe-O bond lengths and Fe-O-Fe bond angles are plotted in Figs. 9.5(c-e). The superexchange interactions between d^5 orbitals of Fe^{3+} in the frustrated triangle are interpretated according to the by the Goodenough-Kanamori-Anderson (GKA) rules [134][135][136], which determines its sign and strength. For Fe^{3+}-O-Fe^{3+} bonds the coupling is AFM for both the 90° and 180° bond angles. As previously reported [150, 155], the strength of the J_i superexchange interactions depends on the Fe–O–Fe bond angle (θ_i) according to the following formula:

$$J_i(\theta) = J_{90^\circ}\sin^2\theta_i + J_{180^\circ}\cos^2\theta_i \tag{9.2}$$

where the parameters J_{90° and J_{180° are specific of the bonding characteristics. Fig. 9.5(f) shows the evolution of the J_5 coupling parameter calculated from the refined Fe-O-Fe angle (θ_5) using Eq. (9.2). We used $J_{90^\circ} \approx 0.75$ meV and $J_{180^\circ} \approx 14.0$ meV, obtained from DFT based calculations in Ref. [156]. It should be mentioned that the evolution of J_5 in Fig. 9.5(f) is an approximation and reflects only the effect of bond angle variations. The J_{90° and J_{180° parameters depend not only on the Fe–O–Fe bond angle, but also on the Fe-O bond lengths in tetrahedral coordination.

On cooling, the evolution of J_5 indicates an abrupt decrease in the strength of the magnetic coupling between the two tetrahedral Fe4-Fe4 pairs, starting at approximately $T_{N2} \sim 500$ K. Furthermore, this weakening of J_5 is accompanied by a strengthening of both the J_8 and J_9 couplings, as it can be deduced from

TABLE 9.2: Fe-O-Fe bond angle (Θ) and Fe-O distances (d_1 and d_2) for the J_5, J_8 and J_9 superexchange couplings in the frustrating triangle, obtained from the refined atomic coordinates at 300 K (AF2) and 510 K (AF1).

	T=300 K			**T=500 K**		
Fe-O-Fe path	d_1 (Å)	d_2 (Å)	θ_i (deg)	d_1 (Å)	d_2 (Å)	θ_i (deg)
J_5: Fe4-O6-Fe4'	1.872 (1)	1.843 (1)	111.6 (1)	1.867 (1)	1.841 (1)	112.3 (1)
J_8: Fe3-O4'-Fe4'	2.053 (1)	1.857 (1)	121.5 (1)	2.066 (1)	1.870 (1)	121.1 (1)
J_9: Fe3-O4-Fe4	1.857 (1)	2.053 (1)	125.2 (1)	1.870 (1)	2.066 (1)	124.7 (1)

the increase of their bond angles (θ_8 and θ_9) and the reduction of the corresponding Fe-O interatomic distances [see Fig. 9.5(c-d)]. Table 9.2 summarizes the values of the Fe-O-Fe bond angles and interatomic distances for J_5, J_8 and J_9 and its comparison between 510 K (AF1) and 300 K (AF2). The small structural variations observed have a great relevance on the magnetic ordering of the frustrated Fe3 and Fe4 sites.

Summarizing, the ordering of the Fe3r and Fe4t magnetic moments in the AF1-AF2 transition is compatible with the variations observed in the magnetic couplings of the J_5, J_8, and J_9 triangle, which undergoes a relaxation of the spin magnetic frustration due to the structural evolution affecting mainly the spins at the Fe3 and Fe4 sublattices.

9.5 Neutron investigation of the magnetostructural response of ε-Fe_2O_3 under magnetic field

9.5.1 Magnetostrictive effects under magnetic field at the ultra-hard ferrimagnetic order

As seen in previous sections of this chapter, the magnetostrictive mechanisms play an undeniable role on the emergence and properties of the high temperature ferrimagnetic phases in ε-Fe_2O_3, as well as on its outstanding magnetocrystalline anisotropy. In order to gain insight on the possible magneto-structural mechanism that gives rise to the unique super-hard phase (FM2) in this exotic trivalent iron oxide, neutron diffraction measurements were conducted at the high-intensity D20 diffractometer using a cryomagnet allowing to apply fields up to 5 T. For this, several NPD patterns were collected at 300 K between 0 and 5 T with a step of 0.5 T between them. The refinement of the CM magnetic reflections in the neutron patterns showed a nearly constant increase of the average moments at the different collinear Fe sublattices [see Fig. 9.7(a)]. The absence of strong anomalies in the evolution of the magnetic intensities and refined moments are compatible with an inversion of the direction of the collinear spins, which are oriented along a direction, as the neutron intensities resulting from these two magnetic order states would be undistinguishable to our unpolarized NPD. However, the Rietveld analysis of the nuclear intensities are rather appealing. The evolution of the average $\langle \mathrm{Fe-O} \rangle$ average interatomic distance and the Δ distortion at the four nonequivalent coordinated FeO_n sites shown

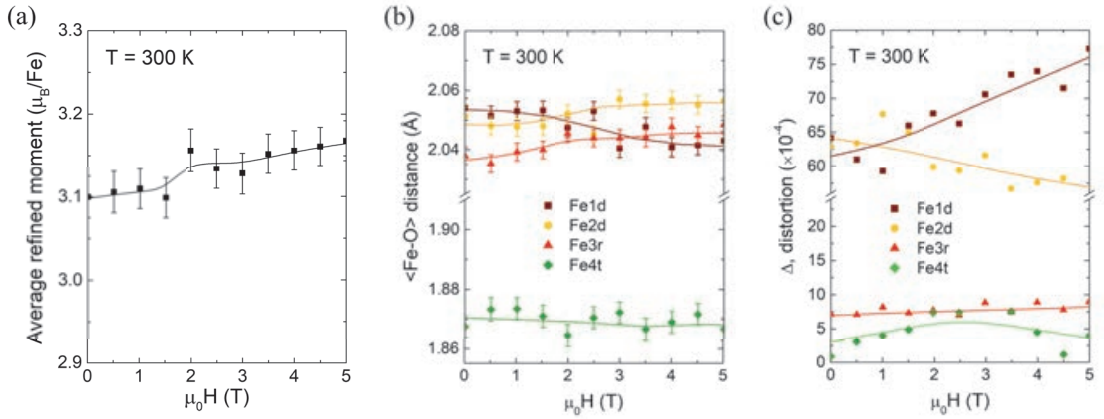

FIGURE 9.7: Magnetic field dependence of different magnetic and structural parameters at the super-hard AF2 phase obtained from NPD fits (D20@ILL, λ = 1.54 Å) at 300 K. (a) Evolution of the average ordered magnetic moment at the Fe sites. (b-c) Variation of the $\langle Fe - O \rangle$ average interatomic distance and distortion Δ at the different Fe^{3+} coordination polyhedra.

in Figs. 9.7(b-c) evidence the existence of atomic shifts under magnetic field that can give insights on the origin of the huge coercive field of the super-hard phase.

Although this investigation is still ongoing and measurements along complete [-H,H] cycles are required to fully characterize the mechanism behind the ferrimagnetic swithching, the results presented in this section are in the line of a magnetostriction-based mechanism, where the huge coercivity (20 kOe at RT) result from the necessary field to provoke subtle atomic shifts able to release some Fe-O-Fe exchange couplings in the frustrated structure during the magnetization switching, allowing finally the propagation of the reverse magnetization state.

9.5.2 Suppression of the ICM magnetic order under magnetic field

The magnetic response of the low temperature ICM magnetic order to external magnetic fields has also been been investigated. To the date, nothing is known about the effect of magnetic fields on the this phase beyond the bulk magnetic characterization, which revealed a critical reduction of the large coercivity at the FM2 ferrimagnetic from 20 kOe to 0.8 kOe, and of the remnant and the saturation magnetization [see Fig. 8.4 in Chapter 8]. To better understand this behaviour, isothermal NPD measurements were carried out up to 5 T at different temperatures below $T_{N2} \sim 150$ K. Measurements were performed at 10 K,

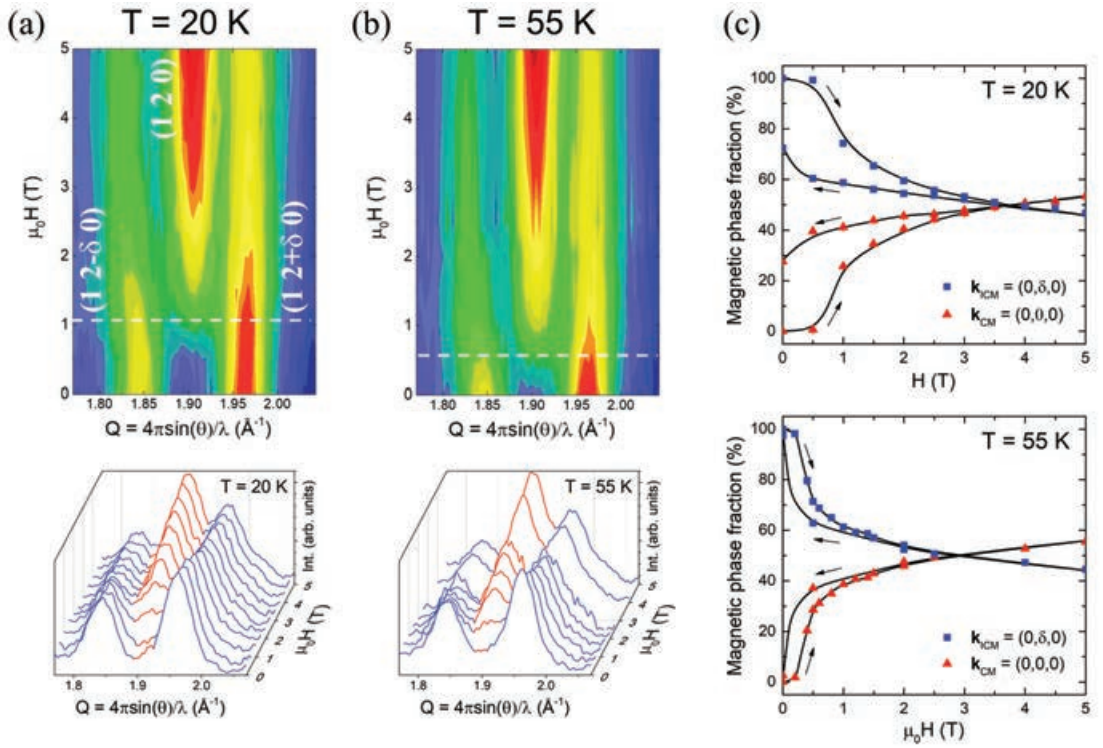

FIGURE 9.8: Neutron diffraction under magnetic fields on ε-Fe_2O_3 nanoparticles (D20@ILL, λ = 1.54 Å). 2D Q-H projections and contour maps showing the isothermal magnetic field dependence (up to 5 T) of the neutron-diffracted intensities around the (1 2 0) magnetic reflection, measured at (a) 20 K and (b) 55 K, both below $T_{ICM} \approx 150$ K. The intensity of the (1 2$\pm\delta$ 0) magnetic satellites is transferred to the CM (1 2 0) satellites due to the suppression of the ICM phase at rather low magnetic fields. (c) Field dependence of magnetic phase fractions of the ICM and the field-induced CM magnetic phases, obtained by fitting the magnetic reflections associated to its respective propagation vectors, $\mathbf{k}_{ICM}$ = (0,δ,0) (blue squares) and $\mathbf{k}_{CM}$ = (0,0,0) (red triangles).

20 K, 55 K and 75 K after cooling the sample in zero field.

The neutrons revealed that under applied magnetic fields ranging from 0 T to 1 T, the low temperature magnetic order [with magnetic propagation vector $\mathbf{k}_{ICM}$ = (0,δ,0)] undergoes an incommensurate-to-commensurate transition, as it can be observed from the Q-H contour maps of the magnetic intensities at 20 K and 55 K, plotted in Figs. 9.8(a-b). The evolution of the (1 2$\pm\delta$ 0) peaks illustrate a strong reduction of the ICM satellites, indicating that the ICM order is suppressed in favour of a field-induced CM magnetic order with the same propagation vector as that of the high temperature ferrimagnetic phases. It should be noticed that for none of the temperatures the total transformation of the ICM into CM magnetic order is achieved at the maximum magnetic field applied (5 T), as reflected by the refined magnetic phase fractions plotted in

Fig. 9.8(c). Likely, the coexistence of CM and ICM magnetic domains could be attributed to the magnetic anisotropy of the ICM order. Since we have a random distribution of nanoparticle orientations, the projection of the maximum magnetic field that is effectively applied along the magnetic easy axis of each monocrystalline particle can range from 0 T to 5 T, thus causing a virtual coexistence of the two separated phases and a broadening of the magnetic transition.

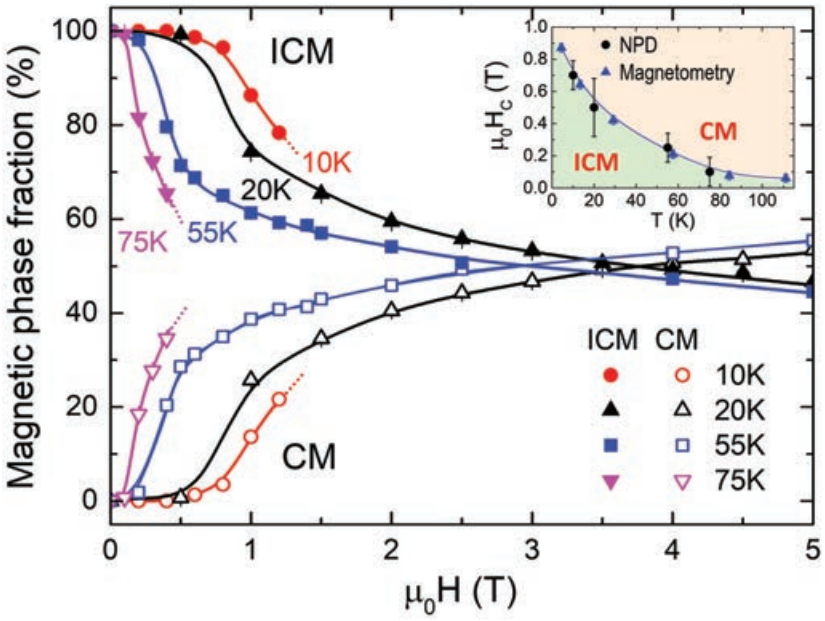

FIGURE 9.9: Evolution upon increasing magnetic field of the relative ICM and CM magnetic phase fractions, obtained from neutron neutron diffraction patterns at different fixed temperatures (10 K, 20 K, 55 K and 75 K). Filled points correspond to the ICM phase, and empty points to the CM one. Inset: Dependence with the temperature of the approximate critical field of the induced magnetic transition obtained from the maximum slope in the curves. The H_C values obtained from macroscopic susceptibility measurements are also shown for comparison.

The ICM-CM magnetic-field-induced transition was monitored at different temperatures, as illustrated in Fig. 9.9. The critical field of the magnetic transition (H_C) versus temperature, determined from each set of isothermal measurements, is shown as an inset in this figure. We observe that the ICM phase is more stable at lower temperatures, and the critical field decreases as we approach to the ordering temperature of the incommensurate phase (AF2-ICM, $T_{N2} \sim 150$ K). The remanent signal in the magnetization curves is well explained by the remanence of the certain amount of the CM phase, and low critical fields needed to transform the ICM phase into the CM also agrees with the magnetic coercivity values obtained in bulk magnetzation measurements.

9.6 Summary

In the this chapter we have investigated the puzzling magneto-structural properties of polycrystalline ε-Fe_2O_3 and its effects on the successive magnetic phases. First, on a detailed synchrotron X-ray thermodiffraction study in a wide temperature range between 100 K and and 925 K, we have shown from the evolution of the lattice constants and the linear thermal expansion coefficients that the ordering of the ultra-hard ferrimagnetic phase (FM2) at $T_{N2} \approx 500$ K is concurrent with a strong anisotropic exchange-striction effect, caused by the ordering of the two frustrated Fe3r and Fe4t collinear sublattices. By carefully refining the atomic coordinates we have fully determined evolution of the $Pna2_1$ structure, which allowed to obtain the evolution of bond lengths and angles in the Fe-O-Fe superexchange paths in the J_5, J_8, and J_9 triangle, where spin frustration is enhanced by the strong coupling between the Fe4t-Fe4t tetrahedral pairs (J_5). A sharp decrease of the Fe4-O-Fe4 angle (J_5), which is accompained by an increase in the bond angle between the two other Fe-Fe pairs (J_8 and J_9), produces a weakening of the frustrating J_5 superexchange coupling, while J_8 and J_9 are strengthened. The release of the magnetic frustration favours the ordering of the Fe3r and Fe4t sublattices, which lead to the super-hard ferrimagnetic order with strong magnetocrystalline anisotropy.
Subsequently, we presented the results of a first neutron diffraction study under magnetic fields, which revealed several noteworthy issues towards the understanding the complex magnetism in ε-Fe_2O_3. On the one hand, we give unprecedented evidences that the ferrimagnetic switching at the ultra-hard FM2 phase is inherently correlated to the displacement of some atoms in the structure. The magnetostriction mechanism driving the ferrimagnetic switching at RT is probably related to the unconventional ferroelectric swithching mechanism proposed to explain the ferroelectric polarization at RT in ε-Fe_2O_3 thin films, which is based on subtle atomic displacements favored by an intermediate nonpolar $Pbcn$ state [73]. On the other hand, we have revealed that the incommensurate magnetic order below $T_{ICM} \approx 150$ K can be suppressed by applying remarkably low magnetic fields (below 1 T). The commensurate field-induced magnetic order with null propagation vector replacing the ICM order is likely similar to the ferrimagnetic CM phase. The model for the ICM order proposed in Chapter 8, based on periodic anti-phase (AP) domains, allows to consistently understand this field-induced magnetic transition as the consequence of switching of the AP magnetic domains. The switching of the

AP domains would be driven by a similar magnetostrictive mechanism as in the ferrimagnetic switching in the super-hard AF2 phase. Although this mechanism is still not well understood, the parallelism with the mechanism to the polarization reversal suggests that at the boundary regions connecting the successive anti-phase magnetic domains (the anti-phase bondaries, APBs), the structure adopts locally an intermediate nonpolar state. Among the nonpolar symmetries closest to the $Pna2_1$ space group, the $Pbcn$ one arises as the most likely candidate. According to the first-principles calculations by K. Xu *et al.* [157], the energy barrier associated to the nonpolar $Pbcn$ state in ε-Fe_2O_3 is only 85 meV/f.u., much lower than the barrier calculated for the $Pnna$ phase of $GaFeO_3$ (0.6 [158], 0.5 [157] or -1.3 eV/f.u. [159]).

Part IV

General conclusions and publications

General conclusions

In this thesis, we have investigated the relevance and effects of magnetic frustration in correlated iron based oxides, where the unusually high stability of their interesting magnetic and ferroic properties stem from the strong magnetic couplings involving Fe cations. Along this manuscript, the $YBaCuFeO_5$ and ε-Fe_2O_3 ferrite systems were addressed in two main parts, in which synchrotron and neutron techniques were selectively combined to characterize different aspects related to their complex magnetism and the impact of its coupled structural properties, as well as their magnetoelectric response and the effects of external magnetic fields. The main conclusions obtained in this work have already been presented in the last section of each chapter. However, an overall view of the major highlights is summarized breafly in this chapter.

Investigating the family of spin-induced $YBaCuFeO_5$ multiferroics with high-T_c chiral magnetism

- The magnetic phase diagram of $YBaCuFeO_5$, where magnetic frustration is strictly driven by Fe^{3+} [Cu^{2+}] chemical disorder, is extended to nearly fully disordered compounds, increasing the stability of the helimagnetic order up to $T_S \approx 366$ K by means of optimized quenching processes. The stability of the modulated order cannot overcome the stability of the collinear order, leading to a Lifshitz multicritical point (LP) which divides the phase diagram into paramagnetic (PM), collinear (AF1) and spiral (AF2) phases, which coexist at the LP. The triple point driven by Fe/Cu disorder sets a limit to the thermal stability and a critical end point for the formation of the spiral. Above the critical disorder ($n_d^c \gtrapprox 0.47$) the system enters in the *phase-separated regime*, characterized by the presence of magnetic phase segregation.

• In contrast with the usual assumption in previous reports, we find that in YBCFO there is a critical threshold of disorder or minimum frustration level, determined at $n_0 \approx 0.112$, below which a long-range spiral magnetic state cannot be formed. If the concentration of AFM Fe-Fe bonds is too low, the dipolar interaction (mediated by spin waves) between individual canted spins in the vicinity of the separated Fe/Fe bonds decay without forming a coherent spiral. Bipyramids with strong AFM coupling can then favour short-ranged minority regions with tendency to $k_z = 0$.

• We have described how the magnetic anisotropy of the spirals phase in YBCFO can be controlled keeping invariant its chemical composition through the degree of B-site chemical disorder, which is linearly related to the tilting of the rotation plane of the spins in the spiral. Favorurably to ferroelectricity in the DM scenario, increasing the level of Fe/Cu disorder increases the cycloidal component ($\mathbf{Q} \perp \mathbf{q}_S$) of the spiral.

• The degree of Fe/Cu cation disorder has a relevant impact on the YBCFO structure. On the one hand, the pyramid height at the Cu-rich pyramid site is more elongated than in the Fe-rich one in virtue of the Jahn-Teller distortion between basal and apical distances around Cu^{2+}, as confirmed by the longer[shorter] bond lengths between Cu[Fe] and the apical oxygen. On the other hand, B-site disorder tends to make uniform the two nominal MO_5 pyramids, which become practically indistinguishable when a nearly random Fe/Cu distributions is reached. Hence, increasing Fe/Cu randomness inherently results in additional lattice effects (decrease [increase] of d_t [d_s]) that also contribute to frustration through the tuning of the magnetic exchange couplings.

• In the aim of finding alternative strategies to upgrade the properties of $YBaCuFeO_5$, B-site divalent non-JT substitutions have been explored. The investigation of different families of $YBa(Cu,M)FeO_5$ layered perovskites (M = Co, Zn, Mg) validates an extraordinarily efficient way to enhance the stability of the spiral order, in which the strong overall contraction of the bipyramidal thickness, caused by the dilution of JT Cu^{2+} ions in the structure, enhance the strong AFM couplings in Fe_2O_9 improper bipyramids, thus raising the magnetic frustration. Maximum stabilities of the spiral, are reached at the tri-critical point, far beyond RT: $T_S \sim 355$ K in Co-samples and 340 K in Zn-doped compounds, keeping just a moderate disorder.

• Among the different divalent B-site substitutions investigated, qualitative significant differences on the doping dependence of the magnetic phase

diagram stem from the character of coupled spin pairs at the bipyramids. In particular, the replacement of FM Cu^{2+}/Fe^{2+} pairs by AFM Co^{2+}/Fe^{2+} (and Co^{2+}/Cu^{2+}) dimers (in $CoMO_9$ bipyramids) leads to an *induced phase separation* characterized by collinear AFM regions (AF3, k_z = 0). Remarkably, this phase separation is avoided by using the non-magnetic Zn^{2+} cation (instead of Co), producing an advantageous single magnetic spiral state below T_S.

• In Zn substituted samples prepared using different cooling methods we have extended the incommensurate modulation (q_s) achieving the largest magnetic discommensuration never seen in this family of compounds (q_s = 0.201, giving a twist angle $\varphi = 72.47(5)^\circ$ in the spiral). Regarding the magnetic anisotropy, inserting divalent Co or Zn at the Cu site has interestingly different impacts on the the tilting of the chiral easy plane. While Co produces a systematic reorientation towards a nearly cycloidal spin order ($\mathbf{Q} \perp \mathbf{q}_S$), highly favorable to ferroelectricity, the effect of Zn is in the opposite direction and leads to a less favourable inclined helix-type spiral order.

• Besides the steric effects produced by chemical substitutions, the structural evolution in YBCFO under hydrostatic pressure reveals that up to 20 GPa the distance separating successive bilayers is rather uncompressible, whereas the bilayer thickness displays much higher compressibility. This validates the possibility of further stabilizing the spiral order by the effect of external pressure.

• The succesful growth of high quality YBCFO single crystals by a modified Traveling Solvent Floating Zone (TSFZ) technique is reported. The B-site disorder of different single crystals, thoroughly quantified by SXRPD and SCND measurements, reveals that inherently to the slow pulling rates of the TSFZ technique the resulting perovskites display high levels of Fe/Cu cationic order. In good agreement with the extrapolated minimal critical threshold in powder samples ($n_0 \approx 0.112$), magnetic diffraction evidenced that the modulated spiral order is lacking only in single crystals with Fe/Cu disorder below $n_d \lessapprox 0.112$. A single crystal above this threshold ($n_d \approx 0.30$) is the only one adopting the incommensurate state with $T_S \approx 195$ K. Noteworthily, in ordered crystals, a detailed NPD characterization of the magnetic moments at the two seggregated collinear domains [k_z = 1/2 (AF1) and k_z = 0 (AF3)] confirms that the latter are associated to regions in the crystal with higher cationic disorder where the Fe-Cu ferromagnetic coupling between spins sharing a bipyramid becomes antiferromagnetic. Noteworthily, a detailed NPD characterization in ordered crystals, allows to confirm that the AF3 collinear domains with k_z =

0 translational symmetry are associated to minoritary regions in the crystal with higher cationic disorder, where the Fe-Cu ferromagnetic coupling between spins sharing a bipyramid becomes antiferromagnetic.

• The combination of several single crystal studies allowed to overcome the limitations of NPD to elucidate the real magnetic nature of the presumed spiral magnetic order in YBCFO. The picture emerging from different complementary quantum-beam techniques, which include (i) unpolarized single-crystal neutron diffraction (SCND), (ii) spherical neutron polarimetry (SNP) and (iii) synchrotron resonant magnetic X-ray scattering (RMXS), unambiguously converges to a solution that requires the combination of two perpendicular modulations to give a non-collinear circular helicoidal order below $\mathrm{T_S}$ = 195 K, in which the interplay of the modulation and the transition temperature matches the prediction of the Scaramucci model. Whereas equally populated ± 1 magnetic chiral domains were found in crystals of macroscopic size using neutrons, RMXS allowed to resolve spatial inhomogeneities in the chiral domain populations of the helicoidal phase.

• The above mentioned investigations on the YBCFO single crystal also allowed to determine with precision that the spins are parallel to the tetragonal ab plane both in the spiral phase and in the preceding AF1 collinear order above $\mathrm{T_S}$. In the latter, collinear moments were also found to be aligned along the diagonal axis. On the other hand, the fact that the slightly decompensated volume fractions of the AF1 conjugated (twin) domains differ from the nearly identical fractions of chiral domains in AF2, suggests that the former can generate indistinctly any of the two types of chiralities below $\mathrm{T_S}$. Interestingly, SCND results also unveil a deviation from collinearity between $\mathbf{m}_1$ and $\mathbf{m}_2$ moments in the chemical cell, characterized as a magnetic phase $\varphi'_{\mathrm{S}} = 172(1)^\circ$, which is not predicted in the model.

• The absence of magnetoelectric response in the studied YBCFO crystal is concluded after the unability to modify the population of chiral domains under electrical fields parallel to (1-1 0) (SNP) and to (0 1 0) direction (RMXS by circularly polarized x-rays with linear polarimetry analysis). where the spin rotation plane of the circular helix was parallel to the ab plane. This result is in agreement with a purely helical magnetic spiral in the DM scenario for the multiferroicity of this system.

• The anisotropy of the magnetic spiral response in YBCFO single crystals is related to the in-plane orientation of the helix. Bulk susceptibility and SCND measurements, show that field-induced transitions at relatively low fields (1-7

T range) occur when H is applied parallel to the in-plane direction ($H \parallel b$), and no changes occur (up to 9 T) for H applied along the perpendicular direction ($H \parallel c$). Neutron experiments reveal that the field-induced transition is associated to the suppression of the spiral and the emergence of a CM order with the same wave vector as the in the high temperature AF1 phase.

Outlook: The search of strategies for the fabrication of single crystals enhancing the cycloidal component in the spiral order, as well as its thermal stability, are imperative, and will allow the study of the magnetoelectric response of this family under a variety of conditions. The understanding of the experimental results presented in this work provides several important clues to define and inspire these new design strategies that could be also applied to materials in the form of epitaxial thin films and heterostructures.
This research also opens the door to the combination of selected A- and B-site cation substitutions. Some which could also help to bring about a depression of the conductivity. Some of these research lines are already being developed in our group (CMEOS) in parallel to the work presented in this Thesis.

Magnetostructural properties of ε-Fe_2O_3, a high-T_C multiferroic with superhard ferrimagnetism

- Contrary to what was stablished in the literature, the magnetoelectric ε-Fe_2O_3 polymorph displays a soft ferrimagnetic order phase (FM1) above the ultra-hard ferrimagnetic order (FM2) that extends to much higher temperatures, between 500 K and 850 K. The PM-AF1-AF2 successive magnetic transitions have been thoroughly studied in the whole temperature range, and have been fully described using the magnetic space groups approach. Both AF1 and AF2 magnetic orders adopt the magnetic space group $Pna'2'_1$ (n. 33.147), and the soft to ultra-hard ferrimagnetism is activated by the magnetic ordering of the regular octahedral and tetrahedral frustrated sites: Fe3r and Fe4t. The small FM component persisting up to $T_{N1} \approx 850$ K is explained from a slightly dissimilar magnetization at the antiparallel Fe1d and Fe2d sublattices.

- The SXRPD structural study across the FM1-FM2 (soft-hard) ferrimagnetic transition unveils the magnetostructural effects behind the ordering of the Fe3r and Fe4t sublattices. The evolution of the bond lengths and angles in the the triangularly frustrated Fe-O-Fe superexchange interactions disclose a strong reduction of the spin frustration, mainly originated by the weakening

of the strongly coupled Fe4t-Fe4t tetrahedral pairs. The Fe3r and Fe4t sublattices become ordered as a result of this, triggering the onset of the super-hard ferrimagnetic order.

- For the ICM magnetic order emerging below the super-hard FM2 phase ($T_{ICM} \sim 150$ K), different helimagnetic, spiral and collinear models proposed in the literature were analyzed in the light of a neutron diffraction investigation and the results from earlier Mössbauer and NFS studies. It has been confirmed that the ground magnetic order in ε-Fe_2O_3 is compatible with a collinear ordering with periodic anti-phase domains with magnetic moments along a. The stabilization of this phase is likely subsequent to magnetostructural effects linked to the collapse of the macroscopic Fe orbital moment between 85-150 K. These preparatory structural changes are very likely associated to the narrow anti-phase boundary regions separating the periodic magnetic domains, that could imply the appearance, locally, of an inversion center (*i.e.* a nonpolar symmetry).
- The neutron diffraction study under magnetic fields provides evidence of a magnetostriction mechanism driving the ferrimagnetic switching at the ultra-hard FM2 phase. The reversal of the magnetic moments likely implies the transformation into a symmetrically equivalent nonpolar $Pna2_1$ structures. The huge coercive fields to achieve the switching of the magnetization are then a consequence of the necessary atomic displacements between these two symmetric structures that could be associated to an intermediate nonpolar $Pbcn$ state. A similar mechanism could also explain the suppression of the low temperature ICM order by the effect of magnetic fields as the consequence of the switching of the anti-phase (AP) domains, where probably a $Pbcn$ nonpolar intermediate state localized at the anti-phase bondaries (APBs) separates the symmetric magnetic/structural domains.

Publications

- *Helimagnets by disorder: Its role on the high-temperature magnetic spiral in the $YBaCuFeO_5$ perovskite*, **Arnau Romaguera**, Xiaodong Zhang, Oscar Fabelo, Francois Fauth, Javier Blasco and José Luis García-Muñoz, **Physical Review Research** 4 043188 (2022) [18pp].
  DOI: doi.org/10.1103/PhysRevResearch.4.043188
- *Magnetic properties of a highly ordered single crystal of the layered perovskite $YBaCuFe_{0.95}Mn_{0.05}O_5$*, Xiaodong Zhang, **Arnau Romaguera**, Felip Sandiumenge, Oscar Fabelo, Javier Blasco, Javier Herrero-Martín and José Luis García-Muñoz, **J. of Magnetism and Magnetic Materials** 551 (2022) 169165 [7pp].
  DOI: doi.org/10.1016/j.jmmm.2022.169165
- *Magnetoelastic coupling behaviour of nanocrystalline ε-Fe_2O_3*, José Luis García-Muñoz, **Arnau Romaguera**, Francois Fauth, Josep Nogués and Martí Gich, **J. of Magnetism and Magnetic Materials** 170240 (2022) [16 pp].
  DOI: doi.org/10.1016/j.jmmm.2022.170240
- *Tuning the tilting of the spiral plane by Mn doping in $YBaCuFeO_5$ multiferroic*, X. Zhang, **Arnau Romaguera**, O. Fabelo, F. Fauth, J. Herrero-Martín and J.L. García-Muñoz, **Acta Materialia**, 206 (2021) 116608 [10pp].
  DOI: doi.org/10.1016/j.actamat.2020.116608
- *Ferromagnetic metallic Sr-rich $Ln_{1/2}A_{1/2}CoO_3$ cobaltites with spontaneous spin rotation*, Jessica Padilla-Pantoja, **Arnau Romaguera**, Xiaodong Zhang, Javier Herrero-Martín, Francois Fauth, Javier Blasco and José Luis García-Muñoz, **Physical review B** 104, 054411 (2021).
  DOI: doi.org/10.1103/PhysRevB.104.054411
- *Phase transitions and magnetic structures in Epsilon-Fe_2O_3 nanoparticles*, **Arnau Romaguera**, Z. Ma, J. Herrero-Martín, C. Popescu, J. Ángel Sans, M. Gich, J.L. García-Muñoz, **Acta Cryst.** (2021), A77, C639.
  DOI: doi.org/10.1107/S0108767321090565

- *Magnetic properties of Cr-substituted ε-$(Fe_{1-x}Cr_x)_2O_3$ nanoparticles with epsilon structure*, Zheng Ma, **Arnau Romaguera**, FrancoisFauth, Javier Herrero-Martín, JoseLuis García-Muñoz, Martí Gich, **J. of Magnetism and Magnetic Materials** 506, 166764 (2020)
  DOI: doi.org/10.1016/j.jmmm.2020.166764
- *Ferromagnetic and antiferromagnetic resonances in ε-Fe_2O_3*, Z. Ma, V. V K Thalakkatukalathil, **A. Romaguera**, J. L. García-Muñoz, F. Macià, J. M. Hernandez, M.Gich, Proceedings of the 16èmes Journées de Caractérisation Microondes et Matériaux, 2020, Toulouse, France. [4pp]. publication/349953036
- *Electronic, spin-state and magnetic transitions in $Ba_2Co_9O_{14}$ investigated by x-ray spectroscopies and neutron diffraction*, J. Herrero-Martín, J. Padilla-Pantoja, S. Lafuerza, **A. Romaguera**, F. Fauth, J. S. Reparaz and J. L. García-Muñoz, **Physical review B** 95, 235129 (2017).
  DOI: doi.org/10.1103/PhysRevB.95.235129
- *Unveiling a new high-temperature ordered magnetic phase in ε-Fe_2O_3*, José Luis García-Muñoz, **Arnau Romaguera**, Francois Fauth, Josep Nogués and Martí Gich, **Chemistry of Materials** 29 (22), 9705–9713 (2017)
  DOI: doi/10.1021/acs.chemmater.7b03417
- *Is there a magnetic spiral in $YBaCuFeO_5$? A single crystal neutron study*, **Arnau Romaguera**, Xiaodong Zhang, Oscar Fabelo, J. Alberto Rodríguez-Velamazán, Javier Herrero-Martín and José Luis García-Muñoz. (submitted)

Manuscripts in preparation (advanced stage):

- *Huge stabilization of a cycloidal order in Co-doped $YBaCuFeO_5$*, Xiaodong Zhang, **Arnau Romaguera**, Oscar Fabelo, Javier Herrero-Martín and José Luis García-Muñoz. (manuscript in preparation)
- *Frustrated Jahn-Teller competition in Mn-doped $YBaCuFeO_5$ investigated by x-ray absorption spectroscopy and neutron diffraction*, Xiaodong Zhang, Javier Herrero-Martín, **Arnau Romaguera**, Felip Sandiumenge, Oscar Fabelo and José Luis García-Muñoz. (manuscript in preparation)
- *Phase diagrams and stability of the chiral magnetic phase in B-site substituted $YBaCuFeO_5$*, **Arnau Romaguera**, Xiaodong Zhang, Ruyong Li, Oscar Fabelo, Javier Herrero-Martín and José Luis García-Muñoz. (manuscript in preparation)
- *Origin of the colossal coercivity in the frustrated ε-Fe_2O_3 ferrite*. **Arnau Romaguera**, José Luis García-Muñoz, Zheng Ma, Oscar Fabelo, Javier Herrero-Martín and Martí Gich. (manuscript in preparation)

- *The incommensurate magnetic ground-state in ε-Fe_2O_3*, **Arnau Romaguera**, Jose Luis Garcia-Muñoz, Zheng Ma, Javier Herrero-Martín, Oscar Fabelo, Martí Gich. (manuscript in preparation)
- *The magnetoelectric response of a $YBaCuFeO_5$ crystal investigated by magnetic resonant x-ray scattering (RMXS)*, **Arnau Romaguera**, Javier Herrero-Martín, Gareth Nisbet, Alessandro Bombardi and José Luis García-Muñoz. (manuscript in preparation)

Part V

Appendices

Appendix A

Supplementary information for Chapter 4: *Helimagnets by disorder: its role on the high-temperature magnetic spiral in the YBCFO perovskite*

A.1 Quantitative determination of cation disorder in YBCFO: X-ray versus neutron diffraction

In general, quantifying any fractional occupation of a crystallographic site by one or various chemical species using diffraction methods can be a difficult and elusive task in some cases. Each problem (determination of cation disorder, chemical composition, oxygen content, etc.) requires of an appropriate choice of experimental parameters: type of radiation, wavelength, instrument and sample conditions.

One of the aims of this work is to determine with the maximum accuracy and reliability the cation disorder at the B-sites of the $YBaCuFeO_5$ perovskite, which are occupied by Fe and Cu atoms. To achieve this, the differences between the total scattered radiation by the atoms located at $(1/2, 1/2, z \approx 3/4)$ and those placed at $(1/2, 1/2, z \approx 1/4)$ positions have to be above the instrumental detection limit of the diffractometer.

The capability of X-ray and neutron diffraction techniques to resolve and quantify cation disorder is strongly conditioned by the difference between the scattering lengths of the cations involved. In this sense, the quantitative determination of Fe/Cu disorder in this system has proven to be extremely challenging due to

the similarity of Fe and Cu scattering lengths whether we use X-rays or neutrons. The choice of high-resolution synchrotron X-ray diffraction for describing the Fe/Cu occupancy presents some advantages over neutrons in the present case. Some of them are listed as follows:

(i) First, the occupancy can be refined from synchrotron X-ray patterns collected at room temperature simply using a single phase (the structural phase). The joint refinement of several phases in neutron patterns (nuclear and magnetic) adds uncertainty and may compromise the refined values for the occupancy. X-rays avoid the undesirable interference from magnetic intensities, which are present and coexist with nuclear peaks in our D20 neutron diffractograms up to very high temperatures since Neel temperatures (T_{N1}) are very high in YBCFO.

(ii) Synchrotron X-ray can provide shorter wavelengths that allows to access a much wider Q-range than neutrons. The number of observed nuclear peaks in neutron diffractograms may not be enough to analyze the occupancy.

(iii) Finally, in consideration of the previous points, determining the Cu/Fe chemical disorder using neutrons is not so favorable compared to X-rays in regard to the scattering lengths. Although X-ray scattering lengths are very similar for Fe and Cu due to its proportional dependence with the atomic number [Z(Fe)=26 and Z(Cu)=29], the neutron scattering lengths of the two magnetic cations are also rather similar: 9.45 fm for Fe and 7.72 fm for Cu.

For the above mentioned reasons, most of the structural information presented in this dissertation (including Fe and Cu cation occupancies) was obtained from refinements of synchrotron X-ray powder diffraction (SXRD) diffractograms [Fig. A.1(a)]. D20 neutron data collected with λ = 2.41 Å is not optimized to determine the occupancy. In order to increase the number of observed nuclear peaks in neutron diffractograms, three samples in the two extremes of the YBCFO series (S1, S2 and S7) were also measured on D20 using a shorter wavelength (λ = 1.54 Å) at high temperature, in the paramagnetic state at 490 K, where magnetic peaks are absent [Fig. A.1(b)]. The occupancies obtained from Rietveld refinements are shown in Table A.1. Although thermal agitation effects in these neutron patterns are far greater than in the X-ray data collected at 300 K, Table A.1 shows that the occupancies obtained near 500 K (in the paramagnetic regime) from these additional neutron measurements agree very well within errors and are compatible with synchrotron X-ray results.

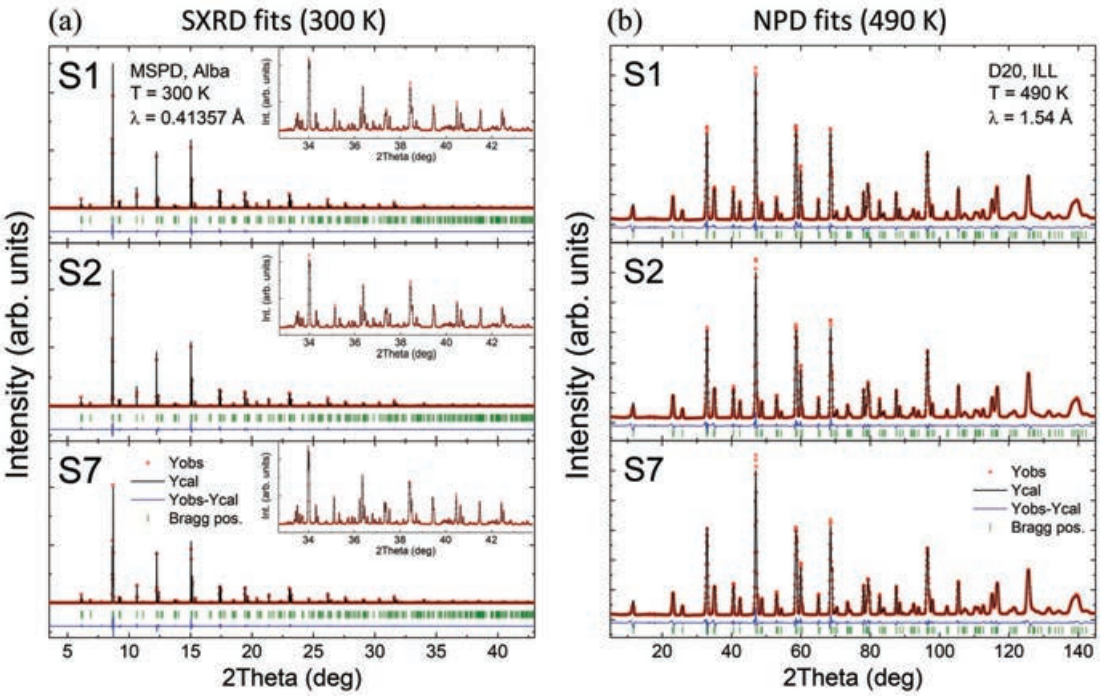

FIGURE A.1: (a) Rietveld fits of the MSPD@Alba synchrotron X-ray diffraction patterns (λ = 0.413570 Å) at 300 K for the S1, S2 and S3 YBCFO samples. Inset: Detail of the high-angles region. (b) Fits of the D20@ILL pure nuclear neutron intensities (λ = 1.54 Å) at 490 K for the same samples. (Black line: calculated pattern, red circles: experimental points, blue line: observed-calculated difference, green bars: position markers of the X-ray and neutron nuclear Bragg reflections).

TABLE A.1: Comparison of the refined Cu/Fe occupancies from Rietveld refinements of MSPD@Alba synchrotron data (λ = 0.413570 Å) at T = 300 K and D20@ILL neutron diffraction data using λ = 1.54 Å at T = 490 K (in the paramagnetic phase) for samples S1, S2 and S7 (end members of the series). Agreement factors from neutron refinements: S1 (R_B: 4.11, R_f: 2.37, χ^2: 169); S2 (R_B: 3.64, R_f: 2.23, χ^2: 182); S3 (R_B: 3.75, R_f: 2.24, χ^2: 213).

		S1	**S2**	**S7**
Synchrotron X-ray MSPD@Alba λ = 0.413570 Å T = 300 K	**Occ(Cu1/Fe2)**	0.706 (29)	0.684 (28)	0.560 (43)
	Occ(Fe1*/Cu2*) = n_d	0.294 (29)	0.316 (28)	0.440 (43)
Neutrons D20@ILL λ = 1.54 Å T = 490 K	**Occ(Cu1/Fe2)**	0.749 (16)	0.688 (16)	0.595 (26)
	Occ(Fe1*/Cu2*) = n_d	0.251 (16)	0.312 (16)	0.405 (26)

A.2 Electrical characterization: polarization

With the aim of probing the ferroelectric properties of these compounds, electric-field dependent polarization P(E) measurements for samples S2, S4 and S5 (300 °C/h cooled, liquid nitrogen quenched and water quenched) were carried out at room temperature (RT) and 77 K. Disc-shaped pellets of 0.5 mm thickness and surface about 50 mm^2 were measured using silver paint as electrodes. At RT the samples show values of resistance of ∼70 kΩ (S2); ∼100 kΩ (S4) and ∼40 MΩ (S5), indicating a strong variation increasing cation disorder. The S5 sample was 400 times more insulating than S4 sample. At ambient temperature the maximum voltage applied for the P(E) cycles was 10 V at frequencies of 100 Hz and 250 Hz (sinusoidal waveform). Fig. A.2 shows that the main contribution at RT is purely resistive and the P(E) loops have the characteristic ellipsoidal shape, which strongly depends on the frequency. For the S5 sample, an ellipsoidal P(E) cycle is also obtained but in this case, as the resistance is higher than for the other two samples, there is also a capacitive contribution (linear dependence of P with E for a pure capacitance) resulting in a dielectric behavior with losses, which strongly depends on the frequency too.

Figs. A.3(a) and A.3(b) report the loops obtained at 77 K for S5 and S2 samples (in the liquid nitrogen cryostat). The samples become more insulating on cooling, and a maximum voltage of 850 V could be applied. Fig. A.3(a) (top panel) show P(E) cycles in sample S5 increasing the voltage at fixed frequency of 250 Hz (sine voltage waveform). The observed ellipsoidal shape corresponds to a lossy dielectric behavior with both resistance and capacitance contributions. Fig. A.3(b) (top panel) show similar measurements for sample S2, in this case using a triangle waveform. Although in this case the shape of the P(E) curve for the triangle voltage waveform is closer to a ferroelectric behavior, the strong dependence of the P(E) curve on the frequency agrees with the absence of ferroelectricity also in the S5 sample. The P(E) curves at the maximum voltage (850 V) are compared for 250 Hz and 100 Hz and using a triangle waveform in the bottom panels, confirming this point. Comparing the two specimens, higher values of P (∼+20%) are measured in S5 respect to the S2 sample. No signs of spontaneous ferroelectricity was detected in these samples.

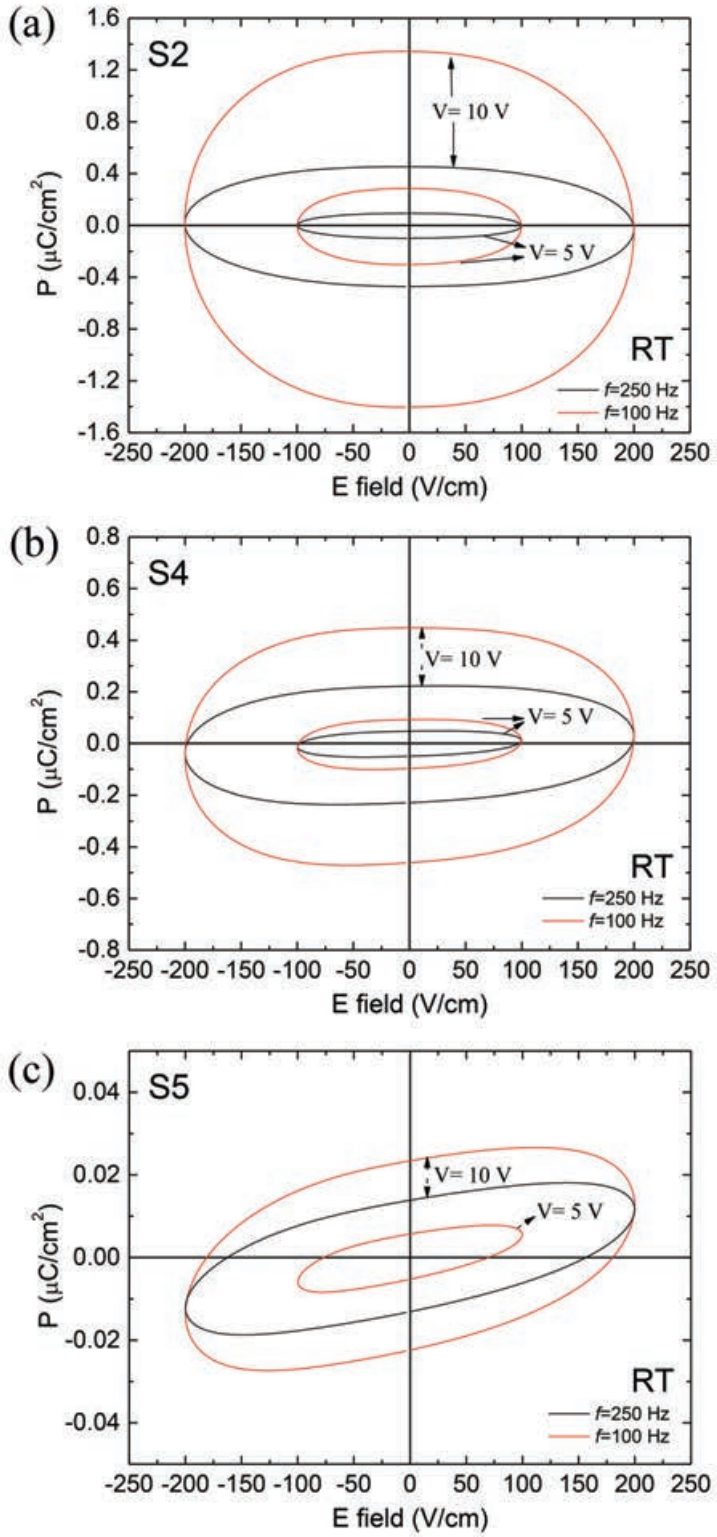

FIGURE A.2: P (E) loops measured at room temperature (RT) at different amplitudes of the electric field (5 V and 10 V) and at two different frequencies (100 Hz and 250 Hz) for (a) S2 cooled at 300 °C/h, (b) S4 liquid nitrogen quenched, and (c) S5 water quenched samples.

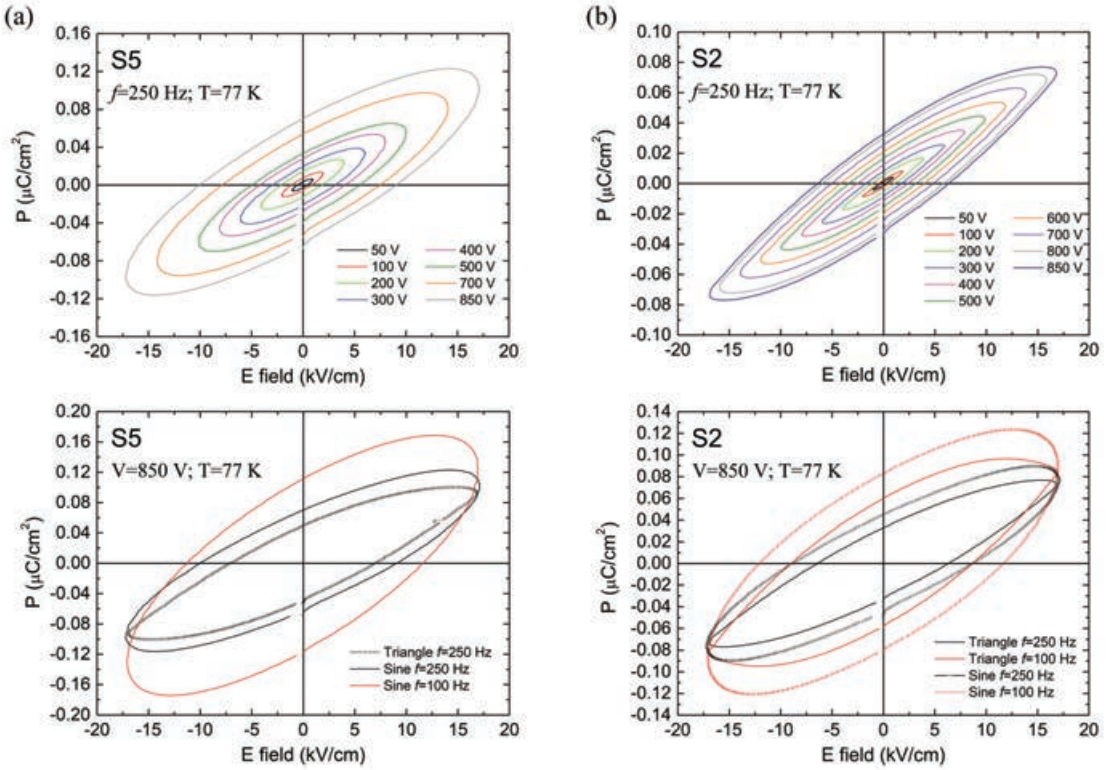

FIGURE A.3: P(E) loops for (a) S5 sample quenched in water and (b) S2 sample cooled at 200 °C/h. Top: P(E) loops measured at 77 K at different amplitudes of the electric field. Bottom: P(E) loops collected at 77 K at two different frequencies of the sinusoidal excitation voltage of 850 V and using a triangle waveform.

Appendix B

Supplementary information for Chapter 5: *Enhancing the spiral stability in YBCFO by B-site divalent non-JT substitutions*

This appendix includes figures and tables that complement the discussion on the effect of B-site chemical doping in Chapter 5. Here we show the fitted SXRPD diffraction patterns measured at the BL06-MSPD beamline of the ALBA Synchrotron Light Facility (Cerdanyola del Vallès, Spain) at 300 K for the structural characterization of the $YBaCu_{1-x}Co_xFeO_5$ and $YBaCu_{1-x}Zn_xFeO_5$ series, and tables showing the corresponding refined structural parameters and agreement factors. Information regarding the YBa(Cu,Co)FeO_5 series, which was studied in collaboration with X. Zhang, can be also found in Ref. [133].

B.1 SXRPD Rietveld fits of Cu/Co-doped samples

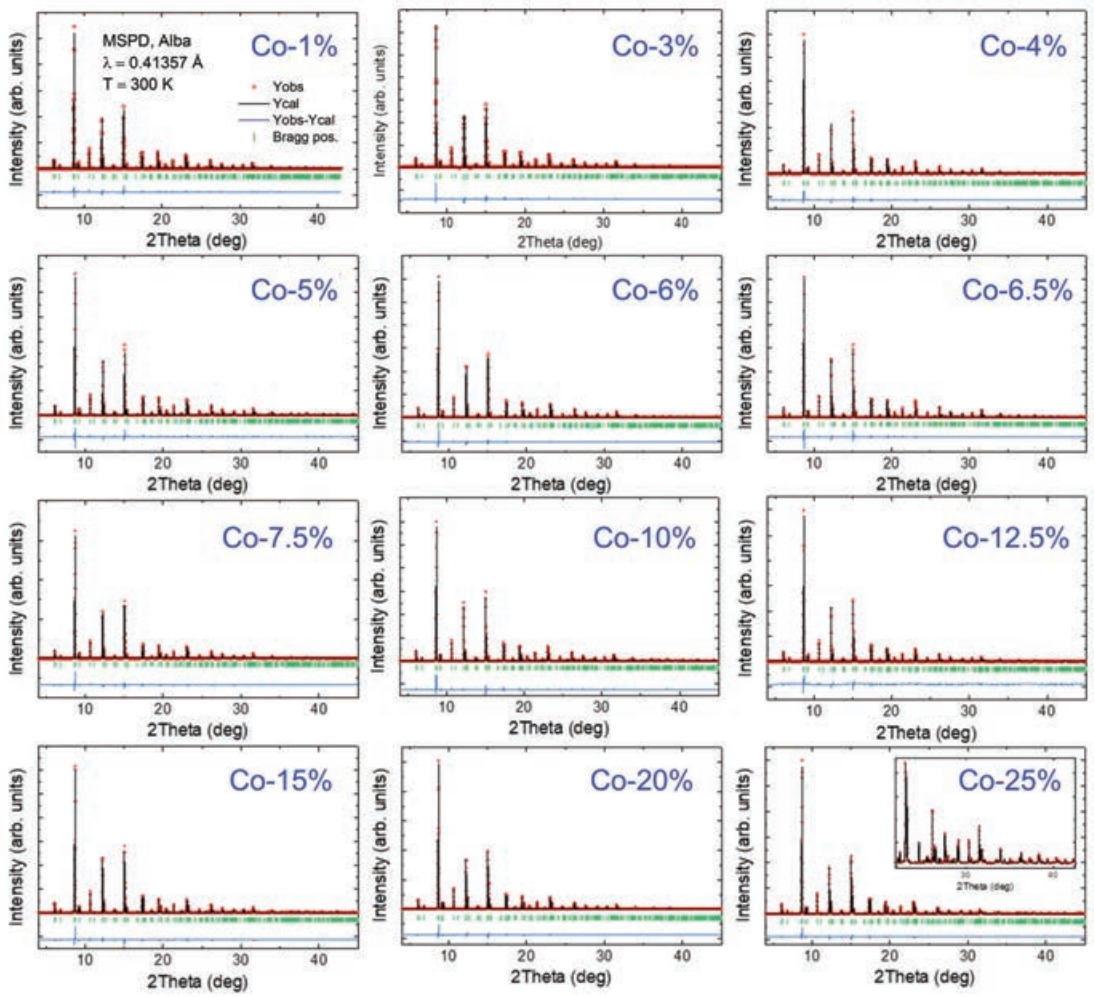

FIGURE B.1: Rietveld refinement (black curve) of the synchrotron X-ray intensities (red circles) at 300 K for the $YBaCu_{1-x}Co_xFeO_5$ samples (with doping values $x = 0.01$, 0.03, 0.04, 0.05, 0.06, 0.065, 0.075, 0.10, 0.125, 0.15, 0.20 and 0.25) prepared with a cooling rate of 300 °C/h. Bottom blue line is the observed-calculated difference, and the row with green bars represents the calculated Bragg positions. Inset: detail of the high-angles region in the Co-25% refinement. Figure adapted from work done in collaboration with X. Zhang, reported in Ref. [133].

TABLE B.1: $YBaCu_{1-x}Co_xFeO_5$ (prepared with 300 °C/h cooling rate). Structural parameters at T = 300 K and agreement factors from Rietveld refinement of MSPD@ALBA synchrotron data (λ=0.413378 Å). [*: minority fraction; n_d (disorder)=Occ Fe1*/(Cu,Co)2*]. The coordinates of each metal [M: (Cu,Co) or Fe] are constrained by z(M1)+z(M2)=1. Values in this table were adapted from work done in collaboration with X. Zhang, reported in Ref. [133].

T=300 K *P4mm*		**Co-1**%	**Co-3**%	**Co-4**%	**Co-5**%	**Co-6**%	**Co-6.5**%	**Co-7.5**%	**Co-10**%	**Co-12.5**%	**Co-15**%	**Co-20**%	**Co-25**%
a=b (Å)		3.87446 (3)	3.87500 (3)	3.87552 (3)	3.87612 (3)	3.87644 (3)	3.87651 (3)	3.87688 (3)	3.87807 (3)	3.87880 (3)	3.87977 (3)	3.88101 (3)	3.88275 (3)
c (Å)		7.66256 (6)	7.66072 (6)	7.65902 (6)	7.65753 (6)	7.65672 (6)	7.65672 (6)	7.65555 (6)	7.65183 (6)	7.64992 (6)	7.64648 (6)	7.64350 (6)	7.63636 (6)
$\Delta_T \equiv$c/2a		0.98886 (1)	0.98848 (1)	0.98813 (1)	0.98778 (1)	0.98760 (1)	0.98758 (1)	0.98733 (1)	0.98655 (1)	0.98612 (1)	0.98543 (1)	0.98473 (1)	0.98337 (1)
V (Å^3)		115.026 (2)	115.030 (2)	115.036 (2)	115.049 (2)	115.056 (2)	115.060 (2)	115.064 (2)	115.079 (2)	115.094 (2)	115.099 (2)	115.128 (2)	115.124 (2)
Y 1*a* (00z)	z/c	0.48823 (32)	0.48854 (33)	0.48811 (26)	0.48877 (23)	0.48806 (29)	0.48848 (28)	0.48923 (37)	0.48960 (27)	0.49015 (27)	0.49049 (28)	0.49101 (29)	0.49174 (29)
Ba 1*a* (00z)	z/c	0	0	0	0	0	0	0	0	0	0	0	0
(Cu,Co)1 1*b* (½ ½ z)	z/c	0.71524 (23)	0.71545 (23)	0.71549 (23)	0.71553 (25)	0.71584 (32)	0.71579 (28)	0.71608 (23)	0.71617 (23)	0.71635 (25)	0.71746 (24)	0.71779 (24)	0.71849 (22)
Fe1* 1*b* (½ ½ z)	z/c	0.75485 (54)	0.75441 (55)	0.75429 (67)	0.75415 (60)	0.75401 (73)	0.75395 (70)	0.75390 (54)	0.75360 (56)	0.75311 (59)	0.75247 (57)	0.75210 (56)	0.75142 (51)
(Cu,Co)2* 1*b* (½ ½ z)	z/c	0.28163 (49)	0.28247 (42)	0.28065 (37)	0.27761 (48)	0.27893 (52)	0.27807 (40)	0.27660 (44)	0.28065 (37)	0.27761 (48)	0.27893 (52)	0.27807 (40)	0.27660 (44)
Fe2 1*b* (½ ½ z)	z/c	0.24515 (54)	0.24559 (55)	0.24571 (67)	0.24585 (60)	0.24599 (73)	0.24605 (70)	0.24610 (54)	0.24640 (56)	0.24689 (59)	0.24753 (57)	0.24790 (56)	0.24858 (51)
O1 1*b* (½ ½ z)	z/c	-0.00318 (234)	-0.00325 (243)	-0.00329 (234)	-0.00359 (278)	-0.00386 (258)	-0.00412 (262)	-0.00455 (256)	-0.00429 (254)	-0.00468 (266)	-0.00389 (263)	-0.00381 (269)	-0.00396 (215)
O2 2*c* (½ 0 z)	z/c	0.30512 (94)	0.30547 (96)	0.30549 (117)	0.30554 (102)	0.30558 (133)	0.30560 (120)	0.30519 (101)	0.30588 (111)	0.30575 (118)	0.30697 (122)	0.30744 (117)	0.30823 (117)
O3 2*c* (½ 0 z)	z/c	0.67389 (93)	0.67443 (95)	0.67459 (116)	0.67485 (102)	0.67497 (133)	0.67531 (120)	0.67484 (99)	0.67629 (108)	0.67649 (115)	0.67847 (118)	0.67992 (113)	0.68164 (113)
Occ (Cu,Co)1/Fe2	$1-n_d$	0.639 (20)	0.638 (20)	0.637 (20)	0.632 (20)	0.632 (20)	0.634 (20)	0.631 (20)	0.632 (20)	0.631 (20)	0.632 (20)	0.631 (20)	0.630 (20)
Occ Fe1*/(Cu,Co)2*)	n_d	0.361 (20)	0.362 (20)	0.363 (20)	0.368 (20)	0.368 (20)	0.366 (20)	0.369 (20)	0.368 (20)	0.369 (20)	0.368 (20)	0.369 (20)	0.370 (20)
χ^2		*70.4*	*69.4*	*49.9*	*72.5*	*63.0*	*74.8*	*78.5*	*82.4*	*65.1*	*75.3*	*53.3*	*52.1*
R_B		*5.35*	*5.34*	*7.81*	*6.00*	*10.2*	*6.77*	*5.41*	*5.45*	*5.46*	*4.73*	*4.33*	*4.65*
R_f		*6.24*	*5.97*	*7.94*	*7.05*	*8.56*	*6.41*	*6.49*	*6.86*	*6.84*	*5.91*	*4.97*	*4.44*

B.2 SXRPD Rietveld fits of Zn/Co-doped samples

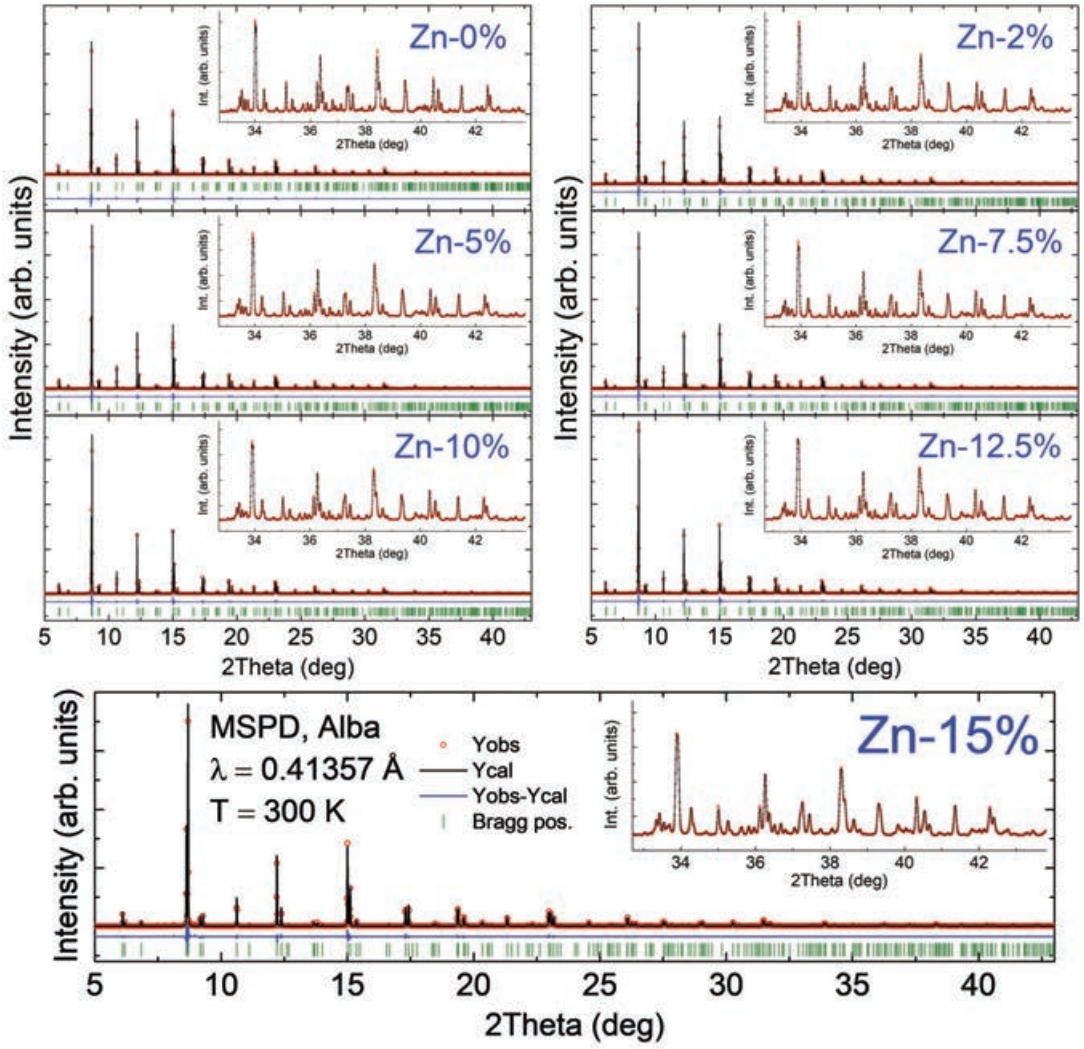

FIGURE B.2: Rietveld refinement (black curve) of the synchrotron X-ray intensities (red circles) at 300 K for the $YBaCu_{1-x}Zn_xFeO_5$ samples (with doping values $x = 0$, 0.02, 0.05, 0.075, 0.1, 0.125 and 0.15) quenched in liquid nitrogen. Bottom blue line is the observed-calculated difference, and the row with green bars represents the calculated Bragg positions. Inset: detail of the high-angles region in the Zn-15% refinement.

TABLE B.2: $YBaCu_{1-x}Zn_xFeO_5$ (quenched in liquid nitrogen). Structural parameters at T = 300 K and agreement factors from Rietveld refinement of MSPD@ALBA synchrotron data (λ=0.413378 Å). [*: minority fraction; n_d (disorder)=Occ Fe1*/(Cu,Zn)2*]. The coordinates of each metal [M: (Cu,Zn) or Fe] are constrained by z(M1)+z(M2)=1.

T=300 K *P4mm*		**Zn-0**%	**Zn-2**%	**Zn-5**%	**Zn-7.5**%	**Zn-10**%	**Zn-12.5**%	**Zn-15**%
a=b (Å)		3.87566 (2)	3.87627 (2)	3.87736 (2)	3.87861 (2)	3.87957 (1)	3.88037 (1)	3.88109 (2)
c (Å)		7.66056 (4)	7.65990 (4)	7.65855 (4)	7.65681 (4)	7.65539 (3)	7.65437 (3)	7.65338 (4)
$\Delta_T \equiv$c/2a		0.988290 (7)	0.988050 (7)	0.987601 (7)	0.987062 (7)	0.986633 (5)	0.986291 (5)	0.985984 (7)
V (Å^3)		115.0675 (13)	115.0934 (13)	115.1380 (13)	115.1860 (13)	115.2216 (10)	115.2536 (10)	115.2817 (13)
Y $1a$ (00z)	z/c	0.4937 (8)	0.49438 (7)	0.4936 (7)	0.4935 (8)	0.4947 (9)	0.4943 (7)	0.4943 (7)
Ba $1a$ (00z)	z/c	0	0	0	0	0	0	0
(Cu,Zn)1 $1b$ (½ ½ z)	z/c	0.71837 (49)	0.71753 (42)	0.71935 (37)	0.72239 (48)	0.72107 (52)	0.72193 (40)	0.72340 (44)
Fe1* $1b$ (½ ½ z)	z/c	0.74578 (94)	0.74505 (84)	0.74611 (81)	0.74489 (89)	0.74689 (99)	0.74818 (78)	0.74937 (76)
(Cu,Zn)2* $1b$ (½ ½ z)	z/c	0.28163 (49)	0.28247 (42)	0.28065 (37)	0.27761 (48)	0.27893 (52)	0.27807 (40)	0.27660 (44)
Fe2 $1b$ (½ ½ z)	z/c	0.25422 (94)	0.25495 (84)	0.25389 (81)	0.25511 (89)	0.25311 (99)	0.25182 (78)	0.25063 (76)
O1 $1b$ (½ ½ z)	z/c	0.0045 (10)	0.0040 (9)	0.0036 (9)	0.0020 (11)	0.0033 (14)	0.0018 (10)	0.0023 (10)
O2 $2c$ (½ 0 z)	z/c	0.3119 (10)	0.3117 (9)	0.3098 (9)	0.3101 (10)	0.3096 (11)	0.3090 (10)	0.3090 (10)
O3 $2c$ (½ 0 z)	z/c	0.6815 (10)	0.6812 (10)	0.6813 (10)	0.6821 (11)	0.6815 (14)	0.6822 (10)	0.6821 (10)
Occ (Cu,Zn)1/Fe2	$1-n_d$	0.613 (28)	0.628 (29)	0.584 (28)	0.590 (20)	0.609 (28)	0.573 (29)	0.595 (31)
Occ Fe1*/(Cu,Zn)2*	n_d	0.387 (28)	0.372 (29)	0.416 (28)	0.410 (20)	0.391 (28)	0.427 (29)	0.405 (31)
χ^2		*57.8*	*74.9*	*84.7*	*92.4*	*79.1*	*112*	*130*
R_B		*3.68*	*2.04*	*2.60*	*2.93*	*2.25*	*4.12*	*2.93*
R_f		*1.8*	*2.86*	*3.17*	*3.58*	*2.72*	*3.18*	*2.93*

Appendix C

Supplementary information for Chapter 7: *Does a magnetic spiral exist in YBCFO? A single crystal investigation*

C.1 Spherical neutron polarimetry: experimental results and calculations

This appendix gathers the complete set of neutron polarimetry measurements and the simulations of the P_{if} terms of the neutron polarization matrices (P) discussed in the Spherical Neutron Polarimetry part in Chapter 7:

- Table C.1 shows the 5 incommensurate reflections investigated in the incommensurate phase (AF2, k_2) with polarized neutrons (measured in D3@ILL at 10 K and 100 K): $(000) + \mathbf{k}$, $(001) + \mathbf{k}$, $(002) + \mathbf{k}$, $(112) - \mathbf{k}$ and $(114) - \mathbf{k}$. For the two last, the polarization elements P_{if} were measured first with positive incident polarization ($P_i > 0$), and then additionally also with negative (inverted) incident polarization ($P_i < 0$), denoted in the table as P_{-if}. The experimental polarization values shown in the table were corrected for the ^{3}He neutron spin filter efficiency from several measurements of P_{zz} on the (111) nuclear reflection. The values obtained from fits to the SNP experimental data using sinusoidal and spiral magnetic models are also shown for comparison. Refinements were done using the Mag2Pol program [98].
- Fig. C.1 shows simulations of the polarization matrix (P_{if}) elements for the neutron polarization matrices (P) at the incommensurate phase for the $(112) - \mathbf{k}$ incommensurate reflection [$\mathbf{k}_2 = (0.5, 0.5, 0.6)$]. They were done using the Mag2Pol program [98] as a function of the magnetic domain populations in

different ICM order models: (a) circular spiral model with chiral magnetic domains (C1, C2) and spins rotating in the ab plane, (b) sinusoidal model with conjugated magnetic domains (D1, D2) along the a axis, and (c) sinusoidal model with the conjugated magnetic domains along the ab diagonal.

TABLE C.1: Best fits of the SNP matrices measured at 10 K and 100 K (AF2 incommensurate phase) using a sinusoidal ($M_I \sim 0$) and spiral ($M_R = M_I$) models. Magnetic models were refined using using Mag2Pol including two types of magnetic domains (twin or chiral domains, depending on the model).

		T = 10 K					T = 100 K				
		AF2 (ICM) $\mathbf{k}_2 = (0.5, 0.5, 0.6)$	**Sinusoidal model ($\mathbf{M_I} \sim 0$)** D1/D2 = 48.9/51.1 (0.9) χ^2=110.46; χ^2_r=1.84		**Spiral model ($\mathbf{M_R} = \mathbf{M_I}$)** C1/C2 = 49.9/50.1 (0.4) χ^2=105.22; χ^2_r=1.75		AF2 (ICM) $\mathbf{k}_2 = (0.5, 0.5, 0.6)$	**Sinusoidal model ($\mathbf{M_I} \sim 0$)** D1/D2 = 47.6/52.4 (0.5) χ^2=105.29; χ^2_r=1.73		**Spiral model ($\mathbf{M_R} = \mathbf{M_I}$)** C1/C2 = 50.0/50.0 (0.3) χ^2=91.61; χ^2_r=1.50	
(hkl)	$\mathbf{P}_{fi}$	**obs**	**cal**	**obs-cal**	**cal**	**obs-cal**	**obs**	**cal**	**obs-cal**	**cal**	**obs-cal**
$(000)+\mathbf{k}$	P_{xx}	-1.006 (15)	-1.000	-0.006	-1.000	-0.006	-0.988 (12)	-1.000	0.013	-1.000	0.013
	P_{xy}	0.020 (18)	0.000	0.020	0.000	0.020	-0.003 (14)	0.000	-0.003	0.000	-0.003
	P_{xz}	-0.036 (18)	0.000	-0.036	0.000	-0.036	-0.051 (14)	0.000	-0.051	0.000	-0.051
	P_{yy}	0.039 (18)	0.000	0.039	-0.002	0.041	0.030 (14)	0.000	0.030	0.000	0.030
	P_{yx}	-0.699 (17)	-0.693	-0.006	-0.708	0.009	-0.737 (13)	-0.704	-0.032	-0.736	0.000
	P_{yz}	0.096 (19)	0.068	0.028	0.085	0.011	0.092 (14)	0.074	0.018	0.071	0.020
	P_{zx}	-0.005 (18)	0.000	-0.005	-0.002	-0.003	-0.003 (14)	0.000	-0.003	0.000	-0.003
	P_{zy}	0.093 (18)	0.068	0.025	0.085	0.008	0.083 (14)	0.074	0.009	0.071	0.011
	P_{zz}	0.711 (17)	0.693	0.018	0.708	0.003	0.739 (12)	0.704	0.035	0.736	0.003
$(112)-\mathbf{k}$	P_{xx}	-1.004 (13)	-1.000	-0.004	-1.000	-0.004	-1.007 (10)	-1.000	-0.007	-1.000	-0.007
	P_{xy}	-0.009 (16)	0.000	-0.009	0.000	-0.009	-0.012 (12)	0.000	-0.012	0.000	-0.012
	P_{xz}	0.015 (16)	0.000	0.015	0.000	0.015	-0.009 (12)	0.000	-0.009	0.000	-0.009
	P_{yy}	0.047 (16)	0.000	0.047	0.003	0.044	0.026 (12)	0.000	0.026	0.000	0.026
	P_{yx}	-0.330 (16)	-0.312	-0.018	-0.316	-0.014	-0.342 (12)	-0.336	-0.005	-0.339	-0.003
	P_{yz}	0.036 (16)	0.040	-0.004	0.050	-0.014	0.036 (12)	0.042	-0.005	0.042	-0.006
	P_{zx}	0.040 (16)	0.000	0.040	0.003	0.037	0.008 (12)	0.000	0.008	0.000	0.008
	P_{zy}	0.041 (16)	0.040	0.001	0.050	-0.010	0.020 (12)	0.042	-0.022	0.042	-0.022
	P_{zz}	0.332 (16)	0.312	0.020	0.316	0.016	0.337 (11)	0.336	0.001	0.339	-0.001
$(112)-\mathbf{k}$	P_{-xx}	1.031 (14)	1.000	0.031	1.000	0.031	1.009 (10)	1.000	0.009	1.000	0.009
	P_{-xy}	0.003 (16)	0.000	0.003	0.000	0.003	-0.004 (12)	0.000	-0.004	0.000	-0.004
	P_{-xz}	0.006 (17)	0.000	0.006	0.000	0.006	-0.014 (12)	0.000	-0.014	0.000	-0.014
	P_{-yy}	-0.031 (16)	0.000	-0.031	0.003	-0.033	0.001 (12)	0.000	0.001	0.000	0.001
	P_{-yx}	0.354 (16)	0.312	0.042	0.316	0.038	0.329 (12)	0.336	-0.007	0.339	-0.009
	P_{-yz}	-0.039 (17)	-0.040	0.001	-0.050	0.012	-0.033 (13)	-0.042	0.009	-0.042	0.010
	P_{-zx}	-0.003 (17)	0.000	-0.003	0.003	-0.006	0.002 (12)	0.000	0.002	0.000	0.002
	P_{-zy}	-0.059 (17)	-0.040	-0.019	-0.050	-0.009	-0.039 (12)	-0.042	0.002	-0.042	0.003
	P_{-zz}	-0.293 (17)	-0.312	0.019	-0.316	0.023	-0.326 (12)	-0.336	0.010	-0.339	0.012
$(001)+\mathbf{k}$	P_{xx}	-0.986 (26)	-1.000	0.014	-1.000	0.014	-1.022 (18)	-1.000	-0.022	-1.000	-0.022
	P_{xy}	0.038 (29)	0.000	0.038	0.000	0.038	0.007 (20)	0.000	0.007	0.000	0.007
	P_{xz}	-0.030 (28)	0.000	-0.030	0.000	-0.030	-0.013 (20)	0.000	-0.013	0.000	-0.013
	P_{yy}	0.040 (27)	0.000	0.040	-0.003	0.043	0.052 (21)	0.000	0.052	0.000	0.052
	P_{yx}	-0.173 (28)	-0.259	0.087	-0.261	0.089	-0.271 (20)	-0.285	0.014	-0.282	0.011
	P_{yz}	0.061 (29)	0.035	0.026	0.045	0.016	0.052 (20)	0.037	0.015	0.038	0.014
	P_{zx}	-0.011 (28)	0.000	-0.011	-0.003	-0.008	0.014 (20)	0.000	0.014	0.000	0.014
	P_{zy}	0.045 (28)	0.035	0.010	0.045	0.000	0.055 (21)	0.037	0.018	0.038	0.017
	P_{zz}	0.266 (29)	0.259	0.006	0.261	0.004	0.295 (20)	0.285	0.010	0.282	0.014
$(002)+\mathbf{k}$	P_{xx}	-1.058 (30)	-1.000	-0.058	-1.000	-0.058	-0.998 (22)	-1.000	0.002	-1.000	0.002
	P_{xy}	0.033 (32)	0.000	0.033	0.000	0.033	0.026 (24)	0.000	0.026	0.000	0.026
	P_{xz}	-0.010 (30)	0.000	-0.010	0.000	-0.010	0.015 (24)	0.000	0.015	0.000	0.015
	P_{yy}	0.020 (32)	0.000	0.020	-0.003	0.023	0.043 (24)	0.000	0.043	0.000	0.043
	P_{yx}	-0.066 (33)	-0.121	0.055	-0.117	0.050	-0.147 (24)	-0.150	0.003	-0.130	-0.017
	P_{yz}	0.000 (33)	0.022	-0.022	0.029	-0.028	-0.033 (23)	0.021	-0.054	0.024	-0.057
	P_{zx}	0.001 (32)	0.000	0.001	-0.003	0.004	0.020 (25)	0.000	0.020	0.000	0.020
	P_{zy}	0.013 (31)	0.022	-0.009	0.029	-0.016	0.025 (25)	0.021	0.004	0.024	0.001
	P_{zz}	0.108 (32)	0.121	-0.014	0.117	-0.009	0.118 (25)	0.150	-0.032	0.130	-0.012
$(114)-\mathbf{k}$	P_{xx}	-0.999 (57)	-1.000	0.001	-1.000	0.001	-0.980 (44)	-1.000	0.020	-1.000	0.020
	P_{xy}	0.016 (50)	0.000	0.016	0.000	0.016	-0.008 (40)	0.000	-0.008	0.000	-0.008
	P_{xz}	0.033 (53)	0.000	0.033	0.000	0.033	0.032 (39)	0.000	0.032	0.000	0.032
	P_{yy}	0.112 (51)	0.000	0.112	0.003	0.109	0.011 (43)	0.000	0.011	0.000	0.011
	P_{yx}	-0.053 (51)	-0.078	0.024	-0.071	0.017	-0.092 (38)	-0.107	0.016	-0.081	-0.011
	P_{yz}	0.090 (54)	0.016	0.073	0.022	0.068	-0.030 (43)	0.015	-0.046	0.018	-0.049
	P_{zx}	0.091 (50)	0.000	0.091	0.003	0.088	0.063 (40)	0.000	0.063	0.000	0.063
	P_{zy}	0.014 (52)	0.016	-0.003	0.022	-0.008	-0.039 (41)	0.015	-0.055	0.018	-0.058
	P_{zz}	0.070 (49)	0.078	-0.008	0.071	-0.001	0.154 (37)	0.107	0.047	0.081	0.073
$(114)-\mathbf{k}$	P_{-xx}	1.008 (57)	1.000	0.008	1.000	0.008	0.973 (48)	1.000	-0.027	1.000	-0.027
	P_{-xy}	-0.118 (52)	0.000	-0.118	0.000	-0.118	0.030 (40)	0.000	0.030	0.000	0.030
	P_{-xz}	-0.151 (48)	0.000	-0.151	0.000	-0.151	-0.006 (44)	0.000	-0.006	0.000	-0.006
	P_{-yy}	-0.114 (51)	0.000	-0.114	0.003	-0.117	-0.033 (40)	0.000	-0.033	0.000	-0.033
	P_{-yx}	0.031 (50)	0.078	-0.047	0.071	-0.040	0.083 (39)	0.107	-0.025	0.081	0.002
	P_{-yz}	-0.021 (56)	-0.016	-0.004	-0.022	0.001	-0.007 (38)	-0.015	0.008	-0.018	0.011
	P_{-zx}	-0.090 (52)	0.000	-0.090	0.003	-0.093	-0.015 (39)	0.000	-0.015	0.000	-0.015
	P_{-zy}	-0.067 (51)	-0.016	-0.050	-0.022	-0.044	-0.001 (39)	-0.015	0.014	-0.018	0.018
	P_{-zz}	-0.050 (52)	-0.078	0.027	-0.071	0.020	-0.034 (40)	-0.107	0.074	-0.081	0.047

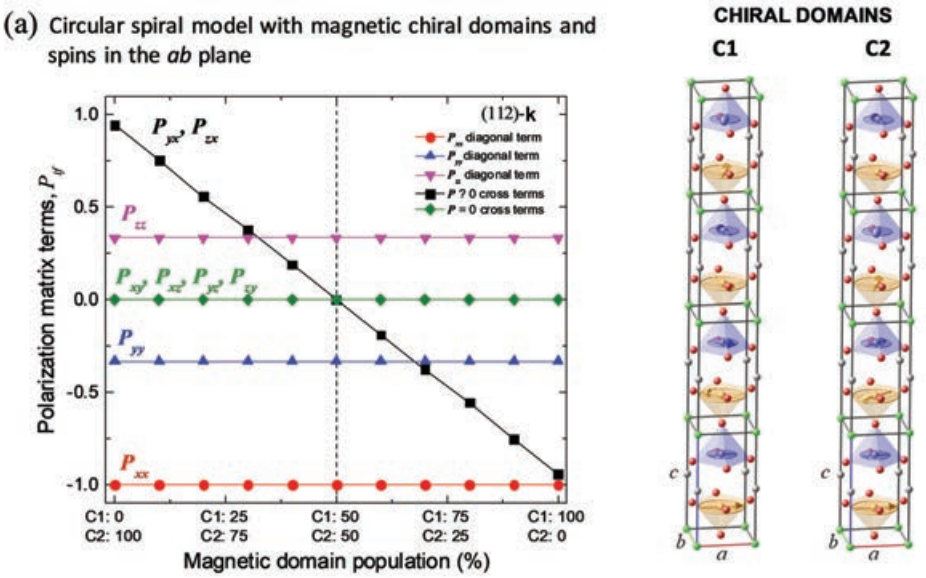

$P_{if}(0,100)$	$P_{if}(50,50)$	$P_{if}(100,0)$
$\begin{pmatrix} -1 & 0 & 0 \\ 0.943 & -0.333 & 0 \\ 0.943 & 0 & 0.333 \end{pmatrix}$	$\begin{pmatrix} -1 & 0 & 0 \\ 0 & -0.333 & 0 \\ 0 & 0 & 0.333 \end{pmatrix}$	$\begin{pmatrix} -1 & 0 & 0 \\ -0.943 & -0.333 & 0 \\ -0.943 & 0 & 0.333 \end{pmatrix}$

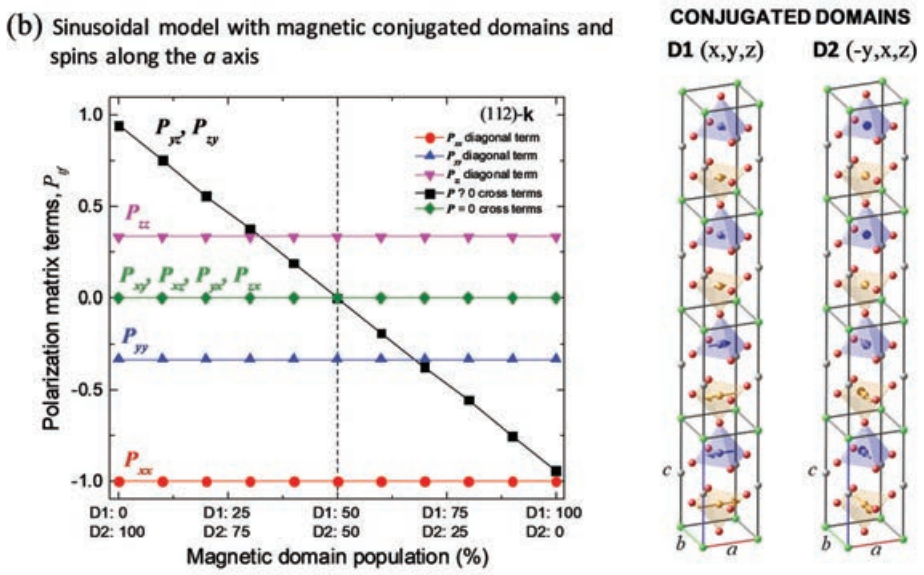

$P_{if}(0,100)$	$P_{if}(50,50)$	$P_{if}(100,0)$
$\begin{pmatrix} -1 & 0 & 0 \\ 0 & -0.333 & 0.943 \\ 0 & 0.943 & 0.333 \end{pmatrix}$	$\begin{pmatrix} -1 & 0 & 0 \\ 0 & -0.333 & 0 \\ 0 & 0 & 0.333 \end{pmatrix}$	$\begin{pmatrix} -1 & 0 & 0 \\ 0 & -0.333 & -0.943 \\ 0 & -0.943 & 0.333 \end{pmatrix}$

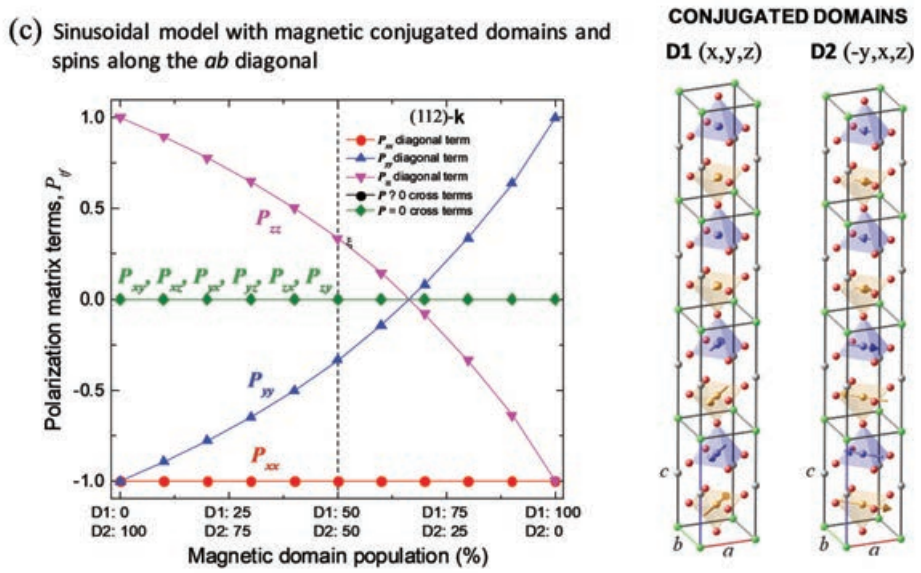

$P_{if}(0,100)$	$P_{if}(50,50)$	$P_{if}(100,0)$
$\begin{pmatrix} -1 & 0 & 0 \\ 0 & -1 & 0 \\ 0 & 0 & 1 \end{pmatrix}$	$\begin{pmatrix} -1 & 0 & 0 \\ 0 & -0.333 & 0 \\ 0 & 0 & 0.333 \end{pmatrix}$	$\begin{pmatrix} -1 & 0 & 0 \\ 0 & 1 & 0 \\ 0 & 0 & -1 \end{pmatrix}$

FIGURE C.1: Simulations of the P_{if} terms of the neutron polarization matrices (P) at the incommensurate phase for the $(112) - \mathbf{k}$ magnetic reflection as a function of the magnetic domain populations in three different models: (a) circular spiral model with chiral magnetic domains (C1, C2) and rotating spins in the ab plane; (b) sinusoidal collinear model with conjugated magnetic domains (D1, D2) along the a/b axis; (c) sinusoidal collinear model with the conjugated magnetic domains (D1, D2) along the ab diagonals of the tetragonal cell.

C.2 Response of the spiral phase to magnetic fields: complementary magnetometry and NPD figures

The supplementary magnetometry and NPD results used in the discussion of the spiral magnetic response under magnetic fields are shown below:

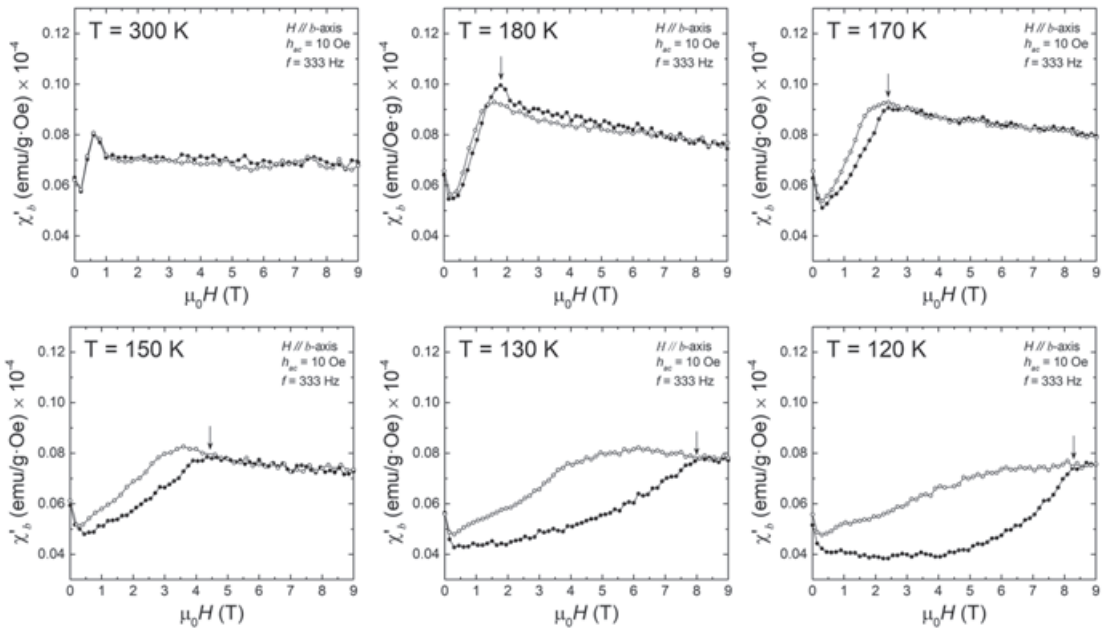

FIGURE C.2: In-phase component of the ac susceptibility versus superimposed dc field amplitudes along b (χ'_b), measured at different temperatures (300 K, 180 k, 170 K, 150 K, 130 K and 120 K). The sample was heated to the collinear phase (above $T_S = 195$ K) and cooled in ZF before recording complete [0T,9T] magnetic field cycles at each fixed temperature.

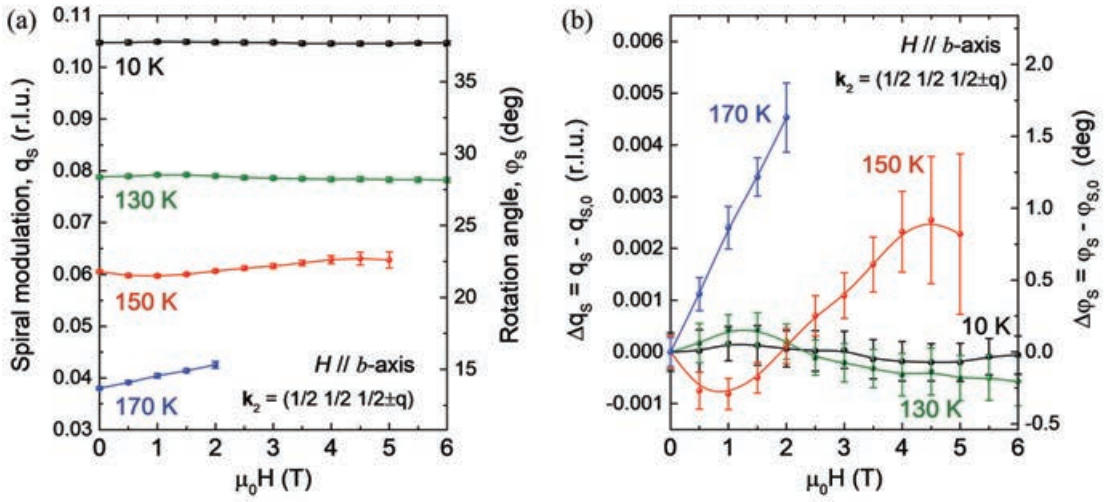

FIGURE C.3: Evolution of the spiral discommensuration in YBCFO single crystal under magnetic fields (D10, ILL). (a) Dependence under magnetic fields along the b axis of q_s obtained from the position of (0.5 0.5 0.5$\pm q$) ICM satellites in the neutron Q_L scans. Isothermal dependencies were measured at 10 K, 130 K, 150 K and 170 K. (b) Variation of q_s respect to its value at zero field ($q_{s,0}$), Δq_s=q_s-$q_{s,0}$. The twist angle φ (canting) formed by two spins of a bipyramid in the spiral phase is also indicated in the right vertical axes ($\varphi = 2\pi q_s$).

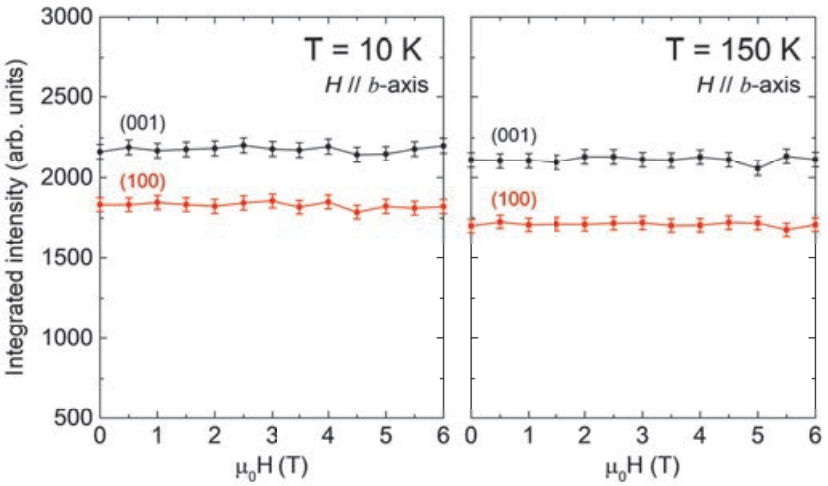

FIGURE C.4: Evolution under magnetic fields applied along b of the integrated (100) and (001) neutron intensities in YBCFO single crystal (D10, ILL). Only nuclear contribution (*i.e.*, no induced FM phase) is observed within the detection limit of the technique.

Appendix D

Supplementary information for Chapter 8: *Complex magnetism investigated in the frustrated ε-Fe_2O_3 multiferroic*

- Fig. D.1(a) shows the Rietveld analysis of a synchrotron X-ray powder diffraction pattern (BL04-MSPD@Alba, λ = 0.41284(6) Å) collected on the ε-Fe_2O_3 sample at RT. All peaks in the diffraction pattern are well fitted using the orthorhombic $Pna2_1$ symmetry corresponding to the ε-Fe_2O_3 phase except for residual traces of α-Fe_2O_3. The amount of hematite (α-Fe_2O_3) impurity in the sample was found to be < 2.3 wt. %.
- Fig. D.1(b) displays a simulation of a neutron diffraction pattern of 50 wt. % ε-Fe_2O_3 and 50 wt. % α-Fe_2O_3 compared to the experimental pattern collected at 305 K (D2B@ILL, λ = 1.594 Å). The two main magnetic peaks from hematite would appear in different positions to those observed in ε-Fe_2O_3.

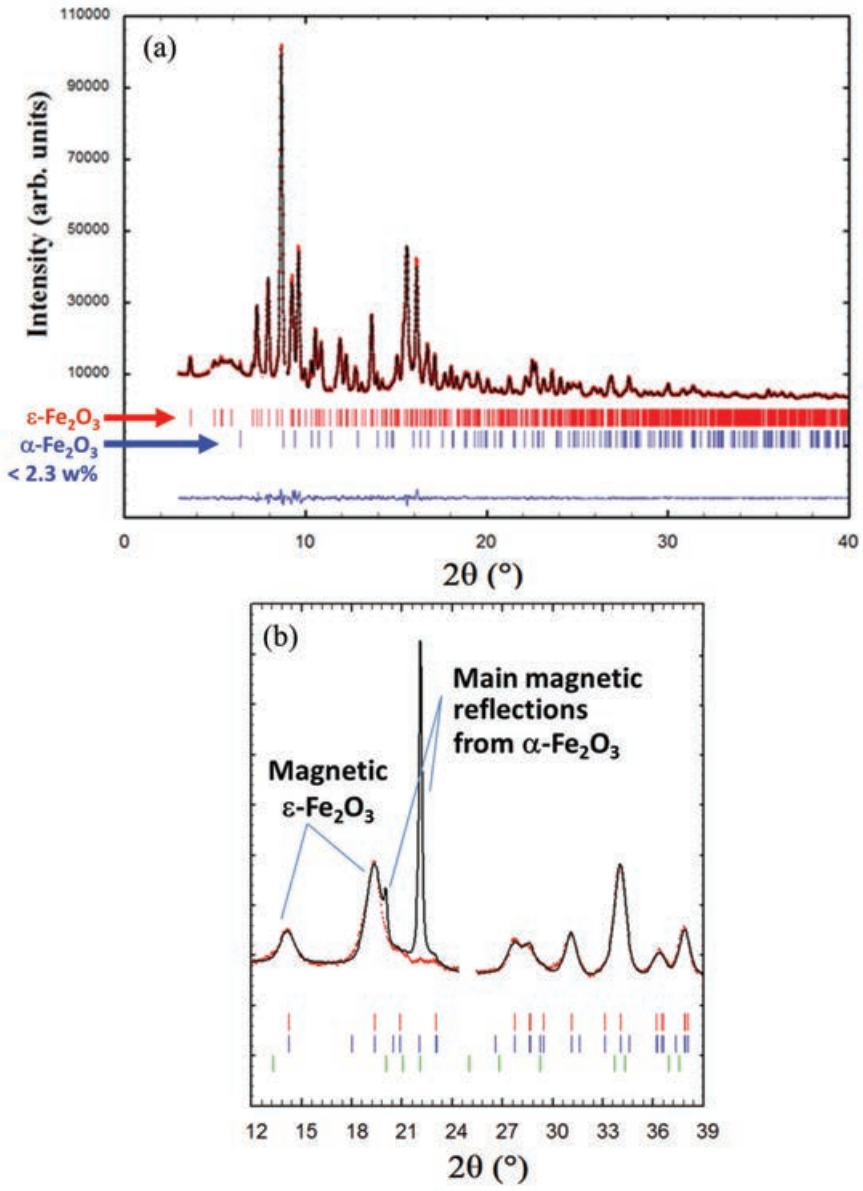

FIGURE D.1: (a) Rietveld fit of the synchrotron X-ray pattern of ε-Fe_2O_3 collected at RT (red circles: experimental points; bottom blue line: difference). The top row of bars (in red) are for ε-Fe_2O_3, and the bottom row (in blue) refers to hematite (α-Fe_2O_3, 2.3(9) % weight). (b) Rietveld calculation (black solid line) of the neutron pattern of ε-Fe_2O_3 compared to the experimental pattern collected at 305 K (red circles: experimental points). The top rows of bars (in red and blue) corresponds to the structural and magnetic phases of ε-Fe_2O_3, while the bottom row (in green) is for the magnetic phase of hematite (ε-Fe_2O_3), which has been included for the calculation in the same proportion as the epsilon-phase.

Bibliography

[1] W. C. Röntgen. "Ueber die durch Bewegung eines im homogenen electrischen Felde befindlichen Dielectricums hervorgerufene electrodynamische Kraft". In: *Annalen der Physik* 271.10 (1888). ISSN: 15213889. DOI: 10.1002/andp.18882711003.

[2] P. Curie. "Sur la symétrie dans les phénomènes physiques, symétrie d'un champ électrique et d'un champ magnétique". In: *Journal de Physique Théorique et Appliquée* 3.1 (1894). ISSN: 0368-3893. DOI: 10.1051/jphystap:018940030039300.

[3] P. Debye. "Bemerkung zu einigen neuen Versuchen über einen magneto-elektrischen Richteffekt". In: *Zeitschrift für Physik* 36.4 (1926). ISSN: 14346001. DOI: 10.1007/BF01557844.

[4] D. N. Astrov. "MAGNETOELECTRIC EFFECT IN CHROMIUM OXIDE D." In: *SOVIET PHYSICS JETP* 13.4 (1961). ISSN: 1520510X.

[5] I. E Dzyaloshinskii. "On the magneto-electrical effect in antiferromagnets". In: *Journal of Experimental and Theoretical Physics* 37.3 (1959). ISSN: 0038-5646.

[6] Elbio Dagotto. "Correlated electrons in high-temperature superconductors". In: *Reviews of Modern Physics* 66.3 (1994). ISSN: 00346861. DOI: 10.1103/RevModPhys.66.763.

[7] *Colossal Magnetoresistive Oxides*. 2000. DOI: 10.1201/9781482287493.

[8] Hans Schmid. "Multi-ferroic magnetoelectrics". In: *Ferroelectrics* 162.1 (1994). ISSN: 15635112. DOI: 10.1080/00150199408245120.

[9] J. Wang et al. “Epitaxial BiFeO3 multiferroic thin film heterostructures”. In: *Science* 299.5613 (2003). ISSN: 00368075. DOI: 10.1126/science.1080615.

[10] T. Kimura et al. “Magnetic control of ferroelectric polarization”. In: *Nature* 426.6962 (2003). ISSN: 00280836. DOI: 10.1038/nature02018.

[11] W. Eerenstein et al. “ Comment on "Epitaxial BiFeO 3 Multiferroic Thin Film Heterostructures" ”. In: *Science* 307.5713 (2005). ISSN: 0036-8075. DOI: 10.1126/science.1105422.

[12] N. Hur et al. “Electric polarization reversal and memory in a multiferroic material induced by magnetic fields”. In: *Nature* 429.6990 (2004). ISSN: 00280836. DOI: 10.1038/nature02572.

[13] Thomas Lottermoser et al. “Magnetic phase control by an electric field”. In: *Nature* 430.6999 (2004). ISSN: 00280836. DOI: 10.1038/nature02728.

[14] Nicola A. Spaldin. *Multiferroics beyond electric-field control of magnetism*. 2020. DOI: 10.1098/rspa.2019.0542.

[15] Sang Wook Cheong and Maxim Mostovoy. *Multiferroics: A magnetic twist for ferroelectricity*. 2007. DOI: 10.1038/nmat1804.

[16] Taka Hisa Arima. *Spin-driven ferroelectricity and magneto-electric effects in frustrated magnetic systems*. 2011. DOI: 10.1143/JPSJ.80.052001.

[17] K. F. Wang, J. M. Liu and Z. F. Ren. “Multiferroicity: The coupling between magnetic and polarization orders”. In: *Advances in Physics* 58.4 (2009). ISSN: 00018732. DOI: 10.1080/00018730902920554.

[18] Shuai Dong et al. “Multiferroic materials and magnetoelectric physics: Symmetry, entanglement, excitation, and topology”. In: *Advances in Physics* 64.5-6 (2015). ISSN: 14606976. DOI: 10.1080/00018732.2015.1114338.

[19] B. Kundys, A. Maignan and Ch Simon. “Multiferroicity with high-TC in ceramics of the YBaCuFeO 5 ordered perovskite”. In: *Applied Physics Letters* 94.7 (2009). ISSN: 00036951. DOI: 10.1063/1.3086309.

[20] Maxim Mostovoy. “Ferroelectricity in spiral magnets”. In: *Physical Review Letters* 96.6 (2006). ISSN: 10797114. DOI: 10.1103/PhysRevLett.96.067601.

[21] Hosho Katsura, Naoto Nagaosa and Alexander V. Balatsky. “Spin current and magnetoelectric effect in noncollinear magnets”. In: *Physical Review Letters* 95.5 (2005). ISSN: 00319007. DOI: 10.1103/PhysRevLett.95.057205.

[22] Sumio Ishihara. "Electronic ferroelectricity and frustration". In: *Journal of the Physical Society of Japan* 79.1 (2010). ISSN: 00319015. DOI: 10.1143/JPSJ.79.011010.

[23] Manfred Fiebig. *Revival of the magnetoelectric effect*. 2005. DOI: 10.1088/0022-3727/38/8/R01.

[24] L. W. Martin and R. Ramesh. "Multiferroic and magnetoelectric heterostructures". In: *Acta Materialia* 60.6-7 (2012). ISSN: 13596454. DOI: 10.1016/j.actamat.2011.12.024.

[25] J. F. Scott. "Data storage: Multiferroic memories". In: *Nature Materials* 6.4 (2007). ISSN: 14764660. DOI: 10.1038/nmat1868.

[26] Wolfgang Kleemann. "Switching magnetism with electric fields". In: *Physics* 2 (2009). DOI: 10.1103/physics.2.105.

[27] Daniel Khomskii. "Classifying multiferroics: Mechanisms and effects". In: *Physics* 2 (2009). DOI: 10.1103/physics.2.20.

[28] I. Dzyaloshinsky. "A thermodynamic theory of "weak" ferromagnetism of antiferromagnetics". In: *Journal of Physics and Chemistry of Solids* 4.4 (1958). ISSN: 00223697. DOI: 10.1016/0022-3697(58)90076-3.

[29] Tôru Moriya. "New mechanism of anisotropic superexchange interaction". In: *Physical Review Letters* 4.5 (1960). ISSN: 00319007. DOI: 10.1103/PhysRevLett.4.228.

[30] I. A. Sergienko and E. Dagotto. "Role of the Dzyaloshinskii-Moriya interaction in multiferroic perovskites". In: *Physical Review B - Condensed Matter and Materials Physics* 73.9 (2006). ISSN: 10980121. DOI: 10.1103/PhysRevB.73.094434.

[31] Naoto Nagaosa. "Theory of multiferroic behavior in cycloidal helimagnets". In: *Journal of Physics Condensed Matter* 20.43 (2008). ISSN: 09538984. DOI: 10.1088/0953-8984/20/43/434207.

[32] Yoshinori Tokura and Noriaki Kida. "Dynamical magnetoelectric effects in multiferroic oxides". In: *Philosophical Transactions of the Royal Society A: Mathematical, Physical and Engineering Sciences*. Vol. 369. 1951. 2011. DOI: 10.1098/rsta.2011.0150.

[33] Y. J. Choi et al. "Ferroelectricity in an ising chain magnet". In: *Physical Review Letters* 100.4 (2008). ISSN: 00319007. DOI: 10.1103/PhysRevLett.100.047601.

[34] Ivan A. Sergienko, Cengiz Şen and Elbio Dagotto. "Ferroelectricity in the magnetic E-phase of orthorhombic perovskites". In: *Physical Review*

Letters 97.22 (2006). ISSN: 00319007. DOI: 10.1103/PhysRevLett.97.227204.

[35] L. N. Bulaevskii et al. "Electronic orbital currents and polarization in Mott insulators". In: *Physical Review B - Condensed Matter and Materials Physics* 78.2 (2008). ISSN: 10980121. DOI: 10.1103/PhysRevB.78.024402.

[36] I. Tsukada et al. "Significant suppression of weak ferromagnetism in (La1.8Eu0.2)CuO4". In: *Physical Review B - Condensed Matter and Materials Physics* 67.22 (2003). ISSN: 1550235X. DOI: 10.1103/PhysRevB.67.224401.

[37] M. Tovar et al. "Weak ferromagnetism and spin-glass-like behavior in the rare-earth cuprates R2CuO4 (R=Tb, Dy, Ho, Er, Tm, and Y)". In: *Physical Review B* 45.9 (1992). ISSN: 01631829. DOI: 10.1103/PhysRevB.45.4729.

[38] A. B. Harris. "Landau analysis of the symmetry of the magnetic structure and magnetoelectric interaction in multiferroics". In: *Physical Review B - Condensed Matter and Materials Physics* 76.5 (2007). ISSN: 10980121. DOI: 10.1103/PhysRevB.76.054447.

[39] T. Kimura et al. "Magnetoelectric phase diagrams of orthorhombic RMnO3 (R=Gd, Tb, and Dy)". In: *Physical Review B - Condensed Matter and Materials Physics* 71.22 (2005). ISSN: 10980121. DOI: 10.1103/PhysRevB.71.224425.

[40] M F Collins and O A Petrenko. " Review / Synthèse : Triangular antiferromagnets ". In: *Canadian Journal of Physics* 75.9 (1997). ISSN: 0008-4204. DOI: 10.1139/p97-007.

[41] T. Goto et al. "Ferroelectricity and giant magnetocapacitance in perovskite rare-earth manganites". In: *Physical Review Letters* 92.25 I (2004). ISSN: 00319007. DOI: 10.1103/PhysRevLett.92.257201.

[42] T. Kimura et al. "Cupric oxide as an induced-multiferroic with high-TC". In: *Nature Materials* 7.4 (2008). ISSN: 14764660. DOI: 10.1038/nmat2125.

[43] L. Er-Rakho et al. "YBaCuFeO5+δ: A novel oxygen-deficient perovskite with a layer structure". In: *Journal of Solid State Chemistry* 73.2 (1988). ISSN: 1095726X. DOI: 10.1016/0022-4596(88)90141-7.

[44] V. Caignaert et al. "Crystal and magnetic structure of YBaCuFeO5". In: *Journal of Solid State Chemistry* 114.1 (1995). ISSN: 1095726X. DOI: 10.1006/jssc.1995.1004.

[45] A. W. Mombrú et al. "Neutron powder diffraction study (T = 4.2-300 K) and polarization analysis of YBaCuFeO5+δ". In: *Journal of Physics Condensed Matter* 10.6 (1998). ISSN: 09538984. DOI: 10.1088/0953-8984/10/6/008.

[46] M. Morin et al. "Incommensurate magnetic structure, Fe/Cu chemical disorder, and magnetic interactions in the high-temperature multiferroic YBaCuFeO5". In: *Physical Review B - Condensed Matter and Materials Physics* 91.6 (2015). ISSN: 1550235X. DOI: 10.1103/PhysRevB.91.064408.

[47] Mickaël Morin et al. "Tuning magnetic spirals beyond room temperature with chemical disorder". In: *Nature Communications* 7.1 (2016). DOI: 10.1038/ncomms13758.

[48] Tian Shang et al. "Design of magnetic spirals in layered perovskites: Extending the stability range far beyond room temperature". In: *Science Advances* 4.10 (2018). ISSN: 23752548. DOI: 10.1126/sciadv.aau6386.

[49] Xiaodong Zhang et al. "Tuning the tilting of the spiral plane by Mn doping in YBaCuFeO5 multiferroic". In: *Acta Materialia* 206 (2021). ISSN: 13596454. DOI: 10.1016/j.actamat.2020.116608.

[50] M. K. Wu et al. "Superconductivity at 93 K in a new mixed-phase Yb-Ba-Cu-O compound system at ambient pressure". In: *Physical Review Letters* 58.9 (1987). ISSN: 00319007. DOI: 10.1103/PhysRevLett.58.908.

[51] J. Lyu et al. "Weak ferromagnetism linked to the high-temperature spiral phase of YBaCuFeO5". In: *Physical Review Research* 4.2 (Apr. 2022), p. 023008. ISSN: 2643-1564. DOI: 10.1103/PhysRevResearch.4.023008.

[52] Yuji Kawamura et al. "High-temperature multiferroic state of RBaCuFeO5 (R = Y, Lu, and Tm)". In: *Journal of the Physical Society of Japan* 79.7 (2010). ISSN: 00319015. DOI: 10.1143/JPSJ.79.073705.

[53] R. D. Shannon. "Revised effective ionic radii and systematic studies of interatomic distances in halides and chalcogenides". In: *Acta Crystallographica Section A* 32.5 (1976). ISSN: 16005724. DOI: 10.1107/S0567739476001551.

[54] Andrea Scaramucci et al. "Multiferroic Magnetic Spirals Induced by Random Magnetic Exchanges". In: *Physical Review X* 8.1 (2018). ISSN: 21603308. DOI: 10.1103/PhysRevX.8.011005.

[55] Andrea Scaramucci et al. "Spiral order from orientationally correlated random bonds in classical XY models". In: *Physical Review Research* 2.1 (2020). ISSN: 26431564. DOI: 10.1103/PhysRevResearch.2.013273.

[56] Nobuyuki Momozawa et al. “Modification of Helix in (Ba1-xSrx)2Zn2Fe12O22 Due to Applied Magnetic Field”. In: *Journal of the Physical Society of Japan* 54.10 (1985). ISSN: 13474073. DOI: 10.1143/JPSJ.54.3895.

[57] Shigenori Utsumi, Daisuke Yoshiba and Nobuyuki Momozawa. “Super-exchange interactions of (Ba_{1-x}Sr_x)2Zn2Fe12O22 system studied by neutron diffraction”. In: *Journal of the Physical Society of Japan* 76.3 (2007). ISSN: 00319015. DOI: 10.1143/JPSJ.76.034704.

[58] D. E. Cox, W. J. Takei and G. Shirane. “A magnetic and neutron diffraction study of the Cr2O3-Fe2O3 system”. In: *Journal of Physics and Chemistry of Solids* 24.3 (1963). ISSN: 00223697. DOI: 10.1016/0022-3697(63)90199-9.

[59] Seungyeol Lee and Huifang Xu. “Size-Dependent Phase Map and Phase Transformation Kinetics for Nanometric Iron(III) Oxides ($\gamma \rightarrow \rightarrow \alpha$ Pathway)”. In: *Journal of Physical Chemistry C* 120.24 (2016). ISSN: 19327455. DOI: 10.1021/acs.jpcc.6b05287.

[60] Martí Gich et al. “Stabilization of metastable phases in spatially restricted fields: The case of the Fe2O3 polymorphs”. In: *Faraday Discussions* 136 (2007). ISSN: 13596640. DOI: 10.1039/b616097b.

[61] Mihaela Popovici et al. “Optimized synthesis of the elusive Epsilon-Fe2O3 phase via sol-gel chemistry”. In: *Chemistry of Materials* 16.25 (2004). ISSN: 08974756. DOI: 10.1021/cm048628m.

[62] Marin Tadic et al. “Synthesis of metastable hard-magnetic -Fe2O3 nanoparticles from silica-coated akaganeite nanorods”. In: *Nanoscale* 9.30 (2017). ISSN: 20403372. DOI: 10.1039/c7nr03639f.

[63] M. Gich et al. “High- and low-temperature crystal and magnetic structures of ϵ-Fe2O3 and their correlation to its magnetic properties”. In: *Chemistry of Materials* 18.16 (2006). ISSN: 08974756. DOI: 10.1021/cm0609931.

[64] Jian Jin, Shin Ichi Ohkoshi and Kazuhito Hashimoto. “Giant Coercive Field of Nanometer-Sized Iron Oxide”. In: *Advanced Materials* 16.1 (2004). ISSN: 09359648. DOI: 10.1002/adma.200305297.

[65] Asuka Namai et al. “Synthesis of an electromagnetic wave absorber for high-speed wireless communication”. In: *Journal of the American Chemical Society* 131.3 (2009). ISSN: 00027863. DOI: 10.1021/ja807943v.

[66] Asuka Namai et al. “Hard magnetic ferrite with a gigantic coercivity and high frequency millimetre wave rotation”. In: *Nature Communications* 3 (2012). ISSN: 20411723. DOI: 10.1038/ncomms2038.

[67] Alberto López-Ortega et al. *Applications of exchange coupled bi-magnetic hard/soft and soft/hard magnetic core/shell nanoparticles*. 2015. DOI: 10.1016/j.physrep.2014.09.007.

[68] M. Gich et al. "Large coercivity and low-temperature magnetic reorientation in ϵ-Fe2O3 nanoparticles". In: *Journal of Applied Physics* 98.4 (2005). ISSN: 00218979. DOI: 10.1063/1.1997297.

[69] Christelle Kadlec et al. "Electromagnon in ferrimagnetic E-Fe2O3 nanograin ceramics". In: *Physical Review B - Condensed Matter and Materials Physics* 88.10 (2013). ISSN: 10980121. DOI: 10.1103/PhysRevB.88.104301.

[70] M. Gich et al. "Magnetoelectric coupling in ϵ-Fe2O3 nanoparticles". In: *Nanotechnology* 17.3 (2006). ISSN: 09574484. DOI: 10.1088/0957-4484/17/3/012.

[71] Yuan Chieh Tseng et al. "Nonzero orbital moment in high coercivity ϵ-Fe2O3 and low-temperature collapse of the magnetocrystalline anisotropy". In: *Physical Review B - Condensed Matter and Materials Physics* 79.9 (2009). ISSN: 1550235X. DOI: 10.1103/PhysRevB.79.094404.

[72] Martí Gich et al. "Multiferroic iron oxide thin films at room temperature". In: *Advanced Materials* 26.27 (2014). ISSN: 15214095. DOI: 10.1002/adma.201400990.

[73] Xiangxiang Guan et al. "Unconventional Ferroelectric Switching via Local Domain Wall Motion in Multiferroic ϵ-Fe2O3 Films". In: *Advanced Electronic Materials* 6.4 (2020). ISSN: 2199160X. DOI: 10.1002/aelm.201901134.

[74] Badari Narayana Rao et al. "Investigation of ferrimagnetism and ferroelectricity in Al: XFe2- xO3 thin films". In: *Journal of Materials Chemistry C* 8.2 (2020). ISSN: 20507526. DOI: 10.1039/c9tc05390e.

[75] Radek Zboril, Miroslav Mashlan and Dimitris Petridis. *Iron(III) oxides from thermal processes-synthesis, structural and magnetic properties, Mössbauer spectroscopy characterization, and applications*. 2002. DOI: 10.1021/cm0111074.

[76] Yu V. Knyazev et al. "Nuclear forward scattering application to the spiral magnetic structure study in -Fe2 O3". In: *Physical Review B* 101.9 (2020). ISSN: 24699969. DOI: 10.1103/PhysRevB.101.094408.

[77] Marie Yoshikiyo et al. "Study of the Electronic Structure and Magnetic Properties of ϵ-Fe ₂ O ₃ by First-Principles

Calculation and Molecular Orbital Calculations". In: *The Journal of Physical Chemistry C* 116.15 (Apr. 2012), pp. 8688–8691. ISSN: 1932-7447. DOI: 10.1021/jp300769z.

[78] Libor MacHala, Jiří Tuček and Radek Zbořil. *Polymorphous transformations of nanometric iron(III) oxide: A review*. 2011. DOI: 10.1021/cm200397g.

[79] Ma Zheng. "Synthesis and Characterization of Epsilon-Fe2O3 Nanoparticles and Thin Films". In: *TDX (Tesis Doctorals en Xarxa)* (Feb. 2021). URL: http://www.tesisenred.net/handle/10803/671968.

[80] T. Y. Tien and R. M. Garretson. "A floating zone single crystal growing apparatus". In: *Journal of Crystal Growth* 16.2 (1972). ISSN: 00220248. DOI: 10.1016/0022-0248(72)90110-8.

[81] Hanna A. Dabkowska and Antoni B. Dabkowski. "Crystal Growth of Oxides by Optical Floating Zone Technique". In: *Springer Handbook of Crystal Growth*. 2010. DOI: 10.1007/978-3-540-74761-1{_}12.

[82] H. A. Dabkowska and B. D. Gaulin. "Growth of single crystals of selected cuprates by the optical Floating Zone Technique". In: *Journal of Optoelectronics and Advanced Materials*. Vol. 9. 5. 2007.

[83] Yen Chung Lai et al. "Self-adjusted flux for the traveling solvent floating zone growth of YBaCuFeO5 crystal". In: *Journal of Crystal Growth* 413 (2015). ISSN: 00220248. DOI: 10.1016/j.jcrysgro.2014.12.020.

[84] B. Ouladdiaf et al. "OrientExpress: A new system for Laue neutron diffraction". In: *Physica B: Condensed Matter* 385-386 (2006). ISSN: 09214526. DOI: 10.1016/j.physb.2006.05.337.

[85] *Orient Express-ILL Web Page*. URL: https://www.ill.eu/users/instruments/instruments-list/orientexpress/.

[86] Baoping Bob He, Uwe Preckwinkel and Kingsley L Smith. "Fundamentals of Two-Dimensional X-ray Diffraction (XRD2)". In: *Advances in X-ray Analysis* 43 (1999).

[87] Philip Willmott. *An introduction to synchrotron radiation: Techniques and applications*. 2011. DOI: 10.1002/9781119970958.

[88] *MSPD-Alba Web Page*. URL: https://www.cells.es/en/beamlines/bl04-mspd.

[89] Yang Ren and Xiaobing Zuo. "Synchrotron X-Ray and Neutron Diffraction, Total Scattering, and Small-Angle Scattering Techniques for Rechargeable Battery Research". In: *Small Methods* 2.8 (2018). ISSN: 23669608. DOI: 10.1002/SMTD.201800064.

[90] Tapan Chatterji. *Neutron Scattering from Magnetic Materials*. 2006. DOI: 10.1016/B978-0-444-51050-1.X5000-9.

[91] *D1B-ILL Web Page*. URL: https://www.ill.eu/users/instruments/instruments-list/d1b/description/instrument-layout.

[92] *D20-ILL Web Page*. URL: https://www.ill.eu/users/instruments/instruments-list/d20/description/instrument-layout.

[93] *D9-ILL Web Page*. URL: https://www.ill.eu/users/instruments/instruments-list/d9/description/instrument-layout.

[94] *D10-ILL Web Page*. URL: https://www.ill.eu/users/instruments/instruments-list/d10/description/instrument-layout.

[95] *D3-ILL Web Page*. URL: https://www.ill.eu/users/instruments/instruments-list/d3/description/instrument-layout.

[96] *BOREAS-Alba Web Page*. URL: https://www.cells.es/en/beamlines/bl29-boreas.

[97] Juan Rodríguez-Carvajal. "Recent advances in magnetic structure determination by neutron powder diffraction". In: *Physica B: Physics of Condensed Matter* 192.1-2 (1993). ISSN: 09214526. DOI: 10.1016/0921-4526(93)90108-I.

[98] Navid Qureshi. *Mag2pol: A program for the analysis of spherical neutron polarimetry, flipping ratio and integrated intensity data*. 2019. DOI: 10.1107/S1600576718016084.

[99] *Esmeralda-ILL Web Page*. URL: https://www.ill.eu/users/support-labs-infrastructure/software-scientific-tools/esmeralda.

[100] Luis Fuentes-Montero et al. *The Esmeralda suite for Laue diffraction data treatment*. 2015. DOI: 10.13140/RG.2.1.4954.1202.

[101] Clemens Prescher and Vitali B. Prakapenka. *DIOPTAS: A program for reduction of two-dimensional X-ray diffraction data and data exploration*. 2015. DOI: 10.1080/08957959.2015.1059835.

[102] Mois Ilia Aroyo et al. "Bilbao Crystallographic Server: I. Databases and crystallographic computing programs". In: *Zeitschrift fur Kristallographie*. Vol. 221. 1. 2006. DOI: 10.1524/zkri.2006.221.1.15.

[103] J. M. Perez-Mato et al. "Symmetry-Based Computational Tools for Magnetic Crystallography". In: *Annual Review of Materials Research* 45 (2015). ISSN: 15317331. DOI: 10.1146/annurev-matsci-070214-021008.

[104] Mois I. Aroyo et al. "Bilbao Crystallographic Server. II. Representations of crystallographic point groups and space groups". In: *Acta Crystallographica Section A: Foundations of Crystallography*. Vol. 62. 2. 2006. DOI: 10.1107/S0108767305040286.

[105] Branton J. Campbell et al. "ISODISPLACE: A web-based tool for exploring structural distortions". In: *Journal of Applied Crystallography* 39.4 (2006). ISSN: 00218898. DOI: 10.1107/S0021889806014075.

[106] Koichi Momma and Fujio Izumi. "VESTA 3 for three-dimensional visualization of crystal, volumetric and morphology data". In: *Journal of Applied Crystallography* 44.6 (2011). ISSN: 00218898. DOI: 10.1107/S0021889811038970.

[107] François Fauth et al. *The crystallography stations at the Alba synchrotron*. 2015. DOI: 10.1140/epjp/i2015-15160-y.

[108] Wen Chung Liu et al. "X-ray multi-beam resonant diffraction analysis of crystal symmetry for layered perovskite YBaCuFeO5". In: *Journal of Applied Crystallography* 49.5 (2016). ISSN: 16005767. DOI: 10.1107/S1600576716013248.

[109] Yen Chung Lai et al. "Magnetic ordering and dielectric relaxation in the double perovskite YBaCuFeO5". In: *Journal of Physics Condensed Matter* 29.14 (2017). ISSN: 1361648X. DOI: 10.1088/1361-648X/aa5708.

[110] M. K. Srivastava et al. "The effect of orbital-lattice coupling on the electrical resistivity of YBaCuFeO5 investigated by X-ray absorption". In: *Scientific Reports* 9.1 (2019). ISSN: 20452322. DOI: 10.1038/s41598-019-54772-0.

[111] Elena V. Mostovshchikova et al. "Infrared and X-ray absorption spectra of Cu2O and CuO nanoceramics". In: *Solid State Phenomena*. Vol. 190. 2012. DOI: 10.4028/www.scientific.net/SSP.190.683.

[112] Frank M.F. De Groot. "AWARD PAPER: XANES spectra of transition metal compounds". In: *Journal of Physics: Conference Series*. Vol. 190. 2009. DOI: 10.1088/1742-6596/190/1/012004.

[113] Deyang Chen et al. "A Strain-Driven Antiferroelectric-to-Ferroelectric Phase Transition in La-Doped BiFeO3 Thin Films on Si". In: *Nano Letters* 17.9 (2017). ISSN: 15306992. DOI: 10.1021/acs.nanolett.7b03030.

[114] Niéli Daffé et al. "Magnetic anisotropies and cationic distribution in CoFe2O4 nanoparticles prepared by co-precipitation route: Influence of particle size and stoichiometry". In: *Journal of Magnetism and Magnetic*

Materials 460 (2018). ISSN: 03048853. DOI: 10.1016/j.jmmm.2018.03.041.

[115] J. Ghijsen et al. "Electronic structure of Cu2O and CuO". In: *Physical Review B* 38.16 (1988). ISSN: 01631829. DOI: 10.1103/PhysRevB.38.11322.

[116] M. Grioni et al. "Studies of copper valence states with Cu L3 x-ray-absorption spectroscopy". In: *Physical Review B* 39.3 (1989). ISSN: 01631829. DOI: 10.1103/PhysRevB.39.1541.

[117] G. van der Laan et al. "Oxidation state variations in copper minerals studied with Cu 2p X-ray absorption spectroscopy". In: *Journal of Physics and Chemistry of Solids* 53.9 (1992). ISSN: 00223697. DOI: 10.1016/0022-3697(92)90037-E.

[118] J. E. Rodríguez and J. López. "Thermoelectric figure of merit of oxygen-deficient YBCO perovskites". In: *Physica B: Condensed Matter* 387.1-2 (2007). ISSN: 09214526. DOI: 10.1016/j.physb.2006.03.096.

[119] C. De Nadaï et al. "L2,3 x-ray absorption spectroscopy and multiplet calculations for KMF3 and K2NaMF6 (M=Ni, Cu)". In: *Physical Review B - Condensed Matter and Materials Physics* 63.12 (2001). ISSN: 1550235X. DOI: 10.1103/PhysRevB.63.125123.

[120] Xiaodong Zhang et al. "Magnetic properties of a highly ordered single crystal of the layered perovskite YBaCuFe0.95Mn0.05O5". In: *Journal of Magnetism and Magnetic Materials* 551 (2022). ISSN: 03048853. DOI: 10.1016/j.jmmm.2022.169165.

[121] Y. S. Song et al. "Chemical doping-induced flop of ferroelectric polarization in multiferroic Mn0.9Co0.1WO4". In: *Physical Review B - Condensed Matter and Materials Physics* 82.21 (2010). ISSN: 10980121. DOI: 10.1103/PhysRevB.82.214418.

[122] R. M. Hornreich, Marshall Luban and S. Shtrikman. "Critical behavior at the onset of k–> -space instability on the λ line". In: *Physical Review Letters* 35.25 (1975). ISSN: 00319007. DOI: 10.1103/PhysRevLett.35.1678.

[123] R. M. Hornreich. "The Lifshitz point: Phase diagrams and critical behavior". In: *Journal of Magnetism and Magnetic Materials* 15-18.PART 1 (1980). ISSN: 03048853. DOI: 10.1016/0304-8853(80)91100-2.

[124] Harish Chandr Chauhan et al. "Multiple phases with a tricritical point and a Lifshitz point in the skyrmion host Cu2OSeO3". In: *Physical Review*

B 100.16 (2019). ISSN: 24699969. DOI: 10.1103/PhysRevB.100.165143.

[125] Dibyendu Dey et al. "Nature of spiral state and absence of electric polarisation in Sr-doped YBaCuFeO 5 revealed by first-principle study". In: *Scientific Reports* 8.1 (2018). ISSN: 20452322. DOI: 10.1038/s41598-018-20774-7.

[126] N. Hollmann et al. "Local symmetry and magnetic anisotropy in multiferroic MnWO4 and antiferromagnetic CoWO4 studied by soft x-ray absorption spectroscopy". In: *Physical Review B - Condensed Matter and Materials Physics* 82.18 (2010). ISSN: 10980121. DOI: 10.1103/PhysRevB.82.184429.

[127] T. Burnus et al. "Local electronic structure and magnetic properties of LaMn0.5Co0.5O3 studied by x-ray absorption and magnetic circular dichroism spectroscopy". In: *Physical Review B - Condensed Matter and Materials Physics* 77.12 (2008). ISSN: 10980121. DOI: 10.1103/PhysRevB.77.125124.

[128] Maria Elenice Dos Santos et al. "Cation distribution and magnetic characterization of the multiferroic cobalt manganese Co2MnO4 spinel doped with bismuth". In: *Journal of Magnetism and Magnetic Materials* 329 (2013). ISSN: 03048853. DOI: 10.1016/j.jmmm.2012.09.070.

[129] I. Urcelay-Olabarria et al. "Neutron diffraction, magnetic, and magnetoelectric studies of phase transitions in multiferroic Mn 0.90Co 0.10WO4". In: *Physical Review B - Condensed Matter and Materials Physics* 85.9 (2012). ISSN: 10980121. DOI: 10.1103/PhysRevB.85.094436.

[130] J. Blasco et al. "Magnetoelectric and structural properties of Y2CoMnO6: The role of antisite defects". In: *Physical Review B* 93.21 (2016). ISSN: 24699969. DOI: 10.1103/PhysRevB.93.214401.

[131] Sophie Guillemet-Fritsch et al. "Magnetic Properties of Cobalt and Manganese Oxide Spinel Ceramics". In: *12th INTERNATIONAL CERAMICS CONGRESS PART F*. Vol. 67. 2010. DOI: 10.4028/www.scientific.net/ast.67.143.

[132] J. Herrero-Martín et al. "Direct observation of noncollinear order of Co and Mn moments in multiferroic Mn0.85Co0.15WO4". In: *Physical Review B - Condensed Matter and Materials Physics* 91.22 (2015). ISSN: 1550235X. DOI: 10.1103/PhysRevB.91.220403.

[133] Xiaodong Zhang. "Enhancing the High-temperature Chiral Magnetic State in YBaCuFeO5". In: *TDX (Tesis Doctorals en Xarxa)* (July 2023). URL: http://www.tdx.cat/handle/10803/675623.

[134] Junjiro Kanamori. "Superexchange interaction and symmetry properties of electron orbitals". In: *Journal of Physics and Chemistry of Solids* 10.2-3 (1959). ISSN: 00223697. DOI: 10.1016/0022-3697(59)90061-7.

[135] John B. Goodenough. "An interpretation of the magnetic properties of the perovskite-type mixed crystals La1-xSrxCoO3-λ". In: *Journal of Physics and Chemistry of Solids* 6.2-3 (1958). ISSN: 00223697. DOI: 10.1016/0022-3697(58)90107-0.

[136] P. W. Anderson. "New approach to the theory of superexchange interactions". In: *Physical Review* 115.1 (1959). ISSN: 0031899X. DOI: 10.1103/PhysRev.115.2.

[137] M. Pissas. "Magnetic texturing due to the partial ordering of Fe+3 and Cu+2 in NdBaCuFeO5". In: *Journal of Magnetism and Magnetic Materials* 432 (2017). ISSN: 03048853. DOI: 10.1016/j.jmmm.2017.01.083.

[138] Jinchen Wang et al. "Pressure effects on magnetic ground states in cobalt-doped multiferroic Mn1-xCoxWO4". In: *Physical Review B* 93.15 (2016). ISSN: 24699969. DOI: 10.1103/PhysRevB.93.155164.

[139] Agnès Dewaele, Paul Loubeyre and Mohamed Mezouar. "Equations of state of six metals above 94 GPa". In: *Physical Review B - Condensed Matter and Materials Physics* 70.9 (2004). ISSN: 01631829. DOI: 10.1103/PhysRevB.70.094112.

[140] *CYCLOPS-ILL Web Page*. URL: https://www.ill.eu/users/instruments/instruments-list/cyclops/.

[141] T. Chatterji. "Spherical Neutron Polarimetry". In: *Neutron Scattering from Magnetic Materials*. Elsevier, 2005, p. 215.

[142] Navid Qureshi et al. "Proof of the elusive high-temperature incommensurate phase in CuO by spherical neutron polarimetry". In: *Science Advances* 6.7 (2020). ISSN: 23752548. DOI: 10.1126/sciadv.aay7661.

[143] M. Blume. "Polarization Effects in the Magnetic Elastic Scattering of Slow Neutrons". In: *Physical Review* 130.5 (June 1963), pp. 1670–1676. ISSN: 0031-899X. DOI: 10.1103/PhysRev.130.1670.

[144] S V Maleyev, V G Bar'yakhtar and R A Suris. "The scattering of slow neutrons by complex magnetic structures". In: *Soviet Physics - Solid State* 4.12 (1963).

[145] U. Schwertmann R. M Cornell. *The Iron Oixdes: Structures, Properties, Reactions, Occurences and Uses*. 2003.

[146] Giorgio Carraro et al. "Enhanced hydrogen production by photoreforming of renewable oxygenates through nanostructured Fe2O3 polymorphs". In: *Advanced Functional Materials* 24.3 (2014). ISSN: 1616301X. DOI: 10.1002/adfm.201302043.

[147] Jiří Tuček et al. *ϵ-Fe2O3: An advanced nanomaterial exhibiting giant coercive field, millimeter-wave ferromagnetic resonance, and magnetoelectric coupling*. 2010. DOI: 10.1021/cm101967h.

[148] Shunsuke Sakurai et al. "First observation of phase transformation of all four Fe2O 3 phases ($\gamma \rightarrow \epsilon \rightarrow \beta \rightarrow \alpha$-phase)". In: *Journal of the American Chemical Society* 131.51 (2009). ISSN: 00027863. DOI: 10.1021/ja9046069.

[149] E. Tronc, C. Chanéac and J.P. Jolivet. "Structural and Magnetic Characterization of ϵ-Fe2O3". In: *Journal of Solid State Chemistry* 139.1 (Aug. 1998), pp. 93–104. ISSN: 00224596. DOI: 10.1006/jssc.1998.7817.

[150] Shin-ichi Ohkoshi, Asuka Namai and Shunsuke Sakurai. "The Origin of Ferromagnetism in ϵ-Fe ₂ O ₃ and ϵ-Ga _x Fe _{2 x} O ₃ Nanomagnets". In: *The Journal of Physical Chemistry C* 113.26 (July 2009), pp. 11235–11238. ISSN: 1932-7447. DOI: 10.1021/jp901637y.

[151] J. López-Sánchez et al. "Sol-gel synthesis and micro-raman characterization of -Fe2O3 micro- and nanoparticles". In: *Chemistry of Materials* 28.2 (2016). ISSN: 15205002. DOI: 10.1021/acs.chemmater.5b03566.

[152] Akira Kuriki et al. "Diffuse scattering due to geometrical frustration in Mn3O4". In: *Journal of the Physical Society of Japan* 72.2 (2003). ISSN: 00319015. DOI: 10.1143/JPSJ.72.458.

[153] Yu V. Knyazev et al. "Mössbauer Study of the Magnetic Transition in -Fe2O3 Nanoparticles Using Synchrotron and Radionuclide Sources". In: *JETP Letters* 110.9 (2019). ISSN: 10906487. DOI: 10.1134/S0021364019210082.

[154] K. Xu et al. "Origin of Ferrimagnetism and Ferroelectricity in Room-Temperature Multiferroic Fe2O3". In: *Physical Review Applied* 9.4 (2018). ISSN: 2331-7019.

[155] Kiyosi Motida and SyÔdhei Miyahara. "On the 90° Exchange Interaction Between Cations (Cr3+, Mn2+, Fe3+ and Ni2+) in Oxides". In: *Journal of*

the Physical Society of Japan 28.5 (1970). ISSN: 13474073. DOI: 10.1143/JPSJ.28.1188.

[156] K. Knížek, P. Novák and Z. Jirák. "Exchange interactions in -Fe2O3: GGA + U calculations". In: *Journal of Physics Condensed Matter* 33.15 (2021). ISSN: 1361648X. DOI: 10.1088/1361-648X/abdb13.

[157] Imran Ahamed, Ralph Skomski and Arti Kashyap. "Controlling the magnetocrystalline anisotropy of ϵ-Fe2O3". In: *AIP Advances* 9.3 (2019). ISSN: 21583226. DOI: 10.1063/1.5080144.

[158] Somdutta Mukherjee et al. "Room temperature nanoscale ferroelectricity in magnetoelectric GaFeO 3 epitaxial thin films". In: *Physical Review Letters* 111.8 (2013). ISSN: 00319007. DOI: 10.1103/PhysRevLett.111.087601.

[159] Daniel Stoeffler. "First principles study of the electric polarization and of its switching in the multiferroic GaFeO 3 system". In: *Journal of Physics Condensed Matter* 24.18 (2012). ISSN: 09538984. DOI: 10.1088/0953-8984/24/18/185502.